Deformation, reactions, and phase mixing in upper mantle shear zones

Dissertation

zur Erlangung des Doktorgrades

der Naturwissenschaften

vorgelegt beim Fachbereich

Geowissenschaften/ Geographie (FB 11)

der Johann Wolfgang Goethe-Universität

in Frankfurt am Main

von

Sören Matthias Tholen

aus Aachen

Frankfurt am Main (2023)

(D30)

vom Fachbereich 11 - Geowissenschaften/ Geographie der

Johann Wolfgang Goethe - Universität als Dissertation angenommen.

Dekan: Prof. Dr. Joachim Curtius

Prodekan: Prof. Dr. Jürgen Runge

Gutachter: Prof. Dr. Gernold Zulauf

                   Prof. Dr. Reiner Kleinschrodt

Datum der Disputation:

Abstract

Upper mantle shear zones are complex systems where deformation is commonly closely interacting with metamorphic (solid-solid) and/or melt/fluid-rock reactions. Here, feedback processes between deformation, reactions, grain size reduction and phase mixing result in strain weakening and the localization of deformation. The expression of these interlinked processes is portrayed by the microfabrics of strained peridotites and pyroxenites. The present thesis is focusing on these processes and their impact on the deformation in three upper mantle shear zones situated in the peridotite massifs of Lanzo (Italian Alps), Erro-Tobbio (Italian Alps) and Ronda (Betic Cordillera, Spain). In all three shear zones, the presence of melt led to phase mixing either by interstitial crystallization of pyroxenes from a Si-saturated and partially also highly evolved melt or by melt-rock reactions of pyroxene porphyroclasts with a Si-undersaturated melt. The effect of melt on the localization of strain is twofold and variable. Enhanced deformation by melt-wetted boundaries is assumed for all shear zones. Additionally, phase mixing by crystallization of interstitial pyroxenes or melt-rock reactions reduce or maintain the grain size by the formation of fine grained neoblasts and secondary phase boundary pinning. In this regard, pre- to early syn-kinematic, map-scale percolation of OH-bearing, evolved melts in the NW Ronda peridotite massif and the associated crystallization of interstitial pyroxenes result in the activation of grain size sensitive deformation mechanisms in the entire melt-effected area. In the rocks collected at Erro-Tobbio, syn-kinematic melt-rock reactions of pyroxene porphyroclasts and Si-undersaturated melt led to the formation of ultramylonitic neoblast tails (grain size ~10 µm). Compared to the adjacent coarser-grained olivine-dominated matrix, the activation of diffusion creep led to an increase in the strain rate by an order of magnitude within interconnected ultramylonitic layers. Strain localization and softening in ultramylonitic layers are also documented in the Lanzo samples. Neoblast tails of pyroxene porphyroclasts were likewise identified as their precursor. The phase assemblage of the tails, including ortho- and clinopyroxene, olivine, plagioclase, and spinel (± amphibole), and their geochemical trends suggest, unlike in Erro-Tobbio, a formation by continuous net-transfer reactions enhanced by the spinel lherzolite to plagioclase lherzolite transition.

The new results obtained from the three studied shear zones underscore the importance of reactions for the interlinked processes of grain size reduction, phase mixing, strain localization and strain softening in upper mantle shear zones. Concerning strain localization, the nature of the reaction (solid-solid, melt/fluid-rock) seems to play a

subordinate role compared to its timing. Pre- to early syn-kinematic melt-triggered reactions result in strain localization along map-scale shear zones. Late stage syn-kinematic melt-rock or metamorphic reactions under high stress conditions are capable of localizing the deformation along discrete, sub-centimeter thick ultramylonites.

Keywords:

Upper mantle, shear zone, phase mixing, strain localization, deformation mechanisms, grain size reduction, melt-rock reactions, net-transfer reactions, mylonite, ultramylonite, EBSD, Lanzo peridotite, Erro-Tobbio peridotite, Ronda peridotite.

Kurzfassung

Scherzonen des oberen Erdmantels sind komplexe Systeme, in denen Deformation in enger Wechselwirkung mit metamorphen (fest-fest) und/oder Schmelz/Fluid-Reaktionen steht. Rückkopplungsprozesse zwischen Deformation, Reaktionen, Korngrößenreduktion und Phasenmischung sind entscheidend für die Lokalisierung von Deformation und ihre Aufrechterhaltung. Mikrogefüge deformierter Peridotite und Pyroxenite zeugen von solchen Prozessen. In der vorliegenden Studie werden drei Scherzonen der Peridotitmassive Lanzo (Alpen, Italien), Erro-Tobbio (Alpen, Italien) und Ronda (Betische Kordillere, Spanien) mikrogefügekundlich und geochemisch untersucht, um diese Wechselwirkungs- und Rückkopplungsprozesse zu entschlüsseln. Hinweise auf schmelzinduzierte Phasenmischung sind in allen drei Scherzonen vorhanden. Sie geht entweder auf die Kristallisation von interstitiellen Pyroxenen aus Si-reicher oder hoch entwickelter, OH-reicher Schmelze oder auf Reaktionen von Pyroxen-Porphyroklasten mit Si-armer Schmelze zurück. Der Einfluss der Schmelze auf die Lokalisierung der Deformation wirkt sich in zweifacher Hinsicht aus: (1) Eine gegenüber schmelzfreien Gesteinen verringerte Viskosität durch schmelzbenetzte Korn- und Phasengrenzen ist für alle drei Scherzonen anzunehmen. (2) Des Weiteren bedingt Korngrößenreduktion und die Stabilisierung von feinkörnigen Phasenmischungen durch interstitielle Pyroxene und/oder durch Schmelz-Porphyroklast-Reaktionen eine Aktivierung von korngrößenabhängigen Deformationsmechanismen. In der Ronda Scherzone führte die prä- bis synkinematische Kristallisation von Pyroxenen zur Aktivierung von *DRX-Kriechen* (dynamische Rekristallisation mit dominanter Korngrenzmigration) und d*isGBS* (Versetzungskriechen-gestütztes Korngrenzgleiten) im km-skaligen schmelzbeeinflussten Bereich. In den Erro-Tobbio Proben bedingten synkinematische Schmelzreaktionen von Pyroxen-Porphyroklasten und Si-armer Schmelze die Bildung ultramylonitischer Neoblasten (Korngröße ~10 µm) in Porphyroklast-Druckschatten. In miteinander vernetzten, weniger als 1 cm mächtigen Ultramyloniten erhöht sich die Strainrate durch die Aktivierung von Diffusionskriechen im Vergleich zur angrenzenden olivindominierten Matrix um etwa eine Größenordnung. Eine solche Lokalisierung von Deformation mit begleitender Verformungsentfestigung ist auch in Ultramyloniten der Lanzo-Proben zu beobachten. Der Ursprung liegt wie in den Erro-Tobbio-Gesteinen in den Neoblasten von Pyroxen-Porphyroklast-Druckschatten. Die geochemische Zusammensetzung der Neoblasten deutet hier jedoch auf eine Bildung durch kontinuierlich stattfindende Reaktionen hin. Die Zusammensetzung aus Ortho- und Klinopyroxenen, Olivin, Plagioklas und Spinell (± Amphibol) weist auf den Übergang von Spinell- zu Plagioklas-Lherzolith als Auslöser dieser Reaktionen hin.

Die aus den drei Untersuchungsgebieten gewonnenen Daten und Erkenntnisse belegen die fundamentale Bedeutung von Reaktionen für die Lokalisierung und Entfestigung der Verformung in Scherzonen des oberen Erdmantels durch Korngrößenreduktion und

Phasenmischung. Für die Lokalisierung der Deformation scheint die Art der Reaktion (fest-fest-, Schmelz-, Fluid-Reaktionen) im Vergleich zu ihrem Zeitpunkt eine eher untergeordnete Rolle zu spielen. Prä- bis früh synkinematische, durch Schmelze initiierte Reaktionen führen zur Lokalisierung der Deformation im km-Bereich. Spätere synkinematische durch Schmelze oder Metamorphose getriggerte Reaktionen unter hohen Differentialspannungen lokalisieren die Deformation entlang von Ultramyloniten im Subzentimeterbereich.

Schlüsselwörter:

Oberer Erdmantel, Scherzone, Phasenmischung, Lokalisierung von Deformation, Deformationsmechanismen, Korngrößenreduktion, Mylonit, Ultramylonit, EBSD, Lanzo-Peridotit, Erro-Tobbio-Peridotit, Ronda-Peridotit.

Acknowledgments

Table of contents

List of abbreviations

BLG   =   Bulging recrystallization

BSE   =   Backscattered electron

CPO   =   Crystallographic preferred orientation

DRX creep   =   Dislocation creep with strain-energy driven grain-boundary migration as main recovery mechanism (Platt and Behr, 2011)

disGBS   =   Dislocation creep accommodated grain boundary sliding (Hirth and Kohlstedt, 2003)

EBSD   =   Electron backscatter diffraction

ECD   =   Equivalent circular diameter

EDX   =   Energy dispersive X-ray spectroscopy

EPMA   =   Electron probe microanalysis

γ =   Shear strain

FSE   =   Forescattered electrons

GB   =   Grain boundary

GBA   =   Grain and phase boundary alignments as described in Newman et al. (1999)

GBS   =   Grain boundary sliding

GBM   =   Grain boundary migration recrystallization

GOS   =   Grain orientation spread

GND   =   Geometrically necessary dislocation

HTSZ   =   High-temperature mantle shear zone

IPF   =   Inverse pole figure

L   =   Low (LP = low pressure)

MAD   =   Mean angular deviation

mrd   =   Multiple of random distribution

NW-B   =   Northwestern Boundary of the Ronda Peridotite

ODF   =   Orientation distribution function

PB   =   Phase boundary

PFG   =   Porphyroclastic fine-grained

P	=	Pressure

P = Pressure

Pa = Pascal

SEM = Scanning electron microscope

SGR = Subgrain rotation recrystallization

SHRIMP = Sensitive high -resolution ion microprobe

SPO = Shape preferred orientation

T = Temperature

$T_{Al\text{-}Cr\text{-}in\text{-}Opx}$ = Al-Cr in orthopyroxene geothermometer calibrated by Witt-Eickschen and Seck (1991)

$T_{BKN}/T_{2\text{-}pyx}$ = Two-pyroxene geothermometer calibrated by Brey and Köhler (1990)

$T_{Ca\text{-}Opx}/T_{Ca\text{-}in\text{-}opx}$ = Calcium in orthopyroxene geothermometer calibrated by Brey and Köhler (1990)

T_{1Cpx} = Single-Cpx-geothermometer calibrated by Nimis and Taylor (2000)

T_{Ta98} = Two-pyroxene geothermometer calibrated by Taylor (1998)

List of mineral abbreviations and mineral reference color scale

Amph = Amphibole

Cpx = Clinopyroxene

Ol = Olivine

Opx = Orthopyroxene

Pl = Plagioclase

Prg = Pargasite ← same as amphibole

Spl = Spinel

1   Introduction

1.1   Upper mantle shear zones

Large-scale differential motions on the earth's surface are accommodated by slip along faults between rather stable, rigid crustal blocks (e.g., Vauchez et al., 2012). Following the fault structures towards deeper levels, deformation becomes distributed from discrete planes into wide zones when the brittle-ductile transition is crossed (e.g., Handy et al., 2018). In these deformational zones, known as "shear zones", differential movements between lithospheric domains are accommodated by ductile deformation. In particular cases, these shear zones crosscut the entire lithosphere potentially forming boundaries of lithospheric plates (Regenauer-Lieb & Yuen, 2003). In the upper mantle, evidence of deformation localized in shear zones is present at various spatial scales ranging from kilometers to micrometers (e.g., Drury et al., 1991). Peridotite massifs are the largest upper mantle outcrops at the earth's surface. They are subdivided according to their tectonic background in orogenic (alpine type) and ophiolitic, oceanic-derived massifs. In both types the localization of deformation in shear zones is present (e.g., Dijkstra et al., 2004). Moreover, mantle xenoliths often show relict structures of localized, ductile deformation (e.g., Mercier and Nicolas, 1974). Similar to the apparent size variation of deformed peridotite outcrops – from hand specimen to hundreds of km^2 –the thickness of shear zones also varies strongly from cm- to km-scale (Dijkstra et al., 2004). Beside this variation in thickness, deformation microstructures can vary significantly between different xenoliths and/or massifs but also within a single thin section or area of investigation, within a shear zone respectively (see section 1.2). In the following, a short review of the upper mantle and in particular its shear zones in terms of minerology, lithology, deformational microstructures, and its deformation mechanisms provides an introduction for the subsequent case studies of three upper mantle shear zones.

The lithospheric mantle is dominated by three major phases: Olivine (50-80 %), orthopyroxene (20-30 %), and clinopyroxene (0-20 %). Minor abundant phases with amounts <5 % are garnet, spinel, plagioclase and occasionally amphibole or phlogopite (Vauchez et al., 2012). Most important rock types are peridotite (>40 % Ol) and pyroxenite (<40 % Ol; Fig. 1.1). According to their main pyroxene phase and its abundance, they are subdivided into harzburgite (<5 % Cpx), lherzolite (>5 % Cpx, >5 % Opx) and wehrlite (<5 % Opx) (Fig. 1.1; Streckeisen, 1974). Especially in peridotite massifs the association of peridotites with dunite (>90 % Ol) and/or pyroxenite layers, veins or dikes is common (e.g., Nicolas, 1986).
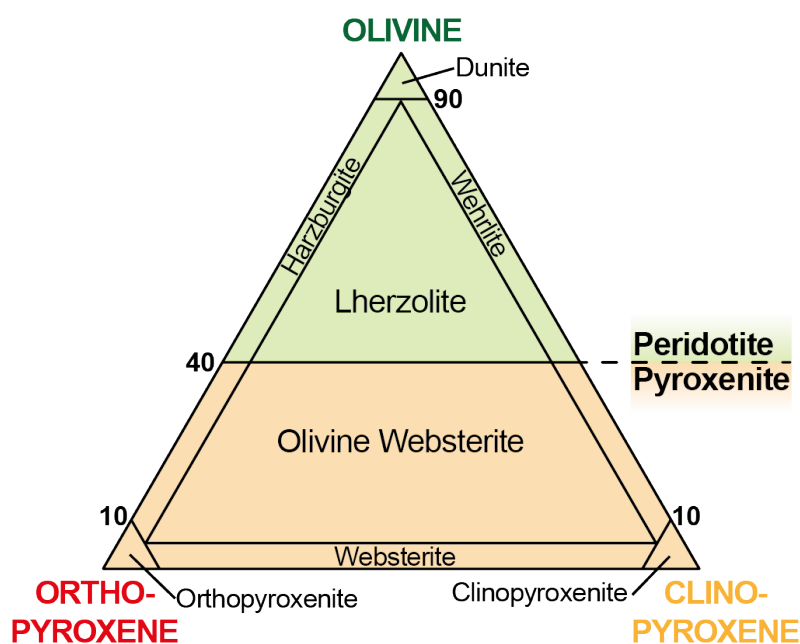
Fig. 1.1. *Classification and nomenclature of ultramafic rocks modified after Streckeisen (1974).*

As the principal composition stays rather constant under most upper mantle conditions, minor phases are often used as indicator for the equilibration depth and for possible metasomatism. Accordingly, peridotites are often classified by the respective prefix of plagioclase, spinel, or garnet (Fig. 1.2). Metasomatism in upper mantle rocks can change the original composition either in a "modal" or "cryptic" way (Dawson, 1984). Modal changes are petrographically visible by replacement structures or by the crystallization of a new secondary phase. In this respect, the presence of pargasitic amphibole indicates H_2O and alkali (Na, K) enrichment either by fluids or by hydrous melts (e.g., Mandler and Grove, 2016). Modal metasomatism due to melts are melt-rock reaction microstructures and the crystallization of interstitial secondary phases (e.g., Rampone et al., 2018). At deeper mantle levels, Si-undersaturated melts cause olivine crystallization and pyroxene dissolution (e.g., Dijkstra et al., 2002). At shallower depth, Si-saturated melts were reported corroding olivine grains and forming pyroxene and plagioclase (e.g., Kaczmarek and Müntener, 2008). Cryptic metasomatism changes only the type and amount of trace and rare earth elements without petrographic evidence (e.g., Kiseeva et al., 2017). Most upper mantle shear zones and sheared peridotites show evidence for reactional changes in their mineralogy by either metasomatism or changing PT conditions (e.g., Dijkstra et al., 2002; Newman et al., 1999). These reactions are thought to play a key role in shear localization and the development of shear zones in the upper mantle (Dijkstra et al., 2004).
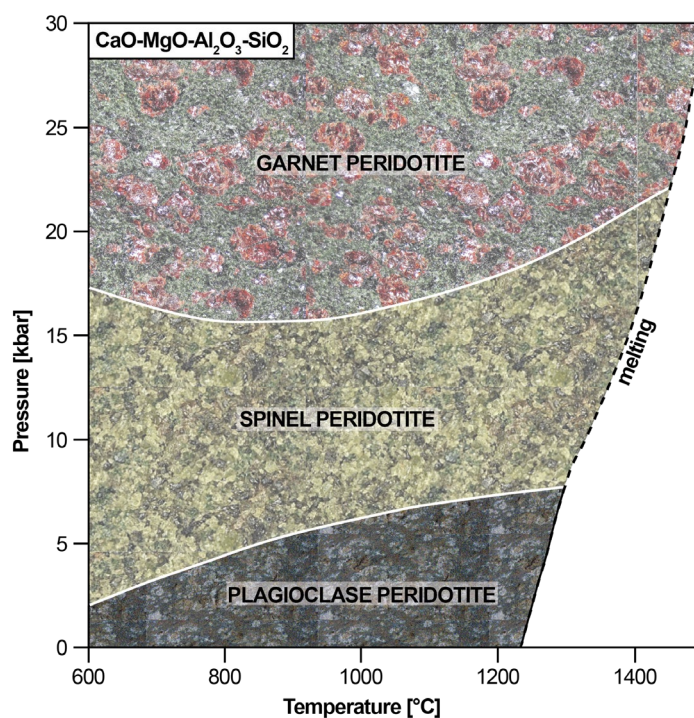
Fig. 1.2. *Stability fields of aluminous phases in peridotites in the CaO-MgO-Al₂O₃-SiO₂ system with exemplary lithology in the background. Modified after Perkins and Anthony (2011).*

1.2   Microstructural classification of deformed mantle rocks

Main strain markers of deformed peridotites are a strong foliation and lineation formed by mineral or mineral aggregate elongation of mostly pyroxenes, spinel, olivine and if present plagioclase. An outstanding marker for both foliation and lineation, are flat, elongated orthopyroxene single crystals with aspect ratios partly exceeding 1:50 (e.g., chapter 2, Fig. 2.4). In highly deformed peridotites, these elongated single crystals, and mono-phase aggregates, as well as assemblages of porphyroclasts with neoblast tails/wings indicate the lineation. The shape of the latter assemblages is commonly described as sigmoidal or delta-shaped (e.g., Newman and Drury, 2010). Additionally, the effect of ductile deformation on pyroxenitic layers or veins is used as indicator for the relative strain intensity. Common deformation structures of pyroxenites are rotated layers parallel to the foliation, folds with axial planes turning parallel to the foliation (intrafolial folds), pinch-and-swell structures and boudins (e.g., Kaczmarek and Müntener, 2008; Précigout et al., 2013).

Classifications of deformed upper-mantle peridotites are mostly based on the grain size and dominant microstructural characteristics. Mercier and Nicolas (1974) distinguished three structural types: The protogranular, the porphyroclastic and the equigranular type. As their classification results from xenolith investigations, it is based on microscale features in the scale of hand specimens and/or thin sections. Geological mapping and microstructural analysis of rocks from various peridotite

massifs led to the classification by Dijkstra et al. (2004). Here, three main types of deformed peridotites in areas of localized deformation are distinguished. Even though the grain size is also the main criteria for classification, the categories of medium to coarse grained tectonite (>4 mm), medium grained tectonite (1-4 mm) and mylonite (1-0.1 mm) are more strongly based on the deformational structures of a bigger area rather than on specific, small-scale microstructures. It must be briefly noted here that by definition mylonites are tectonites (e.g., Turner & Weiss, 1963), which makes the nomenclature of Dijkstra et al. (2004) somewhat misleading. However, for most research on deformed mantle rocks, the applied classification lies between those rather small-scale, microstructural, or larger-scale classifications. Therefore the combination of microstructural and mesoscopic/macroscopic criteria is common (e.g., Czertowicz et al., 2016; Kaczmarek and Tommasi, 2011; Linckens et al., 2011). In general, the differentiation between mylonites and ultramylonites (<50 µm) is commonly accepted. It is, depending on the focus of investigation, flexibly extended by microstructural (porphyroclastic, coarse- or fine-grained) and sequential characteristics (e.g., proto-mylonite). An example of a classification for the increasingly deformed peridotites of the Lanzo shear zone is shown in Figure 2.3 of chapter 2. Due to varying deformation conditions of individual shear zones, ultramylonitic microstructures show variable mean grain sizes ranging between < 15 and 100 µm ECD (equivalent circular diameter). According to the authors of the present research, the distinction between ultramylonitic and mylonitic domains is therefore rather defined by a clear separation of ultramylonitic domains with average grain sizes between < 15-100 µm ECD and coarser grained mylonitic domains (~ 50-200 µm ECD) than by an explicit grain size. The threshold between mylonitic and ultramylonitic grain size is to be determined by microstructural analysis of both domains for a given shear zone. Moreover, in most cases ultramylonitic microstructures form only parts of the overall rock structure. On the sample scale, the classification as ultramylonite therefore mostly refers to rocks consisting of mylonites, which are crosscut by ultramylonitic bands. In this contribution, the occurrence of coherent ultramylonitic bands is accordingly adapted as criteria for an ultramylonite. With the focus on the microscale rather than on macroscale, the classification used in this contribution of ultramylonitic and mylonitic assemblages results straight-forward from the specific analyzed microstructure rather than describing deformed peridotites at a larger scale (m-km).

1.3   Strain localization in the upper mantle: Heterogeneities and strain softening mechanisms

Strain localization in the upper mantle requires on the one hand an initial heterogeneity and/or anisotropy and on the other hand specific deformation mechanisms, which support strain softening. Tommasi and Vauchez (2015) identified several heterogeneity types in the lithospheric mantle as potential "seeds" for strain localization: (1) Large-scale variations in the geothermal gradient as present for hot plumes or the cold lithospheric roots of cratons, (2) major-element and modal heterogeneities as present in the compositional layering of most peridotite massifs, (3) the presence of melt, (4) variations in the hydration state of particularly olivine, (5) grain size heterogeneities and (6) lateral changes of the olivine CPO. Variations in each of these were shown to have a significant effect on the physical properties and in particular on the mechanical strength of the upper mantle (Tommasi & Vauchez, 2015). Additional to these inherent heterogeneities as seeds of strain localization, Regenauer-Lieb et al. (2006) added (7) a numerical-based model of a thermo-mechanical feedback effect from brittle and ductile regions of the lithosphere, which cause strain localization at the brittle-ductile transition and thereby between the lower crust and upper mantle.

Outcrops of deformed peridotites record mostly a complex history of deformation and reactions caused by changing PT conditions and the percolation of melts and/or fluids. Because of the resulting microstructural, mineralogical, and geochemical variations on the small-scale (~m) and the limited extend of massifs or xenoliths, large-scale upper mantle heterogeneities which extend over tens and hundreds of kilometers are difficult to resolve in peridotite massifs and xenoliths. Accordingly, thermal variations and impacts of predominating olivine CPOs are mostly approached by seismic or numerical studies (e.g., Gibert et al., 2003; Knoll et al., 2009; Tommasi et al., 2001, 2009). However, precisely because of their complexity, the study of shear zones from peridotite massifs has the advantage, that at its best, the entire evolution from the depth of the lower lithosphere to the earth's surface is imprinted and accessible in the sheared peridotites. Processes of regional-scale initial weakening and especially the interplay of metasomatism and accompanying melt/fluid-rock reactions, metamorphism, the activity of different deformation mechanisms, phase mixing and grain size evolution under ductile deformation are in the most impressive manner investigable (e.g., Czertowicz et al., 2016; Dijkstra et al., 2002; Kaczmarek and Tommasi, 2011; Linckens et al., 2011).

The localization of strain in the upper mantle depends on both initial heterogeneity and the persistent activity of a weakening/ strain softening mechanisms (Poirier, 1980). Döhmann et al. (2019) modelled the propagation of zones of weakening starting from inclusions tips (= initial heterogeneity) and expanding into shear zones. The width and the localization rate of the developing shear zone were controlled by the amount of rheological weakening. It should be noted that initial heterogeneities could also have an inherent softening effect which may continue or become active again during the evolution of the shear zone. Strain softening mechanisms can be subdivided into four main classes: (1) thermal softening, (2) geometric softening, (3) reaction softening and (4) microstructural softening (e.g., White et al., 1986). Since in peridotite shear zones, reaction and microstructural softening are often interrelated processes, they will be described in one paragraph. The involved deformation mechanisms are revised at the end of this section.

Thermal softening is caused by shear heating, which is based on the conversion of dissipative mechanical work into heat (e.g., Schmalholz and Duretz, 2015). The temperature dependence of the rheology results in a positive feedback of rising temperatures causing softening and thereby enhancing the strain rate (e.g., Kelemen and Hirth, 2007). However, models of thermal softening commonly require a preexisting weakness as for example given by the weaker rheology of fine-grained, mixed mylonites (e.g., Kelemen & Hirth, 2007; Schmalholz & Duretz, 2015).

Geometric softening is indicated by a shape preferred orientation (SPO) or crystallographic/ lattice preferred orientation (CPO). CPOs reflect energetically favorable slip-systems along which dislocations glide and climb commonly referred to as *dislocation creep* (Section 1.4; Passchier & Trouw, 1996). Beside an anisotropy in creep strength, the common alignment in a preferred orientation results in an anisotropy of seismic wave velocities (e.g. Mainprice, 2015). As seismic anisotropy in the upper mantle is rather the rule than the exception, and CPO-producing deformation in the earth's mantle was active for the last 4 G.y., CPO related anisotropy is thought to be of major importance for early shear localization (Tommasi & Vauchez, 2015). However, its importance for the consecutive shear zone evolution with strain localization on various spatial scales is still unclear (e.g., Behr, 1980; Tommasi et al., 2009).

Microstructural softening is often related to grain size reduction and the activity of a grain size-sensitive deformation mechanism (Section 1.4). As shear zones are commonly characterized by either a general small grain size compared to that of the undeformed wall rock or a gradient from coarse grained and undeformed over fine grained, porphyroclastic to even smaller grain sizes in ultramylonites

(e.g., Boudier et al., 1988), grain size reduction, also referred to as "mylonitization" (Cross & Skemer, 2017), is considered to play a key role for strain localization (e.g., Rutter and Brodie, 1988). Apart from dynamic recrystallization and brittle deformation (e.g., Drury et al., 1991; Drury and Urai, 1989), metasomatic and metamorphic reactions are capable of grain size reduction (e.g., Dijkstra et al., 2002; Furusho and Kanagawa, 1999; Newman et al., 1999). Several grain size-sensitive deformation mechanisms were reported:

a. *Diffusion creep* is in general grain size-sensitive due to the dependency of diffusion length and grain size. Depending on the diffusion pathway, it is subdivided into Coble and Nabarro-Herring creep. The former is characterized by diffusion along grain boundaries (Poirier, 1985). In the latter, diffusion occurs throughout the crystal lattice (e.g., Knipe, 1989).

b. *Grain boundary sliding (GBS)* accommodates deformation by the sliding of grains past each other, while the development of voids is prevented by solid state diffusion, crystal-plastic deformation and/or solution and precipitation (Passchier & Trouw, 1996). It can be active in both the dislocation (disGBS) and diffusion creep regime (difGBS) (e.g., Drury et al., 2011; Hansen et al., 2011; Warren and Hirth, 2006). Due to its dependency on the length of diffusion pathways, it is in general grain size sensitive (e.g., Schmid et al., 1977). For the sake of completeness, the activity and importance of GBS in cataclastic shear zones has to be mentioned (e.g., Trouw et al., 2010).

c. Platt and Behr (2011) added an additional grain size-sensitive deformation mechanism by dislocation creep with grain-boundary migration as recovery mechanism (*DRX creep*). Its sensitivity is based on the activity of strain energy driven grain-boundary migration, which Platt and Behr (2011) attest to be no driving force for grain growth under steady state conditions.

1.4   Deformation mechanisms of the upper mantle

Together with deformation experiments on mantle assemblages, microstructural research on deformed peridotites from shear zones of peridotite massifs have led to a profound understanding of the deformation mechanisms operating under upper mantle conditions (e.g., Dijkstra et al., 2004; Hansen et al., 2011; Hirth and Kohlstedt, 2003; Newman and Drury, 2010). In general, high-temperature creep in polycrystalline materials is described by a flow law of the form of equation 1.1. Here, the strain rate ($\dot{\varepsilon}$) depends on the grain size (d) in addition to material-dependent parameters, constants, the differential stress (σ) and

temperature (*T*). Additional to these parameters, it should be noted that the strain rate is also depending on the water content for e.g., olivine under dry (50 ppm H/Si) and water-rich (1000-3000 ppm H/Si) conditions (Fig. 1.3; e.g., Ohuchi et al., 2015), on the presence of melts and fluids along grain boundaries (Hidas et al., 2016; Hirth & Kohlstedt, 1995) and on the presence of a crystallographic preferred orientations (e.g., Knoll et al., 2009). In equation 1.1, the grain size exponent *m* and the stress exponent *n* are decisive for the sensitivity of the strain rate $\dot{\varepsilon}$ to changes in grain size *d* or differential stress σ. Included are more over a material-dependent parameter A, the activation enthalpy Q, the gas constant R and the temperature T.

$$\dot{\varepsilon} = Ad^{-m}\,\sigma^n \exp\left(Q/(R*T)\right) (1.1)$$

As olivine is the most abundant phase of the upper mantle, its flow laws are generally used to predict the rheology of the upper mantle. *Dislocation creep* in olivine is assumed to be active with stress exponents between 3.5 and 7 but with a grain size exponent of $0 < p \le 1$. Thus, the rheology of the upper mantle in the dislocation creep field is strongly stress dependent but relatively insensitive to the grain size (e.g., Faul et al., 2011). With a stress exponent *n* of 2-3.5 and a grain size exponent *p* of 1-2, *dislocation creep accommodated grain boundary sliding* (*DisGBS*) in polycrystalline olivine aggregates was calculated to be grain size- and stress-sensitive (e.g. Hansen et al., 2011a; Hirth and Kohlstedt, 2003). Similar values ($n \approx 4$, $p = 1.33$) were obtained by Platt and Behr (2011) for *DRXcreep*. With stress exponents (*n*) between 1.4 - 3.5 and grain size exponents (*p*) between 2-3, *diffusion creep* in olivine aggregates is sensitive to stress but especially to the grain size (e.g., Faul and Jackson, 2007; Hirth and Kohlstedt, 1995).The individual deformation mechanisms (dislocation creep, diffusion creep, GBS, DisGBS and DRXcreep) are not mutually exclusive and do not necessarily operate independently from each other (Warren & Hirth, 2006). Accordingly, the total strain rate $\dot{\varepsilon}_{total}$ can be formulated as the sum of the individual strain rates accommodated by different deformation mechanisms, here, diffusion creep ($\dot{\varepsilon}_{dif}$), dislocation creep ($\dot{\varepsilon}_{dis}$) and grain boundary sliding ($\dot{\varepsilon}_{GBS}$) (Eqn. 1.2; Précigout et al., 2007). The proportions of the individual mechanisms change due to changes in deformation conditions (Eqn.1.1).

$$\dot{\varepsilon}_{total} = \dot{\varepsilon}_{dif} + \dot{\varepsilon}_{dis} + \dot{\varepsilon}_{GBS} (1.2)$$

For a particular rheological regime, the parameters of a flow law are mostly determined empirically (e.g., Hansen et al., 2011). To identify the dominant deformation mechanism, these values are compared with theoretical values of the different deformation mechanisms. Deformation mechanism maps define areas/

conditions where a particular deformation mechanism is dominant (Fig. 1.3). Due to the inverse relationship between recrystallized grain size of a monomineralic assemblage and differential stress during high-T creep, grain sizes can be used to constrain the paleo differential stress (e.g., Twiss, 1977). Piezometric lines indicating theoretical grain sizes at given differential stresses are commonly added to deformation mechanism maps (Fig. 1.3).
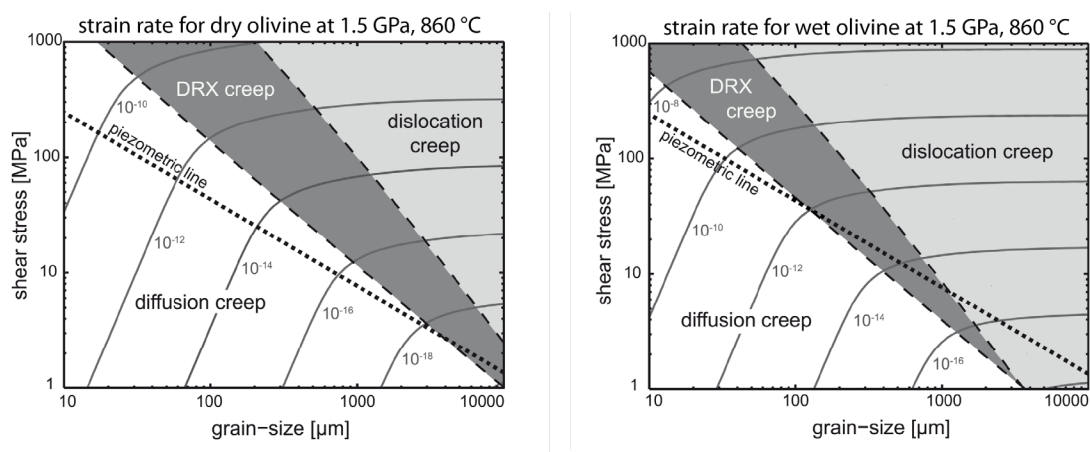
Fig. 1.3. *Olivine deformation mechanism maps at 860 °C and 1.5 GPa lithostatic pressure for dry (left) and wet (376 ppm H/Si) olivine (right). Black dotted line = piezometric line of Van Der Wal and Vissers (1993). Dark grey lines= Lines of constant strain rates (in s⁻¹). DRX creep = Dislocation creep with strain-energy driven grain-boundary migration as main recovery mechanism (Platt and Behr, 2011). Modified after Johanesen and Platt (2015).*

1.5   Mechanisms of phase mixing and its impact on deformation

Microstructural weakening often results from a switch in the dominant deformation mechanism, respectively from dislocation creep via grain boundary sliding to diffusion creep. If the deformational parameters (differential stress, strain rate, temperature, and hydration conditions etc.) are nearly constant, the grain size is the decisive parameter for controlling the dominant deformation mechanism (Fig. 1.3/ Eqn. 1.1). However, fast kinetics in olivine suggest a rapid grain growth and a stabilization of grain size in the dislocation creep or GBS creep field of monomineralic assemblages (De Bresser et al., 2001; Karato, 1989). Equation 1.3 shows the piezometric relationship of single-phase assemblages where the steady state grain size d_{SS} depends on the steady-state stress σ_{SS} in addition to the material-dependent parameters A_1 and q (e.g., Hirth and Kohlstedt, 2015). Following equation 1.3, under high T, upper mantle conditions grains would therefore coarsen after deformation ceases to reduce their interfacial free

energy and thereby counteract long-term strain localization and the reactivation of deformational pathways (e.g., Linckens et al., 2015).

$$d_{SS} = A_1/\sigma_{SS}{}^q \quad (1.3)$$

In contrast to this prediction, ultramylonites with grain sizes indicative for diffusion creep are present in internal parts of many upper mantle shear zones (e.g., Dijkstra et al., 2002; Kaczmarek and Tommasi, 2011; Newman et al., 1999). Here and in most mylonitic peridotites, the assemblage is polymineralic and well mixed. Beside these naturally deformed peridotites, deformation experiments of peridotites (e.g., Cross and Skemer, 2017; Farla et al., 2013; Gilgannon et al., 2020; Linckens et al., 2014; Tasaka et al., 2017) and deformation modelling (e.g., Bercovici and Skemer, 2017) corroborate a significant impact of secondary minerals on the grain size and thus on the rheology. Mixed phases can inhibit grain growth by dragging and pinning of migrating boundaries (= Zener pinning) at temperatures relevant for grain boundary migration (e.g., Herwegh et al., 2011). Thereby, the resulting grain sizes of the primary (d_I) and secondary phase (d_{II}) as well as the maximum primary/ matrix grain size (D_{max}) differ from the flow stress dependent piezometric grain size of single-phase assemblages (Eqn. 1.3) by depending on the volume fraction of the secondary phase (f_{II}) (Eqn. 1.4/1.5) (e.g., Tasaka et al., 2017). For equation 1.4 and 1.5 β and Z are the Zener parameters predicted by Zener in Smith (1948). Beside the fraction, also the spatial distribution of secondary phases has been shown to have a major impact on the grain size evolution (e.g., Herwegh et al., 2011).

$$d_I/d_{II} = \beta/(f_{II})^Z \quad (1.4)$$

and

$$D_{max} = c * d_{II}/f_{II} \quad (1.5)$$

From this, a key role of phase mixing in the localization of strain and its maintenance can be deduced. Several processes have been discussed in the literature, which form phase mixtures in ductile shear zones:

a. *Neighbor switching by grain boundary sliding (GBS/ "Granular flow" in Boullier and Gueguen (1975)) in the dislocation and diffusion creep regime (e.g., Hirth and Kohlstedt, 2003; Précigout et al., 2007; Drury et al., 2011, Farla et al., 2013).* In this process, which is particularly active in fine-grained aggregates, the grains slide past each other accommodating thereby the deformation. Mixing by neighbor switching during GBS is accordingly a mechanical process. Contrary to mixing, deformation experiments by Hiraga et al. (2013) indicate phase aggregation during

GBS. Additionally, Linckens et al. (2014) have shown that phase mixing by the combined process of dynamic recrystallization and GBS requires high amounts of strain. Therefore, these authors remarked that this process does not provide an adequate mechanism for strain localization.

b. *Creep cavitation and subsequent nucleation during GBS* (e.g., Précigout and Stünitz, 2016). In experiments on olivine and diopside composites, Précigout and Stünitz (2016) postulated that phase mixing is achieved when dislocation creep or diffusional mass transport cannot accommodate GBS. At this point, neoblasts precipitate from an aqueous fluid at grain boundaries and instantly fill interstitial grain space forming a mixed assemblage. Further evidence for this process might be found in the work of Platt (2015), where dynamically recrystallized orthopyroxene porphyroclasts form neoblast tails with phase mixing present at their margins. Here, olivine neoblasts were interpreted to crystallize interstitially between the sliding (GBS) grains of the dynamically recrystallized tails.

c. *Geometric phase mixing.* Cross and Skemer (2017) reported the formation of phase mixtures in calcite-anhydrite composites by an entirely mechanical process without cavity formation, diffusion, or reaction. In their torsion experiments, calcite and anhydrite domains were stretched and thinned to 'monolayers' of one or two grain's width at moderate shear strains ($\gamma \geq 6$). Increasing the shear strain ($17 < \gamma < 57$), these layers disaggregated and thereby mixed. Again, it is noted that rheological weakening by the formation of such monolayers would require large strains ($\gamma \leq 100$) in natural settings. Extrapolating these results to the upper mantle, Cross and Skemer (2017) suggests that ultramylonites are rather a consequence and not the cause of shear localization.

d. *Reaction-induced phase mixing.* By the formation of neoblasts, reactions can change the phase assemblage and lead to phase mixing and grain size reduction. In upper mantle shear zones, a variety of reactions were reported, which can be subdivided into the groups of (1) solid-solid or metamorphic, (2) melt-rock, (3) and fluid-rock reactions. (1) Decreasing PT conditions lead to the garnet peridotite–spinel peridotite, and at shallower depth, to the spinel peridotite–plagioclase peridotite transitions (Fig. 1.2, e.g., Furusho and Kanagawa, 1999, Dijkstra et al., 2004). Beside the formation of a new phase (spinel, plagioclase), continuous net-transfer reactions produce additionally neoblasts of the same phase but with a composition adapted to the present PT conditions (e.g., Newman et al., 1999). Additionally, PT-controlled exsolutions in pyroxenes are forming

intracrystalline phase mixtures, which potentially become inter-crystalline during dynamic recrystallization. (2) Melt-rock reactions are based on the disequilibrium between a percolating melt and the host rock, which causes the precipitation of neoblasts and the dissolution of existing grains. The composition of the melt, which in turn changes due to its ascent, controls which phases are dissolved and which are precipitated (e.g., Rampone et al., 2018). Si-undersaturated melts cause olivine crystallization and pyroxene dissolution at deeper mantle depth, and therefore were reported for the early evolution in shear zones (e.g., Dijkstra et al., 2002; Kaczmarek and Müntener, 2008). Si-saturated melts form pyroxene and plagioclase and corrode olivine grains at shallower depth (e.g., Kaczmarek and Müntener, 2008). Additionally, Dijkstra et al. (2002) have shown that, at the microscale, melt-rock reactions and the melt composition are highly dependent on variations of pressure and phase assemblage. (3) Fluid-rock reactions in peridotites cause phase mixing either by precipitation of new phases or dissolution and precipitation of available phases. New phases reportedly formed by crystallization from fluids in mantle rocks are amphibole, chlorite and serpentine (e.g., Hoogerduijn Strating et al., 1993; Précigout et al., 2017; Prigent et al., 2020). In orthopyroxene reaction tails, Kohli and Warren (2020) additionally reported the mixing of tremolite and olivine by hydration reactions at 650-850 °C. Similar to Dijkstra et al. (2002) but here regarding the local fluid rather than the local melt composition, Hidas et al. (2016) suggested that the composition of the fluid is locally controlled by the surrounding minerals. Due to its variations, alternating dissolution and precipitation of olivine and orthopyroxene in the presence of the fluid effectively mixes both phases.

1.6   Research objective

Although the interplay of grain size reduction and phase mixing has been shown to be crucial for strain localization and its maintenance in the upper mantle, a detailed microstructural study that captures and compares phase mixing in multiple shear zones and thereby evaluates its origin and impact on strain localization was so far missing. On the one hand, this can be explained by the wealth of (micro)structural, geochemical, and rheological processes, which naturally deformed peridotites undergo. On the other hand, such a project must be based on existing research, which provides the structural, lithological and large-scale deformational framework and enables to put the microstructural results in the context of the shear zone evolution. Additionally, the required fieldwork

and high resolution geochemical and microstructural analyses are very time consuming.

This microstructural study of samples from the shear zones of the Lanzo ultramafic body (Piemonte Alps, NW Italy), the Erro-Tobbio peridotite (Voltri massif, Ligurian Alps, NW Italy) and the Ronda ultramafic massif (Bethic Cordillera, southern Spain) meets the above-mentioned requirements. All three peridotite massifs were studied and mapped in detail (e.g., Müntener et al., 2005; Obata, 1980; Piccardo and Vissers, 2007). Thereby, the geodynamic framework, the PT conditions and the location and thickness of the targeted shear zones are largely known. Additionally, strain localization, grain size reduction and phase mixing were attested by previous studies (e.g., Kaczmarek and Müntener, 2008; Padovano et al., 2014; Précigout et al., 2007). For each shear zone, a different dominant mixing process has been postulated: For the Lanzo peridotite, the formation of mixed ultramylonites was attributed to melt-rock reactions (Kaczmarek & Müntener, 2008). Phase mixing by metamorphic reactions was suggested in Erro-Tobbio' s ultramylonitic set of shear zones (Hoogerduijn Strating et al., 1993). For the Ronda peridotite, Précigout et al. (2007) proposed grain boundary sliding and neighbor switching as major mixing process. Despite these clearly assigned mixing processes, no detailed analysis of the origin and processes of phase mixing and the formation of the (ultra)mylonites has yet been performed at any of these shear zones. Thereby, the evaluation of other phase mixing processes was mostly neglected, and the importance of phase mixing on the deformation and evolution of the shear zones was generalized and not examined in detail. The standardized microstructural and geochemical analysis carried out in this study on samples taken over the strain gradient of every of the three shear zones enables to identify and evaluate the origin and impact of phase mixing on deformation and strain localization under different conditions. The comparability of the data and their integration in the existing research allows to identify primary phase mixing processes and to decipher their varying impact during the shear zone evolution. Without giving too much away, this work succeeds in identifying a common source of phase mixing that has major implications for the deformation of earth's upper mantle: Reactions.

1.7 Structure of the thesis

This thesis is divided into three main chapters enclosed by the introduction and a conclusion with a brief scientific outlook. The three main chapters consist of the three peer-reviewed publications, each dedicated to one of the project's research areas.

The first publication by Sören Tholen, Jolien Linckens, Catharina Heckel and Marina Kemperle is entitled "Reaction-induced phase mixing and the formation of ultramylonitic bands". It focuses on the Lanzo shear zone (Italy) and was accepted by Tectonophysics (volume 827, Elsevier) for publication as part of the special issue "Deformation processes in the ductile crust and mantle, seismic anisotropy, ocean ridge dynamics: A special issue in honor of Adolphe Nicolas" in January 2022.

The second publication by Jolien Linckens and Sören Tholen is entitled "Formation of ultramylonites in an upper mantle shear zone, Erro-Tobbio, Italy". It was published in the journal Minerals (MDPI) in the special issue of „Mantle Strain Localization – How Minerals Deform at Deep Plate Interfaces" in September 2021 (volume 2021/11, article number 1036).

The third chapter consists of the publication on the shear zone of the NW Ronda peridotite complex, Spain. The manuscript entitled "Melt-enhanced strain localization and phase mixing in a large-scale mantle shear zone (Ronda peridotite, Spain)" by Sören Tholen, Jolien Linckens and Gernold Zulauf has been published by the Journal Solid Earth (European Geosciences Union – EGU) in October 2023.

The order of the chapters corresponds to the order of investigation and not to the date of publication. References of each chapter are given directly at its end. A figure and table list, as well as the complete appendix are attached at the end of the thesis. Beside additional data and figures, the appendix contains all publications in the original format of the respective journal. Additionally, the thesis is accompanied by a CD that contains the supplementary data and the publications. As the printed version limits the quality of the figures, especially the microstructural ones, all figures are attached as high-resolution versions on the CD. The reader is kindly referred to these if the resolution in the printed version is too low or the image size is too small.

1.8   References Introduction

Behr, H. J. (1980). Polyphase shear zones in the granulite belts along the margins of the Bohemian Massif. *Journal of Structural Geology*, *2*(1–2), 249–254. https://doi.org/10.1016/0191-8141(80)90057-7

Bercovici, D., & Skemer, P. (2017). Grain damage, phase mixing and plate-boundary formation. *Journal of Geodynamics*, *108*, 40–55. https://doi.org/10.1016/j.jog.2017.05.002

Boudier, F., Ceuleneer, G., & Nicolas, A. (1988). Shear zones, thrusts and related magmatism in the Oman ophiolite: Initiation of thrusting on an oceanic ridge. *Tectonophysics*, *151*(1–4), 275–296. https://doi.org/10.1016/0040-1951(88)90249-1

Boullier, A. M., & Gueguen, Y. (1975). SP-Mylonites: Origin of some mylonites by superplastic flow. *Contributions to Mineralogy and Petrology*, *50*(2), 93–104. https://doi.org/10.1007/BF00373329

De Bresser, J. H. P., Ter Heege, J. H., & Spiers, C. J. (2001). Grain size reduction by dynamic recrystallization: Can it result in major rheological weakening? *International Journal of Earth Sciences*, *90*(1), 28–45. https://doi.org/10.1007/s005310000149

Cross, A. J., & Skemer, P. (2017). Ultramylonite generation via phase mixing in high-strain experiments. *Journal of Geophysical Research: Solid Earth*, *122*(3), 1744–1759. https://doi.org/10.1002/2016JB013801

Czertowicz, T. A., Toy, V. G., & Scott, J. M. (2016). Recrystallisation , phase mixing and strain localisation in peridotite during rapid extrusion of sub-arc mantle lithosphere. *Journal of Structural Geology*, *88*, 1–19. https://doi.org/10.1016/j.jsg.2016.04.011

Dawson, J. B. (1984). Contrasting types of upper-mantle metasomatism? *Developments in Petrology*, *11*(2), 289–294. https://doi.org/https://doi.org/10.1016/B978-0-444-42274-3.50030-5.

Dijkstra, A. H., Drury, M. R., Vissers, R. L. M., & Newman, J. (2002). On the role of melt-rock reaction in mantle shear zone formation in the Othris Peridotite Massif (Greece). *Journal of Structural Geology*, *24*(9), 1431–1450. https://doi.org/10.1016/S0191-8141(01)00142-0

Dijkstra, A. H., Drury, M. R., Vissers, R. L. M., Newman, J., & Van Roermund, H. L. M. (2004). Shear zones in the upper mantle: Evidence from alpine- and ophiolite-type peridotite massifs. *Geological Society Special Publication*, *224*, 11–24. https://doi.org/10.1144/GSL.SP.2004.224.01.02

Döhmann, M. J. E. A., Brune, S., Nardini, L., Rybacki, E., & Dresen, G. (2019). Strain Localization and Weakening Processes in Viscously Deforming Rocks: Numerical Modeling Based on Laboratory Torsion Experiments. *Journal of Geophysical Research: Solid Earth*, *124*(1), 1120–1137. https://doi.org/10.1029/2018JB016917

Drury, M. R., & Urai, J. L. (1989). Deformation-related recrystallization processes. *Tectonophysics, 172*, 235–253. https://doi.org/https://doi.org/10.1016/0040-1951(90)90033-5

Drury, M. R., Vissers, R. L. M., Van der Wal, D., & Hoogerduijn Strating, E. H. (1991). Shear localisation in upper mantle peridotites. *Pure and Applied Geophysics PAGEOPH*, *137*(4), 439–460. https://doi.org/10.1007/BF00879044

Drury, M. R., Avé Lallemant, H. G., Pennock, G. M., & Palasse, L. N. (2011). Crystal preferred orientation in peridotite ultramylonites deformed by grain size sensitive creep, étang de Lers, Pyrenees, France. *Journal of Structural Geology*, *33*(12), 1776–1789. https://doi.org/10.1016/j.jsg.2011.10.002

Farla, R. J. M., Karato, S., & Cai, Z. (2013). Role of orthopyroxene in rheological weakening of the lithosphere via dynamic recrystallization. *Proceedings of the National Academy of Sciences of the United States of America*, *110*(41), 16355–16360. https://doi.org/10.1073/pnas.1218335110

Faul, U. H., & Jackson, I. (2007). Diffusion creep of dry, melt-free olivine. *Journal of Geophysical Research: Solid Earth*, *112*(4), 1–14. https://doi.org/10.1029/2006JB004586

Faul, U. H., Fitz Gerald, J. D., Farla, R. J. M., Ahlefeldt, R., & Jackson, I. (2011). Dislocation creep of fine-grained olivine. *Journal of Geophysical Research: Solid Earth*, *116*(1), 1–12. https://doi.org/10.1029/2009JB007174

Furusho, M., & Kanagawa, K. (1999). Transformation-induced strain localization in a lherzolite mylonite from the Hidaka metamorphic belt of central Hokkaido, Japan. *Tectonophysics*, *313*(4), 411–432. https://doi.org/10.1016/S0040-1951(99)00215-2

Gibert, B., Seipold, U., Tommasi, A., & Mainprice, D. (2003). Thermal diffusivity of upper mantle rocks: Influence of temperature, pressure, and the deformation fabric. *Journal of Geophysical Research*, *108*(B8). https://doi.org/10.1029/2002jb002108

Gilgannon, J., Poulet, T., Berger, A., Barnhoorn, A., & Herwegh, M. (2020). Dynamic Recrystallization Can Produce Porosity in Shear Zones. *Geophysical Research Letters*, *47*(7), 1–10. https://doi.org/10.1029/2019GL086172

Handy, M. R., Burgmann, R., Fault, I., & Before, S. (2007). Continental Fault Structure and Rheology from the Frictional-to-Viscous Transition Downward. *Tectonic Faults*, 139–181. https://doi.org/10.7551/mitpress/6703.003.0008

Hansen, L. N., Zimmerman, M. E., & Kohlstedt, D. L. (2011). Grain boundary sliding in San Carlos olivine: Flow law parameters and crystallographic-preferred orientation. *Journal of Geophysical Research: Solid Earth*, *116*(8), 1–16. https://doi.org/10.1029/2011JB008220

Herwegh, M., Linckens, J., Ebert, A., Berger, A., & Brodhag, S. H. (2011). The role of second phases for controlling microstructural evolution in polymineralic rocks: A review. *Journal of Structural Geology*, *33*(12), 1728–1750. https://doi.org/10.1016/j.jsg.2011.08.011

Hidas, K., Tommasi, A., Garrido, C. J., Padrón-Navarta, J. A., Mainprice, D., Vauchez, A., et al. (2016). Fluid-assisted strain localization in the shallow subcontinental lithospheric mantle. *Lithos*, *262*, 636–650. https://doi.org/10.1016/j.lithos.2016.07.038

Hiraga, T., Miyazaki, T., Yoshida, H., & Zimmerman, M. E. (2013). Comparison of microstructures in superplastically deformed synthetic materials and natural mylonites: Mineral aggregation via grain boundary sliding. *Geology*, *41*(9), 959–962. https://doi.org/10.1130/G34407.1

Hirth, G., & Kohlstedt, D. (2003). Rheology of the upper mantle and the mantle wedge: A view from the experimentalists. *Geophysical Monograph Series*, *138*, 83–105. https://doi.org/10.1029/138GM06

Hirth, G., & Kohlstedt, D. L. (1995). Experimental constraints on the dynamics of the partially molten upper mantle: deformation in the diffusion creep regime. *Journal of Geophysical Research*, *100*(B2), 1981–2001. https://doi.org/10.1029/94JB02128

Hoogerduijn Strating, E. H., Rampone, E., Piccardo, G. B., Drury, M. R., & Vissers, R. L. M. (1993). Subsolidus emplacement of mantle peridotites during incipient oceanic rifting and opening of the mesozoic tethys (voltri massif, NW Italy). *Journal of Petrology*, *34*(5), 901–927. https://doi.org/10.1093/petrology/34.5.901

Johanesen, K. E., & Platt, J. P. (2015). Rheology, microstructure, and fabric in a large scale mantle shear zone, Ronda Peridotite, southern Spain. *Journal of Structural Geology*, *73*, 1–17. https://doi.org/10.1016/j.jsg.2015.01.007

Kaczmarek, M. A., & Müntener, O. (2008). Juxtaposition of melt impregnation and high-temperature shear zones in the upper mantle; field and petrological constraints from the lanzo peridotite (Northern Italy). *Journal of Petrology*, *49*(12), 2187–2220. https://doi.org/10.1093/petrology/egn065

Kaczmarek, M. A., & Tommasi, A. (2011). Anatomy of an extensional shear zone in the mantle, Lanzo massif, Italy. *Geochemistry, Geophysics, Geosystems*, *12*(8). https://doi.org/10.1029/2011GC003627

Karato, S. (1989). Grain growth kinetics in olivine aggregates. *Tectonophysics*, *168*(4), 255–273. https://doi.org/10.1016/0040-1951(89)90221-7

Kelemen, P. B., & Hirth, G. (2007). A periodic shear-heating mechanism for intermediate-depth earthquakes in the mantle. *Nature*, *446*(7137), 787–790. https://doi.org/10.1038/nature05717

Kiseeva, E. S., Kamenetsky, V. S., Yaxley, G. M., & Shee, S. R. (2017). Mantle melting versus mantle metasomatism – "The chicken or the egg" dilemma. *Chemical Geology*, *455*, 120–130. https://doi.org/10.1016/j.chemgeo.2016.10.026

Knipe, R. J. (1989). Deformation mechanisms - recognition from natural tectonites. *Journal of Structural Geology*, *11*(1–2), 127–146. https://doi.org/10.1016/0191-8141(89)90039-4

Knoll, M., Tommasi, A., Logé, R. E., & Signorelli, J. W. (2009). A multiscale approach to model the anisotropic deformation of lithospheric plates. *Geochemistry, Geophysics, Geosystems*, *10*(8), 1–18. https://doi.org/10.1029/2009GC002423

Kohli, A. H., & Warren, J. M. (2020). Evidence for a Deep Hydrologic Cycle on Oceanic Transform Faults. *Journal of Geophysical Research: Solid Earth*, *125*(2), 1–23. https://doi.org/10.1029/2019JB017751

Linckens, J., Herwegh, M., Mntener, O., & Mercolli, I. (2011). Evolution of a polymineralic mantle shear zone and the role of second phases in the localization of deformation. *Journal of Geophysical Research: Solid Earth*, *116*(6), 1–21. https://doi.org/10.1029/2010JB008119

Linckens, J., Bruijn, R. H. C., & Skemer, P. (2014). Dynamic recrystallization and phase mixing in experimentally deformed peridotite. *Earth and Planetary Science Letters*, *388*, 134–142. https://doi.org/10.1016/j.epsl.2013.11.037

Linckens, J., Herwegh, M., & Müntener, O. (2015). Small quantity but large effect - How minor phases control strain localization in upper mantle shear zones. *Tectonophysics*, *643*, 26–43. https://doi.org/10.1016/j.tecto.2014.12.008

Mainprice, D. (2015). *Seismic Anisotropy of the Deep Earth from a Mineral and Rock Physics Perspective. Treatise on Geophysics* (Vol. 2). Elsevier B.V. https://doi.org/10.1016/B978-0-444-53802-4.00044-0

Mandler, B. E., & Grove, T. L. (2016). Controls on the stability and composition of amphibole in the Earth's mantle. *Contributions to Mineralogy and Petrology*, *171*(8–9), 1–20. https://doi.org/10.1007/s00410-016-1281-5

Mercier, J. C., & Nicolas, A. (1974). Textures and Fabrics of Upper-Mantle Peridotites as Illustrated by Xenoliths from Basalts. *Journal of Petrology*, *16*(2), 454–487. https://doi.org/https://doi.org/10.1029/RG024i004p00875

Müntener, O., Piccardo, G. B., Polino, R., & Zanetti, A. (2005). Revisiting the Lanzo peridotite (NW-Italy) : "Asthenospherization" of ancient mantle lithosphere. *Ofioliti*, *30*(2), 111–124. https://doi.org/10.4454/ofioliti.v30i2.245

Newman, J., & Drury, M. R. (2010). Control of shear zone location and thickness by initial grain size variations in upper mantle peridotites. *Journal of Structural Geology*, *32*(6), 832–842. https://doi.org/10.1016/j.jsg.2010.06.001

Newman, J., Lamb, W. M., Drury, M. R., & Vissers, R. L. M. (1999). Deformation processes in a peridotite shear zone: Reaction-softening by an H2O-deficient, continuous net transfer reaction. *Tectonophysics*, *303*(1–4), 193–222. https://doi.org/10.1016/S0040-1951(98)00259-5

Nicolas, A. (1986). Structure and petrology of Peridotites: Clues to their geodynamic environment. *Reviews of Geophysics*, *24*(4), 875–895. https://doi.org/10.1029/RG024i004p00875

Obata, M. (1980). The ronda peridotite: Garnet-, spinel-, and plagioclase-lherzolite facies and the P-T trajectories of a high-temprature mantle intrusion. *Journal of Petrology*, *21*(3), 533–572. https://doi.org/10.1093/petrology/21.3.533

Ohuchi, T., Kawazoe, T., Higo, Y., Funakoshi, K. I., Suzuki, A., Kikegawa, T., & Irifune, T. (2015). Dislocation-accommodated grain boundary sliding as the major deformation mechanism of olivine in the Earth's upper mantle. *Science Advances*, *1*(9), 1–11. https://doi.org/10.1126/sciadv.1500360

Padovano, M., Piccardo, G. B., & Vissers, R. L. M. (2015). Tectonic and magmatic evolution of the mantle lithosphere during the rifting stages of a fossil slow-ultraslow spreading basin: Insights from the Erro-Tobbio peridotite (Voltri Massif, NW Italy). In *Geological Society Special Publication* (Vol. 413, pp. 205–238). https://doi.org/10.1144/SP413.7

Passchier, C. W., & Trouw, R. A. J. (1996). *Microtectonics*. Berlin, Heidelberg: Springer. https://doi.org/10.1007/3-540-29359-0

Perkins, D., & Anthony, E. Y. (2011). The evolution of spinel lherzolite xenoliths and the nature of the mantle at Kilbourne Hole, New Mexico. *Contributions to Mineralogy and Petrology*, *162*(6), 1139–1157. https://doi.org/10.1007/s00410-011-0644-1

Piccardo, G. B., & Vissers, R. L. M. (2007). The pre-oceanic evolution of the Erro-Tobbio peridotite (Voltri Massif, Ligurian Alps, Italy). *Journal of Geodynamics*, *43*(4–5), 417–449. https://doi.org/10.1016/j.jog.2006.11.001

Platt, J. P. (2015). Rheology of two-phase systems: A microphysical and observational approach. *Journal of Structural Geology*, *77*, 213–227. https://doi.org/10.1016/j.jsg.2015.05.003

Platt, J. P., & Behr, W. M. (2011). Grainsize evolution in ductile shear zones: Implications for strain localization and the strength of the lithosphere. *Journal of Structural Geology*, *33*(4), 537–550. https://doi.org/10.1016/j.jsg.2011.01.018

Poirier, J.-P. (1980). Shear localization and shear instability in materials in the ductile field. *Journal of Structural Geology*, *2*(1–2), 135–142. https://doi.org/10.1016/0191-8141(80)90043-7

Poirier, J.-P. (1985). *Creep of Crystals*. Cambridge University Press. https://doi.org/10.1017/CBO9780511564451

Précigout, J., & Stünitz, H. (2016). Evidence of phase nucleation during olivine diffusion creep: A new perspective for mantle strain localisation. *Earth and Planetary Science Letters*, *455*, 94–105. https://doi.org/10.1016/j.epsl.2016.09.029

Précigout, J., Gueydan, F., Gapais, D., Garrido, C. J., & Essaifi, A. (2007). Strain localisation in the subcontinental mantle - a ductile alternative to the brittle mantle. *Tectonophysics*, *445*(3–4), 318–336. https://doi.org/10.1016/j.tecto.2007.09.002

Précigout, J., Gueydan, F., Garrido, C. J., Cogné, N., & Booth-Rea, G. (2013). Deformation and exhumation of the Ronda peridotite (Spain). *Tectonics*, *32*(4), 1011–1025. https://doi.org/10.1002/tect.20062

Précigout, J., Prigent, C., Palasse, L., & Pochon, A. (2017). Water pumping in mantle shear zones. *Nature Communications*, *8*. https://doi.org/10.1038/ncomms15736

Prigent, C., Warren, J. M., Kohli, A. H., & Teyssier, C. (2020). Fracture-mediated deep seawater flow and mantle hydration on oceanic transform faults. *Earth and Planetary Science Letters*, *532*, 115988. https://doi.org/10.1016/j.epsl.2019.115988

Rampone, E., Borghini, G., & Basch, V. (2018). Melt migration and melt-rock reaction in the Alpine-Apennine peridotites: Insights on mantle dynamics in extending lithosphere. *Geoscience Frontiers*, *11*(1), 151–166. https://doi.org/10.1016/j.gsf.2018.11.001

Regenauer-Lieb, K., & Yuen, D. A. (2003). Modeling shear zones in geological and planetary sciences: Solid- and fluid-thermal-mechanical approaches. *Earth-Science Reviews*, *63*(3–4), 295–349. https://doi.org/10.1016/S0012-8252(03)00038-2

Regenauer-Lieb, K., Weinberg, R. F., & Rosenbaum, G. (2006). The effect of energy feedbacks on continental strength. *Nature*, *442*(7098), 67–70. https://doi.org/10.1038/nature04868

Rutter, E. H., & Brodie, K. H. (1988). The role of tectonic grain size reduction in the rheological stratification of the lithosphere. *Geologische Rundschau*, *77*(1), 295–307. https://doi.org/10.1007/BF01848691

Schmalholz, S. M., & Duretz, T. (2015). Shear zone and nappe formation by thermal softening, related stress and temperature evolution, and application to the Alps. *Journal of Metamorphic Geology*, *33*(8), 887–908. https://doi.org/10.1111/jmg.12137

Schmid, S. M., Boland, J. N., & Paterson, M. S. (1977). Superplastic flow in finegrained limestone. *Tectonophysics*, *43*(3–4), 257–291. https://doi.org/10.1016/0040-1951(77)90120-2

Smith, C. S. (1948). *Grains, phases, and interphases: An interpretation of microstructure*. *Transactions of the American Institute of Mining and Metallurgical Engineers* (Vol. 175). https://doi.org/10.1007/s11661-010-0215-5

Streckeisen, A. (1974). Classification and Nomenclature of Plutonic Rocks Recommendations. *Neues Jahrbuch Für Mineralogie - Monatshefte*, *63*(4), 773–786. https://doi.org/10.1127/njmm/1973/1973/149

Tasaka, M., Zimmerman, M. E., Kohlstedt, D. L., Stünitz, H., & Heilbronner, R. (2017). Rheological Weakening of Olivine + Orthopyroxene Aggregates Due To Phase Mixing: Part 2. Microstructural Development. *Journal of Geophysical Research: Solid Earth*, *122*(10), 7597–7612. https://doi.org/10.1002/2017JB014311

Tommasi, A., & Vauchez, A. (2015). Heterogeneity and anisotropy in the lithospheric mantle. *Tectonophysics*, *661*, 11–37. https://doi.org/10.1016/j.tecto.2015.07.026

Tommasi, A., Gibert, B., Seipold, U., & Mainprice, D. (2001). Anisotropy of thermal diffusivity in the upper mantle. *Nature*, *411*(6839), 783–786. https://doi.org/10.1038/35081046

Tommasi, A., Knoll, M., Vauchez, A., Signorelli, J. W., Thoraval, C., & Logé, R. (2009). Structural reactivation in plate tectonics controlled by olivine crystal anisotropy. *Nature Geoscience*, *2*(6), 423–427. https://doi.org/10.1038/ngeo528

Trouw, R. A. J., Passchier, C. W., & Wiersma, D. J. (2010). Cataclasites. In R. A. J. Trouw, C. W. Passchier, & D. J. Wiersma (Eds.), *Atlas of Mylonites- and related microstructures* (pp. 7–23). Berlin, Heidelberg: Springer Berlin Heidelberg. https://doi.org/10.1007/978-3-642-03608-8_2

Turner, F. J., & Weiss, L. E. (1963). Structural analysis of metamorphic tectonites. *McGraw-Hill, New York*, 1–594.

Twiss, R. J. (1977). Theory and applicability of a recrystallized grain size paleopiezometer. *Pure and Applied Geophysics PAGEOPH*, *115*(1–2), 227–244. https://doi.org/10.1007/BF01637105

Vauchez, A., Tommasi, A., & Mainprice, D. (2012). Faults (shear zones) in the Earth's mantle. *Tectonophysics*, *558–559*, 1–27. https://doi.org/10.1016/j.tecto.2012.06.006

Van Der Wal, D., & Vissers, R. L. M. (1993). Uplift and emplacement of upper mantle rocks in the western Mediterranean. *Geology*, *21*(12), 1119–1122. https://doi.org/10.1130/0091-7613(1993)021<1119:UAEOUM>2.3.CO;2

Warren, J. M., & Hirth, G. (2006). Grain size sensitive deformation mechanisms in naturally deformed peridotites. *Earth and Planetary Science Letters*, *248*(1–2), 438–450. https://doi.org/10.1016/j.epsl.2006.06.006

White, S. H., Bretan, P. G., & Rutter, E. H. (1986). Fault-zone reactivation: kinematics and mechanisms. *Philosophical Transactions of the Royal Society A: Mathematical, Physical and Engineering Sciences*, *317*, 81–97. https://doi.org/https://doi.org/10.1098/rsta.1986.002

2 Reaction-induced phase mixing and the formation of ultramylonitic bands (Lanzo, Italy)

Sören Tholen[1], Jolien Linckens[1/2], Catharina Heckel[1], Marina Kemperle[3]

[1]Institut für Geowissenschaften, Goethe Universität Frankfurt a.M., Altenhöferallee 1, D-60438

[2]Tata Steel, R&D, Microstructural and Surface Characterization, Beverwijk, NL-1951

[3]Institut für Geologie und Mineralogie, Universität zu Köln, Zülpicher Str. 49b, D-50674

2.1 Abstract

As for most upper mantle shear zones, mylonitic and ultramylonitic peridotites exposed in the northern Lanzo shear zone display thoroughly mixed, fine-grained ($< 25\,\mu m$) bands. The weak crystallographic preferred orientations (CPO) of all their phases are indicative for deformation by diffusion creep. Although interpreted as significantly decreasing the strength of the upper mantle if interconnected, the formation process of fine-grained phase mixtures is still debated. Microstructural analysis of gradually higher strained peridotites of the northern Lanzo shear zone revealed the formation of fine-grained ($< 25\,\mu m$) polymineralic tails adjacent to clino- and orthopyroxene porphyroclasts in mylonitic samples. Phase mixtures (av. 65% phase boundaries) are dominated by neoblasts derived from the porphyroclast (Opx/Cpx) and olivine, with minor abundances (< 10 area-%) of plagioclase, spinel, $\pm$ amphibole. Neoblast microstructures and mixing of phases directly at the border of the pyroxenes, indicate a reaction of pyroxene porphyroclasts to neoblast phase mixtures. Neoblast temperature estimations (~860 °C), their systematic change in composition, and plagioclase/spinel abundances suggest that continuous net-transfer reactions, enhanced by the spinel lherzolite to plagioclase lherzolite transition are likely the main driving forces for the formation of ultramylonitic phase mixtures in the Lanzo shear zone. These reactions were potentially enhanced by the presence of fluid as evidenced by pargasitic amphibole crystallization. Comparing these results to other upper mantle shear zones and

deformed xenoliths, the importance of reactions (melt-rock, fluid-rock and/or metamorphic) for the formation of polymineralic, ultramylonitic bands is confirmed.

Keywords: Phase mixing, metamorphic reactions, spinel-plagioclase lherzolite transition, upper mantle, shear zone, recrystallization, Lanzo peridotite.

2.2   Introduction

Upper mantle shear zones are complex systems where a variety of processes take place through space and time. During deformation, changes in the PT conditions (e.g., Ramsay and Graham, 1970; Vauchez et al., 2012), percolation of melts (e.g., Dijkstra et al., 2002) and fluids (e.g., Précigout et al., 2017) can occur. These processes affect the mineralogy and microstructure of the rock, which in turn have a major control on the rheology of the shear zone. In most upper mantle shear zones, a transition in microstructures from relatively undeformed porphyroclastic tectonites, over protomylonites, mylonites and finally to ultramylonites can be observed (e.g., Newman et al., 1999; Dijkstra et al., 2002; Kaczmarek and Müntener, 2008; Linckens et al., 2015). Mylonites and ultramylonites are fine-grained and often polymineralic deformed rocks (Dijkstra et al., 2002; Kaczmarek and Müntener, 2008; Vissers et al., 1997). In these phase mixtures, second phases can counteract grain growth due to Zener pinning so that the grain sizes remain small (e.g., Linckens et al., 2015). In fine-grained, well-mixed layers, the small grain sizes can cause a switch in the dominant deformation mechanism from dislocation to diffusion creep (e.g., Newman et al., 1999; Dijkstra et al., 2002; Kaczmarek and Tommasi, 2011). Assuming a constant strain rate, this switch decreases the stress and deformation will localize in these layers (Karato and Wu, 1993). If these fine-grained, mixed areas are interconnected, they can further localize the deformation in the shear zones affecting the rheology of the lithosphere (e.g., Brodie and Rutter, 1987; Montési, 2013; Pearce and Wheeler, 2011). The preservation of these weak zones over geological time scales due to Zener pinning and possible subsequent reactivation might be important for the initiation of plate tectonics (Bercovici and Ricard, 2014).

To form fine-grained, well-mixed mylonites and ultramylonites, there needs to be, in addition to grain size reduction, a phase mixing process. Several mixing processes have been described previously. Grain boundary sliding (GBS) can result in phase mixing due to neighbor switching in the dislocation and diffusion creep regime (e.g., Boullier and Gueguen, 1975; Hirth and Kohlstedt, 2003;

Precigout et al., 2007; Drury et al., 2011, Farla et al., 2013). In contrast, Hiraga et al. (2013), report phase aggregation during GBS in deformation experiments. Deformation experiments indicate additionally that relatively high amounts of strain are needed to form phase mixtures by the combined process of dynamic recrystallization and GBS (Linckens et al., 2015). For calcite-anhydrite composites Cross and Skemer (2017) additionally reported the formation of phase mixtures by 'geometric' mixing for torsion experiments. At moderate shear strains ($\gamma \geq 6$) calcite and anhydrite domains were stretched and thinned to 'monolayers' of one or two grain's width. At high shear strains ($17 < \gamma < 57$) their disaggregation led to a thoroughly mixed assemblage. An additional phase mixing process related to GBS is creep cavitation and nucleation (e.g., Précigout and Stünitz, 2016). In the experiments of Précigout and Stünitz (2016) phase mixing is achieved when dislocation creep or diffusional mass transport cannot accommodate GBS, cavities open at grain boundaries and are instantly filled by neoblasts precipitating from an aqueous fluid during diffusion creep. Further evidence for this process might additionally be found in the work of Platt (2015) who described microstructures of recrystallization tails of Opx porphyroclasts from South African xenoliths. Here mixing is restricted to the margins of the tails, where olivine neoblasts were interpreted to crystallize interstitially between dynamically recrystallized grains undergoing grain boundary sliding.

Reaction-induced changes of the phase assemblage can also result in phase mixing. Multiple driving forces for mineralogical changes in upper mantle shear zones were reported, which can be divided into (i) metamorphic reactions, (ii) melt-rock reactions (iii) and fluid-rock reactions. (i) Changes in the PT conditions lead to garnet peridotite–spinel peridotite, and at shallower depth, spinel peridotite–plagioclase peridotite transitions (e.g., Furusho and Kanagawa, 1999, Dijkstra et al., 2004). In addition, PT dependent mineral compositions lead to continuous net-transfer reactions (e.g., Newman et al., 1999). (ii) Percolating melt in disequilibrium with the peridotite leads to melt-rock reactions, which may precipitate neoblasts and dissolve existing grains. Which phases dissolve or precipitate depends on the melt composition, which in turn changes due to its ascent (e.g., Rampone et al., 2018). Si-undersaturated melts cause olivine crystallization and pyroxene dissolution at deeper mantle depth, and therefore occurs at the early stages of the shear zone evolution (e.g., Dijkstra et al., 2002; Kaczmarek and Müntener, 2008). At shallower lithospheric depth, Si-saturated melts can occur, corroding olivine grains and forming pyroxene and plagioclase (e.g., Kaczmarek and Müntener, 2008). Local changes of melt composition have an additional impact on the local melt-rock reaction (Dijkstra et al., 2002).

(iii) Fluid-rock reactions can result in phase mixing by pargasitic amphibole and later stage chlorite/serpentine crystallization (e.g., Hoogerduijn Strating et al., 1993; Précigout et al., 2017; Prigent et al., 2020). In addition, Hidas et al. (2016) inferred that the fluid composition can be locally controlled by the surrounding minerals, allowing alternating dissolution and precipitation of olivine and orthopyroxene, leading to phase mixing. Additionally, Kohli and Warren (2020) reported mylonitic tremolite and olivine mixtures in orthopyroxene reaction tails potentially formed by hydration reactions of lherzolites at 650-850 °C.

To determine what processes are important for phase mixing and the formation of the polymineralic (ultra)mylonites we utilized the northern Lanzo shear zone as a natural laboratory and conducted a detailed microstructural and chemical study. In this mantle shear zone, continuously higher strained fabrics are displayed towards the rather homogenous, thoroughly mixed (ultra)mylonitic center of the shear zone (e.g., Kaczmarek and Müntener, 2008; Kaczmarek and Tommasi, 2011; Linckens et al., 2015). Both melt-rock reactions and the spinel peridotite - plagioclase peridotite transition have been suggested as phase mixing processes (e.g., Kaczmarek and Müntener, 2008; Kaczmarek and Tommasi, 2011). Our study evaluates these and other models for phase mixing by focusing on transitions from porphyroclasts (olivine, orthopyroxene and clinopyroxene) to neoblasts in tails and intracrystalline microstructures. By analyzing the phase content, composition, fabric, texture, and mixing intensity we address where microstructurally, when in the shear zone evolution and by what driving force, phase mixing and the creation of ultramylonitic assemblages occurs. We compare the results to other upper mantle shear zones and deformed xenoliths to highlight the importance of reactions for phase mixing and formation of ultramylonites.

2.3   Geological setting
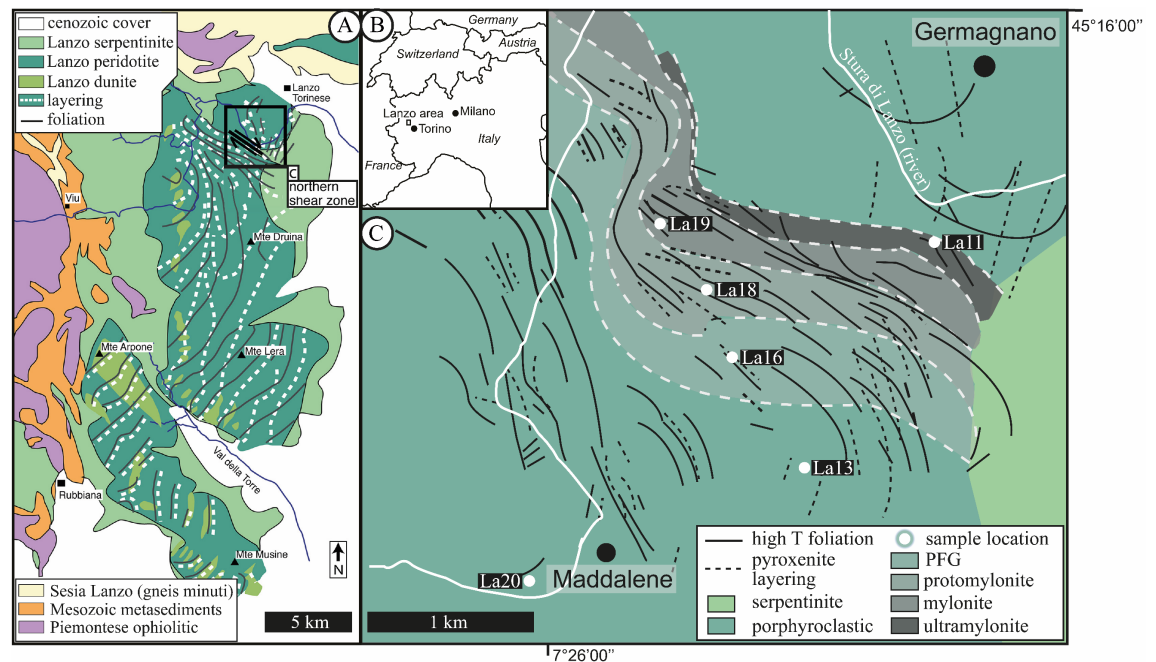
Fig. 2.1. *Overview of the Lanzo massif and a detailed map of the northern shear zone.* ***A.*** *Geological map including peridotite foliation and pyroxenite layering. Map modified after Boudier (1978) and Vieira Duarte et al. (2020).* ***B.*** *Geographic map with the location of the Lanzo area.* ***C.*** *The asymmetrical and anastomising northern shear zone with increasingly strained microstructural texture types (grey coloring) towards the contact to the northeastern hanging wall (PFG= porphyroclastic fine-grained). Sample locations are indicated. Map modified after Kaczmarek and Müntener (2008). For high resolution, see the digital version on the enclosed CD.*

The Lanzo peridotite massif is situated 30 km north-west of Torino, Italy (Fig. 2.1B), and is part of the high-pressure belt of the western Alps (e.g., Müntener et al., 2005). It is divided by two NW-SE striking shear zones into a southern, central, and northern part and covers an area of ~150 km² (Fig. 2.1A) (e.g., Boudier, 1978; Kaczmarek and Müntener, 2008). To the south and east, it is covered by cenozoic sediments of the Po plain (Fig. 2.1A). To the north, continental units of the Sesia-Lanzo zone are exposed (Gneis minuti, Fig. 2.1A). In the West, high-pressure meta-ophiolites (Piemontese ophiolitic, Fig. 2.1A) and mesozoic metasediments are present (Fig. 2.1A; Müntener et al., 2005). Main lithologies are plagioclase lherzolites, spinel lherzolites, pyroxenites and dunites (e.g., Boudier, 1978). Aligned spinel aggregates, plagioclase lenses and elongated orthopyroxene porphyroclasts form the pervasive foliation and lineation (Kaczmarek and Tommasi, 2011). Compositional layering of pyroxene rich and poor cm-scale bands is observed parallel or discordant to the foliation

(Boudier, 1978; Kaczmarek and Tommasi, 2011). The orientation of both foliation and lineation varies: It shifts from N-S to NE-SW in the southern and central part to NW-SE in the northern shear zone area and N-S in the northern part (Fig. 2.1A). Numerous igneous rocks are crosscutting mantle foliation and pyroxenite layering (Kaczmarek and Müntener, 2008, and references therein). The mantle assemblage is surrounded by a 3-5 km thick envelope of foliated serpentinite (Debret et al., 2013). Internally, the mantle assemblage is partially and only slightly serpentinized. For a detailed review of the massif's tectonometamorphic history, see Müntener et al. (2005).

Separating the northern and the central part, a high-temperature mantle shear zone (HTSZ) is exposed (Fig. 2.1A/C) (Kaczmarek and Müntener, 2008, 2005; Kaczmarek and Tommasi, 2011). It is interpreted as the deeper part of a mantle detachment fault between an asthenospheric, southern and a lithospheric, northern block that accommodates the opening of the Piemont-Ligurian ocean, in an ocean-continent transition or an (ultra)slow spreading ridge (Kaczmarek and Müntener, 2008; Kaczmarek and Tommasi, 2011; Müntener et al., 2005). Based on deformation related microstructures, Kaczmarek and Müntener (2008) divided the strained peridotites of Lanzo's northern shear zone into five texture types (Fig. 2.1C). From least deformed to highly deformed, these textures are: porphyroclastic texture, porphyroclastic fine-grained texture, protomylonite, mylonite and mylonite with ultramylonite bands. Main trends with increasing strain are (i) decreasing vol. % of porphyroclasts vs. increasing vol. % of neoblasts, (ii) decreasing grain size and increasing elongation of orthopyroxene porphyroclasts, and (iii) decreasing grain size and increasing phase mixing of matrix neoblasts (Kaczmarek and Müntener, 2008; Kaczmarek and Tommasi, 2011). Additionally, grain size distributions in weak deformed samples are generally more uniform than in higher deformed samples. For a detailed revision of the texture types see Kaczmarek and Müntener (2008). The strain gradient is strongly asymmetrical (Fig. 2.1C). In the SW footwall, the microfabrics gradually change over a width of 1.5 km (Fig. 2.1C; Kaczmarek and Tommasi, 2011). Additionally, the foliation and the pyroxenite layering gradually rotate parallel to the shear plane over a distance of 2-3 km (Fig. 2.1C; Kaczmarek and Tommasi, 2011). In the NE hanging wall, deformed peridotites sharply change (~200 m) into porphyroclastic tectonites and lineation and foliation rotate parallel to the shear zone over a significantly smaller width (< 100 m) (Kaczmarek and Müntener, 2008). Kaczmarek and Müntener (2008) and Kaczmarek and Tommasi (2011) reported a sinistral shear sense for the HTSZ.

The interplay between melt infiltration and deformation in the northern Lanzo shear zone has been studied by Kaczmarek and Müntener (2008; 2010). Shearing associated with melt percolation and melt-rock reactions led to the localization of deformation at temperatures exceeding 1000°C (Kaczmarek and Müntener, 2008). Though most of the observed melt-rock microstructures (orthopyroxene and plagioclase replacing clinopyroxene) and interstitial crystallization of orthopyroxene are interpreted as predating the onset of high-temperature shearing, some were also interpreted as having formed during the deformation (e.g., orthopyroxene replacing deformed olivine, interstitial, anhedral crystallization of orthopyroxene in olivine pressure shadows) (Kaczmarek and Müntener, 2008). Additionally, plagioclase-rich aggregates elongated alongside spinel in the foliation plane might indicate deformation-enhanced melt migration (Müntener et al., 2005). For these microstructures Kaczmarek and Müntener (2008) postulate an incongruent reaction from Al-rich spinel to Cr-spinel and plagioclase in the presence of liquid. Kaczmarek and Müntener (2008) suggested that crystallization of interstitial liquids below the solidus formed areas of olivine, plagioclase, and pyroxenes assemblages. Subsequent deformation localized in these finer grained areas, resulted in well-mixed mylonitic bands. The low permeability of these bands blocked the upward migration of mafic melts which crystallized along the shear zone (Kaczmarek and Müntener, 2008). Kaczmarek and Tommasi (2011) additionally suggested that during late-stage deformation, at relatively low temperatures syntectonic net-transfer reactions, associated with the spinel lherzolite to plagioclase lherzolite transition formed mixed ultramylonitic bands. During the exhumation, seawater-derived fluid infiltration and associated nucleation of amphibole in the deformational center (mylonites and ultramylonites) of the shear zone was reported by Vieira Duarte et al. (2020). The amphibole composition and orientation indicate formation temperatures of 800-850°C and syn-kinematic growth.

2.4   Methods

Samples of the Lanzo shear zone were cut perpendicular to the foliation and parallel to the lineation (*X-Z* section, Fig. 2.4). Thin sections were cut and polished to a thickness of ~30 µm. With an optical light microscope, microstructures of interest were located and categorized for further analyses (electron backscatter diffraction (EBSD) combined with energy dispersive X-ray spectroscopy (EDX), and electron probe microanalysis (EPMA)). As the microstructural focus of this research lies on transitions from porphyroclasts to phase mixtures, porphyroclastic

tectonite (La-20/13) and porphyroclastic fine grained (La16) samples were excluded for further analysis, because in these samples minor phase mixing, recrystallization and reactions occur.

2.4.1 EBSD, EDX and EPMA analysis

For EBSD analysis, thin sections were polished with 0.03 µm colloidal silica. BSE, EBSD and EDX analysis were conducted at the University of Frankfurt and the University of Cologne on carbon coated samples. For EBSD measurements, the Institute of Geoscience in Frankfurt is equipped with a JEOL JSM-6490 scanning electron microscope (SEM). Measurement settings were an acceleration voltage of 15-20 kV and a beam current of ~8 nA. For EBSD data acquisition, the program Flamenco (Oxford Instruments HKL Channel 5) and a Nordlys detector (Oxford Instruments) were used. At the Institute for Geology and Mineralogy in Cologne BSE, EDX and EBSD measurements were conducted with a Zeiss Sigma 300-VP field emission SEM equipped with a NordlysNano detector (Oxford Instruments). The acceleration voltage was set to 20 kV. For the data acquisition the program Aztec was used (Oxford Instruments). The step size was adapted according to grain sizes so that every grain could have at least 10 measurement points (range: 0.5- 5 µm). Depending on step size and acquisition time, EBSD map sizes differ over a wide range. In general, large maps (measurement time > 3h) were obtained using the more stable field emission SEM at the University of Cologne. In Cologne, EDX element maps (O, Mg, Al, Si, Ca, Cr, Mn, and Fe) were obtained simultaneously. At both localities, for the consistency of orientations between sample, measurement and post-processing reference frame was checked by measuring a self-prepared quartz standard. It consists of four synthetic quartz crystals with differently oriented c-axis embedded in epoxy. Known orientations of the single crystals and their position in the standard enables to detect possible rotations affecting the spatial or crystallographic data at any given step during analysis and data handling (e.g., Kilian et al., 2016). The EBSD data were cleaned from systematic misindexing of Ol (similar diffraction patterns for orientations rotated 60° around [100]) with Oxford Instruments HKL Channel 5 software. Subsequently, the data was imported into the MTEX 5.3 MATLAB extension (e.g., Bachmann et al., 2010). All additional data processing and analysis were conducted with MTEX 5.3 (http://mtex-toolbox.github.io/). The

scripts used for cleaning, grain detection (grain internal misorientation < 15°) and subgrain detection (misorientation angle between subgrains < 15°), deletion of incomplete grains at the borders of mapped areas and badly indexed grains, crystallographic and boundary analysis etc. are available on request from the authors. During grain reconstruction, the resulting grains were checked against backscattered/forescattered, band contrast images and EDX data if present. The grain analysis consists of grain size (equivalent circular diameter – ECD) and grain shape (orientation of the grains long axis, aspect ratio). Shape preferred orientations (SPO), defined by the orientation of the long grain axis, include all grains of a given phase. Throughout this manuscript, phase abundances are given by "%" referring to area % of EBSD maps. Phase specific texture maps are colored using the corresponding IPF color key given in Figure 2.2 (Hielscher and Nolze, 2016). The color of each indexed measurement point (pixel) shows which crystal direction is parallel to the X direction of the map which coincides with the lineation of the sample. Grains with similar colors depict therefore similar orientations. Boundary analysis is accomplished by calculating phase specific boundary lengths. Phase (e.g., Ol-Opx) to grain (e.g., Ol-Ol, Opx-Opx) boundary percentages are used to determine the "mixing intensity". In the interest of clarity and length, phase specific boundary analysis is only attached in the supplementary data (S2.1). All pole figures are lower hemisphere plots. A minimum number of 100 grains was used for ODF (orientation distribution function) calculation with grain mean orientations and a consistent halfwidth of 15° (used for all figures). For the calculation, orientations of incomplete grains at the borders of mapped areas were included. Therefore, grain amounts of grain maps can differ from those for orientation calculation. To facilitate the comparison of ODF plots, the color-coding range is consistently fixed from min = 0 mrd (multiple of random distribution) = blue for a random orientation to max = 3 mrd = red (Fig. 2.2). Higher mrds than 3 are also colored red. The maximum mrd is added alongside the J index (Bunge, 1982) (Fig. 2.2). An ODF example including J Index, max mrd value and the amount of analyzed grains is given in Figure 2.2. The plot conventions and its legend apply to all ODFs and pole figures throughout the manuscript. The M index (Skemer et al., 2005) is given alongside all orientation data in the supplementary data (S2.2). Both J and M Index express the strength of

a given ODF. For a detailed evaluation of both see Skemer et al. (2005). An overview of all CPOs is given in the supplementary data (S2.3 and S2.4).

For clarity, the result section will be limited to figures of example microstructures for each microstructure type. Included in these figures are tables and graphs of grain size, modal abundances, aspect ratio, phase boundary %, SPOs and ODFs referring to the depicted microstructure. Average aspect ratios and average grain size are only presented if enough grains were present for a valid statistical statement (n> 25). In contrast, the results presented in the text include all analyzed microstructures of a given microstructure type and therefore numbers and ratios differ from the data shown in the figure. The complete grain, boundary and orientation data are given in the supplementary data (S2.1-S2.4).
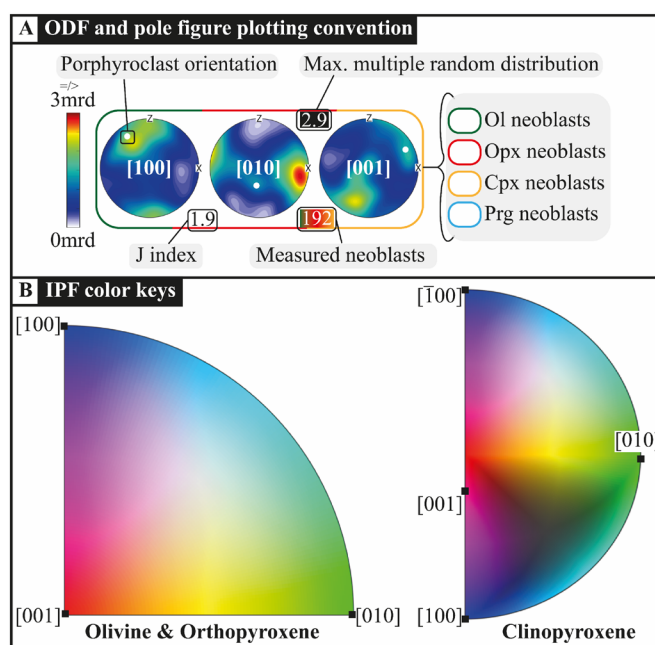
Fig. 2.2. *Plotting conventions and IPF color keys. **A.** Conventions for ODFs and pole figures. ODF colors correspond to mrd (multiple of random distribution). Frame color represents analyzed neoblast phase (green= Ol, red= Opx, orange= Cpx, light blue= Prg). White number against black background shows max mrd. White number against colored background shows the amount of neoblasts analyzed. Black number against white background shows the J Index. From left to right ODFs and pole plots show [100], [010] and [001]. Porphyroclast orientations are given by white dots. **B.** IPF color keys for olivine and orthopyroxene (left) and Clinopyroxene (right).*

Microprobe measurements were conducted using a field emission JEOL JXA-8530F Plus microprobe equipped with 5 wavelength-dispersive spectrometers and located at the Institute of Geoscience at the Goethe University

Frankfurt. Two measuring settings were used: for Cpx and Opx porphyroclasts and neoblasts, a 15 kV acceleration voltage and a 20 nA beam current was used for 20 s (Al, Cr, Ca, Na, Mn, Fe and Ni), 30 s (P, K and Ti) or 40 s (Mg and Si) for peaks and 20 s for background (settings and detection limits in suppl. data S2.5). To detect trace element concentrations of Ol clasts and neoblasts, a trace element protocol was used, with an acceleration voltage of 20 kV, a beam current of 100 nA and extended measuring times up to 150 s for peak, plus 150 s for background (Cr, Al, Ca, and Ti) (suppl. data S2.5). Resulting detection limits were 29 ppm for Cr, 9 ppm for Al, 12 ppm for Ca and 16 ppm for Ti (suppl. data S2.5). For both methods the spot-size was adjusted to the grain size with minimum sizes of 1 μm for small sized neoblasts and maximum 4 μm for porphyroclasts.

2.4.2 Geothermometry

Microprobe data (suppl. data S2.6) were used to calculate equilibrium temperatures of porphyroclasts and neoblasts in mylonitic samples. We used the T_{BKN} two pyroxene geothermometer and the $T_{Ca\,Opx}$ geothermometer calibrated by Brey and Köhler (1990). To check equilibrium, we additionally applied the two-pyroxene   thermometer T_{Ta98} by   Taylor   (1998)   and   the single-Cpx-thermometer T_{1Cpx} by Nimis and Taylor (2000), which were originally calibrated for Grt peridotites. Former studies have shown that T_{BKN} and T_{Ta98} can be applied under relatively low-pressure conditions and outside the garnet stability field (Nimis and Taylor, 2000). T_{BKN} and T_{Ta98} temperature estimates were derived using data from spatially close porphyroclasts. Ca saturation for Ca equilibration in Opx, necessary for the application of Opx geothermometry is assumed by the presence of Cpx in all analyzed samples. Neoblasts are mostly exsolution free, therefore calculated temperatures are thought to be accurate. For both Cpx and Opx porphyroclasts, exsolution lamellae of the respectively other phase are present. We estimated pyroxene porphyroclast temperatures based on the clast chemistry excluding the lamellae. Cpx porphyroclast estimates are therefore minimum temperatures, affected by exsolution and associated diffusion. Even though care was taken to ensure exsolution free measuring areas in Opx porphyroclasts, it cannot be excluded that micro-Cpx-exsolution lamellae (μm) were analyzed as well. Such mixed analysis leads to an increase of e.g., Ca, which results in an overestimation of Opx porphyroclast temperatures. For exchange reactions the Mg-Tschermaks in Opx were calculated after Carswell (1991) and the Ca-Tschermaks in Cpx after Knapp et al. (2013).

2.4.3 Terminology

Mineral abbreviations are used corresponding to Whitney and Evans (2010). Following Kaczmarek and Tommasi (2011) and Kaczmarek and Müntener (2008) we use the term "textures" for the dominant arrangement of grains (size, shape, and orientation) at macroscale (thin section and larger). Accordingly, "textures" define samples by their classification in e.g., porphyroclastic, protomylonite, mylonite. The texture nomenclature was taken from Kaczmarek and Müntener (2008), except the "mylonite with ultramylonitic bands" where we adapt the nomenclature of Linckens et al. (2015) and refer to this texture as "ultramylonite". For a detailed description of the samples, we refer to Linckens et al. (2015). For microstructural descriptions, the term "mylonitic" refers to grain assemblages with mean grain sizes between 25-200 µm equivalent circular diameter (ECD), whereas "ultramylonitic" is used for grain assemblages with average ECD < 25 µm.

The term "dynamic recrystallization" is used for strain-imposed recrystallization processes, which show indicative microstructures of bulging recrystallization (BLG), subgrain rotation recrystallization (SGR) or grain boundary migration (GBM) (Urai et al., 2011). Classical evidence for dynamic recrystallization includes (i) an assemblage of strain free neoblasts surrounding an internally deformed porphyroclasts (where the porphyroclast and neoblast are the same mineral) and (ii) a crystallographic consistency between porphyroclast and surrounding neoblast orientations (e.g., Poirier & Nicolas, 1975). Correspondingly, only microstructures where both criteria are met are addressed as "dynamically recrystallized".

"Grain boundary alignments" (GBAs) are aligned grain and phase boundaries as described in Newman et al. (1999). Grains in these areas are mostly elongated and oriented parallel to each other resulting in GBAs following the long axis of the grains. They mostly form continuous, aligned boundaries over tens to hundreds of µm.

2.5   Microstructures

One texture type can contain multiple different microstructures (Fig. 2.3). In mylonite textures for example, porphyroclasts with relatively coarse-grained neoblast tails coexist with ultramylonitic phase mixtures and dynamically recrystallized Ol areas (e.g., Fig. 2.4B). Therefore, we focus on microstructures and their characteristics rather than on texture types. Three principle microstructural environments were identified in order to evaluate the importance of recrystallization and/or reactions for phase mixing: (i) porphyroclasts and

adjacent neoblast tails enable to identify dynamic recrystallization and reaction processes and their influence on phase mixing, (ii) the analysis of intracrystalline and isolated neoblast assemblages in or between pyroxene porphyroclasts helps to evaluate if a connection to the matrix was crucial for phase mixing, (iii) ultramylonitic bands were analyzed to compare their microstructural characteristics with those of i and ii. For each type (i, ii and iii), analyses were conducted in different texture types (protomylonites, mylonites and ultramylonites), if present. As phase mixing and recrystallization is concentrated in mylonites and ultramylonites (Fig. 2.4B/C) the majority of analyzed microstructures are from those texture types.
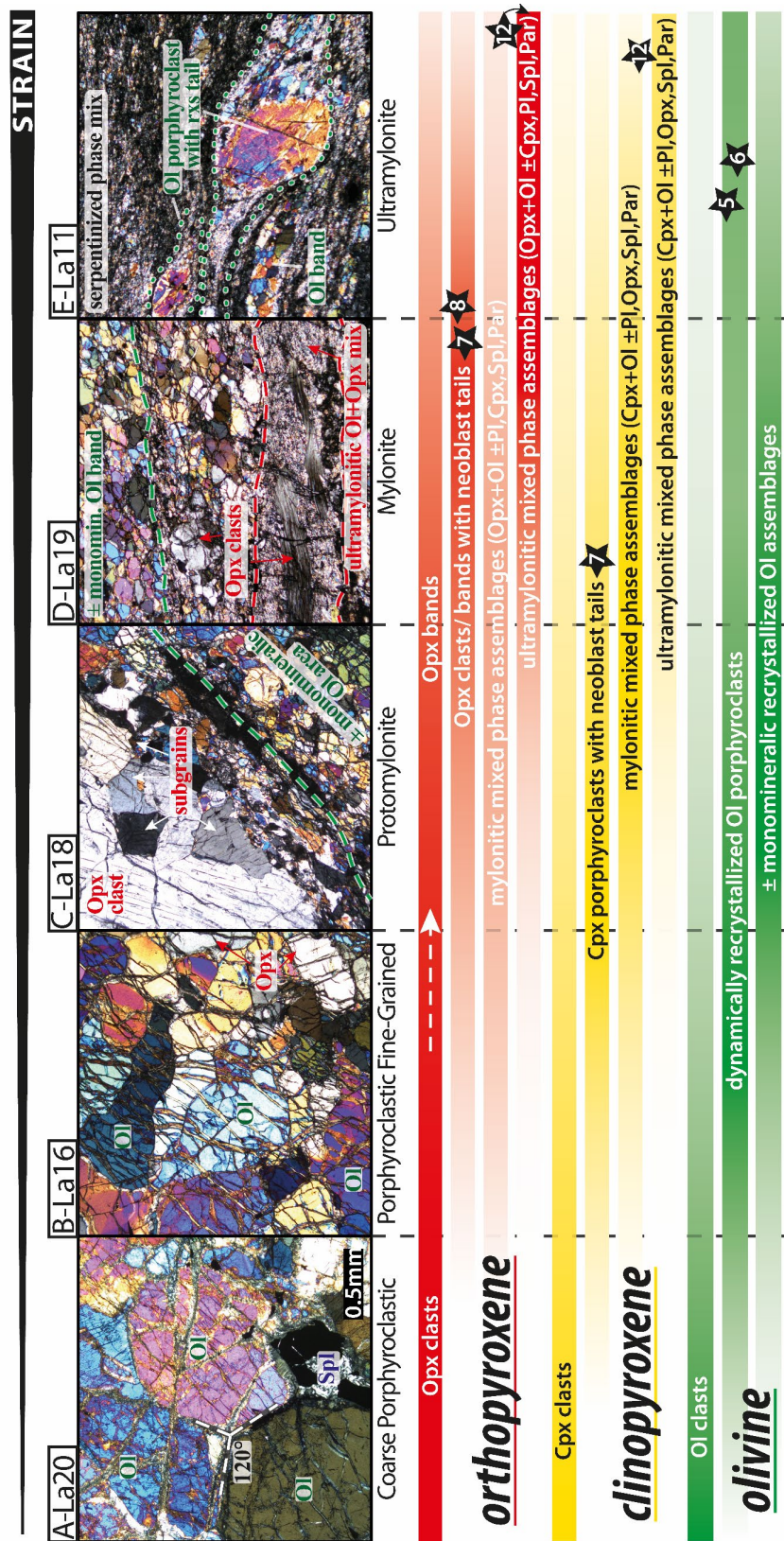
Fig 2. 3. Overview of orthopyroxene (red bars), clinopyroxene (yellow bars) and olivine (green bars) microstructure types and their occurrence with increasing strain (left to right) in the corresponding texture types (polarized light micrographs, texture categories indicated beneath the images). Scale, shown in A, is the same for all micrographs. The bars color intensity indicates the frequency of the respective microstructure in a texture type. Numbers in stars refer to Fig. 2.# where an example of the corresponding microstructure type is shown in detail. For high resolution, see the digital version on the enclosed CD.
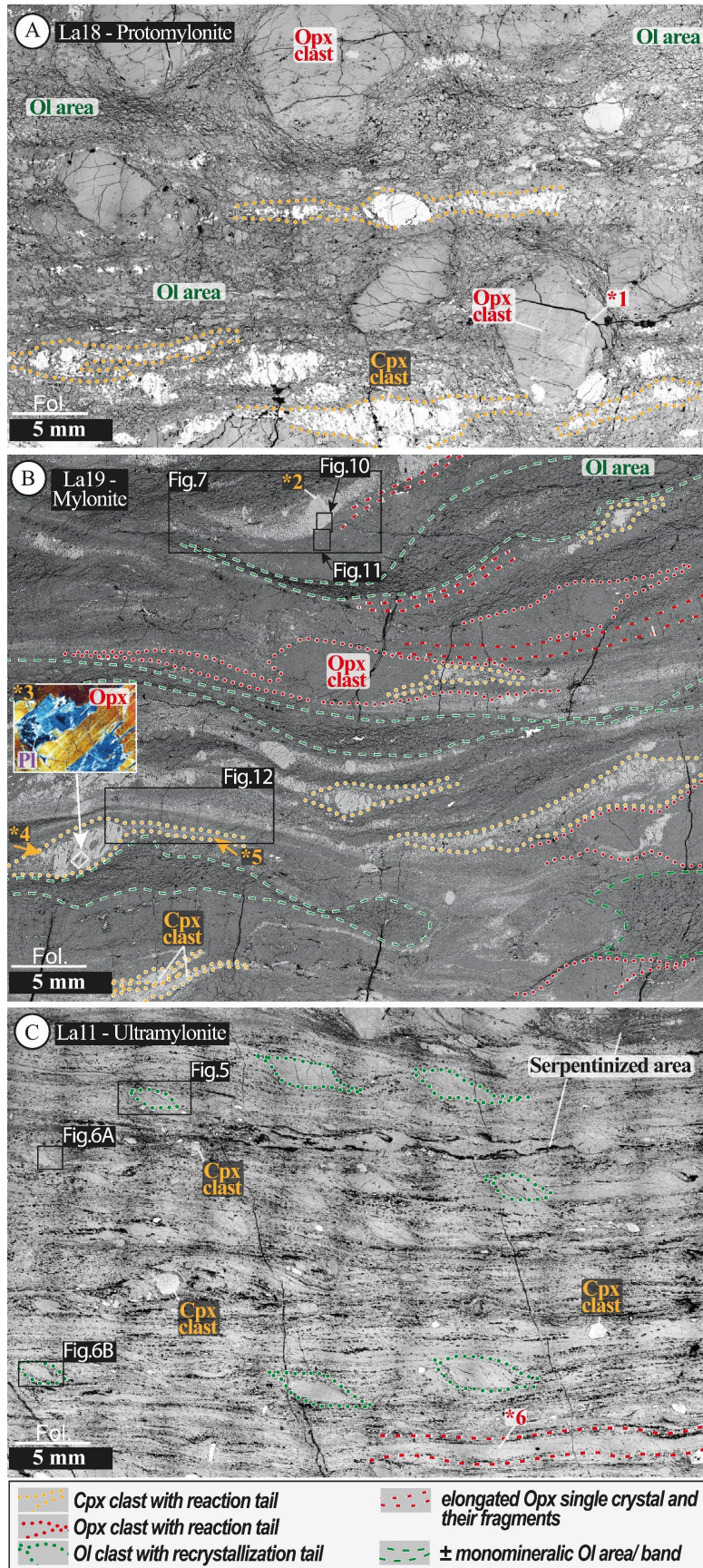
Fig. 2.4. Back-scattered electron (BSE) overviews of increasingly deformed peridotites with analyzed microstructures in black boxes (Fig. number = 2.#).

A. Protomylonitic texture: (*1) Opx porphyroclasts with partly bent Cpx exsolution lamellae.

B. Mylonitic texture: (*2) Cpx porphyroclasts with Opx exsolution lamellae and neoblast tail, (*3) micrograph (polarized light) of intracrystalline Pl+ Opx assemblage in Cpx porphyroclast, (*4) coarse and (*5) fine grained neoblast tails.

C. Ultramylonitic texture: Mixed matrix dominated by Ol and Opx (grey phases) and serpentine (black phase), (*6) fragments of Opx single crystal. For high resolution, see the digital version on the enclosed CD.

2.5.1 Neoblast tails

2.5.1.1 Almost monomineralic tails adjacent to olivine porphyroclasts

Fig. 2.5. *Example microstructure of an olivine porphyroclast with almost monomineralic neoblast tail in the ultramylonite texture (La-11). A-i. Optical micrograph (crossed polarized light). A-ii. Phase map (red grains = Opx, red lines = subgrain boundaries, black lines = grain boundaries, white arrows = lobate porphyroclast boundary). A-iii. Average grain sizes (ECD) excluding the porphyroclast. A-iv. Number of grains per phase. A-v. Average aspect ratio. A-vi. Olivine ODF with porphyroclast orientation (white dots). A-vii. Orthopyroxene ODF. A-viii. Olivine texture map, (black arrows) grains with a similar orientation as the porphyroclast. A-ix. Area percentages. A-x. Grain (GB) and phase boundary percentages (PB). A-xi. Rose diagram of Ol grain long axes. A-xii. Rose diagram of Opx long axes. For high resolution, see the digital version on the enclosed CD.*

Olivine is the dominant phase in all texture types. Internal grain deformation (undulatory extinction, Fig. 2.3A) and dynamic recrystallization of Ol grains are already found in low strained coarse porphyroclastic samples. Olivine grains show lobate boundaries, 120° triple junctions and are elongated in porphyroclastic

samples (La20, La13; Fig. 2.3A/B). Additionally, evidence for dynamic recrystallization of Ol by subgrain rotation recrystallization (SGR) is present in porphyroclastic fine-grained samples (La13; Fig. 2.3B). Almost monomineralic, recrystallized Ol areas and bands in (proto)mylonitic textures (La18, La19; Fig. 2.3C/D) are defined by the absence of a porphyroclast (Fig. 2.4A/B). In these microstructures, Cpx, Opx and Spl are present in places but only as minor phases. The internal deformation of recrystallized Ol grains is small (internal misorientation < 4°), and 120° triple junctions are frequent (Fig. 2.3D). The band length is highly variable between a couple hundred μm to several cm (Fig. 2.4B). Olivine grain size decreases from protomylonite (~630 μm) over mylonite (~250 μm) to ultramylonite (~ 90 μm) (Linckens et al., 2015). To determine the process that led to olivine neoblast formation, the focus of Ol analysis lies on recrystallized porphyroclasts and their transition into neoblasts. Although Ol porphyroclasts are present in all texture types, those with almost monomineralic tails are found in mylonites and more commonly in ultramylonites (Fig. 2.4C). Three microstructures were analyzed (Figs. 2.5, 2.6).

Characteristics for these microstructures are an internally deformed, Ol porphyroclast (Fig. 2.5A-i/viii) adjacent to an almost monomineralic Ol tail (range: 85-98%; Figs. 2.5A-ix, 2.6A/B-v). A relatively coarse grain size (Figs. 2.5A-iii, 2.6A/B-ii) and monomineralic assemblage clearly separate the tail from the mylonitic to ultramylonitic, polyphase matrix (e.g., Fig. 2.5A-i). The porphyroclasts show a rugged grain boundary with indentations of Ol neoblasts (Fig. 2.5A-ii white arrows). Mean Ol neoblast grain size varies between 21 and 46 μm (Figs. 2.5-iii, 2.6A/B-ii). Opx and Cpx neoblasts have a similar, small variability in grain size of 9-15 μm and 8-14 μm. The average Ol aspect ratio is 1.7 (Figs. 2.5A-v, 2.6A/B-iv). Opx neoblasts have similar aspect ratios to Ol (Figs. 2.5A-v, 2.6A/B-iv). In Ol tails, 83% of the total boundaries are grain boundaries (Figs. 2.5A-x, 2.6A/B-vi). 97% of those grain boundaries are Ol-Ol interfaces (suppl. data S2.1). The microstructures exhibit a dependence of the neoblast orientation on the porphyroclast orientation (Fig. 2.5A-vi, 2.6A/B-ix). If neoblasts do not display the same orientation as the porphyroclast, they lay in girdles that include the clast orientation (e.g., Fig. 2.6B-ix). Olivine neoblasts of Figure 2.5A-vi display a rotation of 90° in the foliation plane for [010] and more diffuse rotations for [001], while [100] still display porphyroclast orientations.
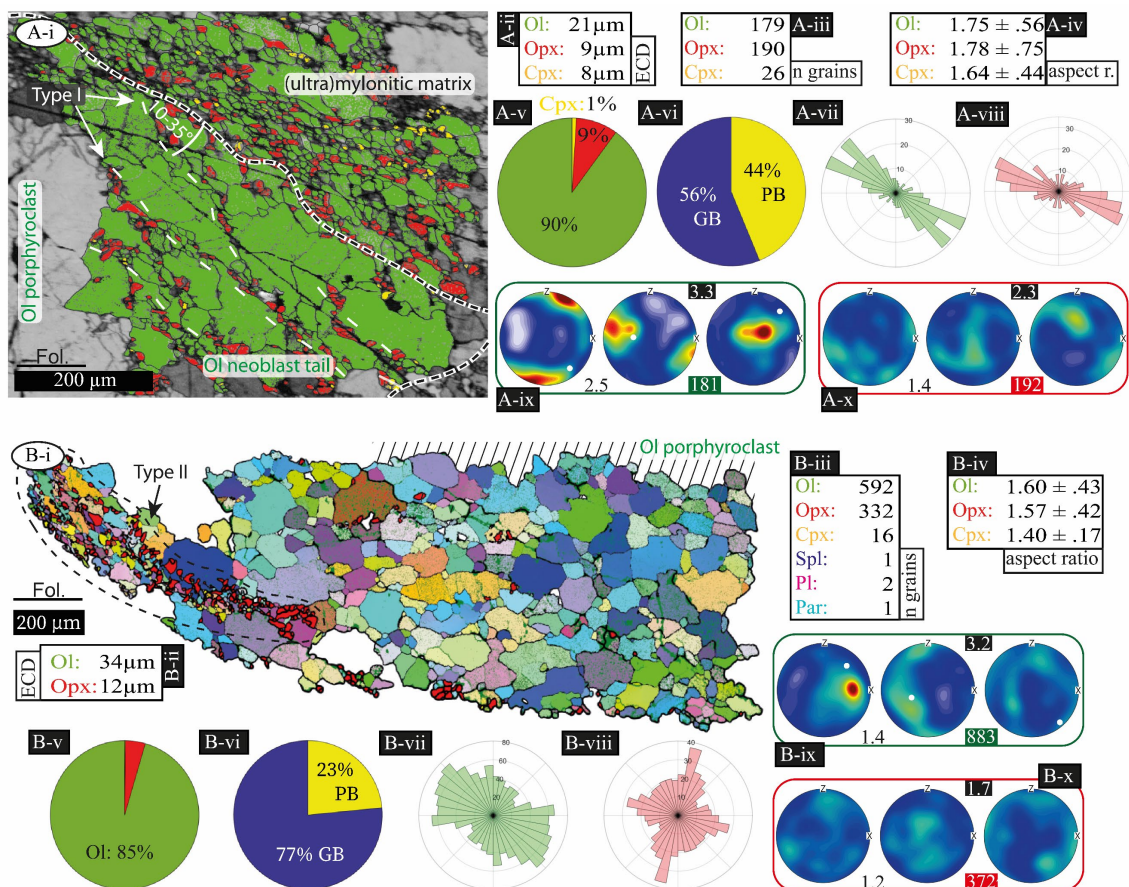
Fig. 2.6. *Phase mixing in neoblast tails of olivine porphyroclasts in the ultramylonite texture type (La-11). **A**-i. Phase map of almost monomineralic Ol tail (black dashed line) with Ol mixing type I (dashed white lines) adjacent to ultramylonitic matrix. The presented data (A-ii-x) is derived from the Ol neoblast tail. A-ii. Average grain size. A-iii. Number of grains. A-iv. Average aspect ratios. A-v. Phase area percentages. A-vi. Phase and grain boundary percentage. A-vii. Rose diagram of Ol neoblast long axes. A-viii. Rose diagram of Opx neoblast long axes. A-ix. ODF of Ol grains. A-x. ODF of Opx neoblasts. **B**-i. Texture map of Ol tail with Opx neoblasts added in red (Mixing type II= inside black dashed line, Ol porphyroclast= black hatched area). B-ii. Average grain size. B-iii. Number of grains. B-vi. Average aspect ratios. B-v. Modal abundances. B-vi. Phase and grain boundary percentages. B-vii. Rose diagram of Ol grain long axes. B-viii. Rose diagram of Opx neoblast long axes. B-ix. ODF of olivine grains. B-x. ODF of Opx neoblasts. High resolution, digital version is included on the CD.*

Some Ol tails contain thin, fine-grained (< 30 μm) trails of Opx-Ol grains. Two types of these trails have been found: one-grain thick trails made of Ol-Opx mixtures (< 25 μm in size) located in between coarser Ol grains (25-100 μm) (Type I; Fig. 2.6A-i); and ~100 μm thick Opx-Ol fine-grained trails at the margin of an Ol neoblast tail (Type II; Fig. 2.6B-i). Type I develops at a small angle (10-35°) to the boundary of tail and matrix (Fig. 2.6A-i). Type I trails have been

observed crosscutting the whole tail, interlinking with other trails, ending at grain boundaries of coarse Ol neoblasts or leaving the thin section plane (Fig. 2.6A-i). A strong SPO has been observed for both Ol and Opx neoblasts (Fig. 2.6A-vii/viii) in this type. Type II mixing is situated at distal parts of the Ol tail (Fig. 2.6B-i) and is connected to an Opx porphyroclast in close vicinity. The smaller grain sizes and the presence of Opx sets the trail apart from the surrounding almost monomineralic Ol tail (Fig. 2.6B-i). The SPO of Opx neoblasts is almost perpendicular to the weak Ol neoblast SPO (Fig. 2.6B-vii/viii). The small spatial extent of both mixing types compared to the entire Ol tails results in only intermediate (Type I: 45% PB; Fig. 2.6A-vi) and low mixing intensities (Type II: 23% PB; Fig. 2.6B-vi).

2.5.1.2 Polymineralic tails adjacent to clinopyroxene porphyroclasts
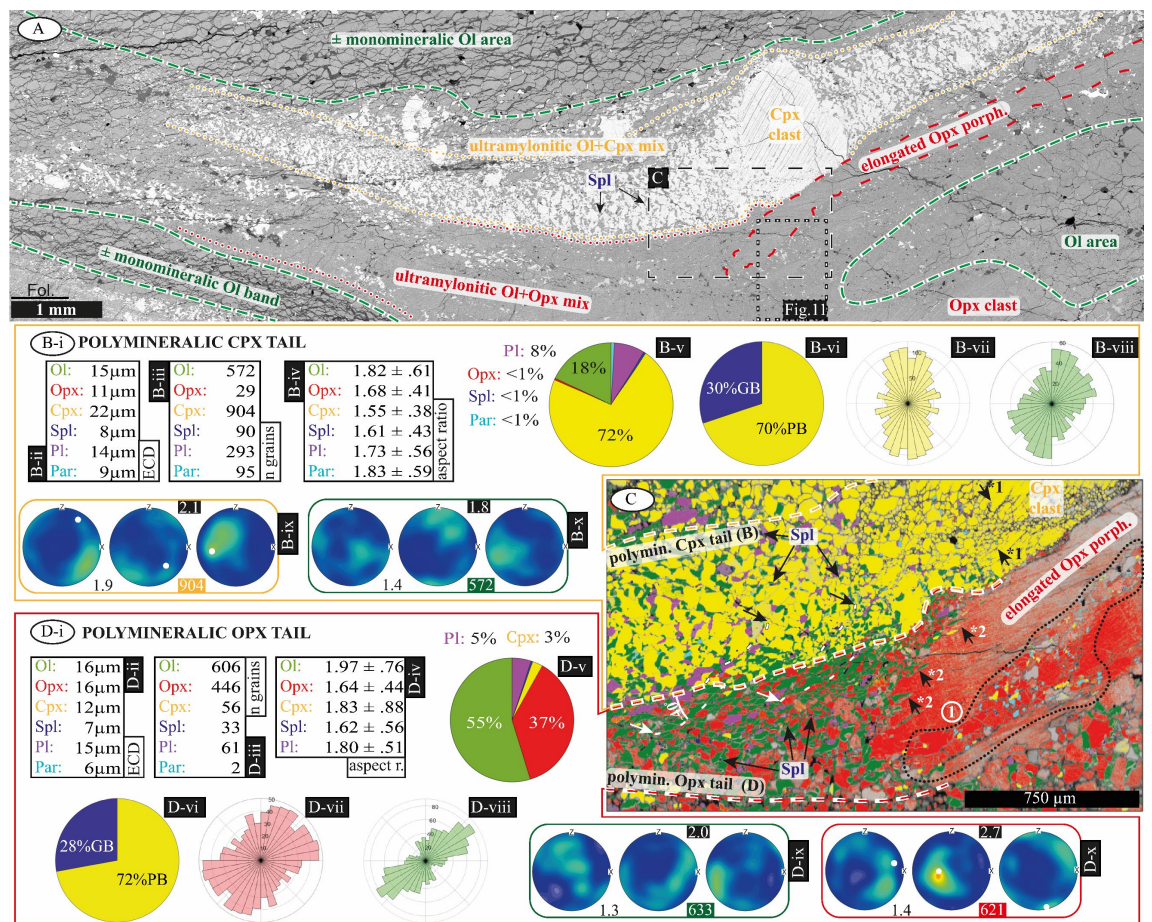
Fig. 2.7. Clino- and orthopyroxene porphyroclast derived polymineralic tails in the mylonitic texture type. **A.** BSE overview image with major microstructures (dashed green = almost monomineralic Ol areas, dashed red = elongated Opx porphyroclast, dotted yellow = Cpx neoblast tail, dotted red = Opx neoblast tail), area of EBSD map (dashed black), and location of Fig. 2.11 indicated.

← ***Fig. 2.7. B**-i. Microstructural data from Cpx neoblast tail marked in C. B-ii. Neoblast av. grain sizes. B-iii. Neoblasts per phase. B-iv. Av. aspect ratio. B-v. Modal abundances. B-vi. Phase and grain boundary percentages. B-vii. SPO of Cpx neoblasts. B-viii. SPO of Ol neoblasts. B-ix. ODF of Cpx neoblasts and porphyroclast orientation. B-x. ODF of Ol neoblasts. **C.** EBSD phase map (location indicated in A, same phase colors as in pie charts B-v and D-v). Annotations are (*1, *2) neoblast indentations in porphyroclasts, (white dashed lines with arrows) grain boundary alignments (GBAs) and (black dotted area 1) intracrystalline Opx neoblast area. **D**-i. Microstructural data from Opx neoblast tail marked in C. D-ii. Neoblast av. grain size. D-iii. Neoblasts per phase. D-iv. Av. neoblast aspect ratio. D-v. Modal abundances. D-vi. Phase and grain boundary percentages. D-vii. SPO of Opx neoblasts. D-viii. SPO of Ol neoblasts. D-ix. ODF of Ol neoblasts. B-x. ODF of Opx neoblasts and porphyroclast orientation. High resolution, digital version is included on the CD.*

Clinopyroxene is present in all analyzed samples. The abundance of Cpx porphyroclasts decreases with increasing strain. Cpx porphyroclasts start to form neoblasts in the porphyroclastic fine-grained texture (Fig. 2.3B). Polymineralic tails adjacent to Cpx porphyroclasts are observed up to mylonitic conditions (Fig. 2.4B). In ultramylonites the amount and the size of Cpx porphyroclasts decreases and polymineralic tails are no longer clearly recognizable (Fig. 2.4C). Opx exsolution lamellae are common. Internal replacement of coarse-grained Cpx porphyroclasts by Opx+Pl is present in all texture types except ultramylonites (e.g., Fig. 2.4B *3).

Tails adjacent to Cpx porphyroclasts are characterized by a single or several Cpx porphyroclasts and a phase mixture of mainly Cpx and Ol (Fig. 2.7A). Secondary phases are Pl, Opx, Spl and Prg. Spl often form small, interstitial neoblasts (Fig. 2.7A/C). Evidence for the relation of the porphyroclast to the polymineralic tails include indentations of Ol and Cpx neoblasts in Cpx porphyroclasts (Fig. 2.7C *1), as well as the distinct boundaries between tail and Ol+Opx dominated adjacent matrix (Fig. 2.7C) and almost monomineralic Ol areas (Fig. 2.7A). In total 6 microstructures were analyzed from mylonitic (La-19) and protomylonitic samples (La-18; suppl. data S2.1). Occasionally, the transition from Cpx tails into Cpx+Ol dominated layers of ultramylonitic bands is visible (e.g., Fig. 2.7A). Beside one Ol dominated tail, Cpx is the dominant phase (av.: 61%, range: 42-86%; suppl. Data S2.1). Olivine makes up between 7 and 48% (av.: 31%). Plagioclase has an abundance of 6% on average (range: 2-8%). Opx forms on average only 2% (range: 0-9%) and occurs more frequently in marginal areas of the tail (e.g., Fig. 2.7). Spl and Prg both cover 1% on average. Cpx forms the biggest neoblasts with an average ECD of 20 μm (range:

10-40 μm). Ol (av. 16 μm, range: 9-30 μm) and Pl (av. 17 μm, range: 10-24 μm) have intermediate neoblast sizes and Opx (av. 12 μm, range: 8-21 μm), Prg (av. 11 μm, range: 8-17 μm) and Spl (on average 8 μm, range: 5-16 μm) form the smallest neoblasts. There is a general trend of decreasing neoblast Cpx grain size going from the protomylonite to the mylonite (Fig. 2.4A/B). However, the range of 9 to 30 μm (av. Cpx ECD) found in different microstructures of a single mylonitic sample (Fig. 2.4B) emphasizes the dependence of neoblast grain size on the location of the porphyroclast tail (Fig. 2.4B *4/*5). Cpx neoblasts display a low aspect ratio of 1.6. Intermixed Opx, Ol and Pl have higher aspect ratios of 1.7 (Opx), 1.8 (Ol), and 1.8 (Pl). 66% of all boundaries are phase boundaries (34% grain boundaries). Cpx-Pl boundaries form 64% (av.) of total Pl phase boundaries (suppl. data S2.1). 75% (av.) of the total Ol boundaries are Ol Cpx phase boundaries. Two different SPOs were found for Cpx neoblasts: (i) long axis aligned subparallel to the foliation (suppl. data S2.7) or (ii) sub perpendicular to the foliation plane/ to the elongation axis of the neoblast tail respectively (Fig. 2.7B-vii). If the aligned Cpx neoblasts of type ii are interconnected in their elongation direction, they form "walls" alternated with Ol "walls" (suppl. data S2.7). Most Cpx neoblasts show a relatively weak CPO (J-index av. 2.2, range 1.3-3.0; e.g., Fig. 2.7B-ix, suppl. data S2.3, S2.4). Stronger Cpx CPOs often show maxima similar to the porphyroclast orientations. Opx CPOs and Ol CPOs are relatively weak with average J indices of 1.6 (range: 1.3-2.1) and 1.4 (range: 1.1-2.0), respectively.

2.5.1.3 Polymineralic tails adjacent to orthopyroxene porphyroclasts
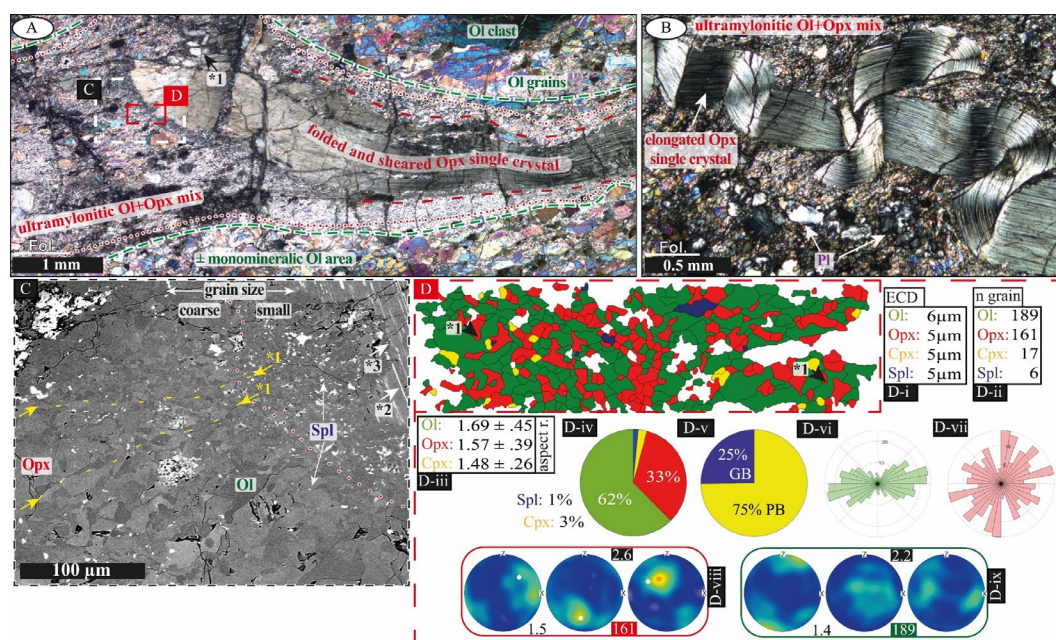
Fig. 2.8. Example microstructure of elongated Opx single crystal with polymineralic tail in the mylonitic texture type. A. Micrograph (crossed polarized light) of (dashed red line) elongated, folded and (*1) sheared Opx single crystal surrounded by (red dots) ultramylonitic Ol+Opx neoblasts. Indicated are (green dashed) Ol areas and location of (white frame) map C and (red frame) EBSD map D. B. Folded, kinked, and sheared Opx single crystal in the mylonitic texture type. C. BSE image of Ol+Opx neoblast mixture with (*1) GBAs, Opx porphyroclast with (*2) Cpx exsolution lamellae and (*3) serrated boundaries. The red dotted line separates areas of smaller and coarser grain size. D. EBSD map of ultramylonitic Ol+Opx mixture in neoblast tail (*1= bottle neck structures). D-i. Average neoblast ECD. D-ii. Number of grains. D-iii. Average aspect ratios. D-iv. Modal abundances. D-v. Grain and phase boundary percentages. D-vi. Ol neoblast SPO. D-vii. Opx neoblast SPO. D-viii. Opx neoblast ODF with the porphyroclast orientation. D-ix. Ol neoblast ODF. High resolution, digital version is included on the CD.

Orthopyroxene porphyroclasts occasionally show evidence for dynamic recrystallization, such as subgrain formation in high stress domains like contacts between large porphyroclasts (Fig. 2.3C) in coarse porphyroclastic, porphyroclastic fine-grained and protomylonitic fabrics.

Furthermore, at these early stages of shear zone evolution, polyphase mixtures containing Opx neoblasts are only observed occasionally in diffuse patches. The proportion of elongated to equiaxial porphyroclasts increases with increasing strain until mylonitic conditions (e.g., Fig. 2.4A/B). Even with elongation in places exceeding the thin section scale (aspect ratio > 1:50) these porphyroclasts are

single crystals. In mylonites, elongated Opx grains are often folded, kinked, and sheared (e.g., Fig. 2.8A/B). In this texture type both equiaxial porphyroclasts and elongated single crystals form neoblast tails. In ultramylonites, only remnants of elongated Opx grains are preserved in the fine-grained polymineralic matrix (Fig. 2.4C). Porphyroclasts and elongated grains display thin (< 10 μm) exsolution lamellae of Cpx (e.g., Fig. 2.8C). In all microstructures, Ol and Opx neoblasts in Opx tails show a linear correlation in grain size but with dependence on the microstructure type (Fig. 2.9).
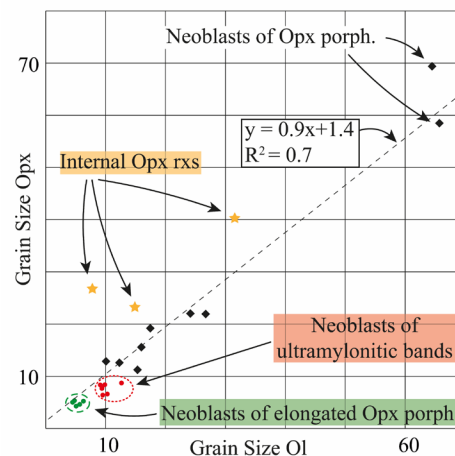
Fig. 2.9. *Grain sizes of Ol and Opx neoblasts from equiaxial Opx tails (black diamonds), internal Opx recrystallization areas (orange stars), ultramylonitic bands (red dots) and elongated Opx single crystal tails (green dots). Linear correlation line (black dashed line) is indicated.*

Polymineralic tails are formed adjacent to equiaxial or elongated Opx porphyroclasts predominantly in mylonites. They are dominated by Ol and Opx ± Cpx, Pl, Prg, Spl (e.g., Fig. 2.7D-v). For porphyroclasts, but more clearly for elongated Opx single crystals, neoblasts are concentrated at porphyroclast boundaries orientated perpendicular to the foliation (Fig. 2.8A). Here, porphyroclast grain boundaries are lobate (Fig. 2.8C *3) and have indentations/embayments filled with Ol neoblasts (Fig. 2.7C *2). Most neoblasts (Opx+Ol) have a highly irregular grain shape with lobate grain boundaries (Fig. 2.8D) and in places bottle neck structures (Fig. 2.8D *1). Small Spl neoblasts are often present as interstitial grains at triple junctions (Fig. 2.8C). The phase mixtures are dominated by Ol (av. 56%, range: 18-62%) and Opx (av. 37%, range: 16-77%; e.g., Fig. 2.7D-v, 2.8D-iv) with both together forming 87-97% (av. 93 %) of the total area-%. Cpx abundances are 2-11% (av. 5%). Accessory minerals

(< 1%) are Spl, Pl and Prg. Mean Ol grain sizes for this microstructure type vary between 4 and 32 µm (av. 13 µm). Opx grain sizes vary between 4 and 40 µm (av. 14 µm). In general, Ol and Opx neoblasts at porphyroclast boundaries display a slightly smaller grain size (~6 µm) than distal neoblasts and have an equiaxial shape (e.g., Fig. 2.8C). Cpx has an average grain size of 10 µm (range: 4-26 µm). Spl, Pl and Prg average grain sizes are 5 µm. Ol and Opx neoblasts have relatively high average aspect ratios of 1.8 (Ol, range: 1.6-2.0) and 1.7 (Opx, range: 1.6-2.0). Thin, elongated neoblasts located at the contact area of Opx+Ol and Cpx+Ol dominated tails have the highest aspect ratios for Ol (2.0) and Opx (2.0) of this study. Here, GBAs are present for up to several hundred micrometers in length following a general SPO dominantly formed by the long axes of Ol neoblasts (Fig. 2.7C white dashed lines). GBAs are oriented oblique (~40°) to the trace of the contact areas. Additionally, GBAs intensify towards the contact area. GBAs are more pronounced with increasing distance to the porphyroclast (Fig. 2.8C). Occasionally, elongated neoblasts of Opx are also present in the center of Opx derived tails (Fig. 2.8C). At transition zones from Opx neoblast tails to almost monomineralic Ol areas, no such grain shapes are observed. Ol and Opx neoblast SPOs are mostly oriented slightly oblique to the foliation (within 20°), with Opx displaying a wider distribution (e.g., Fig. 2.7D-vii/viii). Phase boundaries form on average 65% of all boundaries. The remaining 35% of grain boundaries are dominated by Ol-Ol (av. 66%) and Opx-Opx (av. 31%) boundaries (suppl. data S2.1). On average 75% of Opx boundaries are Opx-Ol, and 55% of Cpx boundaries are Cpx-Ol (suppl. data S2.1). For Pl and Prg, Opx is the main neighboring phase. Besides a generally weak neoblast Opx CPO (J index av. 1.7, range: 1.3 -2.1), Opx porphyroclasts have a strong imprint on the crystallographic orientations of Opx neoblasts (e.g., Fig. 2.8D-viii). For 8 of 10 analyzed Opx neoblast CPOs at least two orientations were identical to the porphyroclast or arranged in girdles together with the clast. Often a maximum is present around porphyroclast orientations (e.g., Fig. 2.8D-viii). A rotation of neoblast orientations has mostly been observed for [001]. Olivine neoblasts show no or weak CPOs with an average J index of 1.6 (range: 1.3-2.2; e.g., Fig. 2.8D-ix).

2.5.2 Intracrystalline and isolated pyroxene microstructures

2.5.2.1   Isolated clinopyroxene microstructures

Fig. 2.10. *Example microstructures of isolated Cpx and interface Cpx-Opx recrystallization in the mylonite texture type. Left BSE overview shows their locations between pyroxene clasts (arrows= exsolution lamellae). **A**-i. Neoblast assemblage between Cpx porphyroclasts (1, 2) with (white arrows) Opx neoblast adjacent to Opx exsolution lamellae. A-ii. Average grain sizes. A-iii. Number of grains per phase. A-iv. Average aspect ratios. A-v. Modal composition. A-vi. Phase and grain boundary percentages. A-vii. Rose diagram of Cpx neoblast long axes. A-viii. ODF of Cpx neoblasts (white dots = Cpx 1 orientations). A-ix. Pole figure of Opx neoblast orientations. **B**-i. Interface neoblast area between Cpx 2 and Opx 3 porphyroclasts (arrows= exsolution lamellae). B-ii. Neoblast av. Grain sizes. B-iii. Grains per phase. B-iv. Average aspect ratio. B-v Modal composition. B-vi. Phase and grain boundary percentages. B-vii. Pole figure of Opx neoblast orientations (red dots= Opx 3 orientations). B-viii. Pole figure of Cpx neoblast orientations (red dots= Cpx '2' orientation). B-ix. Rose diagram of Opx neoblast long axes. B-x. Rose diagram of Cpx neoblast long axes. High resolution, digital version is included on the CD.*

Isolated Cpx recrystallization is restricted in between bigger pyroxene clasts with little or no connection to the matrix (Fig. 2.10). Due to the relatively low abundance of Cpx, only two exemplary microstructures were analyzed, both of them in mylonites (La-19, Fig. 2.10A/B).

The neoblast assemblage is controlled by the bordering porphyroclasts. Close to Cpx porphyroclasts it is dominated by Cpx (88%) with minor abundances of

Opx (6%) and Spl (1%) (Fig. 2.10A-v). Compared to other microstructure types, pargasite has a relatively high abundance of 5% (Fig. 2.10A-v). Opx grains are often adjacent to Opx exsolution lamellae (Fig. 2.10A-i white arrows). Cpx grains form the largest grains (10 µm; Fig. 2.10A-ii). Grain sizes of the secondary phases are: Opx 5 µm, Spl 3 µm, Pl 4 µm and Prg 6 µm (Fig. 2.10A-ii). A well-dispersed second phase content of only 12% creates 40% phase boundaries (Fig. 2.10A-vi). 98% of all grain boundaries are Cpx-Cpx contacts (suppl. data S2.1).

Isolated neoblast areas between Opx and Cpx porphyroclasts are weakly connected to the matrix in the thin section plane (Fig. 2.10B-i). A two-phase mixture of Opx and Cpx is observed (66% Opx, 34% Cpx) with abundances of other phases (Prg, Spl) < 0.5% (Fig. 2.10B-v). Opx and Cpx form similar sized grains (Opx= 9 µm, Cpx= 8 µm; Fig. 2.10B-iii) and have a similar SPO (Fig. 2.10B-ix/x). 45% of the total boundary length are phase boundaries and 55% are grain boundaries (Fig. 2.10B-vi). Both Opx and Cpx form 50% of the grain boundaries (suppl. data S2.1). Also, in regard to phase boundary distribution, Cpx and Opx have an almost identical share of ~60% Cpx-Opx of their total boundaries (suppl. data S2.1).

Only the microstructure displayed in Figure 2.10A contains enough Cpx grains to determine a CPO. Cpx neoblast [001] orientations are similar to the porphyroclast [001] orientation (Fig. 2.10A-viii). The [100] and [010] axes show less dependence on the porphyroclast orientation (Fig. 2.10A-viii). Opx and Cpx neoblast orientations are similar (Fig. 2.10A-viii/ix).

2.5.2.2 Intracrystalline and isolated orthopyroxene microstructures
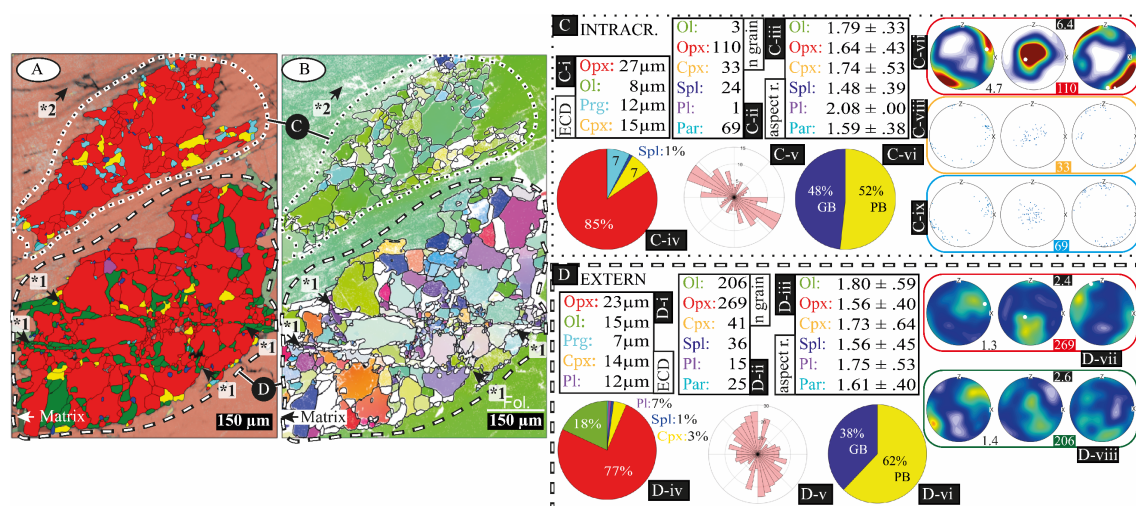
Fig 2.11. *For figure caption see next page.*

←Fig. 2.11. Example of intracrystalline neoblast assemblage in Opx porphyroclast next to a mixed neoblast assemblage connected to matrix (location given in Fig. 2.7A). **A.** *EBSD phase map (phase colors as in ECD, aspect ratio and grain number tables). Annotation for (black dotted line) intracrystalline neoblast area (data in C), (white dashed line) neoblast area in contact with the matrix (data in D), (*1) aligned mixed neoblasts, (*2) crack in the porphyroclast.* **B.** *Texture map. Same annotations as in A.* **C.** *Microstructural data of intracrystalline area (black dotted line in A/B). C-i. Average ECD. C-ii. Grains per phase. C-iii. Average aspect ratio. C-iv. Modal abundances. C-v. Opx neoblast SPO. C-vi. Phase and grain boundary percentages. C-vii. Orthopyroxene ODF. C-viii. Pole figure of Cpx neoblast orientations. C-ix. Pole figure of Prg neoblast orientations.* **D.** *Microstructural data of neoblast area in contact with the matrix (white dashed line in A/B). D-i. Average ECD. D-ii. Grains per phase. D-iii. Average aspect ratio. D-iv. Modal abundances. D-v. Opx neoblast SPO. D-vi. Phase and grain boundary percentages. D-vii. Orthopyroxene ODF. D-viii. Olivine ODF. High resolution, digital version is included on the CD.*

Isolated Opx microstructures are neoblast assemblages not in contact with the Ol-rich matrix. They form either intracrystalline (Fig. 2.11A/B black dotted) or at contacts between two or more pyroxene porphyroclasts (Fig. 2.10B-i). As neoblasts assemblages at Opx-Cpx porphyroclast contacts were already described in section 2.5.2.1, here we focus on intracrystalline neoblast assemblages in Opx porphyroclasts.

Opx is the most abundant phase (85%; Fig. 2.11C-iv). Clinopyroxene and Prg have an identical proportion of 7%, which is the highest Prg proportion of all analyzed microstructures (Fig. 2.11C-iv). Ol is an accessory phase (< 1%). Opx neoblast grain sizes are significantly smaller at the Opx+Cpx porphyroclast interface (av. 9 μm; Fig. 2.10B-ii) than in intracrystalline sites (av. 27 μm; Fig. 2.11C-i). Additionally, in intracrystalline areas Opx neoblasts have larger grain sizes than all other, mostly interstitial phases (Prg av. 12 μm; Cpx av. 15 μm, Spl av. 7 μm; Fig. 2.11C-i). Opx aspect ratios are low (1.64; Fig. 2.11C-viii). Opx grain SPO is perpendicular to the long axis of the host porphyroclast (Fig. 2.11C-v). Intracrystalline areas have 52% phase boundaries and 48% grain boundaries (Fig. 2.11-vi). 90% of these grain boundaries are Opx-Opx contacts (suppl. data S2.1). Pargasite, as the second most abundant phase, is mostly in contact with Opx (80% of the total Prg boundaries are Prg-Opx boundaries). The strong CPO of intracrystalline Opx grains is clearly related to the host porphyroclast orientation (Fig. 2.11C-vii). The orientations of Cpx and Prg neoblasts are similar (Fig. 2.11C-viii/ix).

2.5.3 Ultramylonitic bands

2.5.3.1   Clinopyroxene in ultramylonitic bands

(Ultra)mylonitic matrix assemblages of predominantly Ol and Cpx are present in mylonites and ultramylonites (Fig. 2.12). They are either found as single bands in coarser grained, almost monomineralic Ol matrix or as layers of ultramylonitic bands with multiple Ol+Cpx or Ol+Opx dominated layers (Fig. 2.12). Three examples of Cpx+Ol dominated ultramylonitic bands were analyzed in mylonitic samples (e.g., Fig. 2.12E/G).

Depending on the analyzed area, Ol (av. 52%, range: 41-64%) or Cpx (av. 38 %, range: 26-50%) is the dominant phase (e.g., Fig. 2.12E/G-i). Ol and Cpx together make up, on average, 92% of the total area (range: 90-96 %). The most abundant minor phase is Pl (av. 7%, range: 6-8%). Opx and Spl have, on average, a proportion of 2% and 1%, respectively. Average neoblast grain sizes are Ol 10 μm (range: 9-11 μm), Cpx 9 μm (range: 8-11 μm) and Pl 11 μm (range: 10-11 μm). Unlike the Cpx+Ol assemblages in the tails of Cpx porphyroclasts, where Cpx neoblasts are larger than Ol neoblasts, in the ultramylonitic bands they have a similar grain size within error (e.g., Fig. 2.12E/G-v). Minor phases have average grain sizes of Opx 7 μm (range: 7-8 μm), Spl 5 μm (range: 4-6 μm) and Prg 6 μm (range: 4-9 μm). Average aspect ratios are 1.7 (Cpx), 1.8 (Ol), 1.6 (Opx, Spl) and 1.8 (Prg). Cpx and Ol show mostly a clear SPO (Fig. 2.12E-iii/iv). Long axes of Ol neoblasts are oriented at an angle of 10-15° to the foliation (e.g., Fig. 2.12E-iii, 12G-iv). For Cpx-Ol band of Figure 2.12G a second Cpx maximum is present oriented 90° to the olivine SPO (Fig. 2.12G-iii/iv). Orientation maxima of Cpx show in general a larger spread than Ol maxima (e.g., Fig. 2.9E-iii/iv). Cpx ultramylonitic bands have the highest ratio of phase mixing in all analyzed microstructure types (av. 69% phase boundaries). Opx forms more phase boundaries with Ol (66% of total Opx boundaries) than with Cpx (28% of total Opx boundaries) highlighting the relatively small abundance of Cpx-Opx mixtures (suppl. data S2.1). For Cpx, 76% of boundaries are contacts with Ol and 15% are grain boundaries (suppl. data S2.1). Plagioclase forms most phase boundaries with Ol (40%) and with Cpx (34%). Cpx neoblasts show no (Fig. 2.12G-viii) or weak CPO (av. J index 1.6, range: 1.3-2.0; Suppl. data S2.3). The only Cpx CPO present is defined by [100] perpendicular to the foliation plane, [010] dispersed around Y and [001] dispersed around the lineation (suppl. data S2.3). Olivine neoblasts show absent or very weak CPO (av. J index 1.2 (lowest measured), range: 1.1-1.3).
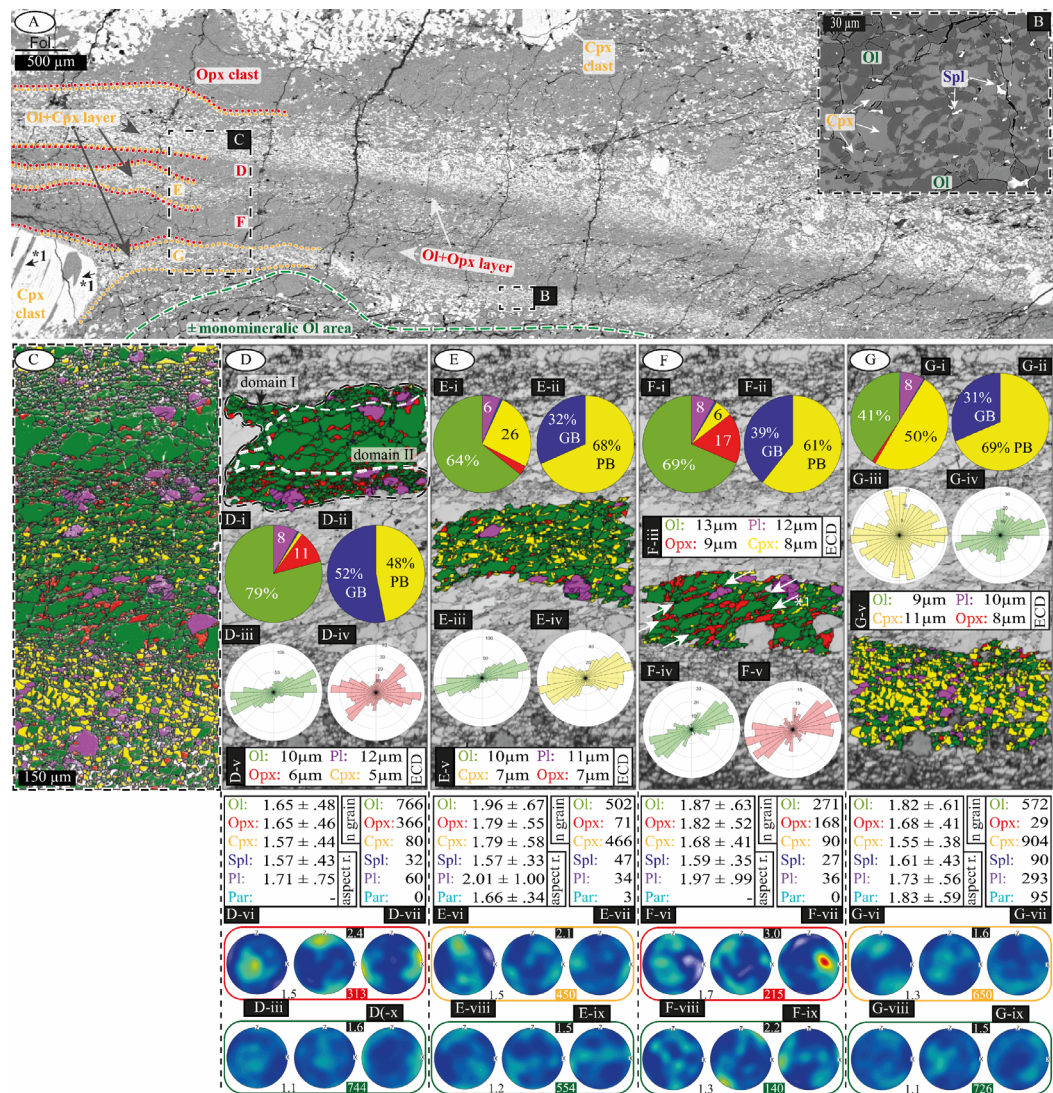
Fig. 2.12. *Ultramylonitic band with layers of predominantly Ol+Opx and Cpx+Ol in the mylonitic texture type.* **A.** *BSE overview with main microstructures and locations of map B, EBSD map C and the analyzed Ol+Opx (D, F) and Ol+Cpx (E, G) layers. Annotated is (*1) intracrystalline replacement of Cpx porphyroclast by Opx+Plg along Opx exsolution lamellae.* **B.** *BSE image of ultramylonitic Cpx+Ol layer with interstitial Spl.* **C.** *EBSD phase map of analyzed microstructures D-G (phase colors as in ECD, aspect ratio and grain number tables).* **D.** *Upper Ol+Opx layer. Finer grained domain I and coarser grained domain II are indicated. D-i. Modal abundances. D-ii. Phase and grain boundary percentages. D-iii. Ol neoblast SPO. D-iv. Opx neoblast SPO. D-v. Average ECD. D-vi. Av. aspect ratio. D-vii. Number of grains. D-viii. Opx neoblast ODF. D-ix. Ol neoblast ODF.* **E.** *Upper Ol+Cpx layer. E-i. Modal abundances. E-ii. Mixing intensity. E-iii. Ol neoblast SPO. E-iv. Cpx neoblast SPO. E-v. Average ECD. High resolution, digital version is included on the CD.*

← *Fig. 2.12. F. E-vi. Av. aspect ratio. E-vii. Grain amounts. E-viii. Cpx neoblast ODF. E-ix. Ol neoblast ODF. Lower Ol+Opx layer. GBAs are indicated with *1 and white dashed lines. F-i. Modal abundances. F-ii. Mixing intensity. F-iii. Average ECD. F-iv. Ol neoblast SPO. F-v. Opx neoblast SPO. F-vi. Av. aspect ratio. F-vii. Number of grains. F-viii. Opx neoblast ODF. F-ix. Ol neoblast ODF. G. Lower Ol+Cpx layer of EBSD map C. G-i. Modal abundances (area %). G-ii. Mixing intensity. G-iii. Cpx neoblast SPO. G-iv. Ol neoblast SPO. G-v. Average ECD. G-vi. Av. aspect ratio. G-vii. Grain amounts. G-viii. Cpx neoblast ODF. G-ix. Ol neoblast ODF.*

2.5.3.2   Orthopyroxene in ultramylonitic bands

Corresponding to matrix areas of Cpx+Ol, Ol+Opx ultramylonitic matrix assemblages also form layers of ultramylonitic bands (Fig. 2.12D/F) or are present as isolated areas in almost monomineralic Ol matrix. At places, the transition from Opx porphyroclast tails into an ultramylonitic bands is visible (Fig. 2.7A).

The microstructures are dominated by Ol (av. 74%, range: 69-79%) and Opx (av. 14%, range: 11-17%). Minor phases are Cpx (av. 4%, range: 1-6%), Pl (8%, range: 0) and Prg (<1%, range: 0-1%) (e.g., Fig. 2.12D/F-i). In the ultramylonitic layer of Figure 2.12D, domains of fine-grained mixed assemblages (Opx, Ol, Pl, Cpx, Spl; domain I) and of coarser grained (>25 μm) Ol neoblasts (domain II) are present. In domain I, Opx and Ol neoblasts yield an average size of 7 μm. Cpx and Spl neoblasts have with 6 and 5 μm similar sizes. Pl (av. 18 μm) forms bigger grains (e.g., Figs. 2.12D-v, 2.12F-iii). In domain II, Opx (av. ECD 6 μm, 11 area %) is present along Ol grain boundaries, sometimes associated with smaller Ol neoblasts (Fig. 2.12D). Fine grained Opx-Ol mixtures along coarser grained Ol neoblasts are also present in other Ol+Opx ultramylonitic layers (Fig. 2.12F *1). In general, grain sizes decrease towards contact areas of neighboring Cpx dominated layers (e.g., Fig. 2.12D). Opx (av. 1.7) and Ol (av. 1.8) neoblasts display high aspect ratios (e.g., Fig. 2.12D/F-vi) and a strong SPO mostly slightly oblique (~25°) to the foliation and parallel to the aligned fine grained Opx+Ol assemblages on Ol grain boundaries (e.g., Fig. 2.12D-iii/iv, 2.12F-iv/v). On average, phase boundaries make up 55% (range: 48-61%) of the total boundaries. 84% (range: 77-90%) of the remaining grain boundaries are Ol-Ol boundaries. Despite Opx being the second most abundant phase, Opx-Opx boundaries only form 8 % (range: 6-10%) of total grain boundaries. Opx neoblasts' [001] axes are aligned parallel to the lineation (Fig. 2.12D/F-viii). Overall, Opx CPOs are the weakest Opx CPOs present in our samples (J index av. 1.5, range: 1.4-1.7). Olivine neoblasts display no CPO (J index av. 1.3, range: 1.1-1.5; e.g., Fig. 2.12D/F-ix).

2.6   Mineral chemistry and thermometry

Geochemical data from pyroxene porphyroclast and neoblasts (mylonitic samples, La 19) were obtained to identify possible compositional changes during the formation of neoblasts. Accordingly, analysis of porphyroclasts, isolated and intracrystalline microstructures with low mixing intensities, and of thoroughly mixed polymineralic tails and ultramylonitic bands were performed. Additionally, Ol porphyroclast and almost monomineralic olivine neoblast assemblages were analyzed for Ol major and trace element abundances in ultramylonitic samples (La-11). Detection limits and the microprobe data are displayed in supplementary data S2.5 and S2.6, respectively. Additional compositional figures of pyroxenes and Ol are displayed in supplementary data S2.8 and S2.9.

→ *Fig. 2.13. Geochemical data from porphyroclasts, neoblasts of intracrystalline/ isolated areas, from porphyroclast tails and ultramylonitic bands. A. Al$_2$O$_3$ vs Cr$_2$O$_3$ of Opx. Arrows illustrate trends of neoblasts (solid) and porphyroclasts (dashed). B. Al$_2$O$_3$ vs TiO$_2$ of Opx. C. Mg# vs Cr$_2$O$_3$ for Opx. D. Al$_2$O$_3$ vs Cr# for Opx. Arrow illustrates trend for porphyroclasts. E. Al$_2$O$_3$ vs Cr$_2$O$_3$ of Cpx. Arrows illustrate trends of neoblasts and porphyroclasts. F. Al$_2$O$_3$ vs TiO$_2$ of Cpx. G. Mg# vs Cr$_2$O$_3$ of Cpx. H. Al$_2$O$_3$ vs Cr# for Cpx. Arrow illustrates trend for porphyroclasts. I. Mg# vs MnO of Ol from almost monomineralic porphyroclast-neoblast assemblages (black outlined symbols) from Cpx+Ol mixtures of Cpx porphyroclast tails (yellow outlined symbols) and from Ol+Opx mixtures in Opx porphyroclast tails (red outlined symbols). J. Al$_2$O$_3$ vs. Ca/ (Ca+Na) of Cpx. High resolution, digital version is included on the CD.*
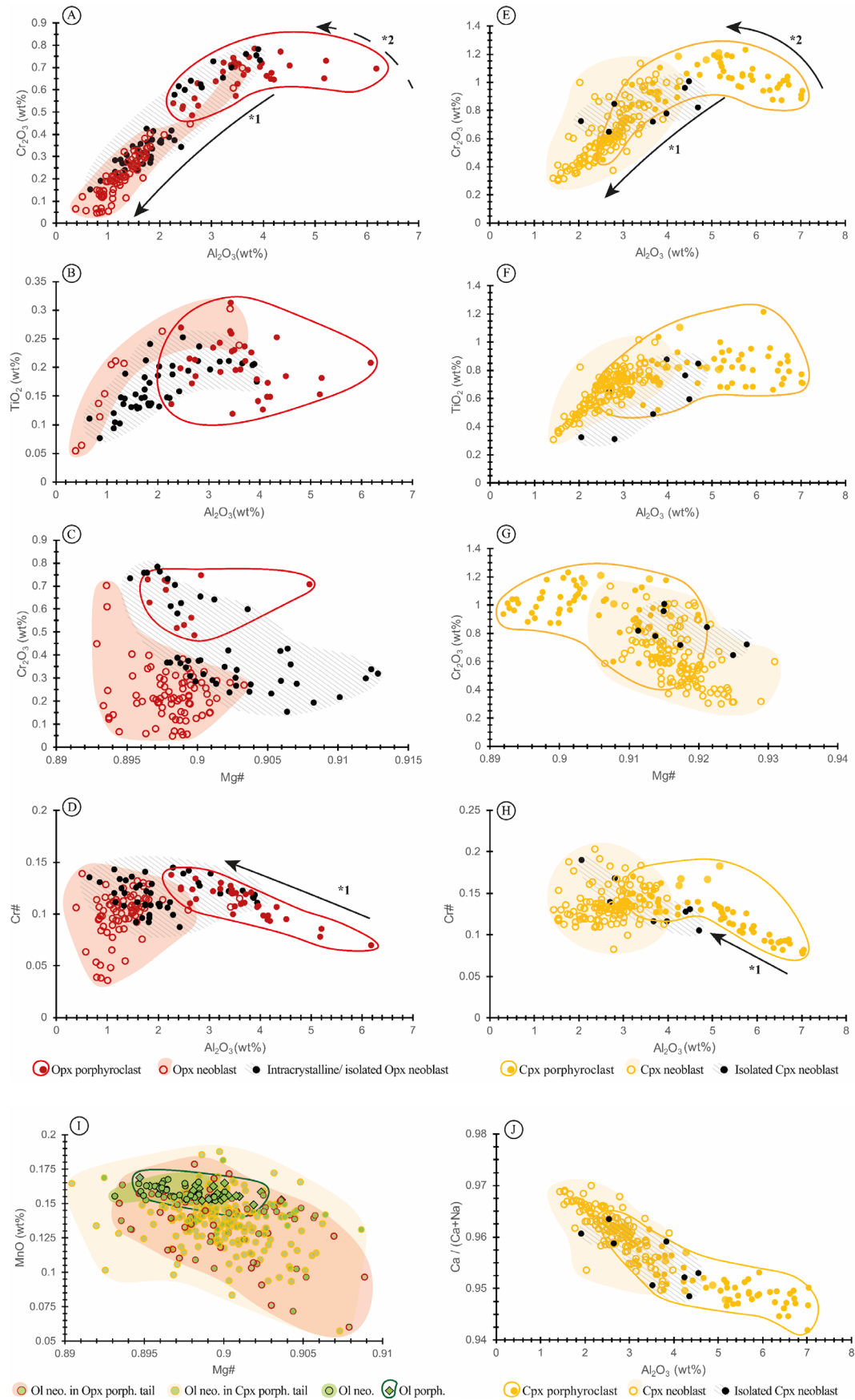
Fig 2.13. For figure caption see previous page.

2.6.1 Orthopyroxene

All analyzed Opx (intracrystalline/isolated and mixed neoblasts/porphyroclasts) is with Mg#s (molar Mg/(Mg+Fe)) exceeding 0.89, enstatite-rich (Fig. 2.13C). A systematic difference between Opx porphyroclasts and neoblasts is present. It is most prominent in the deviation of Al_2O_3 (Fig. 2.13A/B/D) and SiO_2 abundances (suppl. data S2.8) for porphyroclasts and neoblasts and by systematic changes of minor element abundances with respect to Al_2O_3 (Fig. 2.13C, suppl. data S2.8). Al_2O_3 was chosen as comparative oxide for pyroxenes because Al contents in Opx and Cpx decrease due to the transition from spinel to plagioclase facies and therefore correspondent to decreasing pressures (Borghini, 2008). Opx porphyroclasts display Al_2O_3 contents of 2.3 to 6.2 wt.% (Fig. 2.13A/B/C) and between 53.3 and 55.9 wt.% SiO_2 (suppl. data S2.8). In general, lower Al_2O_3 (0.4-3.6 wt.%; Fig. 2.13A/B/D) and higher SiO_2 contents (53.7 57.9 wt.%; suppl. data S2.8) were measured for Opx neoblasts. Isolated, intracrystalline Opx neoblasts show intermediate Al_2O_3 wt.% (Fig. 2.13A). Cr_2O_3 abundances for Opx porphyroclasts vary between 0.5 and 0.8 wt.% (Fig. 2.13A). Opx neoblasts have in general lower values (0.1-0.7 wt.%; Fig. 2.13A/C). Isolated, intracrystalline Opx neoblasts in contrast display the complete Cr_2O_3 range (Fig. 2.13A/C). For all Opx measurements with Al_2O_3 < 4 wt.% Cr_2O_3 decreases systematically with decreasing Al_2O_3 (Fig. 2.13A *1). TiO_2 porphyroclast abundances vary over almost the full spectrum measured between 0.12 and 0.31 wt.% (Fig. 2.13B). Lower TiO_2 abundances (< 0.12 wt.%) are only present for Opx neoblasts where TiO_2 decreases from 0.3 to 0.05 wt.% with decreasing Al_2O_3 content (Fig. 2.13B). For a given Al_2O_3 wt. %, intracrystalline Opx neoblasts tend to have lower TiO_2 abundances than mixed neoblasts (Fig. 2.13B). Systematic differences between porphyroclast Mg#s (range: 0.89-0.9) and neoblast Mg#s (range: 0.89-0.91) are very weak if present at all (Fig. 2.13C). High Mg#s (>0.9) are restricted to isolated, intracrystalline Opx neoblasts (Fig. 2.13C). Opx porphyroclast Cr#s (Cr# = Cr/(Cr+Al); range: 0.07-0.15) lay within the range of neoblast Cr#s (0.04-1.4) (Fig. 2.13D). An increase of Cr# in dependence on decreasing Al_2O_3 is only present for porphyroclast (Fig. 2.13D *1). No significant change in element abundances from porphyroclasts to neoblasts was observed for MnO and CaO (suppl. data S2.8). For FeO, a deviation between high abundances (≥ ~6.7 wt.%) of Opx neoblasts from tails and low abundances (≤ ~6.7 wt.%) for isolated, intracrystalline neoblasts is present (suppl. data S2.8).

2.6.2 Clinopyroxene

In all analyzed Cpx microstructures a systematic difference between the mineral chemistry of porphyroclasts, and neoblasts is present, which is particularly evident in Al_2O_3, SiO_2 wt.% (Fig. 2.13E/F/H/J, suppl. data S2.8) and Mg# (Fig. 2.13G). Cpx porphyroclasts display higher Al_2O_3 contents (3.1-7.0 wt.%) than neoblasts (1.4-4.7 wt. %) (e.g., Fig. 2.13E). SiO_2 contents for porphyroclasts (49.5--53.1 wt.%) are in general lower than for neoblasts (51.3-54.6 wt.%) (suppl. data S2.8). The lowest SiO_2 and the highest Al_2O_3 for Cpx neoblasts were measured in isolated microstructures (suppl. data S2.8, Fig. 2.13E). For porphyroclasts with Al_2O_3 > 4.5 wt.%, Cr_2O_3 contents increase with decreasing Al_2O_3 wt.% (Fig. 2.13E *2). Below 4.5 wt.% Cr_2O_3 abundances decrease with decreasing Al_2O_3 for all measured groups (Fig. 2.13E *1). For TiO_2, Cpx porphyroclasts depict variations (0.5 1.2 wt.%) independent from Al_2O_3 (Fig. 2.13F). TiO_2 neoblasts abundances of isolated and mixed microstructures tend to be lower than in porphyroclasts and decrease with decreasing Al_2O_3 (Fig. 2.13F). Mg#s range from 0.89 to 0.92 for Cpx porphyroclasts and from 0.91 and 0.93 for neoblasts (Fig. 2.13G). As for Opx porphyroclasts, the increase in Cr# coincides with a decrease in the Al_2O_3 content (Fig. 2.13H *1). Neoblast Cr#s mostly scatter around the highest values of porphyroclast Cr#s (Fig. 2.13H). Na2O and CaO abundances in neoblasts follow the trend already displayed in porphyroclasts. Na2O decrease (porph.: 0.8-0.5 wt.%, neo: 0.7-0.4 wt.%) and CaO increase (porph.: 21.4-22.9 wt.%, neo.: 22.1-23.4 wt.%) with Al_2O_3 (suppl. data S2.8). Ca/(Ca+Na) shows higher values for neoblasts than for porphyroclasts and generally increases with decreasing Al_2O_3 content (Fig. 2.13J).

2.6.3 Olivine

Ol porphyroclasts and their corresponding neoblasts display for major elements (Si, Mg, Fe, Mn, (Mg#); Fig. 2.13I, suppl. data S2.9) as well as for Ca (suppl. data S2.9) mostly congruent abundances with only slight variations if present at all (Fig. 2.13I). Most Al, Ti and Cr abundances were below the detection limit (suppl. data S2.9). Ol clasts have similar Mg#s (av. 0.9 ±0.002) as Ol neoblasts (av. 0.897 ±0.002) (Fig. 2.13I). However, for all (n=10) except one microstructure neoblasts display consistently lower Mg#s than their porphyroclast (suppl. data S2.9). Ca contents are lower in Ol porphyroclasts (av. 72 ppm) than in Ol neoblasts (av. 87 ppm). Ti, Cr and Al abundances were despite low detection limits for trace elements not measured in significant amounts in Ol porphyroclast tails (neo. /porph.; suppl. Data S2.9).

Mg#s (range: 0.89-0.91) and Mn abundances (range: 0.06-0.19) from Ol neoblasts of phase mixtures from pyroxene tails are in general more dispersed than those from almost monomineralic Ol assemblages (av. 0.9, range: 0.89-0.9) (Fig. 2.13I, suppl. data S2.9). In general, Ol neoblasts in phase mixtures display slightly higher abundances and higher variabilities for trace elements (Ti, Al, Cr, Ca) than Ol neoblasts of almost monomineralic areas (suppl. data S2.9). Ol neoblasts in Cpx tails have the highest measured trace element abundances (av. Ti 38 ppm, Al 6 ppm, Cr 67 ppm, Ca 398 ppm) (suppl. data S2.9). Ol neoblasts from Opx tails have intermediate trace element abundances (av. Ti: 19 ppm, Al: 12 ppm, Cr 18 ppm, Ca 113 ppm; suppl. data S2.9). In conclusion, Ol neoblasts in phase mixtures display a broader range, and a higher abundance (predominant in Cpx phase mixtures) in trace elements. In addition, these olivines have a broader range of Mg# than Ol neoblasts of almost monomineralic Ol assemblages. However, no trends are observed as present for Opx and Cpx.

2.6.4 Thermometry

Average T estimations for Opx porphyroclasts are 910 ± 21 °C (T_{BKN}), 880 ± 13 °C (T_{Ta98}) and 935 ± 65 °C (T_{Ca-Opx}) (Fig. 2.14A, suppl. data S2.10). In general, the results of the two-pyroxene thermometers (T_{BKN} and T_{Ta98}) and the Ca-in-Opx thermometer are within error (Fig. 2.14A, suppl. data S2.10). Exceptions are two porphyroclasts, which show higher T_{Ca-Opx} temperatures than T_{BKN} and T_{Ta98} estimates of the same data (Fig. 2.14A). For isolated Opx microstructures all average T estimates (857 ± 36 °C (T_{BKN}), 814 ± 34 °C (T_{Ta98}), 858 ± 12 °C (T_{Ca-Opx}) and 829 ± 37 °C (T_{1Cpx}), Fig. 2.14A, suppl. data S2.10) overlap in their standard deviation (Fig. 2.14A, suppl. data S2.10). Temperature calculations for neoblasts in mixed assemblages derived from Opx porphyroclasts are 886 ± 4 °C (T_{BKN}), 828 ± 31 °C (T_{Ta98}), 854 ± 39 °C (T_{Ca-Opx}) and 867 ± 10 °C (T_{1Cpx}) (Fig. 2.14A, suppl. data S2.10). They agree for a given geothermometer (T_{BKN} / $T_{Ca\,Opx}$) for all measured microstructures (Fig. 2.14A).

Cpx porphyroclast T estimations are on average 891 ± 25 °C (T_{BKN}), 864 ± 34 °C (T_{Ta98}) and 851 ± 30 (T_{1Cpx}) (Fig. 2.14B, suppl. data S2.10). The T_{BKN} estimations all lie in a close range between 862 °C and 924 °C (Fig. 2.14B). T_{1Cpx} estimations for Cpx porphyroclasts yield systematically lower T (range: 817-891 °C; Fig. 2.14B). Isolated Cpx neoblasts yield average T (°C) estimates of 837 ± 8 (T_{BKN}), 797 ± 10 T_{Ta98}), 880 ± 35 (T_{Ca-Opx}) and 811 ± 12 (T_{1Cpx}) (Fig. 2.14B). Neoblasts in mixed assemblages derived from Cpx porphyroclasts have estimates (°C) of 871 ± 14 (T_{BKN}), 841 ± 22 (T_{Ta98}), 885 ± 25 (T_{Ca-Opx}) and 859 ± 16 (T_{1Cpx}) (Fig. 2.14B, suppl. data S2.10). Calculated

Ts for different geothermometers are in general consistent for all measured microstructures in multiple samples (Fig. 2.14B, suppl. data S2.10). In addition, T estimations of the different geothermometers agree with each other within error. Data from assemblages of ultramylonitic bands are separated according to their composition. Ol+Opx dominated layers yield average T (°C) estimates of 859 ± 32 (T_{BKN}), 814 ± 21 (T_{Ta98}), 831 ± 22 (T_{Ca-Opx}) and 838 ± 25 (T_{1Cpx}) (Fig. 2.14C, suppl. data S2.10). Cpx+Ol dominated ultramylonitic layers yield similar average T estimates of 858 ± 18 (T_{BKN}), 818 ± 18 (T_{Ta98}), 833 ± 17 (T_{Ca-Opx}) and 841 ± 20 (T_{1Cpx}) (Fig. 2.14C, suppl. data S2.10).
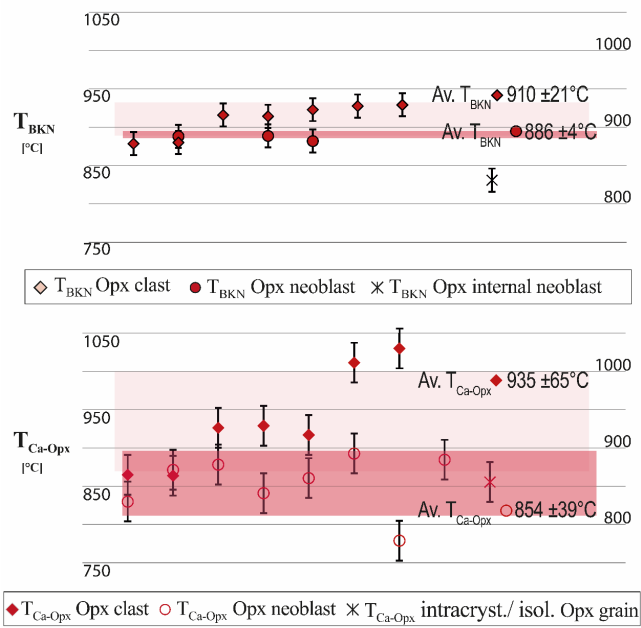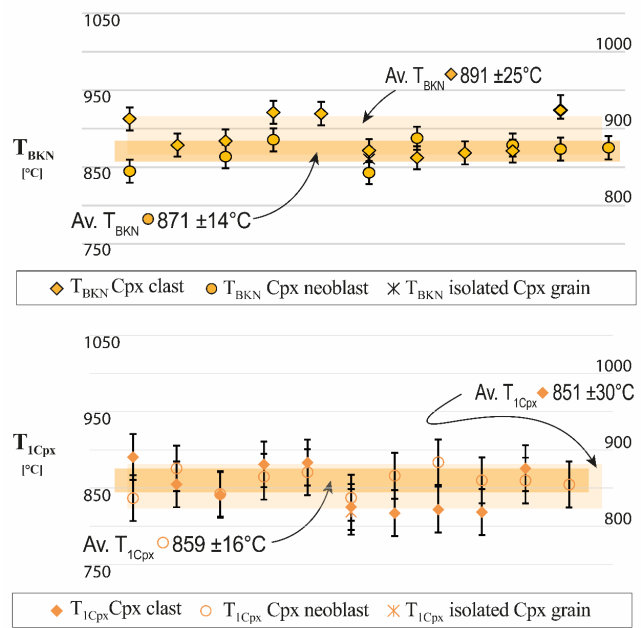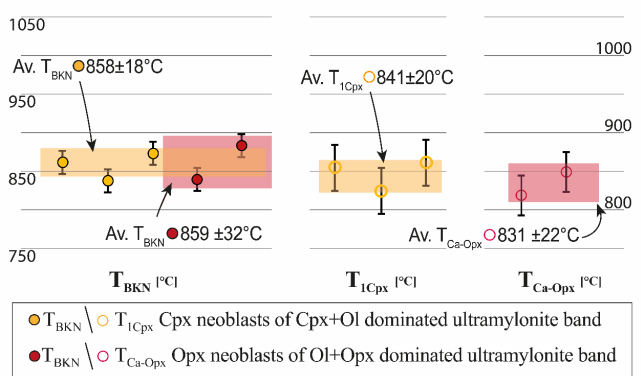
Fig. 2.14. *Geothermal estimations for porphyroclasts (Opx/ Cpx= diamond symbols), neoblasts from intracrystalline and isolated microstructures (Opx/ Cpx= cross symbols), neoblasts of polymineralic tails and ultramylonitic bands (Opx/ Cpx= circle symbols). Displayed are results from T_{BKN}, T_{Ca-Opx} (Brey and Köhler, 1990) and T_{1Cpx} geothermometers (Nimis and Taylor, 2000). High resolution, digital version is included on the CD.*

2.7   Discussion

During the shear zone evolution, porphyroclasts of all three primary phases (Ol, Cpx and Opx) formed tails of neoblasts. Where olivine formed mainly monomineralic tails (Figs. 2.5 and 2.6; av.: 17% phase and 83% grain boundaries), the ortho- and clinopyroxene porphyroclasts formed polymineralic tails of the original pyroxene and olivine, with minor amounts of the other pyroxene, spinel, and plagioclase (Figs. 2.7, 2.8). These polymineralic tails are well mixed (av.: ~65% phase and ~35% grain boundaries) and continue into ultramylonitic bands in some cases (Figs. 2.5, 2.12). In the following, possible formation processes of almost monomineralic olivine and polymineralic pyroxene tails will be discussed and their role on phase mixing processes will be evaluated.

2.7.1   Olivine porphyroclasts

Dynamic recrystallization of Ol porphyroclasts is observed in low strained samples (coarse porphyroclastic texture; Fig. 2.3A), underlining olivine's role as weakest phase under most upper mantle conditions (Boullier and Gueguen, 1975; Karato and Wu, 1993). No phase mixing, related to dynamic recrystallization, was observed in low strained textures (coarse porphyroclastic, fine grained porphyroclastic). Nevertheless, dynamic recrystallization has been shown to be the driving force of grain size reduction and strain localization during early shear zone evolution in Lanzo (Kaczmarek and Tommasi, 2011).

Ol porphyroclast tails in mylonites and ultramylonites have an almost monomineralic assemblage and low mixing intensities (Figs. 2.5, 2.6). Often, associated neoblasts have a small to moderate deviation in misorientation angle (0-40°) from the porphyroclast orientation (Fig. 2.5F) with grain CPOs clearly related to clast orientations (Figs. 2.5G, 2.6A-x, 2.6B-ix). These results are consistent with those by Kaczmarek and Tommasi (2011) who also reported the internal deformation of Ol porphyroclasts (e.g., Fig. 2.5F) with a high density of subgrains and the predominance of small rotation angles (<15°) in correlated Ol misorientation histograms. Following Kaczmarek and Tommasi (2011), dynamic recrystallization of Ol porphyroclasts by SGR is therefore plausible to explain the formation of almost monomineralic tails in mylonite and ultramylonite samples. Contradictory for SGR are high misorientation angles of several grains directly at porphyroclast grain boundaries (Fig. 2.5F). However, rotations of individual grains accommodating ongoing deformation in the recrystallization tail could explain the variety and the presence of high misorientation angles (Sakai et al., 2014). Elongated, irregular grain shapes and lobate boundaries of distal grains and

their bigger grain size compared to those close to the Ol porphyroclast (Fig. 2.5B) indicate grain growth by GBM recrystallization in the tail (Fig. 2.5B). Following Kilian et al. (2011) who suggested a precipitation of K-feldspar along aligned grain boundaries and in cavities formed during dynamic recrystallizations (SGR+GBM), mixing structures along bigger Ol grains inside of recrystallization tail (Fig. 2.6A-I type I) and also on their edges (Fig. 2.6B-I type II) could indicate precipitation of Opx neoblasts during dislocation creep. Similarly, Czertowicz et al. (2016) reported microstructures similar as type I (Fig. 2.6A), with Opx neoblasts along Ol grain boundaries in the Anita Peridotite, New Zealand. Following Menegon et al. (2015), Czertowicz et al. (2016) suggest a precipitation of Opx from fluids in creep cavitations along Ol grain boundaries. The chemical components required for the Opx precipitation are thought to be mobilized along the grain boundaries.

2.7.2 Internal recrystallization of Opx and Cpx porphyroclasts

Pyroxenes rarely show evidence of porphyroclast recrystallization in coarse porphyroclastic and porphyroclastic fine grained textures (Fig. 2.3A/B). If present, formation of subgrains was observed to be limited to small areas close to the grain boundary (Fig. 2.3C).

In the (proto)mylonites, isolated and intracrystalline pyroxene microstructures have a host-phase dominated assemblage, low mixing intensities and neoblast orientations depending on the porphyroclast orientation (Figs. 2.10A/B, 2.11C). Phase mixing of Opx and Cpx is spatially dependent on exsolution lamellae of the porphyroclasts, resulting in low mixing intensities. The relatively high amount of Ti-pargasite (Prg) in isolated microstructures (Figs. 2.10A-v, 2.11C-iv), emphasizes the presence of liquids during neoblast formation and their rather late formation in terms of the shear zone evolution with T < 1050°C (Kaczmarek and Müntener, 2008). Consequently, high mobility of the fluid along fractures in porphyroclasts (e.g., Fig. 2.11A/B *2) and at grain boundaries is required. The relatively strong CPOs of isolated Opx and Cpx microstructures (Figs. 2.10A-viii, 2.11B/C-vii) often coincide with similar orientations of intermixed neoblasts of Prg and Cpx/Opx, respectively (Figs. 2.10A-ix, 2.11C-viii/ix). Concordance of amphibole (tremolite) and Cpx CPOs was reported by Kohli and Warren (2020) for deformed peridotites from the Shaka Transform Fault. The inherited amphibole CPO was explained by the shared, monoclinic crystal structure and a topo- or epitactic growth (Kohli and Warren, 2020; Putnis et al., 2006). Even at neoblast areas between Opx and Cpx clasts, phase mixing intensities are intermediate with neoblasts concentrating at boundaries of their respective host (Fig. 2.10B).

Low mixing intensities, orientations depending on the porphyroclast, and host phase dominated assemblages with high amounts of pargasite indicate fluid assisted dynamic recrystallization as formation process. A formation of pargasite by a local hydrous, Si-saturated melt is unlikely. Melt-rock reactions of such melt should be observable along grain boundaries in the matrix and especially at almost monomineralic Ol areas. Contrary, these microstructures are isolated and intracrystalline. As Figure 2.11 demonstrates neoblast tails adjacent to the intracrystalline microstructures which should be in contact with such melts rather show the crystallization of Ol neoblasts which would not be expected with hydrous Si-saturated melt. However, the small number of isolated pyroxene microstructures analyzed is only suitable for assumptions on the formation process behind pargasite.

2.7.3 Polymineralic tails adjacent to pyroxene porphyroclasts

Tails derived from the pyroxene porphyroclasts are different from Ol recrystallization tails and isolated and intracrystalline pyroxene recrystallization. The pyroxene derived tails are polymineralic, showing high mixing intensities. Furthermore, they show no similarity between porphyroclast and neoblast orientations. The most striking pattern for these microstructures is the occurrence of Ol and host phase neoblasts with secondary Pl and Spl directly at grain boundaries of the porphyroclasts (e.g., Figs. 2.7, 2.8). The Opx and Cpx dominated tails can be clearly distinguished in the samples (Fig. 2.4B). These observations indicate that these polymineralic tails were formed by reactions rather than by dynamic recrystallization. These reactions could be melt-rock reactions or metamorphic reactions.

2.7.3.1 Melt-rock reactions

Beside the replacement of Cpx by Opx+Pl at exsolution lamellae in Cpx porphyroclasts (e.g., Fig. 2.4B *4) no other melt-rock reaction described by previous studies (vermicular Opx growing at expense of deformed Ol, replacement of elongate Spl by undeformed Pl) were found in the studied microstructures. As most evidence of melt-rock reactions was described in low strain textures (Kaczmarek and Müntener, 2008; Müntener et al., 2005) and the replacement of Cpx is only present inside of porphyroclasts of higher strain textures these melt-rock reactions are interpreted to occur prior to the formation of the analyzed microstructures. Consistently, Müntener and Piccardo (2003) and Müntener et al. (2005) interpret the melt presence as a diffuse porous melt flow at a regional scale.

Melt-rock interactions in the northern Lanzo shear zone region were expressed by reactions 2.I and 2.II of Kaczmarek and Müntener (2008).
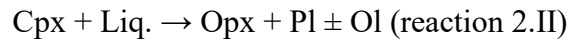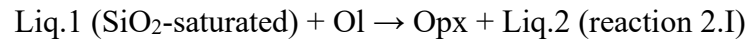
$$Liq.1 \ (SiO_2\text{-saturated}) + Ol \rightarrow Opx + Liq.2 \ (reaction \ 2.I)$$

$$Cpx + Liq. \rightarrow Opx + Pl \pm Ol \ (reaction \ 2.II)$$

Following Kaczmarek and Müntener (2008), these reactions lead to neoblast crystallization, which were subsequently deformed under moderate, broadly distributed stress. Fine grained, mixed assemblages found in mylonites (Ol+Pl+Opx) were thought to represent interstitial melts that crystallized once the solidus was hit. This led to the interpretation of melt presence during localized shearing (Kaczmarek and Müntener, 2008). Our observation, that ultramylonitic phase-mixtures of Opx+Ol and Cpx+Ol derive from polymineralic tails of pyroxene porphyroclasts, contradicts the melt-rock reactions 2.I and 2.II. To form Ol-rich phase mixtures close to pyroxenes, the melt would have to be Si-undersaturated. Locally Si-undersaturated melt due to dissolution and crystallization with differing phases (reaction 2.III) was described for the Othris peridotite (Dijkstra et al., 2002):

$$Opx + SiO_2\text{-undersaturated melt} \leftrightarrow Ol + SiO_2\text{-saturated melt (reaction 2.III)}$$
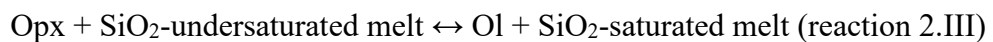
In regard to the observed microstructures, reaction (2.III) could explain the irregular margins of Opx porphyroclasts with numerous Ol embayments (e.g., Fig. 2.7C), combined with elongated Opx and Ol neoblasts in the surrounding mixed assemblage (e.g., Fig. 2.8B) which were also described for Othris peridotites (Dijkstra et al., 2002). Melt assisted shearing, melt-rock reactions, and the formation of a fine grained ultramylonitic matrix was also reported by Degli Alessandrini (2018) in sheared metagabbros of the lower crust. In the case of the Lanzo lherzolite, Cpx can also react with the melt (2.III), forming olivine. However, Si-undersaturated melt causing pyroxene dissolution and Ol crystallization cannot explain the occurrence of Pl (av. 6%) in phase mixtures of recrystallized Cpx porphyroclasts. As Pl grains are not interstitial, similar sized as Cpx and Ol neoblast and already present close to the Cpx porphyroclasts (Fig. 2.7C) a later stage formation of Pl seems implausible. Furthermore, Dijkstra et al. (2002) reported evidence of these reactions in tectonite protoliths, thus in the early shear zone evolution, and therefore postulated a formation temperature for those corrosion/dissolution reactions and the formation of fine-grained assemblages of 1100 °C. For the Lanzo shear zone, no such microstructures were observed in the less deformed textures (i.e., coarse-grained, and fine-grained porphyroclastic textures). Neoblasts from Opx and Cpx tails, as well as from ultramylonitic bands yield uniform temperatures ($869 \pm 18°$ C (T_{BKN}), $831 \pm 24°$ C (T_{Ta98}),

$862 \pm 37°$ C (T_{Ca-Opx}) and $856 \pm 18°$ C (T_{1Cpx}). As most geothermometers give a similar average calculated temperature (within error), estimates are thought to be accurate. Taylor (1998) showed that T_{BKN} overestimates temperatures of fertile peridotite (Nimis and Grütter, 2010). Accordingly, T_{Ta98} estimates are generally lower than T_{BKN} (Fig. 2.14). Differences between estimates of porphyroclast and neoblasts are thought to depict the degree of porphyroclast equilibration. In contrast to Kaczmarek and Müntener (2008) who observed compositional zoning of Opx porphyroclasts, most of our porphyroclast-neoblast pairs give similar calculated temperatures (Fig. 2.14), which indicates that porphyroclasts reached equilibrium with the neoblasts, possibly by enhanced diffusion. Lower temperature estimates for ultramylonites from previous work (La-11, 740 ± 16 °C (T_{Ca-Opx}), Linckens et al., 2015) however demonstrate that the innermost part of the shear zone accumulated strain over a longer interval of temperature. Therefore, our estimations of pyroxene reaction microstructures in mylonites, clustering around 860 °C (range T_{BKN}: 836-888 °C; Fig. 2.14), is consistent with estimates by Kaczmarek and Müntener (2008), whereas Linckens et al. (2015) give a minimum, subsolidus temperature for crystallization and phase mixing. Both T estimates are significantly lower than the formation temperature of phase mixtures postulated for Othris (Dijkstra et al., 2002).

2.7.3.2   Subsolidus net-transfer reactions

Subsolidus continuous net-transfer reactions, resulting from changing PT conditions, have been shown to be capable of forming (ultra)mylonitic Ol+ host phase mixtures (Dijkstra et al., 2004; Hidas et al., 2013; Newman et al., 1999). Kaczmarek and Tommasi (2011) already suggested that such reactions may have led to domains of intermixed two- or three-phase assemblages in the ultramylonites of Lanzo. Beside the exchange of PT sensitive elements (e.g., Al and Cr in pyroxenes; Ca in Opx), continuous net-transfer reactions as result of the Spl lherzolite to Pl lherzolite transition, lead to a systematic change of modal abundances and in the composition of reactants due to the crystallization of a new Al phase (Pl) (e.g., Rampone et al., 1993; Borghini et al., 2010). Previous studies have shown that the shear zone's activity has been under decreasing PT conditions of the transition from spinel to plagioclase peridotite facies, e.g., associated with continuous reactions involving plagioclase and spinel (Kaczmarek and Müntener, 2010, 2008; Kaczmarek and Tommasi, 2011). Olivine and Cpx neoblasts in Cpx tails are often associated with Pl (6%, 22% Pl-Ol boundaries, 64% Pl-Cpx boundaries of total Pl boundaries) and interstitial Spl (1 %, 44% Spl-Ol boundaries, 44% Spl-Cpx boundaries of total Spl boundaries, e.g., Fig. 2.7). The amount of Pl present in pyroxene tails varies between Cpx

tails (av. 6%) and Opx tails (av. 2%). In total, the obtained Pl abundances agree with field observations (1-5 wt. %) and are at the lower range of experimental (5-15 wt.%) literature data for Pl peridotites formed by this facies transition (Borghini et al., 2010; Furusho and Kanagawa, 1999; Newman et al., 1999). Furthermore, Pl is more abundant in areas where small amounts of coarse grained Spl is present, indicating an influence of the spinel-plagioclase transition expressed by:

Al-rich spinel$_0$ + Al-rich pyroxene$_0$ =

plagioclase + olivine + Al-poor pyroxene$_1$ + Cr-rich spinel$_1$

(reaction 2.IV; Borghini et al., 2010)

$2 (1-x) MgSiO_3 + (1-x) CaMgSi_2O_6 + MgAl_{2(1-x)}Cr_2xO_4 =$

enstatite + diopside + Cr-spinel

$(1-x) CaAl_2Si_2O_8 + 2 (1-x) Mg_2SiO_4 + x MgCr_2O_4$

anorthite + forsterite + Mg-Cr spinel (picochromite)

(reaction 2.V; Furusho and Kanagawa, 1999)
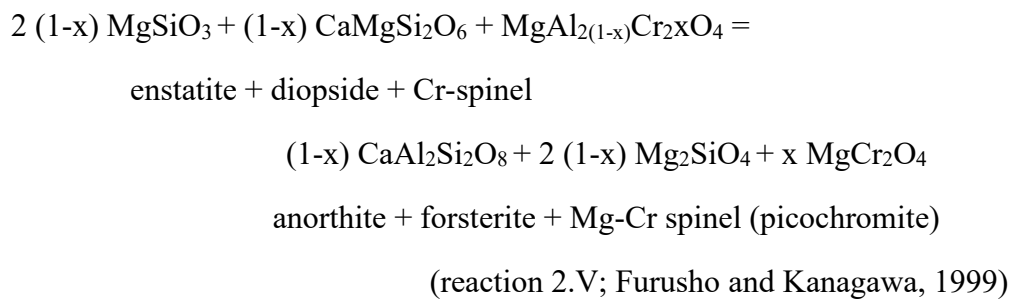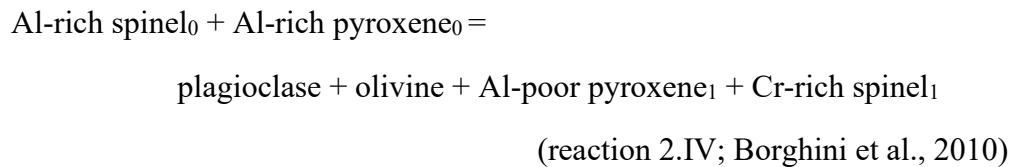
Microstructural observations of small, interstitial Spl (Figs. 2.7C, 2.12B) in neoblast phase mixtures coincide with observations from Borghini et al. (2010) and Furusho and Kanagawa (1999). Spl abundances (0.5-2%) measured in pyroxene tails are in the range of those reported by Borghini et al. (2010) (0.5-4 wt.%) and Furusho and Kanagawa (1999) (1.3-1.6 wt.%). As Cr-rich spinel remains stable within the plagioclase stability field down to pressures as low as ca. 0.3 GPa, spinel-plagioclase reactions (2.IV, 2.V) are thought to be continuous within the Pl stability field (Borghini et al., 2010). Clinopyroxene Ca/(Ca+Na) ratios increase with decreasing pressure (Borghini et al., 2010). Correspondingly, Cpx neoblasts exhibit higher Ca/(Na+Ca) ratios (i.e., lower pressures) than the porphyroclasts (Fig. 2.13J). Slightly higher amounts of Na2O in Pl of neoblasts compared to porphyroclastic abundances reported by Kaczmarek and Müntener (2008) in the mylonitic texture type could be explained by higher amounts of pargasitic amphibole in the former texture (Niida and Green, 1999). Variations of the Cr# (Fig. 2.13D/H), the decrease of Cr_2O_3 (Fig. 2.13A/E) and the significant Al decrease for neoblasts of both pyroxenes (Fig. 2.13A/E) in the Pl stability field in lherzolite compositions (Pl-out: 0.8-1.5 GPa, Borghini et al. (2010) and reference therein) agree with the predicted influence of Pl crystallization

combined with the Cr-Al partitioning between spinel and both pyroxenes by reactions 2.VII and 2.VIII:

$$MgAl_2O_4 + 2\ MgCrAlSiO_6 + 2\ CaMgSi_2O_6 =$$
$$MgCr_2O_4 + 2\ CaAl_2Si_2O_8 + 2\ Mg_2SiO_4$$
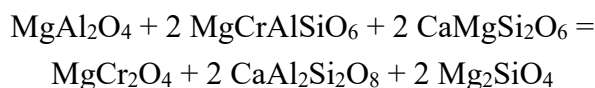
spinel + MgCr-Ts + diopside = Mg-chromite + anorthite + forsterite

(reaction 2.VII; Borghini et al., 2010)

$$MgAl_2O_4 + 2\ CaCrAlSiO_6 + 2\ Mg_2Si_2O_6 =$$
$$MgCr_2O_4 + 2\ CaAl_2Si_2O_8 + 2\ Mg_2SiO_4$$
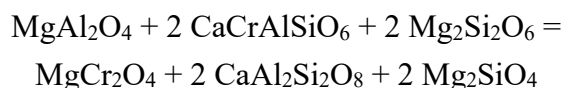
spinel + CaCr-Ts + enstatite = Mg-chromite + anorthite + forsterite

(reaction 2.VIII; Borghini et al., 2010)

Cr#s of pyroxenes and Spl increase with decreasing pressure (Borghini et al., 2010). Correspondingly, Cr# and Cr_2O_3 abundances increase for pyroxene porphyroclasts with decreasing Al_2O_3 content (Figs. 2.13D/H *1, 2.13A/E *2). For pyroxene neoblasts in porphyroclast tails, Cr# display no pronounced positive correlation to Al_2O_3 but scatter around the porphyroclast Cr# values (Fig. 2.13D/H). As variations of Cr# and Al_2O_3 abundance are present in neoblasts of a single pyroxene tail (e.g., Fig. 2.13D) Al-Cr partitioning seems to be dependent on the local equilibrium governed by the presence of Spl and Pl at relatively fixed PT conditions (reaction 2.IX; Borghini et al., 2010).

$$MgCr_2O_4 + CaAl_2Si_2O_8 = MgCrAlSiO_6 + CaCrAlSiO_6$$
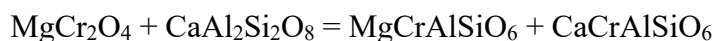
Mg-chromite + anorthite = MgCr-Ts + CaCr-Ts

(reaction 2.IX; Borghini et al., 2010)

Kaczmarek and Müntener (2008) reported a highly variable Spl composition with respect to TiO_2, Cr- and Mg-number. Variations within a single sample are reported to be as large as the total range of all samples in the strain gradient. Especially the high Ti contents are at odds with Spl formation solely by subsolidus reactions and support a melt inherited component (Borghini et al., 2010; Kaczmarek and Müntener, 2008). Increased homogenization in the extensive deformed samples reported by Kaczmarek and Müntener (2008) suggests further that the timing of this melt-induced change was prior to ultramylonitic band formation. As interstitial Spl in pyroxene reaction tails were too small for microprobe measurement, their composition remains unfortunately unknown.

Borghini et al. (2010) reported the modal amount of Pl to progressively decrease with increasing pressure along with a concomitant decrease in modal Ol and an increase in Opx, Cpx and Spl abundances following the reaction:

$$0.12 \ Pl_0 + 0.13 \ Ol + 0.02 \ Spl_0 + 0.3 \ Cpx_0 + 0.43 \ Opx_0 =$$

$$0.05 \ Spl_1 + 0.37 \ Cpx_1 + 0.58 \ Opx_1$$

(reaction 2.X; Borghini et al., 2010)

Corresponding to reaction (2.X), we observe a replacement of both pyroxenes by a mixture of Ol and minor Pl along with the host phase in neoblast tails of pyroxenes (Figs. 2.7, 2.8). A clear connection to the matrix is crucial for the neoblast assemblage and mixing intensity: Isolated microstructures (Opx (Fig. 2.11C), Cpx (Fig. 2.10A), Cpx-Opx interface (Fig. 2.10B) show, despite the presence of Prg, host phase dominated assemblages and low mixing intensities. Therefore, geochemical changes due to the presence of fluid did not extensively modify the neoblast composition or mixing intensity.

In addition to mantle shear zones (e.g., Furusho and Kanagawa, 1999; Newman et al., 1999), phase mixing by heterogenous nucleation due to chemical disequilibrium was also reported in lower crustal shear zones (e.g., Degli Alessandrini, 2018; Kruse and Stünitz, 1999). Depending on the formation mechanism, Kruse and Stünitz (1999) reported for mylonites from the Jotun nappe (Norway) either the formation of monomineralic tails of plagioclase, hornblende and pyroxenes by dynamic recrystallization or phase mixtures of hornblende+Pl or Cpx+Pl in reaction tails. For lower crustal mylonites, highly lobate, serrated boundaries of reacted porphyroclasts similar to those of pyroxene porphyroclasts reaction tails (Figs. 2.7, 2.8) were reported as evidence for diffusion driven (re)crystallization (Gower and Simpson, 1992; Kruse and Stünitz, 1999; Martelat et al., 1999; Zulauf et al., 2002). Combining our results with the experimental observations of Borghini et al. (2009) and the field implications of Furusho and Kanagawa (1999), Newman & Drury (2010) and Newman et al. (1999) we consider that continuous net-transfer reactions due to the Spl lherzolite to Pl lherzolite transition are a potential driving force for the formation of ultramylonitic mixed assemblages in pyroxene porphyroclast tails. As formerly elaborated by Hidas et al. (2016), these syn-kinematic net-transfer reactions are catalyzed by fluids. Syn-kinematic amphibole precipitation and fluid channeling in the center of deformation of the Lanzo shear zone were postulated by Kaczmarek and Tommasi (2011) and Vieira Duarte et al. (2020). Although the amount of amphibole in pyroxene tails seems to be low (av. ~1%), Hidas et al. (2016) have

shown that for a peridotitic composition at corresponding PT conditions, fluid saturation is reached at 1.0-1.4 wt.% amphibole. Additionally, Vieira Duarte et al. (2020) argue for a syn-kinematic growth and deformation of Cl-bearing amphibole between 800-850° C which coincides with neoblasts temperatures.

The fact that reaction-induced formation of ultramylonitic phase mixtures occurs only in strongly deformed textures and increases with deformation (Fig. 2.4) further indicates a strain dependent formation. Deformation experiments on Pl+Ol aggregates have shown positive feedback of deformation and reactions for dry and wet conditions (de Ronde and Stünitz, 2007). An enhanced rate of the An (Pl) to Spl transformation was explained by an increase in nucleation rate due to deformation-induced defects (free dislocations, dislocation pileups, subgrain walls) and locally increased Gibbs free energy (de Ronde and Stünitz, 2007). With the onset of mechanical weakening, neoblasts are transported from the reaction interface, maintaining a high chemical potential and a continuous nucleation of reaction products can occur (de Ronde and Stünitz, 2007). In our samples, this coupling of deformation, diffusion and nucleation is microstructurally corroborated by the formation of elongated polymineralic tails parallel to the foliation and with main porphyroclast reaction interfaces at boundaries perpendicular to the lineation (Fig. 2.7), by increasing neoblast elongation towards distal parts of the tail (Fig. 2.8C) and by increasing amount and length of GBAs towards the border of the tails (Fig. 2.7C). Additionally, neoblast grain sizes are smaller in pyroxene reaction tails embedded in ultramylonitic bands than those in mylonitic areas (e.g., Fig. 2.4B *4/*5).

2.7.3.3   Phase mixing by grain boundary sliding

The polymineralic tails derived from the pyroxene porphyroclasts are formed by reactions, however, grain boundary sliding (GBS) could be an additional phase mixing process during deformation. Grain boundary sliding (GBS) is thought to be active in both dislocation creep regime and diffusion creep regime (Drury et al., 2011; Hirth and Kohlstedt, 2003; Miyazaki et al., 2013; Warren and Hirth, 2006). Most microstructural evidence for GBS is found in ultramylonitic phase mixtures by continuous phase and grain boundaries alignments (Fig. 2.7C white dotted lines) (e.g., Kohlstedt et al., 1976; Newman et al., 1999). GBAs are interpreted as preferred sliding plains during GBS along grain and phase boundaries which are mostly subparallel to the foliation (Dijkstra et al., 2002; Drury et al., 2011; Newman et al., 1999). Neoblasts along GBAs show no increase in mixing (Fig. 2.7C) which was previously observed in experiments of Hiraga et al. (2013). GBAs of the wall like structures in in Cpx reaction tails

(suppl. data S2.7) display significantly different angles to the foliation (70-90°) and are aligned subparallel to porphyroclasts boundaries and are partially parallel to exsolution lamellae of the Cpx clast (suppl. data S2.7). Similar high angles to the tensile direction were also observed by Hiraga et al. (2013). The subparallel orientation to the porphyroclast grain boundary/exsolution lamellae suggests an influence of the clast orientation on neoblast grain shape. However, neoblast CPOs do not show a strong relation to the clast orientation (suppl. data S2.3, S2.4). Additionally, aggregation is significantly weaker than shown by Hiraga et al. (2013) questioning the importance of GBS for these microstructures.

In conclusion, grain boundary sliding in our samples seems to lead to phase aggregation and not to phase mixing. Only in Ol recrystallization tails (Fig. 2.6), GBS combined with creep cavitation and nucleation seems to be accountable for the little mixing present in these microstructures.

2.7.4 Ultramylonite bands

Ultramylonitic bands have a mixed phase assemblage dominated by Ol (> 50%) and either Cpx (av. 38%) or Opx (av. 14%). Similar to reaction tails of pyroxene porphyroclasts minor phases are Pl (av. 8%), Spl (~1%) and Prg (<1%). Pyroxene CPOs are not present or very weak (Opx: av. J index: Opx 1.5, Cpx 1.6). Ol neoblasts mostly form no CPO. Average grain sizes in Cpx+Ol ultramylonitic layers (~10 µm) tend to be bigger than those in Ol+Opx layers (~6 µm). Interestingly, neoblasts in pyroxene porphyroclast tails show a similar trend of bigger grain sizes in Cpx derived tails than in Opx ones (e.g., Fig. 2.7). Similar modal abundances in Ol porphyroclast tails and in ultramylonitic Opx+Ol layers could suggest that these layers derived from strongly deformed, Ol recrystallization tails. However, the transitions from neoblast tails to ultramylonitic bands (Fig. 2.12, 2.4B), the presence of the same phases, similar modal abundances, and high mixing intensities in tails and bands suggest the straightforward interpretation that the origin of the ultramylonite bands are the pyroxene reaction tails. Ultramylonitic grain sizes and weak to no CPO indicate deformation by diffusion creep of the ultramylonitic bands. Their interconnectivity (Fig. 2.4B), their mixed assemblage (64% (Cpx+Ol) and 55% (Ol+Opx) phase boundaries) and their anastomosing microstructures around almost monomineralic Ol areas and porphyroclast-neoblast assemblages suggest that deformation is localized in the ultramylonitic bands/ in the ultramylonitic matrix in the ultramylonite texture. Interestingly, diffusion creep in these bands is combined with strong SPOs and elongated grain shapes (Fig. 2.12C) of pyroxenes and olivine.

Some observations however indicate additional deformation mechanisms. Domains with fine-grained Ol+Opx mixture at grain boundaries of coarse-grained Ol in ultramylonitic Ol+Opx layers (Fig. 2.9F) suggest precipitation of neoblasts during diffusion creep accommodated GBS in creep cavitations similar than mixing structures type I in Ol porphyroclast tails (Fig. 2.7A-i). Interestingly, neoblasts present in tails adjacent to elongated single Opx crystals display smaller grain sizes than in the ultramylonitic bands (Fig. 2.9). This could indicate a certain degree of grain growth in the ultramylonites.

2.7.5 Comparison with other mantle shear zones and the significance of reaction-induced phase mixing

As seen for Lanzo, most mantle shear zones/sheared peridotites show evidence for reaction involved changes in their mineralogy (phase composition and abundances) during their evolution from upper mantle depth to the earth surface. These changes are either due to melt, fluid and/or changing PT conditions (phase transitions and continuous net transfer reactions). The significance of the reaction-induced changes for the generation of phase mixtures becomes clear through a comparison with other sheared peridotites. Initial strain localization is not regarded here.

Melt-rock reactions were reported for Othris, Greece (Dijkstra et al., 2002), Lanzo, Italy (Kaczmarek and Müntener, 2008) and the Table Mountain massif, Newfoundland (Suhr, 1993). Evidence for extensive fluid-rock reactions was observed in the central Ronda peridotite, Spain (Hidas et al., 2016), were limited fluid availability led locally to dissolution-precipitation creep. This process caused the precipitation of elongated Opx at Ol grain boundaries, leading to phase mixing. A similar process is suggested for phase mixing in the Anita peridotite, New Zealand (Czertowicz et al., 2016). In these ultramylonites, the Opx also forms along Ol grain boundaries, which is thought to be the result of Opx precipitation in creep cavitation bands between Ol grains (Czertowicz et al., 2016). Creep cavitation can form during GBS (Fusseis et al., 2009), or due to SGR (Gilgannon et al., 2020). At higher fluid volumes, amphibole or chlorite may form, depending on PT conditions, resulting in fine-grained mixed reaction products, as in Erro-Tobbio (Hoogerduijn Strating et al., 1993; Linckens and Tholen, 2021) and in dredged peridotites from the Shaka and Prince Edward Oceanic Transform Faults (Kohli and Warren, 2020; Prigent et al., 2020). Mineral reactions driven by the change in PT conditions were interpreted as driving force for recrystallization and phase mixing in the Turon de Técouère, France (Newman et al., 1999), in the Twin Sisters Massif, USA (Toy et al., 2009), in the Uenzaru peridotite, Japan

(Furusho and Kanagawa, 1999), and in Lanzo, Italy by Kaczmarek and Tommasi (2011) and this study. Remarkably, all the above-mentioned shear zones display (ultra)mylonitic, thoroughly mixed assemblages, whether as patches or coronas around porphyroclasts or as interconnected bands.

As a counterpart, only a few shear zones were found to deform without concomitant chemical reactions: for the north-western border of the Ronda peridotite, Spain (e.g., Precigout et al. 2007), dynamic recrystallization was found to be the only weakening mechanism responsible for strain localization. Continuous deformation accommodated partly by grain boundary sliding resulted in neighbor-switching and the scattering of Opx neoblasts. Accordingly, microstructures typical for reaction-induced recrystallization as reported herein were not observed. No ultramylonites were formed during deformation and the grain sizes remained relatively large (mean grain sizes of 150-220 μm; Précigout et al., 2017). For pyroxenites of the Beni Bousera peridotite, Morocco, Frets et al. (2012) reported that most deformation was accommodated by dislocation creep of pyroxenes (SGR and GBR dynamic recrystallization). High stress deformation is thought to drive compositional homogenization by mechanical mixing. However, Frets et al. (2012) also reported syn- to late-kinematic reactions that crystallize pyroxenes at the expense of garnets. Skemer et al. (2009) reported fine-grained, mixed domains of Ol+Opx which are associated with relict Opx porphyroclasts for a high-strain shear zone from the Josephine Peridotite, USA. Like for Lanzo, the authors argue that for the formation of these mixed domains, the onset of Opx recrystallization is crucial. On the basis of subgrain boundaries in Opx porphyroclasts, and equiaxial neoblasts a formation by dynamic recrystallization rather than by chemical reactions was suggested. However, a recent study of Kumamoto et al. (2019) has shown, that these shear zones record extensive melt-rock interaction and elevated water concentrations. In summary, the following can be said for these shear zones: even if deformation is mostly accommodated by dynamic recrystallization, the phase mixing present seems to be due to reactions.

Deformation in peridotites with little or no reaction-induced change by metasomatism and/or phase transitions were only reported for sheared xenoliths. For South African kimberlites, Skemer and Karato (2008) show microstructures of dynamically recrystallized Opx porphyroclasts forming equigranular neoblast mosaics with straight grain boundaries and no to little phase mixing over the total length of neoblast tails. Sheared xenoliths from Lesotho and South Africa display extensive dynamic recrystallization of Opx, Cpx and Ol (suppl. data S2.11). Despite the simultaneous dynamic recrystallization of all three phases no phase

mixing occurs (suppl. data S2.11). Although this list is not exhaustive, a correspondence with our results from the northern Lanzo shear zone is apparent. Extensive phase mixing and the formation of (ultra)mylonitic assemblages are only observed when reactions occur (due to melt-rock, fluid-rock reactions and/or metamorphism).

2.8 Conclusions

- Ultramylonitic, polymineralic tails form adjacent to ortho- and clinopyroxene porphyroclast in mylonitic rocks in the Lanzo shear zone.

- Transitions from these tails to ultramylonitic bands with similar mixing intensities, compositions and phase abundances in bands and tails suggest: ultramylonitic bands/matrix derive from pyroxene tails.

- Mineralogical assemblages and phase abundances in pyroxene tails depend primarily on the parent porphyroclast. Clinopyroxene porphyroclasts form clinopyroxene + olivine assemblages. Orthopyroxene porphyroclasts form olivine + orthopyroxene assemblages. Minor phases in both phase mixtures are plagioclase, spinel and pargasitic amphibole.

- Mixing intensities of pyroxene microstructures strongly depend on the connection to the matrix: high phase mixing intensities are only observed in porphyroclast tails embedded in the matrix.

- Polymineralic tails are suggested to form by net-transfer reactions, enhanced by the spinel lherzolite – plagioclase lherzolite transition.

- Minor amphibole occurrence in ultramylonitic phase mixtures suggests that reactions were catalyzed by the presence of a fluid.

- Grain boundary sliding plus cavity nucleation has only a minor importance for phase mixing in tails of dynamically recrystallized olivine porphyroclasts.

- Other upper mantle shear zones confirm that extensive phase mixing and the formation of (ultra)mylonitic assemblages are reaction-induced (melt-rock, fluid-rock, continuous net-transfer, and phase-transition).

Acknowledgments

2.9   References chapter 2

Bachmann, F., Hielscher, R., Schaeben, H. (2010). Texture analysis with MTEX- Free and open source software toolbox. *Solid State Phenom*. 160, 63–68. https://doi.org/10.4028/www.scientific.net/SSP.160.63

Borghini, G. (2008). The spinel- to plagioclase-facies transition in mantle peridotites: Natural and experimental constraints. *Plinius* 34, 43–45.

Borghini, G., Fumagalli, P., Rampone, E. (2010). The stability of plagioclase in the upper mantle: Subsolidus experiments on fertile and depleted lherzolite. *J. Petrol*. 51, 229–254. https://doi.org/10.1093/petrology/egp079

Boudier, F. (1978). Structure and petrology of the Lanzo peridotite massif (Piedmont Alps). *Geol. Soc. Am. Bull*. 7606. https://doi.org/10.1130/0016-7606(1978)89<1574

Boullier, A.M., Gueguen, Y. (1975). SP-Mylonites: Origin of some mylonites by superplastic flow. *Contrib. to Mineral. Petrol*. 50, 93–104. https://doi.org/10.1007/BF00373329

Brey, G.P., Köhler, T. (1990). Geothermobarometry in four-phase lherzolites II. new thermobarometers, and practical assessment of existing thermobarometers. *J. Petrol*. 31, 1353–1378. https://doi.org/10.1093/petrology/31.6.1353

Brodie, K.H., Rutter, E.H. (1987). The role of transiently fine-grained reaction products in syntectonic metamorphism: natural and experimental examples. *Can. J. Earth Sci*. 24, 556–564. https://doi.org/10.1139/e87-054

Bunge, H.-J. (1982). Orientation Distributions, in: *Texture Analysis in Materials Science*. Butterworths, London. https://doi.org/10.1016/B978-0-408-10642-9.50008-8

Carswell, D.A. (1991). The garnet-orthopyroxene Al barometer: problematic application to natural garnet lherzolite assemblages. *Mineral. Mag*. 55, 19–31. https://doi.org/10.1180/minmag.1991.055.378.03

Cross, A.J., Skemer, P. (2017). Ultramylonite generation via phase mixing in high-strain experiments. *J. Geophys. Res. Solid Earth* 122, 1744–1759. https://doi.org/10.1002/2016JB013801

Czertowicz, T.A., Toy, V.G., Scott, J.M. (2016). Recrystallisation, phase mixing and strain localisation in peridotite during rapid extrusion of sub-arc mantle lithosphere. *J. Struct. Geol*. 88, 1–19. https://doi.org/10.1016/j.jsg.2016.04.011

de Ronde, A.A., Stünitz, H. (2007). Deformation-enhanced reaction in experimentally deformed plagioclase-olivine aggregates. *Contrib. to Mineral. Petrol*. 153, 699–717. https://doi.org/10.1007/s00410-006-0171-7

Debret, B., Nicollet, C., Andreani, M., Schwartz, S., Godard, M. (2013). Three steps of serpentinization in an eclogitized oceanic serpentinization front (Lanzo Massif - Western Alps). *J. Metamorph. Geol*. 31, 165–186. https://doi.org/10.1111/jmg.12008

Degli Alessandrini, G. (2018). Deformation Mechanisms and Strain Localization in the Mafic Continental Lower Crust. *Dr. Diss. Univ.* Plymouth, U.K. https://doi.org/https://pearl.plymouth.ac.uk/handle/10026.1/12799?show=full

Dijkstra, A.H., Drury, M.R., Vissers, R.L.M., Newman, J. (2002). On the role of melt-rock reaction in mantle shear zone formation in the Othris Peridotite Massif (Greece). *J. Struct. Geol.* 24, 1431–1450. https://doi.org/10.1016/S0191-8141(01)00142-0

Dijkstra, A.H., Drury, M.R., Vissers, R.L.M., Newman, J., Van Roermund, H.L.M. (2004). Shear zones in the upper mantle: Evidence from alpine- and ophiolite-type peridotite massifs. *Geol. Soc. Spec. Publ.* 224, 11–24. https://doi.org/10.1144/GSL.SP.2004.224.01.02

Drury, M.R., Avé Lallemant, H.G., Pennock, G.M., Palasse, L.N. (2011). Crystal preferred orientation in peridotite ultramylonites deformed by grain size sensitive creep, étang de Lers, Pyrenees, France. *J. Struct. Geol.* 33, 1776–1789. https://doi.org/10.1016/j.jsg.2011.10.002

Farla, R.J.M., Karato, S., Cai, Z. (2013). Role of orthopyroxene in rheological weakening of the lithosphere via dynamic recrystallization. *Proc. Natl. Acad. Sci. U. S. A.* 110, 16355–16360. https://doi.org/10.1073/pnas.1218335110

Frets, E., Tommasi, A., Garrido, C.J., Padrón-Navarta, J.A., Amri, I., Targuisti, K. (2012). Deformation processes and rheology of pyroxenites under lithospheric mantle conditions. *J. Struct. Geol.* 39, 138–157. https://doi.org/10.1016/j.jsg.2012.02.019

Furusho, M., Kanagawa, K. (1999). Transformation-induced strain localization in a lherzolite mylonite from the Hidaka metamorphic belt of central Hokkaido, Japan. *Tectonophysics* 313, 411–432. https://doi.org/10.1016/S0040-1951(99)00215-2

Gower, R.J.W., Simpson, C. (1992). Phase boundary mobility in naturally deformed, high-grade quartzofeldspathic rocks: evidence for diffusional creep. *J. Struct. Geol.* 14, 301–313. https://doi.org/10.1016/0191-8141(92)90088-E

Hidas, K., Garrido, C.J., Tommasi, A., Padrón-Navarta, J.A., Thielmann, M., Konc, Z., Frets, E., Marchesi, C. (2013). Strain localization in pyroxenite by reaction-enhanced softening in the shallow subcontinental lithospheric mantle. *J. Petrol.* 54, 1997–2031. https://doi.org/10.1093/petrology/egt039

Hidas, K., Tommasi, A., Garrido, C.J., Padrón-Navarta, J.A., Mainprice, D., Vauchez, A., Barou, F., Marchesi, C. (2016). Fluid-assisted strain localization in the shallow subcontinental lithospheric mantle. *Lithos* 262, 636–650. https://doi.org/10.1016/j.lithos.2016.07.038

Hielscher, R., Nolze, G. (2016). IPF coloring of crystal orientation data. *J. Appl. Crystallogr.* 49, 1786–1802.

Hiraga, T., Miyazaki, T., Yoshida, H., Zimmerman, M.E. (2013). sliding Comparison of microstructures in superplastically deformed synthetic materials and natural mylonites: Mineral aggregation via grain boundary sliding. *Geology* 41(9), 959-962. https://doi.org/10.1130/G34407.1

Hirth, G., Kohlstedt, D. (2003). Rheology of the upper mantle and the mantle wedge: A view from the experimentalists. *Geophys. Monogr. Ser.* 138, 83–105. https://doi.org/10.1029/138GM06

Hoogerduijn Strating, E.H., Rampone, E., Piccardo, G.B., Drury, M.R., Vissers, R.L.M. (1993). Subsolidus emplacement of mantle peridotites during incipient oceanic rifting and opening of the mesozoic tethys (voltri massif, NW Italy). *J. Petrol.* 34, 901–927. https://doi.org/10.1093/petrology/34.5.901

Kaczmarek, M.A., Müntener, O. (2010). The variability of peridotite composition across a mantle shear zone (Lanzo massif, Italy): Interplay of melt focusing and deformation. *Contrib. to Mineral. Petrol.* 160, 663–679. https://doi.org/10.1007/s00410-010-0500-8

Kaczmarek, M.A., Müntener, O. (2008). Juxtaposition of melt impregnation and high-temperature shear zones in the upper mantle; field and petrological constraints from the lanzo peridotite (Northern Italy). *J. Petrol.* 49, 2187–2220. https://doi.org/10.1093/petrology/egn065

Kaczmarek, M.A., Müntener, O. (2005). Exhumation of mantle lithosphere: Field relations, and interaction processes between magmatism and deformation (field trip to the northern lanzo peridotite). *Ofioliti* 30, 125–134. https://doi.org/10.4454/ofioliti.v30i2.246

Kaczmarek, M.A., Tommasi, A. (2011). Anatomy of an extensional shear zone in the mantle, Lanzo massif, Italy. *Geochemistry, Geophys. Geosystems 12.* https://doi.org/10.1029/2011GC003627

Karato, S., Wu, P. (1993). Rheology of the upper mantle: A synthesis. *Science* (80-.). 260, 771–778. https://doi.org/10.1126/science.260.5109.771

Kilian, R., Bestmann, M., Heilbronner, R, (2016). Absolute orientations from EBSD measurements - as easy as it seems? *Geophys. Res. Abstr.* 18, 8221.

Kilian, R., Heilbronner, R., Stünitz, H. (2011). Quartz grain size reduction in a granitoid rock and the transition from dislocation to diffusion creep. *J. Struct. Geol.* 33, 1265–1284. https://doi.org/10.1016/j.jsg.2011.05.004

Knapp, N., Woodland, A.B., Klimm, K. (2013). Experimental constraints in the CMAS system on the Ca-Eskola content of eclogitic clinopyroxene. *Eur. J. Mineral.* 25, 579–596. https://doi.org/10.1127/0935-1221/2013/0025-2326

Kohli, A.H., Warren, J.M. (2020). Evidence for a Deep Hydrologic Cycle on Oceanic Transform Faults. J. Geophys. Res. Solid Earth 125, 1–23. https://doi.org/10.1029/2019JB017751

Kohlstedt, D.L., Goetze, C., Durham, W.B., Vander Sande, J. (1976). New technique for decorating dislocations in olivine. *Science* (80-.). 191, 1045–1046. https://doi.org/10.1126/science.191.4231.1045

Kruse, R., Stünitz, H. (1999). Deformation mechanisms and phase distribution in mafic high-temperature mylonites from the Jotun Nappe, southern Norway. *Tectonophysics* 303, 223–249. https://doi.org/10.1016/S0040-1951(98)00255-8

Kumamoto, K.M., Warren, J.M., Hauri, E.H. (2019). Evolution of the Josephine Peridotite Shear Zones: 1. Compositional Variation and Shear Initiation. *Geochemistry, Geophys. Geosystems* 20, 5765–5785. https://doi.org/10.1029/2019GC008399

Linckens, J., Herwegh, M., Mntener, O. (2011). Linking temperature estimates and microstructures in deformed polymineralic mantle rocks. *Geochemistry, Geophys. Geosystems* 12, 1–19. https://doi.org/10.1029/2011GC003536

Linckens, J., Herwegh, M., Müntener, O. (2015). Small quantity but large effect - How minor phases control strain localization in upper mantle shear zones. *Tectonophysics* 643, 26–43. https://doi.org/10.1016/j.tecto.2014.12.008

Linckens, J., Tholen, S. (2021). Formation of ultramylonites in an upper mantle shear zone, erro-tobbio, italy. *Minerals* 11. https://doi.org/10.3390/min11101036

Martelat, J.E., Schulmann, K., Lardeaux, J.M., Nicollet, C., Cardon, H. (1999). Granulite microfabrics and deformation mechanisms in southern Madagascar. *J. Struct. Geol.* 21, 671–687. https://doi.org/10.1016/S0191-8141(99)00052-8

Menegon, L., Fusseis, F., Stünitz, H., Xiao, X. (2015). Creep cavitation bands control porosity and fluid flow in lower crustal shear zones. *Geology* 43. https://doi.org/10.1130/G36307.1

Miyazaki, T., Sueyoshi, K., Hiraga, T. (2013). Olivine crystals align during diffusion creep of Earth's upper mantle. *Nature* 502, 321–326. https://doi.org/10.1038/nature12570

Montési, L.G.J. (2013). Fabric development as the key for forming ductile shear zones and enabling plate tectonics. *J. Struct. Geol.* 50, 254–266. https://doi.org/10.1016/j.jsg.2012.12.011

Müntener, O., Piccardo, G.B. (2003). Melt migration in ophiolitic peridotites: The message from Alpine-Apennine peridotites and implications for embryonic ocean basins. *Geol. Soc. Spec. Publ.* 218, 69–89. https://doi.org/10.1144/GSL.SP.2003.218.01.05

Müntener, O., Piccardo, G.B., Polino, R., Zanetti, A. (2005). Revisiting the Lanzo peridotite (NW-Italy): "Asthenospherization" of ancient mantle lithosphere. *Ofioliti* 30, 111–124. https://doi.org/10.4454/ofioliti.v30i2.245

Newman, J., Drury, M.R. (2010). Control of shear zone location and thickness by initial grain size variations in upper mantle peridotites. *J. Struct. Geol.* 32, 832–842. https://doi.org/10.1016/j.jsg.2010.06.001

Newman, J., Lamb, W.M., Drury, M.R., Vissers, R.L.M. (1999). Deformation processes in a peridotite shear zone: Reaction-softening by an H2O-deficient, continuous net transfer reaction. *Tectonophysics* 303, 193–222. https://doi.org/10.1016/S0040-1951(98)00259-5

Niida, K., Green, D.H. (1999). Stability and chemical composition of pargasitic amphibole in MORB pyrolite under upper mantle conditions. *Contrib. to Mineral. Petrol.* 135, 18–40. https://doi.org/10.1007/s004100050495

Nimis, P., Grütter, H. (2010). Internally consistent geothermometers for garnet peridotites and pyroxenites. *Contrib. to Mineral. Petrol.* 159, 411–427. https://doi.org/10.1007/s00410-009-0455-9

Nimis, P., Taylor, W.R. (2000). Single clinopyroxene thermobarometry for garnet peridotites. Part I. Calibration and testing of a Cr-in-Cpx barometer and an enstatite-in-Cpx thermometer. *Contrib. to Mineral. Petrol.* 139, 541–554. https://doi.org/10.1007/s004100000156

Pearce, M.A., Wheeler, J. (2011). Grain growth and the lifetime of diffusion creep deformation. *Geol. Soc. Spec. Publ.* 360, 257–272. https://doi.org/10.1144/SP360.15

Platt, J.P. (2015). Rheology of two-phase systems: A microphysical and observational approach. *J. Struct. Geol.* 77, 213–227. https://doi.org/10.1016/j.jsg.2015.05.003

Poirier, J.-P., Nicolas, A. (1975). Deformation-Induced Recrystallization Due to Progressive Misorientation of Subgrains, with Special Reference to Mantle Peridotites. *J. Geol.* 83, 707–720. https://doi.org/10.1086/628163

Précigout, J., Gueydan, F., Gapais, D., Garrido, C.J., Essaifi, A. (2007). Strain localisation in the subcontinental mantle - a ductile alternative to the brittle mantle. *Tectonophysics* 445, 318–336. https://doi.org/10.1016/j.tecto.2007.09.002

Précigout, J., Prigent, C., Palasse, L., Pochon, A. (2017). Water pumping in mantle shear zones. *Nat. Commun.* 8. https://doi.org/10.1038/ncomms15736

Précigout, J., Stünitz, H. (2016). Evidence of phase nucleation during olivine diffusion creep: A new perspective for mantle strain localization. *Earth Planet. Sci. Lett.* 455, 94–105. https://doi.org/10.1016/j.epsl.2016.09.029

Prigent, C., Warren, J.M., Kohli, A.H., Teyssier, C. (2020). Fracture-mediated deep seawater flow and mantle hydration on oceanic transform faults. *Earth Planet. Sci. Lett.* 532, 115988. https://doi.org/10.1016/j.epsl.2019.115988

Putnis, A., Niedermeier, D., Putnis, C. (2006). From epitaxy to topotaxy: The migration of reaction interfaces through crystals. *Geochim. Cosmochim. Acta* 70. https://doi.org/10.1016/j.gca.2006.06.1479

Rampone, E., Borghini, G., Basch, V. (2018). Melt migration and melt-rock reaction in the Alpine-Apennine peridotites: Insights on mantle dynamics in extending lithosphere Geoscience Frontiers Melt migration and melt-rock reaction in the Alpine-Apennine peridotites: Insights on mantle dynamics in. *Geosci. Front.* https://doi.org/10.1016/j.gsf.2018.11.001

Rampone, E., Piccardo, G.B., Vannucci, R., Bottazzi, P., Ottolini, L. (1993). Subsolidus reactions monitored by trace element partitioning: the spinel- to plagioclase-facies transition in mantle peridotites. *Contrib. to Mineral. Petrol.* 115, 1–17. https://doi.org/10.1007/BF00712974

Ramsay, J.G., Graham, R.H. (1970). Strain variation in shear belts. *Can. J. Earth Sci.* 7, 786–813. https://doi.org/10.1139/e70-078

Sakai, T., Belyakov, A., Kaibyshev, R., Miura, H., Jonas, J.J. (2014). Dynamic and post-dynamic recrystallization under hot, cold and severe plastic deformation conditions. *Prog. Mater. Sci.* 60, 130–207. https://doi.org/10.1016/j.pmatsci.2013.09.002

Sibson, R.H. (1977). Fault rocks and fault mechanisms. *J. Geol. Soc. London.* 133, 191–213. https://doi.org/10.1144/gsjgs.133.3.0191

Skemer, P., Karato, S.I. (2008). Sheared lherzolite xenoliths revisited. *J. Geophys. Res. Solid Earth* 113, 1–14. https://doi.org/10.1029/2007JB005286

Skemer, P., Katayama, I., Jiang, Z., Karato, S.I. (2005). The misorientation index: Development of a new method for calculating the strength of lattice-preferred orientation. *Tectonophysics* 411, 157–167. https://doi.org/10.1016/j.tecto.2005.08.023

Skemer, P., Warren, J.M., Kelemen, P.B., Hirth, G. (2009). Microstructural and rheological evolution of a mantle shear zone. *J. Petrol.* 51, 43–53. https://doi.org/10.1093/petrology/egp057

Suhr, G. (1993). Evaluation of upper mantle microstructures in the Table Mountain massif (Bay of Islands ophiolite). *J. Struct. Geol.* 15, 1273–1292. https://doi.org/10.1016/0191-8141(93)90102-G

Taylor, W.R. (1998). An experimental test of some geothermometer and geobarometer formulations for upper mantle peridotites with application to the thermobarometry of fertile lherzolite and garnet websterite. *Neues Jahrb. fur Mineral. Abhandlungen* 172, 381–408. https://doi.org/10.1127/njma/172/1998/381

Toy, V.G., Newman, J., Lamb, W.M., Tikoff, B. (2009). The role of pyroxenites in formation of shear instabilities in the mantle: Evidence from an ultramafic ultramylonite, Twin Sisters massif, Washington. *J. Petrol*. 51, 55–80. https://doi.org/10.1093/petrology/egp059

Urai, J.L., Means, W.D., Lister, G.S. (2011). Dynamic recrystallization of minerals 161–199. In: *Mineral and Rock Deformation: Laboratory Studies*. https://doi.org/10.1029/gm036p0161

Vauchez, A., Tommasi, A., Mainprice, D. (2012). Faults (shear zones) in the Earth's mantle. Tectonophysics 558–559, 1–27. https://doi.org/10.1016/j.tecto.2012.06.006

Vieira Duarte, J.F., Kaczmarek, M.A., Vonlanthen, P., Putlitz, B., Müntener, O. (2020). Hydration of a Mantle Shear Zone Beyond Serpentine Stability: A Possible Link to Microseismicity Along Ultraslow Spreading Ridges? *J. Geophys. Res. Solid Earth* 125, 1–24. https://doi.org/https://doi.org/10.1029/2020JB019509

Vissers, R.L.M., Drury, M.R., Newman, J., Fliervoet, T.F. (1997). Mylonitic deformation in upper mantle peridotites of the North Pyrenean Zone (France): Implications for strength and strain localization in the lithosphere. *Tectonophysics* 279, 303–325. https://doi.org/10.1016/S0040-1951(97)00128-5

Warren, J.M., Hirth, G. (2006). Grain size sensitive deformation mechanisms in naturally deformed peridotites. *Earth Planet. Sci. Lett*. 248, 438–450. https://doi.org/10.1016/j.epsl.2006.06.006

Whitney, D.L., Evans, B.W. (2010). Abbreviations for names of rock-forming minerals. *Am. Mineral*. 95, 185–187. https://doi.org/10.2138/am.2010.3371

Zulauf, G., Dörr, W., Fiala, J., Kotková, J., Maluski, H., Valverde-Vaquero, P. (2002). Evidence for high-temperature diffusional creep preserved by rapid cooling of lower crust (North Bohemian shear zone, Czech Republic). *Terra Nov.* 14, 343–354. https://doi.org/10.1046/j.1365-3121.2002.00424.x

3 Formation of ultramylonites in an upper mantle shear zone (Erro-Tobbio, Italy)

Jolien Linckens[1/2], Sören Tholen[1]

[1]Institut für Geowissenschaften, Goethe Universität Frankfurt a.M., Altenhöferallee 1, D-60438

[2]Tata Steel, R&D, Microstructural and Surface Characterization, Beverwijk, NL-1951

3.1 Abstract

Deformation in the upper mantle is localized in shear zones. In order to localize strain, weakening has to occur, which can be achieved by a reduction in grain size. In order for grains to remain small and preserve shear zones, phases have to mix. Phase mixing leads to dragging or pinning of grain boundaries which slows down or halts grain growth. Multiple phase mixing processes have been suggested to be important during shear zone evolution. The importance of a phase mixing process depends on the geodynamic setting. This study presents detailed microstructural analysis of spinel bearing shear zones from the Erro-Tobbio peridotite (Italy) that formed during pre-alpine rifting. The first stage of deformation occurred under melt-free conditions, during which clinopyroxene and olivine porphyroclasts dynamically recrystallized. With ongoing extension, silica-undersaturated melt percolated through the shear zones and reacted with the clinopyroxene neoblasts, forming olivine-clinopyroxene layers. Furthermore, the melt reacted with orthopyroxene porphyroclasts, forming fine-grained polymineralic layers (ultramylonites) adjacent to the porphyroclasts. Strain rates in these layers are estimated to be about an order of magnitude faster than within the olivine-rich matrix. This study demonstrates the importance of melt-rock reactions for grain size reduction, phase mixing and strain localization in these shear zones.

Keywords: Ultramylonite, shear zone, phase mixing, EBSD, Erro-Tobbio peridotite, melt-rock reaction.

Authors contribution: *Jolien Linckens;* Field campaign, analysis (EBSD), text and image composition*. Sören Tholen:* Field campaign, sample preparation, analysis (microscopy, EPMA, EBSD), data processing, image and text editing (mainly review).

3.2 Introduction

Strain in the upper mantle is inhomogeneously distributed. The deformation is localized in zones of high strain, i.e., shear zones. Shear zones control the deformation of the upper mantle (e.g., Bürgmann and Dresen, 2008; Drury et al. ,1991; Vissers et al., 1995) and are important for plate tectonics (e.g., Bercovici, 2003; Tackley, 2000). It is therefore essential to know why, how, and when strain localizes.

Initiation of strain localization occurs when certain domains in the upper mantle are weaker than others. Compositional (e.g., presence of melt or fluids), physical (e.g., temperature) and microstructural variations (e.g., grain size, crystallographic preferred orientation (CPO)) in the upper mantle can influence the viscosity (review in Tommasi and Vauchez, 2015). The viscosity of olivine, the volumetrically dominant mineral in the upper mantle, decreases when it incorporates water (Mei and Kohlstedt, 2000; Mei and Kohlstedt, 2000; Tasaka et al., 2015), and when small fractions (0.03-0.04) of melt are present (Hirth and Kohlstedt, 1995a, 1995b; Zimmerman and Kohlstedt, 2004). An increase in temperature decreases the strength of olivine and pyroxenes (the main minerals in the upper mantle) (e.g., Bürgmann and Dresen, 2008; Hansen et al., 2011; Hirth and Kohlstedt, 2003). A smaller grain size leads to a decrease in viscosity when deformation occurs by diffusion, or by dislocation-accommodated grain boundary sliding (disGBS) (e.g., Hansen et al., 2011; Hirth and Kohlstedt, 2003). When dislocation creep is dominant, a CPO develops. A CPO has an influence on olivine strength, as olivine is viscously anisotropic (e.g., Hansen et al., 2012; Skemer et al., 2013; Tommasi et al., 2009). During ductile deformation, the pre-existing variations in viscosity can cause the initiation of strain localization, leading to the formation of shear zones in the upper mantle (e.g., Dijkstra et al., 2002; Regenauer-Lieb and Yuen, 2004; Skemer et al., 2013). In addition, at lower temperatures and high stresses, the occurrence of brittle processes (seismic) followed by ductile processes (post-seismic creep) leads to strain localization in the upper mantle (e.g., Drury et al., 1991; Matysiak and Trepmann, 2012).

In order for strain to remain localized with ongoing ductile deformation, a positive feedback process between deformation and weakening has to occur, i.e., strain softening (Drury et al., 1991). Strain softening processes can be divided in four classes (Drury et al., 1991): thermal softening, geometrical softening, reaction softening and microstructural softening.

Thermal softening originates from shear heating, which is strain-rate dependent (Kelemen and Hirth, 2007). With increasing temperature, the strain rate increases, leading to an increase in temperature, leading to a positive feedback. Recent models show that shear heating is important in the generation of intermediate depth earthquakes (50-300 km) in a narrow temperature interval (600-800 °C) (e.g., Kelemen and Hirth, 2007; Thielmann et al., 2015). However, the models also show that this process can only occur in pre-existing

well-mixed fine-grained shear zones. The mixing of phases is necessary in order for other minerals to pin the migrating olivine grain boundary during grain growth occurring under static (Evans et al., 2001) or dynamic (Drury and Urai, 1989) conditions at the elevated temperatures. Otherwise, rapid grain growth in olivine (Karato, 1989) would lead to strain hardening during deformation, negating the strain softening. Large-scale models also show the importance of the positive feedback during shear heating in order to develop large-scale lithospheric faults (e.g., Regenauer-Lieb and Yuen, 2004).

Geometrical softening is due to the evolution of an olivine CPO. The strength of the CPO will increase with increasing strain, when strain is accommodated by dislocation creep, leading to a positive feedback (e.g., Bystricky et al., 2000; Hansen et al., 2012). This process has been suggested as being important for shear localization in an upper mantle shear zone with no large grain size variation (Skemer et al., 2013) and for the reactivation of pre-existing shear zones (Tommasi et al., 2009).

Reaction softening is caused by the formation of weak interconnected fine-grained polyphase bands of olivine and other minerals (e.g., olivine-opx, olivine-amphibole) or interconnected bands of a weak mineral (e.g., talc, serpentine) (Drury et al., 1991). When the grain size in the polyphase bands is small enough they can deform by diffusion creep and lead to strain softening, which has been observed in natural shear zones (e.g., Newman et al., 1999). The fine grain size in polyphase material can persist due to the pinning process (e.g., Drury and Urai, 1989; Evans et al., 2001; Linckens et al., 2011). The viscosity of the polyphase bands is either determined by the mineral that is interconnected in the bands (Handy, 1994) or by a composite rheology (e.g., (Ji et al., 2003; Tasaka et al., 2013). Reactions in the upper mantle can be caused by the infiltration of fluids or melts or a change in PT conditions (metamorphic reactions). Melts and fluids can preferentially infiltrate in shear zones due to creep cavitation formed during grain boundary sliding (Fusseis et al., 2009; Précigout et al., 2019, 2017), leading to a positive feedback mechanism and strain softening (e.g., Downes, 1990; Hidas et al., 2016; Kaczmarek and Müntener, 2008; Mei et al., 2002). The importance of reactions for the evolution of deformation has been determined in natural shear zones, be it metamorphic reactions (e.g., Newman et al., 1999), melt rock reactions (e.g., Dijkstra et al., 2002b) or hydration reactions (e.g., (Hoogerduijn Strating et al., 1993).

Microstructural softening occurs when the grain size decreases during dislocation creep due to dynamic recrystallization (Drury and Urai, 1989; Urai et al., 1986) or during brittle deformation. The steady state olivine grain size during dislocation creep depends on stress (Van der Wal et al., 1993). However, dislocation creep is a grain size-independent deformation mechanism, and therefore the reduction in grain size will not result in a softening. A softening does occur when there is a change from dislocation creep to a grain size-dependent deformation mechanism. It has been shown in deformation experiments on olivine that disGBS is an important deformation mechanism under upper mantle

conditions (Hansen et al., 2011). This process is grain size-sensitive and a reduction in grain size during deformation would result in softening (e.g., Précigout et al., 2007; Précigout and Gueydan, 2009). An even larger factor of softening will occur when the deformation process changes to diffusion creep, which has a larger grain size sensitivity. In order to keep the olivine grain size small, it is also important that phase mixing occurs during this softening process (e.g., Dijkstra et al., 2002a; Hansen and Warren, 2015; Hirth and Kohlstedt, 2003; Linckens et al., 2015).

The evolution of microstructures from outside to the center of upper mantle shear zones often shows the evolution from a coarse-grained (millimeter sized) microstructure to a well-mixed fine-grained (tens of microns) microstructure (e.g., Hidas et al., 2016; Jaroslow et al., 1996; Platt, 2015; Skemer et al., 2009; Warren and Hirth, 2006). It has been shown that the olivine grain size depends on the amount of other minerals present (Hansen and Warren, 2015; Linckens et al., 2015, 2011; Tasaka et al., 2013), indicating the effectiveness of pinning to inhibit grain growth. Large-scale models show the importance of pinning in preserving shear zones and therefore in the generation of plate tectonics (Bercovici and Ricard, 2014, 2013). The models, microstructural evolution in mantle shear zones, and several softening processes indicate the importance of grain size reduction and phase mixing processes on shear zone development. Recent studies have focused on phase mixing processes. Reactions (e.g., Kaczmarek and Müntener, 2008; Newman et al., 1999; Précigout and Stünitz, 2016), grain boundary sliding (e.g., Ashby and Verrall, 1973; Farla et al., 2013; Linckens et al., 2014; Warren and Hirth, 2006), creep cavitation and nucleation (e.g., (Précigout and Stünitz, 2016) and dissolution-precipitation (Hidas et al., 2016) can lead to the mixing of phases.

However, in order to determine which phase mixing processes are important during upper mantle shear zone evolution, shear zones from different geodynamic settings have to be studied in detail. In addition, the effect of the phase mixing process on strain localization is important to quantify. For this purpose, we analyzed the microstructures of the Erro-Tobbio peridotite in the Ligurian Alps, Northwest Italy. The peridotite was exhumed during rifting in Late Carboniferous-Permian times (e.g., Piccardo et al., 2014; Rampone et al., 2005). The first shear zones occurred during a first melt-free stage of rifting (thinning of the lithosphere by a factor of 2 (Padovano et al., 2015)). After the first stage, ongoing thinning of the lithosphere leads to decompression melting of the asthenosphere and to melt percolation in the shear zones under spinel-facies conditions (e.g., Padovano et al., 2015; Piccardo et al., 2014). Melts that reached the plagioclase-facies conditions in the Erro-Tobbio peridotites were silica-saturated due to extensive melt-rock reactions (e.g., Piccardo et al., 2014; Rampone et al., 2005). These melts formed plagioclase-enriched peridotites and gabbronorite pods (e.g., Piccardo et al., 2014).

Due to the extensive melt percolation during deformation, the spinel bearing shear zones of the Erro-Tobbio peridotite are ideal to analyze the importance of melt-rock reactions

on phase mixing and strain localization. Our detailed microstructural analysis shows the importance of reactions of silica-undersaturated melts with dynamically recrystallized clinopyroxene (cpx) neoblasts and orthopyroxene (opx) porphyroclasts to form fine-grained mixtures of cpx + olivine ± opx ± spinel and mixtures of opx + olivine ± cpx ± spinel, respectively. The opx-rich fine-grained layers interconnect to form ultramylonitic layers on a thin section scale. The strain rate in these layers is estimated to be one order of magnitude faster than in the olivine-rich matrix.

3.3   Geological Setting

The Erro-Tobbio peridotite is located in the Voltri Massif in the Ligurian Alps, Northwest Italy and is a remnant of the Jurassic Ligurian Tethys (Piccardo and Vissers, 2007). The peridotite exhumed due to extension of the subcontinental lithosphere during Late Carboniferous-Permian times (Rampone et al., 2005). Ongoing exhumation occurred during the opening of the Tethys in Jurassic times (Vissers et al., 1995).

The exhumation took place along five generations of shear zones, active at progressively decreasing PT conditions from spinel tectonite, plagioclase-, hornblende-, chlorite-bearing peridotite mylonites and serpentine mylonites (Hoogerduijn Strating et al., 1993). Opx and spinel clusters in lithospheric spinel peridotites have been interpreted as being breakdown products from garnet (Drury et al., 1991). Spinel tectonites and mylonites occur in kilometer-scale shear zones, were the fine-grained mylonites are superimposed on less-deformed tectonites (Padovano et al., 2015; Piccardo et al., 2014). Temperatures calculated with pyroxene geothermometers give a temperature of 960-970 °C (Rampone et al., 2005) for the spinel tectonites. These shear zones are thought to form during the early melt-free extension of the subcontinental lithosphere (e.g., Piccardo and Vissers, 2007). As a consequence of this early thinning of the lithosphere, near-adiabatic upwelling of the asthenosphere led to decompression melting and percolation of MORB-type melts during progressive extension (Piccardo and Vissers, 2007). This is evidenced by spinel harzburgites and dunites at several locations that are parallel to the spinel lherzolite tectonites and mylonites, indicating that silica-undersaturated melt is percolated by channeled porous flow along the pre-existing spinel-facies shear zones (Piccardo et al., 2014). Locally, the spinel peridotites are transformed to plagioclase-enriched peridotites (e.g., Padovano et al., 2015; Piccardo and Vissers, 2007). The high amount of plagioclase (frequently more than 10-15%), indicates that the plagioclase is not metamorphic but formed due to the interstitial crystallization of silica-saturated melt (Piccardo and Vissers, 2007). During ongoing exhumation, deformation occurred in these plagioclase peridotites, forming plagioclase peridotite tectonites and shear zones in the south of Erro-Tobbio (e.g., Hoogerduijn Strating et al., 1993; Padovano et al., 2015). These shear zones cut the spinel shear zones at a high angle

(Linckens et al., 2014). Geothermometry calculations indicate a temperature of 910-960 °C for the plagioclase tectonites (Rampone et al., 2005).

In the hornblende-bearing mylonites the pyroxene porphyroclasts show a syntectonic breakdown to very fine-grained (2-30 µm) mixtures of olivine + amphibole + clinopyroxene + spinel ± orthopyroxene (Mei et al., 2002). The formation of these fine-grained bands and the local occurrence of hornblende porphyroclasts within the olivine matrix indicate pre- and syn-kinematic infiltration of fluids (Mei et al., 2002). The pyroxenes geothermometry calculations give temperatures of 790-880 °C for the amphibole-bearing shear zones (Rampone et al., 2005). The last stages of exhumation at low temperatures and pressures are indicated by the occurrence of chlorite-bearing (500-800 °C) and serpentine (300-500 °C) mylonites (Mei et al., 2002).

Following exhumation, subduction took place during the closing of the Jurassic Ligurian Tethys to eclogite-facies conditions during the Alpine collision. Subsequent rapid exhumation within a serpentine subduction channel occurred, preserving the almost unaltered peridotites (e.g., Piccardo, 2013).

All four samples were taken within the tectonite-mylonite peridotite, located to the west of Lake Badana (Fig. 3.1a). In the field, clasts of mainly orthopyroxene are clearly visible, and some show a component of simple shear (Fig. 3.1b). Thin opx-rich layers alternating with olivine-rich layers are observed (Fig. 3.1b). Some of the layers include elongated spinel clasts (Fig. 3.1b).

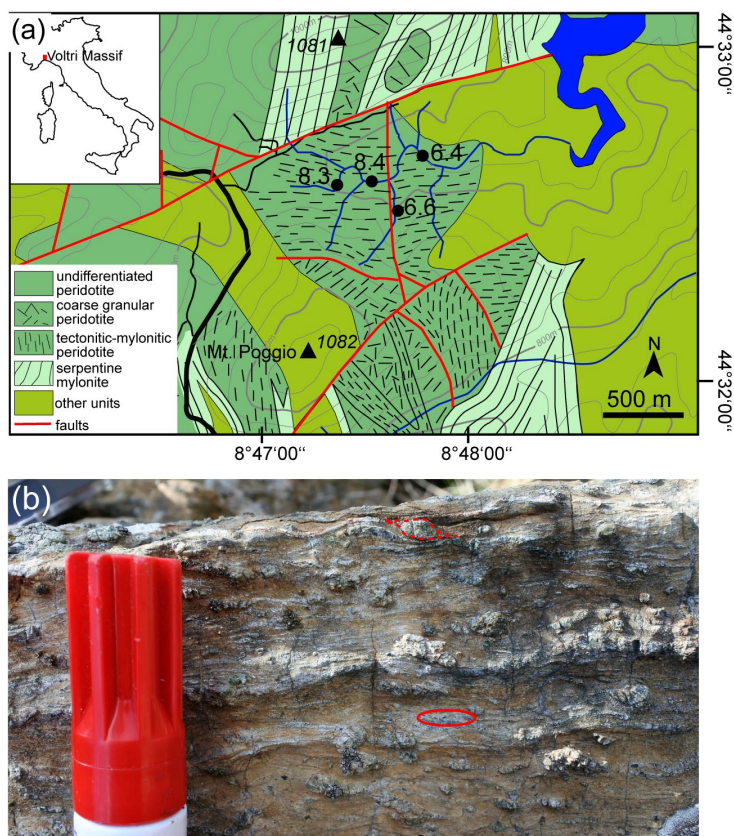*Fig. 3.1. (a) Geological map of the field area with sample locations (black circles) modified after Hoogerduijn Strating et al. (1993), Padovano et al. (2015). (b) Field photo of the spinel-bearing mylonites (location of Sample 6.4). In the red circle is a trail of elongated spinel. The dotted red line is a sigma opx porphyroclast indicating sinistral shear. High resolution, digital version is included on the CD.*

3.4   Materials and Methods

Samples were cut perpendicular to the foliation and parallel to the lineation (*X-Z* section). Thin sections were cut and polished to a thickness of ~30 μm. With an optical light microscope, representative microstructures were determined and selected for further analysis.

For electron backscatter diffraction analysis (EBSD) analysis, thin sections were polished for approximately 15 min with colloidal silica. Combined EBSD and energy dispersive X-ray analysis (EDX) were conducted at the Goethe University in Frankfurt (Germany) and the University of Cologne (Germany) on carbon-coated samples. At the Institute of Geoscience in Frankfurt, a JEOL JSM-6490 scanning electron microscope (SEM) was used. Measurement settings for EBSD were an acceleration voltage of 15 kV and a beam current of ~8 nA. For data acquisition, the program Flamenco (Oxford Instruments HKL Channel 5) and a Nordlys camera (Oxford Instruments) were used. At the Institute for Geology and Mineralogy in Cologne, EDX and EBSD measurements were conducted with a Zeiss Sigma 300-VP field emission SEM equipped with a NordlysNano detector (Oxford Instruments). The acceleration voltage was set to 20 kV. For the data acquisition, the program Aztec was used (Oxford Instruments). The step size was adapted to measured grain sizes in order for every grain to have at least 10 measurement points. The total range of step sizes is from 1-2.22 μm. In Cologne, element maps (O, Mg, Al, Si, Ca, Cr, Mn, Fe) were obtained simultaneously.

The EBSD data were cleaned from systematic misindexing of olivine (similar diffraction patterns for orientations rotated 60° around [100]) with Oxford Instruments HKL Channel 5 software. Subsequently, the data were loaded into the MTEX 5.6 extension for MATLAB (e.g., Bachmann et al., 2010) (http://mtex-toolbox.github.io/). All additional data processing and analysis were conducted with MTEX 5.6 (http://mtex-toolbox.github.io/). The MTEX script used for cleaning, grain detection (grain internal misorientation <15°) and subgrain detection (misorientation angle between subgrains <15°), deletion of boundary and badly indexed grains, crystallographic and boundary analysis, etc., is available on request from the authors. During grain reconstruction, resulting data were continuously checked against backscattered/forescattered, band contrast images and EDX data if present. The equivalent circular diameter (ECD) was calculated for all grains. EBSD and EDX maps were used to calculate phase abundances by area percentage. Throughout the text and the figures, phase abundances are given by "%" referring to area %. Grain boundary analysis was accomplished by calculating phase-specific boundary lengths. Phase (e.g., ol-opx) to grain (e.g., ol-ol, opx-opx) boundary percentages were used to determine the "mixing intensity". Pole figures (lower hemisphere orientation density plots) of the main phases were plotted with MTEX. A minimum number of 100 orientations (one point per grain)

was used. ODF calculation was performed with grain mean orientations and a consistent halfwidth of 15°. To be able to compare the orientation density plots, the color coding is consistently depicted from min = 0 mrd (multiple of random distribution) = blue for a random orientation to max = 3 mrd = red. Higher mrds than 3 are also colored red. The J-index and M-index were calculated for the CPO, which is a measurement of the strength of a CPO (Bunge, 1982; Skemer et al., 2005). The M-index is 0 for a completely random fabric and 1 for a single crystal fabric.

Microprobe measurements were conducted using a JEOL JXA-8530F Plus microprobe with field emission located at the Institute of Geoscience at the Goethe University Frankfurt. The microprobe is equipped with 5 wavelength-dispersive spectrometers. The acceleration voltage was 15 kV and a beam current of 20 nA was used for 20 s (Al, Cr, Ca, Na, Mn, Fe, Ni), 30 s (K, Ti) or 40 s (Mg, Si) peak and 20 s background measuring time. The spot-size was adjusted to the grain size with minimum spot sizes of 1 μm for small grained neoblasts and maximum 4 μm for porphyroclasts. Microprobe data were used to calculate equilibration temperatures of neoblast assemblages and porphyroclasts. Neoblasts are mostly exsolution free, therefore calculated T estimates are thought to be accurate. In opx porphyroclasts with cpx exsolution lamellae, we calculated temperatures based on the host porphyroclast chemistry, ignoring exsolution lamellae. Temperature estimates are therefore minimum estimates. We used the two pyroxene geothermometer ($T_{2\text{-pyx}}$) and Ca in opx geothermometer ($T_{Ca\text{-in-opx}}$) calibrated by Brey and Köhler (1990). In addition, we used the Al and Cr in the opx ($T_{Al\text{-Cr-in-opx}}$) geothermometer calibrated by Witt-Eickschen and Seck (1991).

3.5   Results
3.5.1 Sample Description

All thin sections show polymineralic (opx + ol + cpx ± spinel) ultramylonite layers with a small grain size (~10 μm) that can cross-cut the whole thin section (Fig. 3.2). Often there are well-preserved domains in between serpentine-filled cracks (Fig. 3.2a, bottom right and Fig. 3.3a,b). Often, fine horizontal cracks go through the layers (Fig. 3.3c). The grains in these layers have a very irregular form (Fig. 3.3d). The sample with the lowest amount of opx porphyroclasts also has the thinnest (down to 200 μm) polymineralic layers (Fig. 3.2d). In the samples with more opx porphyroclasts, the polymineralic layers can be up to 900 μm thick (Fig. 3.2a).
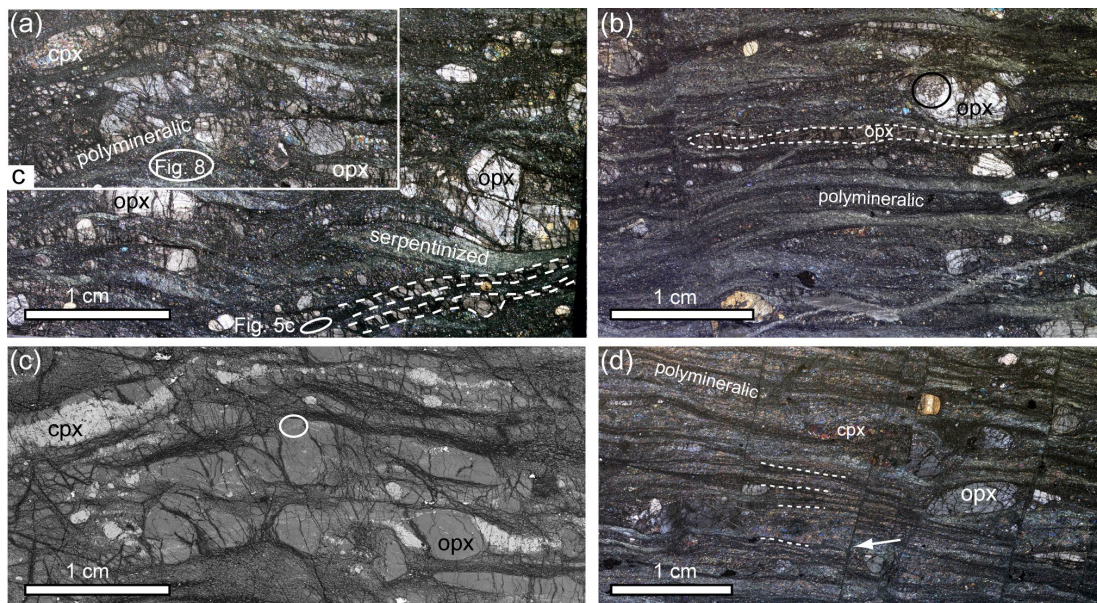
Fig. 3.2. *Overview of the thin sections.* ***(a)*** *Optical microscope image of Sample 6.6 under crossed polarized light. Opx porphyroclasts and some cpx porphyroclasts are visible, within an olivine-rich matrix. There are several fine-grained polymineralic layers visible (dashed white lines). Some of the opx porphyroclasts are elongated. Indicated is the location of Figure 3.5c (white ellipse) and the olivine matrix analyzed with EBSD displayed in Figure 3.8 (white ellipse); also indicated is the location of (c).* ***(b)*** *Optical microscope image of Sample 8.4 under crossed polarized light. The sample is similar to Sample 6.6 but shows fewer opx porphyroclasts and an increasing amount of fine-grained polymineralic layers. Some opx porphyroclasts are elongated as shown by the stippled line. Some opx porphyroclasts are recrystallized (black circle).* ***(c)*** *Part of (a) as backscatter electron (BSE) image. The bright phase is cpx, the medium gray is olivine/opx and the dark is serpentine. The polymineralic layers contain cpx as indicated in the white circle. All the cpx porphyroclasts show tails of smaller, cpx ± olivine neoblasts.* ***(d)*** *Optical microscope image of Sample 8.3 under crossed polarized light. Thin dark layers parallel (dashed lines) to the olivine matrix are fine-grained polymineralic layers. The sample also shows later stage vertical fractures that offset these thin layers (white arrow). High resolution, digital version is included on the CD.*

Fig. 3.3. (a) *Optical microscope image with crossed polarized light of a polymineralic fine-grained layer (ultramylonite) within the olivine-dominant matrix. Location of (b) is indicated.* ***(b)*** *Backscatter electron (BSE) image of part of the fine-grained polymineralic layer. Visible are fine-grained cpx grains (lightest gray) and opx + ol grains within the layer. Gray values for opx and ol are very similar. In addition, in this image cpx grains are visible within the olivine matrix (arrows).* ***(c)*** *Optical microscope image of part of a fine-grained layer with horizontal cracks (dashed red line).* ***(d)*** *BSE image of a fine-grained layer. Darkest grains are opx, gray is olivine and light gray is cpx. Dashed lines show thin elongated opx grains on the border of olivine grains. High resolution, digital version is included on the CD.*

Orthopyroxene clast size ranges from around 0.3 mm up to around 5 mm. Some opx porphyroclasts are elongated and can reach an aspect ratio of up to 20:1 (Fig. 3.2b), however most clasts show small aspect ratios. The porphyroclasts often show undulose extinction. Some porphyroclasts in the samples with small amounts of porphyroclasts (Samples 8.3 and 8.4) show a few subgrains at the border. Some of these porphyroclasts also display some recrystallization at the borders, where dominantly opx occurs (Fig. 3.4g). Some of the opx grains have 120° triple junctions, indicating annealing (Fig. 3.4f). Most opx porphyroclasts show exsolution lamellae of cpx. Some smaller opx porphyroclasts and elongated or folded opx porphyroclasts show a fine-grained polymineralic tail and/or rim (Fig. 3.4a-c, e-f) consisting of olivine, pyroxenes ± spinel. At the border of small opx porphyroclasts and the tips of the elongated opx, olivine grains often occur in embayments (Fig. 3.4a-c). Some opx clasts are kinked and along the kinks small cpx and opx grains occur (Fig. 3.4d).
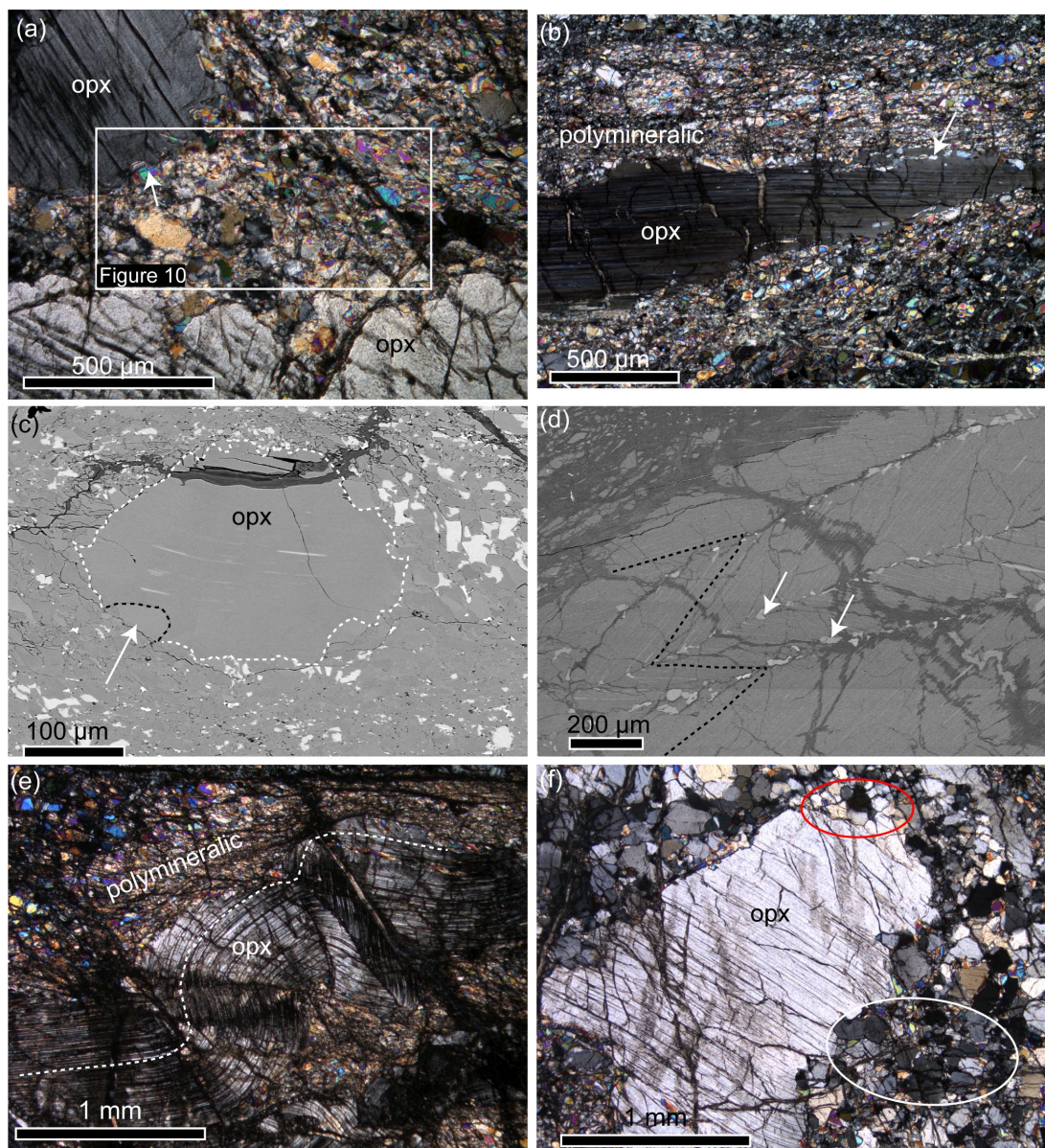
Fig. 3.4. *Orthopyroxene porphyroclasts. (**a**) Optical microscope image under crossed polarized light of an orthopyroxene porphyroclast with olivine embayments (arrow). Indicated is the location of the EBSD map of Figure 3.10. (**b**) Optical microscope image under crossed polarized light of an elongated opx porphyroclasts surrounded by fine-grained polymineralic layers. The porphyroclast shows embayments of olivine (arrow). (**c**) BSE image of an opx porphyroclast (dashed white line) showing cpx exsolution lamellae and olivine embayment (arrow). The porphyroclast is located in a fine-grained polymineralic (opx + ol + cpx + spinel) matrix. (**d**) BSE image of a kinked opx porphyroclast (black dashed line traces a cpx exsolution lamellae) with small cpx (white arrows) on the kinks and grains at the border. (**e**) Folded opx porphyroclasts with cpx exsolution lamellae and a fine-grained polymineralic rim. (**f**) Orthopyroxene porphyroclast surrounded by relatively coarse grains of opx (compared to (e)). Some opx grains show close to 120° interfacial angles at triple junctions (red circle). The area in the white circle includes, besides opx, smaller grains of olivine, cpx and spinel. High resolution, digital version is included on the CD.*
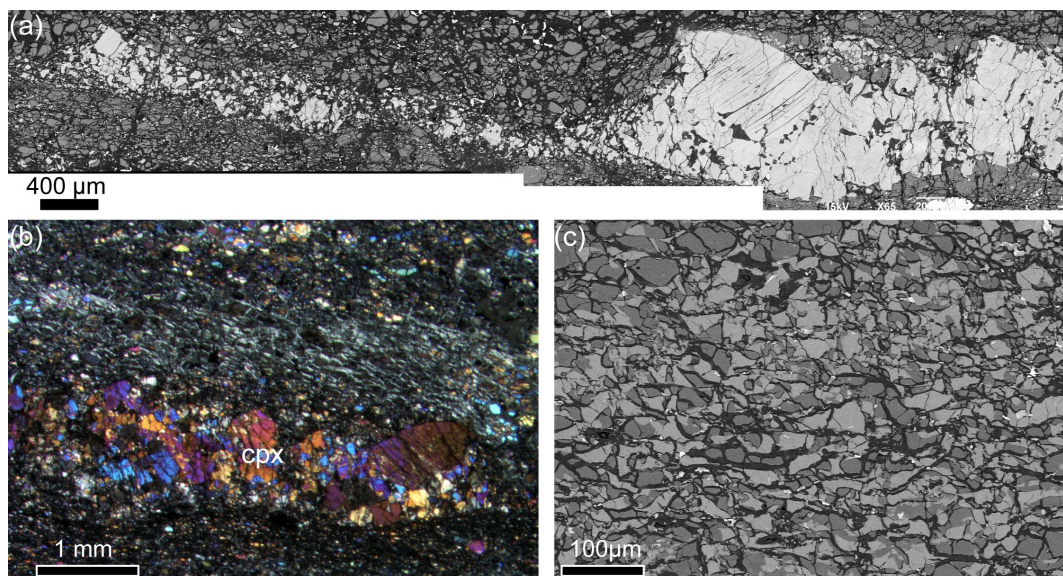
Fig. 3.5. (a) *BSE image of recrystallized cpx porphyroclasts adjacent to the porphyroclast cpx neoblasts, and further away a tail of cpx + olivine.* ***(b)*** *Optical microscope image with crossed polarizers of a recrystallized cpx layer.* ***(c)*** *BSE image of cpx and olivine grains in the matrix (ROI 32). High resolution, digital version is included on the CD.*

Clinopyroxene porphyroclasts occur in all samples and range in size from 190 µm to 2.7 mm. Commonly they show opx exsolution lamellae (Fig. 3.5a). Most cpx porphyroclasts show a rim or tail of smaller cpx grains (Fig. 3.5a,b), and further away from the porphyroclast the cpx neoblasts are intermixed with olivine grains (Fig. 3.5b). In some samples these tails are thin, and they can extend up to 2 cm to form cpx-rich layers (Fig. 3.2c/ 5a). Cpx grains are also prominent in some areas within the olivine-rich matrix (Fig. 3.5c).

Parts of the olivine matrix are highly serpentinized and individual grains are difficult to distinguish under the optical microscope. Where individual grains can be observed the average grain size in the matrix is around 60 µm. No olivine porphyroclasts are observed.

Porphyroclasts of spinel occur in all samples (range in sizes 0.3-1.4 mm); some porphyroclasts form clusters with opx. Some spinel porphyroclasts are stretched (aspect ratios up to 5) in the foliation. Smaller spinel grains occur in the olivine matrix (Fig. 3.5c), and within recrystallized rims and tails of the pyroxene clasts.

3.5.2 EBSD Data

3.5.2.1   Clinopyroxene

Two recrystallized cpx porphyroclasts were mapped with EBSD (Table 3.1, Fig. 3.6/ S3.1). The mapped areas consist mainly of clinopyroxene (95% and 87%, Fig. 3.6/ S3.1). The other phases are olivine (4% and 5%), enstatite (<1% and 4%) and spinel (<1% and 5%). These maps consist of 75% and 53% grain boundaries (Table 3.1), with average cpx grain sizes of 36 μm and 30 μm, respectively. In the map shown in Figure 3.6, small grains of cpx are observed in between larger cpx grains. These small grains are associated with small opx and spinel grains. Small olivine grains (15 ± 7 μm) occur with cpx in phase mixtures at the border of the recrystallized tail (Fig. 3.6c). The cpx grain size in these phase mixtures is much smaller than the grains close to the porphyroclast border. The cpx CPO is related to the clast orientation (Fig. 3.6d/ S3.1). A few cpx grains show a large internal misorientation up to 8° (Fig. 3.6b). The small cpx grains at the border of the recrystallized area, intermixed with olivine, show no internal misorientations (Fig. 3.6b). The olivine grains show no clear CPO (Fig. 3.6d).

Map Name	Type	Olivine		Opx		Cpx		Spinel		Pargasite		PB
		Area	Grain Size	Area	Grain Size	Area	Grain Size	Area	Grain Size	Area	Grain Size	
ROI 12	cpx rxs	5	15 ± 7	4	19 ± 12	87	30 ± 41	5	18 ± 20			47
ROI 16	cpx rxs	4	18 ± 11	<1	18 ± 8	95	36 ± 42	<1	16 ± 6			25
ROI 33	cpx rxs with ol	33	10 ± 6	1		66	11 ± 9	<1				63
ROI 32	olivine + cpx	58	16 ± 8	3	12 ± 4	37	15 ± 7	3	9 ± 4			64
ROI 20	small opx rxs	48	16 ± 12	45	15 ± 12	6	12 ± 8	1	9 ± 3			72
ROI 24	small opx rxs	66	12 ± 8	32	12 ± 10	1	8 ± 3					61
ROI 25	large opx rxs	33	14 ± 8	50	17 ± 15	15	15 ± 11	2	10 ± 5			73
ROI 25	Olivine	88	45 ± 30	7	27 ± 11	3	28 ± 10	2	27 ± 10			45
ROI 31	Olivine	73	23 ± 16	15	17 ± 9	9	17 ± 9	2	10 ± 5			68
ROI 13	Ultramylonite	62	12 ± 7	29	12 ± 7	9	11 ± 5					67
ROI 14	Ultramylonite	76	5 ± 4	16	4 ± 3	6	4 ± 2	1	3 ± 1	<1		52
ROI 19	Ultramylonite	51	11 ± 7	39	10 ± 8	7	9 ± 5	3	8 ± 9	<1	7 ± 2	66
ROI 23	Ultramylonite	75	9 ± 6	21	8 ± 4	4	7 ± 4					52

Table 3.1. *Area percentages and grain sizes (μm), with the standard deviation, of all analyzed phases. The last column shows the proportion of phase boundaries (PB) of the total boundary length as a percentage.*
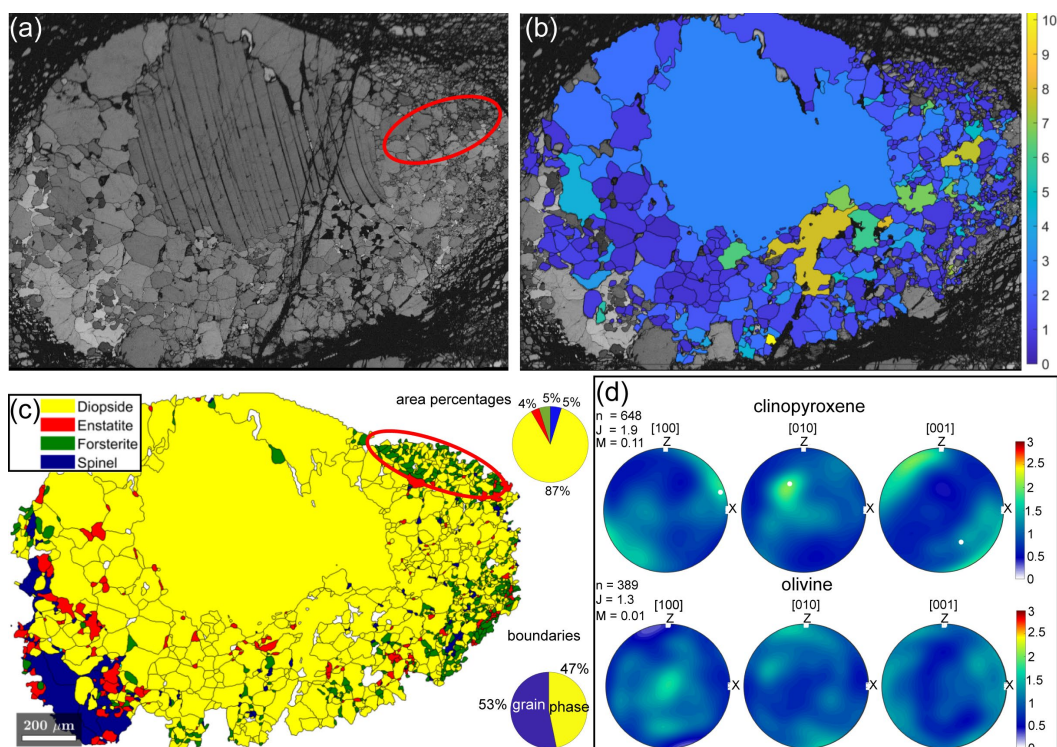
Fig. 3.6. (a) *Band contrast image of a recrystallized cpx porphyroclast (ROI12). The red circle shows an area with fine-grained layers in between larger grains.* ***(b)*** *Grain orientation spread (GOS) map of diopside, displaying the internal misorientation of the grains.* ***(c)*** *Phase map. The red circle shows mixed olivine and cpx domains at the border of the clast.* ***(d)*** *Clinopyroxene and olivine CPO. High resolution, digital version is included on the CD.*

The map of smaller cpx porphyroclasts (Fig. 3.7) shows olivine grains directly at the porphyroclast border, and in contrast to the other two analyzed porphyroclasts, it has a relatively high proportion (63%) of phase boundaries. The phase mixture consists of 66% cpx and 33% olivine, with a small amount of spinel (1%) and opx (<1%). The recrystallized opx grain sizes are smaller (average 11 µm ± 9 µm) for this cpx porphyroclast than for the other two cpx porphyroclasts (Table 3.1). The grain size is similar to the olivine grain size (10 ± 6 µm, Table 3.1). The clinopyroxenes show a weak CPO related to the host orientation. No olivine CPO is observed (Fig. 3.7).
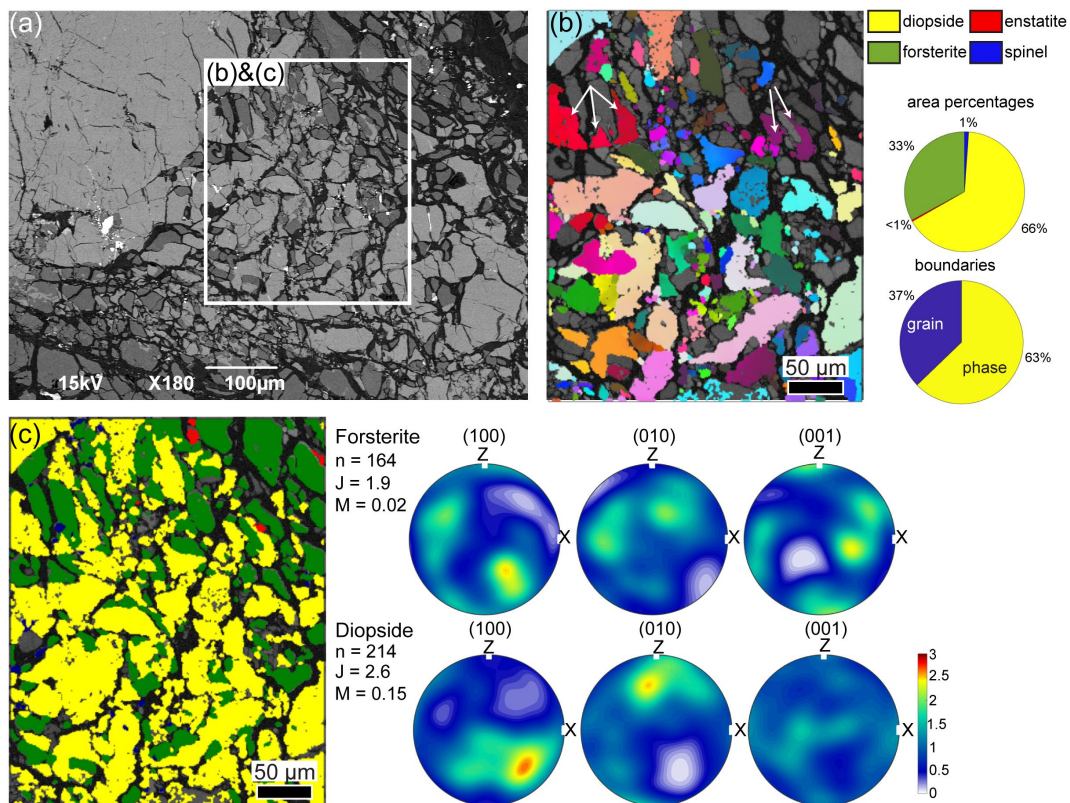
Fig. 3.7. (a) *BSE image of a cpx porphyroclast with recrystallized tail of olivine and cpx neoblasts.* ***(b)*** *Diopside orientation map of the recrystallization tail (ROI33). White arrows show one grain of diopside with irregular boundaries and olivine in between.* ***(c)*** *Phase map of the same area as in (b). The CPOs of clinopyroxene and olivine are also shown. High resolution, digital version is included on the CD.*

In addition to the cpx porphyroclasts, an olivine + cpx matrix domain was analyzed with EBSD (Fig. 3.5c/ 8). The cpx- (37%) and olivine (58%)-rich matrix contains small amounts of opx and spinel (both 3%) (Fig. 3.5c). A large amount of serpentine occurs, which makes the boundary and grain size analyses more prone to errors. The map consists of 64% phase boundaries. Both olivine and cpx grain sizes are relatively small (16 ± 8 µm and 15 ± 7 µm, respectively; Table 3.1). The [001] axes of olivine are oriented parallel to the lineation and the [100] axes are oriented perpendicular to the foliation (Fig. 3.8). The (100) planes of diopside are orientated perpendicular to the lineation and the [001] axes are oriented parallel to the foliation.

A map of the cpx-poor (9%) olivine matrix (73%) was also analyzed (Table 3.1, Fig. 3.8/ S3.2), which contains 15% opx. Due to the well-dispersed pyroxene grains, the phase boundaries make up 68% of the total boundaries. The olivine grain size in this matrix is slightly bigger (23 ± 16 µm), but within error, than the olivine grain size of the cpx-rich matrix. The grain sizes of the other minerals are similar (Table 3.1). The olivine CPO is weak (J-index of 1.6, M-index of 0.04) with the [100] axes parallel to X and [001] axes perpendicular to the foliation (Fig. 3.8).
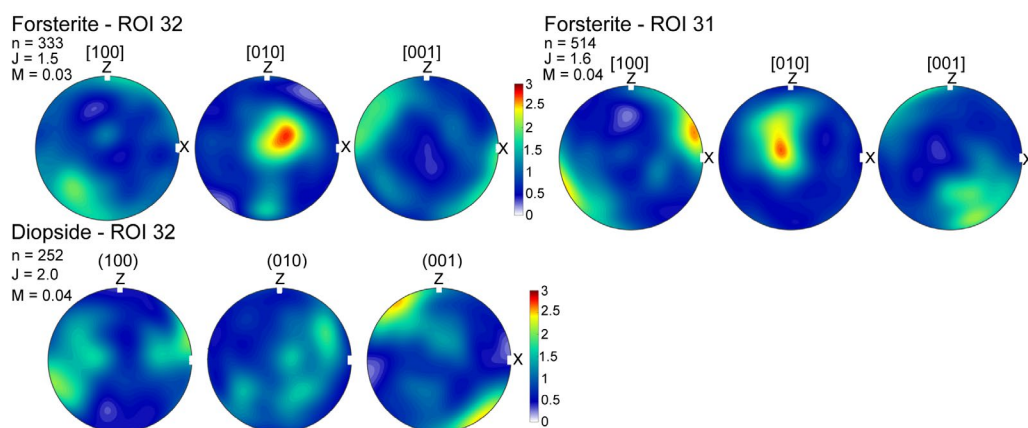
Fig. 3.8. *Forsterite and diopside CPO of the matrix displayed in Figure 3.6c (ROI32) and of the olivine matrix (ROI31).*

3.5.2.2   Orthopyroxene

Three maps of recrystallized opx clasts were measured (Table 3.1, Fig. 3.9/ 10/ S3.3). The recrystallized tails consist of mainly opx (32-50%) and olivine (33-66%). The cpx abundance is variable (1-15%, Table 3.1), and spinel is an accessory phase (1-2%).
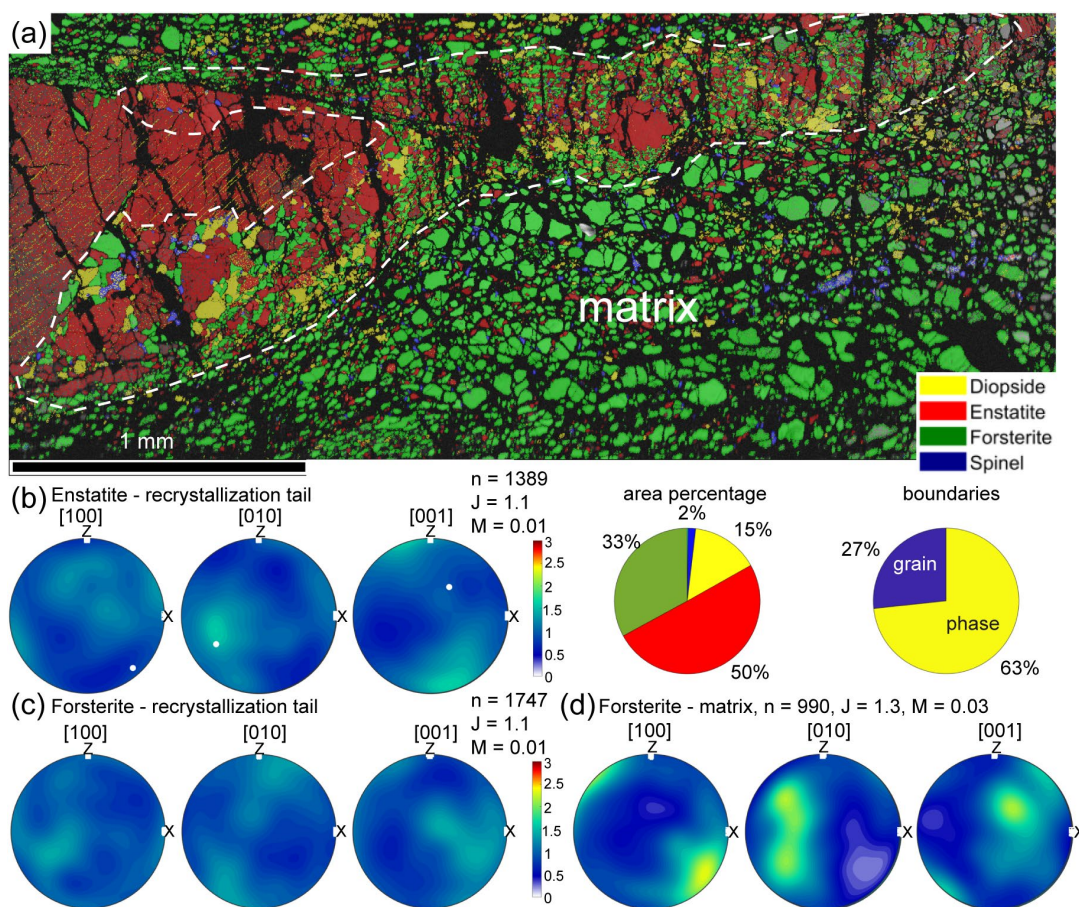
Fig. 3.9. (a) *Phase map of an opx porphyroclast with a recrystallization tail (dashed line) within the olivine matrix; also indicated are the area percentages of the phases and the amount of grain and phase boundaries of the recrystallization tail (ROI25).*

*← **Fig. 3.9. (b)** Pole figure of enstatite orientations in the recrystallization tail. The white dot shows the orientation of the opx porphyroclast. **(c)** Pole figure of forsterite orientations in the recrystallization tail. **(d)** Pole figure of forsterite orientations in the matrix.*

The larger opx porphyroclast shows at the lower border a mixture of relatively coarse-grained opx + ol + cpx ± spinel. These larger opx grains have a relatively large misorientation (up to > 40°) from the opx porphyroclast orientation. The map shows a thin (~100 µm) polymineralic tail extending from the orthopyroxene porphyroclast. The grain sizes in this band are small (opx: 17 ± 15 µm, olivine: 14 ± 8 µm, cpx: 15 ± 11 µm). None of the minerals show a CPO and the J-index and M-index is small for both opx (J = 1.1, M = 0.01) and olivine (J = 1.1, M = 0.01) (Fig. 3.9b,c).

The surrounding olivine-rich matrix (83%) has a larger average grain size (45 ± 30 µm, Table 3.1). Included in the matrix are some (9%) smaller opx grains (27 ± 11 µm), spinel grains (4%, 27 ± 10 µm) and cpx grains (4%, 28 ± 10 µm). The olivine CPO is weak (J-index of 1.3, M-index of 0.03) and shows [100] close to the lineation, [010] close to Y and [001] close to the Z axis (Fig. 3.9d).

The neoblasts adjacent to the small opx porphyroclasts have an inhomogeneous grain size; there are some concentrated lines where very small (~5 µm), mainly orthopyroxene grains occur (Fig. 3.10). Additionally, in these areas pargasite is present, and also visible are embayments of olivine in some larger opx grains of the phase mixture (Fig. 3.10). The phase boundaries are very irregular and lobate. The opx shows a weak CPO (J-index: 1.6, M-index: 0.05), with [001] close to X and [010] perpendicular to the foliation. The orientations of [010] and [001] are close to the porphyroclast orientation (Fig. 3.10). The olivine CPO is relatively weak (J-index: 2.6 and M-index: 0.15), the [100] axes are parallel to X and [010] axes perpendicular to the foliation. Diopside shows a CPO of [100] parallel to Y and [010] perpendicular to the foliation.
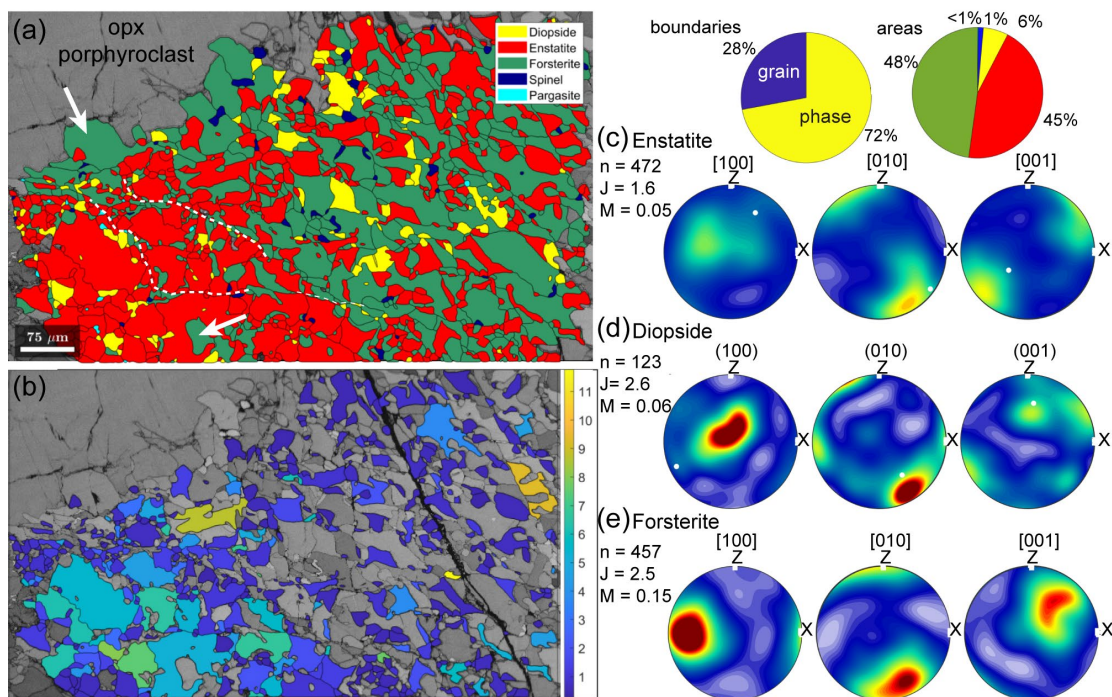
Fig. 3.10. (a) Phase map of a recrystallization tail of an opx porphyroclast (ROI20), located at the top left of the map. The white arrows indicate olivine embayments in the opx porphyroclast and an opx neoblast. The white dashed lines follow cracks along which small grains are visible. Shown at the top right are the grain and phase boundary percentages and area percentages. (b) Band contrast image and the grain orientation spread (GOS) in each enstatite grain. (c-e) CPO of enstatite, diopside and forsterite. High resolution, digital version is included on the CD.

3.5.2.3   Fine-Grained Layers

Four areas were analyzed of different fine-grained polymineralic layers in the thin sections (Table 3.1). One example is shown (Fig. 3.11); the other three are displayed in the supplementary data (Fig. S3.4-S3.6). All layers are dominated by olivine (51-76%) followed by opx (16-39%), cpx (4-9%) and spinel (1-3%). Phase boundaries are dominant and have a similar percentage in all four maps (62-67%). The average grain size ranges from 4-12 µm for all phases (Table 3.1). None of the phases show a CPO in these layers (Fig. 3.11c-d).
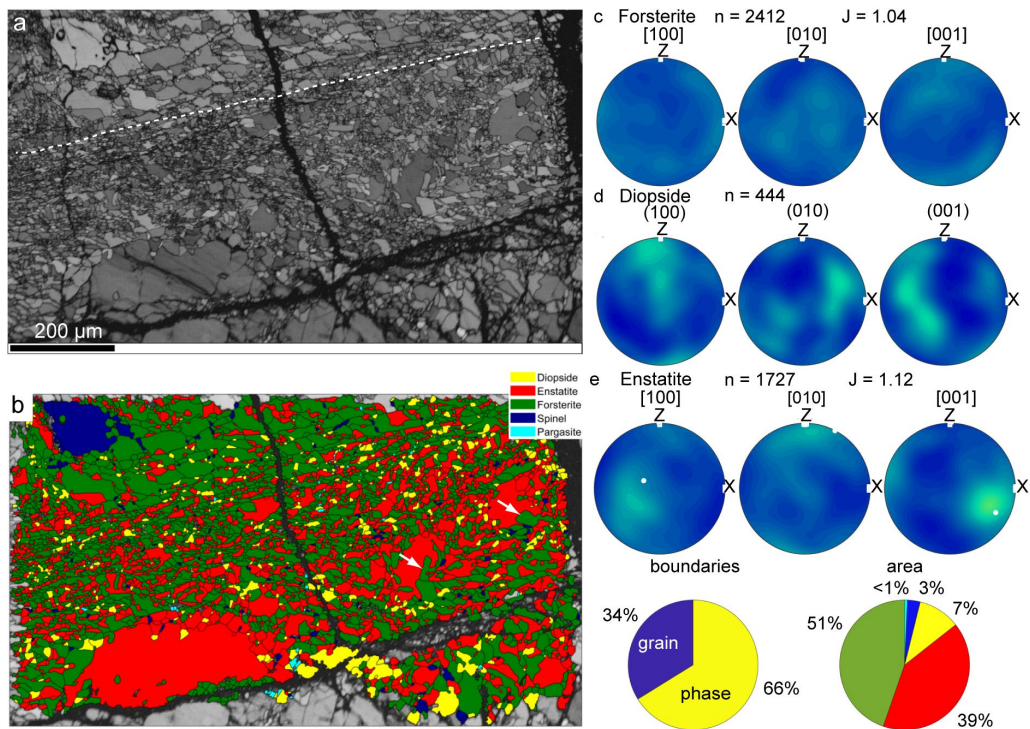
Fig. 3.11. (a) *Band contrast image of a fine-grained layer (ROI19). Cracks, parallel to the layer, go through the fine-grained part of the layer (dashed white line). There are more cracks parallel to this layer. **(b)** Phase map of the fine-grained layer. At the top is an olivine-rich layer with small grains of other phases on the grain boundaries. The grain shapes are very irregular in the fine-grained layer. Bigger opx grains at the right of the map show embayments of olivine (white arrows). **(c-e)** CPO of forsterite, diopside and enstatite. High resolution, digital version is included on the CD.*

3.5.3 Chemical Composition and Geothermal Calculations

The chemical data are shown in Table S3.1. Orthopyroxene shows a correlation between Al_2O_3 (0.92-5.12 wt.%) and Cr_2O_3 (0.04-0.63 wt.%), where porphyroclasts have the highest values, and opx neoblasts in the fine-grained layers the lowest (Fig. 3.12a). The neoblasts show values similar to the fine-grained layers and the range goes up to the lowest values of the porphyroclasts (Fig. 3.12a). A similar difference in composition is shown by CaO (range from 0.26-1.42 wt.%), where the opx in the fine-grained layers shows the lowest values and porphyroclasts the highest values of CaO (Fig. 3.12b). In clinopyroxenes there is a correlation between Cr_2O_3 (range from 0.21-1.08 wt.%) and Al_2O_3 (range from 2.12-6.95 wt.%), where both decrease from porphyroclasts to fine-grained neoblasts (Fig. 3.12d). The neoblasts have values of both Cr_2O_3 and Al_2O_3 spanning the whole range, connecting the fine-grained neoblasts and porphyroclasts (Fig. 3.12c). The values of TiO_2 (range from 0.22-0.72 wt.%) show no dependence on the microstructural site (Fig. 3.12d).

The geothermometry calculations give an average temperature for the neoblasts of 884 ± 58 °C ($T_{Ca-in-opx}$), 823 ± 59 °C ($T_{Al-Cr-in-opx}$) and 853 ± 32 °C (T_{2pyx}) (Table 3.2). These average values are similar, within error. The porphyroclasts show a distinctly higher calculated temperature ($T_{Ca-in-opx}$ 1059 ± 95 °C, $T_{Al-Cr\ in\ opx}$: 1022 ± 47 °C). The calculated temperatures from the fine-grained layers are always lower than the neoblast temperatures, but within error (Table 3.2). The lowest temperatures (775 ± 48 °C) are calculated with the Al-Cr-in-opx geothermometer in the fine-grained layers.
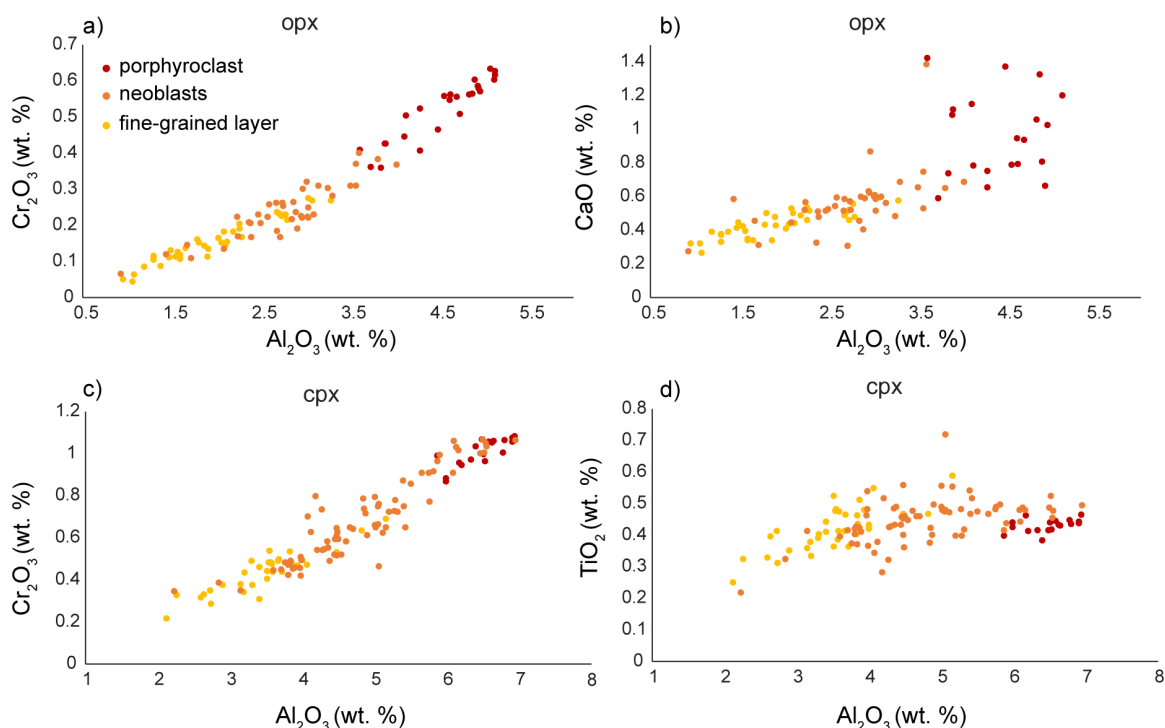
Fig. 3.12. (a) Cr_2O_3 *(wt.%) vs. Al_2O_3 (wt.%) in opx;* **(b)** *CaO vs. Al_2O_3 in opx;* **(c)** *Cr_2O_3 (wt.%) vs. Al_2O_3 (wt.%) in cpx;* **(d)** *TiO_2 (wt.%) vs. Al_2O_3 (wt.%) in cpx. Red symbols are porphyroclast, orange symbols are neoblasts and yellow symbols are grains in fine-grained layers.*

	n	$T_{Ca-in-opx}$	$T_{Al-Cr-in-opx}$	n	T_{2-pyx}
porphyroclasts	4 (24)	1059 ± 95	1022 ± 47		
neoblasts	6 (50)	884 ± 58	823 ± 59	6 (19)	853 ± 32
fine-grained	6 (29)	846 ± 38	775 ± 48	5 (14)	843 ± 30

Table 3.2. *Results of geothermometry calculations for porphyroclasts, neoblasts and neoblasts in fine-grained layers. "n" indicates how many porphyroclasts or different areas were measured and in brackets the total number of measurements is given. The temperatures are averages in °C with their standard deviation.*

3.6   Discussion

3.6.1 Microstructural Evolution

The opx and cpx porphyroclasts both show the formation of smaller recrystallized grains at their borders. The cpx porphyroclasts show mainly cpx neoblasts adjacent to the porphyroclasts, with a small amount of opx neoblasts (4%, Fig. 3.6d). The cpx neoblast CPO is related to the porphyroclast orientation (Fig. 3.6c) and the bigger neoblasts show an internal misorientation (Fig. 3.6b). No olivine embayments are observed in these cpx porphyroclasts (Fig. 3.6/ S3.1). The lack of olivine embayments and the CPO indicate that the neoblasts were formed by dynamic recrystallization of the cpx porphyroclast. The small opx neoblasts are likely coming from exsolution lamellae from the cpx porphyroclasts.

Further away from the cpx porphyroclasts, in recrystallization tails, and adjacent to smaller cpx porphyroclasts, a mixing of olivine and cpx occurs. The irregular shape of the cpx and olivine grains (Fig. 3.5a/ 7a) and the cluster of similar cpx orientations with olivine in between (Fig. 3.7b), suggest that a silica-undersaturated melt percolated through after the dynamic recrystallization stage, dissolving cpx and precipitating olivine. The melt percolation of silica-undersaturated melts occurred during rifting, due to decompression melting of the asthenosphere (Fig. 3.13, Padovano et al., 2015; Piccardo and Vissers, 2007).

In contrast to the bigger cpx porphyroclasts, opx porphyroclasts show rims and/or tails consisting of opx (32-50%) + olivine (33-66%) + cpx (8-15%) ± spinel (1-2%) (Fig. 3.9/ 10). The occurrence of olivine embayments at the borders of opx porphyroclasts and of some bigger neoblasts (Fig. 3.4b,c/ 10e/ 11b) and the formation of fine-grained polymineralic rims surrounding folded and elongated opx porphyroclasts indicate that deformation partially occurred in the presence of a silica-undersaturated melt. The melt-rock reaction combined with ongoing deformation led to the formation of fine-grained (average around 15 μm, Table 3.1) tails adjacent to opx porphyroclasts. Enstatite and forsterite neoblasts next to the big porphyroclasts show no CPO (Fig. 3.9b), indicating that ongoing deformation in these fine-grained layers occurred during diffusion creep. The enstatite neoblasts next to the small opx porphyroclasts show a CPO related to the opx porphyroclast (Fig. 3.10a). In addition, the opx shows some internal misorientation in the bigger neoblasts (Fig. 3.10b), indicating that a combination of dislocation and diffusion creep was active in these layers. This is also indicated by the olivine CPO (Fig. 3.10) that shows an A-type CPO, which is the common slip system in olivine in dry conditions (Karato et al., 2008).

In contrast to cpx porphyroclasts, most opx porphyroclasts show little evidence for dynamic recrystallization prior to melt percolation. This indicates that in the first stage of rifting, prior to melt percolation, dynamic recrystallization of cpx occurred, and likely

olivine porphyroclasts as well (Fig. 3.13). Orthopyroxene porphyroclasts possibly got folded and elongated during these first stages of deformation. With ongoing extension and thinning, decompression melting and infiltration of melt in the shear zones occurred (Linckens et al., 2014). The silica-undersaturated melt reacted with the dynamically recrystallized cpx tails and the opx porphyroclast. These reactions occurred during deformation and fine-grained mixtures formed at the rims of the porphyroclasts. Ongoing deformation under subsolidus conditions led to further grain size reduction and interconnected fine-grained layers (Fig. 3.2/ 3a/ 13) in which deformation could localize. These layers deform by diffusion creep as shown by the lack of CPO of all phases (Fig. 3.11c-e). The layers consist mainly of olivine (51-76%) and opx (16-39%) with a small amount of cpx (4-11%).

The presence of a small amount of amphibole (<1%) in the fine-grained layers (Fig. 3.10a/ 11b) indicates possible fluid/melt infiltration in the later stages of deformation. A late stage of deformation is indicated by horizontal cracks localized within the ultramylonite layers (Fig. 3.11a), and some randomly oriented cracks in recrystallization tails (Fig. 3.10a). Along the horizontal cracks, olivine and opx grain boundaries are aligned. In addition, small-sized, mainly opx grains are found along the cracks (Fig. 3.10b/ 11a).
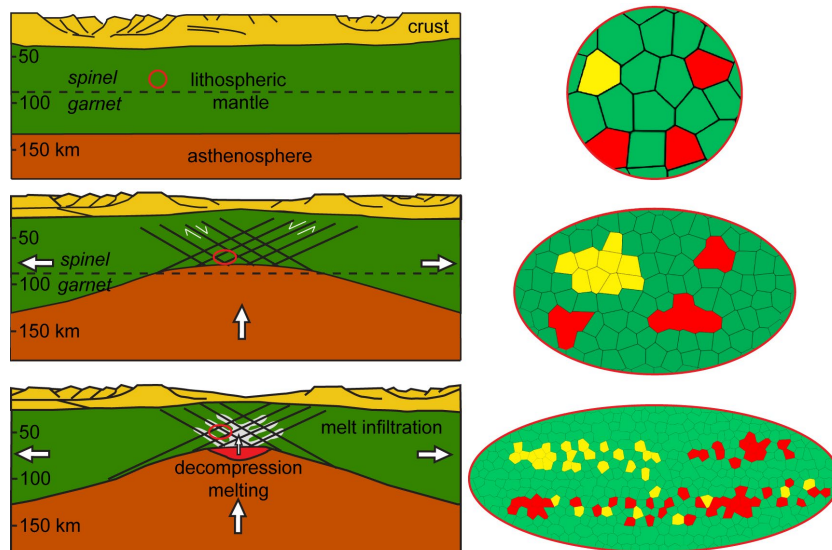
Fig. 3.13. *Sketches of the rifting (modified after* Piccardo et al., 2014) *in the left panels and the corresponding microstructural evolution (located at the red circle and ellipses) in the spinel shear zones of the Erro-Tobbio peridotite in the right panel. The white arrows indicate the movement directions of lithosphere and asthenosphere. The microstructures show the evolution from the undeformed peridotite with large grains of olivine (green), opx (red) and cpx (yellow). During the first stage of thinning, cpx and olivine recrystallize, whereas opx porphyroclasts elongate or remain equigranular. During ongoing thinning melt infiltrates, reacts with the dynamically recrystallized cpx grains and opx porphyroclasts, forming cpx+ol fine-grained layers and opx + ol + cpx fine-grained layers.*

3.6.2 Olivine-Rich Matrix

In order to determine the strain rate contrast between the fine-grained ultramylonite layers and the olivine-rich matrix, the grain size of both is needed. Due to the serpentinization, the olivine grain size of the matrix is difficult to determine. Domains of the matrix that can be analyzed, due to lower amounts of serpentinization, contain relatively high amounts of second phases. Two maps of the matrix that contain second phases (pyroxenes and spinel, totals of 12% and 26%, respectively) give grain sizes of 45 ± 30 μm and 23 ± 16 μm, respectively (Table 3.1). Due to pinning effects, these grain sizes are probably a lower limit of the matrix olivine grain size (Linckens et al., 2015). The pinning effect can also be high as the phases in the matrix are relatively well-mixed, as indicated by the high amount of phase boundaries compared to grain boundaries (45% and 68%, respectively (Table 3.1)). Some parts of the matrix consist of well-mixed (64% phase boundaries) olivine (58%) and cpx (37%) (Fig. 3.6c/ Table 3.1). With the lack of a clear host clast, the high amount of cpx in parts of the matrix is difficult to explain. It is possible that it was formed by extensive reactions of undersaturated silica melt with cpx neoblasts. Alternatively, some cpx enrichment in the olivine matrix could have occurred at the later stages of melt infiltration. In these later stages the melt was possibly enriched in silica due to extensive melt-rock reactions (e.g., Padovano et al., 2015).

The olivine CPO in this cpx-rich matrix shows a C-type CPO with the [001] axes parallel to the lineation and the [100] axes perpendicular to the foliation (Karato et al., 2008). The C-type CPO has been suggested to form when water (Jung and Karato, 2001) or melt (e.g., Tommasi et al., 2006) is present. The olivine CPO in the matrix shows the [100] axes parallel to the lineation and the [001] axes perpendicular to the foliation, which has been classified as the E-type CPO, which is thought to be dominant in water-rich conditions (Karato et al., 2008). In contrast, in the recrystallization tail of a small opx, the A-type CPO was observed (Fig. 3.10), which is suggested to be dominant in dry conditions (Karato et al., 2008). In a few upper mantle shear zones, a transition from A-type to an E-type CPO has been observed to occur with increasing strain localization (i.e., protomylonites to ultramylonites; e.g., Linckens et al., 2011; Park and Jung, 2017). This change in CPO has been suggested to be caused by an increase in water content (Park and Jung, 2017) or a decrease in temperature during strain localization (Linckens et al., 2011). This transition is the opposite of what is observed in the Erro-Tobbio shear zone, where we find the E-type CPO in the olivine matrix.

In the Ronda shear zone, a detailed study on CPO evolution found different CPO types which are related to water content (Précigout et al., 2017). During strain localization, water migrates to the ultramylonites, due to water pumping along grain boundaries. The dry CPO type is found in the drained parts of the shear zone whereas the water-rich CPO is found closer to the ultramylonites. The ultramylonites show a dry CPO type as the fluid is further distributed in new grain boundaries. In the Erro-Tobbio shear zone, the

difference in dry CPO type in the recrystallized layer (Fig. 3.10) compared to the wet CPO type in the matrix (Fig. 3.9) could possibly be related to the same process as described in (Précigout et al., 2017). In this case, the fluid is distributed along the new grain boundaries in the finer-grained areas. However, a more detailed study of the CPO in the different areas of the samples has to be conducted to be able to determine the process responsible for the different CPO types in the Erro-Tobbio shear zone. As the fine-grained layers do not show a CPO (Fig. 3.11), no CPO type can be determined for these layers. In addition, the development of a CPO can be complex, and for the Josephine peridotite the A- and E-type were found in different samples with similar water content (Kumamoto et al., 2019). Here, the pre-existing CPO played a large role in the CPO evolution (Kumamoto et al., 2019). The importance of a pre-existing CPO and geometry of deformation has been shown in a recent study on various natural rock samples (Bernard et al., 2019). This study shows that any of the CPO types (A- to E-types) can form at very low water content and low stresses (Bernard et al., 2019).

In any case, the olivine CPOs suggest that deformation by dislocation creep or dislocation-accommodated grain boundary sliding (disGBS) occurred in the olivine-rich matrix.

3.6.3 Strain Localization

The microstructural evolution indicates the importance of melt-rock reactions for grain size reduction and extensive phase mixing in the shear zone. Due to this grain size reduction, the deformation changes from dislocation creep in the matrix to diffusion creep in the ultramylonite layers.

In order to determine the effect of the decrease in grain sizes and change in de-formation mechanism on the strain rate, a deformation mechanism map has to be generated. For the deformation mechanism map a deformation temperature is needed, which has been calculated for the porphyroclasts, neoblasts and fine-grained neoblasts (Table 3.2).

The microprobe data show a clear trend of decreasing Cr_2O_3 (wt.%), Al_2O_3 (wt.%) and CaO (wt.%) content from porphyroclasts to fine-grained neoblasts (Fig. 3.12). The scatter in CaO (wt.%) in the opx porphyroclasts is related to small exsolution lamellae of cpx. In the cpx the CaO (wt.%) shows a clear trend with decreasing values from the porphyroclasts to the fine-grained neoblasts (Fig. 3.12). The TiO_2 remains at relatively constant values. The geothermometers reflect these trends and show a decrease in calculated temperatures for all three geothermometers, going from porphyroclasts over neoblasts to the fine-grained neoblasts (Table 3.2). The neoblasts show higher temperatures than the fine-grained neoblasts but they are within error. For the deformation map calculations, we used a deformation temperature of 850 °C. With a stress estimate from the olivine matrix calculated with the paleopiezometer and assuming

the stress is similar in both matrix and fine-grained layers, we get a strain rate reduction of about one order of magnitude (Fig. 3.14). The deformation map indicates that the matrix olivine deformed by dislocation creep accommodated by grain boundary sliding (Fig. 3.14). The olivine in the ultramylonite layers deforms at the border between diffusion creep and disGBS (Fig. 3.14). Here we assume a dry olivine flow law, since the importance of disGBS in "wet" conditions has not been determined yet (Hansen et al., 2011). If we assume wet olivine diffusion and dislocation creep flow laws, both matrix olivine and ultramylonite olivine will fall in the diffusion creep field. Due to grain size dependence of diffusion creep, a strain localization in the ultramylonites will also occur.
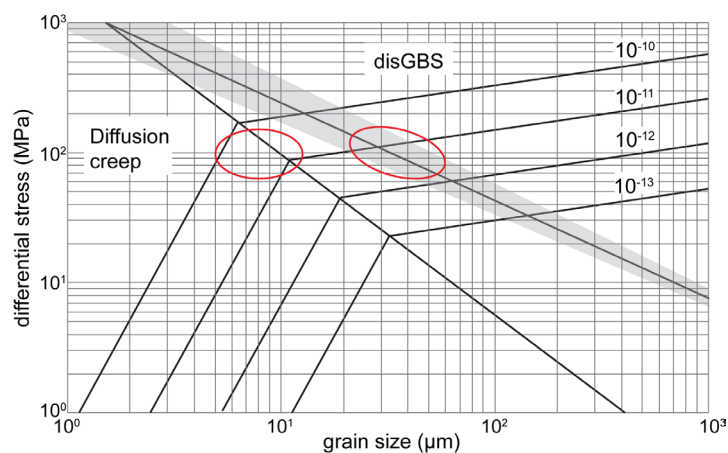
Fig. 3.14. *Olivine deformation mechanism map at 850 °C, showing in light gray the paleopiezometer (Van der Wal et al., 1993). The red circle on the right shows the average olivine grain sizes of the matrix (23-45 μm, Table 3.1) and the corresponding differential stresses calculated with the paleopiezometer. The left circle shows the range of average olivine grain sizes in the ultramylonite layers (5-12 μm, Table 3.1). Diffusion creep flow law from (Hirth and Kohlstedt, 2003) and the disGBS flow law from (Hansen et al., 2011).*

The deformation mechanism map only considers the olivine, as it is the dominant phase in both matrix and the fine-grained layers. However, pyroxenes very likely contribute to the rheology in both the matrix and fine-grained layers. In addition, it has been shown that small melt fractions (0.03-0.04) decrease the viscosity of olivine substantially (Hirth and Kohlstedt, 1995a, 1995b; Zimmerman and Kohlstedt, 2004). Therefore, the effect on the viscosity of the infiltration of the silica undersaturated is twofold. On one hand the melt infiltration during the evolution of the shear zone weakens the complete shear zone, and on the other hand, locally, the melt-rock reactions lead to the formation of the fine-grained ultramylonite layers. This shows the importance of melt-rock reactions for phase mixing, and in turn for strain weakening (Fig. 3.14). The importance of melt-rock reactions for strain weakening have been observed in other peridotites (e.g., Dijkstra et al., 2002b). The observation of the formation of fine-grained layers due to melt percolation is the opposite of what was observed recently in the Finero peridotites in the

southern Alps (Tommasi et al., 2017). The peridotite is a metasomatized mantle section originating in a supra-subduction environment (Tommasi et al., 2017). These authors observed that the percolation of hydrous melts favored olivine grain growth and deformation by dissolution and precipitation. This led to homogenously distributed deformation. Even though pargasite and phlogopite were recrystallized, this recrystallization did not lead to a weakening. This contrasting behavior illustrates the importance of the melt composition and their interaction with the peridotites. In a ridge setting where the asthenosphere melts due to decompression melting, Si-undersaturated melts will percolate the peridotites leading to the melt-rock reactions and strain weakening observed in, for instance, the Erro-Tobbio and Othris peridotite (Dijkstra et al., 2002b).

Acknowledgments

3.7   References chapter 3

Ashby, M. F., & Verrall, R. A. (1973). Diffusion-accomodated Flow and Superplasticity. *Acta Metall.*, *21*(February), 49–163.

Bercovici, D. (2003). The generation of plate tectonics from mantle convection. *Earth and Planetary Science Letters*, *205*(3–4), 107–121. https://doi.org/10.1016/S0012-821X(02)01009-9

Bercovici, D., & Ricard, Y. (2013). Generation of plate tectonics with two-phase grain-damage and pinning: Source-sink model and toroidal flow. *Earth and Planetary Science Letters*, *365*, 275–288. https://doi.org/10.1016/j.epsl.2013.02.002

Bercovici, D., & Ricard, Y. (2014). Plate tectonics, damage and inheritance. *Nature*, *508*(7497), 513–516. https://doi.org/10.1038/nature13072

Bernard, R. E., Behr, W. M., Becker, T. W., & Young, D. J. (2019). Relationships Between Olivine CPO and Deformation Parameters in Naturally Deformed Rocks and Implications for Mantle Seismic Anisotropy. *Geochemistry, Geophysics, Geosystems*, *20*(7), 3469–3494. https://doi.org/10.1029/2019GC008289

Brey, G. P., & Köhler, T. (1990). Geothermobarometry in four-phase lherzolites II. new thermobarometers, and practical assessment of existing thermobarometers. *Journal of Petrology*, *31*(6), 1353–1378. https://doi.org/10.1093/petrology/31.6.1353

Bunge, H.-J. (1982). Orientation Distributions. In *Texture Analysis in Materials Science*. London: Butterworths. https://doi.org/10.1016/B978-0-408-10642-9.50008-8

Bürgmann, R., & Dresen, G. (2008). Rheology of the lower crust and upper mantle: Evidence from rock mechanics, geodesy, and field observations. *Annual Review of Earth and Planetary Sciences*, *36*, 531–567. https://doi.org/10.1146/annurev.earth.36.031207.124326

Bystricky, M., Kunze, K., Burlini, L., & Burg, J. P. (2000). High shear strain of olivine aggregates: Rheological and seismic consequences. *Science*, *290*(5496), 1564–1567. https://doi.org/10.1126/science.290.5496.1564

Dijkstra, A. H., Drury, M. R., & Frijhoff, R. M. (2002). Microstructures and lattice fabrics in the Hilti mantle section (Oman Ophiolite): Evidence for shear localization and melt weakening in the crust-mantle transition zone? *Journal of Geophysical Research: Solid Earth*, *107*(B11), ETG 2-1-ETG 2-18. https://doi.org/10.1029/2001jb000458

Dijkstra, A. H., Drury, M. R., Vissers, R. L. M., & Newman, J. (2002). On the role of melt-rock reaction in mantle shear zone formation in the Othris Peridotite Massif (Greece). *Journal of Structural Geology*, *24*(9), 1431–1450. https://doi.org/10.1016/S0191-8141(01)00142-0

Downes, H. (1990). Shear zones in the upper mantle - Relation between geochemical enrichment and deformation in mantle peridotites. *Geology*, *18*, 374–377. https://doi.org/10.1130/0091-7613(1990)018<0374:SZITUM>2.3.CO;2

Drury, M. R., & Urai, J. L. (1989). Deformation-related recrystallization processes. *Tectonophysics, 172*, 235–253. https://doi.org/https://doi.org/10.1016/0040-1951(90)90033-5

Drury, M. R., Vissers, R. L. M., Van der Wal, D., & Hoogerduijn Strating, E. H. (1991). Shear localisation in upper mantle peridotites. *Pure and Applied Geophysics PAGEOPH*, *137*(4), 439–460. https://doi.org/10.1007/BF00879044

Evans, B., Renner, J., & Hirth, G. (2001). A few remarks on the kinetics of static grain growth in rocks. *International Journal of Earth Sciences*, *90*(1), 88–103. https://doi.org/10.1007/s005310000150

Farla, R. J. M., Karato, S., & Cai, Z. (2013). Role of orthopyroxene in rheological weakening of the lithosphere via dynamic recrystallization. *Proceedings of the National Academy of Sciences of the United States of America*, *110*(41), 16355–16360. https://doi.org/10.1073/pnas.1218335110

Fusseis, F., Regenauer-Lieb, K., Liu, J., Hough, R. M., & De Carlo, F. (2009). Creep cavitation can establish a dynamic granular fluid pump in ductile shear zones. *Nature*, *459*(7249), 974–977. https://doi.org/10.1038/nature08051

Handy, M. R. (1994). Flow laws for rocks containing two non-linear viscous phases: A phenomenological approach. *Journal of Structural Geology*, *16*(3), 287–301. https://doi.org/10.1016/0191-8141(94)90035-3

Hansen, L. N., Zimmerman, M. E., & Kohlstedt, D. L. (2011). Grain boundary sliding in San Carlos olivine: Flow law parameters and crystallographic-preferred orientation. *Journal of Geophysical Research*, *116*(B8), 1–16. https://doi.org/10.1029/2011JB008220

Hansen, L. N., Zimmerman, M. E., & Kohlstedt, D. L. (2012). Laboratory measurements of the viscous anisotropy of olivine aggregates. *Nature*, *492*(7429), 415–417. https://doi.org/10.1038/nature11671

Hansen, Lars N., & Warren, J. M. (2015). Quantifying the effect of pyroxene on deformation of peridotite in a natural shear zone. *Journal of Geophysical Research: Solid Earth*, *120*, 2717–2738. https://doi.org/10.1002/2014JB011584.Received

Hidas, K., Tommasi, A., Garrido, C. J., Padrón-Navarta, J. A., Mainprice, D., Vauchez, A., et al. (2016). Fluid-assisted strain localization in the shallow subcontinental lithospheric mantle. *Lithos*, *262*, 636–650. https://doi.org/10.1016/j.lithos.2016.07.038

Hirth, G., & Kohlstedt, D. (2003). Rheology of the upper mantle and the mantle wedge: A view from the experimentalists. *Geophysical Monograph Series*, *138*, 83–105. https://doi.org/10.1029/138GM06

Hirth, G., & Kohlstedt, D. L. (1995a). Experimental constraints on the dynamics of the partially molten upper mantle: deformation in the diffusion creep regime. *Journal of Geophysical Research*, *100*(B2), 1981–2001. https://doi.org/10.1029/94JB02128

Hirth, G., & Kohlstedt, D. L. (1995b). Experimental constraints on the dynamics of the partially molten upper mantle 2. Deformation in the dislocation creep regime. *J. Geophys. Res.*, *100*(B8), 15441–15449.

Hoogerduijn Strating, E. H., Rampone, E., Piccardo, G. B., Drury, M. R., & Vissers, R. L. M. (1993). Subsolidus emplacement of mantle peridotites during incipient oceanic rifting and opening of the mesozoic tethys (voltri massif, NW Italy). *Journal of Petrology*, *34*(5), 901–927. https://doi.org/10.1093/petrology/34.5.901

Jaroslow, G. E., Hirth, G., & Dick, H. J. B. (1996). Abyssal peridotite mylonites: Implications for grain-size sensitive flow and strain localization in the oceanic lithosphere. *Tectonophysics*, *256*(1-4 SPEC. ISS.), 17–37. https://doi.org/10.1016/0040-1951(95)00163-8

Ji, S., Zhao, P., & Xia, B. (2003). Flow laws of multiphase materials and rocks from end-member flow laws. *Tectonophysics*, *370*(1–4), 129–145. https://doi.org/10.1016/S0040-1951(03)00182-3

Jung, H., & Karato, S. I. (2001). Water-induced fabric transitions in olivine. *Science*, *293*(5534), 1460–1463. https://doi.org/10.1126/science.1062235

Kaczmarek, M. A., & Müntener, O. (2008). Juxtaposition of melt impregnation and high-temperature shear zones in the upper mantle; field and petrological constraints from the lanzo peridotite (Northern Italy). *Journal of Petrology*, *49*(12), 2187–2220. https://doi.org/10.1093/petrology/egn065

Karato, S. (1989). Grain growth kinetics in olivine aggregates. *Tectonophysics*, *168*(4), 255–273. https://doi.org/10.1016/0040-1951(89)90221-7

Karato, S., Jung, H., Katayama, I., & Skemer, P. (2008). Geodynamic Significance of Seismic Anisotropy of the Upper Mantle: New Insights from Laboratory Studies. *Annual Review of Earth and Planetary Sciences*, *36*(1), 59–95. https://doi.org/10.1146/annurev.earth.36.031207.124120

Kelemen, P. B., & Hirth, G. (2007). A periodic shear-heating mechanism for intermediate-depth earthquakes in the mantle. *Nature*, *446*(7137), 787–790. https://doi.org/10.1038/nature05717

Kumamoto, K. M., Warren, J. M., & Hansen, L. N. (2019). Evolution of the Josephine Peridotite Shear Zones: 2. Influences on Olivine Cpo Evolution. *Journal of Geophysical Research: Solid Earth*, *124*(12), 12763–12781. https://doi.org/10.1029/2019JB017968

Linckens, J., Herwegh, M., Mntener, O., & Mercolli, I. (2011). Evolution of a polymineralic mantle shear zone and the role of second phases in the localization of deformation. *Journal of Geophysical Research: Solid Earth*, *116*(6), 1–21. https://doi.org/10.1029/2010JB008119

Linckens, J., Bruijn, R. H. C., & Skemer, P. (2014). Dynamic recrystallization and phase mixing in experimentally deformed peridotite. *Earth and Planetary Science Letters*, *388*, 134–142. https://doi.org/10.1016/j.epsl.2013.11.037

Linckens, J., Herwegh, M., & Müntener, O. (2015). Small quantity but large effect - How minor phases control strain localization in upper mantle shear zones. *Tectonophysics*, *643*, 26–43. https://doi.org/10.1016/j.tecto.2014.12.008

Matysiak, A. K., & Trepmann, C. A. (2012). Crystal-plastic deformation and recrystallization of peridotite controlled by the seismic cycle. *Tectonophysics*, *530–531*, 111–127. https://doi.org/10.1016/j.tecto.2011.11.029

Mei, S., & Kohlstedt, D. . (2000a). Influence of water on plastic deformation of olivine aggregates 1 . Diffusion creep regime environment the charge neutrality condition changes from [Fete - [H • e]. As a consequence , for olivine aggregates the concentration of silicon Particle Size (. *Journal of Geophysical Research*, *105*, 21457–21469.

Mei, S., & Kohlstedt, D. L. (2000b). Influence of water on plastic deformation of olivine aggregates 2. Dislocation creep regime. *Journal of Geophysical Research: Solid Earth*, *105*(B9), 21471–21481. https://doi.org/10.1029/2000jb900180

Mei, S., Bai, W., Hiraga, T., & Kohlstedt, D. L. (2002). Influence of melt on the creep behavior of olivine-basalt aggregates under hydrous conditions. *Earth and Planetary Science Letters*, *201*(3–4), 491–507. https://doi.org/10.1016/S0012-821X(02)00745-8

Newman, J., Lamb, W. M., Drury, M. R., & Vissers, R. L. M. (1999). Deformation processes in a peridotite shear zone: Reaction-softening by an H2O-deficient, continuous net transfer reaction. *Tectonophysics*, *303*(1–4), 193–222. https://doi.org/10.1016/S0040-1951(98)00259-5

Padovano, M., Piccardo, G. B., & Vissers, R. L. M. (2015). Tectonic and magmatic evolution of the mantle lithosphere during the rifting stages of a fossil slow-ultraslow spreading basin: Insights from the Erro-Tobbio peridotite (Voltri Massif, NW Italy). In *Geological Society Special Publication* (Vol. 413, pp. 205–238). https://doi.org/10.1144/SP413.7

Park, M., & Jung, H. (2017). Microstructural evolution of the Yugu peridotites in the Gyeonggi Massif, Korea: Implications for olivine fabric transition in mantle shear zones. *Tectonophysics*, *709*, 55–68. https://doi.org/10.1016/j.tecto.2017.04.017

Piccardo, G. B. (2013). Subduction of a fossil slow-ultraslow spreading ocean: A petrology-constrained geodynamic model based on the Voltri Massif, Ligurian Alps, Northwest Italy. *International Geology Review*, *55*(7), 787–803. https://doi.org/10.1080/00206814.2012.746806

Piccardo, G. B., & Vissers, R. L. M. (2007). The pre-oceanic evolution of the Erro-Tobbio peridotite (Voltri Massif, Ligurian Alps, Italy). *Journal of Geodynamics*, *43*(4–5), 417–449. https://doi.org/10.1016/j.jog.2006.11.001

Piccardo, G. B., Padovano, M., & Guarnieri, L. (2014). The Ligurian Tethys: Mantle processes and geodynamics. *Earth-Science Reviews*, *138*, 409–434. https://doi.org/10.1016/j.earscirev.2014.07.002

Platt, J. P. (2015). Rheology of two-phase systems: A microphysical and observational approach. *Journal of Structural Geology*, *77*, 213–227. https://doi.org/10.1016/j.jsg.2015.05.003

Précigout, J., & Gueydan, F. (2009). Mantle weakening and strain localization: Implications for the long-term strength of the continental lithosphere. *Geology*, *37*(2), 147–150. https://doi.org/10.1130/G25239A.1

Précigout, J., & Stünitz, H. (2016). Evidence of phase nucleation during olivine diffusion creep: A new perspective for mantle strain localisation. *Earth and Planetary Science Letters*, *455*, 94–105. https://doi.org/10.1016/j.epsl.2016.09.029

Précigout, J., Gueydan, F., Gapais, D., Garrido, C. J., & Essaifi, A. (2007). Strain localisation in the subcontinental mantle - a ductile alternative to the brittle mantle. *Tectonophysics*, *445*(3–4), 318–336. https://doi.org/10.1016/j.tecto.2007.09.002

Précigout, J., Prigent, C., Palasse, L., & Pochon, A. (2017). Water pumping in mantle shear zones. *Nature Communications*, *8*. https://doi.org/10.1038/ncomms15736

Précigout, J., Stünitz, H., & Villeneuve, J. (2019). Excess water storage induced by viscous strain localization during high-pressure shear experiment. *Scientific Reports*, *9*(1), 1–9. https://doi.org/10.1038/s41598-019-40020-y

Rampone, E., Romairone, A., Abouchami, W., Piccardo, G. B., & Hofmann, A. W. (2005). Chronology, petrology and isotope geochemistry of the Erro-Tobbio peridotites (Ligurian Alps, Italy): Records of Late Palaeozoic lithospheric extension. *Journal of Petrology*, *46*(4), 799–827. https://doi.org/10.1093/petrology/egi001

Regenauer-Lieb, K., & Yuen, D. (2004). Positive feedback of interacting ductile faults from coupling of equation of state, rheology and thermal-mechanics. *Physics of the Earth and Planetary Interiors*, *142*(1–2), 113–135. https://doi.org/10.1016/j.pepi.2004.01.003

Skemer, P., Katayama, I., Jiang, Z., & Karato, S. (2005). The misorientation index: Development of a new method for calculating the strength of lattice-preferred orientation. *Tectonophysics*, *411*(1–4), 157–167. https://doi.org/10.1016/j.tecto.2005.08.023

Skemer, P., Warren, J. M., Kelemen, P. B., & Hirth, G. (2009). Microstructural and rheological evolution of a mantle shear zone. *Journal of Petrology*, *51*(1–2), 43–53. https://doi.org/10.1093/petrology/egp057

Skemer, P., Warren, J. M., Hansen, L. N., Hirth, G., & Kelemen, P. B. (2013). The influence of water and LPO on the initiation and evolution of mantle shear zones. *Earth and Planetary Science Letters*, *375*, 222–233. https://doi.org/10.1016/j.epsl.2013.05.034

Tackley, P. J. (2000). Mantle convection and plate tectonics: Toward an integrated physical and chemical theory. *Science*, *288*(5473), 2002–2007. https://doi.org/10.1126/science.288.5473.2002

Tasaka, M., Hiraga, T., & Zimmerman, M. E. (2013). Influence of mineral fraction on the rheological properties of forsterite + enstatite during grain-size-sensitive creep: 2. Deformation experiments. *Journal of Geophysical Research: Solid Earth*, *118*(8), 3991–4012. https://doi.org/10.1002/jgrb.50284

Tasaka, M., Zimmerman, M. E., & Kohlstedt, D. L. (2015). Evolution of the rheological and microstructural properties of olivine aggregates during dislocation creep under hydrous conditions. *AGU: Journal of Geophysical Research, Solid Earth*, *121*(iv), 92–113. https://doi.org/10.1002/2015JB012134

Thielmann, M., Rozel, A., Kaus, B. J. P., & Ricard, Y. (2015). Intermediate-depth earthquake generation and shear zone formation caused by grain size reduction and shear heating. *Geology*, *43*(9), 791–794. https://doi.org/10.1130/G36864.1

Tommasi, A., & Vauchez, A. (2015). Heterogeneity and anisotropy in the lithospheric mantle. *Tectonophysics*, *661*, 11–37. https://doi.org/10.1016/j.tecto.2015.07.026

Tommasi, A., Vauchez, A., Godard, M., & Belley, F. (2006). Deformation and melt transport in a highly depleted peridotite massif from the Canadian Cordillera: Implications to seismic anisotropy above subduction zones. *Earth and Planetary Science Letters*, *252*(3–4), 245–259. https://doi.org/10.1016/j.epsl.2006.09.042

Tommasi, A., Knoll, M., Vauchez, A., Signorelli, J. W., Thoraval, C., & Logé, R. (2009). Structural reactivation in plate tectonics controlled by olivine crystal anisotropy. *Nature Geoscience*, *2*(6), 423–427. https://doi.org/10.1038/ngeo528

Tommasi, A., Langone, A., Padrón-Navarta, J. A., Zanetti, A., & Vauchez, A. (2017). Hydrous melts weaken the mantle, crystallization of pargasite and phlogopite does not: Insights from a petrostructural study of the Finero peridotites, southern Alps. *Earth and Planetary Science Letters*, *477*, 59–72. https://doi.org/10.1016/j.epsl.2017.08.015

Urai, J. L., Spiers, C. J., Zwart, H. J., & Lister, G. S. (1986). Weakening of rock salt by water during long-term creep. *Nature*, *324*(1), 554–557.

Vissers, R. L. M., Drury, M. R., Hoogerduijn Strating, E. H., Spiers, C. J., & van der Wal, D. (1995). Mantle shear zones and their effect on lithosphere strength during continental breakup. *Tectonophysics*, *249*(3–4), 155–171. https://doi.org/10.1016/0040-1951(95)00033-J

Van der Wal, D., Chopra, P., Drury, M. R., & Fitz Gerald, J. (1993). Relationships between dynamically recrystallized grain size and deformation conditions in experimentally deformed olivine rocks. *Geophysikal Research Letters*, *20*(14), 1479–1482. https://doi.org/10.1029/93GL01382

Warren, J. M., & Hirth, G. (2006). Grain size sensitive deformation mechanisms in naturally deformed peridotites. *Earth and Planetary Science Letters*, *248*(1–2), 438–450. https://doi.org/10.1016/j.epsl.2006.06.006

Witt-Eickschen, G., & Seck, H. A. (1991). Solubility of Ca and Al in orthopyroxene from spinel peridotite: an improved version of an empirical geothermometer. *Contributions to Mineralogy and Petrology*, *106*(4), 431–439. https://doi.org/10.1007/BF00321986

Zimmerman, M. E., & Kohlstedt, D. L. (2004). Rheological properties of partially molten lherzolite. *Journal of Petrology*, *45*(2), 275–298. https://doi.org/10.1093/petrology/egg089

4 Melt-enhanced strain localization and phase mixing in a large-scale mantle shear zone (Ronda Peridotite, Spain)

Sören Tholen[1], Jolien Linckens[1/2], Gernold Zulauf[1]

[1]Institut für Geowissenschaften, Goethe Universität Frankfurt a.M., Altenhöferallee 1, D-60438, Germany

[2]Tata Steel, R&D, Microstructural and Surface Characterization, Beverwijk, NL-1951, The Netherlands

4.1 Abstract

Strain localization in upper mantle shear zones by grain size reduction and the activation of grain size sensitive deformation mechanisms is closely linked to phase mixing. With its mylonitic grain size (50-100 µm) and well mixed phase assemblage, the km-scale shear zone at the northwestern boundary of the Ronda peridotite is in this respect no exception. In transects across the high-strain "mylonitic" into the low-strain "tectonitic" part of this shear zone four dominant microstructural domains were identified: (1) olivine-rich matrix, (2) mixed matrix, (3) neoblast tails of clinopyroxene porphyroclasts and (4) neoblast tails of orthopyroxene porphyroclasts. In these domains, phase mixing and its impact on strain localization were investigated by a combination of microstructural (optical microscopy), textural (EBSD) and geochemical (EPMA) analysis. The dominant microstructural domain of all samples is the mixed matrix composed of olivine, ortho- and clinopyroxene. Its homogenous distribution of interstitial pyroxenes contradicts mechanical mixing. Instead, extensive phase mixing under near steady-state conditions is documented by the constant grain size and by phase boundary percentages > 60 % for the entire mylonitic unit and all the microstructural domains. Lobate phase boundaries, homogenous phase mixing and secondary phase distribution as well as continuous geochemical trends, independent of the microstructural domain, point to a reaction-driven, metasomatic formation of the mixed matrix and pyroxene porphyroclast tails in the entire shear zone. An OH-bearing metasomatism by small fractions of evolved melts is indicated by amphibole abundance in pyroxene neoblast tails, olivine B-type crystallographic preferred orientations (CPOs), and the microstructural consistency of the grt/spl-mylonites from both major peridotite massifs of the Gibraltar arc, Ronda, and Beni Bousera (Morocco). The established syn-deformational temperatures of 800-900° C at 1.95-2.00 GPa suggest that the metasomatism did not reset the equilibrium temperatures. Consistent geochemistry and phase assemblage in mylonites and tectonites, but a change

from equiaxial (tectonites) to wedge-shaped pyroxenes aligned parallel to the foliation (mylonites) point to a pre- to syn-deformational metasomatism with potential annealing of the tectonites. For the mylonitic mixed matrix, wedge-shaped pyroxenes and neoblast tail formation in pyroxene porphyroclast stress shadows point to the activity of incongruent dissolution-precipitation creep. Beside dissolution-precipitation creep, strong CPOs of all major phases (ol, opx, cpx) suggest additionally dislocation creep as major deformation mechanism in the entire shear zone.

Keywords:

Northwestern Ronda shear zone, phase mixing, EBSD, melt-rock reaction, strain localization.

4.2   Introduction

Deformation in the upper mantle is localized in ductile shear zones. Accommodating most of the deformation in the lithospheric mantle, shear zones have a major imprint on large scale deformation and plate tectonics (Bercovici and Ricard, 2014; Drury et al., 1991). To localize strain, weakening must occur. Weakening in turn is dependent on an initial heterogeneity/anisotropy and a softening mechanism localizing the strain typically first on a heterogeneity and later on in the shear zone itself. In the lithospheric mantle, several types of heterogeneity were identified as potential "seeds" for strain localization: (1) Large-scale variations in the geothermal gradient such as those found in hot plumes or cold lithospheric roots of cratons, (2) major-element and modal heterogeneities as present in the compositional layering of most peridotite massifs, (3) the presence of melt, (4) variations in the hydration state of particularly olivine, (5) grain size heterogeneities and (6) lateral changes of the olivine CPO (e.g., Tommasi and Vauchez, 2015). Strain softening mechanisms that localize and maintain deformation were subdivided into three types (Drury et al., 1991): Thermal softening caused by shear heating and the positive feedback of temperature and strain rate (e.g., Kelemen and Hirth, 2007), geometric softening caused by the anisotropy in creep strength of grains aligned in a CPO (Mameri et al., 2019; White et al., 1980) and microstructural or reaction softening which occurs by grain size reduction and the activity of a grain size sensitive deformation process (Drury and Urai, 1989). Both thermal softening as well as microstructural softening depend on the presence of mixed phase assemblage, either as seed or as stabilization for strain localization (e.g., Kelemen and Hirth, 2007; Linckens et al., 2015). Phase mixing in the upper mantle has been ascribed to several different deformation- or reaction-induced processes. Deformation-induced phase mixing is commonly associated with grain boundary sliding (GBS). During GBS, neighbor switching of grains was reported to form mixtures (e.g., Boullier and Gueguen, 1975; Hirth and Kohlstedt, 2003) but also aggregates (Hiraga et al., 2013). Furthermore, disaggregation of single-phase domains at

high shear strains ("Geometric mixing") was reported by Cross and Skemer (2017). Additionally, nucleation of neoblasts in creep cavitations during GBS leading to phase mixing was reported by Précigout and Stünitz (2016). Reaction-induced phase mixing is bound to either metamorphic (P-T) or metasomatic (melt/fluid) reactions. In the upper mantle, phase transitions from garnet to spinel and to plagioclase peridotites change the phase assemblage and the mineral chemistry of all present phases (e.g., Borghini, 2008). Neoblast formation can thereby lead to phase mixing and, during deformation, to the formation of ultramylonites (Furusho and Kanagawa, 1999; Newman et al., 1999; Tholen et al., 2022). Additionally, the interaction of rock and melt or fluid can cause phase mixing by precipitation of neoblasts and reactions with porphyroclasts/ pristine grains (e.g., Dijkstra et al., 2002; Kaczmarek and Müntener, 2008).

With its decreasing grain size, scattering of pyroxene neoblasts and concurrent diminishing of prior strong olivine CPOs towards the contact to the bordering Jubrique unit, Ronda's NW tectonite/mylonite zone is commonly interpreted as km-scale upper mantle shear zone (Garrido et al., 2011; Précigout et al., 2013, 2007). In contrast to earlier studies on phase mixing in upper mantle shear zones where the mixing depends on metamorphic and metasomatic reactions (Linckens and Tholen, 2021; Tholen et al., 2022) Ronda's mylonites are thought to have little to no metamorphic or metasomatic influence (e.g., Johanesen and Platt, 2015; Précigout et al., 2007). Mechanisms of strain localization and phase mixing operating in Ronda's mylonites were suggested to be bound to grain boundary sliding accommodated by dislocation creep ("DisGBS", Précigout et al., 2007). In this concept, the strain localization is caused by a drop in stress due to the grain size reduction towards the NW boundary of the Ronda peridotite (e.g., Garrido et al., 2011; Précigout et al., 2013). Following Précigout et al. (2007), neighbor-switching during DisGBS leads to scattering of orthopyroxene neoblasts within the matrix. However, Johanesen and Platt (2015) reported thoroughly mixed microstructures with interstitial pyroxenes also in the low strain areas of the SE mylonites and the spinel tectonites (Fig. 4.1). Although mixing in the spinel tectonites was postulated to be melt derived (Johanesen et al., 2014; Soustelle et al., 2009), the mylonites were so far considered to be either completely melt-free (Précigout et al., 2007; Soustelle et al., 2009) or melt-absent during the deformation (Johanesen and Platt, 2015).

To address the genesis and deformational history of NW Ronda shear zone this study focuses on the mylonitic unit with the following research questions: (1) What are the major microstructural domains and how did they form? (2) What is the extent and origin of phase mixing? (3) What is the deformational history and how is it related to the first two research questions, i.e., the formation processes and mixing intensities of the respective microstructural domains? To address these questions, a microstructural and geochemical study was carried out on samples taken across multiple transects from the mylonites into the tectonites (Fig. 4.1).

4.3   Geological setting

The Ronda peridotite, situated in southern Spain, is part of the Betic cordillera (Fig. 4.1). Together with the Rif mountains of N Morocco it forms the Gibraltar arc (= Betic-Rif orogen), which surrounds the Alboran Sea. The Betic cordillera is subdivided into four tectonic domains: The external (1) Sub-Iberian and (2) Maghrebian domains formed by the paleomargins of Iberia and NE Africa, (3) the allochthonous Flysch trough unit comprising Mesozoic to Cenozoic sediments of the oceanic or continental Tethys, and (4) the internal, Alboran domain (Fig. 4.1A) (Booth-Rea et al., 2007). Separated by extensional shear zones and different metamorphic records, the Alboran domain is divided into three main tectonic allochthons (Platt et al., 2006). In ascending order these are the Nevado-Filábride complex, the Alpujárride complex and the Maláguide complex. The lowermost Nevado-Filábride complex records a multistage metamorphic evolution including eclogite facies metamorphism followed by albite-epidote amphibole or greenschist facies overprints during decompression (Platt et al., 2006; Puga et al., 1999). The middle Alpujárride complex underwent HP-LT metamorphism overprinted by decompression and local heating (Balanyá et al., 1997; Platt et al., 2005). The uppermost Maláguide complex is characterized by unmetamorphic rocks or by very low-grade metamorphism (Lonergan, 1993).

The peridotite bodies of Beni Bousera, Ojen, Carratraca and Ronda in sensu stricto are embedded as lenses in the upper Alpujárride complex (Platt et al., 2006). Superimposed on the Ronda peridotite, the Jubrique (or Casares) unit represents a highly attenuated crustal section of ≤ 5 km thickness (Fig. 4.1) (Barich et al., 2014; Obata, 1980). Near the contact to the Ronda peridotite, it displays MP-HT granulite facies kinzigites with melt inclusions (Balanyá et al., 1997; Barich et al., 2014). With increasing distance to the peridotite, the metamorphic conditions decrease to LP-LT phyllites at the contact to the Maláguide complex (Balanyá et al., 1997). In the South and Southeast granitic rocks and migmatites of the Blanca unit underly the Ronda peridotite (Fig. 4.1). Partial melting and deformation of this unit at the contact to the peridotite have been attributed to the emplacement of the Ronda peridotite (Esteban et al., 2008). U-Pb SHRIMP dating of neo crystalline zircon rims from felsic and granitic dykes in this "dynamothermal aureole" point to an emplacement of the Ronda peridotite at 22.3 ± 0.7 Ma (Esteban et al., 2011). Miocene, brittle, top-to-the-N extensional faulting led to the final emplacement of the Alpujárride complex with high cooling rates from 300-100 °C/Ma (Esteban et al., 2004; Platt et al., 2003; Rossetti et al., 2005).
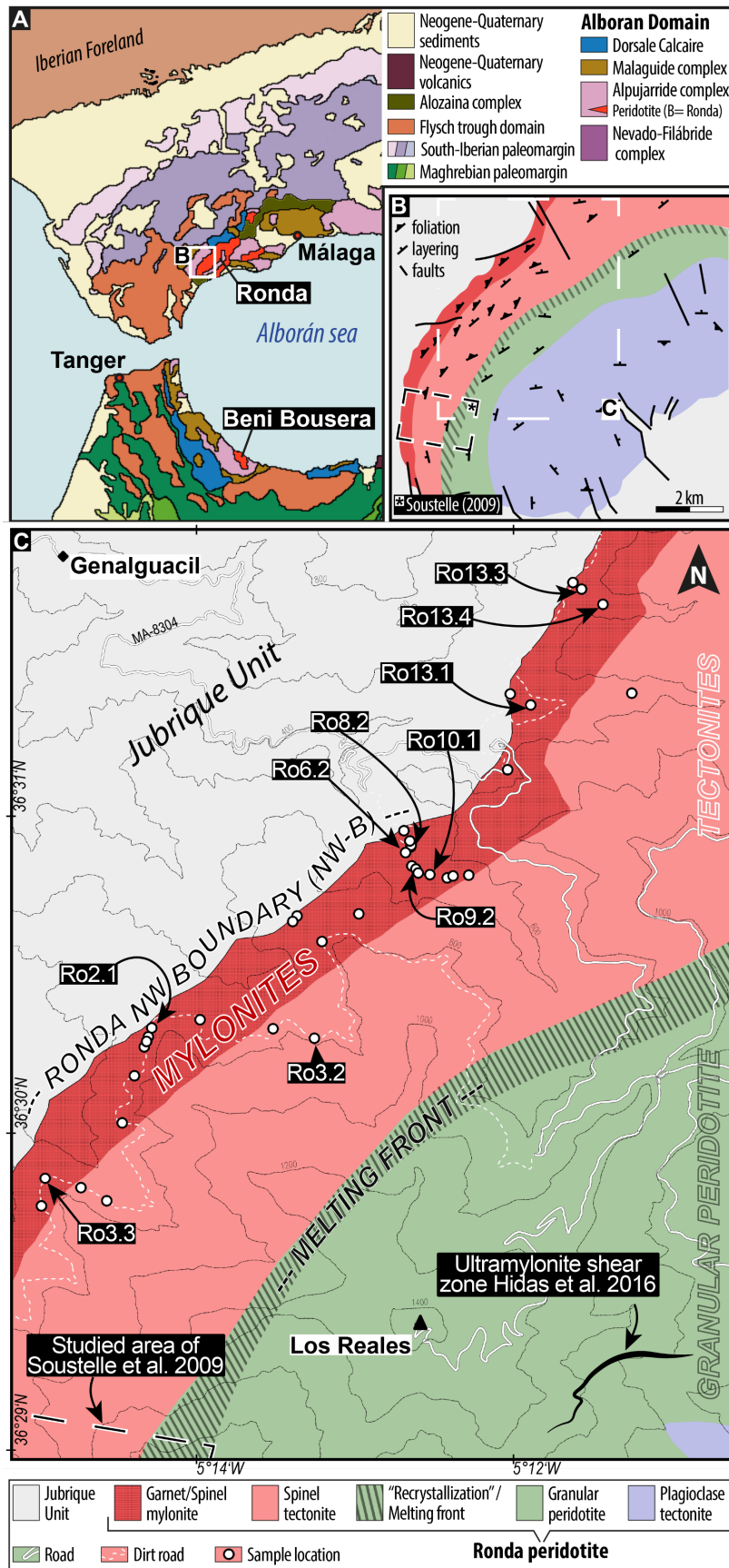
Fig. 4.1. **A:** *Geological overview of the Gibraltar Arc (Betic cordillera and Rif mountains) modified after Suades and Crespo-Blanc (2011). Ronda Peridotite indicated by white box.* **B**: *Schematic structural map of the NW Ronda peridotite with area of investigation indicated (modified after Hidas et al. (2013)). Lithological unit color code same as for C. Studied area of Soustelle et al. (2009) indicated.* **C**: *Close up view on area of investigation with sample locations (modified after Précigout et al. (2013), Van der Wal (1993)). High resolution, digital version is included on the CD.*

4.3.1 The Ronda peridotite

With ca. 300 km^2 areal extent, the Ronda peridotite is the world's largest exposure of subcontinental mantle (Obata, 1980). Its (micro) structural, petrological, and geochemical zoning led to its subdivision into four tectonometamorphic units (Fig. 4.1) (Précigout et al., 2013; Van Der Wal and Vissers, 1996, 1993). From NNW to SSE these are (1) a garnet/spinel-mylonite unit, (2) a spinel-tectonite unit, (3) a coarse-grained granular-peridotite unit, and (4) a plagioclase-tectonite unit. Being aware that tectonites include mylonitic microstructures by definition, the established distinction between "mylonites" and "tectonites" is nevertheless adopted here.

The garnet/spinel mylonites, located along the contact to the Jubrique unit (~500-750 m thickness), are composed of fine-grained, porphyroclastic spl- and grt-bearing peridotites (lherzolites, harzburgites, dunites) (Van Der Wal and Vissers, 1993). Garnet-bearing pyroxenite layers are parallel to the strong foliation and predominantly stretched which leads in places to their pinch-and-swell type boudinage (Précigout et al., 2013; Van Der Wal and Vissers, 1993). Occasionally, the pyroxenite layers show intrafolial folds with their axes-oriented NE-SW slightly dipping towards the NE (Précigout et al., 2013). Graphitized diamonds in garnet-bearing pyroxenites and pre-deformational assemblages of olivine + pyroxenes + garnet found in pressure shadows indicate an origin of great depth (> 150 km) and a pre-mylonitic equilibration in the garnet stability field (1150 °C, 2.4-2.7 GPa (~100 km depth)) (Davies et al., 1993; Garrido et al., 2011). For mylonitic assemblages in the spinel stability field, equilibration conditions of 800-900 °C and 1-2 GPa have been obtained by Johanesen et al. (2014), Garrido et al. (2011) and Van Der Wal and Vissers (1993).

The transition between grt/spl-mylonite and the spl-tectonite remains controversial. Contrary to cross-cutting contacts between mylonites and tectonites described by Van Der Wal and Vissers (1996), Précigout et al. (2007) and Soustelle et al. (2009) postulated a continuous gradient from coarse grained tectonites (grain size of 250-450 µm) to fine-grained mylonites (150-220 µm). Decreasing strain with increasing distance to the NW boundary of the mylonites is also indicated by decreased folding intensity and rotation of pyroxenite layers towards the SE (Précigout et al., 2013). However, Johanesen and Platt (2015) reported for both units (mylonites + tectonites) a consistent grain size of recrystallized olivine (~130 µm) and only an increase in the percentage of the recrystallized olivine grains towards the NW. As the main lithologies (harzburgites, lherzolites) and the foliation and lineation stay similar in tectonites and mylonites, tectonites were interpreted as the weaker deformed counterpart of the mylonites (Van Der Wal and Vissers, 1993). Microstructural and geochemical data indicate additionally, that the tectonites were affected by melt pulses originating from the structurally lower, coarse granular peridotites (Johanesen et al., 2014; Soustelle et al., 2009).

Together with the grt/spl-mylonites, the spl-tectonites form the km-scale NW Ronda shear zone (Fig. 4.1). Its characteristics are the penetrative foliation with subhorizontal stretching lineation defined by cm-scale elongated orthopyroxenes and shear criteria indicating sinistral kinematics and minor coaxial shortening (Balanyá et al., 1997; Précigout and Hirth, 2014; Van Der Wal and Vissers, 1996). The orientation of the foliation and lineation roughly follows the boundaries to the adjacent metasedimentary Jubrique unit in the NW and to the underlying coarse granular-peridotite unit in the SE (Fig. 4.1) (Van Der Wal & Vissers, 1996). In places, foliation and lineation show local variations and weakening (Van Der Wal & Vissers, 1996). For the examined area, the average orientation of the foliation is with ~N50° strike and 80° NW dip in accordance with prior research (Précigout et al., 2013). The shear zone is considered to play a decisive role in the exhumation of the peridotite massif (Johanesen et al., 2014; Précigout et al., 2013).

The coarse granular-peridotite unit is separated from the spl-tectonite unit by a "recrystallization"/ "coarsening" or "melting" front (≤ 400 m) (Lenoir et al., 2001). Here, deformed grains annealed and coarsened, the foliation is lost and garnet-pyroxenite layers are recrystallized as spl-websterites (Garrido and Bodinier, 1999). Lenoir et al. (2001) have shown that the recrystallization front is the boundary/aureole of an area of partial melting (= coarse granular-peridotite unit) with melt extraction < 5%. Secondary cpx, crystallized ahead of the front, indicated a refertilization (Soustelle et al., 2009). The location of the front was shown to be dependent on the peridotite solidus ($\geq$1200 °C, 1.5 GPa) in regard to the temperature gradient within the peridotite body (Lenoir et al., 2001). The coarse granular-peridotite unit itself is mainly composed of unfoliated spinel harzburgite with minor lherzolite and dunite and various types of pyroxenites (Garrido and Bodinier, 1999). The preservation of a strong olivine crystallographic preferred orientation (CPO) and folds of spl pyroxenites corroborates its connection to the overlaying spl-tectonites (Vauchez and Garrido, 2001).

The youngest unit, overprinting the coarse granular-peridotite unit in the southeast, comprises the plagioclase tectonites (Obata, 1980). Their equilibration at pressures of 0.8-0.9 GPa was placed in the context of the massif's exhumation (Hidas et al., 2016). The plagioclase tectonites are composed of spl-free and spl-bearing plagioclase-peridotite layers. The transition between both units records km-scale folding and shearing including the development of a new foliation and the formation of mylonitic and ultramylonitic shear zones, which are tectonically assigned to the decompression of the massif from spinel to plagioclase lherzolite facies prior to the emplacement into the crust (Fig. 4.1; Hidas et al., 2013a).

4.4   Methods

Samples were cut perpendicular to the foliation and parallel to the stretching lineation (*X-Z* section). Thin sections of these sections were polished to a thickness of ~30 μm. After optical analysis by polarization microscopy, electron backscatter diffraction (EBSD) analysis combined with energy dispersive X-ray spectroscopy (EDX), and electron probe microanalysis (EPMA) were performed on carbon coated thin sections. For EBSD and backscattered electron (BSE) analysis, thin sections were polished with 0.03 μm colloidal silica.

Backscattered electron, EBSD and EDX analysis were conducted at the Institute for Geology and Mineralogy - University of Cologne using a Zeiss Sigma 300-VP field emission scanning electron microscope (SEM) equipped with a NordlysNano EBSD detector (Oxford Instruments). For a comprehensive overview, the entire thin sections were scanned in grids simultaneously by BSE and EDX (O, Mg, Al, Si, Ca, Cr, Mn, and Fe; Fig. 4.2). Having identified the microstructures of interest, these were scanned simultaneously by EBSD, EDX, BSE and forescattered electrons (FSE). Measurement settings were an acceleration voltage of 20 kV and a variable step size adapted according to grain sizes. Depending on the step size and acquisition time, EBSD map sizes differ over a wide range. For data acquisition, the program AZtec 4.2 was used (Oxford Instruments). The consistency of orientations between sample, measurement and post-processing reference frame was ensured by the measurement of a quartz standard. It consists of four synthetic quartz crystals embedded in epoxy. The known positions of the quartz single crystals in the standard combined with their known individual orientation enables the operator to identify possible rotations (spatially or crystallographic) of the data during acquisition and processing. Kilian et al. (2016) have shown that such rotations occur often due to unknown orientation in sample material and mistranslations between different processing platforms. Obtained EBSD data was first cleaned by deleting "wild spikes" and filling not indexed points with the average orientation of 6 or more neighbor orientations of the same phase (HKL Channel 5 software - Oxford Instruments). Additionally, the EBSD data were corrected for systematic mis-indexing of olivine due to similar diffraction patterns for orientations rotated 60° around [100]. Secondly, the cleaned data were imported into the MTEX 5.7 MATLAB extension (e.g., Bachmann et al., 2010). All following data processing and analysis were conducted using MTEX (http://mtex-toolbox.github.io/). Orientations of indexed points with high mean angular deviations (MAD > 1) were filled by the mean orientation of the neighboring points. After grain calculation (grain internal misorientation < 15°) grain size specific and inclusion deletion and/or filling was carried out individually for each map. Incomplete grains at the borders of the mapped areas and badly indexed grains were excluded from further analysis. Grain reconstruction of serpentinized olivine grains was achieved by applying a half quadratic filter which preserves subgrain boundaries and fills missing data. An

example is shown for the ol-rich matrix in Figure 4.5. For all other phases, the original cleaned EBSD data was used to preserve the original grain and boundary shape. During the cleaning and reconstruction, the results were checked against backscattered/forescattered, band contrast and microscope images. The EBSD phase assignment was checked by simultaneously obtained EDX maps and/or EDX point measurements. The cleaned EBSD maps were thereupon analyzed for grain and phase properties, boundary properties and orientation properties. Analyzed grain properties are phase abundances by covering area percentage, grain amount, grain size by the equivalent circular diameter (ECD), grain shape by aspect ratio, shape factor and shape preferred orientation (SPO). Phase abundances given by "%" in figures and in the entire manuscript refer to area percentages. Boundary properties are grain (phase A- phase A) and phase (phase A- phase B) boundary percentages calculated by phase specific boundary length. The ratio of total grain to total phase boundary length gives the "mixing intensity" of a microstructure. Orientation properties include phase-specific crystallographic orientations illustrated by pole figures with or without texture. Texture calculation with grain mean orientations and a consistent halfwidth of 15° was achieved by the application of the orientation distribution function (ODF). The M-index (M) and the J-index were calculated from a minimum of 150 grains. Both J-index (Bunge, 1982) and M-index (Skemer et al., 2005), express the strength of a given texture. For a detailed evaluation of both see Skemer et al. (2005). All pole figures are equal-area lower-hemisphere plots. Textures are only displayed for a minimum number of 100 grains per phase. Otherwise, single grain orientations are plotted in the stereo plot as dots. To facilitate the comparison between the texture plots, the color-coding range is fixed according to the maximum of multiple of random distribution (mrd) from blue (mrd= 0) to red (mrd= 3). Higher mrd values are accordingly also colored red. Dislocation densities were calculated in MTEX by resolving the geometrically necessary dislocation content (https://mtex-toolbox.github.io/GND.html) on base of the method of Pantleon (2008).

Microprobe measurements of olivine, clinopyroxene, orthopyroxene, spinel and amphibole were conducted at the Institute of Geosciences - Goethe University Frankfurt a.M. using a field emission JEOL JXA-8530F Plus microprobe equipped with 5 wavelength-dispersive spectrometers. Measuring settings were 15 kV acceleration voltage and 20 nA beam current for 20 s (Al, Cr, Ca, Na, Mn, Fe and Ni), 30 s (P, K and Ti) or 40 s (Mg and Si) peak and 20 s for background measurement (settings and detection limits in S4.1). The same measurement settings and standards were used for the analysis of all phases. The spot-size was adjusted to the grain size with minimum sizes of 1 μm for small neoblasts and maximum 4 μm for porphyroclasts. References to supplementary data are given in the text by an "S" combined with the number of the appendix (e.g., S4.3 for EPMA data).

4.5   Results

Samples were taken from multiple transects of the shear zone over a range from 39 to 703 m distance to the NW boundary of the Ronda peridotite massif ("NW-B"; Fig. 4.1). Sample locations are therefore allocated with their distance [m] to the NW-B (Fig. 4.1). Referring to the established subdivision of the Ronda peridotite developed by Précigout et al. (2013) and Van Der Wal and Bodinier (1996) our samples are dominantly taken from the garnet-spinel mylonites and in greater distance from the NW-B from the spinel tectonites (Fig. 4.1). Both units are composed of lherzolite or harzburgite with minor dunitic lenses. The samples have a highly variable degree of serpentinization. Consistent with previous studies, the foliation is mostly oriented parallel to the NW-B and steeply dipping (65-85°) towards NW (Précigout et al., 2013; Soustelle et al., 2009; Van Der Wal and Vissers, 1996, 1993; Vauchez and Garrido, 2001). Towards the contact the foliation intensifies. The stretching lineation is subhorizontal to shallowly SW dipping (<20°). It is defined by elongated orthopyroxene single crystals, neoblast tails of pyroxene porphyroclasts and olivine-rich lenses stretched in the foliation plane. Towards the contact to the bordering Jubrique metasediments (= NW-B), macroscopic evidence for increasing strain is an increase of porphyroclast elongation and an increase of the mylonitic matrix (Fig. 4.2). The lengthening of orthopyroxene single crystals expands to aspect ratios > 10:1 and length of ~5 cm. The increasing strain is additionally indicated by increasing deformation of partly garnet-bearing pyroxenites, by pinch-and-swell structures (Fig. 4.2D-i), and by boudinage described in detail by Précigout et al. (2013).

4.5.1   Microstructures

Figure 4.2 gives a microstructural overview of representative thin sections with increasing distance to the NW-B. Due to serpentinization and to facilitate phase identification, BSE and Ca-EDX overview scans are shown instead of microscopic images. The proportion of neoblasts in the matrix increases towards the NW-B (Fig. 4.2). Simultaneously, the abundance of porphyroclasts decreases. Nevertheless, deformation features like a clear foliation with marked elongation of porphyroclasts and recrystallized olivine dominated matrix are present in all mylonitic samples (39-502 m distance NW-B, Fig. 4.2). Only the outermost tectonitic sample (703 m distance NW-B) lacks these features and shows a relatively undeformed fabric (Fig. 4.2F). Even though deformation was not as localized in this sample as in those closer to the NW-B, interstitial pyroxenes are present along olivine grain boundaries (Fig. 4.2F-ii). Furthermore, layers consisting of a pyroxene and spinel assemblage crosscut the tectonitic peridotite. Approaching the NW-B, pyroxene porphyroclasts show neoblast tails, which stretch out in the foliation. Simultaneously, pyroxenite layers turn parallel to the foliation and flatten till they disintegrate (Fig. 4.2D-ii) as described in detail in Précigout et al. (2013).

With the focus on phase mixing as well as on reaction and recrystallization processes, we further investigated structures on the micro-scale rather than on thin-section or larger scale. By microscopic analysis and the BSE/EDX element thin section overviews (Fig. 4.2) four major microstructural domains were identified: (1) Olivine-rich matrix, (2) mixed matrix, (3) clinopyroxene neoblast tails, and (4) orthopyroxene neoblast tails. In the following, their microstructural characteristics are presented. Additionally, amphibole-clinopyroxenite veins investigated in three thin sections will be shortly addressed. For reasons of length and clarity, examples of microstructures of each domain are shown which provide its main characteristics and their changes depending on the distance to the NW-B. These figures include pole figures referring to the depicted microstructure. Graphs of the complete microstructural data are presented in Figure 4.3. Average aspect ratios and average grain size are included only if enough grains were present for a valid statistical analysis (n > 100). The presented results include all analyzed microstructures of a given microstructural domain. The complete data is attached as supplementary data (S4.2). Garnet, even if nominally present in a few maps (39 of 41563 analyzed grains), is excluded from further analysis because of its small abundance (< 0.1 % for all microstructural domains) and its susceptibility for mis-indexing with opx especially for small grains. Coarse grained garnet (ECD > 100 µm) was not present in the studied microstructures.
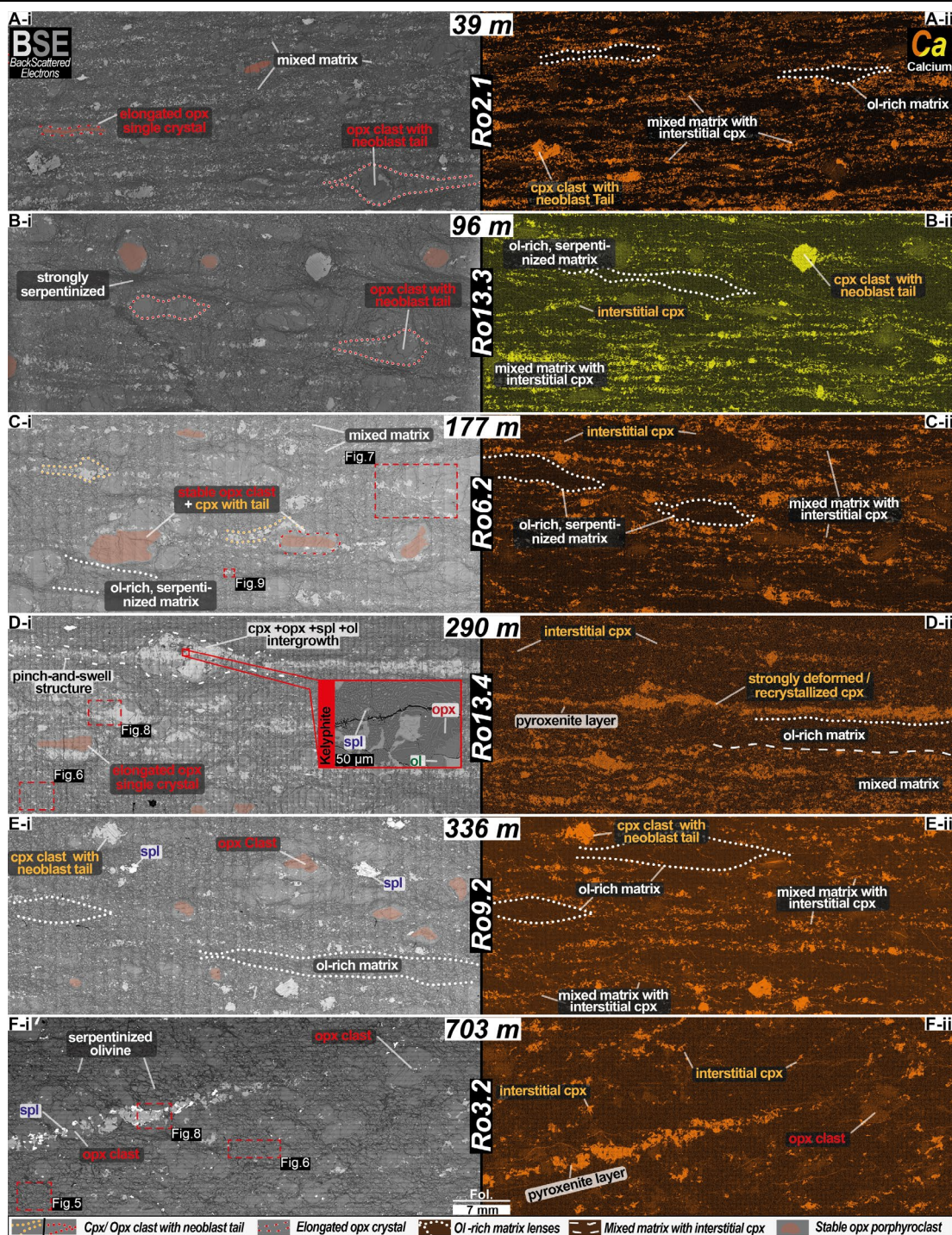
Fig. 4.2. *Electron backscatter (left) and Calcium energy-dispersive X-ray spectroscopy (right) scans of the same thin sections ordered with increasing distance to the NW boundary of the Ronda peridotite (black numbers on white background). Locations of analyzed example microstructures and their Figure # (4.5-4.9) are indicated. Dominant microstructural domains of the NW Ronda shear zone are marked: (1) strongly serpentinized olivine-rich matrix lenses, (2) mixed matrix with interstitial pyroxenes, (3) ortho- and (4) clinopyroxene porphyroclasts with neoblast tails. Note the presence of stable pyroxenes and elongated orthopyroxene. The presence of interstitial cpx (bright colors in EDX images) is indicative for the mixed matrix. D-i includes a close up on a kelyphitic assemblage. High resolution, digital version is included on the CD.*
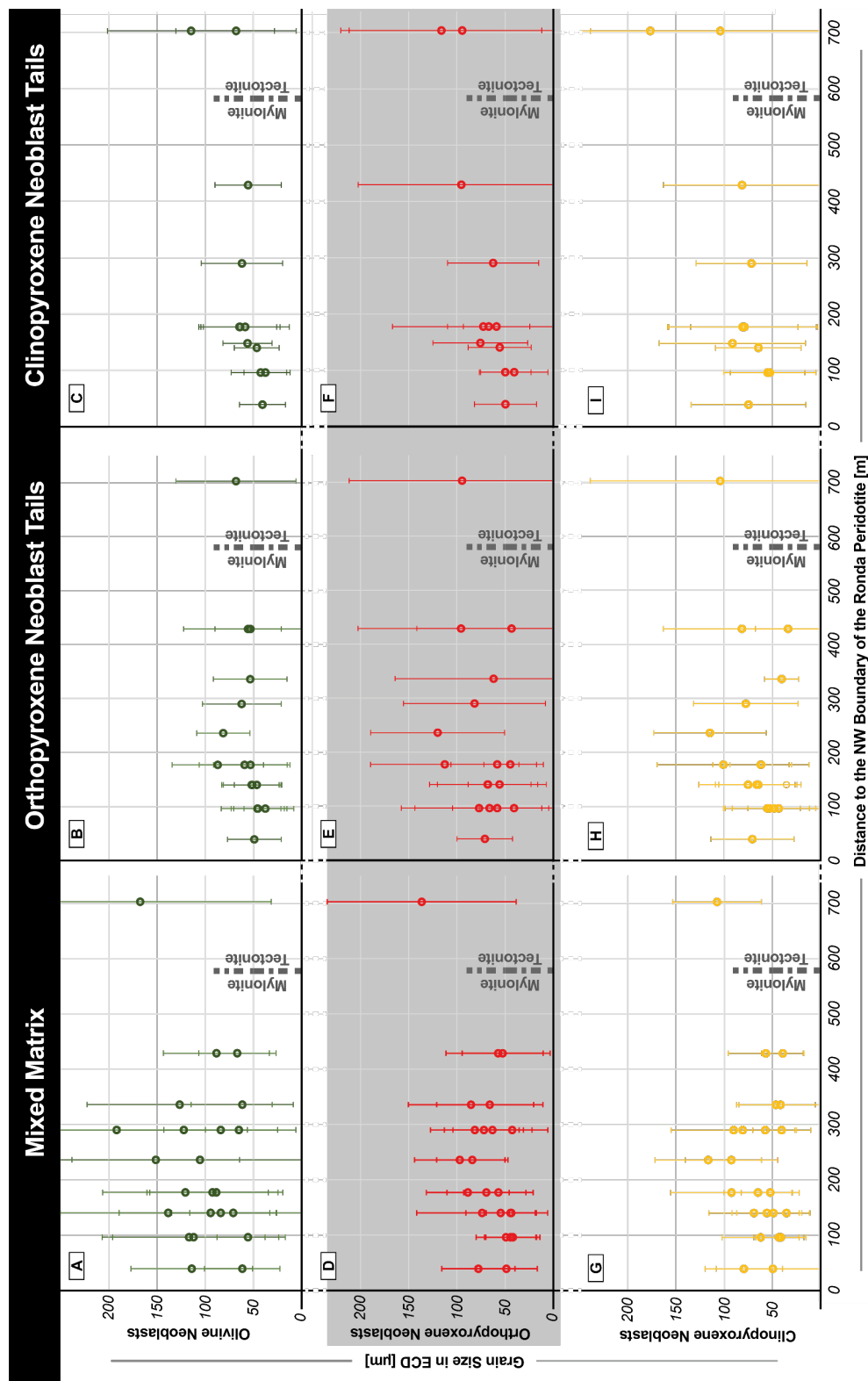
Fig. 4.3a. *Data overview of the major microstructural domains (mixed matrix, orthopyroxene and clinopyroxene porphyroclast neoblast tails) plotted against the distance to the NW-B. The olivine-rich matrix was excluded due to its small database. Each data point represents the average grain size (A-L), area fraction (M,N,O) or phase boundary percentage of the total boundary length (P,Q,R) of one EBSD map of an analyzed microstructure (e.g., Figs. 4.5-4.9). The complete microstructural data is attached in supplementary data 4.2. High resolution, digital version is included on the CD.*
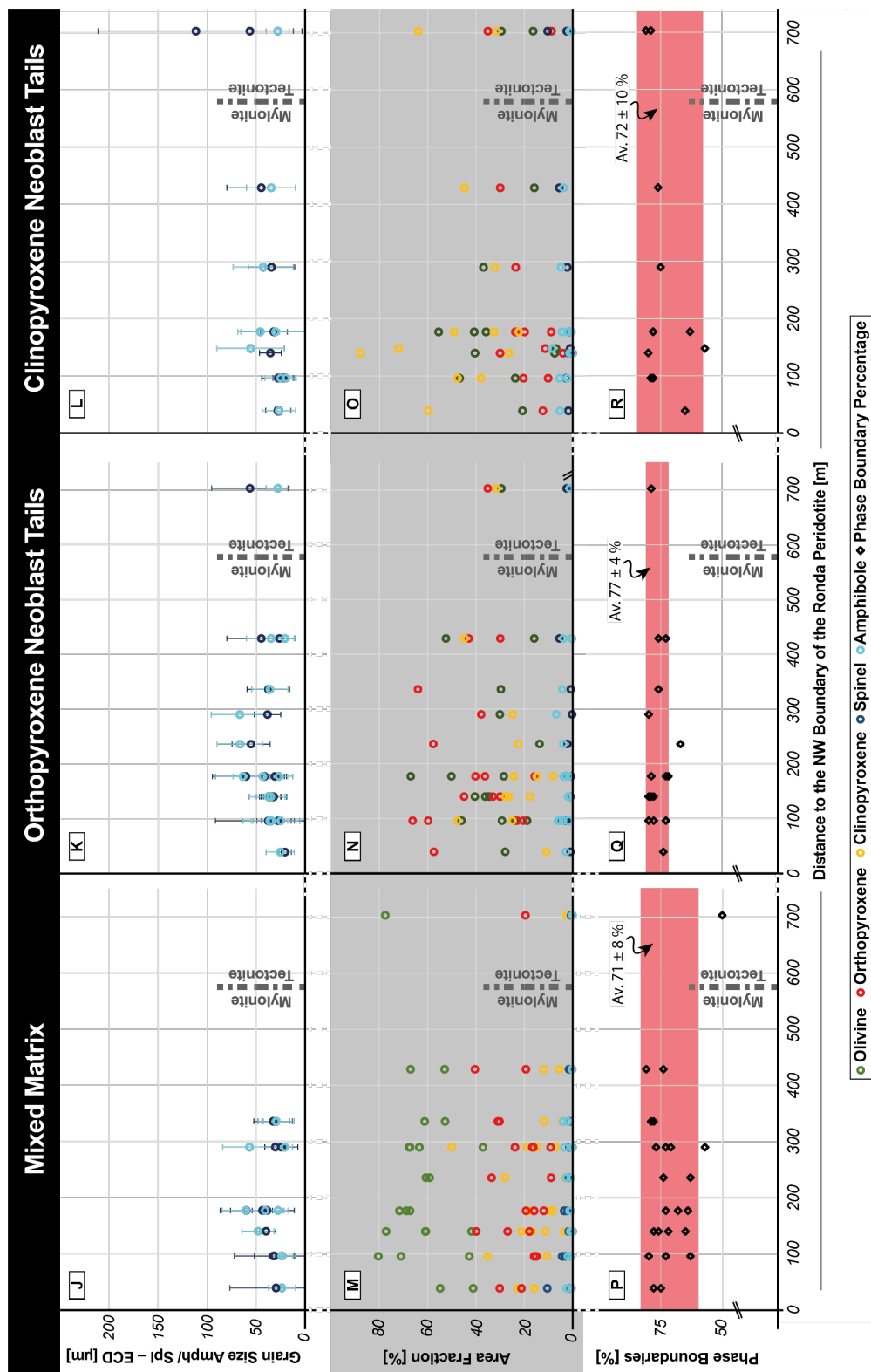
Fig. 4.3b. *Data overview of the major microstructural domains (mixed matrix, orthopyroxene and clinopyroxene porphyroclast neoblast tails) plotted against the distance to the NW-B. The olivine-rich matrix was excluded due to its small database. Each data point represents the average grain size (**A-L**), area fraction (**M,N,O**) or phase boundary percentage of the total boundary length (**P,Q,R**) of one EBSD map of an analyzed microstructure (e.g., Figs. 4.5-4.9). The complete microstructural data is attached in supplementary data 4.2. High resolution, digital version is included on the CD.*
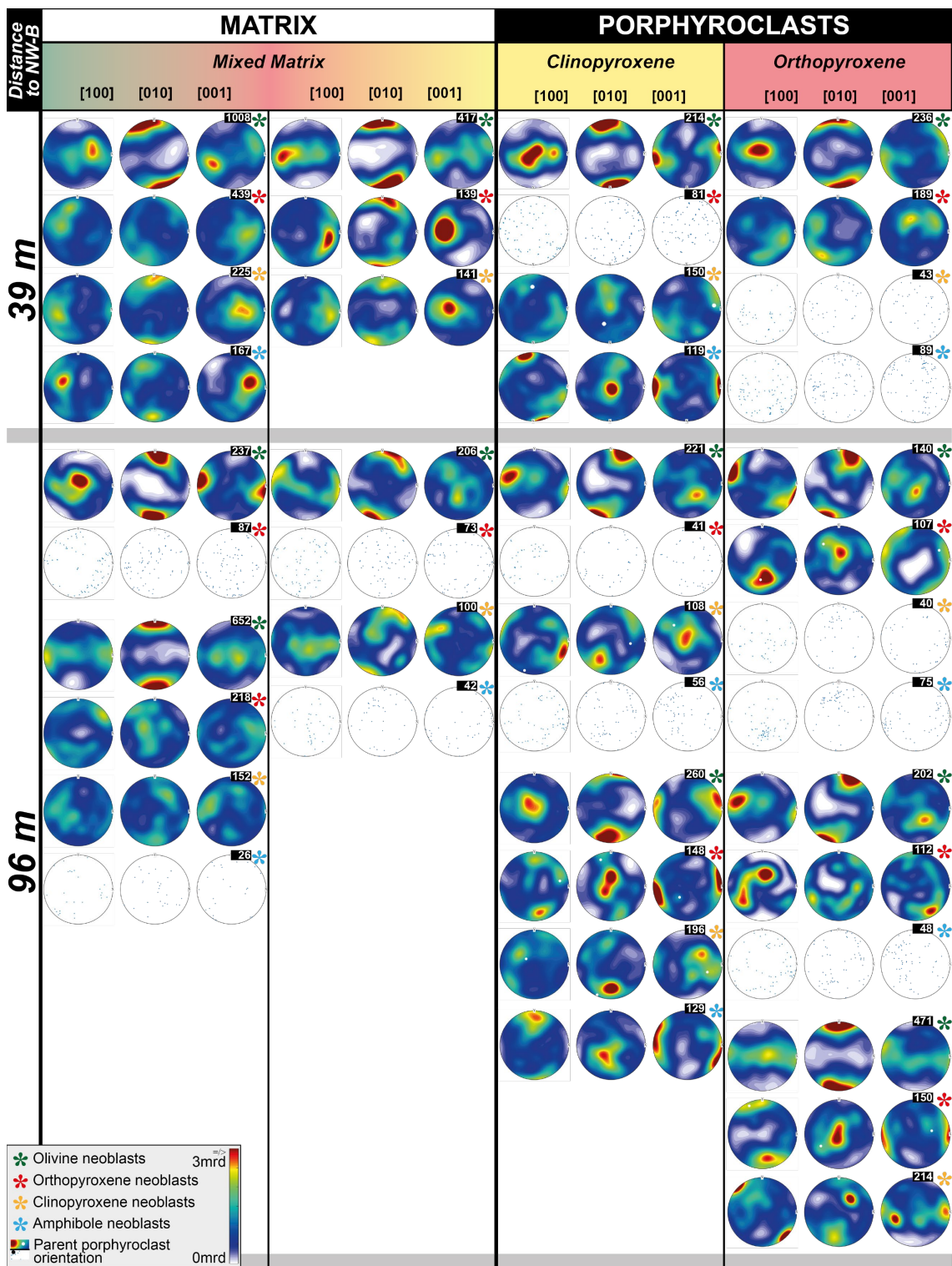
Fig 4.4. *Part 1 of 5. Figure caption on page 129.*
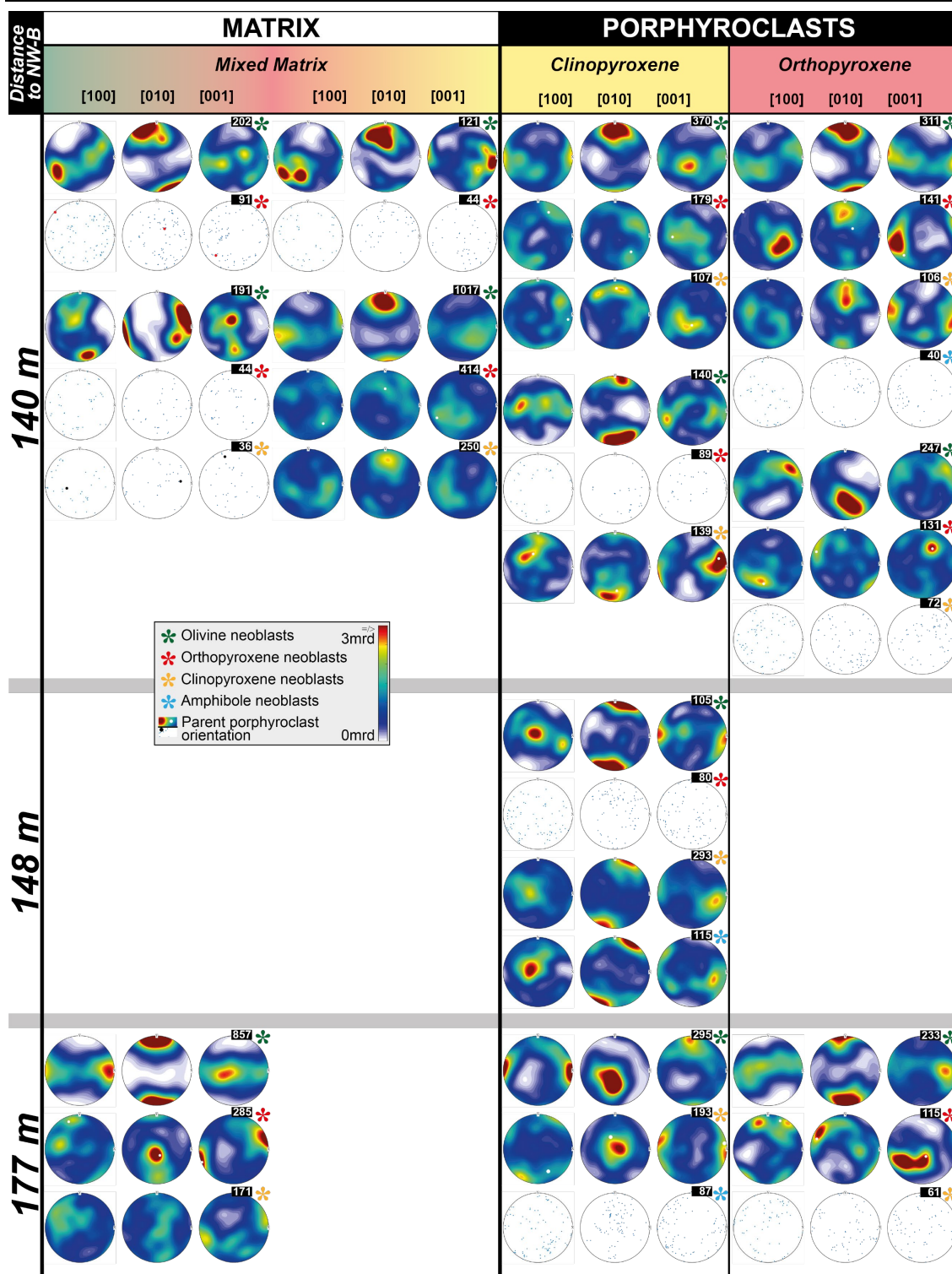
Fig 4.4. Part 2 of 5. Figure caption on page 129.
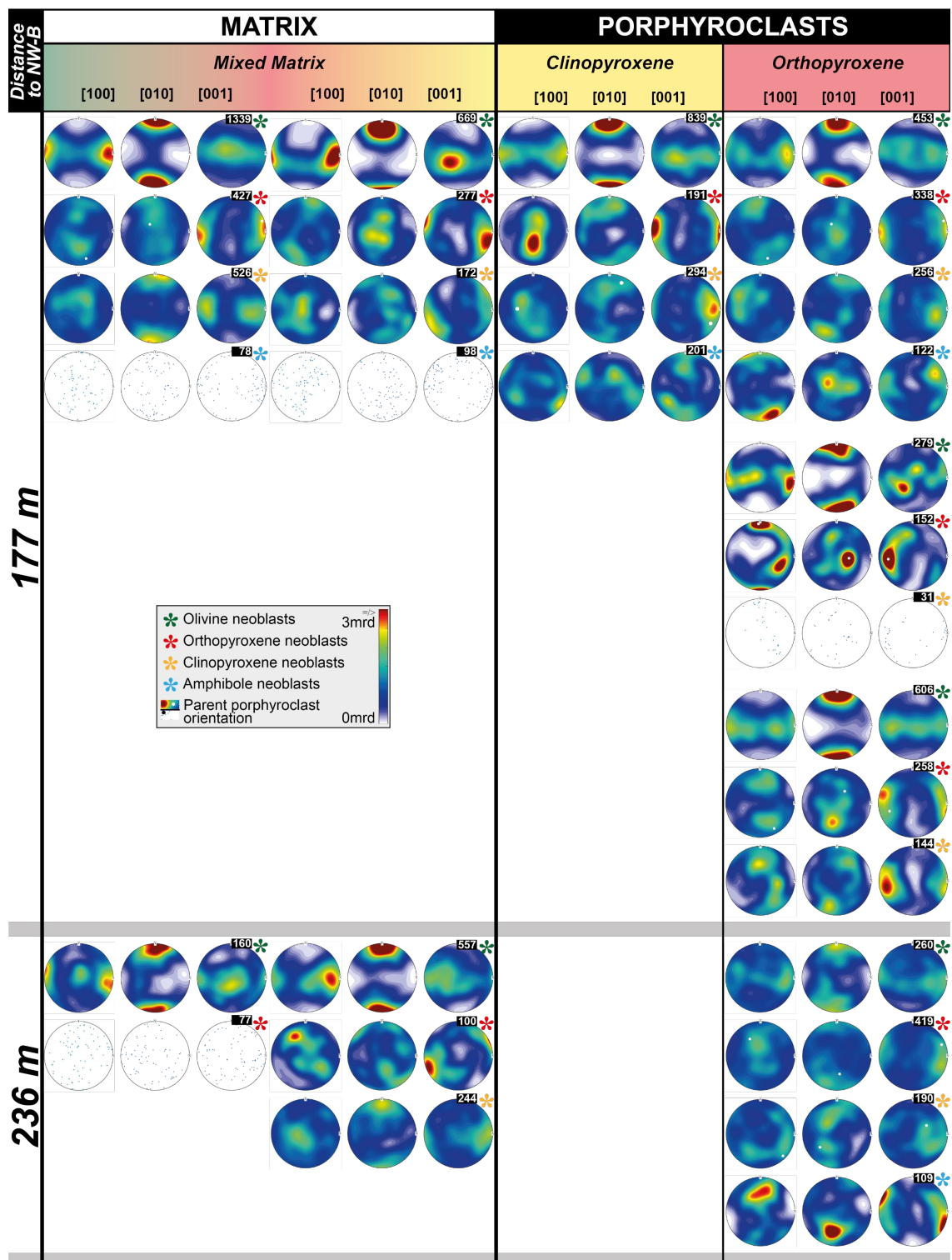
Fig 4.4. *Part 3 of 5. Figure caption on page 129.*
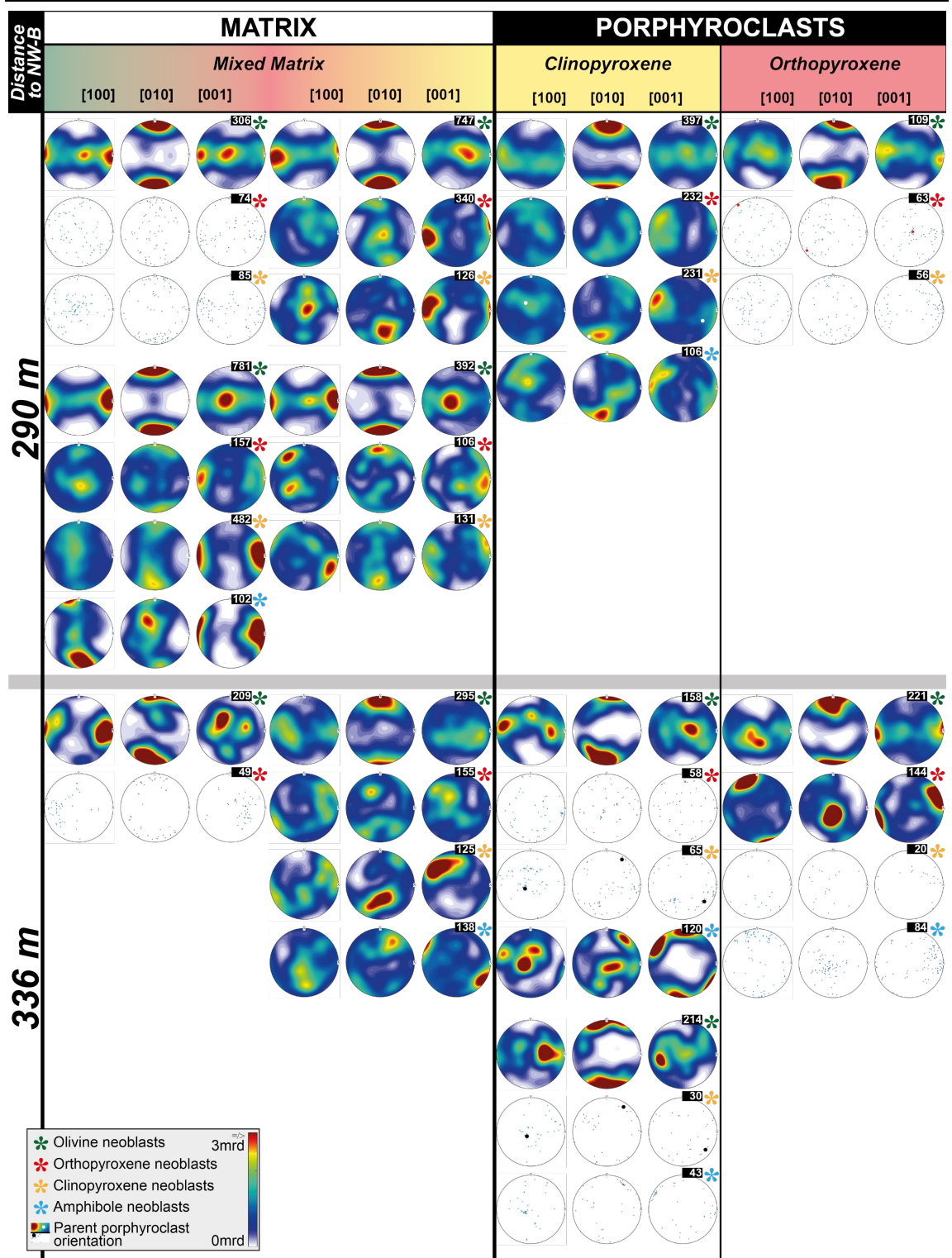
Fig 4.4. Part 4 of 5. Figure caption on page 129.
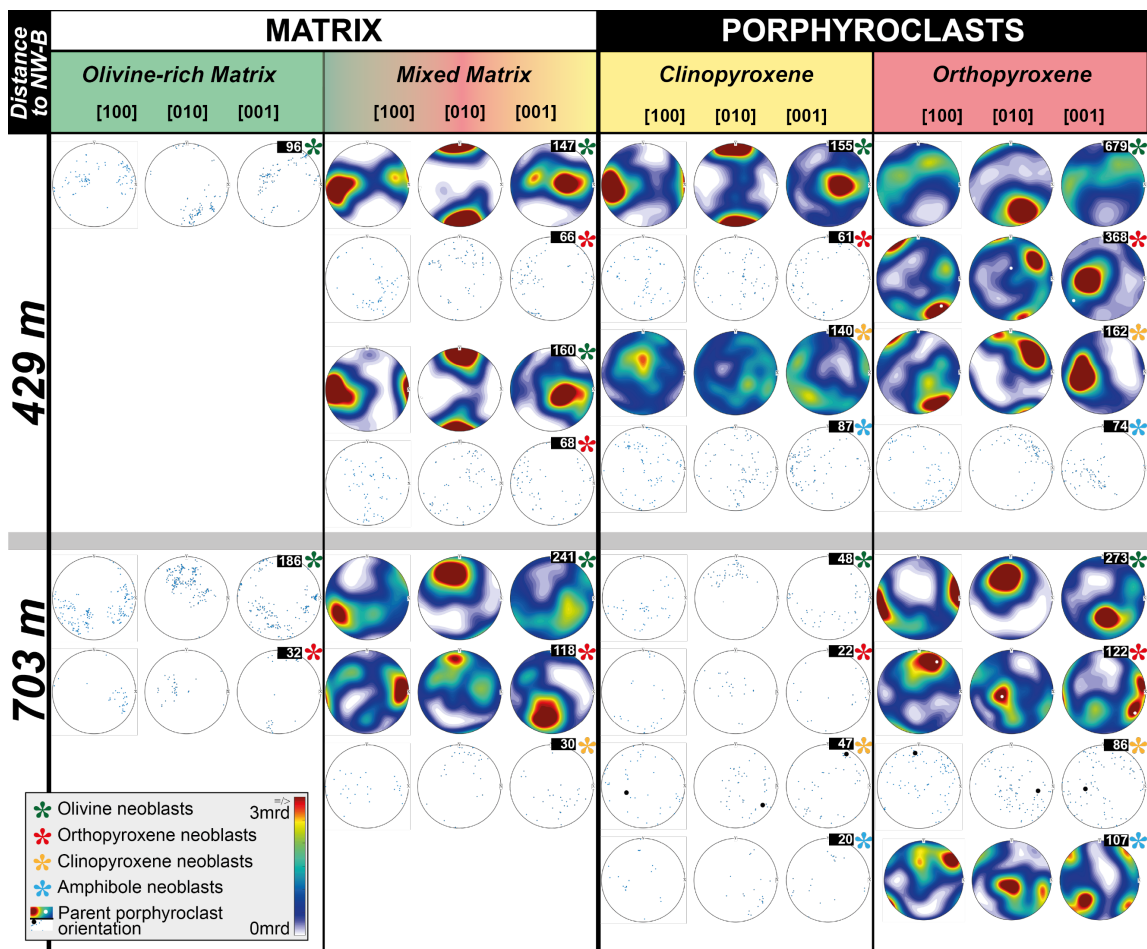
Fig. 4.4. *Part 5 of 5. Orientation data of all microstructural domains plotted per phase and EBSD map as lower pole figures of calculated texture (>100 grains) or dots of grain orientations (<100 grains). White numbers on black indicate number of grains analyzed for the specific phase. Phase is indicated by the color of the asterisk. Grouping of pole figures correspondents to the microstructure: Small spacing indicates neoblasts from the same microstructure. High resolution, digital version is included on the CD.*

4.5.1.1   Matrix domains

The overall olivine dominated matrix forms the major part of all analyzed samples (Fig. 4.2). Due to the presence of interstitial cpx (high Ca counts in Fig. 4.2) and opx, most of this matrix is "mixed" with only parts remaining almost monomineralic, olivine-rich (Ol > 90 %). Nevertheless, lenses of olivine-rich matrix enclosed by mixed matrix are present in all samples (Fig. 4.2). The differentiation between mixed domains and olivine dominated domains becomes increasingly difficult with decreasing distance to the NW-B. In both matrix domains olivine grains are cut by subvertical or subhorizontal serpentine veins. With increasing degree of serpentinization, olivine grain boundaries become increasingly lobate and originally coherent grains are separated into smaller fragments. Coherent crystallographic orientations with bended lattices over span multiple fragments, which were identified as single grains by the analysis of original EBSD data (Fig. 4.5). Due to this discrepancy between calculated fragments and pristine grains, the EBSD data

missing due to serpentinization were filled by applying a half quadratic filter. On the basis of the restored data grain reconstruction of the original grain size could be achieved. Even though this method restores the pristine grain size and preserves the crystal orientations (Fig. 4.5; Bergmann et al. 2016), minor deviations in the shape of the grain boundary might occur.

4.5.1.1.1 Olivine-rich matrix

The olivine-rich matrix is characterized by ol abundance > 90 % and only occasionally occurrence of interstitial secondary phases (Fig. 4.5). In places, coarse pyroxene grains, dominantly opx, are present. Due to the strong serpentinization in olivine-rich domains/ lenses and their abundance limited by the pervasive occurrence of interstitial pyroxenes forming the mixed matrix only two microstructures of the olivine-rich matrix type could be analyzed (e.g., Fig. 4.5). They consist of on average 93 % olivine (range 92-94), 6 % opx (range 6-7) and minor spinel (1 %) and cpx (< 1 %). The average reconstructed olivine grain size is 107 µm (range 103-112; S4.2). With on average 7 % secondary phases, 31,5 % of the total boundary length are phase boundaries. The crystallographic orientations of the olivines are predominantly parallel to each other (Fig. 4.4). Bended lattices and/or subgrain boundaries are often present (Fig. 4.5 – box and dashed line). Cracks within those original grains are filled with serpentine (Fig. 4.5). Orthopyroxenes within the olivine-dominated matrix are oriented with their [001] axis perpendicular to the foliation plane and [100] parallel to the lineation (Fig. 4.4).
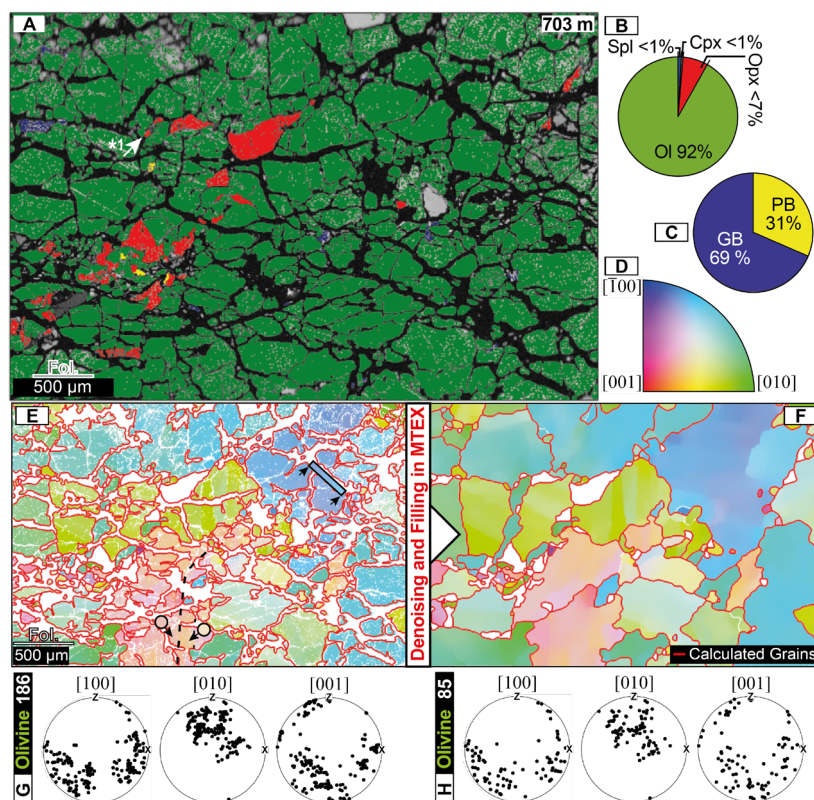
←Fig. 4.5. *A*: *Example microstructure of olivine-rich matrix in sample from 703 m distance to the NW-B. Area percentages (**B**), phase and grain boundary percentages (**C**) are given in pie charts. The olivine orientation colour key for maps E & F is given in **D**. EBSD data reconstruction and denoising, optimized for olivine, is shown in E-H. **E**: Original ol orientations data with calculated grain boundaries (red). Examples of intracrystalline deformation by bending of the crystal lattice (box) and subgrain boundary (dashed line) covering and crossing multiple calculated fragmental grains are annotated. **F**: Denoised and filled ol orientation map with calculated grain boundaries (red). Olivine orientation plots of original (**G**) and reconstructed data (**H**). High resolution, digital version is included on the CD.*

4.5.1.1.2 Mixed matrix

The mixed matrix was defined by less than 90 % olivine and a second phase content dominated by interstitial secondary phases. The microstructures of 23 mixed-matrix domains were analyzed either as subsets of EBSD maps covering pyroxene porphyroclast tail assemblages with adjacent matrix or as individual map. The subsets only consist of the mixed matrix surrounding the porphyroclast-tail assemblage. As mixed matrix microstructures are present in the entire transect (703 to 29 m distance to NW-B), they are present in both mylonitic and tectonitic samples. Characteristics for the mixed matrix are small, interstitial, and irregular/highly lobate pyroxene grains in between coarser grained olivine (Fig. 4.6). The grain shape of pyroxenes and olivine varies between rather equiaxial in tectonitic samples (Fig. 4.6B-i) to elongated olivines and film/wedge-shaped pyroxenes in mylonitic samples (Fig. 4.6A-i). The long side of film-like pyroxenes is mostly parallel to the foliation. Bigger pyroxenes have in general highly irregular grain shapes and protrusions which form intergrow patterns with bordering olivines (Fig. 4.6A-i *1). Indentations of olivine neoblasts in bigger pyroxenes are commonly observed (Fig. 4.6A-i *2). The mineralogical assemblage of the mixed matrix is in general constant for the entire data set and consists of olivine (av. 61 %, range 37-80 %), orthopyroxene (av. 22 %, range 9-40 %), clinopyroxene (av. 14 %, range 2-50 %) and spinel (av. 2 %, range 0-10 %) with occasional amphibole (av. 1 %, range 0-4 %) (Fig. 4.3). Spinel is present as interstitial grains. Phase abundances vary depending on the microstructural setting within one sample but do not significantly change over the distance to the NW-B (Fig. 4.3M). Similar to the olivine-rich matrix, former coarse-grained olivines are cut by serpentine veins. Only in phase mixtures olivine grains are less effected by the serpentinization. Average grain sizes (ECD) are 67 μm for opx (range 42-136), 64 μm for cpx (range 35-117), 41 μm for spinel (range 24-90) and 40 μm for amphibole (range 21-60) (Fig. 4.3, S4.2). Reconstructed olivine grains form in all investigated thin sections and with on average 103 μm (range 55-192) ECD the biggest grains. Over almost the entire mylonitic transect (39-429 distance to the NW-B) grain sizes of all phases of the mixed matrix are similar within uncertainty (1σ, Fig. 4.3). Only

around ~250 m distance to the NW-B, the grain size of both pyroxenes shows an excursion towards coarser sizes. Mixed matrix pyroxenes in the tectonite regime (Fig. 4.6B-i) have coarser grain sizes (Fig. 4.3). Average aspect ratios are 2.03 ±.1 for reconstructed ol, 1.9 ±.2 for opx, 1.9 ±.3 for cpx, 1.8 ±.1 for spinel and 1.8 ±.2 for amphibole (S4.2). In contrast to the grain sizes, the average aspect ratios remain constant over mylonites and tectonites (S4.2). 71 ±8 % of the total boundary length are on average phase boundaries (29 % grain boundaries). Apart from one outlier, all mylonitic mixed matrix domains share this distribution. In tectonite, phase boundaries only form 50 % of the total boundary length. On average 40 % of the total boundary length are olivine-opx boundaries with 48 % of the entire olivine boundaries and 79 % of all opx boundaries being olivine-opx boundaries. Despite the lower abundance of cpx, amphibole forms more phase boundaries with cpx (29 %) than with opx (16 %).

Olivine CPOs are moderate (av. max mrd 10, av. M=0.16). Overall, the A-type olivine CPO is dominant (18 of 23 mixed matrix microstructures; Fig. 4.4). However, transitions to the AG-type by [100] and [001] forming girdles in the foliation plane are present with variable strength (clear AG-type CPO n=3). Clear B-types, which were also reported by Précigout and Hirth (2014) are present in the two samples situated closest to the NW-B. Orthopyroxene CPOs are with an average maximum mrd of 8 and an average M-index of 0.04 the weakest opx CPOs of all investigated domains. In most cases, orthopyroxene's [001] axes are parallel to the lineation. The CPO of opx neoblasts is in places affected by the orientation of larger opx grains within the mixed matrix (Fig. 4.6B-iii). Clinopyroxene CPOs are weak with an average M-index of 0.05 (av. max mrd 18). In most cases, both pyroxenes are oriented parallel to each other and show similar intensities in mrd and M for a given microstructure. In some cases, maxima of pyroxene [100] and [010] orientations are flipped in the sense that clinopyroxene [100] maxima are parallel to orthopyroxene [010] maxima, and cpx [010] display orientations similar to opx [100] (e.g., Fig. 4.6A-iii/iv). Only in four mixed matrix microstructures enough amphibole grains are present to determine a CPO (Fig. 4.4). In general, amphibole orientations are parallel to the present pyroxene and its [001] axes are aligned parallel to the lineation. Neoblasts of ortho- and clinopyroxene and in particular olivine has a high dislocation density, in places concentrated into subgrain boundaries (Fig. 4.7).
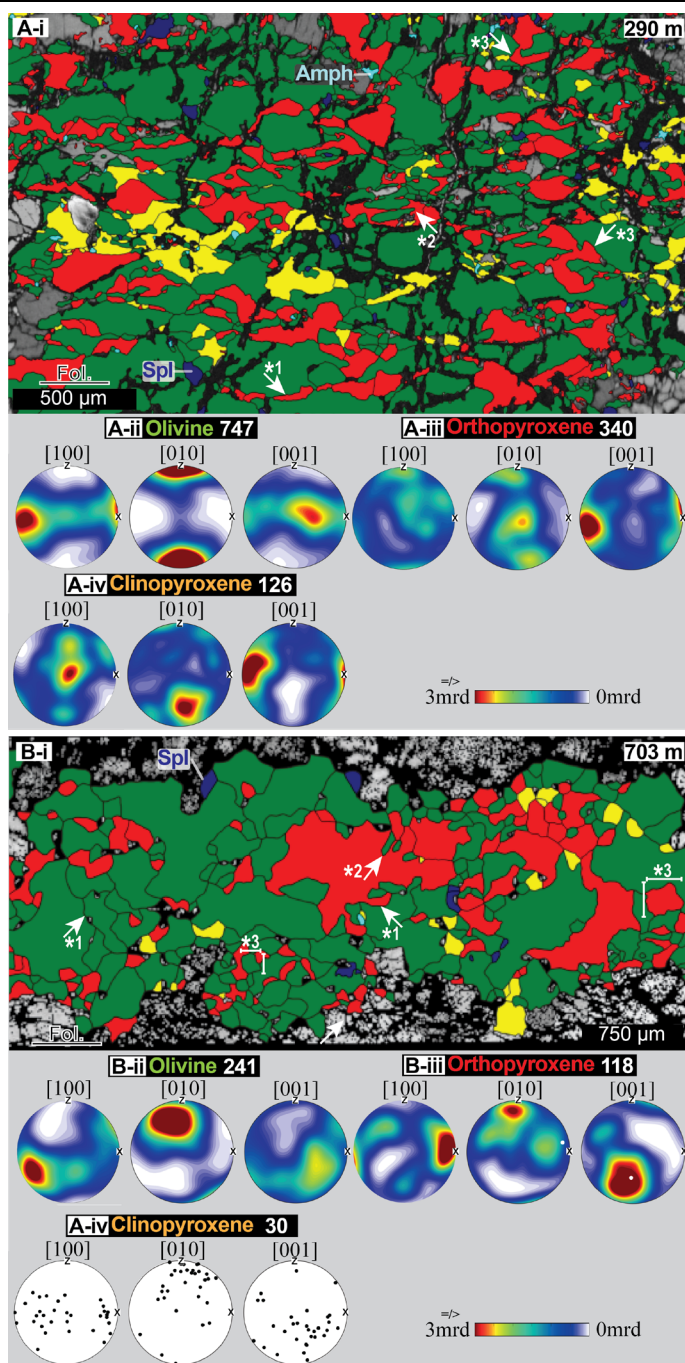
Fig. 4.6. *Example microstructures of the mixed matrix in 290 m (A-i) and 703 m (B-i) distance to the NW-B.* **A**: *Mixed matrix with wedge/film-shaped orthopyroxene (*1) in between coarser olivine, indentations (*2) and highly irregular phase boundaries (*3). CPOs of olivine (A-ii), orthopyroxene (A-iii) and clinopyroxene (A-iv).* **B**: *Mixed matrix of a tectonite sample with highly lobate grain and phase boundaries (*1), indentations (*2) and equiaxial grain shape (*3). CPOs of olivine (B-ii) and orthopyroxene (B-iii) and pole figure of clinopyroxene orientations (A-iv). High resolution, digital version is included on the CD.*
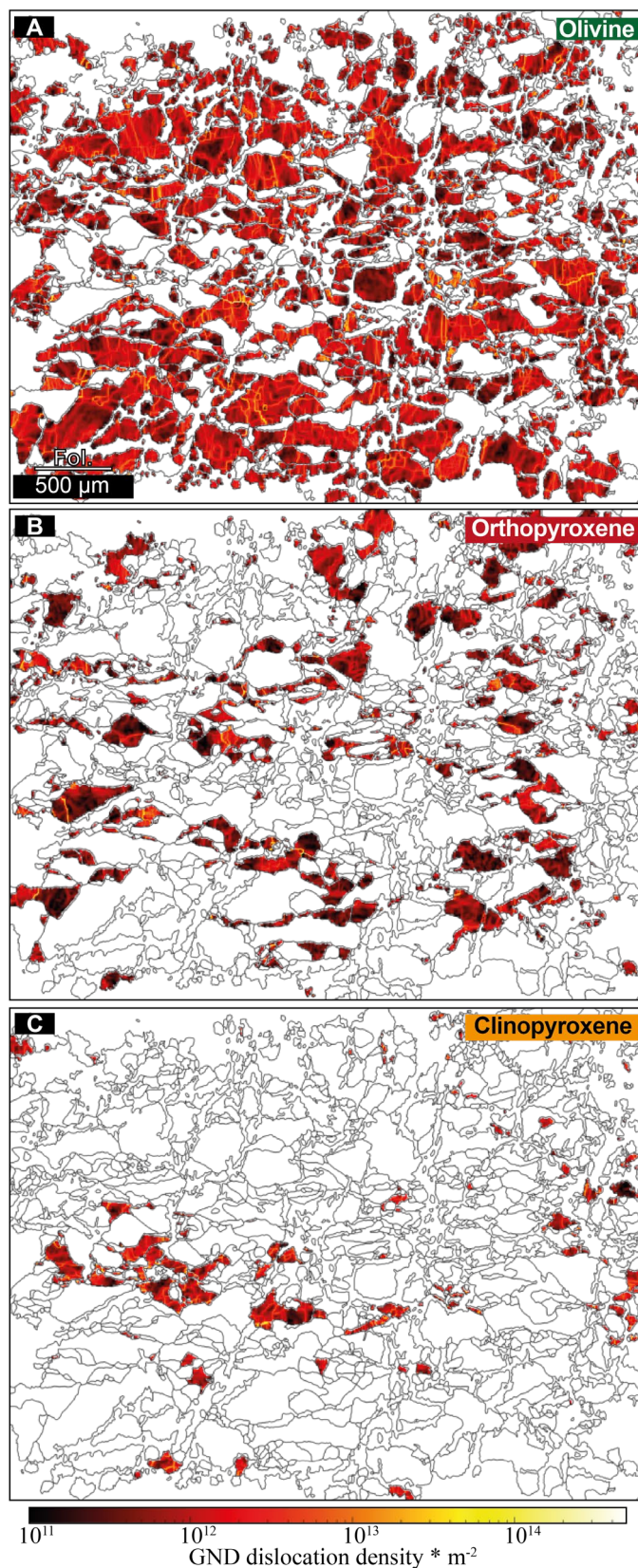
Fig. 4.7. *Geometrically necessary dislocation (GND) density maps for olivine (A), orthopyroxene (B) and clinopyroxene (C) of the mylonitic mixed matrix shown in Figure 4.6A-i. Note grain internal deformation in all phases and the formation of subgrain boundaries visible by bright yellow lines. High resolution, digital version is included on the CD.*

4.5.1.2   Porphyroclast tails

Porphyroclasts are present in all mylonitic samples (Fig. 4.2). In the tectonite sample, the small difference between grain sizes of matrix and porphyroclasts does not allow a clear differentiation between both (Fig. 4.2F). Here, pyroxene is either present in layers consisting of both pyroxenes, spinel, and minor olivine (Fig. 4.9B-i), as clasts, or (Fig. 4.2F-i/ii) as interstitial pyroxenes along grain boundaries of olivine clasts (Fig. 4.6B-i). The isolated pyroxene clasts in tectonites are predominantly orthopyroxenes. In mylonitic samples, the contrast between porphyroclasts and matrix is marked by their strongly differing grain sizes (Fig. 4.2A-E). Most porphyroclasts are pyroxenes. Often clusters of intergrown pyroxenes ± spinel form porphyroclastic assemblages (Fig. 4.2D-i). These assemblages are predominantly present in deformed pyroxenitic layers or in areas with an increased pyroxene proportion (Fig. 4.2C-i lower image half). Occasionally, also garnet surrounded by kelyphitic rims or coarse spinel grains (Fig. 4.2E-i) forms porphyroclasts. As both pyroxenes are present as (porphyro)clasts in tectonites and mylonites, their microstructures were analyzed from 29 to 703 m distance to the NW-B. In mylonitic samples, both pyroxenes show the formation of neoblast tails (Fig. 4.2A-E). Common characteristics of pyroxene neoblast tails are a mixed phase assemblage of both pyroxenes, olivine, amphibole, and spinel. The affiliation of neoblast tails to the parent porphyroclasts is given by the contrast in phase composition and neoblast grain shape between tail and surrounding matrix as well as by neoblast indentations into the parent porphyroclast (Figs. 4.7, 4.8).

4.5.1.2.1 Orthopyroxene porphyroclasts

Orthopyroxene clasts (tectonites) and porphyroclasts (mylonites) are present in all samples. Their shape is variable (Fig. 4.2). However, towards the NW-B highly elongated porphyroclasts (aspect ratios > 1:10) become more abundant. Neoblast formation around opx porphyroclasts is present in all mylonitic samples. Common characteristics of neoblasts are low internal deformation, equiaxial grain shape and often irregular boundaries (Fig. 4.8). At the tectonite-mylonite transition, the formation of neoblasts is weaker and rather arranged in diffuse patches around the porphyroclasts (Fig. 4.8B-i). Here, the mixed neoblasts assemblages are present at the parent clast grain boundary and extend along grain boundaries into the surrounding coarse-grained olivines (Fig. 4.8B-i). With decreasing distance to the NW-B, opx porphyroclast neoblast assemblages become more abundant and form tails within the foliation (Fig. 4.8A-i). The mineralogical assemblage of these tails consists of orthopyroxene (av. 41 %, range 16-66), olivine (av. 34 %, range 14-67), clinopyroxene (av. 20 %, range 1-48), amphibole (av. 3 %, range 1-7) and spinel (av. 2 %, range 1-6) (Fig. 4.3N). Spinel and especially amphibole form mostly interstitial grains. There are no clear trends in the phase assemblage related to the distance to the NW-B (Fig. 4.3N). Amphibole and spinel are constantly present as

secondary phases with standard deviations of ±2 % (amph) and ±1 % (spl) (Fig. 4.3N). For olivine and both pyroxenes, phase abundances in opx neoblast tails can vary in a single thin section in the same magnitude as over the entire shear zone transect. Average grain sizes are 69 μm for opx (range 41-120) and reconstructed ol (range 53-99), 66 μm for cpx (range 34-115), 37 μm for amphibole (range 21-67) and 36 μm for spinel (range 20-56) (Fig. 4.3). Apart from one excursion at around 250 m distance to the NW-B, the grain sizes are largely constant throughout the entire transect (Fig. 4.3). For a given opx tail, grains of both pyroxenes and reconstructed olivine are mostly similar sized (± 10 μm). Amphibole and spinel have similar, small grain sizes with ECDs in general half the size of pyroxene neoblasts. Average aspect ratios are with 1.8 for opx, 1.9 for olivine, 1.8 for cpx, 1.8 for amphibole and 1.9 in general lower than in matrix domains (S4.2). In contrast to the excursion of the grain sizes, aspect ratios remain constant in all mylonitic samples. In the tectonite, the average aspect ratios are higher (S4.2). Phase boundaries clearly dominate (77 ±4 %) over grain boundaries (Fig. 4.3Q). Apart from one outlier, these high phase boundary percentages are present over the entire shear zone (Fig. 4.3Q). Although opx is mostly the predominant phase, olivine forms, on average, most of the phase boundaries (S4.2). Olivine neoblast CPOs are the weakest for all microstructural domains (av. max mrd 9, av. M=0.14). Dominant is the AG-type CPO with girdle distributions of [100] and [001] in the foliation plane (n=11; Fig. 4.4). Transitions to A- or B-type CPOs are formed by point maxima in these girdles (Fig. 4.8A-ii). Two clear A- and B-type CPOs are present for olivine neoblasts in opx tails (Fig. 4.4). Orthopyroxene neoblasts have the strongest opx CPOs of all microstructural domains (av. max mrd 12, av. M=0.07). For almost all orthopyroxene porphyroclast-neoblast assemblages, opx neoblast CPOs are strongly dependent on the parent clast orientation (e.g., Fig. 4.8A/B-iii). This porphyroclast dependence is present in both strong and weak CPOs of orthopyroxene neoblasts. The common orthopyroxene CPO is [001] parallel to the lineation. The [100] and [010] maxima do not show such a clear trend. Clino- and orthopyroxene CPOs are always for [001] and predominantly for [100] and [001] parallel to each other (e.g., Fig. 4.8B-iii/iv). With an average maximum mrd of 19 and an average M-index of 0.19 cpx neoblasts in opx porphyroclast tails form the strongest clinopyroxene CPOs of all microstructural domains. For all orthopyroxene tails, amphibole CPOs are related to the orthopyroxene neoblast CPOs and thereby also parallel to the parent clast orientation (e.g., Fig. 4.8A/B-v).
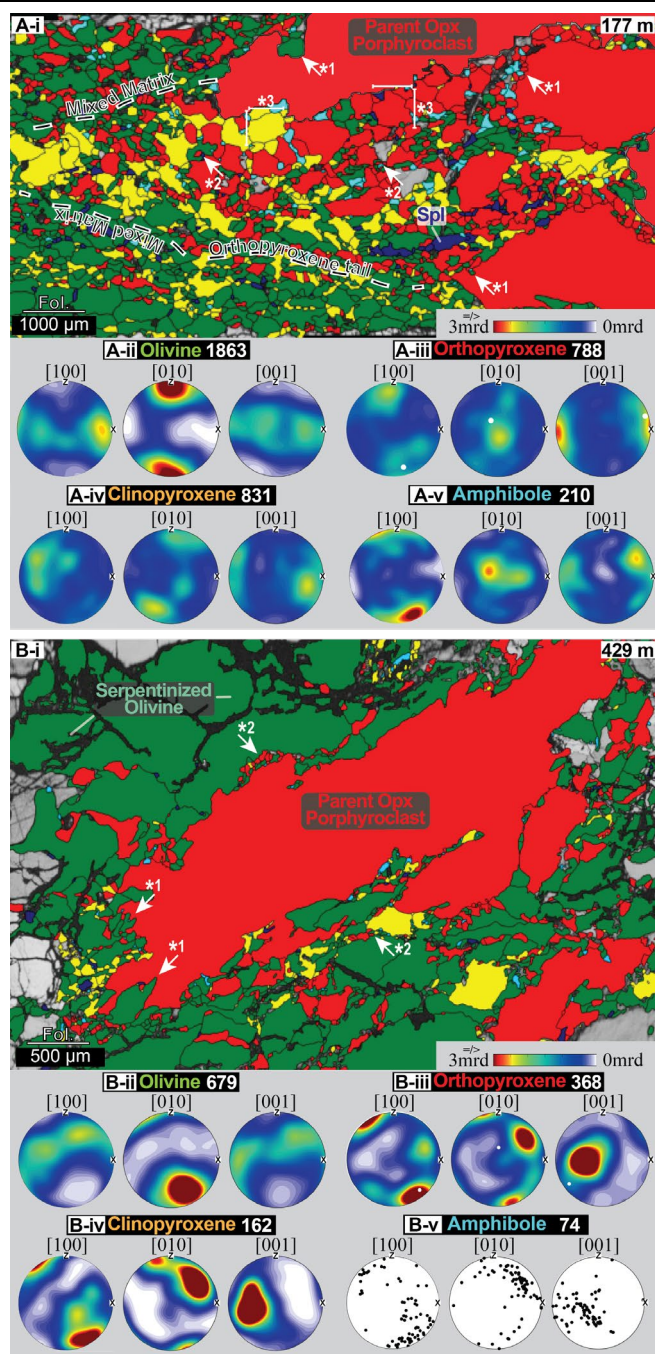
Fig. 4.8. *Example microstructures of orthopyroxene porphyroclasts with neoblasts in 177 m (A-i) and 429 m (B-i) distance to the NW-B. **A**: Neoblast tail of opx and subordinate cpx porphyroclast assemblage. Annotated are neoblast indentations in parent porphyroclasts (*1), interstitial amph and spl (*2) and equigranular grain shape (*3). Note the difference in phase composition and abundances, grain size and shape between neoblast tail and surrounding mixed matrix. CPOs of all present phases are given in A ii-v with white dots in A-iii indicating the parent clast orientation. **B**: Orthopyroxene porphyroclast with neoblast indentations (*1) and fine-grained mixed neoblast assemblages at its boundary (*2). Note the presence of fine-grained mixed neoblast along grain boundaries of the surrounding coarse olivine. CPOs of all present phases are given in B ii-v with white dots in B-iii indicating the parent clast orientation. High resolution, digital version is included on the CD.*

4.5.1.2.2 Clinopyroxene porphyroclasts

In the tectonite, isolated clasts of clinopyroxene are less frequent than those of orthopyroxene (Fig. 4.2F). Here, beside the small, interstitial cpx grains mentioned in the mixed matrix section, coarser clinopyroxene grains are predominantly present in pyroxenite layers consisting of intergrown pyroxenes, spinel, and olivine (Fig. 4.9B-i). Phase boundaries in these are irregular, whereas grain boundaries tend to be straight and angular (Fig. 4.9B-I *1). A differentiation between parent clast and neoblasts is not possible. In mylonitic samples, clinopyroxene porphyroclasts, either present isolated (Fig. 4.2B-ii) or in deformed assemblages of the above-described layers (Fig. 4.2D-ii), form tails of neoblasts, which are sweeping into the foliation. Compared to opx neoblast tails, those of clinopyroxene porphyroclasts are more pronounced both in frequency and in tail length (Fig. 4.2). Additionally, and in contrast to opx neoblast tails, neoblast tails of cpx porphyroclast are also present in mylonitic samples close to the tectonite-mylonite transition (Fig. 4.2E-ii). Neoblast tails of cpx porphyroclasts consist of 48 % clinopyroxene (range 22-88), 27 % olivine (range 7-56), 19 % orthopyroxene (range 4-40), 3 % amphibole (range 0-9) and 2 % spinel (range 1-10). For the major components (cpx, opx, ol) no change in phase abundances is present over the transect (Fig. 4.3O). For the minor phases of amphibole and spinel it seems that in distal parts of the mylonites and in tectonites spinel is the prevailing secondary phase, whereas closer to the NW-B amphibole is more abundant (Fig. 4.3O). In most microstructures, spinel and amphibole occur separated from each other. Average grain sizes are 88 μm for cpx (range 53-177), 83 μm for reconstructed olivine (range 57-137), 70 μm for opx (range 40-116), 38 μm for amphibole (range 20-63) and 44 μm for spinel (range 23-112). The distribution of grain sizes is divided into coarse areas of primary phases (pyroxenes and olivine) and fine-grained areas of thoroughly mixed secondary (amphibole or spinel) and primary phases (Fig. 4.9A-I *3). Primary phase grain sizes are relatively constant over the first 300 m distance to the NW-B (Fig. 4.3). In the distal mylonitic part and in the tectonitic regime, their grain size increases. Amphibole and spinel average grain sizes are about half of the size of primary phases (Fig. 4.3). Their grain sizes tend to be constant over the entire transect. For both primary and secondary phases a slight excursion towards bigger grain sizes around ~280 m distance to the NW-B is present. Average aspect ratios are with 1.8 for cpx, 2.0 for olivine, 1.9 for opx, 1.9 for amphibole and 1.9 in general lower than in matrix domains (S4.2). In contrast to the grain size, aspect ratios are more constant over the entire transect (S4.2). Phase boundaries form on average 72 % (±10 %) of the total boundary length (Fig. 4.2I). This distribution is in general constant over the entire transect, independent of mylonitic or tectonitic unit. Amphibole is mostly affiliated to clinopyroxene (S4.2).

Olivine neoblasts CPOs in tails of clinopyroxene porphyroclasts are variable. Beside the most present A- and B-type (each n=4) transitions to the AG- type with point maxima in [100] and [010] girdles, pure AG-types and one clear E-type are present (Fig. 4.4). Their strength is moderate to strong (av. max mrd 12, av. M=0.15). Clinopyroxene neoblast CPOs are weak (av. max mrd 15, av. M=0.07). In most cases, the parent clinopyroxene porphyroclasts have an imprint on the neoblast orientation (e.g., Fig. 4.9A-iv). However, compared to orthopyroxene, clinopyroxene maxima are often less pronounced and blurred and therefore more variable from their parent clast orientation. The [001] axes are largely parallel to the lineation. Occasionally (n=2), [100] maxima are oriented parallel to the lineation. If present, orthopyroxene neoblasts are parallel to clinopyroxenes with their [001] and show occasionally 90° rotations for [100] and [010]. Amphibole neoblasts are mostly oriented parallel to the pyroxenes (e.g., Fig. 4.9A-v).
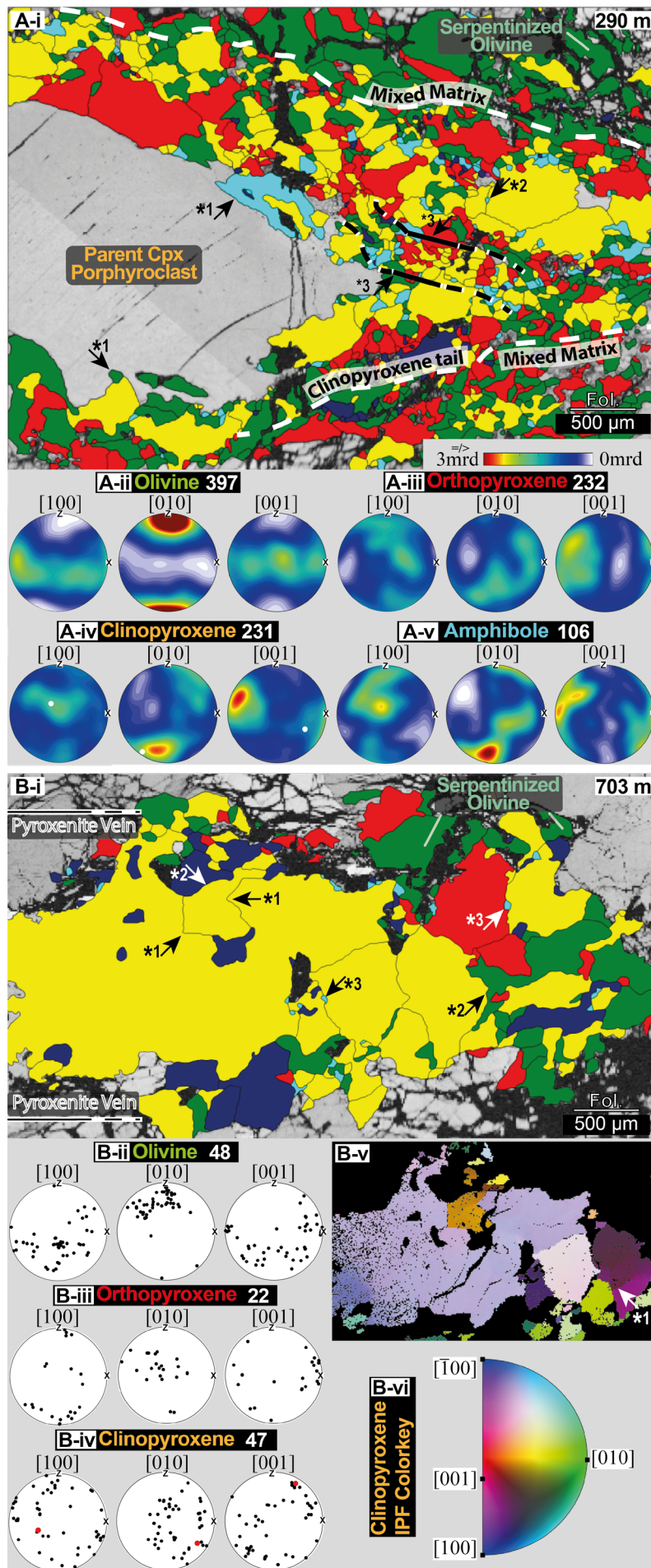
Fig. 4.9. Example microstructures of clinopyroxene porphyroclast with neoblast tail in 290 m (A-i) and cpx-dominated pyroxenite layer at 703 m (B-i) distance to the NW-B. A: Clinopyroxene porphyroclast neoblast tail embedded in the mixed matrix with amphibole/ol indentations (*1) and interstitial amph (*2). Within the tail a band of fine grained neoblasts (*3) is present. CPOs of all phases are given in A ii-v. B: Pyroxenite layer with straight grain (*1) and lobate/irregular phase boundaries (*2) and interstitial amph and spl (*3). Pole figures of ol (B-ii), opx (B-iii) and cpx (B-iv) orientations are given. The cpx orientation map (B-v; colour key in B-vi) shows grain-internal deformation and subgrain boundaries (*1). High resolution, digital version is included on the CD.

4.5.1.3   Clinopyroxene-amphibole veins

In three samples, veins consisting of fine grained (ECD < 10 μm) cpx and amphibole were analyzed. These veins crosscut porphyroclasts, tails and the mixed matrix with an orientation of ~45° to the foliation (Fig. 4.10). In olivine-rich domains no such veins were found. The veins are best visible when crosscutting cpx porphyroclasts or pyroxenite layers (Fig. 4.10). Crosscutting previous structures oblique to the foliation, these veins are attributed to the late evolution of the Ronda peridotite. Because of the focus of this research on the mylonite formation a detailed microstructural investigation was omitted. However, a short revision is given in the geochemistry and the discussion chapters.
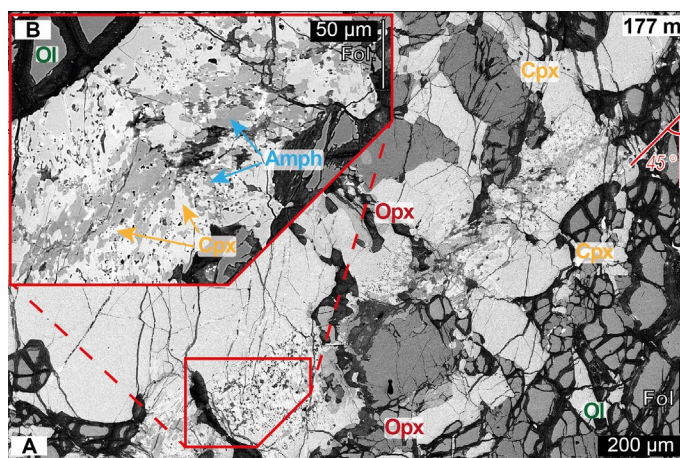
Fig. 4.10*. **A**: Clinopyroxene amphibole vein crosscutting the mixed matrix and a clinopyroxene porphyroclast. Note the ~45° angle between foliation and vein orientation. **B**: Close-up view of vein showing zoning in cpx-rich rim and amph-rich center. High resolution, digital version is included on the CD.*

4.5.2 Mineral chemistry

The major-element compositions of both pyroxenes (opx and cpx), olivine, amphibole and spinel were determined from three samples with different distances to the NW-B (96 m, 177 m, 290 m). Apart from the olivine-rich matrix, all microstructural domains (cpx/opx neoblast tails, mixed matrix) were analyzed for each sample, if present. Neoblast tail measurements include the analysis of the parent pyroxene porphyroclast. There is a general trend for all analyzed phases of decreasing Mg# with increasing distance to the NW-B (Figs. 4.11, 4.12). Coupled to the decrease in Mg# are in most cases an increase in TiO_2 and a decrease in Cr_2O_3 (Figs. 4.11, 4.12). In the following, deviations from this trend and phase specific geochemical variations are presented. Detection limits (S4.1), the complete microprobe data (S4.3) and additional graphs (S4.4) are attached as supplementary data.
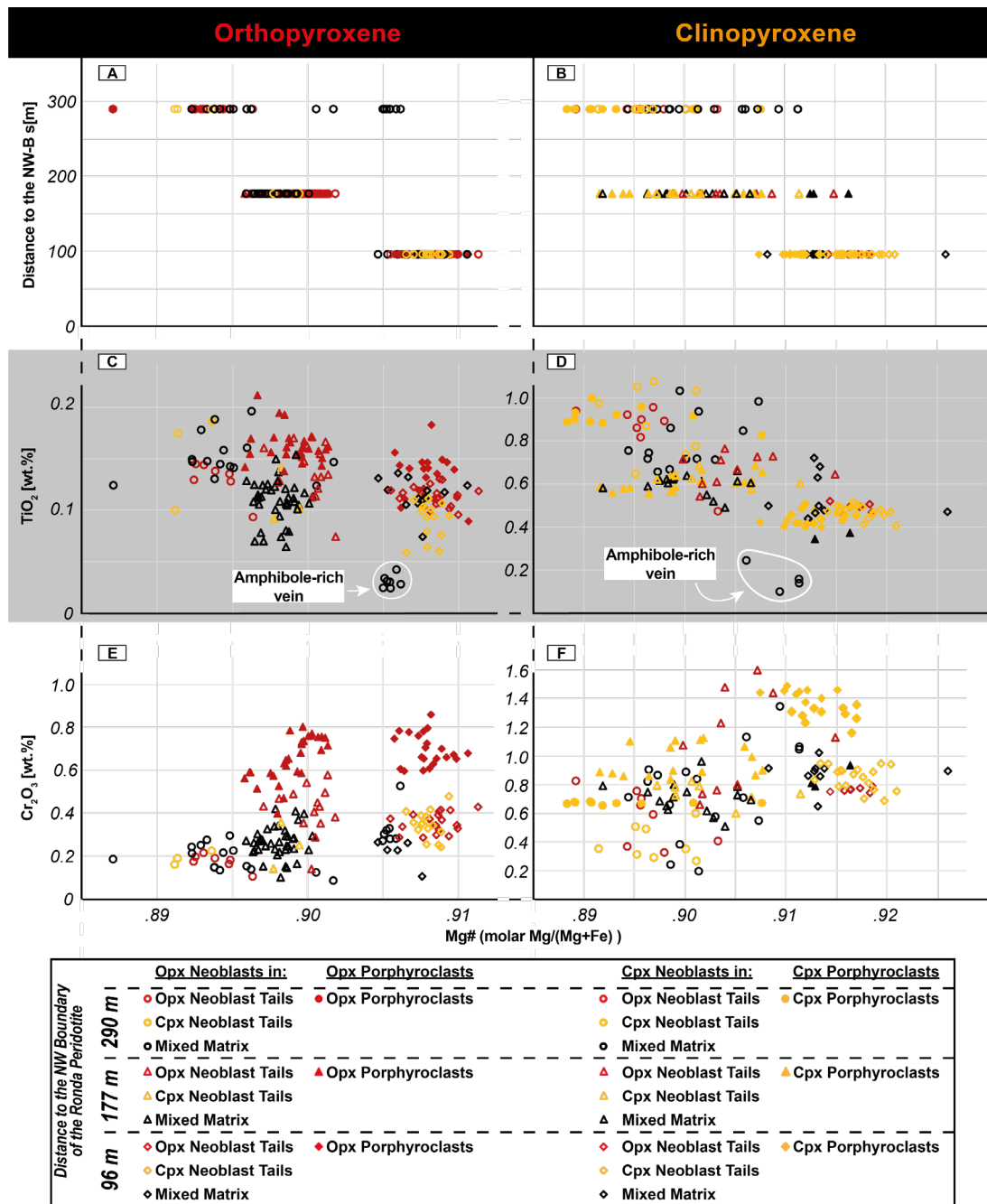
Fig. 4.11. *EPMA data of ortho- and clinopyroxene porphyroclasts and of neoblasts situated at 96 m, 177 m, and 290 m to the NW-B. Neoblasts were analyzed in cpx/opx porphyroclast tails and in the mixed matrix. **A/B**: Mg# against the distance to the NW-B. **C/D**: TiO$_2$ against Mg#. Pyroxenes of clinopyroxene-amphibole vein (Fig. 4.10) are indicated. **E/F**: Cr$_2$O$_3$ against Mg#. High resolution, digital version is included on the CD.*

4.5.2.1   Orthopyroxene

All analyzed orthopyroxenes have with Mg#s (molar Mg/(Mg+Fe)) exceeding 0.89 enstatitic compositions (Fig. 4.11). In general, neoblasts of tails and in the mixed matrix have lower Cr$_2$O$_3$, Al$_2$O$_3$ and TiO$_2$ abundances than opx porphyroclasts of the same sample (Fig. 4.11). The decrease in Mg# with increasing distance to the NW-B is most prominent in opx porphyroclasts but also present for all neoblasts. The complete range of

this trend is from Mg# 0.89 at 290 m distance to Mg# 0.91 at 90 m distance to the NW-B. The Mg# decrease (increase in FeO) is coupled with an increase of TiO_2 and a slight decrease of Cr_2O_3 (Fig. 4.11C/E).

4.5.2.2   Clinopyroxene

All analyzed clinopyroxenes have a diopsitic composition. For each analyzed sample, clinopyroxene porphyroclasts have in general lower Mg#s and higher Al_2O_3 abundances than associated neoblasts. For Na_2O, CaO, Cr_2O_3 and TiO_2, systematic differences between neoblasts and porphyroclasts of a given sample are not present (Figs. 4.11, S4.4). However, the neoblasts have a bigger scatter in their composition of these oxides. For clinopyroxene, the decrease in Mg# is with a range from Mg# 0.89 (290 m) to Mg# 0.93 (90 m distance to the NW-B) more pronounced than for orthopyroxene (Fig. 4.11). Like orthopyroxene, the decrease in Mg# is coupled to a decrease in Cr_2O_3 and an increase in TiO_2 (Fig. 4.11D/F). Additionally, Na_2O increases and CaO decreases with decreasing Mg#. Clinopyroxene neoblasts from a crosscutting amphibole-pyroxenitic vein deviate significantly from all other analysis by markedly lower Al_2O_3 and Na_2O abundances and increased CaO (Figs. 4.11, S4.3).

4.5.2.3   Olivine

All analyzed olivines have a forsteritic composition. Olivine neoblasts follow the trend of decreasing Mg# with increasing distance to the NW-B independent from the microstructural domain (Fig. 4.12A). However, at 290 m distance to the NW-B one group of olivine mixed matrix neoblasts tends to higher Mg#s (Fig. 4.12A). Yet, with lower Mg#s only present in distal samples, the decrease of the Mg# seems to strictly depend on the distance to the NW-B. CaO and NiO abundances do not vary (Figs. 4.12D, S4.4). Most of the Cr_2O_3 and all TiO_2 measurements lie beneath the detection limit and are therefore excluded from further analysis (S4.4).

4.5.2.4   Amphibole

All amphiboles are Ti-Cr-rich pargasites with in general variable abundances of K_2O (range 0-0.78 wt.%), Cr_2O_3 (range 0.19-1.7 wt.%) and TiO_2 (range 0.66-3.76 wt.%) (Figs. 4.12, S4.4). Apart from one measurement carried out on a sample situated at 90 m distance to the NW-B, all amphiboles follow the trend of decreasing Mg# with increasing distance to the NW-B (Fig. 4.12B). Like both pyroxenes, Cr_2O_3 abundances decrease and TiO_2 abundances increase with increasing Mg# (Fig. 4.12E/G). For TiO_2, four measurements show deviations from this trend by lower abundances. There are no systematic differences between amphiboles associated to ortho-, clinopyroxene tails or the mixed matrix. Na_2O and CaO abundances are except for four measurements constant for all samples and all microstructural domains (S4.4).

4.5.2.5 Spinel

Most spinels follow the trend of decreasing Mg# and increasing TiO_2 with increasing distance to the NW-B (Fig. 4.12C). However, coarse grained spinels (ECD ~1 mm) associated with pyroxenes in kelyphitic intergrow at 290 m distance to the NW-B show Mg#s shifted to higher values (Fig. 4.12C). Additionally, spinels associated to cpx neoblast tails have in each sample the highest Mg# (Fig. 4.12C). High Mg#s in these spinels are related to low TiO_2 and Cr_2O_3 values (Fig. 4.12F/H). In contrast to amphibole and both pyroxenes, Cr_2O_3 abundances increase with increasing distance to the NW-B (Fig. 4.12H).
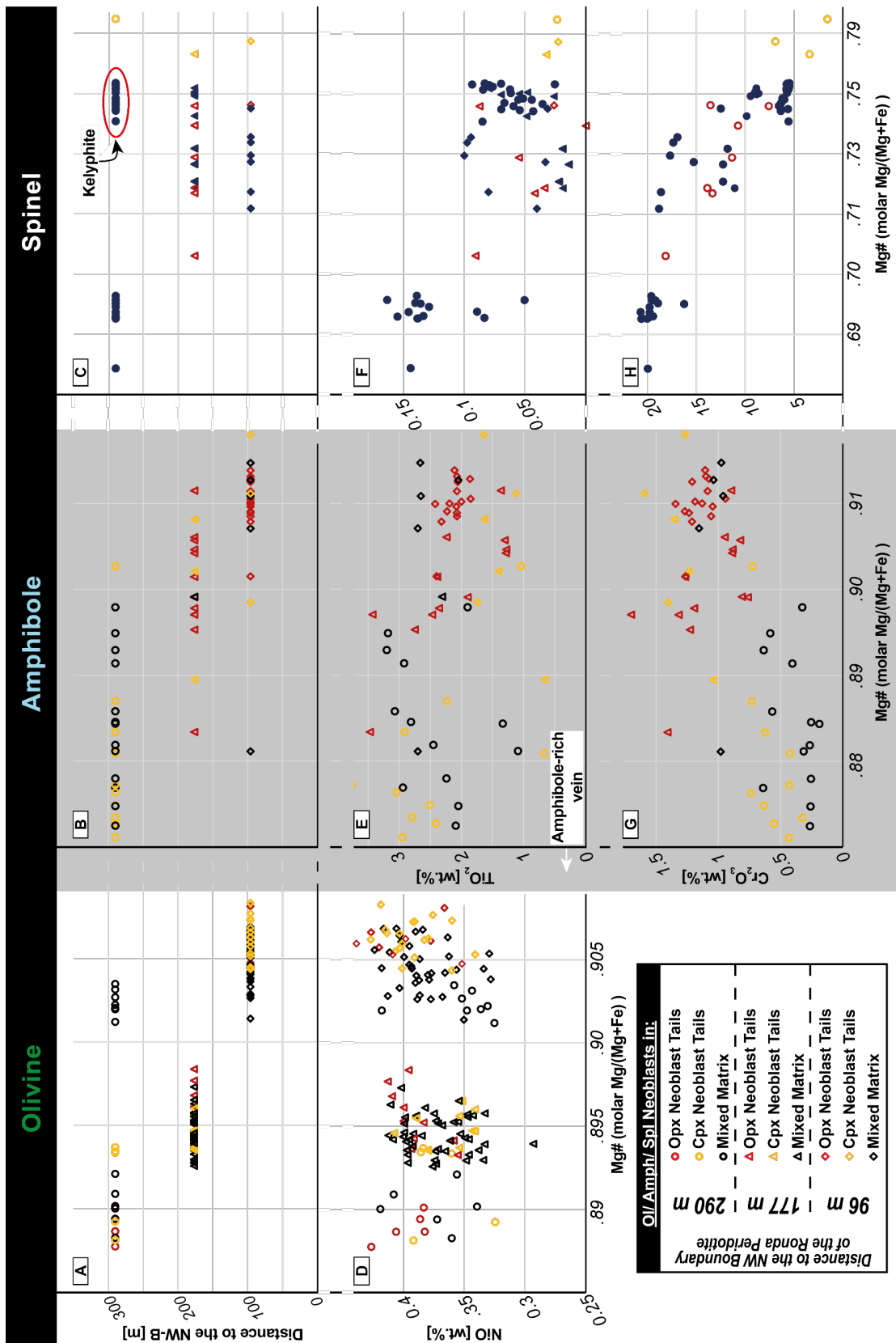
Fig. 4.12. *EPMA data plots of olivine, amphibole, and spinel neoblasts of cpx/opx porphyroclast tails and the mixed matrix at 96 m, 177 m, and 290 m distance to the NW-B. **A/B/C**: Mg# in dependence of the distance to the NW-B. **D**: Mg# against NiO wt.% for olivine neoblasts. **E/F**: Mg# against TiO_2 for amph and spl neoblasts. **G/H**: Mg# against Cr_2O_3 for amph and spl neoblasts. High resolution, digital version is included on the CD.*

4.6 Discussion

4.6.1 Formation of the microstructural domains – Metasomatism by OH-bearing, evolved melt

4.6.1.1 Genesis of the mixed matrix

As the dominant microstructure of all analyzed samples, from 29 to 700 m distance to the NW-B, the mixed matrix is of particular importance for understanding the formation and evolution of the entire shear zone. Its constant microstructural characteristics are (1) a phase assemblage of interstitial secondary grains (opx, spl ± cpx) distributed in between coarse-grained pyroxenes and olivine, (2) high mixing intensities formed by the dispersed distribution of secondary phases and (3) highly lobate phase boundaries and irregular grain shapes. All three characteristics indicate a formation by reactions (e.g. Dijkstra et al., 2002; Hidas et al., 2016; Newman et al., 1999; Tholen et al., 2022). Potential driving forces of such reactions in the upper mantle are metamorphism and/or metasomatism by melt- or fluid-rock interactions.

In other upper mantle shear zones, metamorphic reactions were coupled to the garnet peridotite–spinel peridotite, and at shallower depth, spinel peridotite–plagioclase peridotite transitions which triggered continuous net transfer reactions (e.g. Furusho & Kanagawa, 1999; Newman et al., 1999; Tholen et al., 2022). As phase mixing in the Ronda shear zone is not bound to a specific phase association (grt/spl-bearing), and no plagioclase is present, it is unlikely that metamorphic reactions were the dominant driving force for the neoblast formation in the matrix and in pyroxene tails.

As formerly elaborated by Hidas et al. (2016) in their study on ultramylonitic shear zones in Ronda's SSE plagioclase peridotites (location in Fig. 4.1), syn-kinematic net-transfer, dissolution-precipitation reactions and neoblast crystallization can also be catalyzed by fluids. In this regard, syn-kinematic amphibole precipitation and fluid channeling were also postulated forming mixed phase assemblages and ultramylonites in the center of deformation of the Lanzo shear zone (Vieira Duarte et al., 2020). For a peridotitic composition at shallower upper mantle conditions, Hidas et al. (2016) assume the formation of 1.0–1.4 wt.% amphibole when fluid saturation is reached. However, despite all reported microstructural similarities (high mixing intensity, irregular phase boundaries, interstitial or film-like shapes of orthopyroxenes), there are distinct differences between the NW Ronda shear zone and those mentioned above making a fluid-driven metasomatism unlikely. Firstly, in contrast to the well dispersed amphibole in the matrix reported by Hidas et al. (2016) (~1.6%) and Vieira Duarte et al. (2020) (≤ 30 vol%), amphibole in NW Ronda is mostly limited to pyroxene neoblast tails (av. 3%). In the mixed matrix, amphibole is on average 1%, again mostly associated with coarser grained pyroxenes, especially cpx. The second difference is the lack of

amphibole-bearing ultramylonites and no localization of deformation coinciding with amphibole-rich assemblages (see section 5.3).

Microstructural features such as interstitial grains with low dihedral angles, neoblast indentations in coarse-grained orthopyroxene and highly irregular phase boundaries are furthermore considered as evidence for melt-rock reactions and secondary crystallization from percolating melts (Dijkstra et al., 2002; Stuart et al., 2018; Suhr, 1993). In this regard, the commonly found irregular, highly lobate boundaries between olivine and orthopyroxene suggest a reaction already evoked by Dijkstra et al. (2002) for melt assisted shearing in the Othris peridotite:

Orthopyroxene + low-Si melt ↔ Olivine + high-Si melt (← high stress, → low stress)

(reaction 4.I, Dijkstra et al., 2002)
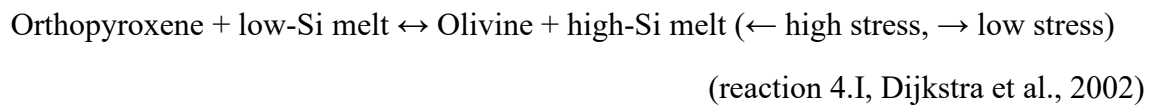
Assuming a formation by percolating melt, the questions arise of its extent and composition. Melt percolation was reported to form lherzolite, plagioclase-bearing peridotite and grt-peridotite replacing harzburgite and dunite in a process called "refertilization" (Beyer et al., 2006; Hu et al., 2020; Müntener & Piccardo, 2003; Le Roux et al., 2007). This process was also ascribed to form cpx-enriched tectonites in the refertilization front a few hundred meters ahead of the melting front between Ronda's coarse grained peridotites and the tectonite unit (Lenoir et al., 2001). The melt origin is ascribed to partial melting (2.5-6.5 % extraction) of the coarse grained peridotites at conditions close to the anhydrous peridotite solidus (T ≥ 1200°C) at 1.5 GPa (Lenoir et al., 2001). In their model, melting was triggered by a rapid, transient heating event (Lenoir et al., 2001). Going further, Soustelle et al. (2009) postulated, that Si-rich melts fertilized the spl-tectonites of the NW Ronda shear zone up to 1.5 km ahead of the melting front. According to these authors, early melt pulses lead to pyroxene and spinel crystallization as irregularly shaped grains, whereas late stage, second-order percolation of evolved melt caused the crystallization of interstitial, undeformed pyroxenes, and spinel with a strongly enriched LREE composition. In contrast to the data of Soustelle et al. (2009), which leaves the mylonitic shear zone melt-unaffected, we present microstructural evidence of melt presence up to the NW boundary of the Ronda massif. However, a change in the modal composition of refertilized lherzolites by neocrystallized pyroxenes, as commonly described for refertilization (e.g., Le Roux et al., 2007), is not documented in both cases. Moreover, syn-kinematic conditions of 800–900 °C and 1.95–2.00 GPa, postulated by Garrido et al. (2011) for the mylonites, refute a large scale, syn-kinematic percolation of refertilizing, basaltic melt, which should reset the temperature.

Similar microstructural evidence for syn-kinematic reactive melt percolation and melt-rock reactions such as irregular grain shape, lobate boundaries and high mixing intensity, have been reported for grt/spl-mylonites of the Beni Bousera peridotite, which forms the Moroccan counterpart of the Ronda massif on the southern limb of the Gibraltar arc (Fig. 4.1; Frets et al., 2014). Syn-kinematic conditions of 850-950° C and ~2.0 GPa, matching those obtained in NW Ronda, led to the assumption of a metasomatism by small fractions of fluids or evolved melts, which did not reset the equilibrium temperatures (Frets et al., 2012, 2014). Amphibole presence in pyroxene neoblast tails (see section 5.1.2), ubiquitous evidence of reaction-derived microstructures and pyroxene crystallization and syn-kinematic PT conditions of 800–900 °C and 1.95–2.00 GPa point to a similar OH-bearing metasomatism by highly evolved melt in the NW Ronda shear zone. The geochemical imprint of this metasomatism is characterized by an increase in FeO (= decreasing Mg#) and TiO_2 for olivine, pyroxenes, spinel, and amphibole in all microstructural domains towards the melting front/with increasing distance to the NW-B respectively (Fig. 4.13). Interestingly, SE tectonites (data from Soustelle et al., 2009) and mylonites follow the same trend of decreasing Mg# with increasing distance to the NW-B (Fig. 4.13). However, an offset is present between SE tectonites analyzed by Soustelle et al. (2009) which decrease from higher Mg# (~0.92) than the mylonites and NW tectonites (~0.89) analyzed here and by Soustelle et al. (2009) (Fig. 4.13). This possibility of multiphase melt pulses and overprinting of the mylonites by the NW tectonites is only indicated by the present sample set, but the evidence in support is not conclusive. However, for the mixed matrix of all mylonitic and NW tectonitic samples analyzed, a pervasive metasomatism is suggested by interstitial spinel and pyroxene neoblasts, high mixing intensities, highly lobate phase boundaries and irregular grain shape. The low abundance of interstitial pyroxenes in ol-rich matrix suggests that these represent areas little to unaffected by this metasomatism. The presence of amphibole and the geochemical data, although limited to three samples, suggest metasomatism by OH-bearing evolved melt.
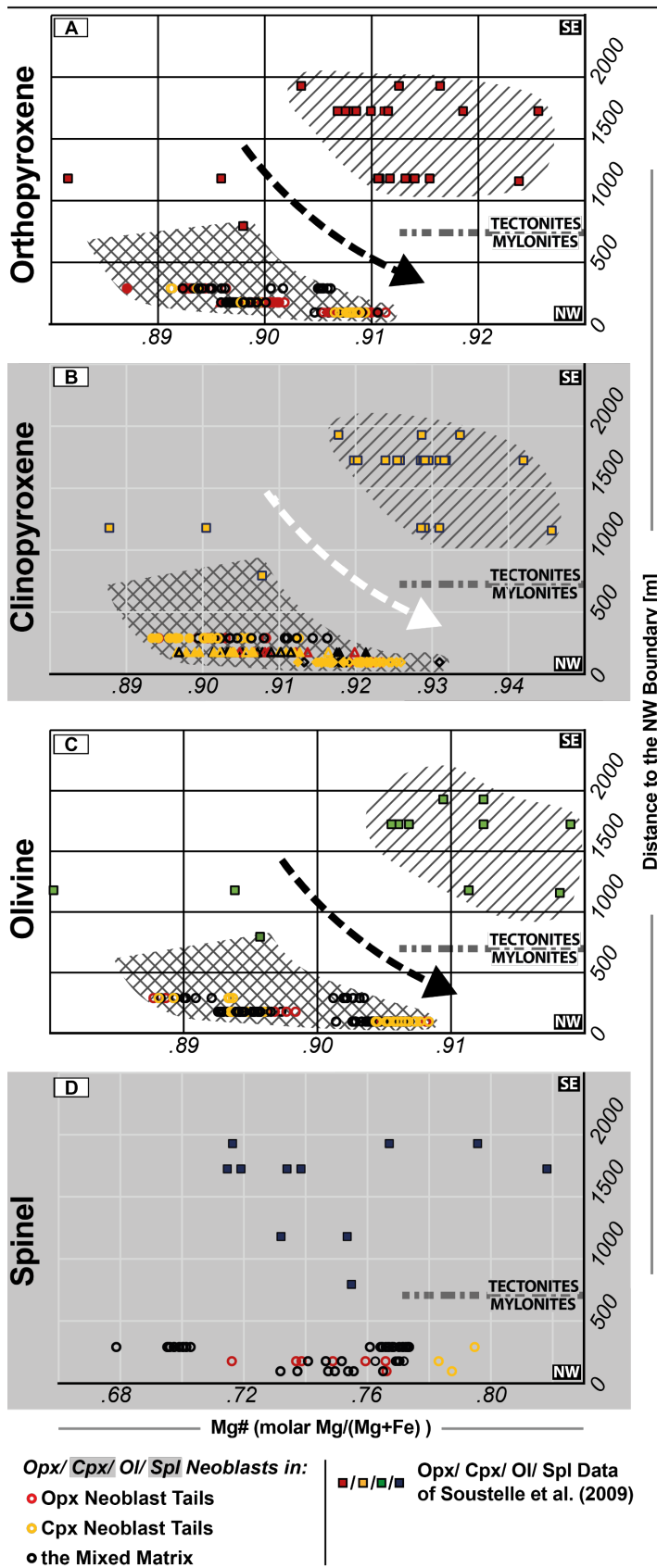
Fig. 4.13. *Mg# data of spinel tectonites (Soustelle et al., 2009) and spl/grt mylonites (this study) vs. distance to the NW-B. The cardinal directions are added by white font on black background. Hatched area: geochemical signature of melt in tectonites; Crosshatched area: geochemical signature of melt in mylonites. Mg# of opx (**A**), cpx (**B**), olivine (**C**) and spl (**D**) plotted against the distance to the NW-B. Location of the studied area by Soustelle et al. (2009) is indicated in Fig. 4.1. Arrows indicate geochemical trend of increasing Mg# towards the NW-B. High resolution, digital version is included on the CD.*

4.6.1.2   On the origin of the pyroxene porphyroclasts and the formation of their neoblast tails

Pyroxene porphyroclasts are present in the entire transect. Especially in the tectonite, cpx porphyroclasts are often associated with pyroxenitic layers, which show a coarse-grained intergrowth of both pyroxenes, olivine, and spinel. Beside their formation by partial crystallization from percolating melts, Garrido and Bodinier (1999) interpreted these websteritic layers to have formed at the expense of garnet-bearing pyroxenites by melt-rock reactions. The kelyphitic structures in pyroxenite layers of mylonites, also described by Van Der Wal and Vissers (1996), corroborate that these assemblages represent at least partially garnet breakdown products. This replacement of garnet-bearing by websteritic assemblages, which was so far associated with the melting/recrystallization front (Garrido and Bodinier, 1999) is present in our samples up to the tectonite-mylonite transition. Straight grain boundaries with 90° angles within the tectonitic pyroxenites suggest that these were partly annealed after having replaced garnet-bearing assemblages.

Boudinage of the pyroxenite layers led to pinch-and-swell structures, which are present already in the SE part of the mylonite zone and described in detail by Précigout et al. (2013). The pyroxene porphyroclast-rich areas and spinel/garnet clusters are interpreted to be the remnants of these pyroxenites. In the same samples (SE mylonites), cpx porphyroclasts form neoblast tails and opx porphyroclasts are bordered by fine-grained patches of neoblasts. From there on, neoblast tails of both pyroxenes form essential microstructural domains in the mylonites. Their characteristics are (1) a polyphase assemblage of cpx, opx, ol, spl and amph with (2) high mixing intensities (av. phase boundary percentages 77 % opx tails, 72 % cpx tails), (3) highly irregular phase boundaries of porphyroclasts and neoblasts and (4) indentations of all neoblast phases into the porphyroclast (Figs. 4.3, 4.8, 4.9). Again, all microstructural characteristics point to a formation by metasomatic reactions. These characteristics remain constant throughout the entire transect suggesting all neoblast tails were formed by the same process from both pyroxene porphyroclasts in all analyzed samples (mylonites/ tectonite).

Amphibole presence and its reaction fabrics suggest, similar to the observations made in the mixed matrix, an OH-bearing metasomatism. Its indentations into the porphyroclasts underline its part of the primary neoblast assemblage. Pargasitic amphibole is stable up to ~3.8 GPa at 1000 °C with its stability strongly depending on the amount of bulk H_2O (Mandler and Grove, 2016). Pargasite-bearing peridotites have been found in peridotite shear zones at similar, syn-kinematic PT conditions to those present in NW Ronda (Garrido et al., 2011; Johanesen et al., 2014: 1.95-2/ 1.5 GPa, 800-900 °C; Hidas et al., 2016; Tholen et al., 2022). The common association of pyroxenes, olivine and amphibole, indentations of amphibole into pyroxene porphyroclasts, also reported by Van der Wal (1993), and the observation that spinel is less abundant in areas with amphibole and vice versa suggest a reaction of pyroxenes, spinel, and amphibole. The replacement of

clinopyroxene and spinel by amphibole in peridotites is commonly attributed to metasomatic reactions (e.g., Blatter and Carmichael, 1998; Bonadiman et al., 2014; Ishimaru et al., 2007). Hydrous melts were observed forming amphibole at the expense of primary orthopyroxene, olivine and clinopyroxene (Rapp et al., 1999; Sen and Dunn, 1995). In their study of xenoliths from Antarctica, Coltorti et al. (2004) suggested a melt-assisted reaction with formation of amphibole at the expense of clinopyroxene and spinel shortly (a few thousand years) before their uplift. Their model implies a two-stage melt-rock evolution with an initial crystallization of pyroxenes, olivine and spinel succeeded by the secondary crystallization of amphibole. However, the composition of associated glass suggests that the metasomizing agent was a Na-alkali silicate melt. For Ronda, the limited geochemical data (3 samples) suggests a Fe-Ti-enriched, OH-bearing melt by constant Na_2O abundances for clinopyroxene clasts and neoblasts and Ti/Fe enrichment for pyroxenes. According to the experimental results of Wang et al. (2021), the composition of the crystallizing amphibole depends on the tectonic setting in addition to the metasomatic melt and peridotite composition. Relatively low Mg# and high Na_2O and TiO_2 abundances of the analyzed amphibole suggest a supra-subduction zone metasomatism (Coltorti et al., 2007). Higher OH abundances in pyroxene neoblast tails are additionally indicated by olivine B-type CPOs, which is often associated with increased concentrations of H/Si (Jung et al., 2006; Jung and Karato, 2001; Mizukami et al., 2004). As no chemical difference is present between neoblast tails and mixed matrix, both microstructural domains are thought to have formed by OH-bearing metasomatism, most likely in the form of a hydrous, evolved melt.

4.6.2 Deformation in the NW Ronda shear zone

4.6.2.1 Differentiation between tectonites and mylonites by deformation-induced microstructures

Although the composition and the microstructures suggest a consistent metasomatic formation of the entire analyzed Ronda shear zone, differences in grain shape and, to a lesser extent, in the grain size between the mylonitic and the tectonitic mixed matrix suggest different deformation conditions and mechanisms of both units. The tectonitic mixed matrix is characterized by small, equiaxial, interstitial grains of both pyroxenes and spinel between coarse pyroxenes and olivine. Neoblast formation in both the tectonitic mixed matrix and around orthopyroxene porphyroclasts at the tectonite-mylonite transition show weak dependence on the foliation. Additionally, tectonitic mixed matrix orthopyroxene neoblasts have a CPO with [001] subperpendicular to the foliation, which is atypical for a deformation-induced CPO (e.g., Jung, 2017) and in most cases strongly connected to the parent clast CPO. Distributed neoblast precipitation, equiaxial neoblast grain shapes and irregular CPO indicate in general weaker deformation and/or a certain degree of post-kinematic annealing in tectonites and

SE mylonites. Nevertheless, strong CPO (A-type CPO, M= 0.2) and lobate grain boundaries indicate deformation of olivine by dislocation creep.

On the other hand, microstructures of the mylonites indicate stronger deformation by (1) film-like pyroxenes orientated along grain boundaries subparallel to the foliation and (2) the increasing abundance of pyroxene neoblast tails elongated in the lineation. Similar film-like microstructures were observed in peridotite mylonites from the Othris shear zone (Dijkstra et al., 2002) and in ultramylonites from the plagioclase-tectonite unit in Ronda (Hidas et al., 2016). For Othris, this microstructure has been associated with the dependence of reaction 4.I on local stress variations (Dijkstra et al., 2002). The "low stress", ol crystallizing variant of reaction 4.I forms highly irregular ol-opx phase boundaries and ol indentations subperpendicular to the foliation. Wedge-shaped pyroxene neoblasts along grain boundaries subparallel to the foliation were interpreted as "high stress" precipitates of reaction 4.I. In NW Ronda, both "low" and "high stress" fabrics are present by film/wedge-shaped pyroxenes in the mixed matrix and at porphyroclast boundaries adjacent to neoblast tails. For fluid-assisted dissolution-precipitation reactions in ultramylonites of Ronda, Hidas et al. (2016) inferred that the fluid composition can be locally controlled by the surrounding minerals, allowing alternating dissolution and precipitation of olivine and orthopyroxene.

Regardless of the type of metasomatic agent, the comparison to the microstructures of Othris and Ronda, in particular the highly lobate phase boundaries and the wedge shaped pyroxenes along the foliation, strongly point to the activity of incongruent, syn-kinematic dissolution-precipitation processes in the mylonitic unit (Hirth & Kohlstedt, 1995). Syn-kinematic diffusion with a stronger effect on smaller grains is additionally indicated by the tendency of mixed matrix pyroxene neoblasts to lower TiO_2 and Cr_2O_3 abundances (Cherniak & Liang, 2012). In addition to grain size sensitive dissolution-precipitation creep, CPOs of olivine and both pyroxenes, increased dislocation densities in neoblasts of the mixed matrix and the elongation of all present grains should result from dislocation creep. The localization of dynamic crystallization processes in olivine neoblasts is corroborated by the highest average M-indices (0.14-0.20) of each microstructural domain, except for cpx in neoblast tails of opx porphyroclasts (M= 0.19), and highest neoblast dislocation densities by GND concentration. Dominant slip systems are (010) in [100] for olivine (A-type, e.g., Karato et al. 2008) and slip on (100) or on (010) with both directed towards [001] for orthopyroxene (Ohuchi et al., 2011; Ross and Nielsen, 1978). In the mylonites, the rheological impact of the olivine-rich matrix is considered to be rather small since it forms competent lenses in the mixed matrix. In the mixed matrix, evidence of both grain size insensitive dislocation creep and grain size sensitive dissolution-precipitation creep corroborate the hypothesis of the activity of a dislocation creep-accommodated grain size sensitive deformation mechanism formerly proposed by Johanesen and Platt (2015) and Précigout et al. (2007). In contrast to dislocation creep

accommodated GBS (DisGBS, Hirth and Kohlstedt, 2003) suggested by Précigout et al. (2007) and Précigout and Hirth (2014), Johanesen and Platt (2015) favor dislocation creep with a grain size sensitivity given by grain boundary migration as dominant recovery mechanism (DRX creep, Platt and Behr, 2011). Because microstructural evidence for both mechanisms is present (GBS: grain and phase boundary alignments; DRX creep: lobate grain boundaries) and DRX creep and DisGBS are dominant under approximately the same conditions of grain size and shear stress (Johanesen and Platt, 2015), neither mechanism can be excluded by this study. However, microstructures of the NW Ronda shear zone indicate the activity of both grain size insensitive dislocation creep and grain size sensitive dissolution-precipitation creep.

4.6.2.2   Timing and effect of metasomatism on deformation

Our data do not permit a firm conclusion about the timing of metasomatism. The dissolution-precipitation creep microstructures which shaped the mylonitic mixed matrix indicate, in accordance with the study of Othris mylonites, that melt was syn-kinematic (Dijkstra et al., 2002). Consistently, Frets et al. (2014) argued for syn- to late-kinematic metasomatism under near-solidus conditions for similar microstructures in the corresponding grt/spl-mylonites of the Beni Bousera peridotite. In addition to enhancing the rate of dissolution-precipitation creep and lubricating grain boundaries for GBS (Hirth & Kohlstedt, 1995), metasomatic melt stimulates grain boundary pinning by crystallized secondary pyroxenes which hinders grain-growth and thereby stabilizes grain size sensitive deformation mechanisms (Linckens et al., 2011). Almost constant neoblast grain sizes in the mylonites indicate a deformation in the melt-affected area at constant stresses. However, microstructures of tectonites, which are interpreted to be formed by the same metasomatism (see section 5.1) indicate weaker deformation. This could be explained either by a pre-kinematic metasomatism or annealing. Evidence for multiphase metasomatism of the tectonite unit brought up by Soustelle et al. (2009) is corroborated by different trends in Mg# of tectonites and mylonites and the final replacement of grt-bearing by websteritic assemblages detected at the tectonite-mylonite transition. Both replacement of grt-bearing pyroxenites and shifting geochemical trends could indicate the tectonite-mylonite transition being an imprint of a later metasomatic front overprinting and annealing mylonitic microstructures under lower stress conditions. As previously discussed in section 5.1.1, additional data of the tectonite-mylonite transition is necessary to address these potential overprinting, annealing relationships of tectonites on mylonites. The controversy of cross-cutting (Van Der Wal and Vissers 1996) versus gradual contact (Précigout et al., 2007; Soustelle et al., 2009) between mylonites and tectonites is most likely part of this context.

4.6.2.3   Strain localization in the northwestern mylonites

A continuous decrease in grain size towards the NW-B (e.g., Obata, 1980; Précigout et al., 2007; Van Der Wal and Vissers, 1996) is not indicated by our data. Neoblast grain sizes of all phases and from all microstructural domains stay constant with minor local excursions over the entire mylonitic shear zone. This observation of constant grain size with regional variations matches the study of Johanesen and Platt (2015) of rather constant grain size of recrystallized olivine (~130 μm) based on optically traced grain boundaries. Accordingly, the average reconstructed olivine grain size of 103 μm for the mixed and 107 μm for the ol-rich matrix lies in the range of average recrystallized olivine grain size reported by Johanesen and Platt (2015) and Frets et al. (2014) for the grt/spl-mylonite unit of both Ronda and Beni Bousera. For the mylonites, the postulated trend of decreasing average grain size with decreasing distance to the NW-B could be explained by the increasing amount of neoblasts and the accompanying increase in the proportion of mixed matrix and neoblast tails.

An increase in strain towards the NW-B is signified by the increase of opx porphyroclast elongation to finally "retort shape" (Johanesen and Platt, 2015). This strain localization is accompanied by the decrease of olivine CPO strength to a minimum of M= 0.09 as formerly reported by Précigout and Hirth (2014). Additionally, the proportion of intact pyroxene porphyroclasts to reacting porphyroclasts decreases towards the NW-B indicating a strain dependence of neoblast tail formation. A positive feedback between deformation and neoblast formation rate was formerly reported by De Ronde and Stünitz (2007) in their experiments for the transition from plagioclase to spinel in olivine+plagioclase aggregates. An enhanced nucleation reaction rate was here explained by increasing deformation-induced defects in the reactant and the deformation-induced transportation of neoblasts away from the reaction interface, which thereby maintains a high chemical potential. For Ronda, a similar mechanism could clear the porphyroclast reaction interface of neoblasts and thereby lead to enhanced neoblast formation and tail elongation. An increasing amount of neoblasts and the stabilization of their small grain size by mixing in turn enhances the share of the grain size sensitive deformation mechanism corroborated by the decrease in CPO strength of olivine. Concomitant with the increase of neoblast tails, the dominant olivine CPO changes within ~150 m distance to the NW-B from an A-type CPO, indicative for low water and intermediate stress conditions, to an AG-type or occasionally a B-type CPO, indicative for increased water content and high stress (e.g., Jung, 2017). The increased presence of olivine B-type CPOs towards the NW-B was formerly interpreted to result from grain boundary sliding (GBS) rather from a change in the dominant slip system (Précigout and Hirth, 2014). However, over the entire mylonitic area, independent of the distance to the NW-B, olivine CPOs from pyroxene neoblast tails are predominantly B- or-AG type (Fig. 4.4). Pyroxene tail microstructures, which include, due to the scanning arrangement, areas of or transitions

to the surrounding matrix, tend to have AG- or A-type olivine CPOs. On the opposite, a stronger B-type is commonly bound to a well-defined neoblast tail without large amounts of the surrounding matrix highlighting the relation between CPO-type and microstructural location. Accordingly, the girdle distributions of olivine's [100] and [001] within the foliation plane present in the AG-type could result from a mix of A- and B-type CPOs. The increased occurrence of amphibole in neoblast tails, especially in association with cpx, documents higher OH abundances. This in turn corroborates the association of B-type CPO to increased concentrations of H/Si (Jung et al., 2006; Jung and Karato, 2001; Mizukami et al., 2004). The correlation of a stronger B-type with increased clinopyroxene abundances observed by Précigout and Hirth (2014), which was at odds with the B-type solely dependent on the increase of GBS towards the NW-B therefore fits with both presented observations: Pronounced presence of amphibole and olivine B-type CPOs in pyroxene neoblast tails and the preferred association of amphibole with clinopyroxene. Accordingly, the decrease of porphyroclasts and the increase in pyroxene neoblast tails towards the NW-B leads to an increase of olivine neoblasts with B-type orientation. However, the formation of olivine B-type CPOs by GBS in the mixed matrix close to the NW-B (< 100 m), suggested by Précigout and Hirth (2014), cannot be ruled out. Although multiphase mixtures crystallized in the metasomatic neoblast tails of pyroxenes, no strain localization as reported for pyroxene reaction tails in other peridotite shear zones occurred in these microstructural domains (Hidas et al., 2013b; Tholen et al., 2022). The main reason for the lack of strain localization might be that all microstructural domains have similar amounts of phase boundaries and similar grain sizes. Therefore, no strain partitioning between the mixed matrix and the tails associated with a switch to a grain size sensitive deformation mechanism was achieved (e.g., Rutter and Brodie, 1988). The strong relation between neoblast and parent porphyroclast orientation implies an inherited orientation of the parent phase neoblasts. The shared orientation of at least one preferred orientation for amphibole and second pyroxene neoblasts with parent phase clast and neoblasts suggests topo- or epitactic growth (Putnis et al., 2006). The increase in finite strain towards the NW-B documented by porphyroclast elongation and neoblast tail formation possibly results from positive feedback between the formation of small, mixed neoblasts and its enhancing and stabilizing effect on grain size sensitive deformation mechanisms (Johanesen and Platt, 2015). Starting with the syn- to early kinematic metasomatic formation of the neoblasts in the mixed matrix and pyroxene porphyroclast tails, the localization of the strain might continue under subsolidus conditions by GBS as suggested by Précigout and Hirth (2014).

4.6.3 Late-stage fluid infiltration

The crosscutting of entire cpx porphyroclasts by amphibole-filled cracks, the replacement of cpx exsolution lamellae by amphibole in opx porphyroclasts (Obata, 1980) and the

formation of amphibole and clinopyroxene-rich veins oblique to the foliation, indicate a late-stage fluid infiltration, which post-dates the melt infiltration and deformation processes discussed above. Since these fabrics are largely restricted to mylonites close to the NW-B, a fluid infiltration originating from the adjacent metasedimentary Jubrique unit seems plausible. Lower Ti abundances for amphibole, clino- and orthopyroxene neoblasts and amphibole Mg#s not comparable (<0.86) to those of other microstructural domains corroborate an independent formation process. Interestingly, the formation of serpentine seems to follow these structures.

4.6.4 Comparison to other upper mantle shear zones and the significance of reactions for localized deformation

Like most studied upper mantle shear zones, the results presented for the Ronda shear zone point to a key-role of reactions in the evolution of upper mantle shear zones (e.g., Dijkstra et al., 2004). A comparison between these studies suggests that the impact of reactions on the evolution of shear zones depends rather on the timing than on the type of reaction:

Tommasi et al. (2017) have shown that hydrous Si-rich melts significantly affect the mechanical strength of the upper mantle and favor a strain localization in the melt-effected region. Additionally, melt-rock reactions in low-strain domains of the Lanzo shear zone document the presence of melt during initial shearing (Kaczmarek and Müntener, 2008). Beside phase mixing by crystallization of pyroxene neoblasts interstitially and at the reacting boundaries of coarser olivine in combination with the activity of a grain size sensitive creep mechanism (Hirth and Kohlstedt, 2003; Platt and Behr, 2011), an additional effect is the reduction of the strength by "wetting" of the phase and grain boundaries (e.g., Hirth and Kohlstedt, 1995). As these effects are solely dependent on the presence of melt, they also are most likely decisive for early localization of strain in the upper mantle.

For syn-kinematic, high stress conditions during the later stages of the shear zone evolution, metasomatic and metamorphic reactions have elsewhere been shown to be important for the formation of ultramylonitic neoblast assemblages either in pyroxene porphyroclast tails or in ultramylonitic bands: In the shear zones of Othris and Erro Tobbio, melt-rock reactions formed ultramylonitic, mixed tails dominated by pyroxene and olivine (Dijkstra et al., 2002; Linckens and Tholen, 2021). Metamorphic reactions in relation to the phase transitions of garnet, spinel and plagioclase triggered reactions at pyroxene porphyroclasts and the formation of ultramylonitic assemblages in shear zones of the Uenzaru peridotite complex, the Turon de Técouère peridotite body and the Lanzo peridotite massif (Furusho and Kanagawa, 1999; Newman et al., 1999; Tholen et al., 2022). Fluid-assisted dissolution-precipitation creep and resulting ultramylonites were reported from shear zones at the transition of plagioclase to granular peridotite unit in

central Ronda (Hidas et al., 2016) and in the Anita Peridotite (Czertowicz et al., 2016). Phase mixing with amphibole and/or chlorite in ultramylonitic assemblages was reported for Erro-Tobbio (Hoogerduijn Strating et al., 1993; Linckens and Tholen, 2021) and the Shaka and Prince Edward transform fault (Kohli and Warren, 2020; Prigent et al., 2020). Diffusion creep and GBS as dominant deformation process in these ultramylonitic assemblages result in a significant reduction in mechanical strength leading to further strain localization in the shear zones if the ultramylonitic areas start to become interconnected (e.g., de Ronde et al., 2005).

Based on the previous research, the observations from NW Ronda can be placed into the following hypothesis: Metasomatic and metamorphic reactions result in reaction softening of the upper mantle by phase mixing and activation of diffusion-driven and grain size sensitive deformation mechanisms, which interacted with dislocation creep. As these reactions are localized, they result in strain localization. The degree of strain localization seems to depend on the timing of the reaction in the course of the shear zone evolution, but not on the nature of the reaction itself. In the case of the NW Ronda shear zone, pre- to early syn-kinematic metasomatism formed the mixed matrix and the neoblast tails over a km-scale area and thereby shaped the early shear zone. High mixing intensities and resulting homogenous grain size in the mylonitic mixed matrix ensured that no further strain localization occurred in porphyroclasts reaction tails. Late stage, syn-kinematic melt/fluid-assisted and/or metamorphic reactions under high stress conditions lead to the formation of mixed ultramylonitic bands, not present in the examined NW Ronda shear zone but described for Othris (Dijkstra et al., 2002), Erro-Tobbio (Linckens and Tholen, 2021), Uenzaru (Furusho and Kanagawa, 1999), Turon de Técouère (Newman et al., 1999) and the coarse granular-peridotite unit of central Ronda (Hidas et al., 2016). In these bands, strain is further localized in the dm- to cm-scale by diffusion creep as dominant deformation mechanism.

4.7   Conclusion

- Metasomatism formed (1) a mixed matrix by crystallization of interstitial pyroxenes and (2) pyroxene porphyroclast neoblast tails by melt-rock reactions in the entire NW Ronda shear zone. Microstructural evidence comprises highly lobate grain boundaries, irregular grain shapes and homogenously dispersed interstitial secondary phases resulting in high mixing intensities. Geochemical analysis and the presence of amphibole indicate a metasomatism by Fe-Ti-enriched, OH-bearing evolved melt, which did not reset the equilibrium temperatures.

- Film/wedge-shaped pyroxenes in the mylonitic mixed matrix point to a pre- to syn-kinematic metasomatism. For the tectonite unit, coarser grain size and

equiaxial grain shapes suggest pre- to early syn-kinematic melt presence and/or annealing, which may be related to multiphase metasomatism. Evidence for the tectonite-mylonite transition as the imprint of a metasomatic front are shifted geochemical trends (Mg#) and the final replacement of garnet-bearing by websteritic assemblages in pyroxenite layers. Due to the limited geochemical data and sample density at the tectonite-mylonite transition further analyses are needed to define the timing of metasomatism and confirm a potential overprint of tectonites on mylonites.

- CPO data and film/wedge-shaped pyroxenes suggest grain size insensitive dislocation creep and grain size sensitive dissolution-precipitation creep as main deformation mechanisms. Grain size sensitive deformation is assisted by the pinning effect operating in the generally strongly mixed assemblages.

- Despite of the nearly constant grain size for the entire mylonite unit a strain gradient towards the NW is documented by increasing elongation of orthopyroxene porphyroclasts. The increase in strain is accompanied by an increase of neoblast abundance and a weakening and change of olivine CPO, both suggesting enhanced grain size sensitive creep.

- Cross-cutting amphibole veins indicate a late-stage fluid infiltration.

- The comparison to other upper mantle shear zones highlights the significance of reactions for localized deformation at different scales. Hypothetically, the degree of strain localization seems to depend more on the timing of the reaction during shear zone evolution than on the type of reaction. Pre- to early syn-kinematic melt infiltration localizes deformation in km-scale melt effected area as present in NW Ronda. Syn kinematic melt/fluid-assisted and/or metamorphic reactions under high stress conditions hypothetically result in the formation of mixed ultramylonitic bands (not present in the investigated NW Ronda shear zone).

Acknowledgments

4.8 References chapter 4

Bachmann, F., Hielscher, R., & Schaeben, H. (2010). Texture analysis with MTEX- Free and open source software toolbox. *Solid State Phenomena*, *160*, 63–68. https://doi.org/10.4028/www.scientific.net/SSP.160.63

Balanyá, J. C., García-Dueñas, V., Azañón, J. M., & Sánchez-Gómez, M. (1997). Alternating contractional and extensional events in the Alpujarride nappes of the Alboran Domain (Betics, Gibraltar Arc). *Tectonics*, *16*(2), 226–238. https://doi.org/10.1029/96TC03871

Barich, A., Acosta-Vigil, A., Garrido, C. J., Cesare, B., Tajčmanová, L., & Bartoli, O. (2014). Microstructures and petrology of melt inclusions in the anatectic sequence of Jubrique (Betic Cordillera, S Spain): Implications for crustal anatexis. *Lithos*, *206–207*(1), 303–320. https://doi.org/10.1016/j.lithos.2014.08.003

Bergmann, R., Chan, R. H., Hielscher, R., Persch, J., & Steidl, G. (2016). Restoration of manifold-valued images by half-quadratic minimization. *Inverse Problems and Imaging*, *10*(2), 281–304. https://doi.org/10.3934/ipi.2016001

Bercovici, D., & Ricard, Y. (2014). Plate tectonics, damage and inheritance. *Nature*, *508*(7497), 513–516. https://doi.org/10.1038/nature13072

Beyer, E. E., Griffin, W. L., & O'Reilly, S. Y. (2006). Transformation of archaean lithospheric mantle by refertilization: Evidence from exposed peridotites in the Western Gneiss Region, Norway. *Journal of Petrology*, *47*(8), 1611–1636. https://doi.org/10.1093/petrology/egl022

Blatter, D. L., & Carmichael, I. S. E. (1998). Plagioclase-free andesites from Zitácuaro (Michoacán), Mexico: Petrology and experimental constraints. *Contributions to Mineralogy and Petrology*, *132*(2), 121–138. https://doi.org/10.1007/s004100050411

Bonadiman, C., Nazzareni, S., Coltorti, M., Comodi, P., Giuli, G., & Faccini, B. (2014). Crystal chemistry of amphiboles: Implications for oxygen fugacity and water activity in lithospheric mantle beneath Victoria Land, Antarctica. *Contributions to Mineralogy and Petrology*, *167*(3), 1–17. https://doi.org/10.1007/s00410-014-0984-8

Booth-Rea, G., Ranero, C. R., Grevemeyer, I., & Martínez-Martínez, J. M. (2007). Crustal types and tertiary tectonic evolution of the Alborán sea, western Mediterranean. *Geochemistry, Geophysics, Geosystems*, *8*(10), 1–25. https://doi.org/10.1029/2007GC001639

Borghini, G. (2008). The spinel- to plagioclase-facies transition in mantle peridotites: Natural and experimental constraints. *Plinius*, *34*(January 2008), 43–45.

Boullier, A. M., & Gueguen, Y. (1975). SP-Mylonites: Origin of some mylonites by superplastic flow. *Contributions to Mineralogy and Petrology*, *50*(2), 93–104. https://doi.org/10.1007/BF00373329

Bunge, H.-J. (1982). Orientation Distributions. In *Texture Analysis in Materials Science*. London: Butterworths. https://doi.org/10.1016/B978-0-408-10642-9.50008-8

Cherniak, D. J., & Liang, Y. (2012). Ti diffusion in natural pyroxene. *Geochimica et Cosmochimica Acta*, *98*, 31–47. https://doi.org/10.1016/j.gca.2012.09.021

Coltorti, M., Beccaluva, L., Bonadiman, C., Faccini, B., Ntaflos, T., & Siena, F. (2004). Amphibole genesis via metasomatic reaction with clinopyroxene in mantle xenoliths from Victoria Land, Antarctica. *Lithos*, *75*(1–2), 115–139. https://doi.org/10.1016/j.lithos.2003.12.021

Coltorti, M., Bonadiman, C., Faccini, B., Grégoire, M., O'Reilly, S. Y., & Powell, W. (2007). Amphiboles from suprasubduction and intraplate lithospheric mantle. *Lithos*, *99*(1–2), 68–84. https://doi.org/10.1016/j.lithos.2007.05.009

Cross, A. J., & Skemer, P. (2017). Ultramylonite generation via phase mixing in high-strain experiments. *Journal of Geophysical Research: Solid Earth*, *122*(3), 1744–1759. https://doi.org/10.1002/2016JB013801

Czertowicz, T. A., Toy, V. G., & Scott, J. M. (2016). Recrystallisation , phase mixing and strain localisation in peridotite during rapid extrusion of sub-arc mantle lithosphere. *Journal of Structural Geology*, *88*, 1–19. https://doi.org/10.1016/j.jsg.2016.04.011

Davies, G. R., Nixon, P. H., Pearson, D. G., & Obata, M. (1993). Tectonic implications of graphitized diamonds from the Ronda peridotite massif, southern Spain. *Geology*, *21*(5), 471–474. https://doi.org/10.1130/0091-7613(1993)021<0471:TIOGDF>2.3.CO;2

Dijkstra, A. H., Drury, M. R., Vissers, R. L. M., & Newman, J. (2002). On the role of melt-rock reaction in mantle shear zone formation in the Othris Peridotite Massif (Greece). *Journal of Structural Geology*, *24*(9), 1431–1450. https://doi.org/10.1016/S0191-8141(01)00142-0

Dijkstra, A. H., Drury, M. R., Vissers, R. L. M., Newman, J., & Van Roermund, H. L. M. (2004). Shear zones in the upper mantle: Evidence from alpine- and ophiolite-type peridotite massifs. *Geological Society Special Publication*, *224*, 11–24. https://doi.org/10.1144/GSL.SP.2004.224.01.02

Drury, M. R., & Urai, J. L. (1989). Deformation-related recrystallization processes. *Tectonophysics, 172*, 235–253. https://doi.org/https://doi.org/10.1016/0040-1951(90)90033-5

Drury, M. R., Vissers, R. L. M., Van der Wal, D., & Hoogerduijn Strating, E. H. (1991). Shear localisation in upper mantle peridotites. *Pure and Applied Geophysics PAGEOPH*, *137*(4), 439–460. https://doi.org/10.1007/BF00879044

Esteban, J. J., Cuevas, J., Tubía, J. M., Sergeev, S., & Larionov, A. (2011). A revised Aquitanian age for the emplacement of the Ronda peridotites (Betic Cordilleras, southern Spain). *Geological Magazine*, *148*(1), 183–187. https://doi.org/10.1017/S0016756810000737

Esteban, José Julián, Sánchez-Rodríguez, L., Seward, D., Cuevas, J., & Tubía, J. M. (2004). The late thermal history of the Ronda area, southern Spain. *Tectonophysics*, *389*(1–2), 81–92. https://doi.org/10.1016/j.tecto.2004.07.050

Esteban, José Julián, Cuevas, J., Vegas, N., & Tubía, J. M. (2008). Deformation and kinematics in a melt-bearing shear zone from the Western Betic Cordilleras (Southern Spain). *Journal of Structural Geology*, *30*(3), 380–393. https://doi.org/10.1016/j.jsg.2007.11.010

Frets, E., Tommasi, A., Garrido, C. J., Padrón-Navarta, J. A., Amri, I., & Targuisti, K. (2012). Deformation processes and rheology of pyroxenites under lithospheric mantle conditions. *Journal of Structural Geology*, *39*(June), 138–157. https://doi.org/10.1016/j.jsg.2012.02.019

Frets, E., Tommasi, A., Garrido, C., Vauchez, A., Mainprice, D., Kamaltarguisti, & Amri, I. (2014). The beni bousera peridotite (rif belt, morocco): An oblique-slip low-angle shear zone thinning the subcontinental mantle lithosphere. *Journal of Petrology*, *55*(2), 283–313. https://doi.org/10.1093/petrology/egt067

Furusho, M., & Kanagawa, K. (1999). Transformation-induced strain localization in a lherzolite mylonite from the Hidaka metamorphic belt of central Hokkaido, Japan. *Tectonophysics*, *313*(4), 411–432. https://doi.org/10.1016/S0040-1951(99)00215-2

Garrido, C. J., & Bodinier, J. L. (1999). Diversity of mafic rocks in the Ronda peridotite: Evidence for pervasive melt-rock reaction during heating of subcontinental lithosphere by upwelling asthenosphere. *Journal of Petrology*, *40*(5), 729–754. https://doi.org/10.1093/petroj/40.5.729

Garrido, C. J., Gueydan, F., Booth-Rea, G., Précigout, J., Hidas, K., Padrón-Navarta, J. A., & Marchesi, C. (2011). Garnet lherzolite and garnet-spinel mylonite in the Ronda peridotite: Vestiges of Oligocene backarc mantle lithospheric extension in the western Mediterranean. *Geology*, *39*(10), 927–930. https://doi.org/10.1130/G31760.1

Hidas, K., Booth-Rea, G., Garrido, C. J., Martínez-Martínez, J. M., Padrón-Navarta, J. A., Konc, Z., et al. (2013). Backarc basin inversion and subcontinental mantle emplacement in the crust: Kilometre-scale folding and shearing at the base of the proto-alborán lithospheric mantle (Betic Cordillera, southern Spain). *Journal of the Geological Society*, *170*(1), 47–55. https://doi.org/10.1144/jgS4.2011-151

Hidas, K., Garrido, C. J., Tommasi, A., Padrón-Navarta, J. A., Thielmann, M., Konc, Z., et al. (2013). Strain localization in pyroxenite by reaction-enhanced softening in the shallow subcontinental lithospheric mantle. *Journal of Petrology*, *54*(10), 1997–2031. https://doi.org/10.1093/petrology/egt039

Hidas, K., Tommasi, A., Garrido, C. J., Padrón-Navarta, J. A., Mainprice, D., Vauchez, A., et al. (2016). Fluid-assisted strain localization in the shallow subcontinental lithospheric mantle. *Lithos*, *262*(October), 636–650. https://doi.org/10.1016/j.lithos.2016.07.038

Hiraga, T., Miyazaki, T., Yoshida, H., & Zimmerman, M. E. (2013). sliding Comparison of microstructures in superplastically deformed synthetic materials and natural mylonites : Mineral aggregation via grain boundary sliding. *Geology (2013) 41 (9), 959–962.* https://doi.org/10.1130/G34407.1

Hirth, G., & Kohlstedt, D. (2003). Rheology of the upper mantle and the mantle wedge: A view from the experimentalists. *Geophysical Monograph Series*, *138*, 83–105. https://doi.org/10.1029/138GM06

Hirth, G., & Kohlstedt, D. L. (1995). Experimental constraints on the dynamics of the partially molten upper mantle: deformation in the diffusion creep regime. *Journal of Geophysical Research*, *100*(B2), 1981–2001. https://doi.org/10.1029/94JB02128

Hoogerduijn Strating, E. H., Rampone, E., Piccardo, G. B., Drury, M. R., & Vissers, R. L. M. (1993). Subsolidus emplacement of mantle peridotites during incipient oceanic rifting and opening of the mesozoic tethys (voltri massif, NW Italy). *Journal of Petrology*, *34*(5), 901–927. https://doi.org/10.1093/petrology/34.5.901

Hu, W. J., Zhong, H., Chu, Z. Y., Zhu, W. G., Bai, Z. J., & Zhang, C. (2020). Ancient Refertilization Process Preserved in the Plagioclase Peridotites: An Example From the Shuanggou Ophiolite, Southwest China. *Journal of Geophysical Research: Solid Earth*, *125*(1), 1–21. https://doi.org/10.1029/2019JB017552

Ishimaru, S., Arai, S., Ishida, Y., Shirasaka, M., & Okrugin, V. M. (2007). Melting and multi-stage metasomatism in the mantle wedge beneath a frontal arc inferred from highly depleted peridotite xenoliths from the avacha volcano, Southern Kamchatka. *Journal of Petrology*, *48*(2), 395–433. https://doi.org/10.1093/petrology/egl065

Johanesen, K., Platt, J. P., Kaplan, M. S., & Ianno, A. J. (2014). A revised thermal history of the Ronda peridotite, S. Spain: New evidence for excision during exhumation. *Earth and Planetary Science Letters*, *393*, 187–199. https://doi.org/10.1016/j.epsl.2014.01.024

Johanesen, K. E., & Platt, J. P. (2015). Rheology, microstructure, and fabric in a large scale mantle shear zone, Ronda Peridotite, southern Spain. *Journal of Structural Geology*, *73*, 1–17. https://doi.org/10.1016/j.jsg.2015.01.007

Jung, H., & Karato, S. I. (2001). Water-induced fabric transitions in olivine. *Science*, *293*(5534), 1460–1463. https://doi.org/10.1126/science.1062235

Jung, Haemyeong. (2017). Crystal preferred orientations of olivine, orthopyroxene, serpentine, chlorite, and amphibole, and implications for seismic anisotropy in subduction zones: a review. *Geosciences Journal*, *21*(6), 985–1011. https://doi.org/10.1007/S4.12303-017-0045-1

Jung, Haemyeong, Katayama, I., Jiang, Z., Hiraga, T., & Karato, S. (2006). Effect of water and stress on the lattice-preferred orientation of olivine. *Tectonophysics*, *421*(1–2), 1–22. https://doi.org/10.1016/j.tecto.2006.02.011

Kaczmarek, M. A., & Müntener, O. (2008). Juxtaposition of melt impregnation and high-temperature shear zones in the upper mantle; field and petrological constraints from the lanzo peridotite (Northern Italy). *Journal of Petrology*, *49*(12), 2187–2220. https://doi.org/10.1093/petrology/egn065

Karato, S., Jung, H., Katayama, I., & Skemer, P. (2008). Geodynamic Significance of Seismic Anisotropy of the Upper Mantle: New Insights from Laboratory Studies. *Annual Review of Earth and Planetary Sciences*, *36*(1), 59–95. https://doi.org/10.1146/annurev.earth.36.031207.124120

Kelemen, P. B., & Hirth, G. (2007). A periodic shear-heating mechanism for intermediate-depth earthquakes in the mantle. *Nature*, *446*(7137), 787–790. https://doi.org/10.1038/nature05717

Kilian, R., Bestmann, M., & Heilbronner, R. (2016). Absolute orientations from EBSD measurements - as easy as it seems ? *Geophysical Research Abstracts*, *18*, 8221.

Kohli, A. H., & Warren, J. M. (2020). Evidence for a Deep Hydrologic Cycle on Oceanic Transform Faults. *Journal of Geophysical Research: Solid Earth*, *125*(2), 1–23. https://doi.org/10.1029/2019JB017751

Lenoir, X., Garrido, C. J., Bodinier, J. L., Dautria, J. M., & Gervilla, F. (2001). The recrystallization front of the Ronda periodite: Evidence for melting and thermal erosion of subcontinental lithospheric mantle beneath the Alboran basin. *Journal of Petrology*, *42*(1), 141–158. https://doi.org/10.1093/petrology/42.1.141

Linckens, J., & Tholen, S. (2021). Formation of ultramylonites in an upper mantle shear zone, erro-tobbio, italy. *Minerals*, *11*(10). https://doi.org/10.3390/min11101036

Linckens, J., Herwegh, M., Mntener, O., & Mercolli, I. (2011). Evolution of a polymineralic mantle shear zone and the role of second phases in the localization of deformation. *Journal of Geophysical Research: Solid Earth*, *116*(6), 1–21. https://doi.org/10.1029/2010JB008119

Linckens, J., Herwegh, M., & Müntener, O. (2015). Small quantity but large effect - How minor phases control strain localization in upper mantle shear zones. *Tectonophysics*, *643*, 26–43. https://doi.org/10.1016/j.tecto.2014.12.008

Lonergan, L. (1993). Timing and kinematics of deformation in the Malaguide Complex, internal zone of the Betic Cordillera, southeast Spain. *Tectonics*, *12*(2), 460–476. https://doi.org/10.1029/92TC02507

Mameri, L., Tommasi, A., Signorelli, J., & Hansen, L. N. (2019). Predicting viscoplastic anisotropy in the upper mantle: a comparison between experiments and polycrystal plasticity models. *Physics of the Earth and Planetary Interiors*, *286*(October 2018), 69–80. https://doi.org/10.1016/j.pepi.2018.11.002

Mandler, B. E., & Grove, T. L. (2016). Controls on the stability and composition of amphibole in the Earth's mantle. *Contributions to Mineralogy and Petrology*, *171*(8–9), 1–20. https://doi.org/10.1007/s00410-016-1281-5

Mizukami, T., Wallis, S. R., & Yamamoto, J. (2004). Natural examples of olivine lattice preferred orientation patterns with a flow-normal a-axis maximum. *Nature*, *427*(6973), 432–436. https://doi.org/10.1038/nature02179

Müntener, O., & Piccardo, G. B. (2003). Melt migration in ophiolitic peridotites: The message from Alpine-Apennine peridotites and implications for embryonic ocean basins. *Geological Society Special Publication*, *218*(Anonymous 1972), 69–89. https://doi.org/10.1144/GSL.SP.2003.218.01.05

Newman, J., Lamb, W. M., Drury, M. R., & Vissers, R. L. M. (1999). Deformation processes in a peridotite shear zone: Reaction-softening by an H2O-deficient, continuous net transfer reaction. *Tectonophysics*, *303*(1–4), 193–222. https://doi.org/10.1016/S0040-1951(98)00259-5

Obata, M. (1980). The ronda peridotite: Garnet-, spinel-, and plagioclase-lherzolite facies and the P-T trajectories of a high-temprature mantle intrusion. *Journal of Petrology*, *21*(3), 533–572. https://doi.org/10.1093/petrology/21.3.533

Ohuchi, T., Karato, S., & Fujino, K. (2011). Strength of single-crystal orthopyroxene under lithospheric conditions. *Contributions to Mineralogy and Petrology*, *161*(6), 961–975. https://doi.org/10.1007/s00410-010-0574-3

Pantleon, W. (2008). Resolving the geometrically necessary dislocation content by conventional electron backscattering diffraction. *Scripta Materialia*, *58*(11), 994–997. https://doi.org/10.1016/j.scriptamat.2008.01.050

Passchier, C. W., & Trouw, R. A. J. (1996). *Microtectonics*. Springer, Berlin, Heidelberg: Springer-Verlag Berlin Heidelberg. https://doi.org/10.1007/3-540-29359-0

Platt, J. P., & Behr, W. M. (2011). Grainsize evolution in ductile shear zones: Implications for strain localization and the strength of the lithosphere. *Journal of Structural Geology*, *33*(4), 537–550. https://doi.org/10.1016/j.jsg.2011.01.018

Platt, J. P., Argles, T. W., Carter, A., Kelley, S. P., Whitehouse, M. J., & Lonergan, L. (2003). Exhumation of the Ronda peridotite and its crustal envelope: Constraints from thermal modelling of a P-T-time array. *Journal of the Geological Society*, *160*(5), 655–676. https://doi.org/10.1144/0016-764902-108

Platt, J. P., Kelley, S. P., Carter, A., & Orozco, M. (2005). Timing of tectonic events in the Alpujárride Complex, Betic Cordillera, southern Spain. *Journal of the Geological Society*, *162*(3), 451–462. https://doi.org/10.1144/0016-764903-039

Platt, J. P., Anczkiewicz, R., Soto, J. I., Kelley, S. P., & Thirlwall, M. (2006). Early Miocene continental subduction and rapid exhumation in the western Mediterranean. *Geology*, *34*(11), 981–984. https://doi.org/10.1130/G22801A.1

Précigout, J., & Hirth, G. (2014). B-type olivine fabric induced by grain boundary sliding. *Earth and Planetary Science Letters*, *395*, 231–240. https://doi.org/10.1016/j.epsl.2014.03.052

Précigout, J., & Stünitz, H. (2016). Evidence of phase nucleation during olivine diffusion creep : A new perspective for mantle strain localisation, *455*, 94–105. https://doi.org/10.1016/j.epsl.2016.09.029

Précigout, J., Gueydan, F., Gapais, D., Garrido, C. J., & Essaifi, A. (2007). Strain localisation in the subcontinental mantle - a ductile alternative to the brittle mantle. *Tectonophysics*, *445*(3–4), 318–336. https://doi.org/10.1016/j.tecto.2007.09.002

Précigout, J., Gueydan, F., Garrido, C. J., Cogné, N., & Booth-Rea, G. (2013). Deformation and exhumation of the Ronda peridotite (Spain). *Tectonics*, *32*(4), 1011–1025. https://doi.org/10.1002/tect.20062

Prigent, C., Warren, J. M., Kohli, A. H., & Teyssier, C. (2020). Fracture-mediated deep seawater flow and mantle hydration on oceanic transform faults. *Earth and Planetary Science Letters*, *532*, 115988. https://doi.org/10.1016/j.epsl.2019.115988

Puga, E., Nieto, J. M., Díaz De Federico, A., Bodinier, J. L., & Morten, L. (1999). Petrology and metamorphic evolution of ultramafic rocks and dolerite dykes of the Betic Ophiolitic Association (Mulhacen Complex, SE Spain): Evidence of eo-Alpine subduction following an ocean-floor metasomatic process. *Lithos*, *49*(1–4), 23–56. https://doi.org/10.1016/S0024-4937(99)00035-3

Putnis, A., Niedermeier, D. R. D., & Putnis, C. V. (2006). From epitaxy to topotaxy: The migration of reaction interfaces through crystals. *Geochimica et Cosmochimica Acta*, *70*(18), A509. https://doi.org/10.1016/j.gca.2006.06.1479

Rapp, R. P., Shimizu, N., Norman, M. D., & Applegate, G. S. (1999). Reaction between slab-derived melts and peridotite in the mantle wedge: Experimental constraints at 3.8 GPa. *Chemical Geology*, *160*(4), 335–356. https://doi.org/10.1016/S0009-2541(99)00106-0

de Ronde, A. A., & Stünitz, H. (2007). Deformation-enhanced reaction in experimentally deformed plagioclase-olivine aggregates. *Contributions to Mineralogy and Petrology*, *153*(6), 699–717. https://doi.org/10.1007/s00410-006-0171-7

de Ronde, A. A., Stünitz, H., Tullis, J., & Heilbronner, R. (2005). Reaction-induced weakening of plagioclase-olivine composites. *Tectonophysics*, *409*(1–4), 85–106. https://doi.org/10.1016/j.tecto.2005.08.008

Ross, J. V., & Nielsen, K. C. (1978). High-temperature flow of wet polycrystalline enstatite. *Tectonophysics*, *44*, 233–261. https://doi.org/10.1016/0040-1951(78)90072-0

Rossetti, F., Faccenna, C., & Crespo-Blanc, A. (2005). Structural and kinematic constraints to the exhumation of the Alpujarride Complex (Central Betic Cordillera, Spain). *Journal of Structural Geology*, *27*(2), 199–216. https://doi.org/10.1016/j.jsg.2004.10.008

Le Roux, V., Bodinier, J. L., Tommasi, A., Alard, O., Dautria, J. M., Vauchez, A., & Riches, A. J. V. (2007). The Lherz spinel lherzolite: Refertilized rather than pristine mantle. *Earth and Planetary Science Letters*, *259*(3–4), 599–612. https://doi.org/10.1016/j.epsl.2007.05.026

Rutter, E. H., & Brodie, K. H. (1988). The role of tectonic grain size reduction in the rheological stratification of the lithosphere. *Geologische Rundschau*, *77*(1), 295–307. https://doi.org/10.1007/BF01848691

Sen, C., & Dunn, T. (1995). Experimental modal metasomatism of a spinel lherzolite and the production of amphibole-bearing peridotite. *Contributions to Mineralogy and Petrology*, *119*(4), 422–432. https://doi.org/10.1007/BF00286939

Skemer, P., Katayama, I., Jiang, Z., & Karato, S. (2005). The misorientation index: Development of a new method for calculating the strength of lattice-preferred orientation. *Tectonophysics*, *411*(1–4), 157–167. https://doi.org/10.1016/j.tecto.2005.08.023

Soustelle, V., Tommasi, A., Bodinier, J. L., Garrido, C. J., & Vauchez, A. (2009). Deformation and reactive

melt transport in the mantle lithosphere above a large-scale partial melting domain: The Ronda peridotite Massif, Southern Spain. *Journal of Petrology*, *50*(7), 1235–1266. https://doi.org/10.1093/petrology/egp032

Stuart, C. A., Piazolo, S., & Daczko, N. R. (2018). The recognition of former melt flux through high-strain zones, (May 2017). https://doi.org/10.1111/jmg.12427

Suades, E., & Crespo-blanc, A. (2011). Onshore study of syn-orogenic olistostromic deposits in the Gibraltar Arc : a tool to reveal mountain front uplift. Presentation during *EGU 2011*.

Suhr, G. (1993). Evaluation of upper mantle microstructures in the Table Mountain massif (Bay of Islands ophiolite). *Journal of Structural Geology*, *15*(11), 1273–1292. https://doi.org/10.1016/0191-8141(93)90102-G

Tholen, S., Linckens, J., Heckel, C., & Kemperle, M. (2022). Reaction-induced phase mixing and the formation of ultramylonitic bands. *Tectonophysics*, *827*(December 2021). https://doi.org/10.1016/j.tecto.2022.229230

Tommasi, A., & Vauchez, A. (2015). Heterogeneity and anisotropy in the lithospheric mantle. *Tectonophysics*, *661*, 11–37. https://doi.org/10.1016/j.tecto.2015.07.026

Tommasi, A., Langone, A., Padrón-Navarta, J. A., Zanetti, A., & Vauchez, A. (2017). Hydrous melts weaken the mantle, crystallization of pargasite and phlogopite does not: Insights from a petrostructural study of the Finero peridotites, southern Alps. *Earth and Planetary Science Letters*, *477*, 59–72. https://doi.org/10.1016/j.epsl.2017.08.015

Vauchez, A., & Garrido, C. J. (2001). Seismic properties of an asthenospherized lithospheric mantle: Constraints from lattice preferred orientations in peridotite from the Ronda massif. *Earth and Planetary Science Letters*, *192*(2), 235–249. https://doi.org/10.1016/S0012-821X(01)00448-4

Van der Wal, D. (1993). Deformation process in mantle peridotites with emphasis on the Ronda peridotite of SW Spain. *Geologica Ultraiectina* (Vol. 102).

Van Der Wal, D., & Bodinier, J.-L. (1996). Origin of the recrystallisation front in the Ronda peridotite by km-scale pervasive porous melt flow. *Contributions to Mineralogy and Petrology*, *122*(4), 387–405. https://doi.org/10.1007/s004100050135

Van Der Wal, D., & Jean-Louis, B. (1996). Origin of the recrystallisation front in the Ronda peridotite by km-scale pervasive porous melt flow. *Contributions to Mineralogy and Petrology*, *122*(4), 387–405. https://doi.org/10.1007/s004100050135

Van Der Wal, D., & Vissers, R. L. M. (1993). Uplift and emplacement of upper mantle rocks in the western Mediterranean. *Geology*. https://doi.org/10.1130/0091-7613(1993)021<1119:UAEOUM>2.3.CO;2

Van Der Wal, D., & Vissers, R. L. M. (1996). Structural petrology of the Ronda peridotite, SW Spain: Deformation history. *Journal of Petrology*, *37*(1), 23–43. https://doi.org/10.1093/petrology/37.1.23

Wang, C., Liang, Y., & Xu, W. (2021). Formation of Amphibole-Bearing Peridotite and Amphibole-Bearing Pyroxenite Through Hydrous Melt-Peridotite Reaction and In Situ Crystallization: An Experimental Study. *Journal of Geophysical Research: Solid Earth*, *126*(3). https://doi.org/10.1029/2020JB019382

White, S. H., Burrows, S. E., Carreras, J., Shaw, N. D., & Humphreys, F. J. (1980). On mylonites in ductile shear zones. *Journal of Structural Geology*, *2*(1–2), 175–187. https://doi.org/10.1016/0191-8141(80)90048-6

5 Summary and outlook

With this microstructural and geochemical study of the shear zones cutting through the peridotites of Lanzo, Erro-Tobbio and Ronda, we quantified and localized phase mixing in diverse upper mantle deformational settings and identified its driving forces. Thereby, a comparative framework is established, which emphasizes the importance of reactions for shear localization in the upper mantle from initial strain localization via the formation of large-scale shear zones to highly localized deformation at late stages of the shear zone evolution. As conclusion, the three research areas are comparatively reviewed, which leads to the major implications of this project and its scientific outlook.

Early stages of the Lanzo shear zone evolution are characterized by melt-induced phase mixing and a km-scale deformation (Kaczmarek & Müntener, 2008). At this stage, mixing is ascribed to melt-rock reactions and interstitial pyroxene crystallization. Subsequently, strain was progressively localized towards the deformational center, where ultramylonitic bands were formed during the final stages of ductile deformation. The ultramylonitic, thoroughly mixed phase assemblages forming those bands have their origin at the boundaries of reacting pyroxene porphyroclasts. Here, neoblasts are formed at the expense of porphyroclasts by continuous net-transfer reactions triggered by the spinel-lherzolite to plagioclase-lherzolite transition. Due to their small grain size (equivalent circular diameter - ECD: 10-20 μm), the dominant deformation mechanism is expected to have been diffusion creep whose activity localizes the deformation in ultramylonitic bands. The mixed phase assemblage counteracts grain growth and therefore ensures the maintenance of strain localization in these bands. In the shear zone of the Erro-Tobbio peridotite, neoblast tails of clinopyroxene porphyroclasts, with limited amount of phase mixing, indicate that initial deformation in the shear zone was accommodated by dynamic recrystallization. Accordingly, the deformation was largely accommodated by dislocation creep, which is thought to be the dominant deformation mechanism of the upper mantle if strain is not localized (Tommasi & Vauchez, 2015). Syn-deformational intrusion of melts triggered the next step of strain localization in the shear zone's evolution. By reactions of Si-undersaturated melt with pyroxene porphyroclasts, ultramylonitic phase mixtures were formed in their neoblast tails. Weak to absent CPOs and a small grain size in the ultramylonitic assemblages suggest diffusion creep as dominant deformation mechanism. As the latter works at low differential stress, the strain rate will increase resulting in strain localization. The shear zone cutting through the peridotite of northwestern Ronda records potentially multiple melt-impulses

originating from below a structurally deeper "melting front" within the Ronda peridotite complex (Soustelle et al., 2009). Strain localization is thought to be controlled by a km-scale melt infiltration of the entire today's area of deformed peridotites in northwestern Ronda. Microstructurally, the OH-bearing melt with locally variant Si-compositions led to the crystallization of interstitial pyroxenes and melt-rock reactions. Si-undersaturated melt formed thoroughly mixed neoblast tails at the expense of pyroxene porphyroclasts. Si-saturated melt formed the mixed matrix by crystallization of interstitial pyroxenes on olivine grain boundaries. Melt-enhanced deformation and the dominance of a dislocation-creep accommodated but grain size sensitive deformation mechanism localized the deformation in the melt-affected area (for an evaluation of the potential deformation mechanisms see chapter 4 and Précigout et al., 2007, 2014; Johanesen and Platt, 2015).

When comparing the new data and results obtained from the three research areas, it becomes obvious that major phase-mixing during the evolution of upper mantle shear zones is decisively dependent on reactions and/or metasomatism. Microstructurally, intensive mixed phase assemblages are either present in neoblast tails of reacting pyroxene porphyroclasts or as mixed matrix formed by interstitial crystallization from a melt or fluid. Phase compositions in neoblast tails are variable, depending on the reaction type and the parent porphyroclast. Nevertheless, common microstructural characteristics like neoblast indentations into parent clasts, highly lobate porphyroclast and neoblast boundaries and the largely absence of subgrains in the porphyroclasts corroborate the reaction-induced formation of those tails. As these highly mixed assemblages are already present at parent clast grain boundaries, mechanical mixing by grain boundary sliding and neighbor switching or dissolution and precipitation in creep cavitations could be excluded as formational process. Although the nature of the reactions is variable (metamorphic, melt/fluid-controlled), phase mixing intensities in neoblast tails of reacting porphyroclasts of all three shear zones are comparably high (av. 65-77 % phase boundary percentage). Consequently, for reaction tails of porphyroclasts, the reaction type seems to be of minor importance for the formation of phase mixtures and its intensity. In the shear zone of the Ronda peridotite, the crystallization of interstitial pyroxenes by a highly evolved, OH-bearing melt and its melt-rock reactions with coarse grained olivines led to the formation of a mixed matrix with similar mixing intensities (av. 71 %) like in the reaction tails of pyroxene porphyroclasts described above. In contrast to the localized phase mixing on micro-scale in pyroxene porphyroclast reaction tails and the resultant

ultramylonitic bands, the phase mixing by crystallization and melt-rock reactions is here of regional-scale (~ 2 km thickness). For all analyzed shear zones, reaction-induced phase mixing, whether by the formation of pyroxene reactions tails or by the precipitation of interstitial grains, significantly increases the mixing intensity. In addition to its insensitivity to the reaction type, the effective timing of the reaction with respect to the shear zone evolution seems to have equally little influence on the mixing intensity: Melt precipitates and melt-rock reactions at pyroxene porphyroclasts during large-scale, pre- to syn-deformational stages of the Ronda shear zone led to similar phase mixing intensities like reactions at pyroxene porphyroclasts during late-stage, highly localized shearing in Lanzo's ultramylonitic bands. Although the mixing intensity seems to be independent on the timing of the reactions with respect to the shear zone evolution, this timing seems to be decisive for the type and the intensity of the strain localization. Evidence for large-scale phase mixing (~km) was only observed by melt-driven crystallization of interstitial pyroxenes in previously olivine-dominated areas (Ronda, Lanzo). Both enhanced deformation by melt-wetted grain boundaries and the reduction of grain size by second phase pinning plus the subsequent activation of a grain size sensitive deformation mechanism potentially drive the strain localization in the km-scale, melt-effected areas. Strong CPOs, a grain size between 50 and 200 μm, and alignments of straight grain boundary corroborate that at this particular stage and scale of strain localization, both dislocation creep and grain size sensitive creep mechanisms are active. Potential prevailing, grain size-sensitive deformation mechanisms are grain boundary sliding accompanied by dislocation creep (DisGBS, e.g., Hirth and Kohlstedt (2003)) or dislocation creep accommodated grain-boundary migration (DRX creep, e.g., Platt and Behr (2011)). As these strain localizing processes are independent from additional initiating processes or heterogeneities, melt percolation is potentially one major driving force for initial strain localization and the formation of shear zones in the upper mantle. The impact of highly localized phase mixing in porphyroclast reaction tails on strain localization seems to be strongly dependent on the timing of the reaction. In the Ronda shear zone, reaction tails of both pyroxenes with similar mixing intensities like those in porphyroclast tails in the shear zones of Lanzo and Erro-Tobbio do not localize deformation. Strong CPOs and similar grain sizes and mixing intensities compared to the surrounding mixed matrix either suggest the activity of equal deformation mechanisms in both microstructural domains. In contrast, the ultramylonitic grain size of pyroxene reaction tails of the shear zones of Lanzo and Erro-Tobbio and their transitions into

ultramylonitic bands, which are strongly delimited from bordering mylonitic areas or lenses, indicate an intense localization of deformation. Ultramylonitic grain sizes of tail and band neoblasts and their weak to absent CPOs corroborate the dominance of diffusion creep, which in turn accounts for higher strain rates and thus for the localization of deformation. The limitation of ultramylonites to the center of shear zones and their association with highly stretched orthopyroxene single crystals corroborate a formation of these reaction tails under high-stress conditions at an elevated stage of the shear zone evolution.

To summarize, reactions, including melt precipitation, have been identified as major driving force for phase mixing in upper mantle shear zones. Different reaction types (melt, fluid, metamorphic) form phase assemblages of similar mixing intensities. The timing of the reaction with respect to the shear zone evolution seems to be decisive for the mode and extent of strain localization. Pre- to early syn-kinematic melt percolation favors large-scale strain localization by dislocation creep accommodated grain size sensitive deformation mechanisms and melt-enhanced deformation. Reactions at pyroxene porphyroclasts at late stages of the shear zone evolution result in ultramylonitic phase assemblages in which diffusion creep localizes the strain in cm-scale ultramylonitic bands.

Having outlined the interplay of phase mixing and strain localization in the evolution of the upper mantle shear zones of Lanzo, Erro-Tobbio and Ronda, several follow-up questions shape the scientific outlook of this project. The localization of strain in microstructural domains is strongly dependent on a smaller grain size and its stability in the areas of localization. Following the piezometric relationship (introduction, Eqn. 1.3) and its adjustment to the second phases (introduction, Eqn. 1.4/1.5), grain sizes evolve depending on differential stress, strain rate, second phase fraction and its distribution. However, even though neoblasts in pyroxene reaction tails are formed by reactions and not by dynamic crystallization, their grain size seems to strongly depend on the deformational framework: High-strain domains have ultramylonitic, whereas moderately strained samples show mylonitic neoblasts. The impact of stress, strain, and the associated internal deformation of pyroxene porphyroclasts on the formation of reaction tails and in particular their neoblast grain size is, as it controls the dominant deformation mechanism within those assemblages, of major importance for potential strain localization. The database compiled by this project provides an excellent framework to approach this question from a microstructural point of view. However, to explore the dependence of

stress on neoblast grain size in reaction tails additional piezometric analysis on the presented samples is necessary. Deformation experiments with the focus on reactions at pyroxenes porphyroclasts covering multiple stress conditions could in this regard crosscheck the microstructural implications of piezometric derived stress conditions. Furthermore, a comparative study with reaction-free but highly strained peridotites, as present in multiple xenoliths (e.g. Kimberley, South Africa (Tholen et al., 2022)), is planned to evaluate phase mixing in reaction-free environments with dominant dynamic crystallization. In combination with the reaction-driven phase mixing studied in Lanzo, Erro-Tobbio and Ronda, this study aims for a comprehensive overview of deformational regimes present in the upper mantle. Hereby, the role of reactions for phase mixing drawn from this thesis could be consolidated and extended to additional deformational settings. As the results of the present study outline the importance of reactions for strain localization in the upper mantle based on a microstructural perspective, its integration into the larger context of geodynamics and plate tectonics remains to be accomplished. Fundamentally in this regard are the introduction of a rheological model for mixed assemblages and the implementation of deformational regimes and reaction-controlled rheology in numerical models. The demanding task in creating a dynamic model of the upper mantle is therefore to integrate and connect metasomatism, metamorphism and deformation, which, as shown, are the cornerstones of strain localization.

6   Zusammenfassung und Ausblick

Die vorliegende mikrogefügekundliche und geochemische Studie befasst sich mit der Lokalisierung und Quantifizierung von Phasenmischung in Scherzonen des oberen Erdmantels unter unterschiedlichen Deformationsbedingungen. Das so geschaffene Rahmenwerk und die in dieses eingeordneten Studien weiterer Scherzonen unterstreichen die herausragende Bedeutung von Mineralreaktionen, mit oder ohne Beteiligung von Fluiden und/oder Schmelzen, für die Lokalisierung von Deformation im oberen Erdmantel. Von der initialen Lokalisierung der Deformation über die Bildung km-mächtigen Scherzonen bis hin zur Konzentration der Deformation in cm-schmalen Ultramyloniten bestimmen Reaktionen die Phasenmischung. Zum Abschluss dieser Arbeit sollen die drei Studien vergleichend rekapituliert werden, um mit den Hauptschlussfolgerungen und einem kurzen wissenschaftlichen Ausblick abzuschließen.

Das initiale Stadium der Lanzo-Scherzone ist durch schmelzinduzierte Phasenmischung und km-breite Deformation gekennzeichnet (Kaczmarek und Müntener, 2008). Die in diesem Stadium entstehenden Protomylonite haben durch Schmelz-Gesteins-Reaktionen und interstitiell kristallisierte Pyroxene eine gemischte Phasenzusammensetzung. In der folgenden Scherzonenentwicklung lokalisiert sich die Deformation in Myloniten und zuletzt in Ultramyloniten. Die Grenze zwischen mylonitischen und ultramylonitischen Mikrostrukturen ist scharf. Der Ursprung der stark durchmischten Ultramylonite liegt in Druckschatten von Pyroxen-Porphyroklasten wo sich feinkörnige Neoblasten bilden (Äquivalentdurchmesser (*ECD*): 10-20 μm). Die Komponenten der Neoblasten sowie die geochemische Zusammensetzung von Porphyroklasten und Neoblasten deuten auf eine Bildung durch kontinuierliche Reaktionen hin, welche durch den Übergang von Spinell- zu Plagioklas-Lherzolithen ausgelöst wurden. Aufgrund der geringen Korngröße ist der dominierende Deformationsmechanismus der Ultramylonite das Diffusionskriechen. Die hierdurch reduzierte mechanische Spannung bei konstanter Strainrate lokalisiert die Deformation in den miteinander verbundenen Ultramylonit-Bändern. Die Phasenmischung wirkt hierbei dem Kornwachstum durch *Zener-Pinning* entgegen und gewährleistet so die Aufrechterhaltung von Diffusionskriechen und Deformationslokalisierung.

In der nordwestlichen Scherzone des Erro-Tobbio Peridotitmassivs deutet die schwach durchmischte, klinopyroxenreiche Zusammensetzung von Neoblasten in Druckschatten von Klinopyroxen-Porphyroklasten auf dynamische Rekristallisation hin. Der dabei

dominierende Deformationsmechanismus des Versetzungskriechens ist auch in der Erro-Tobbio Scherzone symptomatisch für Bedingungen von nicht lokalisierter, großskaliger Deformation im oberen Erdmantel (z.B. Tommasi und Vauchez, 2015). Die Lokalisierung der Deformation in Scherzonen geht mit Schmelzintrusion in die sich deformierenden Peridotite einher: Reaktionen von Si-untersättigter Schmelze mit Pyroxen-Porphyroklasten bilden stark durchmischte, ultramylonitische Neoblast-Zusammensetzungen in deren Druckschatten. Schwache bis fehlende CPOs und kleine Korngrößen (*ECD*: 5-12 µm) deuten auf Diffusionskriechen als dominanten Deformationsmechanismus hin. Wie auch in der Scherzone von Lanzo führt Diffusionskriechen zur Lokalisierung der Deformation in den Ultramyloniten.

Auch die Scherzone des nordwestlichen Ronda-Peridotitmassivs weist Spuren von möglicherweise multiplen Schmelzintrusionen auf (Soustelle et al., 2009). Der Ursprung der Schmelze ist unterhalb einer strukturell tieferliegenden Schmelzfront zu verorten. Lokale Variationen in der Zusammensetzung der OH-reichen, differenzierten Schmelze führten sowohl zur Kristallisation von interstitiellen Pyroxenen als auch zu Schmelzreaktionen mit Pyroxen-Porphyroklasten. Die daraus resultierende Phasenmischung und Korngrößenreduktion bedingten die Aktivierung eines korngrößenabhängigen Deformationsmechanismus.

Die gewonnen Daten und Erkenntnisse der drei Studien zeigen, dass Phasenmischung in Scherzonen des oberen Mantels maßgeblich von metasomatischen und/oder metamorphen Reaktionen abhängt. Intensive Phasenmischung ist entweder in Druckschatten reagierender Pyroxen-Porphyroklasten oder in der durch interstitielle Kristallisation gemischten Matrix vorhanden. Die Neoblast-Phasenzusammensetzung in Druckschatten ist je nach Reaktionstyp und Ausgangs-Porphyroklast unterschiedlich. Gemeinsame mikrostrukturelle Merkmale wie Einbuchtungen von Neoblasten in Mutterklasten, stark lobate Porphyroklast- und Neoblast-Korn- und Phasengrenzen sowie das weitgehende Fehlen von Subkörnern in den Porphyroklasten sprechen für die Bildung der Neoblasten durch Reaktionen. Eine mechanische Mischung der Neoblasten durch Korngrenzgleiten ist wegen der starken Durchmischung unmittelbar an den Korngrenzen von Mutterklasten auszuschließen. Obwohl die Reaktionstypen variieren (Schmelze, Fluid, Metamorphose), sind die Mischungsintensitäten der Neoblasten in Druckschatten aller drei Scherzonen vergleichbar hoch (⌀ 65-77 % Phasengrenzen). Der Reaktionstyp ist für die Bildung der Neoblasten und deren Mischungsintensität folglich von geringer Bedeutung. In der Scherzone des NW Ronda Peridotitmassivs führte die Kristallisation

von interstitiellen Pyroxenen und Schmelz-Gesteins-Reaktionen mit grobkörnigen Olivinen zur Bildung einer gemischten Matrix mit ähnlichen Mischungsintensitäten (⬗ 71 %) wie in den Pyroxen-Porphyroklast-Druckschatten. Im Gegensatz zur lokalisierten Phasenmischung und Korngrößenverkleinerung in Druckschatten von Porphyroklasten und den daraus resultierenden ultramylonitischen Bändern der Scherzonen von Lanzo und Erro-Tobbio ist Phasenmischung in der Ronda Scherzone durch interstitielle Kristallisation und Schmelz-Gesteins-Reaktionen im gesamten schmelzbeeinflussten Gebiet zu beobachten (~2 km Mächtigkeit). In allen untersuchten Scherzonen erhöhten Reaktionen, sei es durch die Bildung von Neoblasten in Druckschatten von Pyroxen-Porphyroklasten oder durch die Kristallisation von interstitiellen Körnern, die Mischungsintensität erheblich. Ebenso wie der Reaktionstyp scheint der Zeitpunkt der Reaktion eine untergeordnete Rolle für die Mischungsintensität zu spielen: Kristallisation und Schmelz-Porphyroklast-Reaktionen im initialen Stadium der Ronda-Scherzone führen zu ähnlichen Phasenmischungsintensitäten wie Reaktionen an Pyroxen-Porphyroklasten während der späten, stark lokalisierten Deformation in ultramylonitischen Bändern von Lanzo und Erro-Tobbio. Für die Intensität der Deformationslokalisierung scheint dieser Zeitpunkt jedoch ausschlaggebend: Eine großräumige Phasenmischung wurde nur durch schmelzinduzierte Kristallisation von interstitiellen Pyroxenen in zuvor olivindominierten Gebieten beobachtet (Ronda, Lanzo). Sowohl die verstärkte Strainrate durch schmelzbenetzte Korn- und Phasengrenzen als auch die Aktivierung eines korngrößensensiblen Deformationsmechanismus, welcher auf der Verringerung der Korngröße durch Neoblast-Kristallisation sowie deren Aufrechterhaltung durch *Zener-Pinning* basieren, lokalisieren die Deformation in km-großen, schmelzbeeinflussten Bereichen. Starke CPOs, Korngrößen zwischen 50 und 200 µm und in der Foliation ausgerichtete Korngrenzen bestätigen, dass in diesem Stadium sowohl Versetzungskriechen als auch , korngrößensensitive Deformationsmechanismen aktiv waren. Dominant sind hier wahrscheinlich die Mechanismen Korngrenzengleiten (*DisGBS*, Hirth und Kohlstedt (2003)), oder Korngrenzmigration (*DRX creep,* Platt und Behr (2011)). Da diese schmelzbedingte Lokalisierung der Deformation unabhängig von vorherigen Heterogenität bzw. weiterer Initialprozesse ist, ist Schmelzperkolation dieser Studie zu Folge entscheidend für die initiale Lokalisierung von Deformation und somit ausschlaggebend für die Bildung von Scherzonen im oberen Erdmantel. Ob Deformationslokalisierung in den ultramylonitischen Neoblasten, welche aus den

Reaktionen an Pyroxen-Porphyroklasten hervorgehen, auftritt, ist maßgeblich von dem Zeitpunkt der Reaktion abhängig. Obwohl die Neoblastzusammensetzung der Druckschatten von Pyroxen-Porphyroklasten der Ronda Scherzone ähnliche Mischungsintensitäten wie die von den Scherzonen Lanzo und Erro-Tobbio aufweisen, kommt es zu keiner Lokalisierung. Kongruente Korngrößen und Mischungsintensität von Neoblasten in Druckschatten und der sie umgebenden gemischten Matrix deuten in Ronda auf die Aktivität gleicher Deformationsmechanismen in beiden Bereichen hin. Im Gegensatz dazu konzentriert sich die Deformation in den Scherzonen von Lanzo und Erro-Tobbio in ultramylonitischen Bändern, welche deutlich von mylonitischen Bereichen abgegrenzt sind. Geringe Korngrößen und schwach entwickelte CPOs bestätigen Diffusionskriechen als dominanten Deformationsmechanismus. Das auf das deformative Zentrum der Scherzone begrenzte Vorkommen der Ultramylonite und ihre Assoziation mit stark gelängten Orthopyroxen-Einkristallen bestätigt die Bildung der Neoblasten unter hoher mechanischer Spannung während eines späten Stadiums der Scherzonenentwicklung.

Reaktionen, interstitielle Kristallisation eingeschlossen, können somit als Hauptgrund für Phasenmischung in Scherzonen des oberen Mantels identifiziert werden. Unterschiedliche Reaktionspartner (Schmelze, Fluid, feste Phasen) bilden Neoblast-Zusammensetzungen mit ähnlichen Mischungsintensitäten. Der Zeitpunkt der Reaktion in Hinblick auf die Entwicklung der Scherzone scheint entscheidend für die Art und das Ausmaß der Lokalisierung der Deformation zu sein. Schmelzperkolation in frühen Stadien der Scherzonenentwicklung begünstigt großräumige Lokalisierung durch die Aktivierung von korngrößenabhängigen Deformationsmechansimen und schmelzbenetzte Korn- und Phasengrenzen. Reaktionen an Korngrenzen von Pyroxen-Porphyroklasten in späteren Stadien der Scherzonenentwicklung bilden ultramylonitische Neoblast-Zusammensetzungen in Druckschatten von Pyroxen-Porphyroklasten. Durch deren Vernetzung zu Bändern wird Diffusionskriechen aktiviert, welches durch höhere Strainraten die Deformation im Zentimeterbereich lokalisiert.

Die Erkenntnisse über das Zusammenspiel von Phasenmischung und Deformations-Lokalisierung in Scherzonen des oberen Erdmantels führen direkt zu mehreren Folgefragestellungen. Die Lokalisierung von Deformation hängt stark von einer geringen Korngröße und deren Stabilität ab. Nach der piezometrischen Gleichung (Einleitung, Gl. 1.3) und ihrer Anpassung an die Zweitphasen (Einleitung, Gl. 1.4/1.5) entwickeln sich Korngrößen in Abhängigkeit von der Differentialspannung, der Strainrate sowie dem

Anteil und der Verteilung von Zweitphasen. Obwohl Neoblasten in Druckschatten von Pyroxen-Porphyroklasten durch Reaktionen und nicht durch dynamische Kristallisation gebildet werden, scheint ihre Korngröße stark von den Deformationsbedingungen abzuhängen: Stark deformierte Proben weisen ultramylonitische (Lanzo, Erro-Tobbio Scherzonen), mäßig beanspruchte Proben mylonitische Neoblasten auf (Ronda Scherzone). Der Einfluss von mechanischer Spannung, Verformung und der damit verbundenen korninternen Deformation von Pyroxen-Porphyroklasten auf die Bildung von Neoblasten in deren Druckschatten und insbesondere deren Neoblast-Korngröße ist von großer Bedeutung für die Lokalisierung von Deformation, da diese den dominanten Deformationsmechanismus kontrolliert. Die im Rahmen dieses Projekts erhobenen Daten bieten einen hervorragenden Rahmen, um die Fragestellung von Deformationsbedingungen und Neoblast-Korngröße aus mikrostruktureller Sicht anzugehen. Um jedoch die Abhängigkeit der mechanischen Spannung von der Neoblast-Korngröße in Druckschatten zu untersuchen, wären zusätzliche piezometrische Analysen der Proben erforderlich. Darüber hinaus könnten Deformationsexperimente mit Schwerpunkt auf Reaktionen an Pyroxen-Porphyroklasten unter verschiedenen Spannungsbedingungen deren mikrostrukturelle Auswirkungen gegenprüfen. Weiterhin ist eine vergleichende Studie mit reaktionsfreien, jedoch stark deformierten Peridotit-Xenolithen (z.B. Kimberley, Südafrika) geplant, um Phasenmischung in reaktionsfreien Umgebungen mit dominanter dynamischer Kristallisation zu untersuchen. In Kombination mit der reaktionsgetriebenen Phasenmischung von Lanzo, Erro-Tobbio und Ronda zielt diese Studie auf einen umfassenden Überblick über die Deformationsregime im oberen Erdmantel.

Die vorliegende Studie legt die Bedeutung von Reaktionen für Lokalisierung der Deformation im oberen Erdmantel aus der mikrostrukturellen Perspektive dar. Die Integration dieser Erkenntnisse in den größeren Kontext der Geodynamik und Plattentektonik steht jedoch noch aus. Grundlegend hierfür sind die Einführung eines rheologischen Modells für Phasenmischungen und die Implementierung von Deformationsregimen und reaktionsgesteuerter Rheologie in numerische Modelle. Die anspruchsvolle Aufgabe der Erstellung eines dynamischen Modells des oberen Erdmantels erfordert, wie die Ergebnisse dieser Arbeit belegen, die Integration und Verbindung von Schmelzbildung, Fluidaktivität, Metasomatose, Metamorphose und Deformation.

6.1   References summary and outlook

Hirth, G., & Kohlstedt, D. (2003). Rheology of the upper mantle and the mantle wedge: A view from the experimentalists. *Geophysical Monograph Series*, *138*, 83–105. https://doi.org/10.1029/138GM06

Kaczmarek, M. A., & Müntener, O. (2008). Juxtaposition of melt impregnation and high-temperature shear zones in the upper mantle; field and petrological constraints from the lanzo peridotite (Northern Italy). *Journal of Petrology*, *49*(12), 2187–2220. https://doi.org/10.1093/petrology/egn065

Platt, J. P., & Behr, W. M. (2011). Grainsize evolution in ductile shear zones: Implications for strain localization and the strength of the lithosphere. *Journal of Structural Geology*, *33*(4), 537–550. https://doi.org/10.1016/j.jsg.2011.01.018

Soustelle, V., Tommasi, A., Bodinier, J. L., Garrido, C. J., & Vauchez, A. (2009). Deformation and reactive melt transport in the mantle lithosphere above a large-scale partial melting domain: The Ronda peridotite Massif, Southern Spain. *Journal of Petrology*, *50*(7), 1235–1266. https://doi.org/10.1093/petrology/egp032

Tholen, S., Linckens, J., Heckel, C., & Kemperle, M. (2022). Reaction-induced phase mixing and the formation of ultramylonitic bands. *Tectonophysics*, *827*(December 2021). https://doi.org/10.1016/j.tecto.2022.229230

Tommasi, A., & Vauchez, A. (2015). Heterogeneity and anisotropy in the lithospheric mantle. *Tectonophysics*, *661*, 11–37. https://doi.org/10.1016/j.tecto.2015.07.026

List of figures

Chapter 1- Introduction

Chapter 2 – Lanzo – Reaction-induced phase mixing and the formation of ultramylonitic bands

Chapter 3 – Erro-Tobbio – Formation of ultramylonites in an upper mantle shear zone

Chapter 4 – Ronda – Melt-enhanced strain localization and phase mixing in a large-scale mantle shear zone

List of tables

Chapter 3 – Erro-Tobbio – Formation of ultramylonites in an upper mantle shear zone

Appendix chapter 2 – Lanzo – Reaction-induced phase mixing and the formation of ultramylonitic bands

S2.1   –   Grain and boundary data (attached as Excel file on CD)

S2.2   –   Grain orientation data including Aspect Ratio, Shape Factor, Paris Factor (attached as Excel file on CD)

S2.3   –   Additional CPO data 1 (attached below & on CD)

S2.4   –   Additional CPO data 2 (attached below & on CD)

S2.5   –   EPMA measurement settings and detection limits (attached below & on CD)

S2.6   –   Microprobe data (attached below & on CD)

S2.7   –   Microstructure of Cpx porphyroclast (attached below & on CD)

S2.8   –   Additional graphs of pyroxene geochemistry (attached as Excel file on CD)

S2.9   –   Additional graphs of olivine geochemistry (attached as Excel file on CD)

S2.10   –   Additional geothermometric data (attached below & on CD)

S2.11   –   Microstructure of Lesotho Xenolith (attached below & on CD)

Publication   –   "Reaction-induced phase mixing and the formation of ultramylonitic bands" by Sören Tholen, Jolien Linckens, Catharina Heckel, Marina Kemperle published in *Tectonophysics,* 827 (2022), (attached below & on CD)
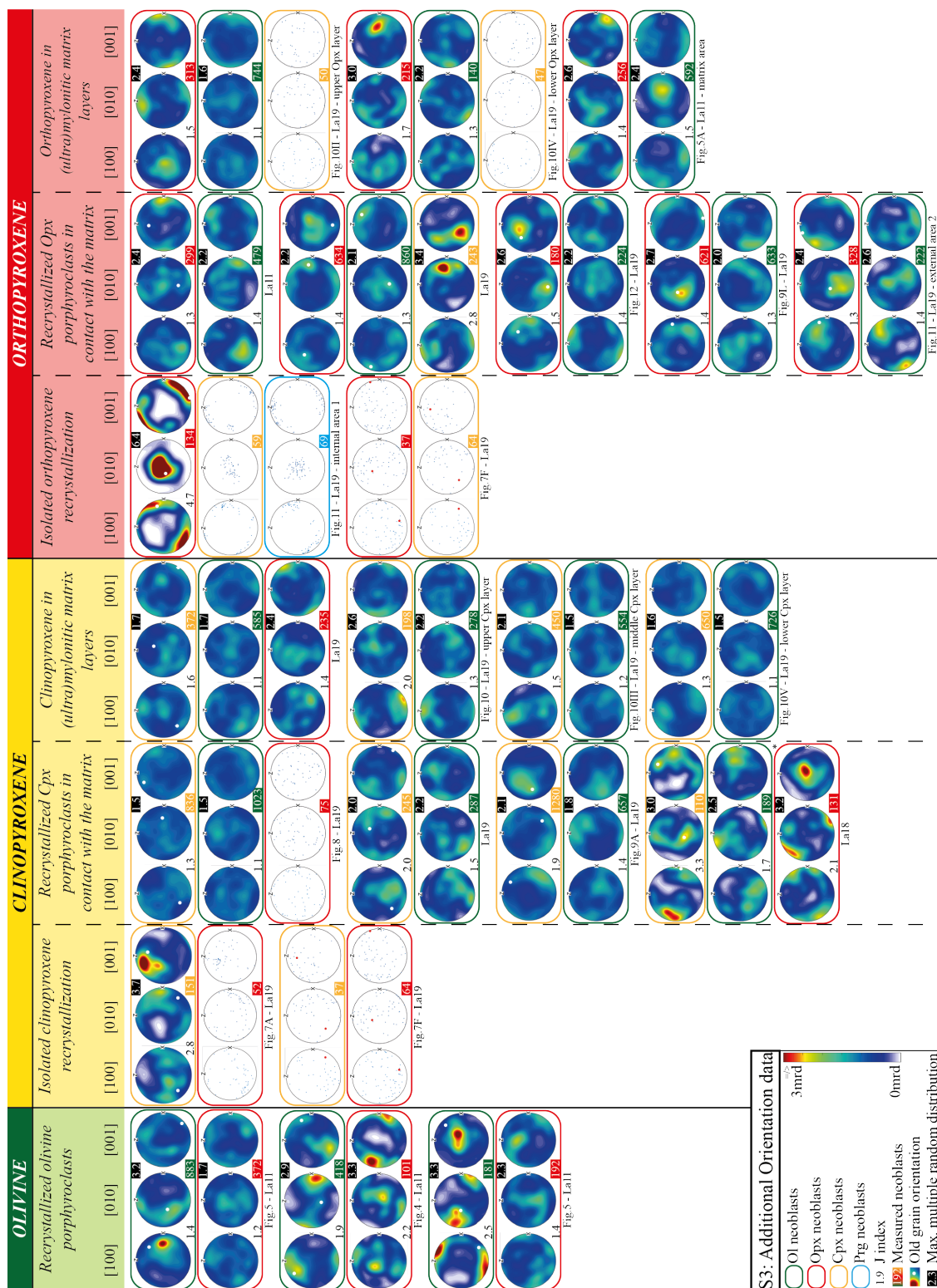
S2.3 –*Additional CPO data 1. For optimal resolution, the reader is referred to the version attached on the CD.*
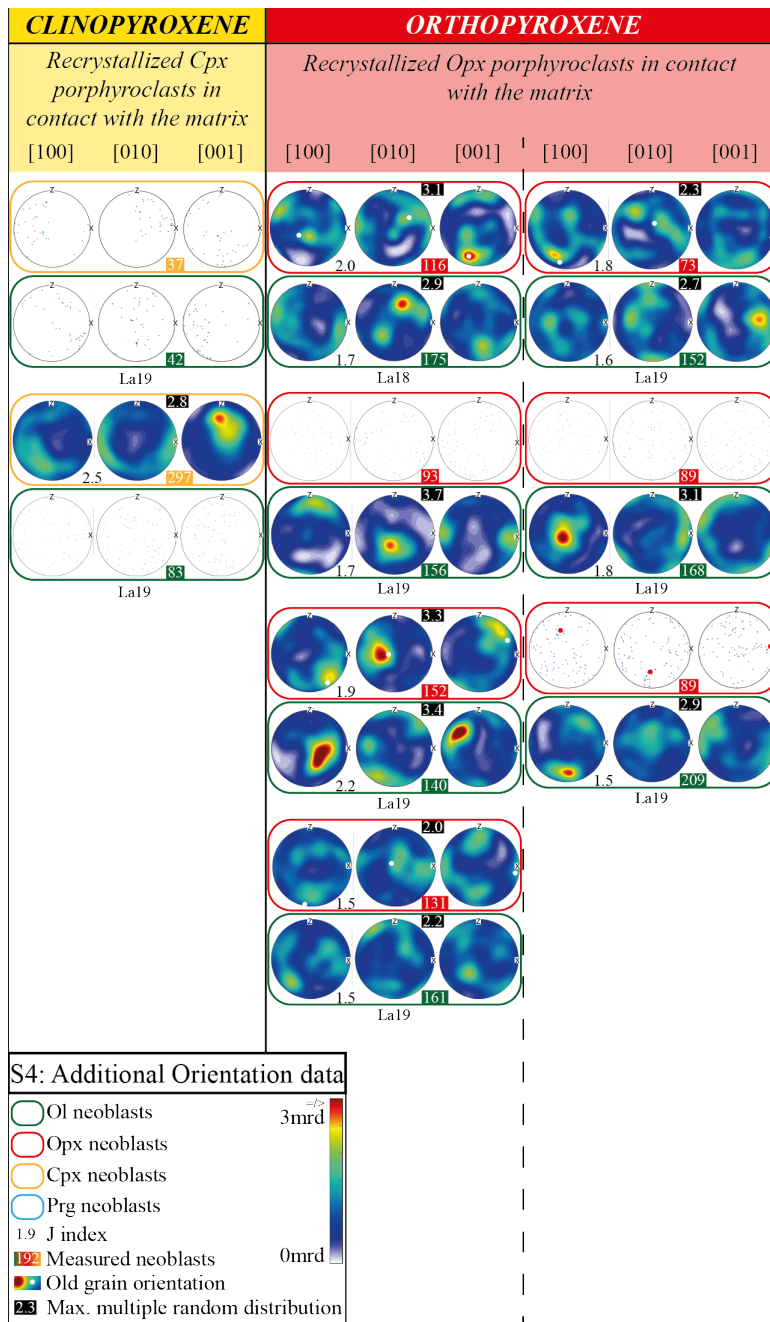
S2.4 –*Additional CPO data 2. For optimal resolution, the reader is referred to the version attached on the CD.*

Cpx and Opx recrystallization measurements				
Element	Crystal	Meas. t peak (s)	Meas. t back(s)	Detect. Limit (ppm)
Al	TAP	30	15	49
Si	TAP	30	15	65
Cr	PETL	30	15	101
Ca	PETL	30	15	44
K	PETL	30	15	28
Ti	PETL	30	15	53
Na	TAPL	20	15	42
Mg	TAPL	40	15	27
Mn	LIFH	20	15	121
Fe	LIFH	20	15	123
Ni	LIFH	20	15	153

Trace elements olivine measurements				
Element	Crystal	Meas. t peak (s)	Meas. t back (s)	Detect. Limit (ppm)
Si	TAP	60	60	40
Ca	TAP	150	150	11
Ti	PETH	150	150	16
Cr	PETL	150	150	28
Mn	LIFL	40	20	63
Al	TAPL	150	150	9
Fe	LIFL	60	30	53
Mg	TAP	60	30	47
Ni	LIFL	20	20	65

S2.5 – *Measurement settings and detection limits for Cpx and Opx recrystallization and trace element olivine measurement.*

Olivine

Texture t.: Ultramylonite

ROI*	La11_2ROI1		La11_2ROI3		La11_2ROI7		La11_2ROI6	La11_1ROI7	La11_1ROI1		La11_1ROI2		La11_1ROI3	
	Clast	Neoblast	Clast	Neoblast	Clast	Neoblast	Neoblast	Neoblast	Clast	Neoblast	Clast	Neoblast	Clast	Neoblast
	(n=3)	(n=6)	(n=4)	(n=7)	(n=3)	(n=5)	(n=5)	(n=6)	(n=3)	(n=2)	(n=3)	(n=5)	(n=3)	(n=4)
SiO_2 (wt%)	40.44	40.29	40.36	40.10	40.40	40.29	40.36	40.17	40.25	40.19	40.16	40.06	40.43	40.33
TiO_2 (ppm)	12	11	5	6	11	7	12	9	16	31	14	9	9	13
Al_2O_3 (ppm)	5	5	1	3	5	5	3	4	1	301	0	1	18	1
Cr_2O_3 (ppm)	6	9	8	2	3	11	6	16	5	38	4	4	1	15
FeO (wt%)	10.03	10.16	9.85	9.99	10.01	9.96	10.13	9.94	9.9	10.25	9.77	10.13	9.91	10.13
MnO (wt%)	0.16	0.16	0.16	0.16	0.16	0.16	0.16	0.15	0.16	0.16	0.15	0.16	0.16	0.16
NiO (wt%)	0.37	0.37	0.36	0.35	0.39	0.38	0.37	0.39	0.37	0.39	0.38	0.37	0.38	0.37
MgO (wt%)	49.67	49.17	49.46	49.26	49.16	49.21	49.23	49.12	48.86	48.71	49.32	48.82	49.32	48.92
CaO (ppm)	35	125	38	39	26	103	43	52	99	96	81	96	91	119
Total (wt%)	100.67	100.17	100.19	99.86	100.12	100.01	100.26	99.78	99.55	99.77	99.79	99.55	100.22	99.93
Mg#	0.898	0.896	0.900	0.898	0.898	0.898	0.897	0.898	0.898	0.894	0.900	0.896	0.899	0.896
Cr#	0.528	0.490	0.833	0.667	0.500	0.625	0.833	0.680	0.750	0.061	1.000	1.000	-	-

S2.6 –EPMA data (1 of 13).

Olivine

Texture t.	Ultramylonite								Mylonite			
ROI*	La11_1ROI4		La11_1ROI5		La11_1ROI6		La11_1ROI7		La19_2ROI33		La19_2ROI32	La19_2ROI5
	Clast	Neoblast	Clast	Neoblast	Clast	Neoblast	Clast	Neoblast	Inclusion	Neoblast	Neoblast	Neoblast
	(n=3)	(n=4)	(n=3)	(n=4)	(n=3)	(n=6)	(n=3)	(n=4)	(n=1)	(n=4)	(n=5)	(n=3)
SiO_2 (wt%)	40.45	40.14	40.34	40.13	40.56	40.44	40.55	40.43	40.7	40.73	40.64	40.55
TiO_2 (ppm)	17	12	10	8	6	9	8	5	89	36	39	32
Al_2O_3 (ppm)	0	3	2	2	1	6	3	4	25	16	52	10
Cr_2O_3 (ppm)	4	18	5	6	8	14	16	1	169	58	75	37
FeO (wt%)	10.09	10.08	9.69	9.77	9.67	10	9.69	9.94	9.39	9.38	9.2	9.5
MnO (wt%)	0.16	0.16	0.16	0.16	0.15	0.16	0.15	0.15	0.15	0.14	0.14	0.15
NiO (wt%)	0.36	0.35	0.36	0.34	0.37	0.38	0.37	0.37	0.36	0.37	0.38	0.38
MgO (wt%)	49.06	49.08	49.01	48.94	49.4	49.18	49.6	49.38	49.84	49.81	49.85	49.87
CaO (ppm)	93	105	108	124	88	100	76	83	1203	335	448	260
Total (wt%)	100.14	99.83	99.58	99.36	100.17	100.17	100.38	100.28	100.65	100.49	100.29	100.49
Mg#	0.897	0.897	0.900	0.899	0.901	0.898	0.901	0.899	0.904	0.904	0.906	0.903
Cr#	1.000	0.706	0.500	0.750	1.000	0.681	0.675	0.500	0.778	0.588	0.542	0.670

S2.6 –EPMA data (2 of 13).

Olivine

Texture t.	Mylonite			
ROI*	La19_2ROI34		La19_2ROI17	La11_1ROI35
	Clast	Neoblast	Neoblast	Neoblast
	(n=4)	(n=5)	(n=4)	(n=6)
SiO$_2$ (wt%)	40.44	40.46	40.68	40.57
TiO$_2$ (ppm)	20	17	19	23
Al$_2$O$_3$ (ppm)	8	9	12	6
Cr$_2$O$_3$ (ppm)	13	25	18	12
FeO (wt%)	9.53	9.53	9.33	9.55
MnO (wt%)	0.15	0.15	0.14	0.15
NiO (wt%)	0.37	0.37	0.38	0.38
MgO (wt%)	49.67	49.69	50.04	49.85
CaO (ppm)	304	101	113	104
Total (wt%)	100.25	100.23	100.6	100.52
Mg#	0.903	0.903	0.905	0.903
Cr#	0.538	0.625	0.448	0.593

S2.6 –EPMA data (3 of 13).

Olivine

Texture t.	Mylonite – Opx recrystallization microstructures						Mylonite – Ultramylonitic Ol+ Opx layers		
ROI*	La19_2ROI20	La19_2ROI22	La19_2ROI21	La19_2ROI3	La11_1ROI17	La19_1ROI9	La19_1ROI18	La19_1ROI22	La19_1ROI22
	Neoblast	Neoblast	Neoblast	Neoblast	Neoblast	Neoblast	Neoblast	Neoblast	Neoblast
	(n=26)	(n=15)	(n=1)	(n=15)	(n=16)	(n=20)	(n=7)	(n=15)	(n=14)
SiO_2 (wt%)	40.83	40.82	40.7	40.63	40.72	40.79	40.76	40.77	40.60
TiO_2 (wt%)	0.01			0.01	0.01	0.01		0.01	0.01
Al_2O_3 (wt%)				0.01	0.02	0.01			0.01
Cr_2O_3 (wt%)	0.01	0.02	0.03	0.03	0.02	0.02	0.01		0.01
FeO (wt%)	9.62	9.72	8.94	9.56	9.49	9.65	9.59	9.91	9.80
MnO (wt%)	0.13	0.12	0.01	0.12	0.14	0.14	0.1	0.14	0.14
NiO (wt%)	0.38	0.36	0.39	0.39	0.38	0.37	0.35	0.37	0.37
MgO (wt%)	49.02	49.14	49.46	49.14	48.89	49.18	48.95	48.95	48.82
CaO (wt%)		0.01	0.04	0.02	0.03	0.01	0.03	0.02	0.02
Na_2O (wt%)			0.01						
K_2O (wt%)									
Total (wt%)	100.01	100.20	99.62	99.61	99.69	100.17	99.79	100.19	99.78
Mg#	0.901	0.900	0.908	0.902	0.902	0.901	0.901	0.898	0.899
Cr#	0.870	0.975	1.000	0.815	0.761	0.920	0.755	0.940	0.821

S2.6 –EPMA data (4 of 13).

Olivine

Texture t.	Mylonite – Cpx recrystallization microstructures								
ROI*	La19_2ROI16	La19_2ROI27	La19_2ROI13	La19_2ROI3	La19_2ROI34	La19_1ROI17	La19_1ROI26	La19_1ROI24.1	La19_1ROI24.2
	Neoblast	Neoblast	Neoblast	Neoblast	Neoblast	Neoblast	Neoblast	Neoblast	Neoblast
	(n=7)	(n=5)	(n=9)	(n=10)	(n=16)	(n=2)	(n=8)	(n=7)	(n=8)
SiO_2 (wt%)	40.90	40.86	40.45	40.35	40.71	40.97	40.85	40.95	40.60
TiO_2 (wt%)	0.01	0.01	0.01	0.01	0.01	0.02		0.01	
Al_2O_3 (wt%)	0.01						0.02	0.03	
Cr_2O_3 (wt%)	0.02	0.01	0.02	0.02	0.01	0.03	0.02		0.02
FeO (wt%)	9.74	9.87	9.7	9.81	10.09	9.55	9.88	9.80	9.60
MnO (wt%)	0.13	0.15	0.15	0.14	0.13	0.13	0.14	0.14	0.14
NiO (wt%)	0.37	0.37	0.36	0.36	0.37	0.36	0.36	0.34	0.38
MgO (wt%)	49.07	48.94	48.80	48.77	48.94	48.83	48.82	48.92	48.81
CaO (wt%)	0.05	0.02	0.06	0.06	0.04	0.12	0.05	0.08	0.04
Na_2O (wt%)									
K_2O (wt%)									
Total (wt%)	100.29	100.22	99.54	99.52	100.29	100.02	100.14	100.27	99.59
Mg#	0.900	0.898	0.900	0.899	0.896	0.901	0.898	0.899	0.901
Cr#	0.828	0.800	1.000	0.725	0.975	0.983	0.532	0.736	0.938

S2.6 – EPMA data (5 of 13).

Olivine

Texture t.	Mylonite – Cpx rxs			Mylonite – Ultramylonitic Cpx+ Ol layers		
ROI*	La19_1ROI27.2	La19_1ROI27.1	La19_1ROI22	La19_1ROI22	La19_1ROI22	La19_1ROI22
	Neoblast	Neoblast	Neoblast	Neoblast	Neoblast	Neoblast
	(n=6)	(n=11)	(n=7)	(n=4)	(n=9)	
SiO_2 (wt%)	40.31	40.84	41.09	41.08	41.05	
TiO_2 (wt%)	0.01		0.01	0.01	0.01	
Al_2O_3 (wt%)					0.01	
Cr_2O_3 (wt%)	0.01	0.03	0.01	0.01	0.02	
FeO (wt%)	9.78	9.70	9.77	9.82	9.59	
MnO (wt%)	0.14	0.14	0.14	0.15	0.14	
NiO (wt%)	0.36	0.37	0.36	0.38	0.37	
MgO (wt%)	48.78	49.11	49.11	49.11	48.82	
CaO (wt%)	0.05	0.07	0.05	0.05	0.06	
Na_2O (wt%)						
K_2O (wt%)						
Total (wt%)	99.45	100.25	100.53	100.61	100.07	
Mg#	0.899	0.900	0.900	0.899	0.901	
Cr#	0.818	0.941	1.000	1.000	0.830	

S2.6 –EPMA data (6 of 13).

Orthopyroxene

Texture t.	Mylonite – Opx recrystallization microstructures												
ROI*	La19_2ROI20			La19_2ROI22		La19_2ROI21		La19_2ROI3			La19_1ROI14		
	Clast Int.	Clast Av.	Neoblast	Clast Int.	Neoblast	Clast Av.	Neoblast Int.	Clast Int.	Clast Av.	Neoblast	Clast Int.	Clast Av.	Neoblast Int.
	(n=4)	(n=6)	(n=9)	(n=5)	(n=16)	(n=6)	(n=2)	(n=3)	(n=4)	(n=11)	(n=2)	(n=6)	(n=17)
SiO_2 (wt%)	54.19	54.30	57.17	54.54	56.82	54.49	55.33	54.86	55.05	56.06	54.94	54.79	56.24
TiO_2 (wt%)	0.16	0.16	0.14	0.15	0.19	0.20	0.22	0.23	0.24	0.18	0.17	0.21	0.15
Al_2O_3 (wt%)	5.14	4.83	1.02	4.03	1.35	3.59	2.92	3.59	3.31	1.48	2.94	3.33	1.75
Cr_2O_3 (wt%)	0.67	0.67	0.15	0.67	0.24	0.73	0.67	0.72	0.67	0.27	0.60	0.67	0.33
FeO (wt%)	6.73	6.76	6.86	6.67	6.92	6.66	6.68	6.85	6.80	7.04	6.48	6.61	6.54
MnO (wt%)	0.13	0.14	0.16	0.15	0.17	0.15	0.17	0.15	0.16	0.16	0.15	0.14	0.15
NiO (wt%)	0.09	0.09	0.07	0.09	0.07	0.09	0.09	0.10	0.09	0.07	0.09	0.09	0.07
MgO (wt%)	32.23	32.25	34.05	32.81	33.86	32.61	32.95	32.57	32.66	34.04	33.02	32.84	33.69
CaO (wt%)	0.48	0.55	0.40	0.47	0.49	0.64	0.51	0.65	0.77	0.42	0.61	0.53	0.46
Na_2O (wt%)	0.02	0.02	0.01	0.01	0.01	0.02	0.01	0.02	0.02	0.01	0.01	0.01	0.01
K_2O (wt%)													
Total (wt%)	99.85	99.78	100.3	99.59	100.11	99.17	99.55	99.73	99.76	99.73	99.01	99.22	99.40
Mg#	0.895	0.895	0.899	0.898	0.897	0.897	0.898	0.894	0.895	0.896	0.901	0.899	0.902
Cr#	0.082	0.087	0.088	0.101	0.107	0.120	0.133	0.120	0.122	0.110	0.124	0.120	0.113

S2.6 –EPMA data (7 of 13).

Orthopyroxene

Texture t.	Mylonite – Opx recrystallization microstructures									Mylonite – Ultramylonitic Opx+ Ol layers	
ROI*	La19_1ROI17			La19_1ROI9			La19_1ROI18			La19_1ROI22	La19_1ROI22
	Clast Av.	Neoblast Int.	Neoblast	Clast Int.	Clast Av.	Neoblast	Clast Int.	Clast Av.	Neoblast	Neoblast	Neoblast
	(n=3)	(n=16)	(n=9)	(n=4)	(n=5)	(n=4)	(n=1)	(n=5)	(n=3)	(n=5)	(n=8)
SiO_2 (wt%)	56.27	56.34	56.39	55.17	55.11	56.62	55.65	55.62	55.94	56.96	57.12
TiO_2 (wt%)	0.23	0.15	0.22	0.22	0.23	0.21	0.20	0.20	0.10	0.10	0.13
Al_2O_3 (wt%)	2.03	1.66	1.52	3.36	3.37	1.51	2.44	2.79	0.76	0.97	1.05
Cr_2O_3 (wt%)	0.47	0.35	0.29	0.71	0.72	0.22	0.52	0.54	0.10	0.08	0.11
FeO (wt%)	6.41	6.34	6.75	6.67	6.59	6.85	6.59	6.62	7.17	6.97	6.80
MnO (wt%)	0.15	0.16	0.16	0.15	0.15	0.17	0.16	0.15	0.18	0.16	0.17
NiO (wt%)	0.07	0.09	0.07	0.08	0.08	0.08	0.09	0.07	0.07	0.07	0.07
MgO (wt%)	33.63	33.90	33.80	32.73	32.56	33.92	32.73	32.96	34.71	34.51	34.04
CaO (wt%)	0.53	0.4	0.53	0.93	1.15	0.55	1.00	0.64	0.29	0.37	0.43
Na_2O (wt%)	0.02		0.01	0.03	0.04	0.01	0.03	0.01	0.00	0.01	
K_2O (wt%)											
Total (wt%)	99.81	99.44	99.73	100.04	99.99	100.13	99.40	99.62	99.32	100.18	99.92
Mg#	0.903	0.905	0.899	0.897	0.899	0.898	0.899	0.899	0.896	0.898	0.899
Cr#	0.133	0.121	0.112	0.125	0.125	0.88	0.124	0.116	0.081	0.049	0.064

S2.6 –EPMA data (8 of 13).

Orthopyroxene

Texture t.	Mylonite – Opx neoblast in Cpx recrystallization microstructures									
ROI*	La19_2ROI16	La19_2ROI27	La19_2ROI13	La19_2ROI31	La19_1ROI17	La19_1ROI26	La19_1ROI24.2	La19_1ROI27.2	La19_1ROI27.1	
	Neoblast	Neoblast	Neoblast	Neoblast	Neoblast Int.	Neoblast	Neoblast	Neoblast	Exsolution	Neob.
	(n=1)	(n=2)	(n=2)	(n=3)	(n=2)	(n=1)	(n=1)	(n=3)	(n=1)	(n=1)
SiO_2 (wt%)	57.18	57.05	56.51	56.56	56.39	56.72	56.57	55.39	54	54.41
TiO_2 (wt%)	0.17	0.17	0.18	0.20	0.12	0.19	0.20	0.16	0.17	0.21
Al_2O_3 (wt%)	1.16	1.10	1.41	1.49	1.42	1.58	1.55	1.23	5.74	4.36
Cr_2O_3 (wt%)	0.16	0.16	0.26	0.21	0.30	0.22	0.22	0.20	0.69	0.68
FeO (wt%)	6.90	6.90	6.73	6.84	6.67	6.91	6.62	6.89	6.76	6.96
MnO (wt%)	0.16	0.17	0.16	0.16	0.16	0.18	0.16	0.17	0.15	0.18
NiO (wt%)	0.07	0.07	0.06	0.07	0.05	0.04	0.09	0.08	0.09	0.07
MgO (wt%)	33.90	34.15	33.77	33.81	33.50	34.13	33.46	34.25	31.85	32.52
CaO (wt%)	0.46	0.45	0.50	0.57	0.57	0.50	0.61	0.44	0.63	0.62
Na_2O (wt%)	0.01	0.01	0.01	0.01	0.01	0.01	0.01		0.02	0.01
K_2O (wt%)										
Total (wt%)	100.17	100.22	99.58	99.93	99.19	100.48	99.39	98.79	100.10	100.01
Mg#	0.897	0.898	0.899	0.898	0.900	0.898	0.900	0.899	0.9894	0.893
Cr#	0.083	0.089	0.107	0.087	0.129	0.087	0.086	0.092	0.075	0.095

S2.6 –EPMA data (9 of 13).

Clinopyroxene

Texture t. — Mylonite – Cpx recrystallization microstructures

ROI*	La19_2ROI16			La19_2ROI27		La19_2ROI13			La19_2ROI31			La19_2ROI34		
	Clast Int.	Clast Av.	Neoblast	Clast Int.	Neoblast	Clast Int.	Clast Av.	Neoblast	Clast Int.	Clast Av.	Neob.	Clast Int.	Clast Av.	Neob.
	(n=3)	(n=4)	(n=10)	(n=1)	(n=10)	(n=5)	(n=5)	(n=9)	(n=2)	(n=4)	(n=11)	(n=5)	(n=7)	(n=7)
SiO_2 (wt%)	52.86	52.85	53.66	51.74	52.95	50.57	50.57	52.53	50.65	50.93	52.53	50.66	50.91	52.8
TiO_2 (wt%)	0.68	0.70	0.47	0.71	0.62	0.85	0.85	0.68	0.82	0.85	0.68	0.73	0.74	0.7
Al_2O_3 (wt%)	3.32	3.29	1.85	3.45	2.56	5.98	5.98	2.81	5.90	5.08	2.83	5.36	5.01	2.67
Cr_2O_3 (wt%)	0.91	0.89	0.40	0.97	0.63	1.04	1.04	0.71	1.07	1.05	0.65	1.2	1.16	0.57
FeO (wt%)	2.86	2.85	2.60	2.66	2.70	3.07	3.07	2.71	3.09	2.96	3.76	3.04	3.01	2.81
MnO (wt%)	0.08	0.08	0.08	0.08	0.08	0.08	0.08	0.07	0.10	0.09	0.08	0.09	0.09	0.09
NiO (wt%)	0.04	0.04	0.05	0.01	0.05	0.05	0.05	0.04	0.02	0.02	0.04	0.05	0.04	0.05
MgO (wt%)	16.30	16.27	17.03	16.10	16.69	15.04	15.04	16.44	15.15	15.42	16.56	15.53	15.68	16.74
CaO (wt%)	22.36	22.46	23.05	22.29	22.51	22.32	22.32	22.66	22.01	22.14	22.51	21.94	21.96	22.6
Na_2O (wt%)	0.59	0.58	0.43	0.58	0.52	0.65	0.65	0.51	0.66	0.65	0.51	0.67	0.65	0.49
K_2O (wt%)														
Total (wt%)	99.99	100.02	99.62	98.59	99.29	99.65	99.65	99.16	99.46	99.19	99.15	99.26	99.26	99.52
Mg#	0.910	0.911	0.921	0.915	0.917	0.897	0.897	0.915	0.898	0.903	0.915	0.901	0.903	0.914
Cr#	0.156	0.154	0.126	0.158	0.139	0.106	0.106	0.144	0.109	0.124	0.131	0.131	0.136	0.126

S2.6 –EPMA data (10 of 13).

Clinopyroxene

Texture t.	Mylonite –Cpx recrystallization microstructures												
ROI*	La19_1ROI17_Internal			La19_1ROI17_External			La19_1ROI26			La19_1ROI24.2			La19_1ROI24S
	Clast Int.	Clast Av.	Neo. Int.	Clast Int.	Clast Av.	Neo. Ex.	Clast Int.	Clast Av.	Neoblast	Clast Int.	Clast Av.	Neoblast	Neoblast
	(n=1)	(n=4)	(n=7)	(n=2)	(n=2)	(n=19)	(n=1)	(n=5)	(n=12)	(n=3)	(n=8)	(n=11)	(n=7)
SiO_2 (wt%)	50.31	51.21	52.04	50.64	50.97	52.51	51.09	51.90	52.69	50.92	51.40	52.76	52.78
TiO_2 (wt%)	0.80	0.71	0.57	0.86	0.91	0.71	0.81	0.75	0.71	0.92	0.82	0.70	0.69
Al_2O_3 (wt%)	5.92	4.88	3.44	5.80	5.67	2.94	5.16	4.19	3.07	5.34	4.58	3.01	2.66
Cr_2O_3 (wt%)	1.02	1.06	0.81	0.99	0.97	0.81	1.21	1.02	0.70	1.04	0.96	0.64	0.63
FeO (wt%)	2.89	2.62	2.51	2.92	2.94	2.58	2.83	2.76	2.73	2.84	2.81	2.76	2.65
MnO (wt%)	0.05	0.07	0.08	0.06	0.06	0.08	0.06	0.08	0.08	0.09	0.08	0.08	0.09
NiO (wt%)	0.05	0.03	0.03	0.03	0.01	0.03	0.01	0.05	0.04	0.02	0.03	0.04	0.04
MgO (wt%)	14.82	15.29	16.05	14.97	15.11	16.30	15.26	15.79	16.74	15.17	15.53	16.50	16.49
CaO (wt%)	22.58	22.53	22.61	22.45	22.32	22.64	22.46	22.45	22.58	22.43	22.54	22.48	22.66
Na_2O (wt%)	0.61	0.62	0.57	0.62	0.62	0.54	0.68	0.62	0.53	0.66	0.61	0.51	0.49
K_2O (wt%)													
Total (wt%)	99.05	99.01	98.72	99.32	99.59	99.15	99.57	99.60	99.61	99.42	99.34	99.48	99.17
Mg#	0.901	0.912	0.919	0.901	0.901	0.918	0.906	0.911	0.915	0.905	0.908	0.913	0.917
Cr#	0.103	0.130	0.41	0.103	0.103	0.156	0.136	0.140	0.131	0.115	0.125	0.212	0.137

S2.6 –EPMA data (11 of 13).

Clinopyroxene

Texture t.	Mylonite – Cpx recrystallization microstructures						Mylonite – Internal Cpx	Mylonite – Ultramylonitic Cpx+ Ol layers		
ROI*	La19_1ROI27.2			La19_1ROI27.1			La19_1ROI17Interface	La19_1ROI22		
	Clast Int.	Clast Av.	Neoblast	Clast Int.	Clast Av.	Neoblast	Neoblast	Neoblast	Neoblast	Neoblast
	(n=5)	(n=10)	(n=8)	(n=3)	(n=8)	(n=4)	(n=11)	(n=6)	(n=11)	(n=10)
SiO_2 (wt%)	49.99	50.51	52.76	50.44	50.45	53.04	52.19	53.76	53.19	53.22
TiO_2 (wt%)	0.76	0.91	0.68	0.79	0.79	0.66	0.67	0.56	0.62	0.67
Al_2O_3 (wt%)	6.66	5.61	2.75	6.26	6.13	2.38	3.41	2.07	2.42	2.40
Cr_2O_3 (wt%)	0.90	0.91	0.63	1.01	1.00	0.52	0.93	0.41	0.53	0.55
FeO (wt%)	3.01	2.89	2.70	3.09	6.05	2.66	2.39	2.62	2.62	2.67
MnO (wt%)	0.08	0.08	0.08	0.09	0.08	0.07	0.07	0.08	0.07	0.08
NiO (wt%)	9.05	0.04	0.05	0.03	0.03	0.03	0.05	0.04	0.05	0.44
MgO (wt%)	14.75	15.11	16.63	14.94	14.97	16.90	16.00	17.02	16.66	16.73
CaO (wt%)	22.25	22.42	22.64	22.00	22.13	22.75	22.69	23.04	23.01	22.75
Na_2O (wt%)	0.71	0.67	0.50	0.66	0.66	0.74	0.61	0.44	0.49	0.49
K_2O (wt%)										
Total (wt%)	99.15	99.16	99.41	99.32	99.30	99.48	99.00	100.04	99.68	99.60
Mg#	0.897	0.903	0.917	0.896	0.897	0.919	0.923	0.921	0.919	0.918
Cr#	0.083	0.103	0.133	0.098	0.102	0.128	0.160	0.11	0.126	0.134

S2.6 –EPMA data (12 of 13).

| S6 –Clinopyroxene				
Texture t.	Mylonite – Cpx neoblast in Opx recrystallization microstructures			
ROI*	La19_2ROl22	La19_2ROl3	La19_2ROl14	
	Neoblast	Neoblast	Neoblast	
	(n=5)	(n=5)	(n=2)	
SiO$_2$ (wt%)	53.07	52.92	51.52	
TiO$_2$ (wt%)	0.68	0.67	0.73	
Al$_2$O$_3$ (wt%)	2.46	2.63	3.62	
Cr$_2$O$_3$ (wt%)	0.55	0.66	0.63	
FeO (wt%)	2.81	2.78	2.91	
MnO (wt%)	0.08	0.07	0.08	
NiO (wt%)	0.05	0.05	0.05	
MgO (wt%)	16.75	16.79	16.10	
CaO (wt%)	22.70	22.61	22.42	
Na$_2$O (wt%)	0.45	0.50	0.49	
K$_2$O (wt%)				
Total (wt%)	99.61	99.67	98.52	
Mg#	0.914	0.915	0.908	
Cr#	0.133	0.144	0.106	

S2.6 –EPMA data (13 of 13).
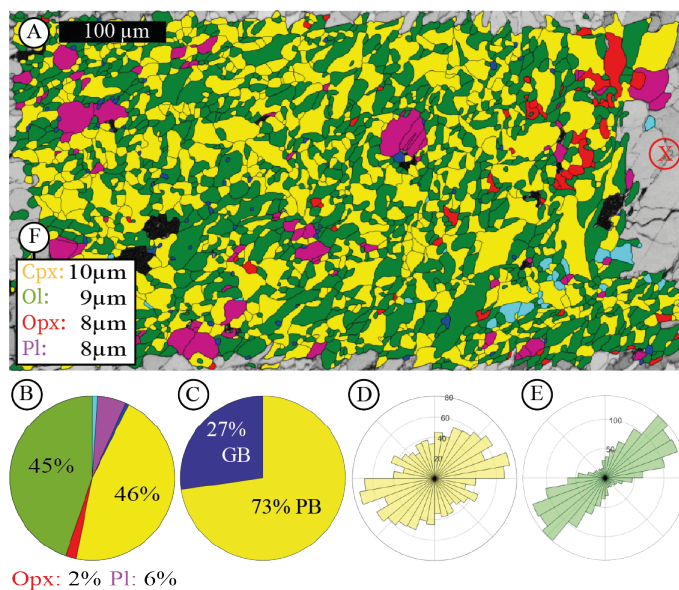
*S2.7 – (A) Microstructure of Cpx porphyroclast in contact to the matrix in the mylonite texture type (red X = parent clast). **B**. Phase composition in area percentages. **C**. Phase and grain boundary percentages. **D**. SPO for Cpx neoblast long axes. **E**. SPO of Ol neoblast long axes. Note the Cpx and Ol dominated phase composition with relatively high amounts of anorthite-rich plagioclase (B) and high phase boundary percentages (C). Cyan colored phase is pargasite. Dark blue phase is Spl. Black are not/ badly indexed regions. For optimal resolution, the reader is referred to the version attached on the CD.*

T (°C)	Orthopyroxene recrystallization				Clinopyroxene recrystallization				(Ultra)mylonitic assemblages			
	T_{BKN}	T_{TA98}	$T_{Ca\text{-}Opx}$	T_{1Cpx}	T_{BKN}	T_{TA98}	$T_{Ca\text{-}Opx}$	T_{1Cpx}	T_{BKN}	T_{TA98}	$T_{Ca\text{-}Opx}$	T_{1Cpx}
Porphyroclast Interior	879	879	865	-	913	913	-	891				
	880	866	864	-	879	879	-	855				
	916	897	926	-	884	861	-	841				
	914	897	929	-	921	898	-	881		*no data*		
	923	868	917	-	920	902	-	883				
	928	883	1011	-	871	831	-	825				
	929	871	1030	-	862	826	-	817				
	910 ±21	880 ±13	935 ±65	-	869	829	-	822				
					871	825	-	819				
					924	877	-	876				
					891 ±25	864 ±34	-	851 ±30				
Internal Neoblasts	-	-	878	-	831	790	855	802				
	882	838	861	855	843	804	904	819		*no data*		
	831	790	855	802	837 ±8	797 ±10	880 ±35	811 ±12				
	857 ±36	814 ±34	858 ±12	829 ±37								
Neoblasts	-	-	830	-	845	820	858	837	836	799	815	820
	888	852	871	873	-	-	-	876	881	828	846	855
	889	793	841	873	864	825	875	842	859 ±32	814 ±21	831 ±22	838 ±25
	-	-	885	-	885	847	900	865	861	828	815	852
	-	-	893	-	-	-	-	- 871	837	801	846	820
	-	-	779	-	860	822	885	837	873	836	841	858
	882	838	851	855	888	847	873	866	858 ±18	818 ±18	833 ±17	841 ±20
	886 ±4	828 ±31	854 ±39	867 ±10	-	-	-	884				
					875	839	917	855				
					879	838	852	860				
					873	887	919	860				
					871 ±14	841 ±22	885 ±25	859 ±16				
Error	± 15	± 31	± 26	± 30	± 15	± 31	± 26	± 30	± 15	± 31	± 26	± 30

S2.10 – *Overview of T estimates by the T_{BKN}, T_{TA98}, $T_{Ca\text{-}Opx}$, and T_{1Cpx} geothermometers. Temperatures (°C) are given for porphyroclast interiors, internal neoblasts and neoblasts for ortho-, clinopyroxene recrystallization microstructures and (ultra)mylonitic assemblages (Opx, Cpx). Symbols used in Fig. 2.14 are indicated next to mean T and its standard deviation for estimations of a given geothermometer and microfabric. The calibration error is given in the last row (light grey). For optimal resolution, the reader is referred to the version attached on the CD.*
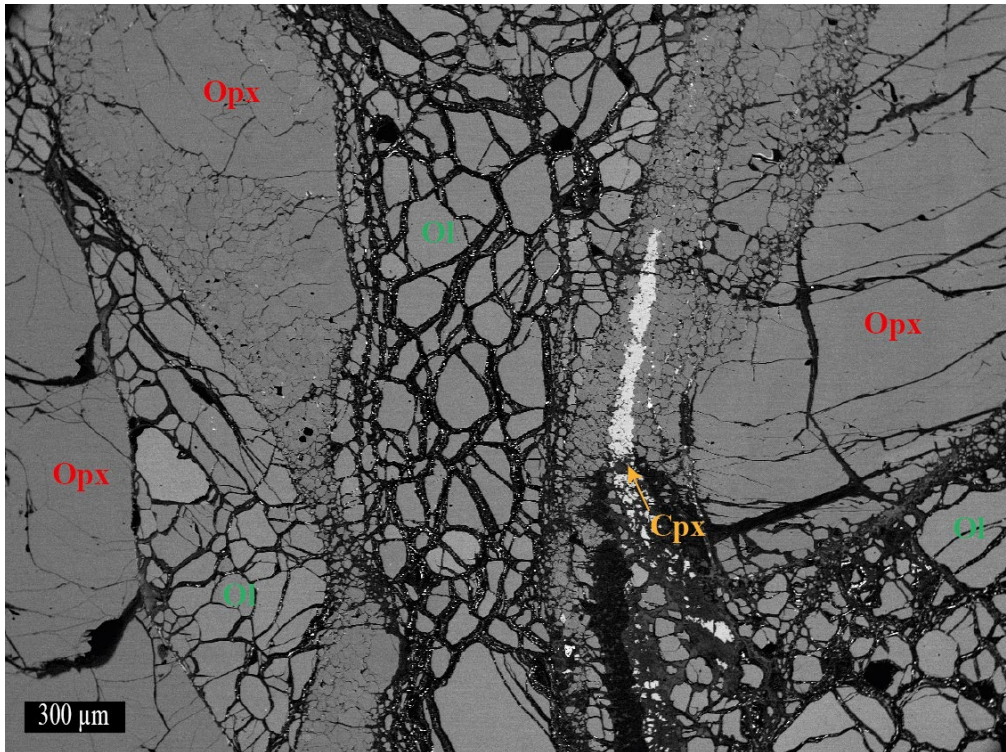
S2.11 *– Dynamic recrystallization in strained xenolith from Kimberly, South Africa. Note, despite extensive simultaneous recrystallization of all phases, no phase mixing is present between the phases. For optimal resolution, the reader is referred to the version attached on the CD.*

Reaction-induced phase mixing and the formation of ultramylonitic bands

Sören Tholen [a,*], Jolien Linckens [a], Catharina Heckel [a], Marina Kemperle [b]

[a] Institute of Geosciences, Goethe University Frankfurt, Altenhöferallee 1, D-60438 Frankfurt a.M., Germany
[b] Institute of Geology and Mineralogy, University of Cologne, Zülpicher Str. 49b, D-50674 Köln, Germany

ARTICLE INFO

ABSTRACT

As for most upper mantle shear zones, mylonitic and ultramylonitic peridotites exposed in the northern Lanzo shear zone display thoroughly mixed, fine-grained (< 25 μm) bands. The weak crystallographic preferred orientations (CPO) of all their phases are indicative for deformation by diffusion creep. Although interpreted as significantly decreasing the strength of the upper mantle if interconnected, the formation process of fine-grained phase mixtures is still debated. Microstructural analysis of gradually higher strained peridotites of the northern Lanzo shear zone revealed the formation of fine-grained (< 25 μm) polymineralic tails adjacent to clino- and orthopyroxene porphyroclasts in mylonitic samples. Phase mixtures (av. 65% phase boundaries) are dominated by neoblasts derived from the porphyroclast (Opx/Cpx) and olivine, with minor abundances (< 10 area-%) of plagioclase, spinel ± amphibole. Neoblast microstructures and mixing of phases directly at the border of the pyroxenes, indicate a reaction of pyroxene porphyroclasts to neoblast phase mixtures. Neoblast temperature estimations (~860 °C), their systematic change in composition, and plagioclase/spinel abundances suggest that continuous net-transfer reactions, enhanced by the spinel lherzolite to plagioclase lherzolite transition are likely the main driving forces for the formation of ultramylonitic phase mixtures in the Lanzo shear zone. These reactions were potentially enhanced by the presence of fluid as evidenced by pargasitic amphibole crystallization. Comparing these results to other upper mantle shear zones and deformed xenoliths, the importance of reactions (melt-rock, fluid-rock and/or metamorphic) for the formation of polymineralic, ultramylonitic bands is confirmed.

1. Introduction

Upper mantle shear zones are complex systems where a variety of processes take place through space and time. During deformation, changes in the PT-conditions (e.g., Ramsay and Graham, 1970; Vauchez et al., 2012), percolation of melts (e.g., Dijkstra et al., 2002) and fluids (e.g., Précigout et al., 2017) can occur. These processes affect the mineralogy and microstructure of the rock, which in turn have a major control on the rheology of the shear zone. In most upper mantle shear zones, a transition in microstructures from relatively undeformed porphyroclastic tectonites, over protomylonites, mylonites and finally to ultramylonites can be observed (e.g., Newman et al., 1999; Dijkstra et al., 2002; Kaczmarek and Müntener, 2008; Linckens et al., 2015). Mylonites and ultramylonites are fine-grained and often polymineralic deformed rocks (Dijkstra et al., 2002; Kaczmarek and Müntener, 2008; Vissers et al., 1997). In these phase mixtures, second-phases can counteract grain growth due to Zener pinning so that the grain sizes remain small (e.g., Linckens et al., 2015). In fine-grained, well-mixed layers, the small grain sizes can cause a switch in the dominant deformation mechanism from dislocation to diffusion creep (e.g., Newman et al., 1999; Dijkstra et al., 2002; Kaczmarek and Tommasi, 2011). Assuming a constant strain rate, this switch decreases the stress and deformation will localize in these layers (Karato and Wu, 1993). If these fine-grained, mixed areas are interconnected, they can further localize the deformation in the shear zones affecting the rheology of the lithosphere (e.g., Brodie and Rutter, 1987; Montési, 2013; Pearce and Wheeler, 2011). The preservation of these weak zones over geological time scales due to Zener pinning and possible, subsequent reactivation might be important for the initiation of plate tectonics (Bercovici and Ricard, 2014).

In order to form fine-grained, well-mixed mylonites and ultramylonites, there needs to be, in addition to grain size reduction, a phase mixing process. Several mixing processes have been described previously. Grain boundary sliding (GBS) can result in phase mixing due to neighbor switching in the dislocation and diffusion creep regime (e.g., Boullier and Gueguen, 1975; Hirth and Kohlstedt, 2003; Précigout et al., 2007; Drury et al., 2011; Farla et al., 2013). In contrast, Hiraga et al.

(2013), report phase aggregation during GBS in deformation experiments. Deformation experiments indicate additionally that relatively high amounts of strain are needed to form phase mixtures by the combined process of dynamic recrystallization and GBS (Linckens et al., 2015). For calcite-anhydrite composites Cross and Skemer (2017) additionally reported the formation of phase mixtures by 'geometric' mixing for torsion experiments. At moderate shear strains ($\gamma \geq 6$) calcite and anhydrite domains were stretched and thinned to 'monolayers' of one or two grain's width. At high shear strains ($17 < \gamma < 57$) their disaggregation led to a thoroughly mixed assemblage. An additional phase mixing process related to GBS is creep cavitation and nucleation (e.g., Précigout and Stünitz, 2016). In the experiments of Précigout and Stünitz (2016) phase mixing is achieved when dislocation creep or diffusional mass transport cannot accommodate GBS, cavities open at grain boundaries and are instantly filled by neoblasts precipitating from an aqueous fluid during diffusion creep. Further evidence for this process might additionally be found in the work of Platt (2015) who described microstructures of recrystallization tails of Opx porphyroclasts from South African xenoliths. Here mixing is restricted to the margins of the tails, where olivine neoblasts were interpreted to crystallize interstitially between dynamically recrystallized grains undergoing grain boundary sliding.

Reaction-induced changes of the phase assemblage can also result in phase mixing. Multiple driving forces for mineralogical changes in upper mantle shear zones were reported, which can be divided into (i) metamorphic reactions, (ii) melt-rock reactions (iii) and fluid-rock reactions. (i) Changes in the PT-conditions lead to garnet peridotite–spinel peridotite, and at shallower depth, spinel peridotite–plagioclase peridotite transitions (e.g Furusho and Kanagawa, 1999; Dijkstra et al., 2004). In addition, PT dependent mineral compositions lead to continuous net-transfer reactions (e.g., Newman et al., 1999). (ii) Percolating melt in disequilibrium with the peridotite leads to melt-rock reactions, which may precipitate neoblasts and dissolve existing grains. Which phases dissolve or precipitate depend on the melt composition, which in turn changes due to its ascent (e.g., Rampone et al., 2018). In particular, Si-undersaturated melts cause olivine crystallization and pyroxene dissolution at deeper mantle depth, and therefore occurs at the early stages of the shear zone evolution (e.g., Dijkstra et al., 2002; Kaczmarek and Müntener, 2008). At shallower lithospheric depth, Si-saturated melts can occur, corroding olivine grains and forming pyroxene and plagioclase (e.g., Kaczmarek and Müntener, 2008). Local changes of melt composition have an additional impact on the local melt-rock reaction (Dijkstra et al., 2002). (iii) Fluid-rock reactions can result in phase mixing by pargasitic amphibole and later stage chlorite/serpentine crystallization (e.g., Hoogerduijn Strating et al., 1993; Précigout et al., 2017; Prigent et al., 2020). In addition, Hidas et al. (2016) inferred that the fluid composition can be locally controlled by the surrounding minerals, allowing alternating dissolution and precipitation of olivine and orthopyroxene, leading to phase mixing. Additionally, Kohli and Warren (2020) reported mylonitic tremolite and olivine mixtures in orthopyroxene reaction tails potentially formed by hydration reactions of lherzolites at 650–850 °C.

In order to determine what processes are important for phase mixing and the formation of the polymineralic (ultra)mylonites we utilized the northern Lanzo shear zone as a natural laboratory and conducted a detailed microstructural and chemical study. In this mantle shear zone, continuously higher strained fabrics are displayed towards the rather homogenous, thoroughly mixed (ultra)mylonitic center of the shear zone (e.g., Kaczmarek and Müntener, 2008; Kaczmarek and Tommasi, 2011; Linckens et al., 2015). Both melt-rock reactions and the spinel peridotite - plagioclase peridotite transition have been suggested as phase mixing processes (e.g., Kaczmarek and Müntener, 2008; Kaczmarek and Tommasi, 2011). Our study evaluates these and other models for phase mixing by focusing on transitions from porphyroclasts (olivine, orthopyroxene and clinopyroxene) to neoblasts in tails and intracrystalline microstructures. By analyzing the phase content,

composition, fabric, texture and mixing intensity we address where microstructurally, when in the shear zone evolution and by what driving force, phase mixing and the creation of ultramylonitic assemblages occurs. We compare the results to other upper mantle shear zones and deformed xenoliths to highlight the importance of reactions for phase mixing and formation of ultramylonites.

2. Geological setting

The Lanzo peridotite massif is situated 30 km north-west of Torino, Italy (Fig. 1B), and is part of the high pressure belt of the western Alps (e.g., Müntener et al., 2005). It is divided by two NW-SE striking shear zones into a southern, central and northern part and covers an area of ~150 km^2 (Fig. 1A) (e.g., Boudier, 1978; Kaczmarek and Müntener, 2008). To the south and east, it is covered by cenozoic sediments of the Po plain (Fig. 1A). To the north, continental units of the Sesia-Lanzo zone are exposed (Gneis minuti, Fig. 1A). In the West, high-pressure meta-ophiolites (Piemontese ophiolitic, Fig. 1A) and mesozoic meta-sediments are present (Fig. 1A; Müntener et al., 2005). Main lithologies are plagioclase lherzolites, spinel lherzolites, pyroxenites and dunites (e.g., Boudier, 1978). Aligned spinel aggregates, plagioclase lenses and elongated orthopyroxene porphyroclasts form the pervasive foliation and lineation (Kaczmarek and Tommasi, 2011). Compositional layering of pyroxene rich and poor cm-scale bands is observed parallel or discordant to the foliation (Boudier, 1978; Kaczmarek and Tommasi, 2011). The orientation of both, foliation and lineation, varies: it shifts from N-S to NE-SW in the southern and central part to NW-SE in the northern shear zone area and N-S in the northern part (Fig. 1A). Numerous igneous rocks are crosscutting mantle foliation and pyroxenite layering (Kaczmarek and Müntener, 2008, and references therein). The mantle assemblage is surrounded by a 3–5 km thick envelope of foliated serpentinite (Debret et al., 2013). Internally, the mantle assemblage is partially and only slightly serpentinized. For a detailed review of the massif's tectonometamorphic history, see Müntener et al. (2005).

Separating the northern and the central part, a high-temperature mantle shear zone (HTSZ) is exposed (Fig. 1A/C) (Kaczmarek and Müntener, 2005, 2008; Kaczmarek and Tommasi, 2011). It is interpreted as the deeper part of a mantle detachment fault between an asthenospheric, southern and a lithospheric, northern block that accommodates the opening of the Piemont-Ligurian ocean, in an ocean-continent transition or an (ultra)slow spreading ridge (Kaczmarek and Müntener, 2008; Kaczmarek and Tommasi, 2011; Müntener et al., 2005). Based on deformation related microstructures, Kaczmarek and Müntener (2008) divided the strained peridotites of Lanzo's northern shear zone into five texture types (Fig. 1C). From least deformed to highly deformed, these textures are: porphyroclastic texture, porphyroclastic fine-grained texture, protomylonite, mylonite and mylonite with ultramylonite bands. Main trends with increasing strain are (i) decreasing vol % of porphyroclasts vs. increasing vol% of neoblasts, (ii) decreasing grain size and increasing elongation of orthopyroxene porphyroclasts, and (iii) decreasing grain size and increasing phase mixing of matrix neoblasts (Kaczmarek and Müntener, 2008; Kaczmarek and Tommasi, 2011). Additionally, grain size distributions in lower deformed samples are generally more uniform than in higher deformed samples. For a detailed revision of the texture types see Kaczmarek and Müntener (2008). The strain gradient is strongly asymmetrical (Fig. 1C). In the SW footwall, the microfabrics gradually change over a width of 1.5 km (Fig. 1C; Kaczmarek and Tommasi, 2011). Additionally, the foliation and the pyroxenite layering gradually rotate parallel to the shear plane over a distance of 2–3 km (Fig. 1C; Kaczmarek and Tommasi, 2011). In the NE hanging wall, deformed peridotites sharply change (~200 m) into porphyroclastic tectonites and lineation and foliation rotate parallel to the shear zone over a significantly smaller width (< 100 m) (Kaczmarek and Müntener, 2008). Kaczmarek and Müntener (2008) and Kaczmarek and Tommasi (2011) reported a sinistral shear sense for the
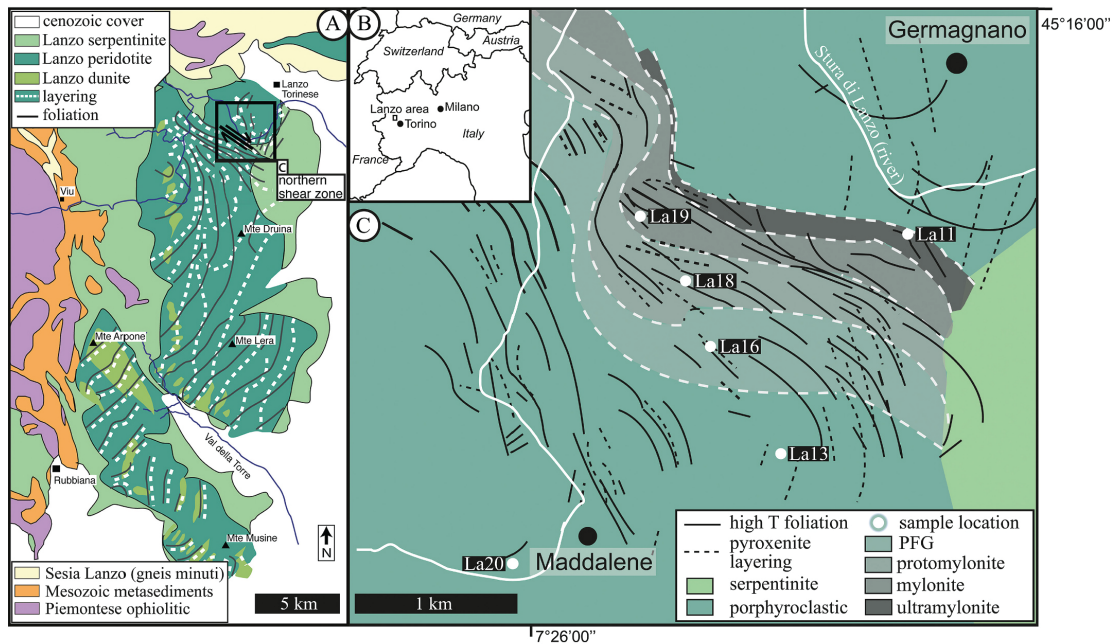
Fig. 1. Overview of the Lanzo massif and a detailed map of the northern shear zone. A. Geological map including peridotite foliation and pyroxenite layering. Map modified after Boudier (1978) and Vieira Duarte et al. (2020). B. Geographic map with the location of the Lanzo area C. The asymmetrical and anastomising northern shear zone with increasingly strained microstructural texture types (grey coloring) towards the contact to the northeastern hanging wall (PFG = porphyroclastic fine-grained). Sample locations are indicated. Map modified after Kaczmarek and Müntener (2008).

HTSZ.

The interplay between melt infiltration and deformation in the northern Lanzo shear zone has been studied by Kaczmarek and Müntener (2008, 2010). Shearing associated with melt percolation and melt-rock reactions led to the localization of deformation at temperatures exceeding 1000 °C (Kaczmarek and Müntener, 2008). Though most of the observed melt-rock microstructures (orthopyroxene and plagioclase replacing clinopyroxene) and interstitial crystallization of orthopyroxene are interpreted as predating the onset of high-temperature shearing, some were also interpreted as having formed during the deformation (e. g., orthopyroxene replacing deformed olivine, interstitial, anhedral crystallization of orthopyroxene in olivine pressure shadows) (Kaczmarek and Müntener, 2008). Additionally, plagioclase-rich aggregates elongated alongside spinel in the foliation plane might indicate deformation-enhanced melt migration (Müntener et al., 2005). For these microstructures Kaczmarek and Müntener (2008) postulate an incongruent reaction from Al-rich spinel to Cr-spinel and plagioclase in the presence of liquid. Kaczmarek and Müntener (2008) suggested that crystallization of interstitial liquids below the solidus formed areas of olivine, plagioclase, and pyroxenes assemblages. Subsequent deformation localized in these finer grained areas, resulted in well-mixed mylonitic bands. The low permeability of these bands blocked the upward migration of mafic melts which crystallized along the shear zone (Kaczmarek and Müntener, 2008). Kaczmarek and Tommasi (2011) additionally suggested that during late-stage deformation, at relatively low temperatures syntectonic net-transfer reactions, associated with the spinel lherzolite to plagioclase lherzolite transition formed mixed ultramylonitic bands. During the exhumation, seawater-derived fluid infiltration and associated nucleation of amphibole in the deformational center (mylonites and ultramylonites) of the shear zone was reported by Vieira Duarte et al. (2020). The amphibole composition and orientation

indicate formation temperatures of 800–850 °C and synkinematic growth.

3. Methods

Samples of the Lanzo shear zone were cut perpendicular to the foliation and parallel to the lineation (X-Z section, Fig. 4). Thin sections were cut and polished to a thickness of ~30 μm. With an optical light microscope, microstructures of interest were located and categorized for further analyses (electron backscatter diffraction (EBSD) combined with energy dispersive X-ray spectroscopy (EDX), and electron probe microanalysis (EPMA)). As the microstructural focus of this research lies on transitions from porphyroclasts to phase mixtures, porphyroclastic tectonite (La-20/13) and porphyroclastic fine grained (La16) samples were excluded for further analysis, because in these samples minor phase mixing, recrystallization and reactions occur.

3.1. EBSD, EDX and EPMA analysis

For EBSD analysis, thin sections were polished with 0.03 μm colloidal silica. BSE, EBSD and EDX analysis were conducted at the University of Frankfurt and the University of Cologne on carbon coated samples. For EBSD measurements, the Institute of Geoscience in Frankfurt is equipped with a JEOL JSM-6490 scanning electron microscope (SEM). Measurement settings were an acceleration voltage of 15–20 kV and a beam current of ~8 nA. For EBSD data acquisition, the program Flamenco (Oxford Instruments HKL Channel 5) and a Nordlys detector (Oxford Instruments) were used. At the Institute for Geology and Mineralogy in Cologne BSE, EDX and EBSD measurements were conducted with a Zeiss Sigma 300-VP field emission SEM equipped with a NordlysNano detector (Oxford Instruments). The acceleration voltage

was set to 20 kV. For the data acquisition the program Aztec was used (Oxford Instruments). The step size was adapted according to grain sizes so that every grain could have at least 10 measurement points (range: 0.5–5 μm). Depending on step size and acquisition time, EBSD map sizes differ over a wide range. In general, large maps (measurement time > 3 h) were obtained using the more stable field emission SEM at the University of Cologne. In Cologne, EDX element maps (O, Mg, Al, Si, Ca, Cr, Mn and Fe) were obtained simultaneously. At both localities, for the consistency of orientations between sample, measurement and post-processing reference frame was checked by measuring a self-prepared quartz standard. It consists of four synthetic quartz crystals with differently oriented c-axis embedded in epoxy. Known orientations of the single crystals and their position in the standard enables to detect possible rotations affecting the spatial or crystallographic data at any given step during analysis and data handling (e.g., Kilian et al., 2016). The EBSD data were cleaned from systematic misindexing of Ol (similar diffraction patterns for orientations rotated 60° around [100]) with Oxford Instruments HKL Channel 5 software. Subsequently, the data were imported into the MTEX 5.3 MATLAB extension (e.g., Bachmann et al., 2010). All additional data processing and analysis were conducted with MTEX 5.3 (http://mtex-toolbox.github.io/). The scripts used for cleaning, grain detection (grain internal misorientation <15°) and subgrain detection (misorientation angle between subgrains <15°), deletion of incomplete grains at the borders of mapped areas and badly indexed grains, crystallographic and boundary analysis etc. are available on request from the authors. During grain reconstruction, the resulting grains were checked against backscattered/forescattered, band contrast images and EDX data if present. The grain analysis consists of grain size (equivalent circular diameter – ECD) and grain shape (orientation of the grains long axis, aspect ratio). Shape preferred orientations (SPO), defined by the orientation of the long grain axis, include all grains of a given phase. Throughout this manuscript, phase abundances are given by "%" referring to area % of EBSD maps. Phase specific texture maps are colored using the corresponding IPF color key given in fig. 2 (Hielscher and Nolze, 2016). The color of each indexed measurement point (pixel) shows which crystal direction is parallel to the X direction of the map which coincides with the lineation of the sample. Grains with similar colors depict therefore similar orientations. Boundary analysis is accomplished by calculating phase specific boundary lengths. Phase (e.g., Ol-Opx) to grain (e.g., Ol-Ol, Opx-Opx) boundary percentages are used to determine the "mixing intensity". In the interest of clarity and length, phase specific boundary analysis is only attached in the supplementary data (S1). All pole figures are lower hemisphere plots. A minimum number of 100 grains was used for ODF (orientation distribution function) calculation with grain mean orientations and a consistent halfwidth of 15° (used for all figures). For the calculation, orientations of incomplete grains at the borders of mapped areas were included. Therefore, grain amounts of grain maps can differ from those for orientation calculation. To facilitate the comparison of ODF plots, the color coding range is consistently fixed from min = 0 mrd (multiple of random distribution) = blue for a random orientation to max = 3 mrd = red (Fig. 2). Higher mrds than 3 are also colored red. The maximum mrd and the amount of analyzed grains is added alongside the J index (Bunge, 1982) (Fig. 2). An ODF example is given in fig. 2. The plot conventions and its legend apply to all ODFs and pole figures throughout the manuscript. The M index (Skemer et al., 2005) is given alongside all orientation data in the supplementary data (S2). Both, J and M Index, express the strength of a given ODF. For a detailed evaluation of both see Skemer et al. (2005). An overview of all CPOs is given in the supplementary data (S3 and S4).

For clarity, the result section will be limited to figures of example microstructures for each microstructure type. Included in these figures are tables and graphs of grain size, modal abundances, aspect ratio, phase boundary %, SPOs and ODFs referring to the depicted microstructure. Average aspect ratios and average grain size are only presented if enough grains were present for a valid statistical statement (*n*
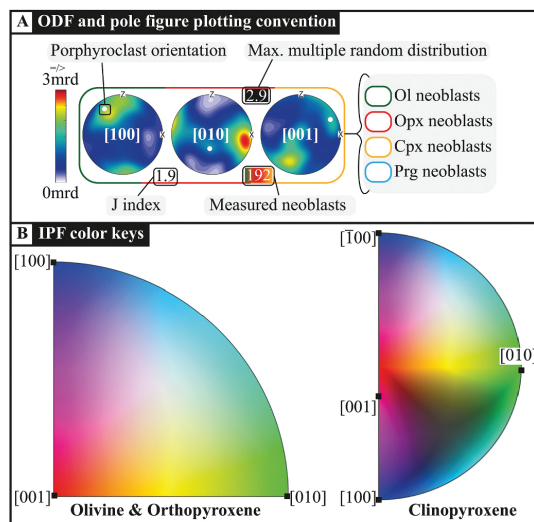

Fig. 2. Plotting conventions and IPF color keys. A. Conventions for ODFs and pole figures. ODF colors correspond to mrd (multiple of random distribution). Frame color represents analyzed neoblast phase (green = Ol, red = Opx, orange = Cpx, light blue = Prg). White number against black background shows max mrd. White number against colored background shows the amount of neoblasts analyzed. Black number against white background shows the J Index. From left to right ODFs and pole plots show [100], [010] and [001]. Porphyroclast orientations are given by white dots. B. IPF color keys for olivine and orthopyroxene (left) and Clinopyroxene (right). (For the interpretation of the reference color, the reader is referred to the web version of this article.)

> 25). In contrast, the results presented in the text include all analyzed microstructures of a given microstructure type and therefore numbers and ratios differ from the data shown in the figure. The complete grain, boundary and orientation data are given in the supplementary data (S1-S4).

Microprobe measurements were conducted using a field emission JEOL JXA-8530F Plus microprobe equipped with 5 wavelength-dispersive spectrometers and located at the Institute of Geoscience at the Goethe University Frankfurt. Two measuring settings were used: for Cpx and Opx porphyroclasts and neoblasts, a 15 kV acceleration voltage and a 20 nA beam current was used for 20 s (Al, Cr, Ca, Na, Mn, Fe and Ni), 30 s (P, K and Ti) or 40 s (Mg and Si) for peaks and 20 s for background (settings and detection limits in suppl. data S5). In order to detect trace element concentrations of Ol clasts and neoblasts, a trace element protocol was used, with an acceleration voltage of 20 kV, a beam current of 100 nA and extended measuring times up to 150 s for peak, plus 150 s for background (Cr, Al, Ca and Ti) (suppl. data S5). Resulting detection limits were 29 ppm for Cr, 9 ppm for Al, 12 ppm for Ca and 16 ppm for Ti (suppl. data S5). For both methods the spot-size was adjusted to the grain size with minimum sizes of 1 μm for small sized neoblasts and maximum 4 μm for porphyroclasts.

3.2. Geothermometry

Microprobe data (suppl. data S6) were used to calculate equilibrium temperatures of porphyroclasts and neoblasts in mylonitic samples. We used the T_{BKN} two pyroxene geothermometer and the T_{Ca-Opx} geothermometer calibrated by Brey and Köhler (1990). To check equilibrium, we additionally applied the two-pyroxene thermometer T_{TA98} by Taylor (1998) and the single-Cpx-thermometer T_{1Cpx} by Nimis and Taylor (2000), which were originally calibrated for Grt peridotites.

Former studies have shown that T_{BKN} and T_{TA98} can be applied under relatively low pressure conditions and outside the garnet stability field (Nimis and Taylor, 2000). T_{BKN} and T_{TA98} temperature estimates were derived using data from spatially close porphyroclasts. Ca saturation for Ca equilibration in Opx, necessary for the application of Opx geo-thermometry is assumed by the presence of Cpx in all analyzed samples. Neoblasts are mostly exsolution free, therefore calculated temperatures are thought to be accurate. For both Cpx and Opx porphyroclasts, exsolution lamellae of the respectively other phase are present. We estimated pyroxene porphyroclast temperatures based on the clast chemistry excluding the lamellae. Cpx porphyroclast estimates are therefore minimum temperatures, affected by exsolution and associated diffusion. Even though care was taken to ensure exsolution free measuring areas in Opx porphyroclasts, it cannot be excluded that micro-Cpx-exsolution lamellae (μm) were analyzed as well. Such mixed analysis leads to an increase of e.g. Ca, which results in an over-estimation of Opx porphyroclast temperatures. For exchange reactions the Mg-Tschermaks in Opx were calculated after Carswell (1991) and the Ca-Tschermaks in Cpx after Knapp et al. (2013).

3.3. Terminology

Mineral abbreviations are used corresponding to Whitney and Evans (2010). Following Kaczmarek and Tommasi (2011) and Kaczmarek and Müntener (2008) we use the term "textures" for the dominant arrangement of grains (size, shape and orientation) at macroscale (thin section and larger). Accordingly, "textures" define samples by their classification in e.g. porphyroclastic, protomylonite, mylonite. The texture nomenclature was taken from Kaczmarek and Müntener (2008), except the "mylonite with ultramylonitic bands" where we adapt the nomenclature of Linckens et al. (2015) and refer to this texture as "ultramylonite". For a detailed description of the samples, we refer to Linckens et al. (2015). For microstructural descriptions, the term "mylonitic" refers to grain assemblages with mean grain sizes between 25 and 200 μm equivalent circular diameter (ECD), whereas

"ultramylonitic" is used for grain assemblages with average ECD < 25 μm.

The term "dynamic recrystallization" is used for strain imposed recrystallization processes, which show indicative microstructures of bulging recrystallization (BLG), subgrain rotation recrystallization (SGR) or grain boundary migration (GBM) (Urai et al., 2011). Classical evidences for dynamic recrystallization include (i) an assemblage of strain free neoblasts surrounding an internally deformed porphyroclasts (where the porphyroclast and neoblast are the same mineral) and (ii) a crystallographic consistency between porphyroclast and surrounding neoblast orientations (e.g., Poirier and Nicolas, 1975). Correspondingly, only microstructures where both criteria are met are addressed as "dynamically recrystallized".

"Grain boundary alignments" (GBAs) are aligned grain and phase boundaries as described in Newman et al. (1999). Grains in these areas are mostly elongated and oriented parallel to each other resulting in GBAs following the long axis of the grains. They mostly form continuous, aligned boundaries over tens to hundreds of μm.

4. Microstructures

One texture type can contain multiple different microstructures (Fig. 3). In mylonite textures for example, porphyroclasts with relatively coarse-grained neoblast tails coexist with ultramylonitic phase mixtures and dynamically recrystallized Ol areas (e.g. Fig. 4B). Therefore, we focus on microstructures and their characteristics rather than on texture types. Three principle microstructural environments were identified in order to evaluate the importance of recrystallization and/or reactions for phase mixing: (i) porphyroclasts and adjacent neoblast tails enable to identify dynamic recrystallization and reaction processes and their in-fluence on phase mixing, (ii) the analysis of intracrystalline and isolated neoblast assemblages in or between pyroxene porphyroclasts helps to evaluate if a connection to the matrix was crucial for phase mixing, (iii) ultramylonitic bands were analyzed to compare their microstructural characteristics with those of i and ii. For each type (i, ii and iii), analyses
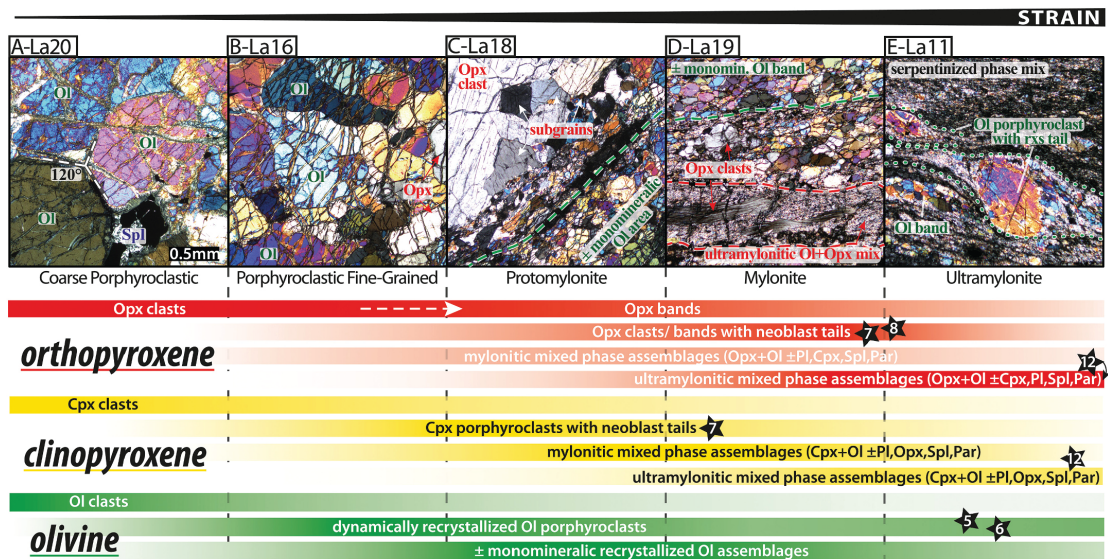

Fig. 3. Overview of orthopyroxene (red bars), clinopyroxene (yellow bars) and olivine (green bars) microstructure types and their occurrence with increasing strain (left to right) in the corresponding texture types (polarized light micrographs, texture categories indicated beneath the images). Scale, shown in A, is the same for all micrographs. The bars color intensity indicates the frequency of the respective microstructure in a texture type. Numbers in stars refer to Fig. # where an example of the corresponding microstructure type is shown in detail.
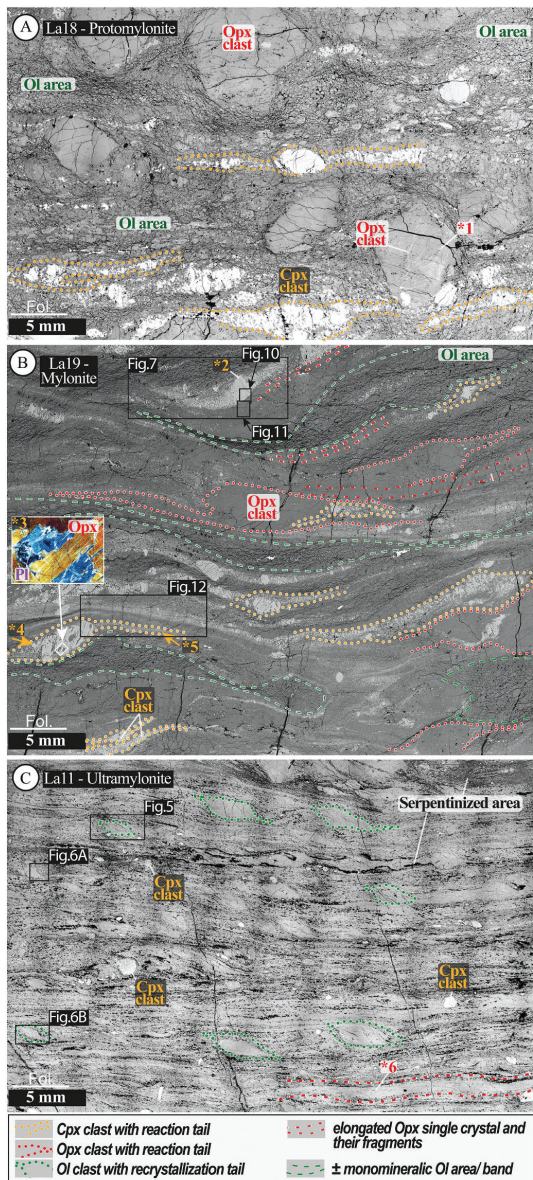
Fig. 4. Backscattered electron (BSE) overviews of increasingly deformed peridotites with analyzed microstructures in black boxes. A. Protomylonitic texture: (*1) Opx porphyroclasts with partly bent Cpx exsolution lamellae. B. Mylonitic texture: (*2) Cpx porphyroclasts with Opx exsolution lamellae and neoblast tail, (*3) micrograph (polarized light) of intracrystalline Pl + Opx assemblage in Cpx porphyroclast, (*4) coarse and (*5) fine grained neoblast tails. C. Ultramylonitic texture: Mixed matrix dominated by Ol and Opx (grey phases) and serpentine (black phase), (*6) fragments of Opx single crystal.

were conducted in different texture types (protomylonites, mylonites and ultramylonites), if present. As phase mixing and recrystallization is concentrated in mylonites and ultramylonites (Fig. 4B/C) the majority of analyzed microstructures is from those texture types.

4.1. Neoblast tails

4.1.1. Almost monomineralic tails adjacent to olivine porphyroclasts

Olivine is the dominant phase in all texture types. Internal grain deformation (undulatory extinction, Fig. 3A) and dynamic recrystallization of Ol grains are already found in low strained coarse porphyroclastic samples. Olivine grains show lobate boundaries, 120° triple junctions and are elongated in porphyroclastic samples (La20, La13; Fig. 3A/B). Additionally, evidence for dynamic recrystallization of Ol by subgrain rotation recrystallization (SGR) is present in porphyroclastic fine-grained samples (La13; Fig. 3B). Almost monomineralic, recrystallized Ol areas and bands in (proto)mylonitic textures (La18, La19; Fig. 3C/D) are defined by the absence of a porphyroclast (Fig. 4A/B). In these microstructures, Cpx, Opx and Spl are present in places but only as minor phases. The internal deformation of recrystallized Ol grains is small (internal misorientation <4°), and 120° triple junctions are frequent (Fig. 3D). The band length is highly variable between a couple hundred μm to several cm (Fig. 4B). Olivine grain size decreases from protomylonite (~630 μm) over mylonite (~250 μm) to ultramylonite (~90 μm) (Linckens et al., 2015). In order to determine the process that led to olivine neoblast formation, the focus of Ol analysis lies on recrystallized porphyroclasts and their transition into neoblasts. Although Ol porphyroclasts are present in all texture types, those with almost monomineralic tails are found in mylonites and more commonly in ultramylonites (Fig. 4C). Three microstructures were analyzed (Fig. 5, 6).

Characteristic for these microstructures are an internally deformed, Ol porphyroclast (Fig. 5A-i/viii) adjacent to an almost monomineralic Ol tail (range: 85–98%; Fig. 5A-ix, 6A/B-v). A relatively coarse grain size (Fig. 5A-iii, 6A/B-ii) and monomineralic assemblage clearly separate the tail from the mylonitic to ultramylonitic, polyphase matrix (e.g., Fig. 5A-i). The porphyroclasts show a rugged grain boundary with indentations of Ol neoblasts (Fig. 5A-ii white arrows). Mean Ol neoblast grain size varies between 21 and 46 μm (Fig. 5-iii, 6A/B-ii). Opx and Cpx neoblasts have a similar, small variability in grain size of 9–15 μm and 8–14 μm. The average Ol aspect ratio is 1.7 (Fig. 5A-v, 6A/B-iv). Opx neoblast have similar aspect ratios to Ol (Fig. 5A-v, 6A/B-iv). In Ol tails, 83% of the total boundaries are grain boundaries (Fig. 5A-x, 6A/B-vi). 97% of those grain boundaries are Ol-Ol interfaces (suppl. data S1). The microstructures exhibit a dependence of the neoblast orientation on the porphyroclast orientation (Fig. 5A-vi, 6A/B-ix). If neoblasts do not display the same orientation as the porphyroclast, they lay in girdles that include the clast orientation (e.g., Fig. 6B-ix). Olivine neoblasts of fig. 5A-vi display a rotation of 90° in the foliation plane for [010] and more diffuse rotations for [001], while [100] still display porphyroclast orientations.

Some Ol tails contain thin, fine-grained (< 30 μm) trails of Opx-Ol grains. Two types of these trails have been found: one-grain thick trails made of Ol-Opx mixtures (< 25 μm in size) located in between coarser Ol grains (25–100 μm) (Type I; Fig. 6A-i); and ~ 100 μm thick Opx-Ol fine-grained trails at the margin of an Ol neoblast tail (Type II; Fig. 6B-i). Type I develops at a small angle (10–35°) to the boundary of tail and matrix (Fig. 6A-i). Type I trails have been observed crosscutting the whole tail, interlinking with other trails, ending at grain boundaries of coarse Ol neoblasts or leaving the thin section plane (Fig. 6A-i). A strong SPO has been observed for both Ol and Opx neoblasts (Fig. 6A-vii/viii) in this type. Type II mixing is situated at distal parts of the Ol tail (Fig. 6B-i) and is connected to an Opx porphyroclast in close vicinity. The smaller grain sizes and the presence of Opx sets the trail apart from the surrounding almost monomineralic Ol tail (Fig. 6B-i). The SPO of Opx neoblasts is almost perpendicular to the weak Ol neoblast SPO (Fig. 6B-vii/viii). The small spatial extent of both mixing types
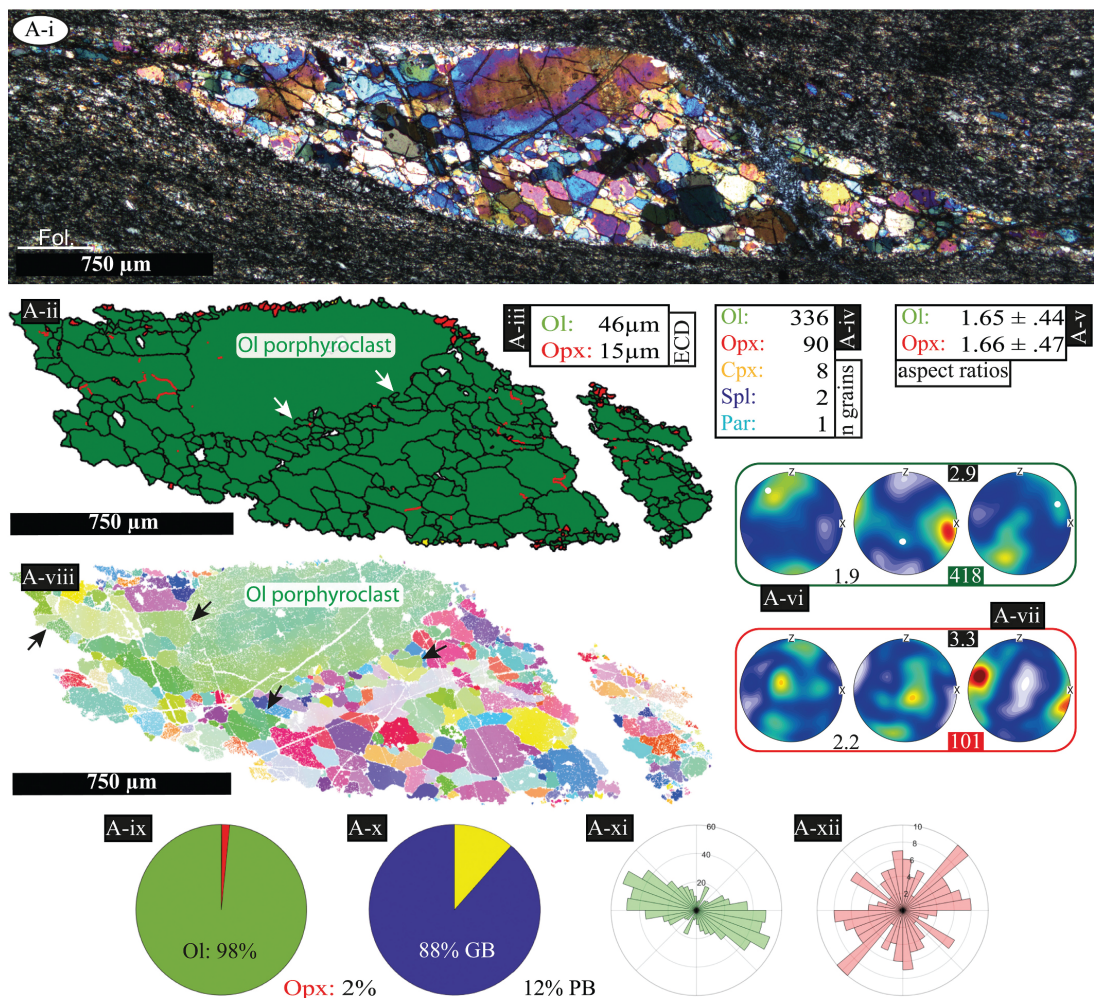
Fig. 5. Example microstructure of an olivine porphyroclast with almost monomineralic neoblast tail in the ultramylonite texture (La-11). A-i. Optical micrograph (crossed polarized light). A-ii. Phase map (red grains = Opx, red lines = subgrain boundaries, black lines = grain boundaries, white arrows = lobate porphyroclast boundary). A-iii. Average grain sizes (ECD) excluding the porphyroclast. A-iv. Number of grains per phase. A-v. Average aspect ratio. A-vi. Olivine ODF with porphyroclast orientation (white dots). A-vii. Orthopyroxene ODF. A-viii. Olivine texture map, (black arrows) grains with a similar orientation as the porphyroclast. A-ix. Area percentages. A-x. Grain (GB) and phase boundary percentages (PB). A-xi. Rose diagram of Ol grain long axes. A-xii. Rose diagram of Opx long axes. (For the interpretation of the texture map by the reference (Fig. 2), the reader is referred to the web version of this article.)

compared to the entire Ol tails results in only intermediate (Type I: 45% PB; Fig. 6A-vi) and low mixing intensities (Type II: 23% PB; Fig. 6B-vi).

4.1.2. Polymineralic tails adjacent to clinopyroxene porphyroclasts

Clinopyroxene is present in all analyzed samples. The abundance of Cpx porphyroclasts decreases with increasing strain. Cpx porphyroclasts start to form neoblasts in the porphyroclastic fine-grained texture (Fig. 3B). Polymineralic tails adjacent to Cpx porphyroclasts are observed up to mylonitic conditions (Fig. 4B). In ultramylonites the amount and the size of Cpx porphyroclasts decreases and polymineralic tails are no longer clearly recognizable (Fig. 4C). Opx exsolution lamellae are common. Internal replacement of coarse-grained Cpx porphyroclasts by Opx + Pl is present in all texture types except

ultramylonites (e.g., Fig. 4B *3).

Tails adjacent to Cpx porphyroclasts are characterized by a single or several Cpx porphyroclasts and a phase mixture of mainly Cpx and Ol (Fig. 7A). Secondary phases are Pl, Opx, Spl and Prg. Spl often forms small, interstitial neoblasts (Fig. 7A/C). Evidence for the relation of the porphyroclast to the polymineralic tails include indentations of Ol and Cpx neoblasts in Cpx porphyroclasts (Fig. 7C *1), as well as the distinct boundaries between tail and Ol + Opx dominated adjacent matrix (Fig. 7C) and almost monomineralic Ol areas (Fig. 7A). In total 6 microstructures were analyzed from mylonitic (La-19) and protomylonitic samples (La-18; suppl. data S1). Occasionally, the transition from Cpx tails into Cpx + Ol dominated layers of ultramylonitic bands is visible (e. g., Fig. 7A). Beside one Ol-dominated tail, Cpx is the dominant phase
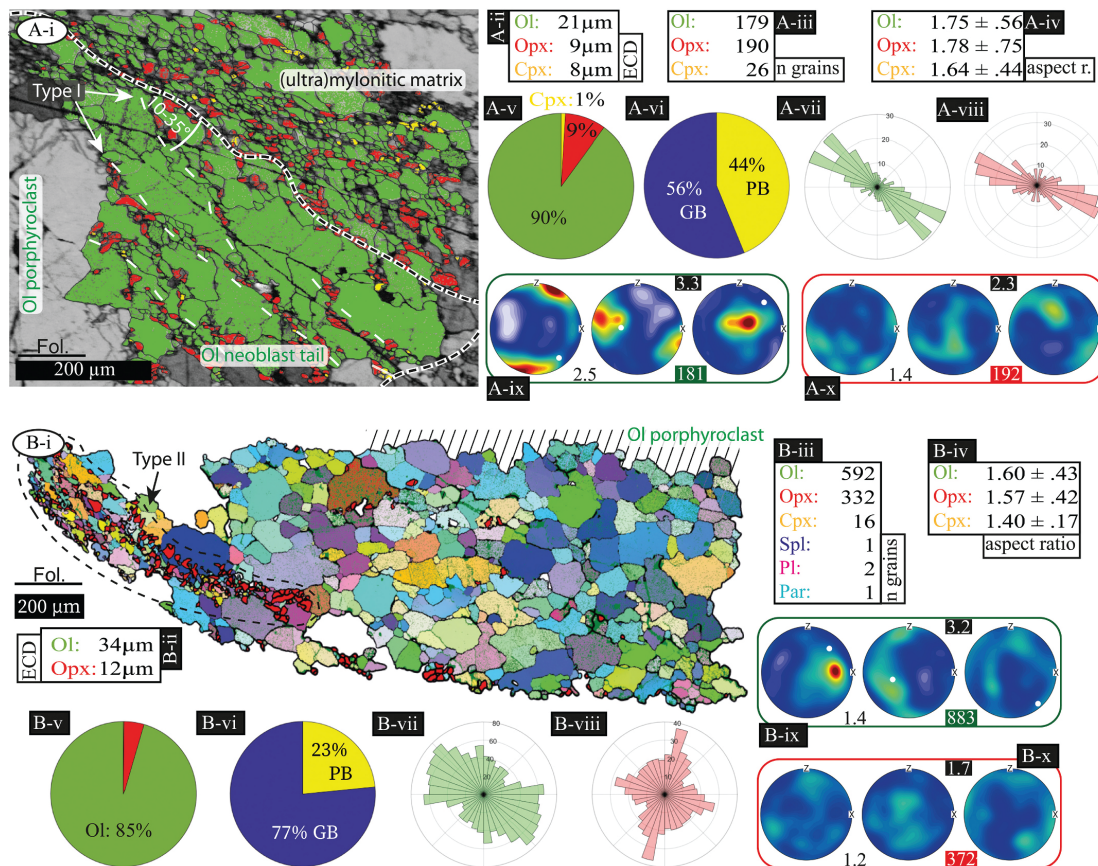
Fig. 6. Phase mixing in neoblast tails of olivine porphyroclasts in the ultramylonite texture type (La-11). A-i. Phase map of almost monomineralic Ol tail (black dashed line) with Ol mixing type I (dashed white lines) adjacent to ultramylonitic matrix. Presented data (A-ii-x) is derived from the Ol neoblast tail. A-ii. Average grain size. A-iii. Number of grains. A-iv. Average aspect ratios. A-v. Phase area percentages. A-vi. Phase and grain boundary percentage. A-vii. Rose diagram of Ol neoblast long axes. A-viii. Rose diagram of Opx neoblast long axes. A-ix. ODF of Ol grains. A-x. ODF of Opx neoblasts. B-i. Texture map of Ol tail with Opx neoblasts added in red (Mixing type II = inside black dashed line, Ol porphyroclast = black hatched area). B-ii. Average grain size. B-iii. Number of grains. B-vi. Average aspect ratios. B-v. Modal abundances. B-vi. Phase and grain boundary percentages. B-vii. Rose diagram of Ol grain long axes. B-viii. Rose diagram of Opx neoblast long axes. B-ix. ODF of olivine grains. B-x. ODF of Opx neoblasts. (For the interpretation of the texture map by the reference (Fig. 2), the reader is referred to the web version of this article.)

(av.: 61%, range: 42–86%; suppl. data S1). Olivine makes up between 7 and 48% (av.: 31%). Plagioclase has an abundance of 6% on average (range: 2–8%). Opx forms on average only 2% (range: 0–9%) and occurs more frequently in marginal areas of the tail (e.g. Fig. 7). Spl and Prg both cover 1% on average. Cpx forms the biggest neoblasts with an average ECD of 20 μm (range: 10–40 μm). Ol (av. 16 μm, range: 9–30 μm) and Pl (av. 17 μm, range: 10–24 μm) have intermediate neoblast sizes and Opx (av. 12 μm, range: 8–21 μm), Prg (av. 11 μm, range: 8–17 μm) and Spl (on average 8 μm, range: 5–16 μm) form the smallest neoblasts. There is a general trend of decreasing neoblast Cpx grain size going from the protomylonite to the mylonite (Fig. 4A/B). However, the range of 9 to 30 μm (av. Cpx ECD) found in different microstructures of a single mylonitic sample (Fig. 4B) emphasizes the dependence of neoblast grain size on the location of the porphyroclast tail (Fig. 4B *4/*5). Cpx neoblasts display a low aspect ratio of 1.6. Intermixed Opx, Ol and Pl have higher aspect ratios of 1.7 (Opx), 1.8 (Ol), and 1.8 (Pl). 66% of all boundaries are phase boundaries (34% grain boundaries). Cpx-Pl boundaries form 64% (av.) of total Pl phase boundaries (suppl. data

S1). 75% (av.) of the total Ol boundaries are Ol-Cpx phase boundaries. Two different SPOs were found for Cpx neoblasts: (i) long axis aligned subparallel to the foliation (suppl. data S7) or (ii) sub-perpendicular to the foliation plane/ to the elongation axis of the neoblast tail respectively (Fig. 7B-vii). If the aligned Cpx neoblasts of type ii are interconnected in their elongation direction, they form "walls" alternated with Ol "walls" (suppl. data S7). Most Cpx neoblasts show a relatively weak CPO (J-index av. 2.2, range 1.3–3.0; e.g. Fig. 7B-ix, suppl. data S3, S4). Stronger Cpx CPOs often show maxima similar to the porphyroclast orientations. Opx CPOs and Ol CPOs are relatively weak with average J indices of 1.6 (range: 1.3–2.1) and 1.4 (range: 1.1–2.0), respectively.

4.1.3. Polymineralic tails adjacent to orthopyroxene porphyroclasts

Orthopyroxene porphyroclasts occasionally show evidence for dynamic recrystallization, such as subgrain formation in high stress domains like contacts between large porphyroclasts (Fig. 3C) in coarse porphyroclastic, porphyroclastic fine-grained and protomylonitic fabrics. Furthermore, at these early stages of shear zone evolution,
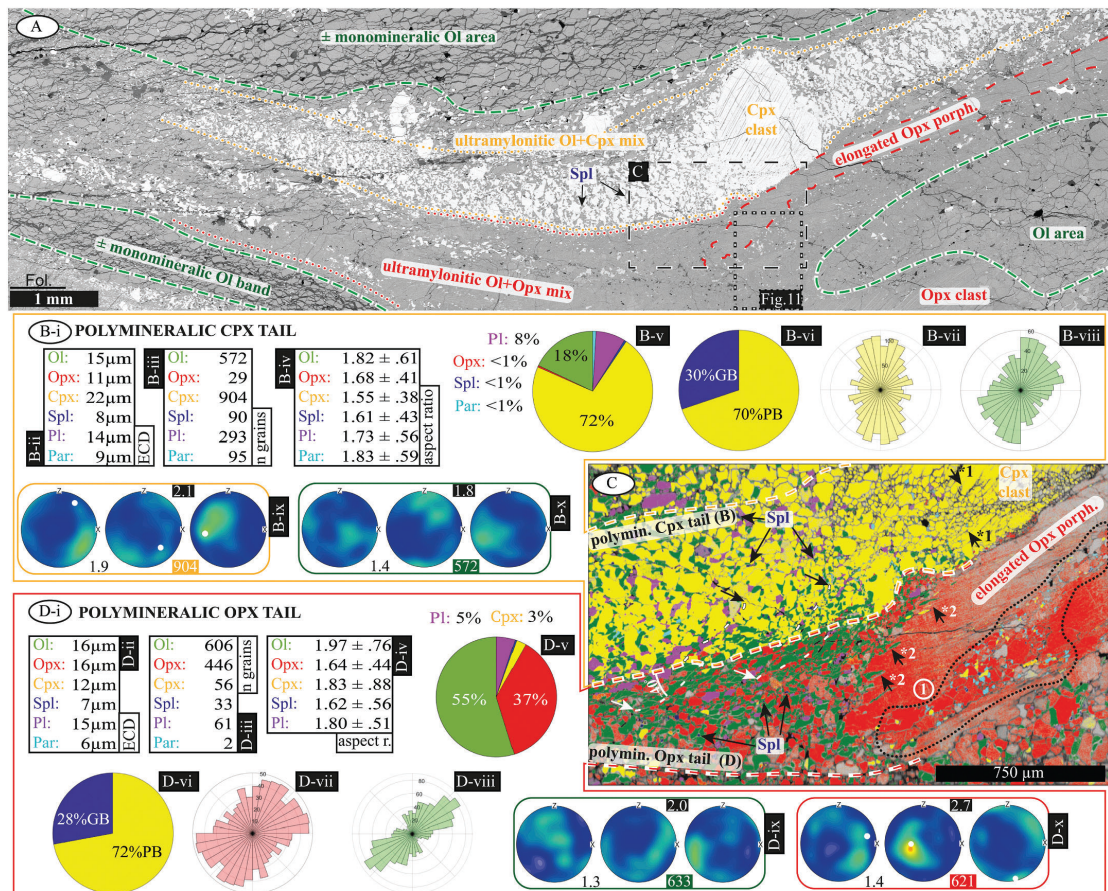
Fig. 7. Clino- and orthopyroxene porphyroclast derived polymineralic tails in the mylonitic texture type. A. BSE overview image with major microstructures (dashed green = almost monomineralic Ol areas, dashed red = elongated Opx porphyroclast, dotted yellow = Cpx neoblast tail, dotted red = Opx neoblast tail), area of EBSD map (dashed black), and location of Fig. 11 indicated. B-i. Microstructural data from Cpx neoblast tail marked in C. B-ii. Neoblast av. grain sizes. B-iii. Neoblasts per phase. B-iv. Av. aspect ratio. B-v. Modal abundances. B-vi. Phase and grain boundary percentages. B-vii. SPO of Cpx neoblasts. B-viii. SPO of Ol neoblasts. B-ix. ODF of Cpx neoblasts and porphyroclast orientation. B-x. ODF of Ol neoblasts. C. EBSD phase map (location indicated in A, same phase colors as in pie charts B-v and D-v). Annotations are (*1, *2) neoblast indentations in porphyroclasts, (white dashed lines with arrows) grain boundary alignments (GBAs) and (black dotted area 1) intracrystalline Opx neoblast area. D-i. Microstructural data from Opx neoblast tail marked in C. D-ii. Neoblast av. grain size. D-iii. Neoblasts per phase. D-iv. Av. neoblast aspect ratio. D-v. Modal abundances. D-vi. Phase and grain boundary percentages. D-vii. SPO of Opx neoblasts. D-viii. SPO of Ol neoblasts. D-ix. ODF of Ol neoblasts. B-x. ODF of Opx neoblasts and porphyroclast orientation.

polyphase mixtures containing Opx neoblasts are only observed occasionally in diffuse patches. The proportion of elongated to equiaxial porphyroclasts increases with increasing strain until mylonitic conditions (e.g., Fig. 4A/B). Even with elongation in places exceeding the thin section scale (aspect ratio > 1:50) these porphyroclasts are single crystals. In mylonites, elongated Opx grains are often folded, kinked, and sheared (e.g. Fig. 8A/B). In this texture type both, equiaxial porphyroclasts and elongated single crystals form neoblast tails. In ultramylonites, only remnants of elongated Opx grains are preserved in the fine-grained polymineralic matrix (Fig. 4C). Porphyroclasts and elongated grains display thin (< 10 μm) exsolution lamellae of Cpx (e.g. Fig. 8C). In all microstructures, Ol and Opx neoblasts in Opx tails show a linear correlation in grain size but with dependence on the microstructure type (Fig. 9).

Polymineralic tails are formed adjacent to equiaxial or elongated Opx porphyroclasts predominantly in mylonites. They are dominated by Ol and Opx ± Cpx, Pl, Prg, Spl (e.g. Fig. 7D-v). For porphyroclasts, but more clearly for elongated Opx single crystals, neoblasts are concentrated at porphyroclast boundaries orientated perpendicular to the foliation (Fig. 8A). Here, porphyroclast grain boundaries are lobate (Fig. 8C *3) and have indentations/embayments filled with Ol neoblasts (Fig. 7C *2). Most neoblasts (Opx + Ol) have a highly irregular grain shape with lobate grain boundaries (Fig. 8D) and in places bottle neck structures (Fig. 8D *1). Small Spl neoblasts are often present as interstitial grains at triple junctions (Fig. 8C). The phase mixtures are dominated by Ol (av. 56%, range: 18–62%) and Opx (av. 37%, range: 16–77%; e.g. Fig. 7D-v, 8D-iv) with both together forming 87–97% (av. 93%) of the total area-%. Cpx abundances are 2–11% (av. 5%). Accessory minerals (< 1%) are Spl, Pl and Prg. Mean Ol grain sizes for this microstructure type vary between 4 and 32 μm (av. 13 μm). Opx grain
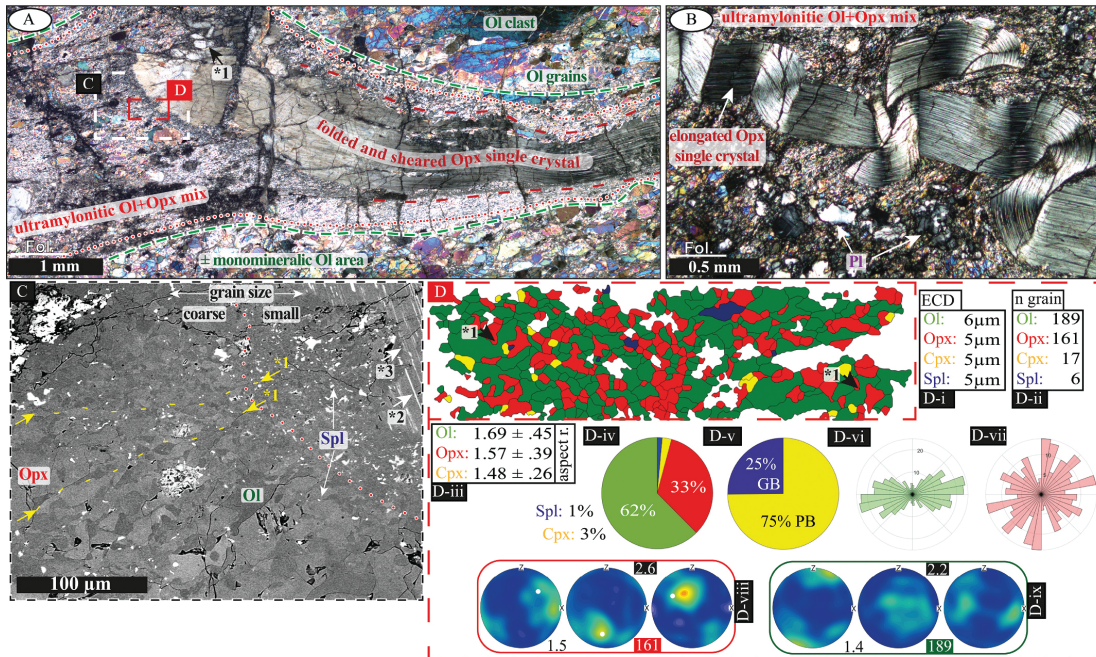
Fig. 8. Example microstructure of elongated Opx single crystal with polymineralic tail in the mylonitic texture type. A. Micrograph (crossed polarized light) of (dashed red line) elongated, folded and (*1) sheared Opx single crystal surrounded by (red dots) ultramylonitic Ol + Opx neoblasts. Indicated are (green dashed) Ol areas and location of (white frame) map C and (red frame) EBSD map D. B. Folded, kinked and sheared Opx single crystal in the mylonitic texture type. C. BSE image of Ol + Opx neoblast mixture with (*1) GBAs, Opx porphyroclast with (*2) Cpx exsolution lamellae and (*3) serrated boundaries. Red dotted line separates areas of smaller and coarser grain size. D. EBSD map of ultramylonitic Ol + Opx mixture in neoblast tail (*1 = bottle neck structures). D-i. Average neoblast ECD. D-ii. Number of grains. D-iii. Average aspect ratios. D-iv. Modal abundances. D-v. Grain and phase boundary percentages. D-vi. Ol neoblast SPO. D-vii. Opx neoblast SPO. D-viii. Opx neoblast ODF with the porphyroclast orientation. D-ix. Ol neoblast ODF.
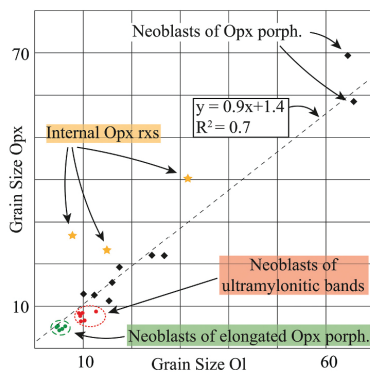

Fig. 9. Grain sizes of Ol and Opx neoblasts from equiaxial Opx tails (black diamonds), internal Opx recrystallization areas (orange stars), ultramylonitic bands (red dots) and elongated Opx single crystal tails (green dots). Linear correlation line (black dashed line) is indicated.

sizes vary between 4 and 40 μm (av. 14 μm). In general, Ol and Opx neoblasts at porphyroclast boundaries display a slightly smaller grain size (~6 μm) than distal neoblasts and have an equiaxial shape (e.g., Fig. 8C). Cpx has an average grain size of 10 μm (range: 4–26 μm). Spl, Pl and Prg average grain sizes are 5 μm. Ol and Opx neoblasts have

relatively high average aspect ratios of 1.8 (Ol, range: 1.6–2.0) and 1.7 (Opx, range: 1.6–2.0). Thin, elongated neoblasts located at the contact area of Opx + Ol and Cpx + Ol dominated tails have the highest aspect ratios for Ol (2.0) and Opx (2.0) of this study. Here, GBAs are present for up to several hundred micrometers in length following a general SPO dominantly formed by the long axes of Ol neoblasts (Fig. 7C white dashed lines). GBAs are oriented oblique (~40°) to the trace of the contact. Additionally, GBAs intensify towards the contact area. GBAs are more pronounced with increasing distance to the porphyroclast (Fig. 8C). Occasionally, elongated neoblasts of Opx are also present in the center of Opx derived tails (Fig. 8C). At transition zones from Opx neoblast tails to almost monomineralic Ol areas, no such grain shapes are observed. Ol and Opx neoblast SPOs are mostly oriented slightly oblique to the foliation (within 20°), with Opx displaying a wider distribution (e.g., Fig. 7D-vii/viii). Phase boundaries form on average 65% of all boundaries. The remaining 35% of grain boundaries are dominated by Ol-Ol (av. 66%) and Opx-Opx (av. 31%) boundaries (suppl. data S1). On average 75% of Opx boundaries are Opx-Ol, and 55% of Cpx boundaries are Cpx-Ol (suppl. data S1). For Pl and Prg, Opx is the main neighboring phase. Beside a generally weak neoblast Opx CPO (J index av. 1.7, range: 1.3–2.1), Opx porphyroclasts have a strong imprint on the crystallographic orientations of Opx neoblasts (e.g. Fig. 8D-viii). For 8 of 10 analyzed Opx neoblast CPOs at least two orientations were identical to the porphyroclast or arranged in girdles together with the clast. Often a maximum is present around porphyroclast orientations (e.g., Fig. 8D-viii). A rotation of neoblast orientations has mostly been observed for [001]. Olivine neoblasts show no or weak CPOs with an average J index of 1.6 (range: 1.3–2.2; e.g. Fig. 8D-ix).

4.2. Intracrystalline and isolated pyroxene microstructures

4.2.1. Isolated clinopyroxene microstructures

Isolated Cpx recrystallization is restricted in-between bigger pyroxene clasts with little or no connection to the matrix (Fig. 10). Due to the relatively low abundance of Cpx, only two exemplary microstructures were analyzed, both of them in mylonites (La-19, Fig. 10A/B).

The neoblast assemblage is controlled by the bordering porphyroclasts. Close to Cpx porphyroclasts it is dominated by Cpx (88%) with minor abundances of Opx (6%) and Spl (1%) (Fig. 10A-v). Compared to other microstructure types, pargasite has a relatively high abundance of 5% (Fig. 10A-v). Opx grains are often adjacent to Opx exsolution lamellae (Fig. 10A -i white arrows). Cpx grains form the largest grains (10 μm; Fig. 10A-ii). Grain sizes of the secondary phases are: Opx 5 μm, Spl 3 μm, Pl 4 μm and Prg 6 μm (Fig. 10A-ii). A well-dispersed second phase content of only 12%, creates 40% phase boundaries (Fig. 10A-vi). 98% of all grain boundaries are Cpx-Cpx contacts (suppl. data S1).

Isolated neoblast areas between Opx and Cpx porphyroclasts are weakly connected to the matrix in the thin section plane (Fig. 10B-i). A two-phase mixture of Opx and Cpx is observed (66% Opx, 34% Cpx) with abundances of other phases (Prg, Spl) < 0.5% (Fig. 10B-v). Opx and Cpx form similar sized grains (Opx = 9 μm, Cpx = 8 μm; Fig. 10B-iii) and have a similar SPO (Fig. 10B-ix/x). 45% of the total boundary length are phase boundaries and 55% are grain boundaries (Fig. 10B-vi). Both Opx and Cpx form 50% of the grain boundaries (suppl. data S1). Also, in regard to phase boundary distribution, Cpx and Opx have an almost identical share of ~60% Cpx-Opx of their total boundaries (suppl. data S1).

Only the microstructure displayed in fig. 10A contains enough Cpx grains to determine a CPO. Cpx neoblast [001] orientations are similar to the porphyroclast [001] orientation (Fig. 10A-viii). The [100] and [010] axes show less dependence on the porphyroclast orientation (Fig. 10A-viii). Opx and Cpx neoblast orientations are similar (Fig. 10A-viii/ix).

4.2.2. Intracrystalline and isolated orthopyroxene microstructures

Isolated Opx microstructures are neoblast assemblages not in contact to the Ol-rich matrix. They form either intracrystalline (Fig. 11A/B black dotted) or at contacts between two or more pyroxene porphyroclasts (Fig. 10B-i). As neoblast assemblages at Opx-Cpx porphyroclast contacts were already described in section 4.2.1, here we focus on intracrystalline neoblast assemblages in Opx porphyroclasts.

Opx is the most abundant phase (85%; Fig. 11C-iv). Clinopyroxene and Prg have an identical proportion of 7%, which is the highest Prg proportion of all analyzed microstructures (Fig. 11C-iv). Ol is an accessory phase (< 1%). Opx neoblast grain sizes are significantly smaller at the Opx + Cpx porphyroclast interface (av. 9 μm; Fig. 10B-ii) than at intracrystalline sites (av. 27 μm; Fig. 11C-i). Additionally, in intracrystalline areas Opx neoblasts have larger grain sizes than all other, mostly interstitial phases (Prg av. 12 μm; Cpx av. 15 μm; Spl av. 7 μm; Fig. 11C-i). Opx aspect ratios are low (1.64; Fig. 11C-viii). Opx grain SPO is perpendicular to the long axis of the host porphyroclast (Fig. 11C-
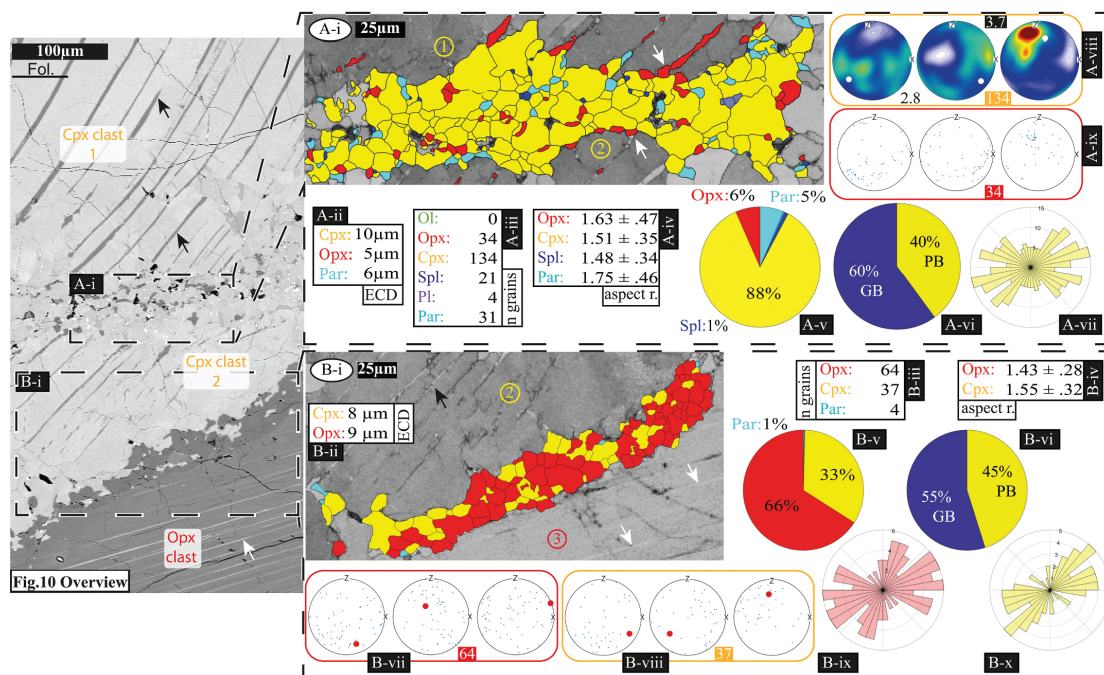

Fig. 10. Example microstructures of isolated Cpx and interface Cpx-Opx recrystallization in the mylonite texture type. Left BSE overview shows their locations between pyroxene clasts (arrows = exsolution lamellae). A-i. Neoblast assemblage between Cpx porphyroclasts (1, 2) with (white arrows) Opx neoblast adjacent to Opx exsolution lamellae. A-ii. Average grain sizes. A-iii. Number of grains per phase. A-iv. Average aspect ratios. A-v. Modal composition. A-vi. Phase and grain boundary percentages. A-vii. Rose diagram of Cpx neoblast long axes. A-viii. ODF of Cpx neoblasts (white dots = Cpx 1 orientations). A-ix. Pole figure of Opx neoblast orientations. B-i. Interface neoblast area between Cpx 2 and Opx 3 porphyroclasts (arrows = exsolution lamellae). B-ii. Neoblast av. Grain sizes. B-iii. Grains per phase. B-iv. Average aspect ratio. B-v Modal composition. B-vi. Phase and grain boundary percentages. B-vii. Pole figure of Opx neoblast orientations (red dots = Opx 3 orientations). B-viii. Pole figure of Cpx neoblast orientations (red dots = Cpx '2' orientation). B-ix. Rose diagram of Opx neoblast long axes. B-x. Rose diagram of Cpx neoblast long axes.
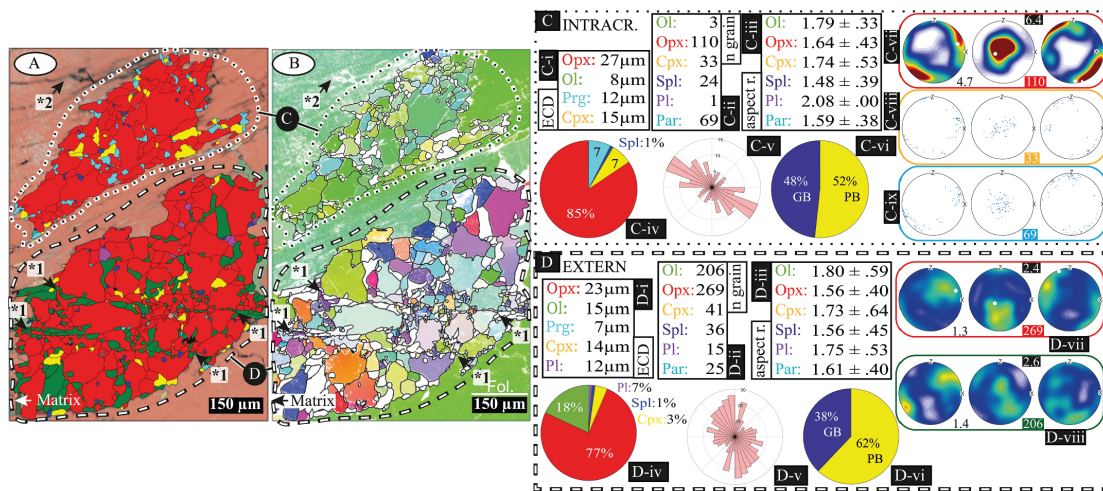
S. Tholen et al.

Fig. 11. Example of intracrystalline neoblast assemblage in Opx porphyroclast next to a mixed neoblast assemblage connected to the matrix (location given in Fig. 7A). A. EBSD phase map (phase colors as in ECD, aspect ratio and grain number tables). Annotation for (black dotted line) intracrystalline neoblast area (data in C), (white dashed line) neoblast area in contact with the matrix (data in D), (*1) aligned mixed neoblasts, (*2) crack in the porphyroclast. B. Texture map. Same annotations as in A. C. Microstructural data of intracrystalline area (black dotted line in A/B). C-i. Average ECD. C-ii. Grains per phase. C-iii. Average aspect ratio. C-iv. Modal abundances. C-v. Opx neoblast SPO. C-vi. Phase and grain boundary percentages. C-vii. Orthopyroxene ODF. C-viii. Pole figure of Cpx neoblast orientations. C-ix. Pole figure of Prg neoblast orientations. D. Microstructural data of neoblast area in contact with the matrix (white dashed line in A/B). D-i. Average ECD. D-ii. Grains per phase. D-iii. Average aspect ratio. D-iv. Modal abundances. D-v. Opx neoblast SPO. D-vi. Phase and grain boundary percentages. D-vii. Orthopyroxene ODF. D-viii. Olivine ODF. (For the interpretation of the texture map by the reference (Fig. 2), the reader is referred to the web version of this article.)

v). Intracrystalline areas have 52% phase boundaries and 48% grain boundaries (Fig. 11-vi). 90% of these grain boundaries are Opx-Opx contacts (suppl. data S1). Pargasite, as second most abundant phase, is mostly in contact with Opx (80% of the total Prg boundaries are Prg-Opx boundaries). The strong CPO of intracrystalline Opx grains is clearly related to the host porphyroclast orientation (Fig. 11C-vii). The orientations of Cpx and Prg neoblasts are similar (Fig. 11-viii/ix).

4.3. Ultramylonitic bands

4.3.1. Clinopyroxene in ultramylonitic bands

(Ultra)mylonitic matrix assemblages of predominantly Ol and Cpx are present in mylonites and ultramylonites (Fig. 12). They are either found as single bands in coarser grained, almost monomineralic Ol matrix or as layers of ultramylonitic bands with multiple Ol + Cpx and Ol + Opx dominated layers (Fig. 12). Three examples of Cpx + Ol dominated ultramylonitic bands were analyzed in mylonitic samples (e. g., Fig. 12E/G).

Depending on the analyzed area, Ol (av. 52%, range: 41–64%) or Cpx (av. 38%, range: 26–50%) is the dominant phase (e.g., Fig. 12E/G-i). Ol and Cpx together make up, on average 92% of the total area (range: 90–96%). The most abundant minor phase is Pl (av. 7%, range: 6–8%). Opx and Spl have, on average, a proportion of 2% and 1%, respectively. Average neoblast grain sizes are Ol 10 µm (range: 9–11 µm), Cpx 9 µm (range: 8–11 µm) and Pl 11 µm (range: 10–11 µm). Unlike the Cpx + Ol assemblages in the tails of Cpx porphyroclasts, where Cpx neoblasts are larger than Ol neoblasts, in the ultramylonitic bands they have a similar grain size within error (e.g., Fig. 12E/G-v). Minor phases have average grain sizes of Opx 7 µm (range: 7–8 µm), Spl 5 µm (range: 4–6 µm) and Prg 6 µm (range: 4–9 µm). Average aspect ratios are 1.7 (Cpx), 1.8 (Ol), 1.6 (Opx, Spl) and 1.8 (Prg). Cpx and Ol show mostly a clear SPO (Fig. 12E-iii/iv). Long axes of Ol neoblasts are oriented at an angle of 10–15° to the foliation (e.g., Fig. 12E-iii, 12G-iv). For Cpx-Ol band of fig. 12G a second Cpx maximum is present oriented 90° to the olivine

SPO (Fig. 12G-iii/iv). Orientation maxima of Cpx show in general a larger spread than Ol maxima (e.g., Fig. 9E-iii/iv). Cpx ultramylonitic bands have the highest ratio of phase mixing in all analyzed microstructure types (av. 69% phase boundaries). Opx forms more phase boundaries with Ol (66% of total Opx boundaries) than with Cpx (28% of total Opx boundaries) highlighting the relatively small abundance of Cpx-Opx mixtures (suppl. data S1). For Cpx, 76% of boundaries are contacts with Ol and 15% are grain boundaries (suppl. data S1). Plagioclase forms most phase boundaries with Ol (40%) and with Cpx (34%) (Fig. 12G-viii). Cpx neoblasts show no (Fig. 12G-viii) or weak CPO (av. J index 1.6, range: 1.3–2.0; Suppl. data S3). The only Cpx CPO present is defined by [100] perpendicular to the foliation plane, [010] dispersed around Y and [001] dispersed around the lineation (suppl. data S3). Olivine neoblasts show absent or very weak CPO (av. J index 1.2 (lowest measured), range: 1.1–1.3).

4.3.2. Orthopyroxene in the ultramylonitic bands

Corresponding to matrix areas of Cpx + Ol, Ol + Opx ultramylonitic matrix assemblages also form layers of ultramylonitic bands (Fig. 12D/ F) or are present as isolated areas in almost monomineralic Ol matrix. At places, the transition from Opx porphyroclast tails into an ultramylonitic bands is visible (Fig. 7A).

The microstructures are dominated by Ol (av. 74%, range: 69–79%) and Opx (av. 14%, range: 11–17%). Minor phases are Cpx (av. 4%, range: 1–6%), Pl (8%, range: 0) and Prg (<1%, range: 0–1%) (e.g., Fig. 12D/F-i). In the ultramylonitic layer of fig. 12D, domains of fine-grained mixed assemblages (Opx, Ol, Pl, Cpx, Spl; domain I) and of coarser grained (>25 µm) Ol neoblasts (domain II) are present. In domain I, Opx and Ol neoblasts yield an average size of 7 µm. Cpx and Spl neoblasts have with 6 and 5 µm similar sizes. Pl (av. 18 µm) forms bigger grains (e.g., Fig. 12D-v, 12F-iii). In domain II, Opx (av. ECD 6 µm, 11 area-%) is present along Ol grain boundaries, sometimes associated with smaller Ol neoblasts (Fig. 12D). Fine grained Opx-Ol mixtures along coarser grained Ol neoblasts are also present in other Ol + Opx
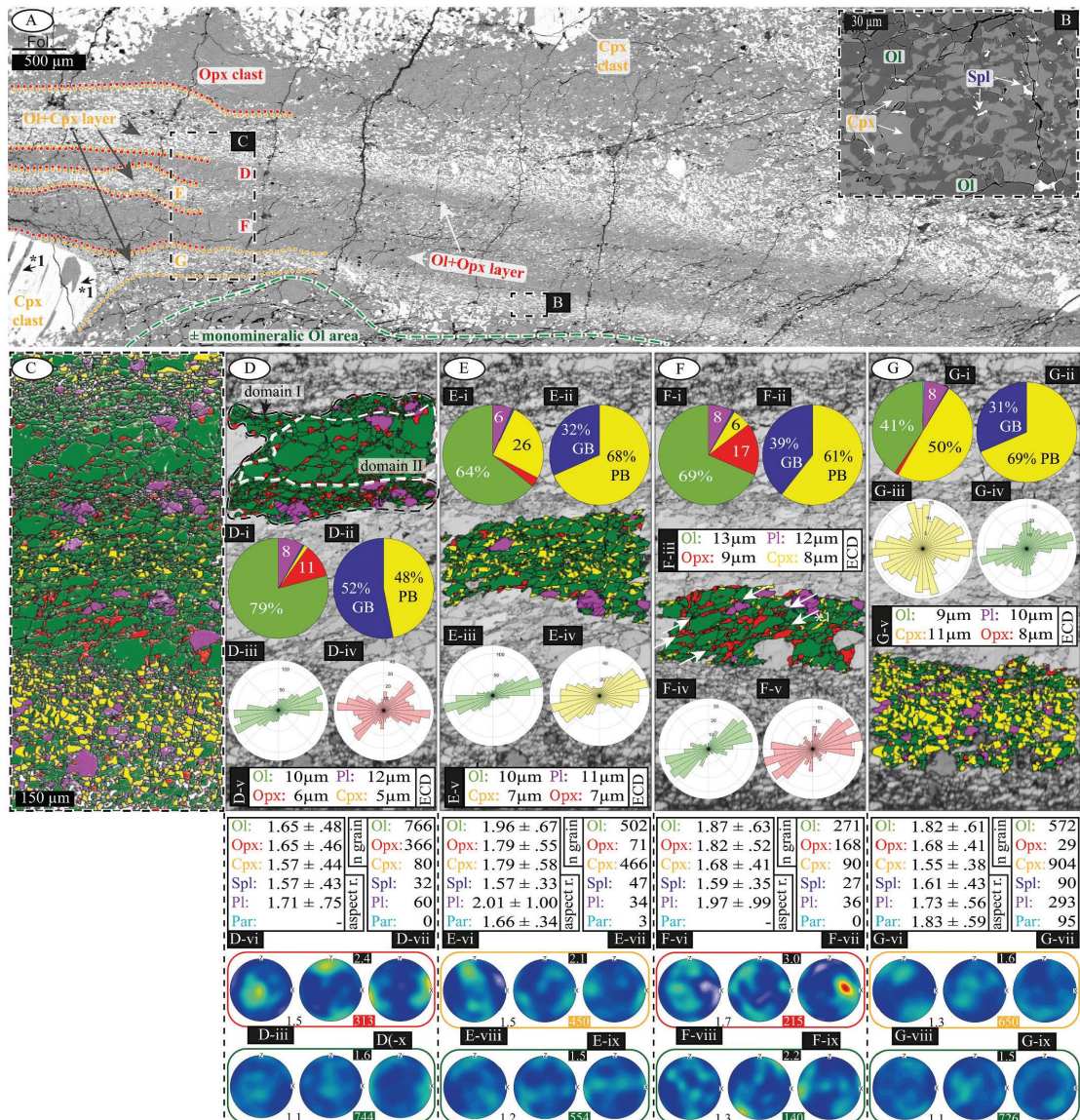
Fig. 12. Ultramylonitic band with layers of predominantly Ol + Opx and Cpx + Ol in the mylonitic texture type. A. BSE overview with main microstructures and locations of map B, EBSD map C and the analyzed Ol + Opx (D, F) and Ol + Cpx (E, G) layers. Annoted is (*1) intracrystalline replacement of Cpx porphyroclast by Opx + Plg along Opx exsolution lamellae. B. BSE image of ultramylonitic Cpx + Ol layer with interstitial Spl. C. EBSD phase map of analyzed microstructures D-G (phase colors as in ECD, aspect ratio and grain number tables). D. Upper Ol + Opx layer. Finer grained domain I and coarser grained domain II are indicated. D-i. Modal abundances. D-ii. Phase and grain boundary percentages. D-iii. Ol neoblast SPO. D-iv. Opx neoblast SPO. D-v. Average ECD. D-vi. Av. aspect ratio. D-vii. Number of grains. D-viii. Opx neoblast ODF. D-ix. Ol neoblast ODF. E. Upper Ol + Cpx layer. E-i. Modal abundances. E-ii. Mixing intensity. E-iii. Ol neoblast SPO. E-iv. Cpx neoblast SPO. E-v. Average ECD. E-vi-. Av. aspect ratio. E-vii. Grain amounts. E-viii. Cpx neoblast ODF. E-ix. Ol neoblast ODF. F. Lower Ol + Opx layer. GBAs are indicated with *1 and white dashed lines. F-i. Modal abundances. F-ii. Mixing intensity. F-iii. Average ECD. F-iv. Ol neoblast SPO. F-v. Opx neoblast SPO. F-vi. Av. aspect ratio. F-vii. Number of grains. F-viii. Opx neoblast ODF. F-ix. Ol neoblast ODF. G. Lower Ol + Cpx layer of EBSD map C. G-i. Modal abundances. G-ii. Mixing intensity. G-iii. Cpx neoblast SPO. G-iv. Ol neoblast SPO. G-v. Average ECD. G-vi. Av. aspect ratio. G-vii. Grain amounts. G-viii. Cpx neoblast ODF. G-ix. Ol neoblast ODF.

ultramylonitic layers (Fig. 12F *1). In general, grain sizes decrease towards contact areas of neighboring Cpx dominated layers (e.g., Fig. 12D). Opx (av. 1.7) and Ol (av. 1.8) neoblasts display high aspect ratios (e.g., Fig. 12D/F-vi) and a strong SPO mostly slightly oblique (~25°) to the foliation and parallel to the aligned fine grained Opx + Ol assemblages on Ol grain boundaries (e.g., Fig. 12D-iii/iv, 12F-iv/v). On

average, phase boundaries make up 55% (range: 48–61%) of the total boundaries. 84% (range: 77–90%) of the remaining grain boundaries are Ol-Ol boundaries. Despite Opx being the second most abundant phase, Opx-Opx boundaries only form 8% (range: 6–10%) of total grain boundaries. Opx neoblasts' [001] axes are aligned parallel to the lineation (Fig. 12D/F-viii). Overall, Opx CPOs are the weakest Opx CPOs
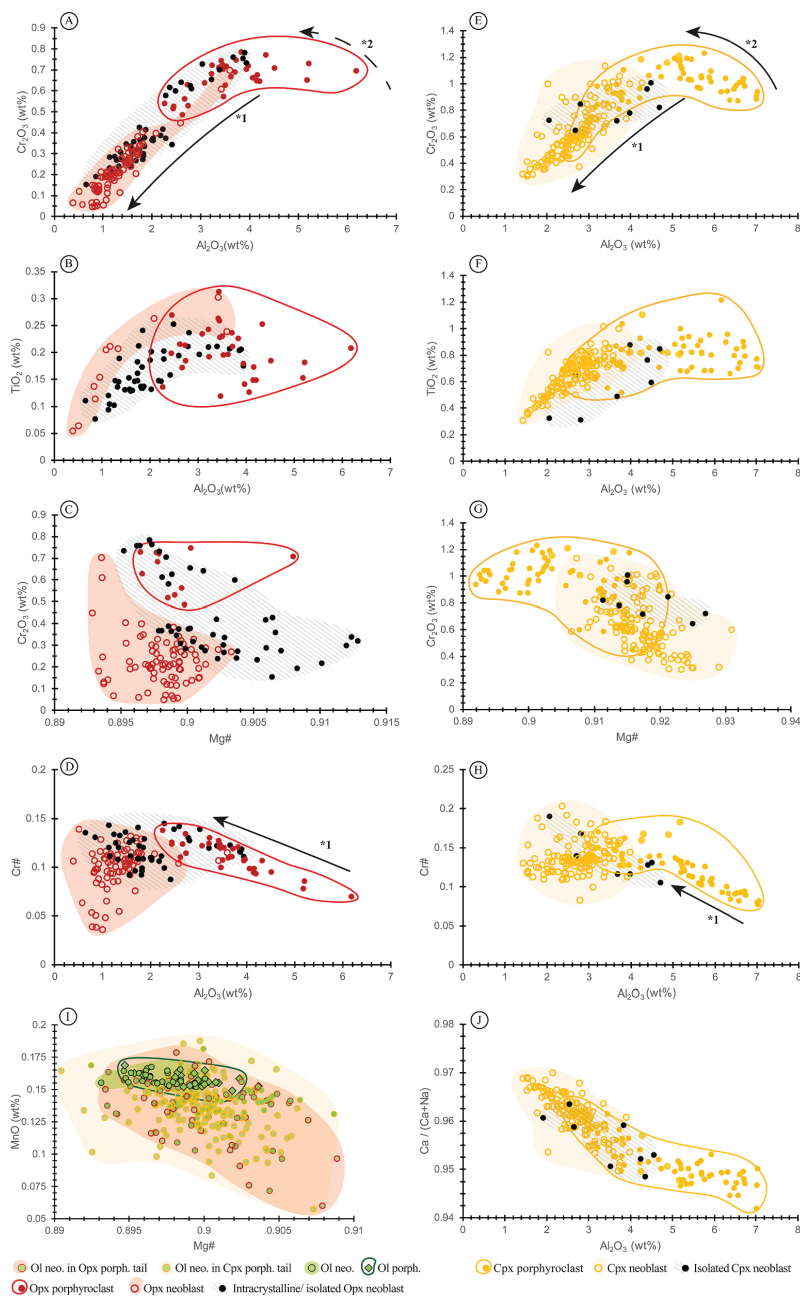

Fig. 13. Geochemical data from porphyroclasts, neoblasts of intracrystalline/ isolated areas, from porphyroclast tails and ultramylonitic bands. A. Al_2O_3 vs Cr_2O_3 of Opx. Arrows illustrate trends of neoblasts (solid) and porphyroclasts (dashed). B. Al_2O_3 vs TiO_2 of Opx. C. Mg# vs Cr_2O_3 for Opx. D. Al_2O_3 vs Cr# for Opx. Arrow illustrates trend for porphyroclasts. E. Al_2O_3 vs Cr_2O_3 of Cpx. Arrows illustrate trends of neoblasts and porphyroclasts. F. Al_2O_3 vs TiO_2 of Cpx. G. Mg# vs Cr_2O_3 of Cpx. H. Al_2O_3 vs Cr# for Cpx. Arrow illustrates trend for porphyroclasts. I. Mg# vs MnO of Ol from almost monomineralic porphyroclast-neoblast assemblages (black outlined symbols) from Cpx + Ol mixtures of Cpx porphyroclast tails (yellow outlined symbols) and from Ol + Opx mixtures in Opx porphyroclast tails (red outlined symbols). J. Al_2O_3 vs Ca/ (Ca + Na) of Cpx.

present in our samples (J index av. 1.5, range: 1.4–1.7). Olivine neoblasts display no CPO (J index av. 1.3, range: 1.1–1-5; e.g. Fig. 12D/F-ix).

5. Mineral chemistry and thermometry

Geochemical data from pyroxene porphyroclast and neoblasts (mylonitic samples, La-19) were obtained to identify possible compositional changes during the formation of neoblasts. Accordingly, analysis of porphyroclasts, isolated and intracrystalline microstructures with low mixing intensities, and of thoroughly mixed polymineralic tails and ultramylonitic bands were performed. Additionally, Ol porphyroclast and almost monomineralic olivine neoblast assemblages were analyzed for Ol major and trace element abundances in ultramylonitic samples (La-11). Detection limits and the microprobe data are displayed in supplementary data S5 and S6, respectively. Additional compositional figures of pyroxenes and Ol are displayed in supplementary data S8 and S9.

5.1. Orthopyroxene

All analyzed Opx (intracrystalline/isolated and mixed neoblasts/ porphyroclasts) is with Mg#s (molar Mg/(Mg + Fe)) exceeding 0.89, enstatite rich (Fig. 13C). A systematic difference between Opx porphyroclasts and neoblasts is present. It is most prominent in the deviation of Al_2O_3 (Fig. 13A/B/D) and SiO_2 abundances (suppl. data S8) for porphyroclasts and neoblasts and by systematic changes of minor element abundances with respect to Al_2O_3 (Fig. 13C, suppl. Data S8). Al_2O_3 was chosen as comparative oxide for pyroxenes because Al contents in Opx and Cpx decrease due to the transition from spinel to plagioclase facies and therefore correspondent to decreasing pressures (Borghini, 2008). Opx porphyroclasts display Al_2O_3 contents of 2.3 to 6.2 wt% (Fig. 13A/B/C) and between 53.3 and 55.9 wt% SiO_2 (suppl. data S8). In general, lower Al_2O_3 (0.4–3.6 wt%; Fig. 13A/B/D) and higher SiO_2 contents (53.7–57.9 wt%; suppl. data S8) were measured for Opx neoblasts. Cr_2O_3 abundances for Opx porphyroclasts vary between 0.5 and 0.8 wt% (Fig. 13A). Opx neoblasts have in general lower values (0.1–0.7 wt%; Fig. 13A/C). Isolated, intracrystalline Opx neoblasts in contrast display the complete Cr_2O_3 range (Fig. 13A/C). For all Opx measurements with $Al_2O_3 < 4$ wt% Cr_2O_3 decreases systematically with decreasing Al_2O_3 (Fig. 13A *1). TiO_2 porphyroclast abundances vary over almost the full spectrum measured between 0.12 and 0.31 wt% (Fig. 13B). Lower TiO_2 abundances (< 0.12 wt%) are only present for Opx neoblasts where TiO_2 decreases from 0.3 to 0.05 wt% with decreasing Al_2O_3 content (Fig. 13B). For a given Al_2O_3 wt%, intracrystalline Opx neoblasts tend to have lower TiO_2 abundances than mixed neoblasts (Fig. 13B). Systematic differences between porphyroclast Mg#s (range: 0.89–0.9) and neoblast Mg#s (range: 0.89–0.91) are very weak if present at all (Fig. 13C). High Mg#s (>0.9) are restricted to isolated, intracrystalline Opx neoblasts (Fig. 13C). Opx porphyroclast Cr#s (Cr# = Cr/((Cr + Al); range: 0.07–0.15) lay within the range of neoblast Cr#s (0.04–1.4) (Fig. 13D). An increase of Cr# in dependence on decreasing Al_2O_3 is only present for porphyroclasts (Fig. 13D *1). No significant change in element abundances from porphyroclasts to neoblasts was observed for MnO and CaO (suppl. data S8). For FeO, a deviation between high abundances ($\geq$ ~6.7 wt%) of Opx neoblasts from tails and low abundances ($\leq$ ~6.7 wt%) for isolated, intracrystalline neoblasts is present (suppl. data S8).

5.2. Clinopyroxene

In all analyzed Cpx microstructures a systematic difference between the mineral chemistry of porphyroclasts, and neoblasts is present, which is particularly evident in Al_2O_3, SiO_2 wt% (Fig. 13E/F/H/J, suppl. data S8) and Mg# (Fig. 13G). Cpx porphyroclasts display higher Al_2O_3

contents (3.1–7.0 wt%) than neoblasts (1.4–4.7 wt%) (e.g., Fig. 13E). SiO_2 contents for porphyroclasts (49.5–53.1 wt%) are in general lower than for neoblasts (51.3–54.6 wt%) (suppl. data S8). The lowest SiO_2 and the highest Al_2O_3 for Cpx neoblasts were measured in isolated microstructures (suppl. data S8, Fig. 13E). For porphyroclasts with $Al_2O_3 > 4.5$ wt%, Cr_2O_3 contents increase with decreasing Al_2O_3 wt% (Fig. 13E *2). Below 4.5 wt% Cr_2O_3 abundances decrease with decreasing Al_2O_3 for all measured groups (Fig. 13E *1). For TiO_2, Cpx porphyroclasts depict variations (0.5–1.2 wt%) independent from Al_2O_3 (Fig. 13F). TiO_2 neoblasts abundances of isolated and mixed microstructures tend to be lower than in porphyroclasts and decrease with decreasing Al_2O_3 (Fig. 13F). Mg#s range from 0.89 to 0.92 for Cpx porphyroclasts and from 0.91 and 0.93 for neoblasts (Fig. 13G). As for Opx porphyroclasts, the increase in Cr# coincides with a decrease in the Al_2O_3 content (Fig. 13H *1). Neoblast Cr#s mostly scatter around the highest values of porphyroclast Cr#s (Fig. 13H). Na_2O and CaO abundances in neoblasts follow the trend already displayed in porphyroclasts. Na_2O decrease (porph.: 0.8–0.5 wt%, neo: 0.7–0.4 wt%) and CaO increase (porph.: 21.4–22.9 wt%, neo.: 22.1–23.4 wt%) with Al_2O_3 (suppl. data S8). Ca/(Ca + Na) shows higher values for neoblasts than for porphyroclasts and generally increases with decreasing Al_2O_3 content (Fig. 13 J).

5.3. Olivine

Ol porphyroclasts and their corresponding neoblasts display for major elements (Si, Mg, Fe, Mn, (Mg#); Fig. 13I, suppl. data S9) as well as for Ca (suppl. data S9) mostly congruent abundances with only slight variations if present at all (Fig. 13I). Most Al, Ti and Cr abundances were below the detection limit (suppl. data S9). Ol clasts have similar Mg#s (av. 0.9 ± 0.002) as Ol neoblasts (av. 0.897 ± 0.002) (Fig. 13I). However, for all ($n = 10$) except one microstructure neoblasts display consistently lower Mg#s than their porphyroclast (suppl. data S9). Ca contents are lower in Ol porphyroclasts (av. 72 ppm) than in Ol neoblasts (av. 87 ppm). Ti, Cr and Al abundances were despite low detection limits for trace elements not measured in significant amounts in Ol porphyroclast tails (neo./porph.; suppl. data S9).

Mg#s (range: 0.89–0.91) and Mn abundances (range: 0.06–0.19) from Ol neoblasts of phase mixtures from pyroxene tails are in general more dispersed than those from almost monomineralic Ol assemblages (av. 0.9, range: 0.89–0.9) (Fig. 13I, suppl. data S9). In general, Ol neoblasts in phase mixtures display slightly higher abundances and higher variabilities for trace elements (Ti, Al, Cr, Ca) than Ol neoblasts of almost monomineralic areas (suppl. data S9). Ol neoblasts in Cpx tails have the highest measured trace element abundances (av. Ti 38 ppm, Al 36 ppm, Cr 67 ppm, Ca 398 ppm) (suppl. data S9). Ol neoblasts from Opx tails have intermediate trace element abundances (av. Ti: 19 ppm, Al: 12 ppm, Cr 18 ppm, Ca 113 ppm; suppl. data S9). In conclusion, Ol neoblasts in phase mixtures display a broader range, and a higher abundance (predominant in Cpx phase mixtures) in trace elements. In addition, these olivines have a broader range of Mg# than Ol neoblasts of almost monomineralic Ol assemblages. However, no trends are observed as present for Opx and Cpx.

5.4. Thermometry

Average T estimations for Opx porphyroclasts are 910 ± 21 °C (T_{BKN}), 880 ± 13 °C (T_{Ta98}) and 935 ± 65 °C (T_{Ca-Opx}) (Fig. 14A, suppl. data S10). In general, the results of the two-pyroxene thermometers (T_{BKN} and T_{Ta98}) and the Ca-in-Opx thermometer are within error (Fig. 14A, suppl. data S10). Exceptions are two porphyroclasts, which show higher T_{Ca-Opx} temperatures than T_{BKN} and T_{Ta98} estimates of the same data (Fig. 14A). For isolated Opx microstructures all average T estimates (857 ± 36 °C (T_{BKN}), 814 ± 34 °C (T_{Ta98}), 858 ± 12 °C (T_{Ca-Opx}) and 829 ± 37 °C (T_{1Cpx}), Fig. 14A, suppl. data S10) overlap in their standard deviation (Fig. 14A, suppl. data S10). Temperature
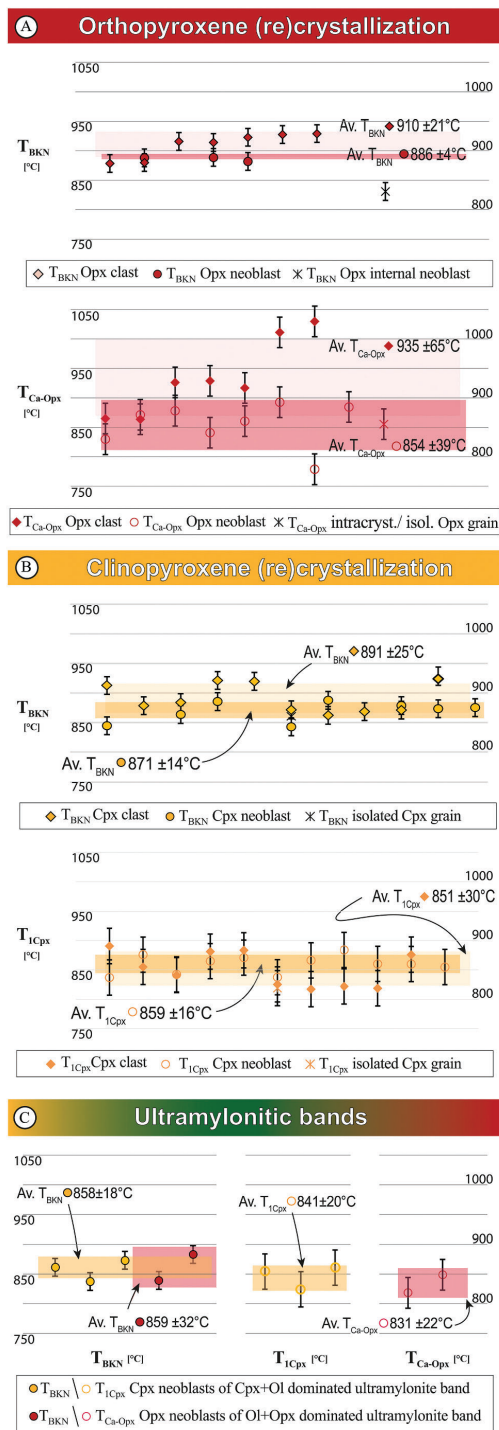
Fig. 14. Geothermal estimations for porphyroclasts (Opx/ Cpx = diamond symbols), neoblasts from intracrystalline and isolated microstructures (Opx/ Cpx = cross symbols), neoblasts of polymineralic tails and ultramylonitic bands (Opx/ Cpx = circle symbols). Displayed are results from T_{BKN}, T_{Ca-Opx} (Brey and Köhler, 1990) and T_{1Cpx} geothermometers (Nimis and Taylor, 2000).

calculations for neoblasts in mixed assemblages derived from Opx porphyroclasts are $886 \pm 4\,°C$ (T_{BKN}), $828 \pm 31\,°C$ (T_{Ta98}), $854 \pm 39\,°C$ (T_{Ca-Opx}) and $867 \pm 10\,°C$ (T_{1Cpx}) (Fig. 14A, suppl. data S10). They agree for a given geothermometer (T_{BKN}/ T_{Ca-Opx}) for all measured microstructures (Fig. 14A).

Cpx porphyroclast T estimations are on average $891 \pm 25\,°C$ (T_{BKN}), $864 \pm 34\,°C$ (T_{Ta98}) and 851 ± 30 (T_{1Cpx}) (Fig. 14B, suppl. data S10). The T_{BKN} estimations all lie in a close range between $862\,°C$ and $924\,°C$ (Fig. 14B). T_{1Cpx} estimations for Cpx porphyroclasts yield systematically lower T (range: 817–891 °C; Fig. 14B). Isolated Cpx neoblasts yield average T (°C) estimates of 837 ± 8 (T_{BKN}), 797 ± 10 (T_{Ta98}), 880 ± 35 (T_{Ca-Opx}) and 811 ± 12 (T_{1Cpx}) (Fig. 14B). Neoblasts in mixed assemblages derived from Cpx porphyroclasts have estimates (°C) of 871 ± 14 (T_{BKN}), 841 ± 22 (T_{Ta98}), 885 ± 25 (T_{Ca-Opx}) and 859 ± 16 (T_{1Cpx}) (Fig. 14B, suppl. data S10). Calculated Ts for different geothermometers are in general consistent for all measured microstructures in multiple samples (Fig. 14B, suppl. data S10). In addition, T estimations of the different geothermometers agree with each other within error.

Data from assemblages of ultramylonitic bands are separated according to their composition. Ol + Opx dominated layers yield average T (°C) estimates of 859 ± 32 (T_{BKN}), 814 ± 21 (T_{Ta98}), 831 ± 22 (T_{Ca-Opx}) and 838 ± 25 (T_{1Cpx}) (Fig. 14C, suppl. data S10). Cpx + Ol dominated ultramylonitic layers yield similar average T (°C) estimates of 858 ± 18 (T_{BKN}), 818 ± 18 (T_{Ta98}), 833 ± 17 (T_{Ca-Opx}) and 841 ± 20 (T_{1Cpx}) (Fig. 14C, suppl. data S10).

6. Discussion

During the shear zone evolution, porphyroclasts of all three primary phases (Ol, Cpx and Opx) formed tails of neoblasts. Where olivine formed mainly monomineralic tails (Fig. 5 and 6; av.: 17% phase and 83% grain boundaries), the ortho- and clinopyroxene porphyroclasts formed polymineralic tails of the original pyroxene and olivine, with minor amounts of the other pyroxene, spinel and plagioclase (Fig. 7, 8). These polymineralic tails are well mixed (av.: ~65% phase and ~ 35% grain boundaries) and continue into ultramylonitic bands in some cases (Fig. 5 and 12). In the following, possible formation processes of almost monomineralic olivine and polymineralic pyroxene tails will be discussed and their role on phase mixing processes will be evaluated.

6.1. Olivine porphyroclasts

Dynamic recrystallization of Ol porphyroclasts is observed in low strained samples (coarse porphyroclastic texture; Fig. 3A), underlining olivine's role as weakest phase under most upper mantle conditions (Boullier and Gueguen, 1975; Karato and Wu, 1993). No phase mixing, related to dynamic recrystallization, was observed in low strained textures (coarse porphyroclastic, fine-grained porphyroclastic). Nevertheless, dynamic recrystallization has been showed to be the driving force of grain size reduction and strain localization during early shear zone evolution in Lanzo (Kaczmarek and Tommasi, 2011).

Ol porphyroclast tails in mylonites and ultramylonites have an almost monomineralic assemblage and low mixing intensities (Fig. 5, 6). Often, associated neoblasts have a small to moderate deviation in misorientation angle (0–40°) from the porphyroclast orientation (Fig. 5F) with grain CPOs clearly related to clast orientations (Fig. 5G, 6A-x, 6B-ix). These results are consistent with those by Kaczmarek and Tommasi (2011) who also reported the internal deformation of Ol porphyroclasts (e.g., Fig. 5F) with a high density of subgrains and the

predominance of small rotation angles (<15°) in correlated Ol misorientation histograms. Following Kaczmarek and Tommasi (2011), dynamic recrystallization of Ol porphyroclasts by SGR is therefore plausible to explain the formation of almost monomineralic tails in mylonite and ultramylonite samples. Contradictory for SGR are high misorientation angles of several grains directly at porphyroclast grain boundaries (Fig. 5F). However, rotations of individual grains accommodating ongoing deformation in the recrystallization tail could explain the variety and the presence of high misorientation angles (Sakai et al., 2014). Elongated, irregular grain shapes and lobate boundaries of distal grains and their bigger grain size compared to those close to the Ol porphyroclast (Fig. 5B) indicate grain growth by GBM recrystallization in the tail (Fig. 5B). Following Kilian et al. (2011) who suggested a precipitation of K-feldspar along aligned grain boundaries and in cavities formed during dynamic recrystallizations (SGR + GBM), mixing structures along bigger Ol grains inside of recrystallization tail (Fig. 6A-I type I) and also on their edges (Fig. 6B-I type II) could indicate precipitation of Opx neoblasts during dislocation creep. Similarly, Czertowicz et al. (2016) reported microstructures similar as type I (Fig. 6A), with Opx neoblasts along Ol grain boundaries in the Anita Peridotite, New Zealand. Following Menegon et al. (2015), Czertowicz et al. (2016) suggest a precipitation of Opx from fluids in creep cavitations along Ol grain boundaries. The chemical components required for the Opx precipitation are thought to be mobilized along the grain boundaries.

6.2. Internal recrystallization of Opx and Cpx porphyroclasts

Pyroxenes rarely show evidence of porphyroclast recrystallization in coarse porphyroclastic and porphyroclastic fine grained textures (Fig. 3A/B). If present, formation of subgrains is restricted to small areas close to the grain boundary (Fig. 3C).
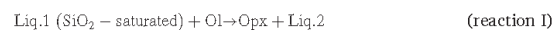
In the (proto)mylonites, isolated and intracrystalline pyroxene microstructures have a host-phase dominated assemblage, low mixing intensities and neoblast orientations depending on the porphyroclast orientation (Fig. 10A/B, 11C). Phase mixing of Opx and Cpx is spatially dependent on exsolution lamellae of the porphyroclasts, resulting in low mixing intensities. The relatively high amount of Ti-pargasite (Prg) in isolated microstructures (Fig. 10A-v and 11C-iv), emphasizes the presence of liquids during neoblast formation and their rather late formation in terms of the shear zone evolution with $T < 1050\,°C$ (Kaczmarek and Müntener, 2008). Consequently, high mobility of the fluid along fractures in porphyroclasts (e.g., Fig. 11A/B *2) and at grain boundaries is required. The relatively strong CPOs of isolated Opx and Cpx microstructures (Fig. 10A-viii, 11B/C-vii) often coincide with similar orientations of intermixed neoblasts of Prg and Cpx/Opx, respectively (Fig. 10A-ix and 11C-viii/ix). Concordance of amphibole (tremolite) and Cpx CPOs was reported by Kohli and Warren (2020) for deformed peridotites from the Shaka Transform Fault. The inherited amphibole CPO was explained by the shared, monoclinic crystal structure and a topo- or epitactic growth (Kohli and Warren, 2020; Putnis et al., 2006). Even at neoblast areas between Opx and Cpx clasts, phase mixing intensities are intermediate with neoblasts concentrating at boundaries of their respective host (Fig. 10B). Low mixing intensities, orientations depending on the porphyroclast and host phase dominated assemblages with high amounts of pargasite indicate fluid assisted dynamic recrystallization as formation process. A formation of pargasite by a local hydrous, Si-saturated melt is unlikely. Melt-rock reactions of such melt should be observable along grain boundaries in the matrix and especially at almost monomineralic Ol areas. Contrary, these microstructures are isolated and intracrystalline. As fig. 11 demonstrates neoblast tails adjacent to the intracrystalline microstructures which should be in contact with such melts rather show the crystallization of Ol neoblasts which would not be expected with hydrous Si-saturated melt. However, the small number of isolated pyroxene microstructures analyzed is only suitable for assumptions on the formation process behind pargasite.

### 6.3. Polymineralic tails adjacent to pyroxene porphyroclasts

Tails derived from the pyroxene porphyroclasts are different from Ol recrystallization tails and isolated and intracrystalline pyroxene recrystallization. The pyroxene derived tails are polymineralic, showing high mixing intensities. Furthermore, they show no similarity between porphyroclast and neoblast orientations. The most striking pattern for these microstructures is the occurrence of Ol and host phase neoblasts with secondary Pl and Spl directly at grain boundaries of the porphyroclasts (e.g., Fig. 7, 8). The Opx and Cpx dominated tails can be clearly distinguished in the samples (Fig. 4B). These observations indicate that these polymineralic tails were formed by reactions rather than by dynamic recrystallization. These reactions could be melt-rock reactions or metamorphic reactions.

6.3.1. Melt-rock reactions

Beside the replacement of Cpx by Opx + Pl at exsolution lamellae in Cpx porphyroclasts (e.g. Fig. 4B *4) no other melt-rock reaction described by previous studies (vermicular Opx growing at expense of deformed Ol, replacement of elongate Spl by undeformed Pl) were found in the studied microstructures. As most evidence of melt-rock reactions were described in low strain textures (Kaczmarek and Müntener, 2008; Müntener et al., 2005) and the replacement of Cpx is only present inside of porphyroclasts of higher strain textures these melt-rock reactions are interpreted to occur prior to the formation of the analyzed microstructures. Consistently, Müntener and Piccardo (2003) and Müntener et al. (2005) interpret the melt presence as a diffuse porous melt flow at a regional scale. Melt-rock interactions in the northern Lanzo shear zone region were expressed by reactions I and II of Kaczmarek and Müntener (2008).

Liq.1 $(SiO_2 - saturated) + Ol \rightarrow Opx + Liq.2$ (reaction I)

$Cpx + Liq. \rightarrow Opx + Pl \pm Ol$ (reaction II)

Following Kaczmarek and Müntener (2008), these reactions lead to neoblast crystallization, which were subsequently deformed under moderate, broadly distributed stress. Fine grained, mixed assemblages found in mylonites (Ol + Pl + Opx) were thought to represent interstitial melts that crystallized once the solidus was hit. This led to the interpretation of melt presence during localized shearing (Kaczmarek and Müntener, 2008). Our observation, that ultramylonitic phase-mixtures of Opx + Ol and Cpx + Ol derive from polymineralic tails of pyroxene porphyroclasts, contradicts the melt-rock reactions I and II. In order to form Ol-rich phase mixtures close to pyroxenes, the melt would have to be Si-undersaturated. Locally Si-undersaturated melt due to dissolution and crystallization with differing phases (reaction III) was described for the Othris peridotite (Dijkstra et al., 2002):

$Opx + SiO_2 - undersaturated\,melt \leftrightarrow Ol + SiO_2 - saturated\,melt$
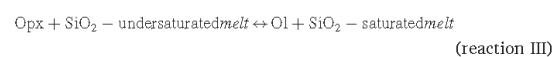
(reaction III)

In regard to the observed microstructures, reaction (III) could explain the irregular margins of Opx porphyroclasts with numerous Ol embayments (e.g. Fig. 7C), combined with elongated Opx and Ol neoblasts in the surrounding mixed assemblage (e.g., Fig. 8B) which were also described for Othris peridotites (Dijkstra et al., 2002). Melt assisted shearing, melt-rock reactions and the formation of a fine grained ultramylonitic matrix was also reported by Degli Alessandrini (2018) in sheared metagabbros of the lower crust. In the case of the Lanzo lherzolite, Cpx can also react with the melt (III), forming olivine. However, Si-undersaturated melt causing pyroxene dissolution and Ol crystallization cannot explain the occurrence of Pl (av. 6%) in phase mixtures of recrystallized Cpx porphyroclasts. As Pl grains are not interstitial, similar sized as Cpx and Ol neoblast and already present close to the Cpx porphyroclasts (Fig. 7C) a later stage formation of Pl seems implausible. Furthermore, Dijkstra et al. (2002) reported evidence of these reactions in tectonite protoliths, thus in the early shear zone evolution, and
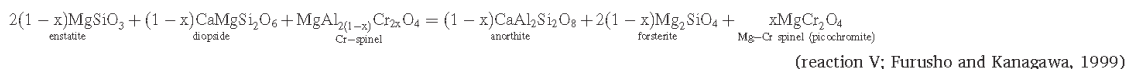
therefore postulated a formation temperature for those corrosion/ dissolution reactions and the formation of fine-grained assemblages of 1100 °C. For the Lanzo shear zone, no such microstructures were observed in the less deformed textures (i.e. coarse-grained and fine-grained porphyroclastic textures). Neoblasts from Opx and Cpx tails, as well as from ultramylonitic bands yield uniform temperatures (869 ± 18 °C (T_{BKN}), 831 ± 24 °C (T_{Ta98}), 862 ± 37 °C (T_{Ca-Opx}) and 856 ± 18 °C (T_{1Cpx}). As most geothermometers give a similar average calculated temperature (within error), estimates are thought to be accurate. Taylor (1998) showed that T_{BKN} overestimates temperatures of fertile peridotite (Nimis and Grütter, 2010). Accordingly, T_{Ta98} estimates are generally lower than T_{BKN} (Fig. 14). Differences between estimates of porphyroclast and neoblasts are thought to depict the degree of porphyroclast equilibration. In contrast to Kaczmarek and Müntener (2008) who observed compositional zoning of Opx porphyroclasts, most of our porphyroclast-neoblast pairs give similar calculated temperatures

shear zone's activity has been under decreasing PT conditions of the transition from spinel to plagioclase peridotite facies, e.g. associated with continuous reactions involving plagioclase and spinel (Kaczmarek and Müntener, 2008, 2010; Kaczmarek and Tommasi, 2011). Olivine and Cpx neoblasts in Cpx tails are often associated with Pl (6%, 22% Pl-Ol boundaries, 64% Pl-Cpx boundaries of total Pl boundaries) and interstitial Spl (1%, 44% Spl-Ol boundaries, 44% Spl-Cpx boundaries of total Spl boundaries, e.g. Fig. 7). The amount of Pl present in pyroxene tails varies between Cpx tails (av. 6%) and Opx tails (av. 2%). In total, the obtained Pl abundances agree with field observations (1–5 wt.-%) and are at the lower range of experimental (5–15 wt%) literature data for Pl peridotites formed by this facies transition (Borghini et al., 2010; Furusho and Kanagawa, 1999; Newman et al., 1999). Furthermore, Pl is more abundant in areas where small amounts of coarse grained Spl is present, indicating an influence of the spinel-plagioclase transition expressed by:

$$Al-rich\ spinel_0 + Al-rich\ pyroxene_0 \leftrightarrow plagioclase + olivine + Al-poor\ pyroxene_1 + Cr-rich\ spinel_1 \qquad \text{(reaction IV; Borghini et al., 2010)}$$

and

$$2(1-x)MgSiO_3 + (1-x)CaMgSi_2O_6 + MgAl_{2(1-x)}Cr_{2x}O_4 = (1-x)CaAl_2Si_2O_8 + 2(1-x)Mg_2SiO_4 + xMgCr_2O_4$$
$$\underset{\text{enstatite}}{} \quad \underset{\text{diopside}}{} \quad \underset{\text{Cr-spinel}}{} \quad \underset{\text{anorthite}}{} \quad \underset{\text{forsterite}}{} \quad \underset{\text{Mg-Cr spinel (picochromite)}}{}$$

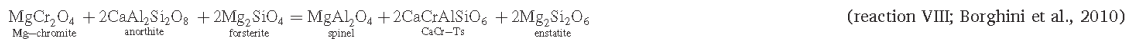$$\text{(reaction V; Furusho and Kanagawa, 1999)}$$

(Fig. 14), which indicates that porphyroclasts reached equilibrium with the neoblasts, possibly by enhanced diffusion. Lower temperature estimates for ultramylonites from previous work (La-11, 740 ± 16 °C (T_{Ca-Opx}), Linckens et al., 2015) however demonstrate that the innermost part of the shear zone accumulated strain over a longer interval of temperature. Therefore, our estimations of pyroxene reaction microstructures in mylonites, clustering around 800 °C (range T_{BKN}: 836–888 °C; Fig. 14), is consistent with estimates by Kaczmarek and Müntener (2008), whereas Linckens et al. (2015) give a minimum, sub-solidus temperature for crystallization and phase mixing. Both T estimates are significantly lower than the formation temperature of phase mixtures postulated for Othris (Dijkstra et al., 2002).
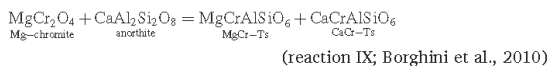
6.3.2. Sub-solidus net-transfer reactions

Sub-solidus continuous net-transfer reactions, resulting from changing PT conditions, have been shown to be capable of forming (ultra)mylonitic Ol + host phase mixtures (Dijkstra et al., 2004; Hidas et al., 2013; Newman et al., 1999). Kaczmarek and Tommasi (2011) already suggested that such reactions may have led to domains of intermixed two- or three-phase assemblages in the ultramylonites of Lanzo. Beside the exchange of PT sensitive elements (e.g. Al and Cr in pyroxenes; Ca in Opx), continuous net-transfer reactions as result of the Spl lherzolite to Pl lherzolite transition, lead to a systematic change of modal abundances and in the composition of reactants due to the crystallization of a new Al phase (Pl) (e.g., Rampone et al., 1993; Borghini et al., 2010). Previous studies have shown that the

Microstructural observations of small, interstitial Spl (Fig. 7C, 12B) in neoblast phase mixtures coincide with observations from Borghini et al. (2010) and Furusho and Kanagawa (1999). Spl abundances (0.5–2%) measured in pyroxene tails are in the range of those reported by Borghini et al. (2010) (0.5–4 wt%) and Furusho and Kanagawa (1999) (1.3–1.6 wt%). As Cr-rich spinel remains stable within the plagioclase stability field down to pressures as low as ca. 0.3 GPa, spinel-plagioclase reactions (IV, V) are thought to be continuous within the Pl stability field (Borghini et al., 2010). Clinopyroxene Ca/(Ca + Na) ratios increase with decreasing pressure (Borghini et al., 2010). Correspondingly, Cpx neoblasts exhibit higher Ca/(Na + Ca) ratios (i.e. lower pressures) than the porphyroclasts (Fig. 13 J). Slightly higher amounts of Na_2O in Pl of neoblasts compared to porphyroclastic abundances reported by Kaczmarek and Müntener (2008) in the mylonitic texture type could be explained by higher amounts of pargasitic amphibole in the former texture (Niida and Green, 1999). Variations of the Cr# (Fig. 13D/ H), the decrease of Cr_2O_3 (Fig. 13A/E) and the significant Al decrease for neoblasts of both pyroxenes (Fig. 13A/E) in the Pl stability field in lherzolite compositions (Pl-out: 0.8–1.5 GPa, Borghini et al. (2010) and reference therein) agree with the predicted influence of Pl crystallization combined with the Cr-Al partitioning between spinel and both pyroxenes by reactions VII and VIII:
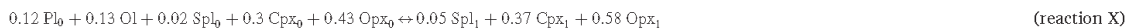
$$MgCr_2O_4 + 2CaAl_2Si_2O_8 + 2Mg_2SiO_4 = MgAl_2O_4 + 2MgCrAlSiO_6 + 2CaMgSi_2O_6$$
$$\underset{\text{Mg-chromite}}{} \quad \underset{\text{anorthite}}{} \quad \underset{\text{forsterite}}{} \quad \underset{\text{spinel}}{} \quad \underset{\text{MgCr-Ts}}{} \quad \underset{\text{diopside}}{}$$

$$\text{(reaction VII; Borghini et al., 2010)}$$

$$\underset{\text{Mg–chromite}}{MgCr_2O_4} + \underset{\text{anorthite}}{2CaAl_2Si_2O_8} + \underset{\text{forsterite}}{2Mg_2SiO_4} = \underset{\text{spinel}}{MgAl_2O_4} + \underset{\text{CaCr–Ts}}{2CaCrAlSiO_6} + \underset{\text{enstatite}}{2Mg_2Si_2O_6}$$

(reaction VIII; Borghini et al., 2010)

Cr#s of pyroxenes and Spl increase with decreasing pressure (Borghini et al., 2010). Correspondingly, Cr# and Cr_2O_3 abundances increase for pyroxene porphyroclasts with decreasing Al_2O_3 content (Fig. 13D/H *1, 13A/E *2). For pyroxene neoblasts in porphyroclast tails, Cr# display no pronounced positive correlation to Al_2O_3 but scatter around the porphyroclast Cr# values (Fig. 13D/H). As variations of Cr# and Al_2O_3 abundance are present in neoblasts of a single pyroxene tail (e.g., Fig. 13D) Al-Cr partitioning seems to be dependent on the local equilibrium governed by the presence of Spl and Pl at relatively fixed PT conditions (reaction IX; Borghini et al., 2010).

$$\underset{\text{Mg–chromite}}{MgCr_2O_4} + \underset{\text{anorthite}}{CaAl_2Si_2O_8} = \underset{\text{MgCr–Ts}}{MgCrAlSiO_6} + \underset{\text{CaCr–Ts}}{CaCrAlSiO_6}$$

(reaction IX; Borghini et al., 2010)

Kaczmarek and Müntener (2008) reported a highly variable Spl composition with respect to TiO_2, Cr- and Mg-number. Variations within a single sample are reported to be as large as the total range of all samples in the strain gradient. Especially the high Ti contents are at odds with Spl formation solely by subsolidus reactions and support a melt inherited component (Borghini et al., 2010; Kaczmarek and Müntener, 2008). Increased homogenization in the extensive deformed samples reported by Kaczmarek and Müntener (2008) suggests further that the timing of this melt-induced change was prior to ultramylonitic band formation. As interstitial Spl in pyroxene reaction tails were too small for microprobe measurement, their composition remains unfortunately unknown. Borghini et al. (2010) reported the modal amount of Pl to progressively decrease with increasing pressure along with a concomitant decrease in modal Ol and an increase in Opx, Cpx and Spl abundances following the reaction:

and Drury (2010) and Newman et al. (1999) we consider that continuous net-transfer reactions due to the Spl lherzolite to Pl lherzolite transition are a potential driving force for the formation of ultramylonitic mixed assemblages in pyroxene porphyroclast tails. As formerly elaborated by Hidas et al. (2016), these synkinematic net-transfer reactions are catalyzed by fluids. Synkinematic amphibole precipitation and fluid channeling in the center of deformation of the Lanzo shear zone were postulated by Kaczmarek and Tommasi (2011) and Vieira Duarte et al. (2020). Although the amount of amphibole in pyroxene tails seems to be low (av. ~1%), Hidas et al. (2016) have shown that for a peridotitic composition at corresponding PT-conditions, fluid saturation is reached at 1.0–1.4 wt% amphibole. Additionally, Vieira Duarte et al. (2020) argue for a synkinematic growth and deformation of Cl-bearing amphibole between 800 and 850 °C which coincides with neoblasts temperatures.

The fact that reaction-induced formation of ultramylonitic phase mixtures occurs only in strongly deformed textures and increase with deformation (Fig. 4) further indicates a strain dependent formation. Deformation experiments on Pl + Ol aggregates have shown a positive feedback of deformation and reactions for dry and wet conditions (de Ronde and Stünitz, 2007). An enhanced rate of the An (Pl) to Spl transformation was explained by an increase in nucleation rate due to deformation-induced defects (free dislocations, dislocation pile-ups, subgrain walls) and locally increased Gibbs free energy (de Ronde and Stünitz, 2007). With the onset of mechanical weakening, neoblasts are transported from the reaction interface, maintaining a high chemical potential and a continuous nucleation of reaction products can occur (de Ronde and Stünitz, 2007). In our samples, this coupling of deformation, diffusion and nucleation is microstructurally corroborated by the for-

$$0.12\,Pl_0 + 0.13\,Ol + 0.02\,Spl_0 + 0.3\,Cpx_0 + 0.43\,Opx_0 \leftrightarrow 0.05\,Spl_1 + 0.37\,Cpx_1 + 0.58\,Opx_1$$

(reaction X)

Corresponding to reaction (X), we observe a replacement of both pyroxenes by a mixture of Ol and minor Pl along with the host phase in neoblast tails of pyroxenes (Fig. 7 and 8). A clear connection to the matrix is crucial for the neoblast assemblage and mixing intensity: Isolated microstructures (Opx (Fig. 11C), Cpx (Fig. 10A), Cpx-Opx interface (Fig. 10B) show, despite the presence of Prg, host phase dominated assemblages and low mixing intensities. Therefore, geochemical changes due to the presence of fluid did not extensively modify the neoblast composition or mixing intensity.

In addition to mantle shear zones (e.g., Furusho and Kanagawa, 1999; Newman et al., 1999), phase mixing by heterogenous nucleation due to chemical disequilibrium was also reported in lower crustal shear zones (e.g., Degli Alessandrini, 2018; Kruse and Stünitz, 1999). Depending on the formation mechanism, Kruse and Stünitz (1999) reported for mylonites from the Jotun nappe (Norway) either the formation of monomineralic tails of plagioclase, hornblende and pyroxenes by dynamic recrystallization or phase mixtures of hornblende+Pl or Cpx + Pl in reaction tails. For lower crustal mylonites, highly lobate, serrated boundaries of reacted porphyroclasts similar to those of pyroxene porphyroclasts reaction tails (Fig. 7, 8) were reported as evidence for diffusion-driven (re)crystallization (Gower and Simpson, 1992; Kruse and Stünitz, 1999; Martelat et al., 1999; Zulauf et al., 2002). Combining our results with the experimental observations of Borghini et al. (2010) and the field implications of Furusho and Kanagawa (1999), Newman

mation of elongated polymineralic tails parallel to the foliation and with main porphyroclast reaction interfaces at boundaries perpendicular to the lineation (Fig. 7), by increasing neoblast elongation towards distal parts of the tail (Fig. 8C) and by increasing amount and length of GBAs towards the border of the tails (Fig. 7C). Additionally, neoblast grain sizes are smaller in pyroxene reaction tails embedded in ultramylonitic bands than those in mylonitic areas (e.g., Fig. 4B *4/*5).

6.3.3. Phase mixing by grain boundary sliding

The polymineralic tails derived from the pyroxene porphyroclasts are formed by reactions, however, grain boundary sliding (GBS) could be an additional phase mixing process during deformation. Grain boundary sliding (GBS) is thought to be active in both dislocation creep regime and diffusion creep regime (Drury et al., 2011; Hirth and Kohlstedt, 2003; Miyazaki et al., 2013; Warren and Hirth, 2006). Most microstructural evidence for GBS are found in ultramylonitic phase mixtures by continuous phase and grain boundaries alignments (Fig. 7C white dotted lines) (e.g., Kohlstedt et al., 1976; Newman et al., 1999). GBAs are interpreted as preferred sliding plains during GBS along grain and phase boundaries which are mostly subparallel to the foliation (Dijkstra et al., 2002; Drury et al., 2011; Newman et al., 1999). Neoblasts along GBAs show no increase in mixing (Fig. 7C) which was previously observed in experiments of Hiraga et al. (2013). GBAs of the wall like structures in in Cpx reaction tails (suppl. data S7) display

significantly different angles to the foliation (70–90°) and are aligned subparallel to porphyroclasts boundaries and are partially parallel to exsolution lamellae of the Cpx clast (suppl. data S7). Similar high angles to the tensile direction were also observed by Hiraga et al. (2013). The subparallel orientation to the porphyroclast grain boundary/exsolution lamellae suggests an influence of the clast orientation on neoblast grain shape. However, neoblast CPO do not show a strong relation to the clast orientation (suppl. data S3, S4). Additionally, aggregation is significantly weaker than shown by Hiraga et al. (2013) questioning the importance of GBS for these microstructures.

In conclusion, grain boundary sliding in our samples seems to lead to phase aggregation and not to phase mixing. Only in Ol recrystallization tails (Fig. 6), GBS combined with creep cavitation and nucleation seems to be accountable for the little mixing present in these microstructures (see section 6.1).

6.4. Ultramylonite bands

Ultramylonitic bands have a mixed phase assemblage dominated by Ol (> 50%) and either Cpx (av. 38%) or Opx (av. 14%). Similar to reaction tails of pyroxene porphyroclasts minor phases are Pl (av. 8%), Spl (~1%) and Prg (<1%). Pyroxene CPOs are not present or very weak (Opx: av. J index: Opx 1.5, Cpx 1.6). Ol neoblasts mostly form no CPO. Average grain sizes in Cpx + Ol ultramylonitic layers (~10 μm) tend to be bigger than those in Ol + Opx layers (~6 μm). Interestingly, neoblasts in pyroxene porphyroclast tails show a similar trend of bigger grain sizes in Cpx derived tails than in Opx ones (e.g. Fig. 7). Similar modal abundances in Ol porphyroclast tails and in ultramylonitic Opx + Ol layers could suggest that these layers derived from strongly deformed, Ol recrystallization tails. However, the transitions from neoblast tails to ultramylonitic bands (Fig. 12, 4B), the presence of the same phases, similar modal abundances and high mixing intensities in tails and bands suggest the straightforward interpretation that the origin of the ultramylonite bands are the pyroxene reaction tails. Ultramylonitic grain sizes and weak to no CPO indicate deformation by diffusion creep of the ultramylonitic texture. Their interconnectivity (Fig. 4B), their mixed assemblage (64% (Cpx + Ol) and 55% (Ol + Opx) phase boundaries) and their anastomosing microstructures around almost monomineralic Ol areas and porphyroclast-neoblast assemblages suggest that deformation is localized in the ultramylonitic bands/ in the ultramylonitic matrix in the ultramylonite texture. Interestingly, diffusion creep in these bands is combined with strong SPOs and elongated grain shapes (Fig. 12C) of pyroxenes and olivine.

Some observations however indicate additional deformation mechanisms. Domains with fine-grained Ol + Opx mixture at grain boundaries of coarse-grained Ol in ultramylonitic Ol + Opx layers (Fig. 9F) suggest precipitation of neoblasts during diffusion creep accommodated GBS in creep cavitations similar than mixing structures type I in Ol porphyroclast tails (Fig. 7A-i). Interestingly, neoblasts present in tails adjacent to elongated single Opx crystals display smaller grain sizes than in the ultramylonitic bands (Fig. 9). This could indicate a certain degree of grain growth in the ultramylonites.

6.5. Comparison with other mantle shear zones and the significance of reaction-induced phase mixing

As seen for Lanzo, most mantle shear zones/sheared peridotites show evidence for reaction involved changes in their mineralogy (phase composition and abundances) during their evolution from upper mantle depth to the earth surface. These changes are either due to melt, fluid and/or changing PT-conditions (phase transitions and continuous net transfer reactions). The significance of the reaction-induced changes for the generation of phase mixtures becomes clear through a comparison with other sheared peridotites. Initial strain localization is not regarded here.

Melt-rock reactions were reported for Othris, Greece (Dijkstra et al., 2002), Lanzo, Italy (Kaczmarek and Müntener, 2008) and the Table Mountain massif, Newfoundland (Suhr, 1993). Evidence for extensive fluid-rock reactions was observed in the central Ronda peridotite, Spain (Hidas et al., 2016), were limited fluid availability led locally to dissolution-precipitation creep. This process caused the precipitation of elongated Opx at Ol grain boundaries, leading to phase mixing. A similar process is suggested for phase mixing in the Anita peridotite, New Zealand (Czertowicz et al., 2016). In these ultramylonites, the Opx also forms along Ol grain boundaries, which is thought to be the result of Opx precipitation in creep cavitation bands between Ol grains (Czertowicz et al., 2016). Creep cavitation can form during GBS (Fusseis et al., 2009), or due to SGR (Gilgannon et al., 2020). At higher fluid volumes, amphibole or chlorite may form, depending on PT conditions, resulting in fine-grained mixed reaction products, as in Erro-Tobbio (Hoogerduijn Strating et al., 1993; Linckens and Tholen, 2021) and in dredged peridotites from the Shaka and Prince Edward Oceanic Transform Faults (Kohli and Warren, 2020; Prigent et al., 2020). Mineral reactions driven by the change in PT-conditions were interpreted as driving force for recrystallization and phase mixing in the Turon de Técouère, France (Newman et al., 1999), in the Twin Sisters Massif, USA (Toy et al., 2009), in the Uenzaru peridotite, Japan (Furusho and Kanagawa, 1999), and in Lanzo, Italy by Kaczmarek and Tommasi (2011) and this study. Remarkably, all the above-mentioned shear zones display (ultra)mylonitic, thoroughly mixed assemblages, whether as patches or coronas around porphyroclasts or as interconnected bands.

As a counterpart, only a few shear zones were found to deform without concomitant chemical reactions: for the north-western border of the Ronda peridotite, Spain (e.g., Précigout et al., 2007), dynamic recrystallization was found to be the only weakening mechanism responsible for strain localization. Continuous deformation accommodated partly by grain boundary sliding resulted in neighbor-switching and the scattering of Opx neoblasts. Accordingly, microstructures typical for reaction-induced recrystallization as reported herein were not observed. No ultramylonites were formed during deformation and the grain sizes remained relatively large (mean grain sizes of 150–220 μm; Précigout et al., 2017). For pyroxenites of the Beni Bousera peridotite, Morocco, Frets et al. (2012) reported that most deformation was accommodated by dislocation creep of pyroxenes (SGR and GBR dynamic recrystallization). High stress deformation is thought to drive compositional homogenization by mechanical mixing. However, Frets et al. (2012) also reported syn- to late-kinematic reactions that crystallize pyroxenes at the expense of garnets. Skemer et al. (2009) reported fine-grained, mixed domains of Ol + Opx which are associated with relict Opx porphyroclasts for a high-strain shear zone from the Josephine Peridotite, USA. Like for Lanzo, the authors argue that for the formation of these mixed domains, the onset of Opx recrystallization is crucial. On the basis of subgrain boundaries in Opx porphyroclasts, and equiaxial neoblasts a formation by dynamic recrystallization rather than by chemical reactions was suggested. However, a recent study of Kumamoto et al. (2019) has shown, that these shear zones record extensive melt-rock interaction and elevated water concentrations. In summary, the following can be said for these shear zones: even if deformation is mostly accommodated by dynamic recrystallization, the phase mixing present seems to be due to reactions.

Deformation in peridotites with little or no reaction-induced change by metasomatism and/or phase transitions were only reported for sheared xenoliths. For South African kimberlites, Skemer and Karato (2008) show microstructures of dynamically recrystallized Opx porphyroclasts forming equigranular neoblast mosaics with straight grain boundaries and no to little phase mixing over the total length of neoblast tails. Sheared xenoliths from Lesotho and South Africa display extensive dynamic recrystallization of Opx, Cpx and Ol (suppl. data S11). Despite the simultaneous dynamic recrystallization of all three phases no phase mixing occurs (suppl. data S11). Although this list is not exhaustive, a correspondence with our results from the northern Lanzo shear zone is apparent. Extensive phase mixing and the formation of (ultra)mylonitic

assemblages are only observed when reactions occur (due to melt-rock, fluid-rock reactions and/or metamorphism).

7. Conclusions

- Ultramylonitic, polymineralic tails form adjacent to ortho- and clinopyroxene porphyroclast in mylonitic rocks in the Lanzo shear zone.
- Transitions from these tails to ultramylonitic bands with similar mixing intensities, compositions and phase abundances in bands and tails suggest: ultramylonitic bands/matrix derive from pyroxene tails.
- Mineralogical assemblages and phase abundances in pyroxene tails depend primarily on the parent porphyroclast. Clinopyroxene porphyroclasts form clinopyroxene + olivine assemblages. Orthopyroxene porphyroclasts form olivine + orthopyroxene assemblages. Minor phases in both phase mixtures are plagioclase, spinel and pargasitic amphibole.
- Mixing intensities of pyroxene microstructures strongly depend on the connection to the matrix: high phase mixing intensities are only observed in porphyroclast tails embedded in the matrix.
- Polymineralic tails are suggested to from by net-transfer reactions, enhanced by the spinel lherzolite – plagioclase lherzolite transition.
- Minor amphibole occurrence in ultramylonitic phase mixtures suggests that reactions were catalyzed by the presence of a fluid.
- Grain boundary sliding plus cavity nucleation has only a minor importance for phase mixing in tails of dynamically recrystallized olivine porphyroclasts.
- Other upper mantle shear zones confirm that extensive phase mixing and the formation of (ultra)mylonitic assemblages are reaction-induced (melt-rock, fluid-rock, continuous net-transfer and phase-transition).

Supplementary data to this article can be found online at https://doi.org/10.1016/j.tecto.2022.229230.

Declaration of Competing Interest

The authors declare that they have no known competing financial interests or personal relationships that could have appeared to influence the work reported in this paper.

Acknowledgments

References

Bachmann, F., Hielscher, R., Schaeben, H., 2010. Texture analysis with MTEX- Free and open source software toolbox. Solid State Phenom. 160, 63–68. https://doi.org/10.4028/www.scientific.net/SSP.160.63.

Bercovici, David, Ricard, Yanick, 2014. Plate tectonics, damage and inheritance. Nature 508, 513–516. https://doi.org/10.1038/nature13072.

Borghini, G., 2008. The spinel- to plagioclase-facies transition in mantle peridotites: natural and experimental constraints. Plinius 34, 43–45.

Borghini, G., Fumagalli, P., Rampone, E., 2010. The stability of plagioclase in the upper mantle: Subsolidus experiments on fertile and depleted lherzolite. J. Petrol. 51, 229–254. https://doi.org/10.1093/petrology/egp079.

Boudier, F., 1978. Structure and petrology of the Lanzo peridotite massif (Piedmont Alps). Geol. Soc. Am. Bull. 7606 https://doi.org/10.1130/0016-7606(1978) 89<1574.

Boullier, A.M., Gueguen, Y., 1975. SP-Mylonites: origin of some mylonites by superplastic flow. Contrib. Mineral. Petrol. 50, 93–104. https://doi.org/10.1007/BF00373329.

Brey, G.P., Köhler, T., 1990. Geothermobarometry in four-phase lherzolites II. new thermobarometers, and practical assessment of existing thermobarometers. J. Petrol. 31, 1353–1378. https://doi.org/10.1093/petrology/31.6.1353.

Brodie, K.H., Rutter, E.H., 1987. The role of transiently fine-grained reaction products in syntectonic metamorphism: natural and experimental examples. Can. J. Earth Sci. 24, 556–564. https://doi.org/10.1139/e87-054.

Bunge, H.-J., 1982. Orientation distributions. In: Texture Analysis in Materials Science. Butterworths, London. https://doi.org/10.1016/B978-0-408-10642-9.50008-8.

Carswell, D.A., 1991. The garnet-orthopyroxene Al barometer: problematic application to natural garnet lherzolite assemblages. Mineral. Mag. 55, 19–31. https://doi.org/10.1180/minmag.1991.055.378.03.

Cross, A.J., Skemer, P., 2017. Ultramylonite generation via phase mixing in high-strain experiments. J. Geophys. Res. Solid Earth 122, 1744–1759. https://doi.org/10.1002/2016JB013801.

Czertowicz, T.A., Toy, V.G., Scott, J.M., 2016. Recrystallisation, phase mixing and strain localisation in peridotite during rapid extrusion of sub-arc mantle lithosphere. J. Struct. Geol. 88, 1–19. https://doi.org/10.1016/j.jsg.2016.04.011.

de Ronde, A.A., Stünitz, H., 2007. Deformation-enhanced reaction in experimentally deformed plagioclase-olivine aggregates. Contrib. Mineral. Petrol. 153, 699–717. https://doi.org/10.1007/s00410-006-0171-7.

Debret, B., Nicollet, C., Andreani, M., Schwartz, S., Godard, M., 2013. Three steps of serpentinization in an eclogitized oceanic serpentinization front (Lanzo Massif - Western Alps). J. Metamorph. Geol. 31, 165–186. https://doi.org/10.1111/jmg.12008.

Degli Alessandrini, G., 2018. Deformation Mechanisms and Strain Localization in the Mafic Continental Lower Crust. Dr. Diss. Univ, Plymouth, U.K. https://pearl.plymouth.ac.uk/handle/10026.1/12799?show—full

Dijkstra, A.H., Drury, M.R., Vissers, R.L.M., Newman, J., 2002. On the role of melt-rock reaction in mantle shear zone formation in the Othris Peridotite Massif (Greece). J. Struct. Geol. 24, 1431–1450. https://doi.org/10.1016/S0191-8141(01)00142-0.

Dijkstra, A.H., Drury, M.R., Vissers, R.L.M., Newman, J., Van Roermund, H.L.M., 2004. Shear zones in the upper mantle: Evidence from alpine- and ophiolite-type peridotite massifs. Geol. Soc. Spec. Publ. 224, 11–24. https://doi.org/10.1144/GSL.SP.2004.224.01.02.

Drury, M.R., Avé Lallement, H.G., Pennock, G.M., Palasse, L.N., 2011. Crystal preferred orientation in peridotite ultramylonites deformed by grain size sensitive creep, étang de Lers, Pyrenees, France. J. Struct. Geol. 33, 1776–1789. https://doi.org/10.1016/j.jsg.2011.10.002.

Farla, R.J.M., Karato, S., Cai, Z., 2013. Role of orthopyroxene in rheological weakening of the lithosphere via dynamic recrystallization. Proc. Natl. Acad. Sci. U. S. A. 110, 16355–16360. https://doi.org/10.1073/pnas.1218335110.

Frets, E., Tommasi, A., Garrido, C.J., Padrón-Navarta, J.A., Amri, I., Targuisti, K., 2012. Deformation processes and rheology of pyroxenites under lithospheric mantle conditions. J. Struct. Geol. 39, 138–157. https://doi.org/10.1016/j.jsg.2012.02.019.

Furusho, M., Kanagawa, K., 1999. Transformation-induced strain localization in a lherzolite mylonite from the Hidaka metamorphic belt of central Hokkaido, Japan. Tectonophysics 313, 411–432. https://doi.org/10.1016/S0040-1951(99)00215-2.

Fusseis, Florian, Regenauer-Lieb, Klaus, Liu, Jie, Hough, Robert Michael, 2009. Creep cavitation can establish a dynamic granular fluid pump in ductile shear zones. Nature 459 (7249), 974–977. https://doi.org/10.1038/nature08051.

Gilgannon, James, Poulet, Thomas, Berger, Alfons, Barnhoorn, Auke, Herwegh, Marco, 2020. Dynamic Recrystallization Can Produce Porosity in Shear Zones. Geophysical Research Letters 47 (7), 1–10. https://doi.org/10.1029/2019GL086172.

Gower, R.J.W., Simpson, C., 1992. Phase boundary mobility in naturally deformed, high-grade quartzofeldspathic rocks: evidence for diffusional creep. J. Struct. Geol. 14, 301–313. https://doi.org/10.1016/0191-8141(92)90088-E.

Hidas, K., Garrido, C.J., Tommasi, A., Padrón-Navarta, J.A., Thielmann, M., Konc, Z., Frets, E., Marchesi, C., 2013. Strain localization in pyroxenite by reaction-enhanced softening in the shallow subcontinental lithospheric mantle. J. Petrol. 54, 1997–2031. https://doi.org/10.1093/petrology/egt039.

Hidas, K., Tommasi, A., Garrido, C.J., Padrón-Navarta, J.A., Mainprice, D., Vauchez, A., Barou, F., Marchesi, C., 2016. Fluid-assisted strain localization in the shallow subcontinental lithospheric mantle. Lithos 262, 636–650. https://doi.org/10.1016/j.lithos.2016.07.038.

Hielscher, R., Nolze, G., 2016. IPF coloring of crystal orientation data. J. Appl. Crystallogr. 49, 1786–1802.

Hiraga, T., Miyazaki, T., Yoshida, H., Zimmerman, M.E., 2013. sliding Comparison of microstructures in superplastically deformed synthetic materials and natural mylonites: mineral aggregation via grain boundary sliding. https://doi.org/10.1130/G34407.1.

Hirth, G., Kohlstedt, D., 2003. Rheology of the upper mantle and the mantle wedge: A view from the experimentalists. Geophys. Monogr. Ser. 138, 83–105. https://doi.org/10.1029/138GM06.

Hoogerduijn Strating, E.H., Rampone, E., Piccardo, G.B., Drury, M.R., Vissers, R.L.M., 1993. Subsolidus emplacement of mantle peridotites during incipient oceanic rifting

and opening of the mesozoic tethys (voltri massif, NW Italy). J. Petrol. 34, 901–927. https://doi.org/10.1093/petrology/34.5.901.

Kaczmarek, M.A., Müntener, O., 2005. Exhumation of mantle lithosphere: field relations, and interaction processes between magmatism and deformation (field trip to the northern lanzo peridotite). Ofioliti 30, 125–134. https://doi.org/10.4454/ofioliti.v30i2.246.

Kaczmarek, M.A., Müntener, O., 2008. Juxtaposition of melt impregnation and high-temperature shear zones in the upper mantle; field and petrological constraints from the lanzo peridotite (Northern Italy). J. Petrol. 49, 2187–2220. https://doi.org/10.1093/petrology/egn065.

Kaczmarek, M.A., Müntener, O., 2010. The variability of peridotite composition across a mantle shear zone (Lanzo massif, Italy): Interplay of melt focusing and deformation. Contrib. Mineral. Petrol. 160, 663–679. https://doi.org/10.1007/s00410-010-0500-8.

Kaczmarek, M.A., Tommasi, A., 2011. Anatomy of an extensional shear zone in the mantle, Lanzo massif, Italy. Geochem. Geophys. Geosyst. 12, n/a-n/a. https://doi.org/10.1029/2011GC003627.

Karato, S., Wu, P., 1993. Rheology of the upper mantle: A synthesis. Science (80-.) 260, 771–778. https://doi.org/10.1126/science.260.5109.771.

Kilian, R., Heilbronner, R., Stünitz, H., 2011. Quartz grain size reduction in a granitoid rock and the transition from dislocation to diffusion creep. J. Struct. Geol. 33, 1265–1284. https://doi.org/10.1016/j.jsg.2011.05.004.

Kilian, R., Bestmann, M., Heilbronner, R., 2016. Absolute orientations from EBSD measurements - as easy as it seems ? Geophys. Res. Abstr. 18, 8221.

Knapp, N., Woodland, A.B., Klimm, K., 2013. Experimental constraints in the CMAS system on the Ca-Eskola content of eclogitic clinopyroxene. Eur. J. Mineral. 25, 579–596. https://doi.org/10.1127/0935-1221/2013/0025-2326.

Kohli, A.H., Warren, J.M., 2020. Evidence for a deep hydrologic cycle on oceanic transform faults. J. Geophys. Res. Solid Earth 125, 1–23. https://doi.org/10.1029/2019JB017751.

Kohlstedt, D.L., Goetze, C., Durham, W.B., Vander Sande, J., 1976. New technique for decorating dislocations in olivine. Science (80-.) 191, 1045–1046. https://doi.org/10.1126/science.191.4231.1045.

Kruse, R., Stünitz, H., 1999. Deformation mechanisms and phase distribution in mafic high-temperature mylonites from the Jotun Nappe, southern Norway. Tectonophysics 303, 223–249. https://doi.org/10.1016/S0040-1951(98)00255-8.

Kumamoto, K.M., Warren, J.M., Hauri, E.H., 2019. Evolution of the Josephine Peridotite Shear Zones: 1. Compositional Variation and Shear Initiation. Geochem. Geophys. Geosyst. 20, 5765–5785. https://doi.org/10.1029/2019GC008399.

Linckens, J., Tholen, S., 2021. Formation of ultramylonites in an upper mantle shear zone, erro-tobbio, italy. Minerals 11. https://doi.org/10.3390/min11101036.

Linckens, J., Herwegh, M., Müntener, O., 2015. Small quantity but large effect - How minor phases control strain localization in upper mantle shear zones. Tectonophysics 643, 26–43. https://doi.org/10.1016/j.tecto.2014.12.008.

Martelat, J.E., Schulmann, K., Lardeaux, J.M., Nicollet, C., Cardon, H., 1999. Granulite microfabrics and deformation mechanisms in southern Madagascar. J. Struct. Geol. 21, 671–687. https://doi.org/10.1016/S0191-8141(99)00072-8.

Menegon, L., Fusseis, F., Stünitz, H., Xiao, X., 2015. Creep cavitation bands control porosity and fluid flow in lower crustal shear zones. Geology 43. https://doi.org/10.1130/G36307.1.

Miyazaki, T., Sueyoshi, K., Hiraga, T., 2013. Olivine crystals align during diffusion creep of Earth's upper mantle. Nature 502, 321–326. https://doi.org/10.1038/nature12570.

Montési, L.G.J., 2013. Fabric development as the key for forming ductile shear zones and enabling plate tectonics. J. Struct. Geol. 50, 254–266. https://doi.org/10.1016/j.jsg.2012.12.011.

Müntener, O., Piccardo, G.B., 2003. Melt migration in ophiolitic peridotites: The message from Alpine-Apennine peridotites and implications for embryonic ocean basins. Geol. Soc. Spec. Publ. 218, 69–89. https://doi.org/10.1144/GSL.SP.2003.218.01.05.

Müntener, O., Piccardo, G.B., Polino, R., Zanetti, A., 2005. Revisiting the Lanzo peridotite (NW-Italy) : "Asthenospherization" of ancient mantle lithosphere. Ofioliti 30, 111–124. https://doi.org/10.4454/ofioliti.v30i2.245.

Newman, J., Drury, M.R., 2010. Control of shear zone location and thickness by initial grain size variations in upper mantle peridotites. J. Struct. Geol. 32, 832–842. https://doi.org/10.1016/j.jsg.2010.06.001.

Newman, J., Lamb, W.M., Drury, M.R., Vissers, R.L.M., 1999. Deformation processes in a peridotite shear zone: Reaction-softening by an H2O-deficient, continuous net transfer reaction. Tectonophysics 303, 193–222. https://doi.org/10.1016/S0040-1951(98)00259-5.

Niida, K., Green, D.H., 1999. Stability and chemical composition of pargasitic amphibole in MORB pyrolite under upper mantle conditions. Contrib. Mineral. Petrol. 135, 18–40. https://doi.org/10.1007/s004100050495.

Nimis, P., Grütter, H., 2010. Internally consistent geothermometers for garnet peridotites and pyroxenites. Contrib. Mineral. Petrol. 159, 411–427. https://doi.org/10.1007/s00410-009-0455-9.

Nimis, P., Taylor, W.R., 2000. Single clinopyroxene thermobarometry for garnet peridotites. Part I. Calibration and testing of a Cr-in-Cpx barometer and an enstatite-in-Cpx thermometer. Contrib. Mineral. Petrol. 139, 541–554. https://doi.org/10.1007/s004100000156.

Pearce, M.A., Wheeler, J., 2011. Grain growth and the lifetime of diffusion creep deformation. Geol. Soc. Spec. Publ. 360, 257–272. https://doi.org/10.1144/SP360.15.

Platt, J.P., 2015. Rheology of two-phase systems: A microphysical and observational approach. J. Struct. Geol. 77, 213–227. https://doi.org/10.1016/j.jsg.2015.05.003.

Poirier, J.-P., Nicolas, A., 1975. Deformation-Induced Recrystallization Due to Progressive Misorientation of Subgrains, with Special Reference to Mantle Peridotites. J. Geol. 83, 707–720. https://doi.org/10.1086/628163.

Précigout, J., Stünitz, H., 2016. Evidence of phase nucleation during olivine diffusion creep: a new perspective for mantle strain localisation, 455, pp. 94–105. https://doi.org/10.1016/j.epsl.2016.09.029.

Précigout, J., Gueydan, F., Gapais, D., Garrido, C.J., Essaifi, A., 2007. Strain localisation in the subcontinental mantle - a ductile alternative to the brittle mantle. Tectonophysics 445, 318–336. https://doi.org/10.1016/j.tecto.2007.09.002.

Précigout, J., Prigent, C., Palasse, L., Pochon, A., 2017. Water pumping in mantle shear zones. Nat. Commun. 8 https://doi.org/10.1038/ncomms15736.

Prigent, C., Warren, J.M., Kohli, A.H., Teyssier, C., 2020. Fracture-mediated deep seawater flow and mantle hydration on oceanic transform faults. Earth Planet. Sci. Lett. 532, 115988 https://doi.org/10.1016/j.epsl.2019.115988.

Putnis, A., Niedermeier, D., Putnis, C., 2006. From epitaxy to topotaxy: the migration of reaction interfaces through crystals. Geochim. Cosmochim. Acta - Geochim COSMOCHIM ACTA 70. https://doi.org/10.1016/j.gca.2006.06.1479.

Rampone, E., Piccardo, G.B., Vannucci, R., Bottazzi, P., Ottolini, L., 1993. Subsolidus reactions monitored by trace element partitioning: the spinel- to plagioclase-facies transition in mantle peridotites. Contrib. Mineral. Petrol. 115, 1–17. https://doi.org/10.1007/BF00712974.

Rampone, E., Borghini, G., Basch, V., 2018. Melt migration and melt-rock reaction in the Alpine-Apennine peridotites : insights on mantle dynamics in extending lithosphere Geoscience Frontiers Melt migration and melt-rock reaction in the Alpine-Apennine peridotites : insights on mantle dynamics in. Geosci. Front. https://doi.org/10.1016/j.gsf.2018.11.001.

Ramsay, J.G., Graham, R.H., 1970. Strain variation in shear belts. Can. J. Earth Sci. 7, 786–813. https://doi.org/10.1139/e70-078.

Sakai, T., Belyakov, A., Kaibyshev, R., Miura, H., Jonas, J.J., 2014. Dynamic and post-dynamic recrystallization under hot, cold and severe plastic deformation conditions. Prog. Mater. Sci. 60, 130–207. https://doi.org/10.1016/j.pmatsci.2013.09.002.

Skemer, P., Karato, S.I., 2008. Sheared lherzolite xenoliths revisited. J. Geophys. Res. Solid Earth 113, 1–14. https://doi.org/10.1029/2007JB005286.

Skemer, P., Katayama, I., Jiang, Z., Karato, S.I., 2005. The misorientation index: Development of a new method for calculating the strength of lattice-preferred orientation. Tectonophysics 411, 157–167. https://doi.org/10.1016/j.tecto.2005.08.023.

Skemer, P., Warren, J.M., Kelemen, P.B., Hirth, G., 2009. Microstructural and rheological evolution of a mantle shear zone. J. Petrol. 51, 43–53. https://doi.org/10.1093/petrology/egp057.

Suhr, G., 1993. Evaluation of upper mantle microstructures in the Table Mountain massif (Bay of Islands ophiolite). J. Struct. Geol. 15, 1273–1292. https://doi.org/10.1016/0191-8141(93)90102-G.

Taylor, W.R., 1998. An experimental test of some geothermometer and geobarometer formulations for upper mantle peridotites with application to the thermobarometry of fertile lherzolite and garnet websterite. Neues Jahrb. fur Mineral. Abhandlungen 172, 381–408. https://doi.org/10.1127/njma/172/1998/381.

Toy, V.G., Newman, J., Lamb, W.M., Tikoff, B., 2009. The role of pyroxenites in formation of shear instabilities in the mantle: Evidence from an ultramafic ultramylonite, Twin Sisters massif, Washington. J. Petrol. 51, 55–80. https://doi.org/10.1093/petrology/egp059.

Urai, J.L., Means, W.D., Lister, G.S., 2011. Dynamic recrystallization of minerals 161–199. https://doi.org/10.1029/gm036p0161.

Vauchez, A., Tommasi, A., Mainprice, D., 2012. Faults (shear zones) in the Earth's mantle. Tectonophysics 558–559, 1–27. https://doi.org/10.1016/j.tecto.2012.06.006.

Vieira Duarte, J.F., Kaczmarek, M.A., Vonlanthen, P., Putlitz, B., Müntener, O., 2020. Hydration of a Mantle Shear Zone Beyond Serpentine Stability: A Possible Link to Microseismicity Along Ultraslow Spreading Ridges? J. Geophys. Res. Solid Earth 125, 1–24. https://doi.org/10.1029/2020JB019509.

Vissers, R.L.M., Drury, M.R., Newman, J., Fliervoet, T.F., 1997. Mylonitic deformation in upper mantle peridotites of the North Pyrenean Zone (France): Implications for strength and strain localization in the lithosphere. Tectonophysics 279, 303–325. https://doi.org/10.1016/S0040-1951(97)00128-5.

Warren, J.M., Hirth, G., 2006. Grain size sensitive deformation mechanisms in naturally deformed peridotites. Earth Planet. Sci. Lett. 248, 438–450. https://doi.org/10.1016/j.epsl.2006.06.006.

Whitney, D.L., Evans, B.W., 2010. Abbreviations for names of rock-forming minerals. Am. Mineral. 95, 185–187. https://doi.org/10.2138/am.2010.3371.

Zulauf, G., Dörr, W., Fiala, J., Kotková, J., Maluski, H., Valverde-Vaquero, P., 2002. Evidence for high-temperature diffusional creep preserved by rapid cooling of lower crust (North Bohemian shear zone, Czech Republic). Terra Nov. 14, 343–354. https://doi.org/10.1046/j.1365-3121.2002.00424.x.

Appendix chapter 3 – Erro-Tobbio - Formation of ultramylonites in an upper mantle shear zone, Erro-Tobbio, Italy

Table S3.1   –   Microprobe data of orthopyroxene and clinopyroxene neoblasts and porphyroclasts in sample 6.4 and 6.8 (attached on CD)

Figure S3.1   –   EBSD data of dynamic recrystallized cpx porphyroclast (ROI16) (attached below & on CD)

Figure S3.2   –   EBSD maps the olivine-rich matrix (attached as Excel file on CD)

Figure S3.3   –   EBSD data of recrystallized opx porphyroclasts (ROI 24) (attached below & on CD)

Figure S3.4   –   EBSD data of fine-grained layer (ROI14) (attached below & on CD)

Figure S3.5   –   EBSD map of fine-grained layer (ROI23) (attached below & on CD)

Figure S3.6   –   EBSD data of fine-grained layer (ROI23) (attached below & on CD)

Publication   –   "Formation of Ultramylonites in an Upper Mantle Shear Zone, Erro-Tobbio, Italy" by Jolien Linckens and Sören Tholen published in *minerals,* 11 (2021), (attached below & on CD)
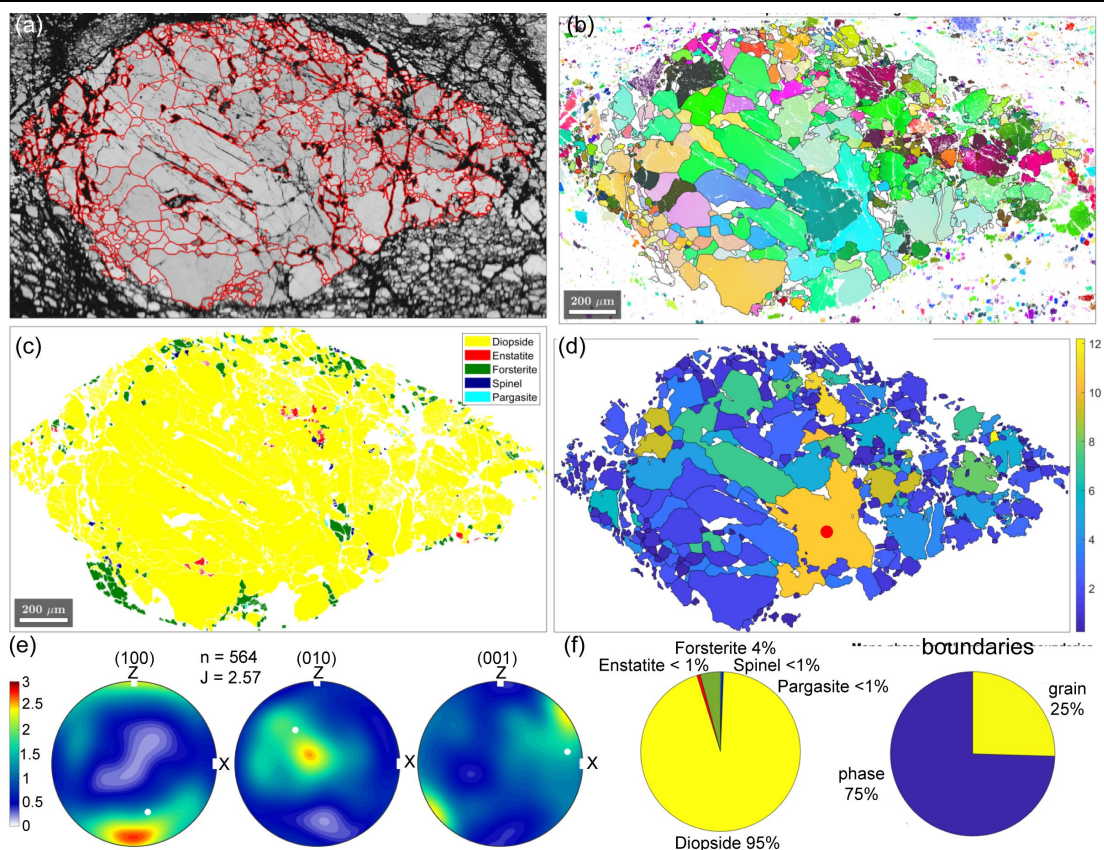
Figure S3.1 *– EBSD data of dynamic recrystallized cpx porphyroclast (ROI16). (**a**) Band contrast image of the complete map and grin boundaries (red lines) of the area used in the grain, orientation and boundary analysis. Scale the same as in (b) and (c). (**b**) Orientation data of diopside. (**c**) Phase map of the area selected for the analysis. (**d**) Grain orientation spread in the diopside grains. Scale the same as in (b) and (c). (**e**) CPO of diopside grains, the white dot indicates the orientation of the grain indicated with the red dot in (d). (**f**) Phase percentages and boundary percentages. For optimal resolution, the reader is referred to the version attached on the CD.*
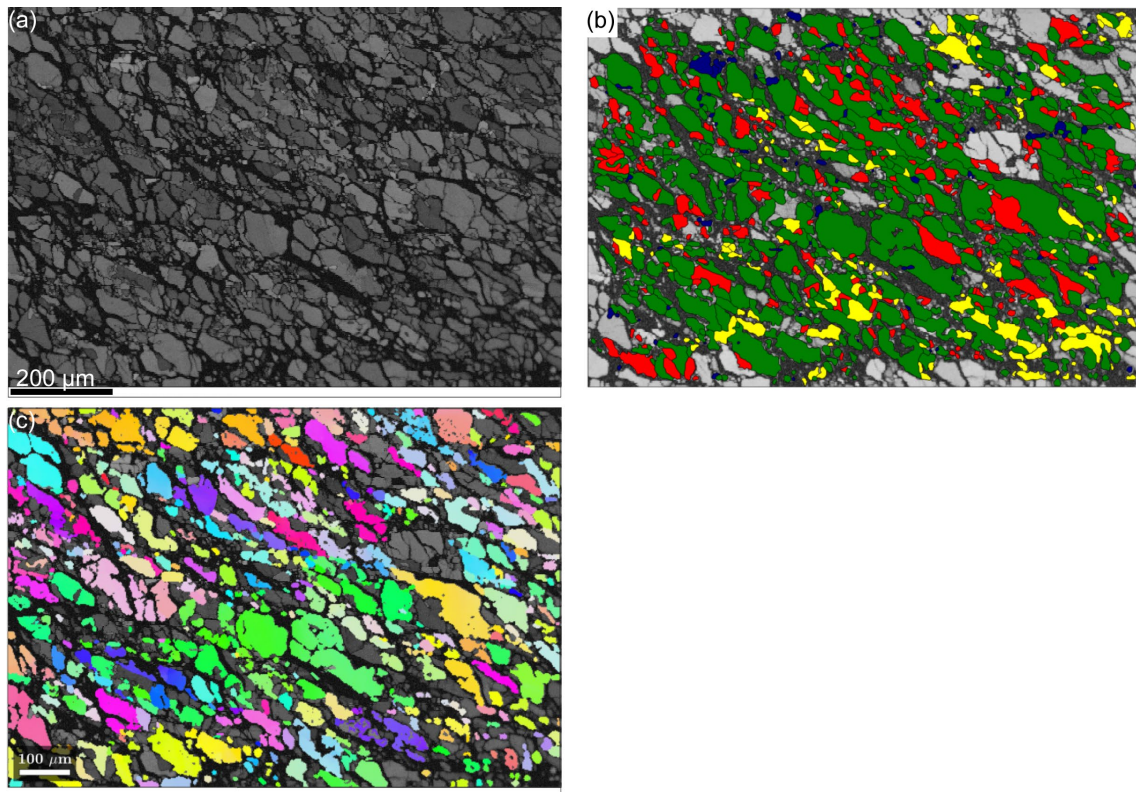
Figure S3.2 – *EBSD maps the olivine-rich matrix. (**a**) Band contrast image. (**b**) Phase map
with forsterite (green), enstatite (red), diopside (yellow) and spinel (blue). Same scale as
(c). (**c**) Olivine orientations. For optimal resolution, the reader is referred to the version
attached on the CD.*
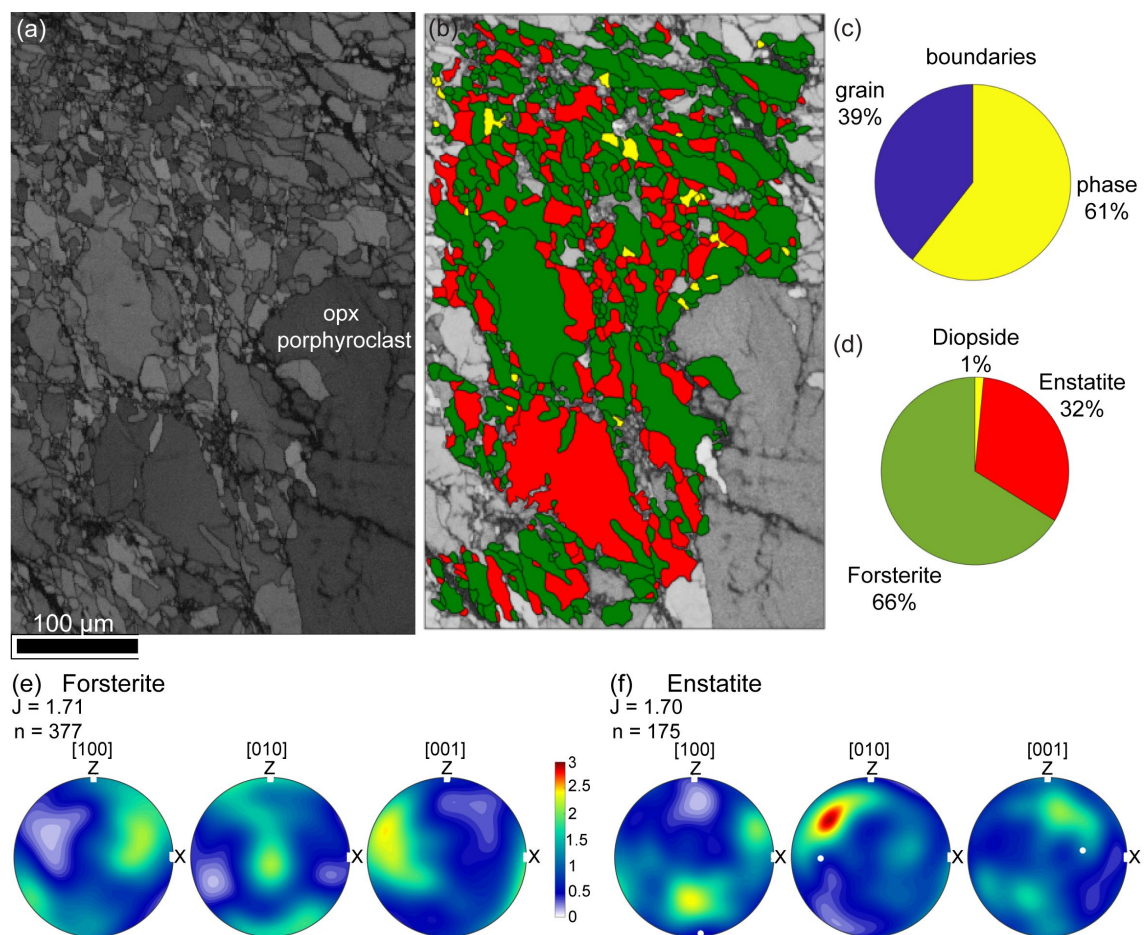
Figure S3.3 *– EBSD data of recrystallized opx porphyroclasts (ROI 24). (**a**) Band contrast (**b**) phase map, colors as in the area percentage pie chart in (d). (**c**) Phase and grain boundary percentages. (**d**) Area percentages of the different phases. (**e**) Forsterite CPO. (**f**) Enstatite CPO. Indicated is the orientation of the porphyroclast (white dot). For optimal resolution, the reader is referred to the version attached on the CD.*
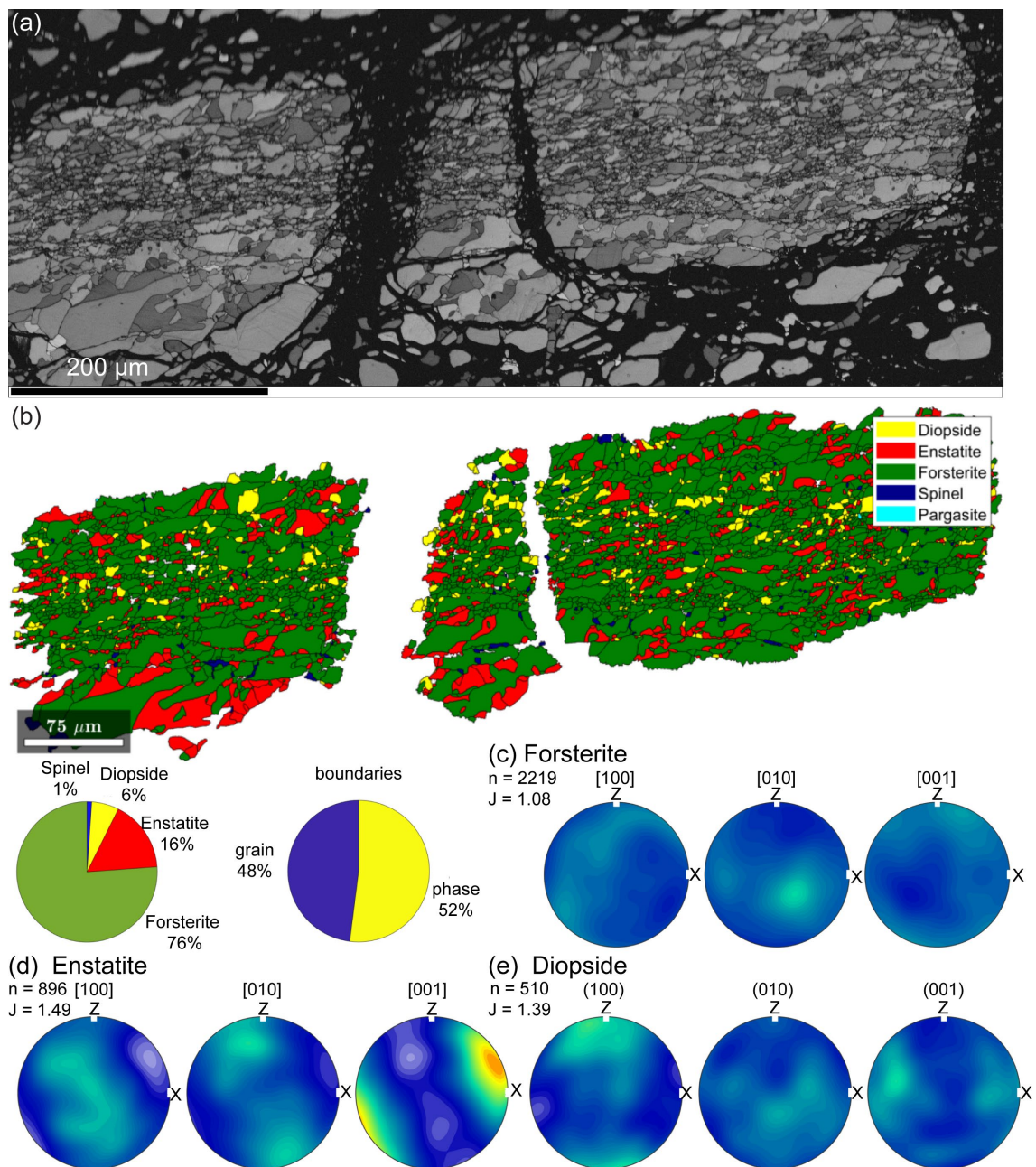
Figure S3.4 – *EBSD data of fine-grained layer (ROI14).* (**a**) *Band contrast image.* (**b**) *Phase map with area % of the phases and the percentage of phase and grain boundaries.* (**c**) *Forsterite CPO.* (**d**) *Enstatite CPO.* (**e**) *Diopside CPO. For optimal resolution, the reader is referred to the version attached on the CD.*
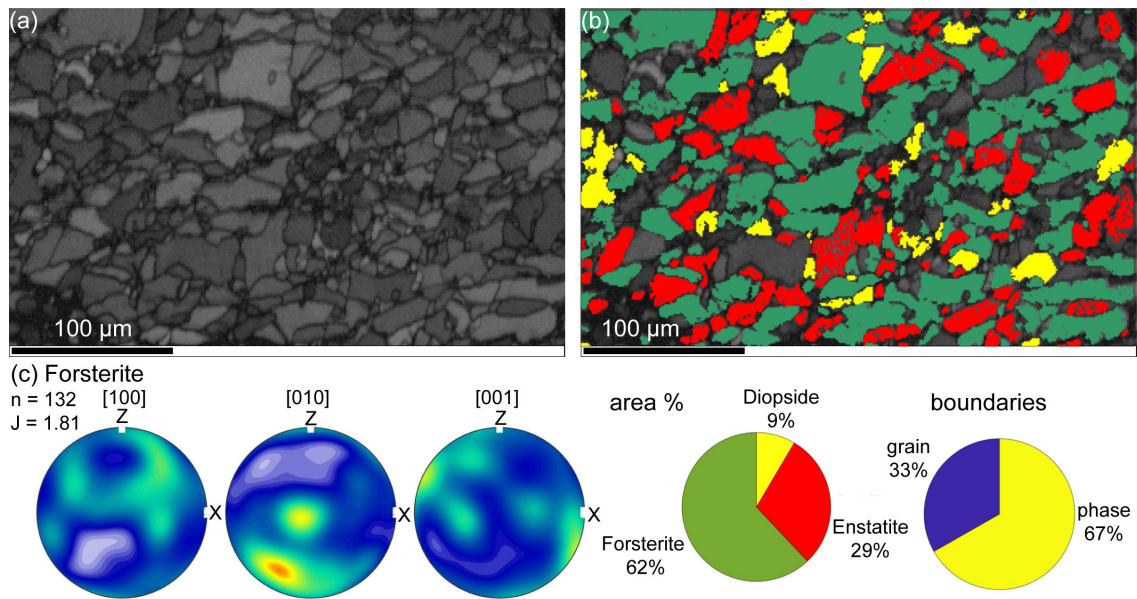
Figure S3.5 – *EBSD map of fine-grained layer (ROI23). (**a**) Band contrast map. (**b**) Phase map, with underneath the pie charts of the area % and boundaries. (**c**) Forsterite CPO. For optimal resolution, the reader is referred to the version attached on the CD.*
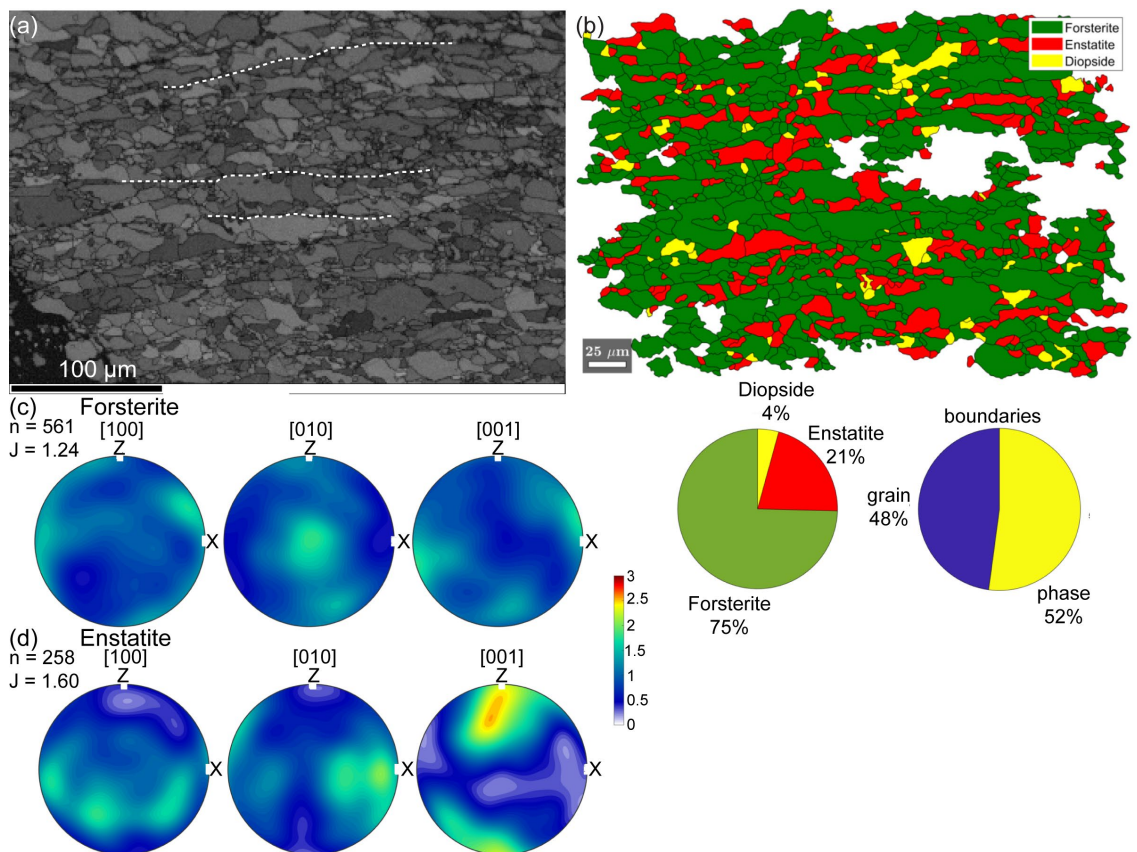
Figure S3.6 – *EBSD data of fine-grained layer (ROI23). (**a**) Band contrast of the area, dashed with lines follow some of the horizontal cracks in the layer. (**b**) Phase map of the area. Below are indicated the area percentages and phase and grain boundary percentages. (**c**) Forsterite CPO. (**d**) Enstatite CPO.*

minerals

MDPI

Article

Formation of Ultramylonites in an Upper Mantle Shear Zone, Erro-Tobbio, Italy

Jolien Linckens * and Sören Tholen *

Institut für Geowissenschaften, Goethe-Universität Frankfurt am Main, Altenhöferallee 1,
60438 Frankfurt am Main, Germany
* Correspondence: Linckens@em.uni-frankfurt.de (J.L.); tholen@geo.uni-frankfurt.de (S.T.)

Abstract: Deformation in the upper mantle is localized in shear zones. In order to localize strain, weakening has to occur, which can be achieved by a reduction in grain size. In order for grains to remain small and preserve shear zones, phases have to mix. Phase mixing leads to dragging or pinning of grain boundaries which slows down or halts grain growth. Multiple phase mixing processes have been suggested to be important during shear zone evolution. The importance of a phase mixing process depends on the geodynamic setting. This study presents detailed microstructural analysis of spinel bearing shear zones from the Erro-Tobbio peridotite (Italy) that formed during pre-alpine rifting. The first stage of deformation occurred under melt-free conditions, during which clinopyroxene and olivine porphyroclasts dynamically recrystallized. With ongoing extension, silica-undersaturated melt percolated through the shear zones and reacted with the clinopyroxene neoblasts, forming olivine–clinopyroxene layers. Furthermore, the melt reacted with orthopyroxene porphyroclasts, forming fine-grained polymineralic layers (ultramylonites) adjacent to the porphyroclasts. Strain rates in these layers are estimated to be about an order of magnitude faster than within the olivine-rich matrix. This study demonstrates the importance of melt-rock reactions for grain size reduction, phase mixing and strain localization in these shear zones.

Keywords: ultramylonite; shear zone; phase mixing; EBSD; Erro-Tobbio peridotite; melt-rock reaction

1. Introduction

Strain in the upper mantle is inhomogeneously distributed. The deformation is localized in zones of high strain, i.e., shear zones. Shear zones control the deformation of the upper mantle (e.g., [1–3]) and are important for plate tectonics (e.g., [4,5]). It is therefore essential to know why, how and when strain localizes.

Initiation of strain localization occurs when certain domains in the upper mantle are weaker than others. Compositional (e.g., presence of melt or fluids), physical (e.g., temperature) and microstructural variations (e.g., grain size, crystallographic preferred orientation (CPO)) in the upper mantle can influence the viscosity (review in [6]). The viscosity of olivine, the volumetrically dominant mineral in the upper mantle, decreases when it incorporates water [7–9], and when small fractions (0.03–0.04) of melt are present [10–12]. An increase in temperature decreases the strength of olivine and pyroxenes (the main minerals in the upper mantle) (e.g., [1,13,14]). A smaller grain size leads to a decrease in viscosity when deformation occurs by diffusion, or by dislocation-accommodated grain boundary sliding (disGBS) (e.g., [13,14]). When dislocation creep is dominant, a CPO develops. A CPO has an influence on olivine strength, as olivine is viscously anisotropic (e.g., [15–17]). During ductile deformation, the pre-existing variations in viscosity can cause the initiation of strain localization, leading to the formation of shear zones in the upper mantle (e.g., [15,18,19]). In addition, at lower temperatures and high stresses, the occurrence of brittle processes (seismic) followed by ductile processes (postseismic creep) leads to strain localization in the upper mantle (e.g., [2,20]).

In order for strain to remain localized with ongoing ductile deformation, a positive feedback process between deformation and weakening has to occur, i.e., strain softening [2]. Strain softening processes can be divided in four classes [2]: thermal softening, geometrical softening, reaction softening and microstructural softening.

Thermal softening originates from shear heating, which is strain-rate dependent [21]. With increasing temperature, the strain rate increases, leading to an increase in temperature, leading to a positive feedback. Recent models show that shear heating is important in the generation of intermediate depth earthquakes (50–300 km) in a narrow temperature interval (600–800 °C) (e.g., [21,22]). However, the models also show that this process can only occur in pre-existing well-mixed fine-grained shear zones. The mixing of phases is necessary in order for other minerals to pin the migrating olivine grain boundary during grain growth occurring under static [23] or dynamic [24] conditions at the elevated temperatures. Otherwise, rapid grain growth in olivine [25] would lead to strain hardening during deformation, negating the strain softening. Large-scale models also show the importance of the positive feedback during shear heating in order to develop large-scale lithospheric faults (e.g., [19]).

Geometrical softening is due to the evolution of an olivine CPO. The strength of the CPO will increase with increasing strain, when strain is accommodated by dislocation creep, leading to a positive feedback (e.g., [17,26]). This process has been suggested as being important for shear localization in an upper mantle shear zone with no large grain size variation [15] and for the reactivation of pre-existing shear zones [16].

Reaction softening is caused by the formation of weak interconnected fine-grained polyphase bands of olivine and other minerals (e.g., olivine-opx, olivine-amphibole) or interconnected bands of a weak mineral (e.g., talc, serpentine) [2]. When the grain size in the polyphase bands is small enough they can deform by diffusion creep and lead to strain softening, which has been observed in natural shear zones (e.g., [27]). The fine grain size in polyphase material can persist due to the pinning process (e.g., [23,24,28]). The viscosity of the polyphase bands is either determined by the mineral that is interconnected in the bands [29] or by a composite rheology (e.g., [30,31]). Reactions in the upper mantle can be caused by the infiltration of fluids or melts or a change in PT conditions (metamorphic reactions). Melts and fluids can preferentially infiltrate in shear zones due to creep cavitation formed during grain boundary sliding [32–34], leading to a positive feedback mechanism and strain softening (e.g., [35–39]). The importance of reactions for the evolution of deformation has been determined in natural shear zones, be it metamorphic reactions (e.g., [27]), melt rock reactions (e.g., [40]) or hydration reactions (e.g., [41]).

Microstructural softening occurs when the grain size decreases during dislocation creep due to dynamic recrystallization [24,42] or during brittle deformation. The steady state olivine grain size during dislocation creep depends on stress [43]. However, dislocation creep is a grain size-independent deformation mechanism, and therefore the reduction in grain size will not result in a softening. A softening does occur when there is a change from dislocation creep to a grain size-dependent deformation mechanism. It has been shown in deformation experiments on olivine that disGBS is an important deformation mechanism under upper mantle conditions [13]. This process is grain size-sensitive and a reduction in grain size during deformation would result in softening (e.g., [44,45]). An even larger factor of softening will occur when the deformation process changes to diffusion creep, which has a larger grain size sensitivity. In order to keep the olivine grain size small, it is also important that phase mixing occurs during this softening process (e.g., [14,18,46,47]).

The evolution of microstructures from outside to the center of upper mantle shear zones often shows the evolution from a coarse-grained (millimeter sized) microstructure to a well-mixed fine-grained (tens of microns) microstructure (e.g., [36,48–51]). It has been shown that the olivine grain size depends on the amount of other minerals present [28,46,47,52], indicating the effectiveness of pinning to inhibit grain growth. Large-scale models show the importance of pinning in preserving shear zones and therefore in

the generation of plate tectonics [53,54]. The models, microstructural evolution in mantle shear zones, and several softening processes indicate the importance of grain size reduction and phase mixing processes on shear zone development. Recent studies have focused on phase mixing processes. Reactions (e.g., [27,37,55], grain boundary sliding (e.g., [51,56–58]), creep cavitation and nucleation (e.g., [55] and dissolution-precipitation [36] can lead to the mixing of phases.

However, in order to determine which phase mixing processes are important during upper mantle shear zone evolution, shear zones from different geodynamic settings have to be studied in detail. In addition, the effect of the phase mixing process on strain localization is important to quantify. For this purpose, we analyzed the microstructures of the Erro-Tobbio peridotite in the Ligurian Alps, Northwest Italy. The peridotite was exhumed during rifting in Late Carboniferous-Permian times (e.g., [59,60]). The first shear zones occurred during a first melt-free stage of rifting (thinning of the lithosphere by a factor of 2 [61]). After the first stage, ongoing thinning of the lithosphere leads to decompression melting of the asthenosphere and to melt percolation in the shear zones under spinel-facies conditions (e.g., [60,61]). Melts that reached the plagioclase-facies conditions in the Erro-Tobbio peridotites were silica-saturated due to extensive melt-rock reactions (e.g., [59,60]). These melts formed plagioclase-enriched peridotites and gabbro-norite pods (e.g., [60]).

Due to the extensive melt percolation during deformation, the spinel bearing shear zones of the Erro-Tobbio peridotite are ideal to analyze the importance of melt-rock reactions on phase mixing and strain localization. Our detailed microstructural analysis shows the importance of reactions of silica-undersaturated melts with dynamically recrystallized clinopyroxene (cpx) neoblasts and orthopyroxene (opx) porphyroclasts to form fine-grained mixtures of cpx + olivine $\pm$ opx $\pm$ spinel and mixtures of opx + olivine $\pm$ cpx $\pm$ spinel, respectively. The opx-rich fine-grained layers interconnect to form ultramylonitic layers on a thin section scale. The strain rate in these layers is estimated to be one order of magnitude faster than in the olivine-rich matrix.

2. Geological Setting

The Erro-Tobbio peridotite is located in the Voltri Massif in the Ligurian Alps, Northwest Italy and is a remnant of the Jurassic Ligurian Tethys [62]. The peridotite exhumed due to extension of the subcontinental lithosphere during Late Carboniferous-Permian times [59]. Ongoing exhumation occurred during the opening of the Tethys in Jurassic times [3].

The exhumation took place along five generations of shear zones, active at progressively decreasing PT conditions from spinel tectonite, plagioclase-, hornblende-, chlorite-bearing peridotite mylonites and serpentine mylonites [41]. Opx and spinel clusters in lithospheric spinel peridotites have been interpreted as being breakdown products from garnet [2]. Spinel tectonites and mylonites occur in kilometer-scale shear zones, were the fine-grained mylonites are superimposed on less-deformed tectonites [61,62]. Temperatures calculated with pyroxene geothermometers give a temperature of 960–970 °C [59] for the spinel tectonites. These shear zones are thought to form during the early melt-free extension of the subcontinental lithosphere (e.g., [62]). As a consequence of this early thinning of the lithosphere, near-adiabatic upwelling of the asthenosphere led to decompression melting and percolation of MORB-type melts during progressive extension [62]. This is evidenced by spinel harzburgites and dunites at several locations that are parallel to the spinel lherzolite tectonites and mylonites, indicating that silica-undersaturated melt is percolated by channeled porous flow along the pre-existing spinel-facies shear zones [61]. Locally, the spinel peridotites are transformed to plagioclase-enriched peridotites (e.g., [61,62]). The high amount of plagioclase (frequently more than 10–15%), indicates that the plagioclase is not metamorphic but formed due to the interstitial crystallization of silica-saturated melt [62]. During ongoing exhumation, deformation occurred in these plagioclase peridotites, forming plagioclase peridotite tectonites and shear zones in the south of Erro-Tobbio (e.g., [41,61]). These shear zones cut the spinel shear zones at a

high angle [58]. Geothermometry calculations indicate a temperature of 910–960 °C for the plagioclase tectonites [59].

In the hornblende-bearing mylonites the pyroxene porphyroclasts show a syntectonic breakdown to very fine-grained (2–30 μm) mixtures of olivine + amphibole + clinopyroxene + spinel ± orthopyroxene [38]. The formation of these fine-grained bands and the local occurrence of hornblende porphyroclasts within the olivine matrix indicate pre- and synkinematic infiltration of fluids [38]. The pyroxenes geothermometry calculations give temperatures of 790–880 °C for the amphibole-bearing shear zones [59]. The last stages of exhumation at low temperatures and pressures are indicated by the occurrence of chlorite-bearing (500–800 °C) and serpentine (300–500 °C) mylonites [38].

Following exhumation, subduction took place during the closing of the Jurassic Ligurian Tethys to eclogite-facies conditions during the Alpine collision. Subsequent rapid exhumation within a serpentine subduction channel occurred, preserving the almost unaltered peridotites (e.g., [63]).

All four samples were taken within the tectonite-mylonite peridotite, located to the west of Lake Badana (Figure 1a). In the field, clasts of mainly orthopyroxene are clearly visible, and some show a component of simple shear (Figure 1b). Thin opx-rich layers alternating with olivine-rich layers are observed (Figure 1b). Some of the layers include elongated spinel clasts (Figure 1b).
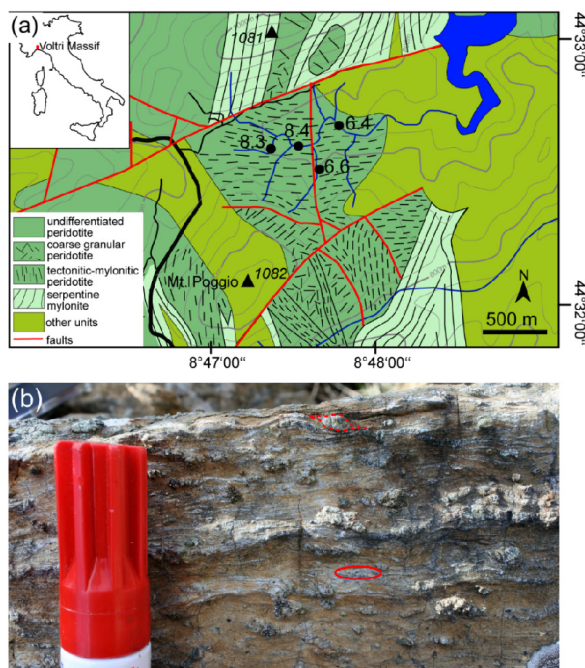
Figure 1. (**a**) Geological map of the field area with sample locations (black circles) modified after [41,61]. (**b**) Field photo of the spinel-bearing mylonites (location of Sample 6.4). In the red circle is a trail of elongated spinel. The dotted red line is a sigma opx porphyroclast indicating sinistral shear.

3. Materials and Methods

Samples were cut perpendicular to the foliation and parallel to the lineation (*XZ* section). Thin sections were cut and polished to a thickness of ~30 μm. With an optical

light microscope, representative microstructures were determined and selected for further analysis.

For electron backscatter diffraction analysis (EBSD) analysis, thin sections were polished for approximately 15 min with colloidal silica. Combined EBSD and energy dispersive X-ray analysis (EDX) were conducted at the Goethe University in Frankfurt (Germany), and the University of Cologne (Germany) on carbon-coated samples. At the Institute of Geoscience in Frankfurt, a JEOL JSM-6490 scanning electron microscope (SEM) was used. Measurement settings for EBSD were an acceleration voltage of 15 kV and a beam current of ~8 nA. For data acquisition, the program Flamenco (Oxford Instruments HKL Channel 5) and a Nordlys camera (Oxford Instruments) were used. At the Institute for Geology and Mineralogy in Cologne, EDX and EBSD measurements were conducted with a Zeiss Sigma 300-VP field emission SEM equipped with a NordlysNano detector (Oxford Instruments). The acceleration voltage was set to 20 kV. For the data acquisition, the program Aztec was used (Oxford Instruments). The step size was adapted to measured grain sizes in order for every grain to have at least 10 measurement points. The total range of step sizes is from 1–2.22 μm. In Cologne, element maps (O, Mg, Al, Si, Ca, Cr, Mn, Fe) were obtained simultaneously.

The EBSD data were cleaned from systematic misindexing of olivine (similar diffraction patterns for orientations rotated 60° around [100]) with Oxford Instruments HKL Channel 5 software. Subsequently, the data were loaded into the MTEX 5.6 extension for MATLAB (e.g., Bachmann et al., 2010) (http://mtex-toolbox.github.io/, accessed on 3 March 2013). All additional data processing and analysis were conducted with MTEX 5.6 (http://mtex-toolbox.github.io/, accessed on 3 March 2013). The MTEX script used for cleaning, grain detection (grain internal misorientation < 15°) and subgrain detection (misorientation angle between subgrains < 15°), deletion of boundary and badly indexed grains, crystallographic and boundary analysis, etc., is available on request from the authors. During grain reconstruction, resulting data were continuously checked against backscattered/forescattered, band contrast images and EDX data if present. The equivalent circular diameter (ECD) was calculated for all grains. EBSD and EDX maps were used to calculate phase abundances by area percentage throughout the text and the figures, phase abundances are given by "%" referring to area %. Grain boundary analysis was accomplished by calculating phase-specific boundary lengths. Phase (e.g., ol-opx) to grain (e.g., ol-ol, opx-opx) boundary percentages were used to determine the "mixing intensity". Pole figures (lower hemisphere orientation density plots) of the main phases were plotted with MTEX. A minimum number of 100 orientations (one point per grain) was used. ODF calculation was performed with grain mean orientations and a consistent halfwidth of 15°. To be able to compare the orientation density plots, the color coding is consistently depicted from min = 0 mrd (multiple of random distribution) = blue for a random orientation to max = 3 mrd = red. Higher mrd's than 3 are also colored red. The J-index and M-index were calculated for the CPO, which is a measurement of the strength of a CPO [64,65]. The M-index is 0 for a completely random fabric and 1 for a single crystal fabric.

Microprobe measurements were conducted using a JEOL JXA-8530F Plus microprobe with field emission located at the Institute of Geoscience at the Goethe University Frankfurt. The microprobe is equipped with 5 wavelength-dispersive spectrometers. The acceleration voltage was 15 kV and a beam current of 20 nA was used for 20 s (Al, Cr, Ca, Na, Mn, Fe, Ni), 30 s (K, Ti) or 40 s (Mg, Si) peak and 20 s background measuring time. The spot-size was adjusted to the grain size with minimum spot sizes of 1 μm for small grained neoblasts and maximum 4 μm for porphyroclasts. Microprobe data were used to calculate equilibration temperatures of neoblast assemblages and porphyroclasts. Neoblasts are mostly exsolution free, therefore calculated T estimates are thought to be accurate. In opx porphyroclasts with cpx exsolution lamellae, we calculated temperatures based on the host porphyroclast chemistry, ignoring exsolution lamellae. Temperature estimates are therefore minimum estimates. We used the two pyroxene geothermometer ($T_{2\text{-pyx}}$) and Ca in opx

geothermometer ($T_{Ca-in-opx}$) calibrated by [66]. In addition, we used the Al and Cr in the opx ($T_{Al-Cr-in-opx}$) geothermometer calibrated by [67].

4. Results

4.1. Sample Description

All thin sections show polymineralic (opx + ol + cpx ± spinel) ultramylonite layers with a small grain size (~10 µm) that can cross-cut the whole thin section (Figure 2). Often there are well-preserved domains in between serpentine-filled cracks (Figure 2a, bottom right and Figure 3a,b). Often, fine horizontal cracks go through the layers (Figure 3c). The grains in these layers have a very irregular form (Figure 3d). The sample with the lowest amount of opx porphyroclasts also has the thinnest (down to 200 µm) polymineralic layers (Figure 2d). In the samples with more opx porphyroclasts, the polymineralic layers can be up to 900 µm thick (Figure 2a).
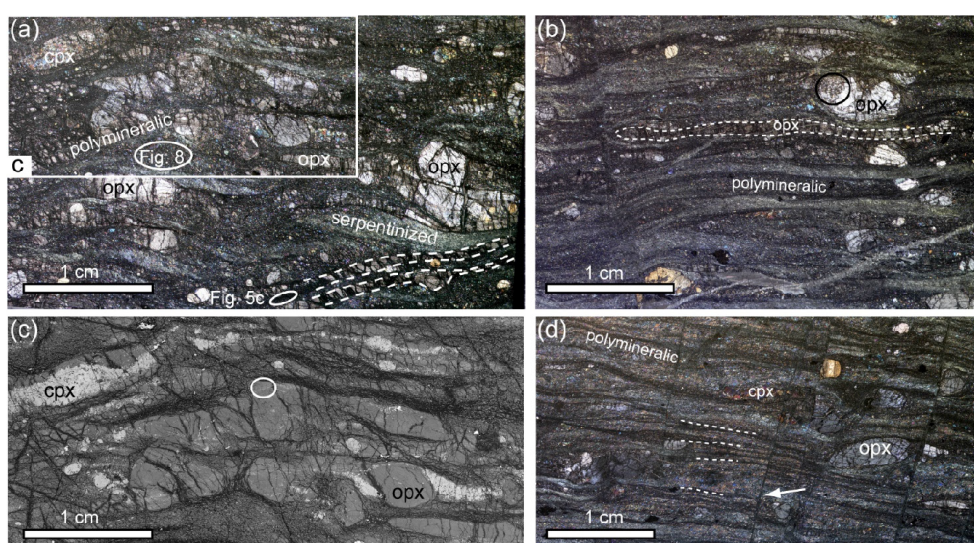
Figure 2. Overview of the thin sections. (**a**) Optical microscope image of Sample 6.6 under crossed polarized light. Opx porphyroclasts and some cpx porphyroclasts are visible, within an olivine-rich matrix. There are several fine-grained polymineralic layers visible (dashed white lines). Some of the opx porphyroclasts are elongated. Indicated is the location of Figure 5c (white ellipse) and the olivine matrix analyzed with EBSD displayed in Figure 8 (white ellipse); also indicated is the location of (**c**). (**b**) Optical microscope image of Sample 8.4 under crossed polarized light. The sample is similar to Sample 6.6 but shows fewer opx porphyroclasts and an increasing amount of fine-grained polymineralic layers. Some opx porphyroclasts are elongated as shown by the stippled line. Some opx porphyroclasts are recrystallized (black circle). (**c**) Part of (**a**) as backscatter electron (BSE) image. The bright phase is cpx, the medium gray is olivine/opx and the dark is serpentine. The polymineralic layers contain cpx as indicated in the white circle. All the cpx porphyroclasts show tails of smaller, cpx ± olivine neoblasts. (**d**) Optical microscope image of Sample 8.3 under crossed polarized light. Thin dark layers parallel (dashed lines) to the olivine matrix are fine-grained polymineralic layers. The sample also shows later stage vertical fractures that offset these thin layers (white arrow).
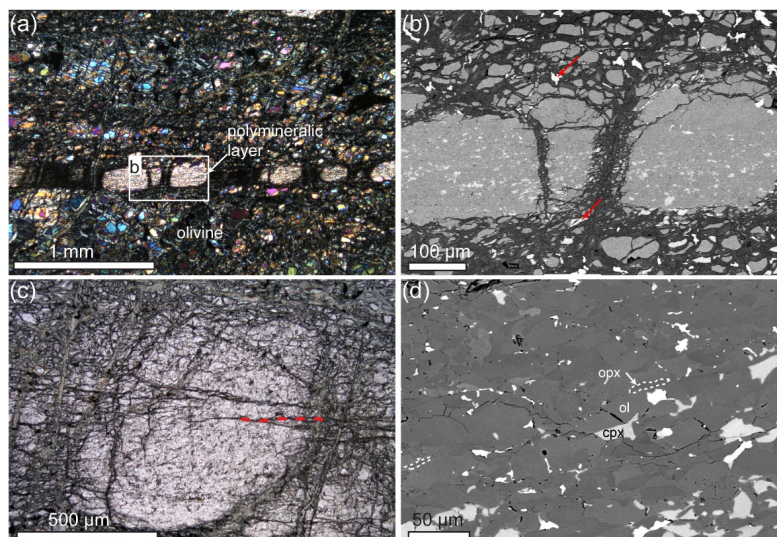
Figure 3. (**a**) Optical microscope image with crossed polarized light of a polymineralic fine-grained layer (ultramylonite) within the olivine-dominant matrix. Location of (**b**) is indicated. (**b**) Backscatter electron (BSE) image of part of the fine-grained polymineralic layer. Visible are fine-grained cpx grains (lightest gray) and opx + ol grains within the layer. Gray values for opx and ol are very similar. In addition, in this image cpx grains are visible within the olivine matrix (arrows). (**c**) Optical microscope image of part of a fine-grained layer with horizontal cracks (dashed red line). (**d**) BSE image of a fine-grained layer. Darkest grains are opx, gray is olivine and light gray is cpx. Dashed lines show thin elongated opx grains on the border of olivine grains.

Orthopyroxene clast size ranges from around 0.3 mm up to around 5 mm. Some opx porphyroclasts are elongated and can reach an aspect ratio of up to 20:1 (Figure 2b), however most clasts show small aspect ratios. The porphyroclasts often show undulose extinction. Some porphyroclasts in the samples with small amounts of porphyroclasts (Samples 8.3 and 8.4) show a few subgrains at the border. Some of these porphyroclasts also display some recrystallization at the borders, where dominantly opx occurs (Figure 4g). Some of the opx grains have 120° triple junctions, indicating annealing (Figure 4f). Most opx porphyroclasts show exsolution lamellae of cpx. Some smaller opx porphyroclasts and elongated or folded opx porphyroclasts show a fine-grained polymineralic tail and/or rim (Figure 4a–c,e,f) consisting of olivine, pyroxenes ± spinel. At the border of small opx porphyroclasts and the tips of the elongated opx, olivine grains often occur in embayments (Figure 4a–c). Some opx clasts are kinked and along the kinks small cpx and opx grains occur (Figure 4d).
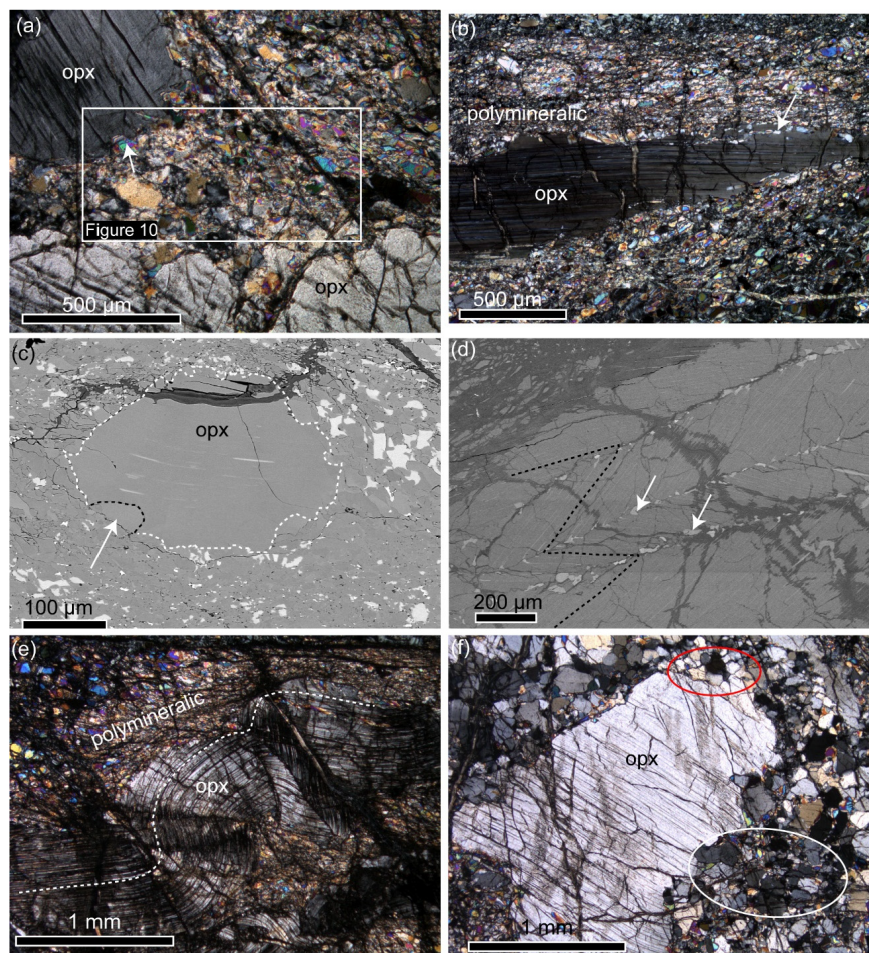
Figure 4. Orthopyroxene porphyroclasts. (**a**) Optical microscope image under crossed polarized light of an orthopyroxene porphyroclast with olivine embayments (arrow). Indicated is the location of the EBSD map of Figure 10. (**b**) Optical microscope image under crossed polarized light of an elongated opx porphyroclasts surrounded by fine-grained polymineralic layers. The porphyroclast shows embayments of olivine (arrow). (**c**) BSE image of an opx porphyroclast (dashed white line) showing cpx exsolution lamellae and olivine embayment (arrow). The porphyroclast is located in a fine-grained polymineralic (opx + ol + cpx + spinel) matrix. (**d**) BSE image of a kinked opx porphyroclast (black dashed line traces a cpx exsolution lamellae) with small cpx (white arrows) on the kinks and grains at the border. (**e**) Folded opx porphyroclasts with cpx exsolution lamellae and a fine-grained polymineralic rim. (**f**) Orthopyroxene porphyroclast surrounded by relatively coarse grains of opx (compared to (**e**)). Some opx grains show close to 120° interfacial angles at triple junctions (red circle). The area in the white circle includes, besides opx, smaller grains of olivine, cpx and spinel.

Clinopyroxene porphyroclasts occur in all samples and range in size from 190 μm to 2.7 mm. Commonly they show opx exsolution lamellae (Figure 5a). Most cpx porphyroclasts show a rim or tail of smaller cpx grains (Figure 5a,b), and further away from the porphyroclast the cpx neoblasts are intermixed with olivine grains (Figure 5b). In some samples these tails are thin and they can extend up to 2 cm to form cpx-rich layers

(Figures 2c and 5a). Cpx grains are also prominent in some areas within the olivine-rich matrix (Figure 5c).
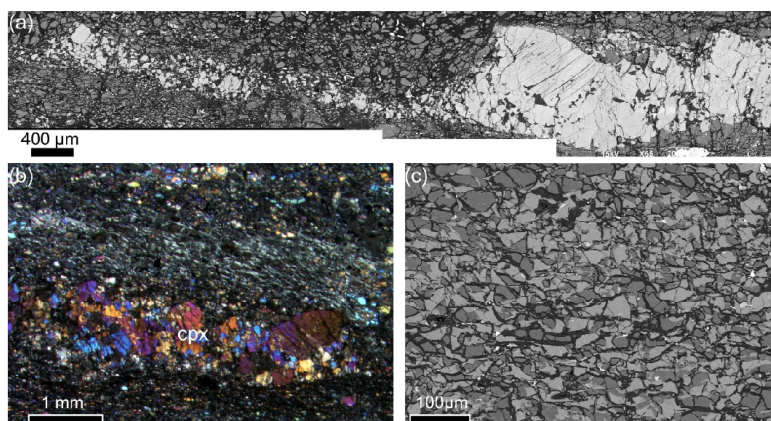

Figure 5. (**a**) BSE image of recrystallized cpx porphyroclasts adjacent to the porphyroclast cpx neoblasts, and further away a tail of cpx + olivine. (**b**) Optical microscope image with crossed polarizers of a recrystallized cpx layer. (**c**) BSE image of cpx and olivine grains in the matrix (ROI 32).

Parts of the olivine matrix are highly serpentinized and individual grains are difficult to distinguish under the optical microscope. Where individual grains can be observed the average grain size in the matrix is around 60 μm. No olivine porphyroclasts are observed.

Porphyroclasts of spinel occur in all samples (range in sizes 0.3–1.4 mm); some porphyroclasts form clusters with opx. Some spinel porphyroclasts are stretched (aspect ratios up to 5) in the foliation. Smaller spinel grains occur in the olivine matrix (Figure 5c), and within recrystallized rims and tails of the pyroxene clasts.

4.2. EBSD Data

4.2.1. Clinopyroxene

Two recrystallized cpx porphyroclasts were mapped with EBSD (Table 1, Figures 6 and S1). The mapped areas consist mainly of clinopyroxene (95% and 87%, Figures 6 and S1). The other phases are olivine (4% and 5%), enstatite (<1% and 4%) and spinel (<1% and 5%). These maps consist of 75% and 53% grain boundaries (Table 1), with average cpx grain sizes of 36 μm and 30 μm, respectively. In the map shown in Figure 6, small grains of cpx are observed in between larger cpx grains. These small grains are associated with small opx and spinel grains. Small olivine grains (15 ± 7 μm) occur with cpx in phase mixtures at the border of the recrystallized tail (Figure 6c). The cpx grain size in these phase mixtures is much smaller than the grains close to the porphyroclast border. The cpx CPO is related to the clast orientation (Figures 6d and S1). A few cpx grains show a large internal misorientation up to 8° (Figure 6b). The small cpx grains at the border of the recrystallized area, intermixed with olivine, show no internal misorientations (Figure 6b). The olivine grains show no clear CPO (Figure 6d).

Table 1. Area percentages and grain sizes (μm), with the standard deviation, of all analyzed phases. The last column shows the proportion of phase boundaries (PB) of the total boundary length as a percentage.

Map Name	Type	Olivine		Opx		Cpx		Spinel		Pargasite		PB
		Area	Grain Size	Area	Grain Size	Area	Grain Size	Area	Grain Size	Area	Grain Size	
ROI 12	cpx rxs	5	15 ± 7	4	19 ± 12	87	30 ± 41	5	18 ± 20			47
ROI 16	cpx rxs	4	18 ± 11	<1	18 ± 8	95	36 ± 42	<1	16 ± 6			25
ROI 33	cpx rxs with ol	33	10 ± 6	1		66	11 ± 9	<1				63
ROI 32	olivine + cpx	58	16 ± 8	3	12 ± 4	37	15 ± 7	3	9 ± 4			64
ROI 20	small opx rxs	48	16 ± 12	45	15 ± 12	6	12 ± 8	1	9 ± 3			72
ROI 24	small opx rxs	66	12 ± 8	32	12 ± 10	1	8 ± 3					61
ROI 25	large opx rxs	33	14 ± 8	50	17 ± 15	15	15 ± 11	2	10 ± 5			73
ROI 25	Olivine	88	45 ± 30	7	27 ± 11	3	28 ± 10	2	27 ± 10			45
ROI 31	Olivine	73	23 ± 16	15	17 ± 9	9	17 ± 9	2	10 ± 5			68
ROI 13	Ultramylonite	62	12 ± 7	29	12 ± 7	9	11 ± 5					67
ROI 14	Ultramylonite	76	5 ± 4	16	4 ± 3	6	4 ± 2	1	3 ± 1	<1		52
ROI 19	Ultramylonite	51	11 ± 7	39	10 ± 8	7	9 ± 5	3	8 ± 9	<1	7 ± 2	66
ROI 23	Ultramylonite	75	9 ± 6	21	8 ± 4	4	7 ± 4					52

Figure 6. (**a**) Band contrast image of a recrystallized cpx porphyroclast (ROI12). The red circle shows an area with fine-grained layers in between larger grains. (**b**) Grain orientation spread (GOS) map of diopside, displaying the internal misorientation of the grains. (**c**) Phase map. The red circle shows mixed olivine and cpx domains at the border of the clast. (**d**) Clinopyroxene and olivine CPO.

The map of smaller cpx porphyroclasts (Figure 7) shows olivine grains directly at the porphyroclast border, and in contrast to the other two analyzed porphyroclasts, it has a relatively high proportion (63%) of phase boundaries. The phase mixture consists of 66% cpx and 33% olivine, with a small amount of spinel (1%) and opx (<1%). The recrystallized opx grain sizes are smaller (average 11 μm ± 9 μm) for this cpx porphyroclast than for the other two cpx porphyroclasts (Table 1). The grain size is similar to the olivine grain size (10 ± 6 μm, Table 1). The clinopyroxenes show a weak CPO related to the host orientation. No olivine CPO is observed (Figure 7).
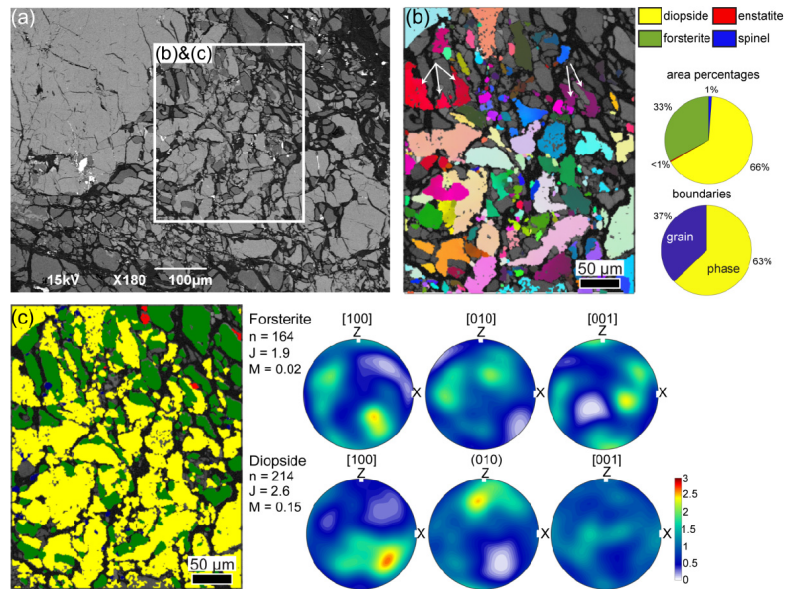
Figure 7. (**a**) BSE image of a cpx porphyroclast with recrystallized tail of olivine and cpx neoblasts. (**b**) Diopside orientation map of the recrystallization tail (ROI33). White arrows show one grain of diopside with irregular boundaries and olivine in between. (**c**) Phase map of the same area as in (**b**). The CPOs of clinopyroxene and olivine are also shown.

In addition to the cpx porphyroclasts, an olivine + cpx matrix domain was analyzed with EBSD (Figures 5c and 8). The cpx- (37%) and olivine (58%)-rich matrix contains small amounts of opx and spinel (both 3%) (Figure 5c). A large amount of serpentine occurs, which makes the boundary and grain size analyses more prone to errors. The map consists of 64% phase boundaries. Both olivine and cpx grain sizes are relatively small (16 ± 8 μm and 15 ± 7 μm, respectively; Table 1). The [001] axes of olivine are oriented parallel to the lineation and the [100] axes are oriented perpendicular to the foliation (Figure 8). The (100) planes of diopside are orientated perpendicular to the lineation and the [001] axes are oriented parallel to the foliation.
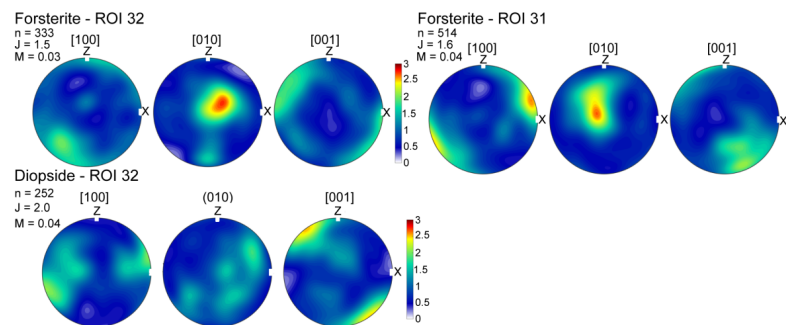
Figure 8. Forsterite and diopside CPO of the matrix displayed in Figure 6c (ROI32) and of the olivine matrix (ROI31).

A map of the cpx-poor (9%) olivine matrix (73%) was also analyzed (Table 1, Figures 8 and S2), which contains 15% opx. Due to the well-dispersed pyroxene grains, the phase boundaries make up 68% of the total boundaries. The olivine grain size in this matrix is slightly bigger (23 $\pm$ 16 μm), but within error, than the olivine grain size of the cpx-rich matrix. The grain sizes of the other minerals are similar (Table 1). The olivine CPO is weak (J-index of 1.6, M-index of 0.04) with the [100] axes parallel to X and [001] axes perpendicular to the foliation (Figure 8).

4.2.2. Orthopyroxene

Three maps of recrystallized opx clasts were measured (Table 1, Figures 9, 10 and S3). The recrystallized tails consist of mainly opx (32–50%) and olivine (33–66%). The clinopyroxene abundance is variable (1–15%, Table 1), and spinel is an accessory phase (1–2%).
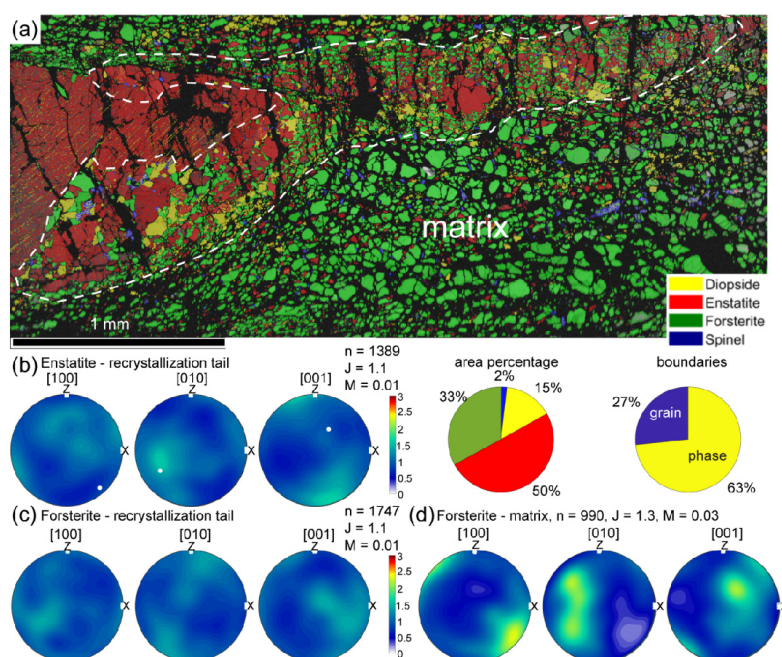
Figure 9. (**a**) Phase map of an opx porphyroclast with a recrystallization tail (dashed line) within the olivine matrix; also indicated are the area percentages of the phases and the amount of grain and phase boundaries of the recrystallization tail (ROI25). (**b**) Pole figure of enstatite orientations in the recrystallization tail. The white dot shows the orientation of the opx porphyroclast. (**c**) Pole figure of forsterite orientations in the recrystallization tail. (**d**) Pole figure of forsterite orientations in the matrix.
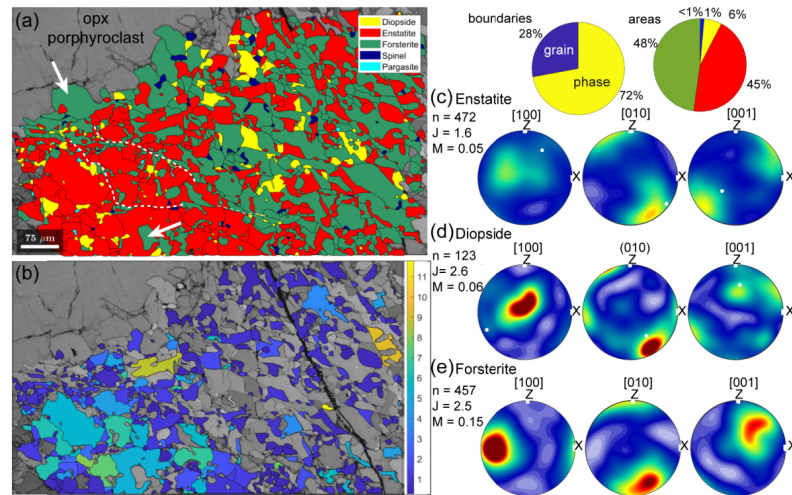
Figure 10. (**a**) Phase map of a recrystallization tail of an opx porphyroclast (ROI20), located at the top left of the map. The white arrows indicate an olivine embayments in the opx porphyroclast and an opx neoblast. The white dashed lines follow cracks along which small grains are visible. Shown at the top right are the grain and phase boundary percentages and area percentages. (**b**) Band contrast image and the grain orientation spread (GOS) in each enstatite grain. (**c**–**e**) CPO of enstatite, diopside and forsterite.

The larger opx porphyroclast shows at the lower border a mixture of relatively coarse-grained opx + ol + cpx ± spinel. These larger opx grains have a relatively large misorientation (up to >40°) from the opx porphyroclast orientation. The map shows a thin (~100 μm) polymineralic tail extending from the orthopyroxene porphyroclast. The grain sizes in this band are small (opx: 17 ± 15 μm, olivine: 14 ± 8 μm, cpx: 15 ± 11 μm). None of the minerals show a CPO and the J-index and M-index is small for both opx (J = 1.1, M = 0.01)) and olivine (J = 1.1, M = 0.01) (Figure 9b,c).

The surrounding olivine-rich matrix (83%) has a larger average grain size (45 ± 30 μm, Table 1). Included in the matrix are some (9%) smaller opx grains (27 ± 11 μm), spinel grains (4%, 27 ± 10 μm) and cpx grains (4%, 28 ± 10 μm). The olivine CPO is weak (J-index of 1.3, M-index of 0.03) and shows [100] close to the lineation, [010] close to Y and [001] close to the Z axis (Figure 9d).

The neoblasts adjacent to the small opx porphyroclasts have an inhomogeneous grain size; there are some concentrated lines where very small (~5 μm), mainly orthopyroxene grains occur (Figure 10). Additionally, in these areas pargasite is present, and also visible are embayments of olivine in some larger opx grains of the phase mixture (Figure 10). The phase boundaries are very irregular and lobate. The opx shows a weak CPO (J-index: 1.6, M-index: 0.05), with [001] close to X and [010] perpendicular to the foliation. The orientations of [010] and [001] are close to the porphyroclast orientation (Figure 10). The olivine CPO is relatively weak (J-index: 2.6 and M-index: 0.15), the [100] axes are parallel to X and [010] axes perpendicular to the foliation. Diopside shows a CPO of [100] parallel to Y and (010) perpendicular to the foliation.

4.2.3. Fine-Grained Layers

Four areas were analyzed of different fine-grained polymineralic layers in the thin sections (Table 1). One example is shown (Figure 11); the other three are displayed in the supplementary data (Figures S4–S6). All layers are dominated by olivine (51–76%) followed by opx (16–39%), cpx (4–9%) and spinel (1–3%). Phase boundaries are dominant

and have a similar percentage in all four maps (62–67%). The average grain size ranges from 4–12 μm for all phases (Table 1). None of the phases show a CPO in these layers (Figure 11c,d).
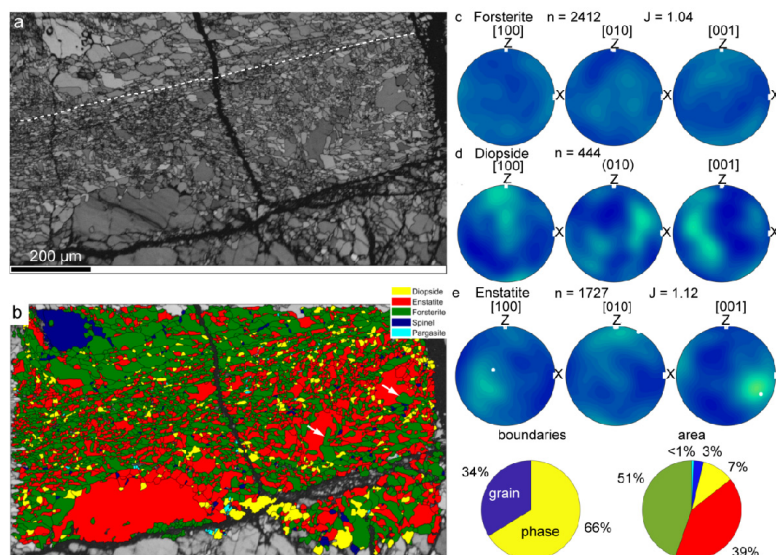

Figure 11. (**a**) Band contrast image of a fine-grained layer (ROI19). Cracks, parallel to the layer, go through the fine-grained part of the layer (dashed white line). There are more cracks parallel to this layer. (**b**) Phase map of the fine-grained layer. At the top is an olivine-rich layer with small grains of other phases on the grain boundaries. The grain shapes are very irregular in the fine-grained layer. Bigger opx grains at the right of the map show embayments of olivine (white arrows). (**c**–**e**) CPO of forsterite, diopside and enstatite.

4.3. Chemical Composition and Geothermal Calculations

The chemical data are shown in Table S1. Orthopyroxene shows a correlation between Al_2O_3 (0.92–5.12 wt.%) and Cr_2O_3 (0.04–0.63 wt.%), where porphyroclasts have the highest values, and opx neoblasts in the fine-grained layers the lowest (Figure 12a). The neoblasts show values similar to the fine-grained layers and the range goes up to the lowest values of the porphyroclasts (Figure 12a). A similar difference in composition is shown by CaO (range from 0.26–1.42 wt.%), where the opx in the fine-grained layers shows the lowest values and porphyroclasts the highest values of CaO (Figure 12b). In clinopyroxenes there is a correlation between Cr_2O_3 (range from 0.21–1.08 wt.%) and Al_2O_3 (range from 2.12–6.95 wt.%), where both decrease from porphyroclasts to fine-grained neoblasts (Figure 12d). The neoblasts have values of both Cr_2O_3 and Al_2O_3 spanning the whole range, connecting the fine-grained neoblasts and porphyroclasts (Figure 12c). The values of TiO_2 (range from 0.22–0.72 wt.%) show no dependence on the microstructural site (Figure 12d).

The geothermometry calculations give an average temperature for the neoblasts of 884 ± 58 °C ($T_{Ca-in-opx}$), 823 ± 59 °C ($T_{Al-Cr-in-opx}$) and 853 ± 32 °C (T_{2pyx}) (Table 2). These average values are similar, within error. The porphyroclasts show a distinct higher calculated temperature ($T_{Ca-in-opx}$ 1059 ± 95 °C, $T_{Al-Cr\ in\ opx}$: 1022 ± 47 °C). The calculated temperatures from the fine-grained layers are always lower than the neoblast temperatures, but within error (Table 2). The lowest temperatures (775 ± 48 °C) are calculated with the Al-Cr-in-opx geothermometer in the fine-grained layers.
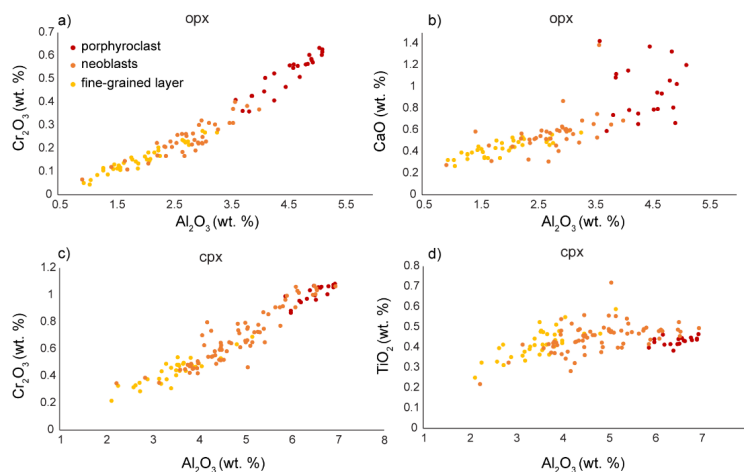
Figure 12. (a) Cr_2O_3 (wt.%) vs. Al_2O_3 (wt.%) in opx; (b) CaO vs. Al_2O_3 in opx; (c) Cr_2O_3 (wt.%) vs. Al_2O_3 (wt.%) in cpx; (d) TiO_2 (wt.%) vs. Al_2O_3 (wt.%) in cpx. Red symbols are porphyroclast, orange symbols are neoblasts and yellow symbols are grains in fine-grained layers.

Table 2. Results of geothermometry calculations for porphyroclasts, neoblasts and neoblasts in fine-grained layers. "n" indicates how many porphyroclasts or different areas in the thin section were measured and in brackets the total number of measurements is given. The temperatures are the averages in °C with their standard deviation.

	n	$T_{Ca-in-opx}$	$T_{Al-Cr-in-opx}$	n	T_{2-pyx}
porphyroclasts	4 (24)	1059 ± 95	1022 ± 47		
neoblasts	6 (50)	884 ± 58	823 ± 59	6 (19)	853 ± 32
fine-grained	6 (29)	846 ± 38	775 ± 48	5 (14)	843 ± 30

5. Discussion

5.1. Microstructural Evolution

The opx and cpx porphyroclasts both show the formation of smaller recrystallized grains at their borders. The cpx porphyroclasts show mainly cpx neoblasts adjacent to the porphyroclasts, with a small amount of opx neoblasts (4%, Figure 6d). The cpx neoblast CPO is related to the porphyroclast orientation (Figure 6c) and the bigger neoblasts show an internal misorientation (Figure 6b). No olivine embayments are observed in these cpx porphyroclasts (Figures 6 and S1). The lack of olivine embayments and the CPO indicate that the neoblasts were formed by dynamic recrystallization of the cpx porphyroclast. The small opx neoblasts are likely coming from exsolution lamellae from the cpx porphyroclasts.

Further away from the cpx porphyroclasts, in recrystallization tails, and adjacent to smaller cpx porphyroclasts, a mixing of olivine and cpx occurs. The irregular shape of the cpx and olivine grains (Figures 5a and 7a) and the cluster of similar cpx orientations with olivine in between (Figure 7b), suggest that a silica-undersaturated melt percolated through after the dynamic recrystallization stage, dissolving cpx and precipitating olivine. The melt percolation of silica-undersaturated melts occurred during rifting, due to decompression melting of the asthenosphere (Figure 13, [61,62]).
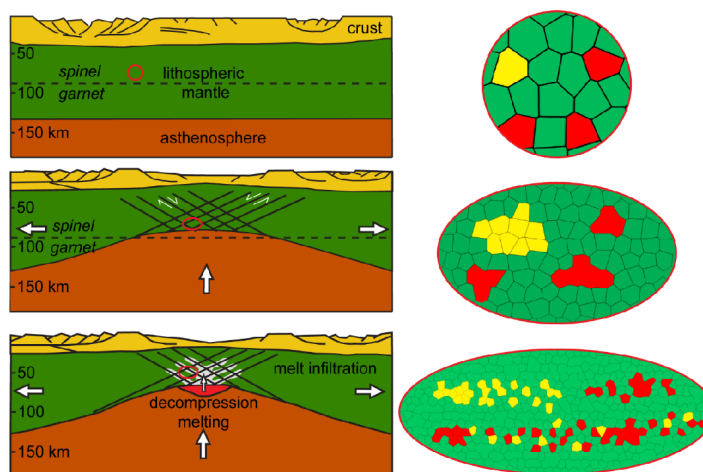
Figure 13. Sketches of the rifting (modified after [61]) in the left panels, and the corresponding microstructural evolution in the spinel shear zones of the Erro-Tobbio peridotite (locations indicated with the red circle and ellipses) in the right panel. The white arrows indicate the movement directions of the lithosphere and asthenosphere. The microstructures show the evolution from the undeformed peridotite with large grains of olivine (green), opx (red) and cpx (yellow). During the first stage of thinning, cpx and olivine recrystallize, whereas opx porphyroclasts elongate or remain equigranular. During ongoing thinning melt infiltrates, reacts with the dynamically recrystallized cpx grains and opx porphyroclasts, forming cpx+ol fine-grained layers and opx + ol + cpx fine-grained layers.

In contrast to the bigger cpx porphyroclasts, opx porphyroclasts show rims and/or tails consisting of opx (32–50%) + olivine (33–66%) + cpx (8–15%) ± spinel (1–2%) (Figures 9 and 10). The occurrence of olivine embayments at the borders of opx porphyroclasts and of some bigger neoblasts (Figures 4b,c, 10e and 11b) and the formation of fine-grained polymineralic rims surrounding folded and elongated opx porphyroclasts indicate that deformation partially occurred in the presence of a silica-undersaturated melt. The melt-rock reaction combined with ongoing deformation led to the formation of fine-grained (average around 15 μm, Table 1) tails adjacent to opx porphyroclasts. Enstatite and forsterite neoblasts next to the big porphyroclasts show no CPO (Figure 9b), indicating that ongoing deformation in these fine-grained layers occurred during diffusion creep. The enstatite neoblasts next to the small opx porphyroclasts show a CPO related to the opx porphyroclast (Figure 10a). In addition, the opx shows some internal misorientation in the bigger neoblasts (Figure 10b), indicating that a combination of dislocation and diffusion creep was active in these layers. This is also indicated by the olivine CPO (Figure 10) that shows an A-type CPO, which is the common slip system in olivine in dry conditions [68].

In contrast to cpx porphyroclasts, most opx porphyroclasts show little evidence for dynamic recrystallization prior to melt percolation. This indicates that in the first stage of rifting, prior to melt percolation, dynamic recrystallization of cpx occurred, and likely olivine porphyroclasts as well (Figure 13). Orthopyroxene porphyroclasts possibly got folded and elongated during these first stages of deformation. With ongoing extension and thinning, decompression melting and infiltration of melt in the shear zones occurred [58]. The silica-undersaturated melt reacted with the dynamically recrystallized cpx tails and the opx porphyroclast. These reactions occurred during deformation and fine-grained mixtures formed at the rims of the porphyroclasts. Ongoing deformation under sub-solidus conditions led to further grain size reduction and interconnected fine-grained layers (Figures 2, 3a and 13) in which deformation could localize. These layers deform by

diffusion creep as shown by the lack of CPO of all phases (Figure 11c–e). The layers consist mainly of olivine (51–76%) and opx (16–39%) with a small amount of cpx (4–11%).

The presence of a small amount of amphibole (<1%) in the fine-grained layers (Figures 10a and 11b) indicates possible fluid/melt infiltration in the later stages of deformation. A late stage of deformation is indicated by horizontal cracks localized within the ultramylonite layers (Figure 11a), and some randomly oriented cracks in recrystallization tails (Figure 10a). Along the horizontal cracks, olivine and opx grain boundaries are aligned. In addition, small-sized, mainly opx grains are found along the cracks (Figures 10b and 11a).

5.2. Olivine-Rich Matrix

In order to determine the strain rate contrast between the fine-grained ultramylonite layers and the olivine-rich matrix, the grain size of both is needed. Due to the serpentinization, the olivine grain size of the matrix is difficult to determine. Domains of the matrix that can be analyzed, due to lower amounts of serpentinization, contain relatively high amounts of second phases. Two maps of the matrix that contain second phases (pyroxenes and spinel, totals of 12% and 26%) give grain sizes of 45 ± 30 μm and 23 ± 16 μm, respectively (Table 1). Due to pinning effects, these grain sizes are probably a lower limit of the matrix olivine grain size [47]. The pinning effect can also be high as the phases in the matrix are relatively well-mixed, as indicated by the high amount of phase boundaries compared to grain boundaries (45% and 68%, respectively (Table 1)). Some parts of the matrix consist of well-mixed (64% phase boundaries) olivine (58%) and cpx (37%) (Figure 6c, Table 1). With the lack of a clear host clast, the high amount of cpx in parts of the matrix is difficult to explain. It is possible that it was formed by extensive reactions of undersaturated silica melt with cpx neoblasts. Alternatively, some cpx enrichment in the olivine matrix could have occurred at the later stages of melt infiltration. In these later stages the melt was possibly enriched in silica due to extensive melt-rock reactions (e.g., [61]).

The olivine CPO in this cpx-rich matrix shows a C-type CPO with the [001] axes parallel to the lineation and the [100] axes perpendicular to the foliation [68]. The C-type CPO has been suggested to form when water [69] or melt (e.g., [70]) is present. The olivine CPO in the matrix shows the [100] axes parallel to the lineation and the [001] axes perpendicular to the foliation, which has been classified as the E-type CPO, which is thought to be dominant at water-rich conditions [68]. In contrast, in the recrystallization tail of a small opx, the A-type CPO was observed (Figure 10), which is suggested to be dominant at dry conditions [68]. In a few upper mantle shear zones, a transition from A-type to an E-type CPO has been observed to occur with increasing strain localization (i.e., protomylonites to ultramylonites; e.g., [28,71]). This change in CPO has been suggested to be caused by an increase in water content [71] or a decrease in temperature during strain localization [28]. This transition is the opposite of what is observed in the Erro-Tobbio shear zone, where we find the E-type CPO in the olivine matrix.

In the Ronda shear zone, a detailed study on CPO evolution found different CPO types which are related to water content [33]. During strain localization, water migrates to the ultramylonites, due to water pumping along grain boundaries. The dry CPO type is found in the drained parts of the shear zone whereas the water-rich CPO is found closer to the ultramylonites. The ultramylonites show a dry CPO type as the fluid is further distributed in new grain boundaries. In the Erro-Tobbio shear zone, the difference in dry CPO type in the recrystallized layer (Figure 10) compared to the wet CPO type in the matrix (Figure 9) could possibly be related to the same process as described in [33]. In this case, the fluid is distributed along the new grain boundaries in the finer-grained areas. However, a more detailed study of the CPO in the different areas of the samples has to be conducted to be able to determine the process responsible for the different CPO types in the Erro-Tobbio shear zone. As the fine-grained layers do not show a CPO (Figure 11), no CPO type can be determined for these layers. In addition, the development of a CPO can be complex, and for the Josephine peridotite the A- and E-type were found in different samples with similar

water content [72]. Here, the pre-existing CPO played a large role in the CPO evolution [72]. The importance of a pre-existing CPO and geometry of deformation has been shown in a recent study on various natural rock samples [73]. This study shows that any of the CPO types (A- to E-types) can form at very low water content and low stresses [73].

In any case, the olivine CPOs suggest that deformation by dislocation creep or dislocation-accommodated grain boundary sliding (disGBS) occurred in the olivine-rich matrix.

5.3. Strain Localization

The microstructural evolution indicates the importance of melt-rock reactions for grain size reduction and extensive phase mixing in the shear zone. Due to this grain size reduction, the deformation changes from dislocation creep in the matrix to diffusion creep in the ultramylonite layers.

In order to determine the effect of the decrease in grain sizes and change in deformation mechanism on the strain rate, a deformation mechanism map has to be generated. For the deformation mechanism map a deformation temperature is needed, which has been calculated for the porphyroclasts, neoblasts and fine-grained neoblasts (Table 2).

The microprobe data show a clear trend of decreasing Cr_2O_3 (wt.%), Al_2O_3 (wt.%) and CaO (wt.%) content from porphyroclasts to fine-grained neoblasts (Figure 12). The scatter in CaO (wt.%) in the opx porphyroclasts is related to small exsolution lamellae of cpx. In the cpx the CaO (wt.%) shows a clear trend with decreasing values from the porphyroclasts to the fine-grained neoblasts (Figure 12). The TiO_2 remains at relatively constant values. The geothermometers reflect these trends and show a decrease in calculated temperatures for all three geothermometers, going from porphyroclasts over neoblasts to the fine-grained neoblasts (Table 2). The neoblasts show higher temperatures than the fine-grained neoblasts but they are within error. For the deformation map calculations, we used a deformation temperature of 850 °C. With a stress estimate from the olivine matrix calculated with the paleopiezometer and assuming the stress is similar in both matrix and fine-grained layers, we get a strain rate reduction of about one order of magnitude (Figure 14). The deformation map indicates that the matrix olivine deformed by dislocation creep accommodated by grain boundary sliding (Figure 14). The olivine in the ultramylonite layers deforms at the border between diffusion creep and disGBS (Figure 14). Here we assume a dry olivine flow law, since the importance of disGBS at "wet" conditions has not been determined yet [13]. If we assume wet olivine diffusion and dislocation creep flow laws, both matrix olivine and ultramylonite olivine will fall in the diffusion creep field. Due to grain size dependence of diffusion creep, a strain localization in the ultramylonites will also occur.
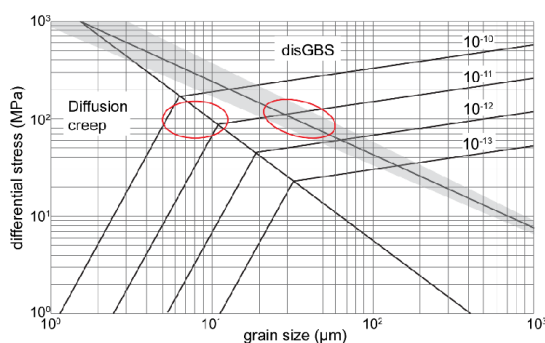

Figure 14. Olivine deformation mechanism map at 850 °C, showing in light gray the paleopiezometer [43]. The red circle on the right shows the average olivine grain sizes of the matrix (23–45 µm, Table 1) and the corresponding differential stresses calculated with the paleopiezometer. The left circle shows the range of average olivine grain sizes in the ultramylonite layers (5–12 µm, Table 1). Diffusion creep flow law from [14] and the disGBS flow law from [13].

The deformation mechanism map only considers the olivine, as it is the dominant phase in both matrix and the fine-grained layers. However, the pyroxenes very likely contribute to the rheology in both the matrix and fine-grained layers. In addition, it has been shown that small melt fractions (0.03–0.04) decrease the viscosity of olivine substantially [10–12]. Therefore, the effect on the viscosity of the infiltration of the silica undersaturated is twofold. On one hand the melt infiltration during the evolution of the shear zone weakens the complete shear zone, and on the other hand, locally, the melt-rock reactions lead to the formation of the fine-grained ultramylonite layers. This shows the importance of melt-rock reactions for phase mixing, and in turn for strain weakening (Figure 14). The importance of melt-rock reactions for strain weakening have been observed in other peridotites (e.g., [40]). The observation of the formation of fine-grained layers due to melt percolation is the opposite of what was observed recently in the Finero peridotites in the southern Alps [74]. The peridotite is a metasomatized mantle section originating in a supra-subduction environment [74]. These authors observed that the percolation of hydrous melts favored olivine grain growth and deformation by dissolution and precipitation. This led to homogenously distributed deformation. Even though pargasite and phlogopite were recrystallized, this recrystallization did not lead to a weakening. This contrasting behavior illustrates the importance of the melt composition and their interaction with the peridotites. In a ridge setting where the asthenosphere melts due to decompression melting, Si-undersaturated melts will percolate the peridotites leading to the melt-rock reactions and strain weakening observed in, for instance, the Erro-Tobbio and Othris peridotite [40].

References

1. Bürgmann, R.; Dresen, G. Rheology of the Lower Crust and Upper Mantle: Evidence from Rock Mechanics, Geodesy, and Field Observations. *Annu. Rev. Earth Planet. Sci.* **2008**, *36*, 531–567. [CrossRef]
2. Drury, M.R.; Vissers, R.L.M.; Wal, D.; Hoogerduijn Strating, E.H. Shear localisation in upper mantle peridotites. *Pure Appl. Geophys.* **1991**, *137*, 439–460. [CrossRef]
3. Vissers, R.L.M.; Drury, M.R.; Hoogerduijn Strating, E.H.; Spiers, C.J.; van der Wal, D. Mantle shear zones and their effect on lithosphere strength during continental breakup. *Tectonophysics* **1995**, *249*, 155–171. [CrossRef]
4. Bercovici, D. The generation of plate tectonics from mantle convection. *Earth Planet. Sci. Lett.* **2003**, *205*, 107–121. [CrossRef]
5. Tackley, P.J. Mantle convection and plate tectonics: Toward an integrated physical and chemical theory. *Science* **2000**, *288*, 2002–2007. [CrossRef] [PubMed]
6. Tommasi, A.; Vauchez, A. Heterogeneity and anisotropy in the lithospheric mantle. *Tectonophysics* **2015**, *661*, 11–37. [CrossRef]

7.   Mei, S.; Kohlstedt, D.L. Influence of water on plastic deformation of olivine aggregates 1. Diffusion creep regime. *J. Geophys. Res. Solid Earth* **2000**, *105*, 21457–21469. [CrossRef]

8.   Mei, S.; Kohlstedt, D.L. Influence of water on plastic deformation of olivine aggregates 2. Dislocation creep regime. *J. Geophys. Res. Solid Earth* **2000**, *105*, 21471–21481. [CrossRef]

9.   Tasaka, M.; Zimmerman, M.E.; Kohlstedt, D.L. Evolution of the rheological and microstructural properties of olivine aggregates during dislocation creep under hydrous conditions. *J. Geophys. Res. Solid Earth* **2015**, *121*, 92–113. [CrossRef]

10. Hirth, G.; Kohlstedt, D.L. Experimental constraints on the dynamics of the partially molten upper mantle: 2. Deformation in the dislocation creep regime. *J. Geophys. Res.* **1995**, *100*, 15411–15449. [CrossRef]

11. Hirth, G.; Kohlstedt, D.L. Experimental constraints on the dynamics of the partially molten upper mantle: Deformation in the diffusion creep regime. *J. Geophys. Res.* **1995**, *100*, 1981–2001. [CrossRef]

12. Zimmerman, M.E.; Kohlstedt, D.L. Rheological Properties of Partially Molten Lherzolite. *J. Petrol.* **2004**, *45*, 275–298. [CrossRef]

13. Hansen, L.N.; Zimmerman, M.E.; Kohlstedt, D.L. Grain boundary sliding in San Carlos olivine: Flow law parameters and crystallographic-preferred orientation. *J. Geophys. Res.* **2011**, *116*, 1–16. [CrossRef]

14. Hirth, G.; Kohlstedt, D.L. Rheology of the upper mantle and the mantle wedge: A view from the experimentalists. In *Inside the Subduction Factory*; Eiler, J., Ed.; Geophysical Monograph; American Geophysical Union: Washington, DC, USA, 2003; Volume 138, pp. 83–105.

15. Skemer, P.; Warren, J.M.; Hansen, L.N.; Hirth, G.; Kelemen, P.B. The influence of water and LPO on the initiation and evolution of mantle shear zones. *Earth Planet. Sci. Lett.* **2013**, *375*, 222–233. [CrossRef]

16. Tommasi, A.; Knoll, M.; Vauchez, A.; Signorelli, J.W.; Thoraval, C.; Logé, R. Structural reactivation in plate tectonics controlled by olivine crystal anisotropy. *Nat. Geosci.* **2009**, *2*, 423–427. [CrossRef]

17. Hansen, L.N.; Zimmerman, M.E.; Kohlstedt, D.L. Laboratory measurements of the viscous anisotropy of olivine aggregates. *Nature* **2012**, *492*, 415–418. [CrossRef]

18. Dijkstra, A.H.; Drury, M.R.; Frijhoff, R.M. Microstructures and lattice fabrics in the Hilti mantle section (Oman Ophiolite): Evidence for shear localization and melt weakening in the crust–mantle transition zone? *J. Geophys. Res.* **2002**, *107*, 1–18. [CrossRef]

19. Regenauer-Lieb, K.; Yuen, D. Positive feedback of interacting ductile faults from coupling of equation of state, rheology and thermal-mechanics. *Phys. Earth Planet. Inter.* **2004**, *142*, 113–135. [CrossRef]

20. Matysiak, A.K.; Trepmann, C.A. Crystal-plastic deformation and recrystallization of peridotite controlled by the seismic cycle. *Tectonophysics* **2012**, *530–531*, 111–127. [CrossRef]

21. Kelemen, P.B.; Hirth, G. A periodic shear-heating mechanism for intermediate-depth earthquakes in the mantle. *Nature* **2007**, *446*, 787–790. [CrossRef]

22. Thielmann, M.; Rozel, A.; Kaus, B.J.P.; Ricard, Y. Intermediate-depth earthquake generation and shear zone formation caused by grain size reduction and shear heating. *Geology* **2015**, *43*, 791–794. [CrossRef]

23. Evans, B.; Renner, J.; Hirth, G. A few remarks on the kinetics of static grain growth in rocks. *Int. J. Earth Sci.* **2001**, *90*, 88–103. [CrossRef]

24. Drury, M.R.; Urai, J.L. Deformation-related recrystallization processes. *Tectonophysics* **1990**, *172*, 235–253. [CrossRef]

25. Karato, S. Grain growth kinetics in olivine aggregates. *Tectonophysics* **1989**, *168*, 255–273. [CrossRef]

26. Bystricky, M.; Kunze, K.; Burlini, L.; Burg, J.-P. High Shear Strain of Olivine Aggregates: Rheological and Seismic Consequences. *Science* **2000**, *290*, 1564–1567. [CrossRef]

27. Newman, J.; Lamb, W.M.; Drury, M.R.; Vissers, R.L.M. Deformation processes in a peridotite shear zone: Reaction-softening by an H2O-deficient, continuous net transfer reaction. *Tectonophysics* **1999**, *303*, 193–222. [CrossRef]

28. Linckens, J.; Herwegh, M.; Müntener, O.; Mercolli, I. Evolution of a polymineralic mantle shear zone and the role of second phases in the localization of deformation. *J. Geophys. Res.* **2011**, *116*, 1–21. [CrossRef]

29. Handy, M. Flow laws for rocks containing two non-linear viscous phases: A phenomenological approach. *J. Struct. Geol.* **1994**, *16*, 287–301. [CrossRef]

30. Ji, S.; Zhao, P.; Xia, B. Flow laws of multiphase materials and rocks from end-member flow laws. *Tectonophysics* **2003**, *370*, 129–145. [CrossRef]

31. Tasaka, M.; Hiraga, T.; Zimmerman, M.E. Influence of mineral fraction on the rheological properties of forsterite + enstatite during grain-size-sensitive creep: 2. Deformation experiments. *J. Geophys. Res. Solid Earth* **2013**, *118*, 3991–4012. [CrossRef]

32. Fusseis, F.; Regenauer-Lieb, K.; Liu, J.; Hough, R.M.; De Carlo, F. Creep cavitation can establish a dynamic granular fluid pump in ductile shear zones. *Nature* **2009**, *459*, 974–977. [CrossRef] [PubMed]

33. Précigout, J.; Prigent, C.; Palasse, L.; Pochon, A. Water pumping in mantle shear zones. *Nat. Commun.* **2017**, *8*. [CrossRef] [PubMed]

34. Précigout, J.; Stünitz, H.; Villeneuve, J. Excess water storage induced by viscous strain localization during high-pressure shear experiment. *Sci. Rep.* **2019**, *9*. [CrossRef] [PubMed]

35. Downes, H. Shear zones in the upper mantle − Relation between geochemical enrichment and deformation in mantle peridotites. *Geology* **1990**, *18*, 374–377. [CrossRef]

36. Hidas, K.; Tommasi, A.; Garrido, C.J.; Padrón-navarta, J.A.; Mainprice, D. Fluid-assisted strain localization in peridotites during emplacement of the shallow subcontinental lithospheric mantle. *Lithos* **2016**, *262*, 636–650. [CrossRef]

37. Kaczmarek, M.-A.; Müntener, O. Juxtaposition of melt impregnation and high-temperature shear zones in the upper mantle; field and petrological constraints from the Lanzo peridotite (Northern Italy). *J. Petrol.* **2008**, *49*, 2187–2220. [CrossRef]
38. Mei, S.; Bai, W.; Hiraga, T.; Kohlstedt, D.L. Influence of melt on the creep behavior of olivine-basalt aggregates under hydrous conditions. *Earth Planet. Sci. Lett.* **2002**, *201*, 491–507. [CrossRef]
39. Holtzman, B.K.; Kohlstedt, D.L.; Zimmerman, M.E.; Heidelbach, F.; Hiraga, T.; Hustoft, J. Melt segregation and strain partitioning: Implications for seismic anisotropy and mantle flow. *Science* **2003**, *301*, 1227–1230. [CrossRef]
40. Dijkstra, A.H.; Drury, M.R.; Vissers, R.L.M.; Newman, J. On the role of melt-rock reaction in mantle shear zone formation in the Othris Peridotite Massif (Greece). *J. Struct. Geol.* **2002**, *24*, 1431–1450. [CrossRef]
41. Hoogerduijn Strating, E.; Rampone, E.; Piccardo, G.; Drury, M.R.; Vissers, R.L. Subsolidus emplacement of mantle peridotites during incipient oceanic rifting and opening of the Mesozoic Tethys (Voltri Massif, NW Italy). *J. Petrol.* **1993**, *34*, 901–927. [CrossRef]
42. Urai, J.L.; Spiers, C.J.; Zwart, H.J.; Lister, G.S. Weakening of rock salt by water during long-term creep. *Nature* **1986**, *324*, 554–557. [CrossRef] [PubMed]
43. Van der Wal, D.; Chopra, P.; Drury, M.R.; Fitz Gerald, J.D. Relationships between dynamically recrystallized grain size and deformation conditions in experimentally deformed olivine rocks. *Geophys. Res. Lett.* **1993**, *20*, 1479–1482. [CrossRef]
44. Précigout, J.; Gueydan, F. Mantle weakening and strain localization: Implications for the long-term strength of the continental lithosphere. *Geology* **2009**, *37*, 147–150. [CrossRef]
45. Précigout, J.; Gueydan, F.; Gapais, D.; Garrido, C.; Essaifi, A. Strain localisation in the subcontinental mantle—A ductile alternative to the brittle mantle. *Tectonophysics* **2007**, *445*, 318–336. [CrossRef]
46. Hansen, L.N.; Warren, J.M. Quantifying the effect of pyroxene on deformation of peridotite in a natural shear zone. *J. Geophys. Res. B Solid Earth* **2015**, *120*, 2717–2738. [CrossRef]
47. Linckens, J.; Herwegh, M.; Müntener, O. Small quantity but large effect—How minor phases control strain localization in upper mantle shear zones. *Tectonophysics* **2015**, *643*, 26–43. [CrossRef]
48. Jaroslow, G.E.; Hirth, G.; Dick, H.J.B. Abyssal peridotite mylonites: Implications for grain-size sensitive flow and strain localization in the oceanic lithosphere. *Tectonophysics* **1996**, *256*, 17–37. [CrossRef]
49. Platt, J.P. Rheology of two-phase systems: A microphysical and observational approach. *J. Struct. Geol.* **2015**, *77*, 213–227. [CrossRef]
50. Skemer, P.; Warren, J.M.; Kelemen, P.B.; Hirth, G. Microstructural and rheological evolution of a mantle shear zone. *J. Petrol.* **2010**, *51*, 43–53. [CrossRef]
51. Warren, J.M.; Hirth, G. Grain size sensitive deformation mechanisms in naturally deformed peridotites. *Earth Planet. Sci. Lett.* **2006**, *248*, 438–450. [CrossRef]
52. Tasaka, M.; Hiraga, T. Influence of mineral fraction on the rheological properties of forsterite + enstatite during grain-size-sensitive creep: 1. Grain size and grain growth laws. *J. Geophys. Res. Solid Earth* **2013**, *118*, 3970–3990. [CrossRef]
53. Bercovici, D.; Ricard, Y. Generation of plate tectonics with two-phase grain-damage and pinning: Source-sink model and toroidal flow. *Earth Planet. Sci. Lett.* **2013**, *365*, 275–288. [CrossRef]
54. Bercovici, D.; Ricard, Y. Plate tectonics, damage and inheritance. *Nature* **2014**, *508*, 513–516. [CrossRef] [PubMed]
55. Précigout, J.; Stünitz, H. Evidence of phase nucleation during olivine diffusion creep: A new perspective for mantle strain localisation. *Earth Planet. Sci. Lett.* **2016**, *455*, 94–105. [CrossRef]
56. Ashby, M.F.; Verrall, R.A. Diffusion-accommodated flow and superplasticity. *Acta Metall.* **1973**, *21*, 149–163. [CrossRef]
57. Farla, R.J.M.; Karato, S.-I.; Cai, Z. Role of orthopyroxene in rheological weakening of the lithosphere via dynamic recrystallization. *Proc. Natl. Acad. Sci. USA* **2013**, *110*, 16355–16360. [CrossRef]
58. Linckens, J.; Bruijn, R.H.C.; Skemer, P. Dynamic recrystallization and phase mixing in experimentally deformed peridotite. *Earth Planet. Sci. Lett.* **2014**, *388*, 134–142. [CrossRef]
59. Rampone, E.; Romairone, A.; Abouchami, W.; Piccardo, G.B.; Hofmann, A.W. Chronology, petrology and isotope geochemistry of the Erro-Tobbio peridotites (Ligurian Alps, Italy): Records of Late Palaeozoic lithospheric extension. *J. Petrol.* **2005**, *46*, 799–827. [CrossRef]
60. Piccardo, G.B.; Padovano, M.; Guarnieri, L. The Ligurian Tethys: Mantle processes and geodynamics. *Earth-Sci. Rev.* **2014**, *138*, 409–434. [CrossRef]
61. Padovano, M.; Piccardo, G.B.; Vissers, R.L.M. Tectonic and magmatic evolution of the mantle lithosphere during the rifting stages of a fossil slow—Ultraslow spreading basin: Insights from the Erro–Tobbio peridotite (Voltri Massif, NW Italy). *Geol. Soc.* **2014**, *413*, 205–238. [CrossRef]
62. Piccardo, G.B.; Vissers, R.L.M. The pre-oceanic evolution of the Erro-Tobbio peridotite (Voltri Massif, Ligurian Alps, Italy). *J. Geodyn.* **2007**, *43*, 417–449. [CrossRef]
63. Piccardo, G.B. Subduction of a fossil slow-ultraslow spreading ocean: A petrology-constrained geodynamic model based on the Voltri Massif, Ligurian Alps, Northwest Italy. *Int. Geol. Rev.* **2013**, *55*, 787–803. [CrossRef]
64. Bunge, H.-J. *Texture Analysis in Materials Science*; Butterworths: London, UK, 1982.
65. Skemer, P.; Katayama, I.; Jiang, Z.; Karato, S. The misorientation index: Development of a new method for calculating the strength of lattice-preferred orientation. *Tectonophysics* **2005**, *411*, 157–167. [CrossRef]

66. Brey, G.P.; Koehler, T. Geothermobarometry in four-phase lherzolites II. New thermobarometers, and practical assessment of existing thermobarometers. *J. Petrol.* **1990**, *31*, 1353–1378. [CrossRef]

67. Witt-Eickschen, G.; Seck, H.A. Solubility of Ca and Al in orthopyroxene from spinel peridotite: An improved version of an empirical geothermometer. *Contrib. to Mineral. Petrol.* **1991**, *106*, 431–439. [CrossRef]

68. Karato, S.; Jung, H.; Katayama, I.; Skemer, P. Geodynamic significance of seismic anisotropy of the upper mantle: New insights from laboratory studies. *Annu. Rev. Earth Planet. Sci.* **2008**, *36*, 59–95. [CrossRef]

69. Jung, H.; Karato, S. Water-induced fabric transitions in olivine. *Science* **2001**, *293*, 1460–1463. [CrossRef] [PubMed]

70. Tommasi, A.; Vauchez, A.; Godard, M.; Belley, F. Deformation and melt transport in a highly depleted peridotite massif from the Canadian Cordillera: Implications to seismic anisotropy above subduction zones. *Earth Planet. Sci. Lett.* **2006**, *252*, 245–259. [CrossRef]

71. Park, M.; Jung, H. Microstructural evolution of the Yugu peridotites in the Gyeonggi Massif, Korea: Implications for olivine fabric transition in mantle shear zones. *Tectonophysics* **2017**, *709*, 55–68. [CrossRef]

72. Kumamoto, K.M.; Warren, J.M.; Hansen, L.N. Evolution of the Josephine Peridotite Shear Zones: 2. Influences on Olivine Cpo Evolution. *J. Geophys. Res. Solid Earth* **2019**, *124*, 12763–12781. [CrossRef]

73. Bernard, R.E.; Behr, W.M.; Becker, T.W.; Young, D.J. Relationships Between Olivine CPO and Deformation Parameters in Naturally Deformed Rocks and Implications for Mantle Seismic Anisotropy. *Geochem. Geophys. Geosystems* **2019**, *20*, 3469–3494. [CrossRef]

74. Tommasi, A.; Langone, A.; Padrón-Navarta, J.A.; Zanetti, A.; Vauchez, A. Hydrous melts weaken the mantle, crystallization of pargasite and phlogopite does not: Insights from a petrostructural study of the Finero peridotites, southern Alps. *Earth Planet. Sci. Lett.* **2017**, *477*, 59–72. [CrossRef]

Appendix chapter 4 – Ronda - Melt-enhanced strain localization and phase mixing in a large-scale mantle shear zone (Ronda Peridotite, Spain)

S4.1   –   EPMA measurement settings and detection limits
(attached below & on CD)

S4.2   –   Microstructural data (attached as Excel file on CD)

S4.3   –   EPMA data (attached as Excel file on CD)

S4.4   –   Additional EPMA graphs Cpx, Ol, Amph (attached below & on CD)

Publication   –   "Melt-enhanced strain localization and phase mixing in a large-scale mantle shear zone (Ronda peridotite, Spain)" by Sören Tholen, Jolien Linckens and Gernold Zulauf published in *Solid Earth (EGU),* 14 (2023), (attached below & on CD)

Element	Crystal	Meas. t peak (s)	Meas. t back (s)	Detect. Limit (ppm)
Al	TAP	30	15	134
Si	TAP	30	15	457
Cr	PETL	30	15	300
Ca	PETL	30	15	128
K	PETL	30	15	363
Ti	PETL	30	15	149
Na	TAPL	20	10	87
Mg	TAPL	40	20	176
Mn	LIFH	20	10	86
Fe	LIFH	20	10	130
Ni	LIFH	20	10	374

S4.1 – *EPMA measurement settings and detection limits.*
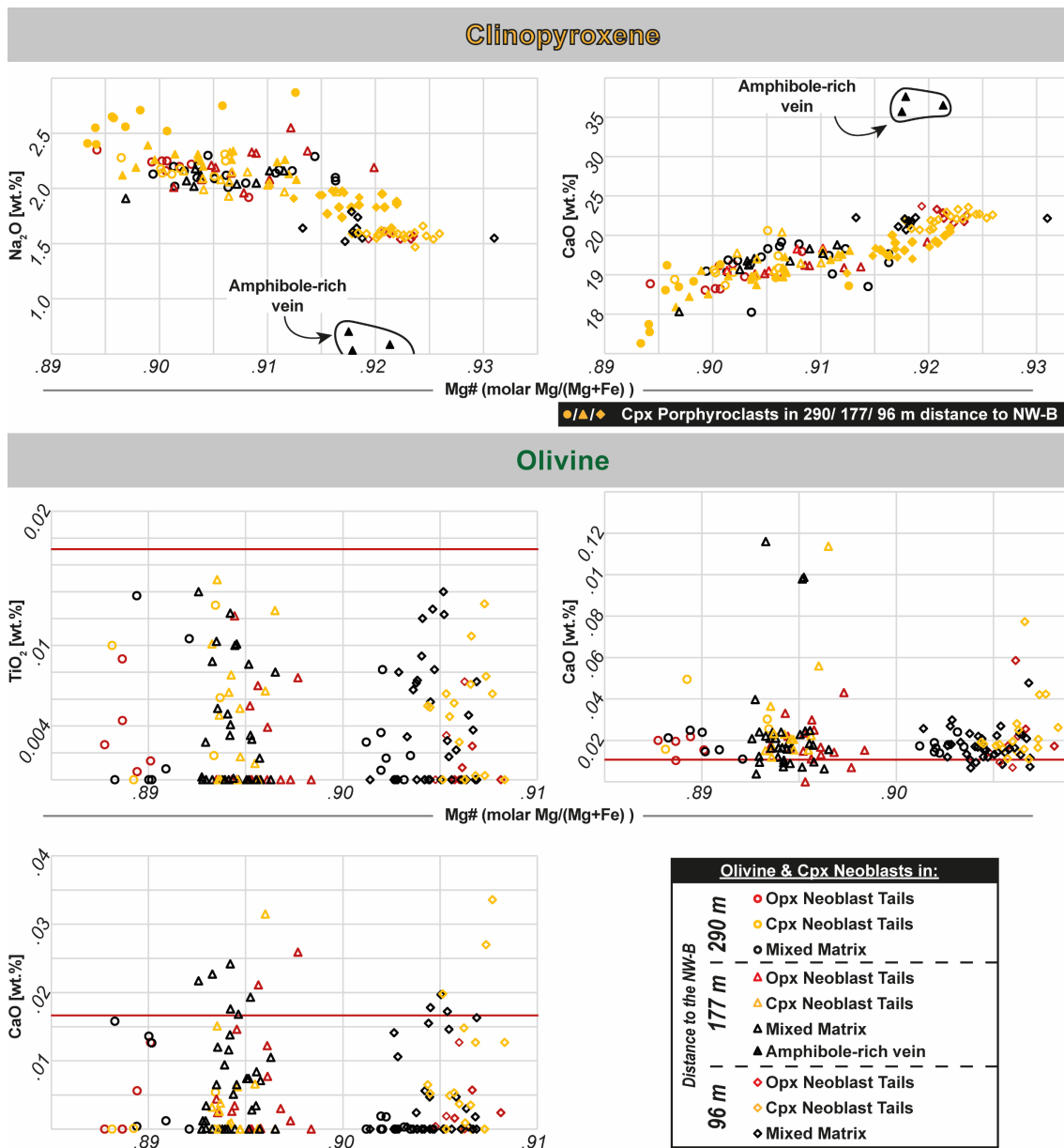
S4.4 (1 of 2) – Additional EPMA graphs clinopyroxene and olivine. For optimal resolution, the reader is referred to the version attached on the CD.
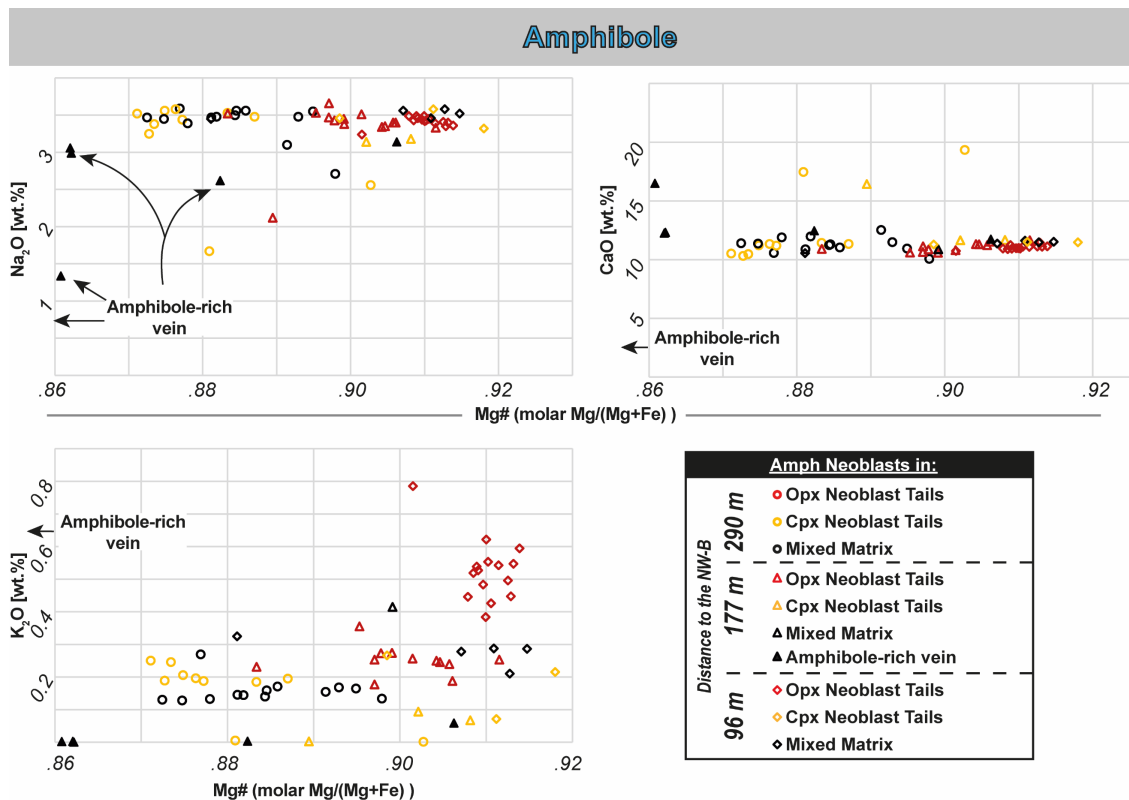
S4.4 (2 of 2) – Additional EPMA graphs amphibole. For optimal resolution, the reader is referred to the version attached on the CD.

Solid Earth

Melt-enhanced strain localization and phase mixing in a large-scale mantle shear zone (Ronda peridotite, Spain)

Sören Tholen[1], Jolien Linckens[1,2], and Gernold Zulauf[1]

[1]Institut für Geowissenschaften, Goethe Universität Frankfurt am Main,
Altenhöferallee 1, 60438 Frankfurt am Main, Germany
[2]Research & Development, Tata Steel, 1970 CA Ijmuiden, the Netherlands

Correspondence: Sören Tholen (tholen@geo.uni-frankfurt.de)

Abstract. Strain localization in upper-mantle shear zones by grain size reduction and the activation of grain-size-sensitive deformation mechanisms is closely linked to phase mixing. With its mylonitic grain size (50–100 µm) and well-mixed phase assemblage, the kilometer-scale shear zone at the northwestern boundary of the Ronda peridotite is, in this respect, no exception. In transects across the high-strain mylonitic into the low-strain tectonitic part of this shear zone, the following four dominant microstructural domains were identified: (1) olivine-rich matrix, (2) mixed matrix, (3) neoblast tails of clinopyroxene porphyroclasts, and (4) neoblast tails of orthopyroxene porphyroclasts. In these domains, phase mixing and its impact on strain localization were investigated by a combination of microstructural (optical microscopy), textural (EBSD), and geochemical (EPMA) analysis. The dominant microstructural domain of all samples is the mixed matrix composed of olivine, orthopyroxene, and clinopyroxene. Its homogenous distribution of interstitial pyroxenes contradicts mechanical mixing. Instead, extensive phase mixing under near-steady-state conditions is documented by the constant grain size and by phase boundary percentages > 60 % for the entire mylonitic unit and all the microstructural domains. Lobate phase boundaries, homogenous phase mixing, and secondary-phase distribution, as well as continuous geochemical trends that are independent of the microstructural domain, point to a reaction-driven, metasomatic formation of the mixed matrix and pyroxene porphyroclast tails in the entire shear zone. An OH-bearing metasomatism by small fractions of evolved melts is indicated by amphibole abundance in pyroxene neoblast tails, olivine B-type-crystallographic-preferred orientations

(CPOs), and the microstructural consistency of the garnet–spinel (grt–spl) mylonites from both major peridotite massifs of the Gibraltar arc, Ronda, and Beni Bousera (Morocco). The established syn-deformational temperature of 800–900 °C at 1.95–2.00 GPa suggests that the metasomatism did not reset the equilibrium temperatures. Consistent geochemistry and phase assemblage in mylonites and tectonites but a change from equiaxial (tectonites) to wedge-shaped pyroxenes aligned parallel to the foliation (mylonites) point to a pre- to syn-deformational metasomatism, with the potential annealing of the tectonites. For the mylonitic mixed matrix, wedge-shaped pyroxenes, and neoblast tail formation in pyroxene porphyroclast stress shadows point to the activity of incongruent dissolution–precipitation creep. Apart from the dissolution–precipitation creep, strong CPOs of all major phases (ol, opx, and cpx) suggest dislocation creep as being the major deformation mechanism in the entire shear zone.

1 Introduction

Deformation in the upper mantle is localized in ductile shear zones. By accommodating most of the deformation in the lithospheric mantle, shear zones have a major imprint on large-scale deformation and plate tectonics (Bercovici and Ricard, 2014; Drury et al., 1991). To localize the strain, weakening must occur. Weakening in turn is dependent on an initial heterogeneity or anisotropy and a softening mechanism that localizes the strain, typically first on a heterogeneity and later on in the shear zone itself. In the lithospheric mantle, several types of heterogeneity were identi-

fied as being potential seeds for strain localization. These include (1) large-scale variations in the geothermal gradient, such as those found in hot plumes or cold lithospheric roots of cratons; (2) major-element and modal heterogeneities, such as those present in the compositional layering of most peridotite massifs; (3) the presence of melt; (4) variations in the hydration state of particularly olivine; (5) grain size heterogeneities; and (6) lateral changes in the olivine crystallographic-preferred orientation (CPO; e.g., Tommasi and Vauchez, 2015). Strain-softening mechanisms that localize and maintain deformation were subdivided into three types (Drury et al., 1991). These are thermal softening, which is caused by shear heating and the positive feedback of temperature and strain rate (e.g., Kelemen and Hirth, 2007); geometric softening, which is caused by the anisotropy in creep strength of grains aligned in a CPO (Mameri et al., 2019; White et al., 1980); and microstructural or reaction softening, which occurs by grain size reduction and the activity of a grain-size-sensitive deformation process (Drury and Urai, 1989). Both thermal softening and microstructural softening depend on the presence of mixed-phase assemblage, which operates either as the seed or as the stabilization for strain localization (e.g., Kelemen and Hirth, 2007; Linckens et al., 2015). Phase mixing in the upper mantle has been ascribed to several different deformation- or reaction-induced processes. Deformation-induced phase mixing is commonly associated with grain boundary sliding (GBS). During GBS, neighbor switching of grains was reported to form not only mixtures (e.g., Boullier and Gueguen, 1975; Hirth and Kohlstedt, 2003) but also aggregates (Hiraga et al., 2013). Furthermore, the disaggregation of single-phase domains at high-shear strains (geometric mixing) was reported by Cross and Skemer (2017). Additionally, nucleation of neoblasts in creep cavitations during GBS leading to phase mixing was reported by Précigout and Stünitz (2016). Reaction-induced phase mixing is bound to either metamorphic $(P - T)$ or metasomatic (melt or fluid) reactions. In the upper mantle, phase transitions from garnet to spinel and plagioclase peridotites change the phase assemblage and the mineral chemistry of all present phases (e.g., Borghini, 2008). Neoblast formation can thereby lead to phase mixing and, during deformation, to the formation of ultramylonites (Furusho and Kanagawa, 1999; Newman et al., 1999; Tholen et al., 2022). Additionally, the interaction of rock and melt or fluid can cause phase mixing by precipitation of neoblasts and reactions with porphyroclasts or pristine grains (e.g., Dijkstra et al., 2002; Kaczmarek and Müntener, 2008).

With its decreasing grain size, the scattering of pyroxene neoblasts and the concurrent diminishing of prior strong olivine CPOs towards the contact to the bordering Jubrique unit, Ronda's NW tectonite and mylonite zone is commonly interpreted as a kilometer-scale upper-mantle shear zone (Garrido et al., 2011;Précigout et al., 2007, 2013). In contrast to earlier studies on phase mixing in upper-mantle shear zones, where the mixing depends on metamorphic and metasomatic reactions (Linckens and Tholen, 2021; Tholen et al., 2022), Ronda's mylonites are thought to have little to no metamorphic or metasomatic influence (e.g., Johanesen and Platt, 2015; Précigout et al., 2007). Mechanisms of strain localization and phase mixing operating in Ronda's mylonites were suggested to be bound to grain boundary sliding accommodated by dislocation creep (DisGBS; Précigout et al., 2007). Using this concept, the strain localization is caused by a drop in stress due to the grain size reduction towards the NW boundary of the Ronda peridotite (e.g., Garrido et al., 2011; Précigout et al., 2013). Following Précigout et al. (2007), neighbor switching during DisGBS leads to the scattering of orthopyroxene neoblasts within the matrix. However, Johanesen and Platt (2015) also reported thoroughly mixed microstructures with interstitial pyroxenes in the low-strain areas of the SE mylonites and the spinel tectonites (Fig. 1). Although mixing in the spinel tectonites was postulated to be melt derived (Johanesen et al., 2014; Soustelle et al., 2009), the mylonites were so far considered to be either completely melt-free (Précigout et al., 2007; Soustelle et al., 2009) or melt-absent during the deformation (Johanesen and Platt, 2015).

To address the genesis and deformational history of the NW Ronda shear zone, this study focuses on the mylonitic unit with the following research questions: (1) what are the major microstructural domains, and how did they form? (2) What is the extent and origin of phase mixing? (3) What is the deformational history, and how is it related to the first two research questions (i.e., the formation processes and mixing intensities of the respective microstructural domains)? To address these questions, a microstructural and geochemical study was carried out on samples taken across multiple transects from the mylonites into the tectonites (Fig. 1).

2 Geological setting

The Ronda peridotite, situated in southern Spain, is part of the Betic Cordillera (Fig. 1). Together with the Rif mountains of northern Morocco, it forms the Gibraltar Arc (the Betic–Rif orogen), which surrounds the Alborán Sea. The Betic Cordillera is subdivided into the following four tectonic domains: the external (1) sub-Iberian and (2) Maghrebian domains, which are formed by the paleomargins of Iberia and NE Africa; (3) the allochthonous Flysch trough unit comprising Mesozoic to Cenozoic sediments of the oceanic or continental Tethys; and (4) the internal Alborán domain (Fig. 1a; Booth-Rea et al., 2007). Separated by extensional shear zones and different metamorphic records, the Alborán domain is divided into three main tectonic allochthons (Platt et al., 2006). In ascending order, these are the Nevado–Filábride Complex, the Alpujárride Complex, and the Maláguide Complex. The lowermost Nevado–Filábride Complex records a multistage metamorphic evolution that includes eclogite facies metamorphism followed by albite-
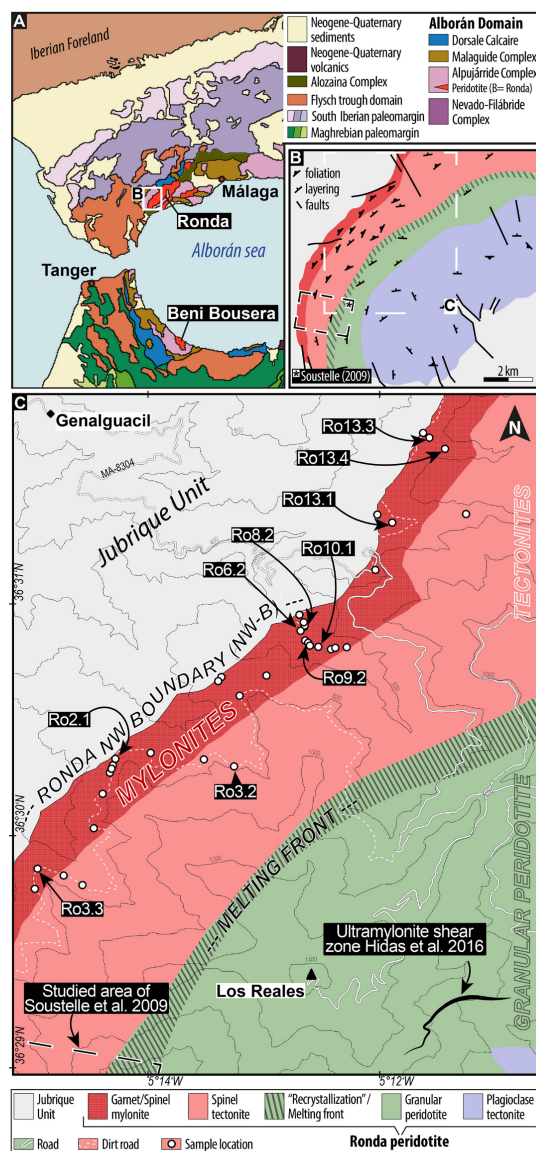
Figure 1. (a) Geological overview of the Gibraltar Arc (Betic Cordillera and Rif mountains), modified after Suades and Crespo-Blanc (2011). Ronda peridotite is indicated by a white box. **(b)** Schematic structural map of the NW Ronda peridotite, with the area of investigation indicated by dashed white box (modified after Hidas et al., 2013b). The lithological unit color code is same as for panel **(c)**. The studied area of Soustelle et al. (2009) is indicated by a dashed black box. **(c)** Close-up view of the area of investigation, with sample locations indicated (modified after Précigout et al., 2013, and Van der Wal, 1993).

epidote amphibole or greenschist facies overprints during decompression (Platt et al., 2006; Puga et al., 1999). The middle Alpujárride Complex underwent high-pressure–low-temperature (HP–LT) metamorphism that was overprinted by decompression and local heating (Balanyá et al., 1997; Platt et al., 2005). The uppermost Maláguide Complex is characterized by unmetamorphic rocks or by very low-grade metamorphism (Lonergan, 1993).

The peridotite bodies of Beni Bousera, Ojén, Carratraca, and Ronda in sensu stricto are embedded as lenses in the upper Alpujárride Complex (Platt et al., 2006). Superimposed on the Ronda peridotite, the Jubrique (or Casares) unit represents a highly attenuated crustal section of ≤ 5 km thickness (Fig. 1; Barich et al., 2014; Obata, 1980). Near the contact to the Ronda peridotite, it displays medium-pressure–high-temperature (MP–HT) granulite facies kinzigites with melt inclusions (Balanyá et al., 1997; Barich et al., 2014). With increasing distance to the peridotite, the metamorphic conditions decrease to low-pressure–low-temperature (LP–LT) phyllites at the contact to the Maláguide Complex (Balanyá et al., 1997). In the south and southeast, granitic rocks and migmatites of the Blanca unit underlie the Ronda peridotite (Fig. 1). Partial melting and deformation of this unit at the contact to the peridotite have been attributed to the emplacement of the Ronda peridotite (Esteban et al., 2008). U–Pb SHRIMP (Sensitive High-Resolution Ion MicroProbe) dating of neocrystalline zircon rims from felsic and granitic dikes in this dynamothermal aureole point to an emplacement of the Ronda peridotite at 22.3 ± 0.7 Ma (Esteban et al., 2011). Miocene, brittle, and top-to-the-north extensional faulting led to the final emplacement of the Alpujárride Complex, with high cooling rates from 300–100 °C Ma^{-1} (Esteban et al., 2004; Platt et al., 2003; Rossetti et al., 2005).

2.1 The Ronda peridotite

With ca. 300 km^2 areal extent, the Ronda peridotite is the world's largest exposure of subcontinental mantle (Obata, 1980). Its (micro)structural, petrological, and geochemical zoning led to its subdivision into four tectonometamorphic units (Fig. 1; Précigout et al., 2013; Van Der Wal and Vissers, 1993, 1996). From NNW to SSE, these are (1) a garnet–spinel (spl–grt) mylonite unit, (2) a spinel–tectonite unit, (3) a coarse-grained granular peridotite unit, and (4) a plagioclase–tectonite unit. Being aware that tectonites include mylonitic microstructures by definition, the established distinction between mylonites and tectonites is nevertheless adopted here.

The garnet–spinel mylonites, located along the contact to the Jubrique unit (~ 500–750 m thickness), are composed of fine-grained, porphyroclastic garnet- and spinel-bearing peridotites (lherzolites, harzburgites, and dunites; Van Der Wal and Vissers, 1993). Garnet-bearing pyroxenite layers are parallel to the strong foliation and predominantly stretched, which leads to their pinch-and-swell-type boudinage in some

places (Précigout et al., 2013; Van Der Wal and Vissers, 1993). Occasionally, the pyroxenite layers show intrafolial folds, with their axes oriented NE–SW and slightly dipping towards the NE (Précigout et al., 2013). Graphitized diamonds in garnet-bearing pyroxenites and pre-deformational assemblages of olivine, both pyroxenes, and garnet found in pressure shadows indicate an origin of great depth (> 150 km) and a pre-mylonitic equilibration in the garnet stability field (1150 °C, 2.4–2.7 GPa; ∼ 100 km depth; Davies et al., 1993; Garrido et al., 2011). For mylonitic assemblages in the spinel stability field, equilibration conditions of 800–900 °C and 1–2 GPa have been obtained by Johanesen et al. (2014), Garrido et al. (2011), and Van Der Wal and Vissers (1993).

The transition between grt–spl mylonite and the spl tectonite remains controversial. Contrary to crosscutting contacts between mylonites and tectonites described by Van Der Wal and Vissers (1996), Précigout et al. (2007) and Soustelle et al. (2009) postulated a continuous gradient from coarse-grained tectonites (grain size of 250–450 µm) to fine-grained mylonites (150–220 µm). Decreasing strain with increasing distance to the NW boundary of the mylonites is also indicated by the decreased folding intensity and rotation of pyroxenite layers towards the SE (Précigout et al., 2013). However, Johanesen and Platt (2015) reported a consistent grain size of recrystallized olivine (∼ 130 µm) for both units (mylonites and tectonites) and only an increase in the percentage of the recrystallized olivine grains towards the NW. As the main lithologies (harzburgites and lherzolites) and the foliation and lineation stay similar in tectonites and mylonites, tectonites were interpreted as being the weaker deformed counterpart of the mylonites (Van Der Wal and Vissers, 1993). Microstructural and geochemical data indicate additionally that the tectonites were affected by melt pulses originating from the structurally lower and coarse granular peridotites (Johanesen et al., 2014; Soustelle et al., 2009).

Together with the grt–spl mylonites, the spl tectonites form the kilometer-scale NW Ronda shear zone (Fig. 1). Its characteristics are the penetrative foliation, with subhorizontal stretching lineation that is defined by centimeter-scale elongated orthopyroxenes and shear criteria which indicate sinistral kinematics and minor coaxial shortening (Balanyá et al., 1997; Précigout and Hirth, 2014; Van Der Wal and Vissers, 1996). The orientation of the foliation and lineation roughly follows the boundaries to the adjacent metasedimentary Jubrique unit in the NW and to the underlying coarse granular peridotite unit in the SE (Fig. 1; Van Der Wal and Vissers, 1996). In some places, foliation and lineation show local variations and weakening (Van Der Wal and Vissers, 1996). For the examined area, the average orientation of the foliation is with ∼ 50° N strike and 80° NW dip, which is in accordance with prior research (Précigout et al., 2013). The shear zone is considered to play a decisive role in the exhumation of the peridotite massif (Johanesen et al., 2014; Précigout et al., 2013).

The coarse granular peridotite unit is separated from the spl tectonite unit by a recrystallization and/or coarsening and melting front (≤ 400 m; Lenoir et al., 2001). Here, the deformed grains annealed and coarsened, the foliation is lost, and garnet-pyroxenite layers are recrystallized as spl websterites (Garrido and Bodinier, 1999). Lenoir et al. (2001) showed that the recrystallization front is the boundary or aureole of an area of partial melting (i.e., the coarse granular peridotite unit) with melt extraction < 5 %. Secondary clinopyroxene (cpx), crystallized ahead of the front, indicated a refertilization (Soustelle et al., 2009). The location of the front was shown to be dependent on the peridotite solidus (≥ 1200 °C, 1.5 GPa) with regard to the temperature gradient within the peridotite body (Lenoir et al., 2001). The coarse granular peridotite unit itself is mainly composed of unfoliated spinel harzburgite, with minor lherzolite and dunite and various types of pyroxenites (Garrido and Bodinier, 1999). The preservation of a strong olivine CPO and folds of spl pyroxenites corroborates its connection to the overlaying spl tectonites (Vauchez and Garrido, 2001).

The youngest unit, overprinting the coarse granular peridotite unit in the SE, comprises the plagioclase tectonites (Obata, 1980). Their equilibration at pressures of 0.8–0.9 GPa was placed in the context of the massif's exhumation (Hidas et al., 2016). The plagioclase tectonites are composed of spl-free and spl-bearing plagioclase–peridotite layers. The transition between both units records kilometer-scale folding and shearing, including the development of a new foliation and the formation of mylonitic and ultramylonitic shear zones, which are tectonically assigned to the decompression of the massif from spinel to plagioclase lherzolite facies prior to the emplacement into the crust (Fig. 1; Hidas et al., 2013a).

3 Methods

Samples were cut perpendicular to the foliation and parallel to the stretching lineation (X–Z section). Thin sections of these sections were polished to a thickness of ∼ 30 µm. After optical analysis by polarization microscopy, electron backscatter diffraction (EBSD) analysis combined with energy-dispersive X-ray spectroscopy (EDX) and electron probe microanalysis (EPMA) were performed on carbon-coated thin sections. For EBSD and backscattered electron (BSE) analysis, thin sections were polished with 0.03 µm colloidal silica.

Backscattered electron, EBSD, and EDX analysis were conducted at the Institute of Geology and Mineralogy, University of Cologne, using a Zeiss Sigma 300 VP field emission scanning electron microscope (SEM) equipped with a NordlysNano EBSD detector (Oxford Instruments). For a comprehensive overview, the entire length of the thin sections was scanned in grids simultaneously by BSE and EDX (O, Mg, Al, Si, Ca, Cr, Mn, and Fe; Fig. 2). Having identified the microstructures of interest, these were scanned si-
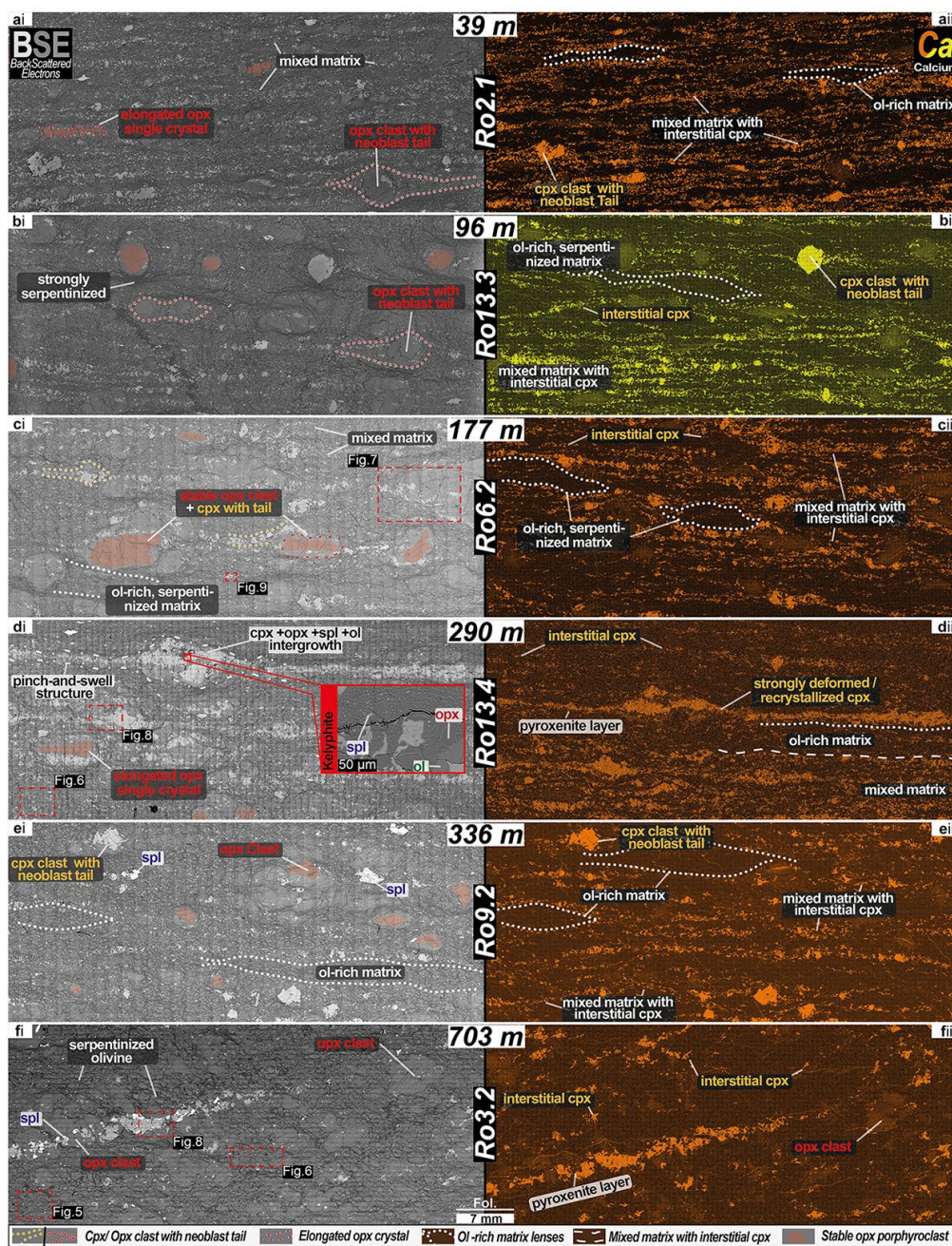
Figure 2. Electron backscatter (ai–fi) and calcium energy-dispersive X-ray spectroscopy (aii–fii) scans of the same thin sections ordered with increasing distance to the NW boundary of the Ronda peridotite (black numbers on white background). The locations of the analyzed example microstructures and their figure number are indicated. Dominant microstructural domains of the NW Ronda shear zone are marked as follows: (1) strongly serpentinized olivine-rich matrix lenses, (2) mixed matrix with interstitial pyroxenes, and (3) ortho- and (4) clinopyroxene porphyroclasts with neoblast tails. Note the presence of stable pyroxenes and elongated orthopyroxene. The presence of interstitial cpx (bright colors in EDX images) is indicative of the mixed matrix. Panel (di) includes a close-up of a kelyphitic assemblage.

multaneously by EBSD, EDX, BSE, and forescattered electrons (FSE). Measurement settings were an acceleration voltage of 20 kV, and a variable step size was adapted according to grain sizes. Depending on the step size and acquisition time, the EBSD map sizes differ over a wide range. For data acquisition, the program AZtec 4.2 was used (Oxford Instruments). The consistency of orientations between sample, measurement, and post-processing reference frame was ensured by the measurement of a quartz standard. It consists of four synthetic quartz crystals embedded in epoxy. The known positions of the quartz single crystals in the standard combined with their known individual orientation enable the operator to identify possible rotations (spatially or crystallographic) of the data during acquisition and processing. Kilian et al. (2016) showed that such rotations occur often due to unknown orientation in sample material and incorrect translations between different processing platforms. The obtained EBSD data were first cleaned by deleting wild spikes and filling points not indexed with the average orientation of six or more neighbor orientations of the same phase (HKL Channel 5 software; Oxford Instruments). Additionally, the EBSD data were corrected for systematic misindexing of olivine due to similar diffraction patterns for orientations rotated 60° at around [100]. Second, the cleaned data were imported into the MTEX 5.7 MATLAB extension (e.g., Bachmann et al., 2010). All of the following data processing and analysis were conducted using MTEX (http://mtex-toolbox.github.io/, last access: 10 October 2023). Orientations of indexed points with high mean angular deviations (MADs > 1) were filled by the mean orientation of the neighboring points. After grain calculation (grain internal misorientation < 15°), grain-size-specific and inclusion deletion and/or filling was carried out individually for each map. Incomplete grains at the borders of the mapped areas and badly indexed grains were excluded from further analysis. Grain reconstruction of serpentinized olivine grains was achieved by applying a half quadratic filter, which preserves subgrain boundaries and fills missing data. An example is shown for the olivine (ol)-rich matrix in Fig. 5. For all other phases, the original cleaned EBSD data were used to preserve the original grain and boundary shape. During the cleaning and reconstruction, the results were checked against backscattered or forescattered, band contrast, and microscope images. The EBSD phase assignment was checked by simultaneously obtained EDX maps and/or EDX point measurements. The cleaned EBSD maps were thereupon analyzed for grain and phase properties, boundary properties, and orientation properties. Analyzed grain properties are phase abundances by covering the area percentage, grain amount, grain size by the equivalent circular diameter (ECD), grain shape by aspect ratio, shape factor, and shape-preferred orientation (SPO). Phase abundances that are given by percentages in figures and in the entire paper refer to area percentages. Boundary properties are grain (phase A–phase A) and phase (phase A–phase B) boundary percentages calculated by a phase-specific bound-

ary length. The ratio of total grain to total phase boundary length gives the mixing intensity of a microstructure. The orientation properties include phase-specific crystallographic orientations that are illustrated by pole figures with or without texture. A texture calculation with grain mean orientations and a consistent half-width of 15° was achieved by the application of the orientation distribution function (ODF). The M index (M) and the J index were calculated from a minimum of 150 grains. Both the J index (Bunge, 1982) and M index (Skemer et al., 2005) express the strength of a given texture. For a detailed evaluation of both, see Skemer et al. (2005). All pole figures are equal-area, lower-hemisphere plots. Textures are only displayed for a minimum number of 100 grains per phase. Otherwise, the single grain orientations are plotted in the stereo plot as dots. To facilitate the comparison between the texture plots, the color-coding range is fixed according to the maximum of multiple of random distribution (mrd) from blue (mrd = 0) to red (mrd = 3). Higher mrd values are accordingly also colored red. Dislocation densities were calculated in MTEX by resolving the geometrically necessary dislocation content (https://mtex-toolbox.github.io/GND.html, last access: 10 October 2023), based on the method of Pantleon (2008).

Microprobe measurements of olivine (ol), clinopyroxene (cpx), orthopyroxene (opx), spinel (spl), and amphibole (amph) were conducted at the Institute of Geosciences at Goethe University, Frankfurt am Main, using a field emission JEOL JXA-8530F Plus microprobe equipped with five wavelength-dispersive spectrometers. The measurement settings were 15 kV acceleration voltage and 20 nA beam current for 20 s (Al, Cr, Ca, Na, Mn, Fe, and Ni), 30 s (P, K, and Ti), or 40 s (Mg and Si) peak and 20 s for background measurement (settings and detection limits are given in Table S1 in the Supplement). The same measurement settings and standards were used for the analysis of all phases. The spot size was adjusted to the grain size, with minimum sizes of 1 μm for small neoblasts and maximum sizes of 4 μm for porphyroclasts.

4 Results

Samples were taken from multiple transects of the shear zone over a range from 39 to 703 m distance to the NW boundary of the Ronda peridotite massif (NW-B; Fig. 1). Sample locations are therefore allocated with their distance (meters) to the NW-B (Fig. 1). Referring to the established subdivision of the Ronda peridotite developed by Précigout et al. (2013) and Van Der Wal and Bodinier (1996), our samples are dominantly taken from the garnet–spinel mylonites and collected at a greater distance from the NW-B from the spinel tectonites (Fig. 1). Both units are composed of lherzolite or harzburgite, with minor dunitic lenses. The samples have a highly variable degree of serpentinization. Consistent with previous studies, the foliation is mostly ori-

ented parallel to the NW-B and steeply dipping (65–85°) towards the NW (Précigout et al., 2013; Soustelle et al., 2009; Van Der Wal and Vissers, 1993, 1996; Vauchez and Garrido, 2001). Towards the NW-B, the foliation intensifies. The stretching lineation is subhorizontal to shallowly SW dipping (< 20°). It is defined by elongated orthopyroxene single crystals, neoblast tails of pyroxene porphyroclasts, and olivine-rich lenses stretched in the foliation plane. Towards the contact to the bordering Jubrique metasediments (at the NW-B), macroscopic evidence of the increasing strain is an increase in the porphyroclast elongation and an increase in the mylonitic matrix (Fig. 2). The lengthening of orthopyroxene single crystals expands to aspect ratios > 10 : 1 and a length of ∼ 5 cm. The increasing strain is additionally indicated by the increasing deformation of partly garnet-bearing pyroxenites, by pinch-and-swell structures (Fig. 2di), and by boudinage, as described in detail by Précigout et al. (2013).

4.1 Microstructures

Figure 2 gives a microstructural overview of representative thin sections, with increasing distance to the NW-B. Due to serpentinization and also to facilitate phase identification, BSE and Ca EDX overview scans are shown instead of microscopic images. The proportion of neoblasts in the matrix increases towards the NW-B (Fig. 2). Simultaneously, the abundance of porphyroclasts decreases. Nevertheless, deformation features, like a clear foliation with the marked elongation of porphyroclasts and a recrystallized olivine-dominated matrix are present in all mylonitic samples (39–502 m distance NW-B; Fig. 2). Only the outermost tectonitic sample (703 m distance NW-B) lacks these features and shows a relatively undeformed fabric (Fig. 2f). Even though the deformation was not as localized in this sample as in those closer to the NW-B, interstitial pyroxenes are present along olivine grain boundaries (Fig. 2fii). Furthermore, layers consisting of a pyroxene and spinel assemblage crosscut the tectonitic peridotite. Approaching the NW-B, pyroxene porphyroclasts show neoblast tails, which stretch out in the foliation. Simultaneously, pyroxenite layers turn parallel to the foliation and flatten until they disintegrate (Fig. 2dii), as described in detail in Précigout et al. (2013).

With the focus on phase mixing and on reaction and recrystallization processes, we further investigated structures on the microscale rather than on the thin section or larger scale. By using microscopic analysis and the BSE or EDX element thin section overviews (Fig. 2), the following four major microstructural domains were identified: (1) olivine-rich matrix, (2) mixed matrix, (3) clinopyroxene neoblast tails, and (4) orthopyroxene neoblast tails. In the following, their microstructural characteristics are presented. Additionally, amphibole–clinopyroxenite veins investigated in three thin sections will be briefly addressed. For reasons of length and clarity, examples of microstructures of each domain are shown, which provide its main characteristics and their

changes, depending on the distance to the NW-B. These figures include pole figures referring to the depicted microstructure. Graphs of the complete microstructural data are presented in Fig. 3. Average aspect ratios and the average grain size are included only if enough grains were present for a valid statistical analysis ($n > 100$). The presented results include all analyzed microstructures of a given microstructural domain. The complete data are given in Table S2. Garnet, even if nominally present in a few maps (39 of 41 563 analyzed grains), is excluded from further analysis because of its small abundance (< 0.1 % for all microstructural domains) and its susceptibility for misindexing with opx, especially for small grains. Coarse-grained garnet (ECD > 100 µm) was not present in the studied microstructures.

4.1.1 Matrix domains

The overall olivine-dominated matrix forms the major part of all analyzed samples (Fig. 2). Due to the presence of interstitial cpx (high Ca counts in Fig. 2) and opx, most of this matrix is mixed, with only parts remaining almost monomineralic and olivine rich (Ol > 90 %). Nevertheless, lenses of the olivine-rich matrix enclosed by the mixed matrix are present in all samples (Fig. 2). The differentiation between mixed domains and olivine-dominated domains becomes increasingly difficult with decreasing distance to the NW-B. In both matrix domains, olivine grains are cut by subvertical or subhorizontal serpentine veins. With an increasing degree of serpentinization, olivine grain boundaries become increasingly lobate, and originally coherent grains are separated into smaller fragments. Coherent crystallographic orientations with bent lattices span multiple fragments, which were identified as being single grains through the analysis of original EBSD data (Fig. 5). Due to this discrepancy between calculated fragments and pristine grains, the EBSD data that were missing due to serpentinization were filled by applying a half-quadratic filter. Based on the restored data, the grain reconstruction of the original grain size could be achieved. Even though this method restores the pristine grain size and preserves the crystal orientations (Fig. 5; Bergmann et al., 2016), minor deviations in the shape of the grain boundary might occur.

Olivine-rich matrix

The olivine-rich matrix is characterized by ol abundance > 90 % and occasional occurrences of interstitial secondary phases (Fig. 5). In some places, coarse pyroxene grains, dominantly opx, are present. Due to the strong serpentinization in olivine-rich domains or lenses and their abundance being limited by the pervasive occurrence of interstitial pyroxenes forming the mixed matrix, only two microstructures of the olivine-rich matrix type could be analyzed (e.g., Fig. 5). They consist of on average 93 % olivine (range 92–94), 6 % opx (range 6–7) and minor spinel (1 %),
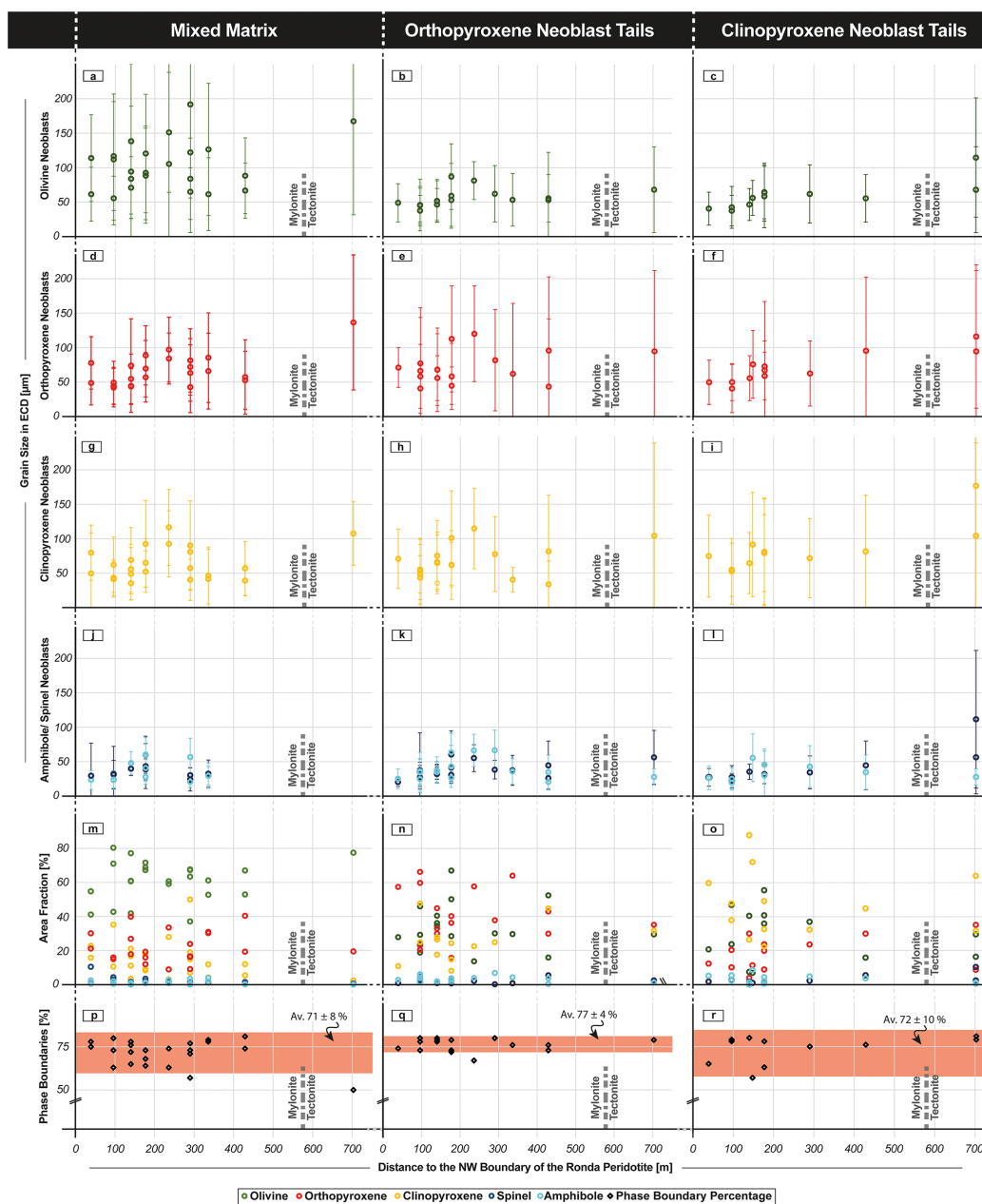
Figure 3. Data overview of the major microstructural domains (mixed matrix, orthopyroxene, and clinopyroxene porphyroclast neoblast tails) plotted against the distance to the NW-B. The olivine-rich matrix was excluded due to its small database. Each data point represents the average grain size **(a–l)**, area fraction **(m–o)**, or phase boundary percentage of the total boundary length **(p–r)** of one EBSD map of an analyzed microstructure (e.g., Figs. 5–9). The complete microstructural data are shown in Table S2.

and cpx ($< 1\%$). The average reconstructed olivine grain size is 107 µm (range 103–112; Table S2). With on average 7 % comprising secondary phases, 31.5 % of the total boundary length are phase boundaries. The crystallographic orientations of the olivines are predominantly parallel to each other (Fig. 4). Bent lattices and/or subgrain boundaries are often present (Fig. 5; box and dashed line). Cracks within those original grains are filled with serpentine (Fig. 5). Orthopyroxenes within the olivine-dominated matrix are oriented with their [001] axis perpendicular to the foliation plane and [100] parallel to the lineation (Fig. 4).

Mixed matrix

The mixed matrix was defined by less than 90 % olivine, and a second-phase content dominated by interstitial secondary phases. The microstructures of 23 mixed-matrix domains were analyzed either as subsets of EBSD maps covering pyroxene porphyroclast tail assemblages with an adjacent matrix or as an individual map. The subsets only consist of the mixed matrix surrounding the porphyroclast tail assemblage. As mixed-matrix microstructures are present in the entire transect (703 to 29 m distance to NW-B), they are present in both mylonitic and tectonitic samples. The characteristics of the mixed matrix are small, interstitial, and irregular and highly lobate pyroxene grains in between coarser-grained olivine (Fig. 6). The grain shape of pyroxenes and olivine varies from being rather equiaxial in the tectonitic samples (Fig. 6bi) to being elongated olivines and film- or wedge-shaped pyroxenes in mylonitic samples (Fig. 6ai). The long side of film-like pyroxenes is mostly parallel to the foliation. Bigger pyroxenes generally have highly irregular grain shapes and protrusions which form intergrowth patterns with bordering olivines (Fig. 6ai *1). Indentations of olivine neoblasts in bigger pyroxenes are commonly observed (Fig. 6ai *2). The mineralogical assemblage of the mixed matrix is in general constant for the entire data set and consists of olivine (avg 61 %; range 37 %–80 %), orthopyroxene (avg 22 %; range 9 %–40 %), clinopyroxene (avg 14 %; range 2 %–50 %), and spinel (avg 2 %; range 0 %–10 %), with occasional amphibole (avg 1 %; range 0 %–4 %; Fig. 3). Spinel is present in the form of interstitial grains. Phase abundances vary, depending on the microstructural setting within one sample, but do not significantly change over the distance to the NW-B (Fig. 3m). Similar to the olivine-rich matrix, former coarse-grained olivines are cut by serpentine veins. Only in phase mixtures are olivine grains less effected by the serpentinization. Average grain sizes (ECD) are 67 µm for opx (range 42–136), 64 µm for cpx (range 35–117), 41 µm for spinel (range 24–90); and 40 µm for amphibole (range 21–60; Fig. 3; Table S2). Reconstructed olivine grains form, with on average 103 µm (range 55–192) ECD, the biggest grains in all investigated thin sections. Almost over the entire mylonitic transect (39–429 distance to the NW-B), the grain sizes of all phases of the mixed ma-

trix are similar within the uncertainty (1σ; Fig. 3). Only at around ~ 250 m distance to the NW-B is an excursion towards coarser sizes observable for both pyroxenes. Mixed-matrix pyroxenes in the tectonite regime (Fig. 6bi) have coarser grain sizes (Fig. 3). The average aspect ratios are 2.03 ± 0.1 for reconstructed ol, 1.9 ± 0.2 for opx, 1.9 ± 0.3 for cpx, 1.8 ± 0.1 for spinel, and 1.8 ± 0.2 for amphibole (Table S2). In contrast to the grain sizes, the average aspect ratios remain constant over mylonites and tectonites (Table S2). On average, $71 \pm 8\%$ of the total boundary length are phase boundaries (29 % grain boundaries). Apart from one outlier, all mylonitic mixed-matrix domains share this distribution. In the tectonite, phase boundaries only form 50 % of the total boundary length. On average, 40 % of the total boundary length are olivine–opx boundaries, with 48 % of the entire olivine boundaries and 79 % of all opx boundaries being olivine–opx boundaries. Despite the lower abundance of cpx, amphibole forms more phase boundaries with cpx (29 %) than with opx (16 %).

Olivine CPOs are moderate (avg max mrd 10; avg $M = 0.16$). Overall, the A-type olivine CPO is dominant (18 of 23 mixed-matrix microstructures; Fig. 4). However, transitions to the AG type by [100] and [001], forming girdles in the foliation plane, are present with variable strength (clear AG-type CPO $n = 3$). Clear B types, which were also reported by Précigout and Hirth (2014) are present in the two samples situated closest to the NW-B. Orthopyroxene CPOs are, with an average maximum mrd of 8 and an average M index of 0.04, the weakest opx CPOs of all investigated domains. In most cases, the orthopyroxene [001] axes are parallel to the lineation. The CPO of opx neoblasts is, in some places, affected by the orientation of larger opx grains within the mixed matrix (Fig. 6biii). Clinopyroxene CPOs are weak, with an average M index of 0.05 (avg max mrd 18). In most cases, both pyroxenes are oriented parallel to each other and show similar intensities in mrd and M for a given microstructure. In some cases, maxima of pyroxene [100] and [010] orientations are flipped in the sense that clinopyroxene [100] maxima are parallel to orthopyroxene [010] maxima, and cpx [010] display orientations similar to opx [100] (e.g., Fig. 6aiii–iv). Only in four mixed-matrix microstructures are enough amphibole grains present to determine a CPO (Fig. 4). In general, amphibole orientations are parallel to the present pyroxene, and its [001] axes are aligned parallel to the lineation. Neoblasts of ortho- and clinopyroxene and olivine in particular has a high dislocation density, which is concentrated into subgrain boundaries in some places (Fig. 7).

4.1.2 Porphyroclast tails

Porphyroclasts are present in all mylonitic samples (Fig. 2). In the tectonite sample, the small difference between grain sizes of matrix and porphyroclasts does not allow a clear differentiation between both (Fig. 2f). Here, pyroxene is either
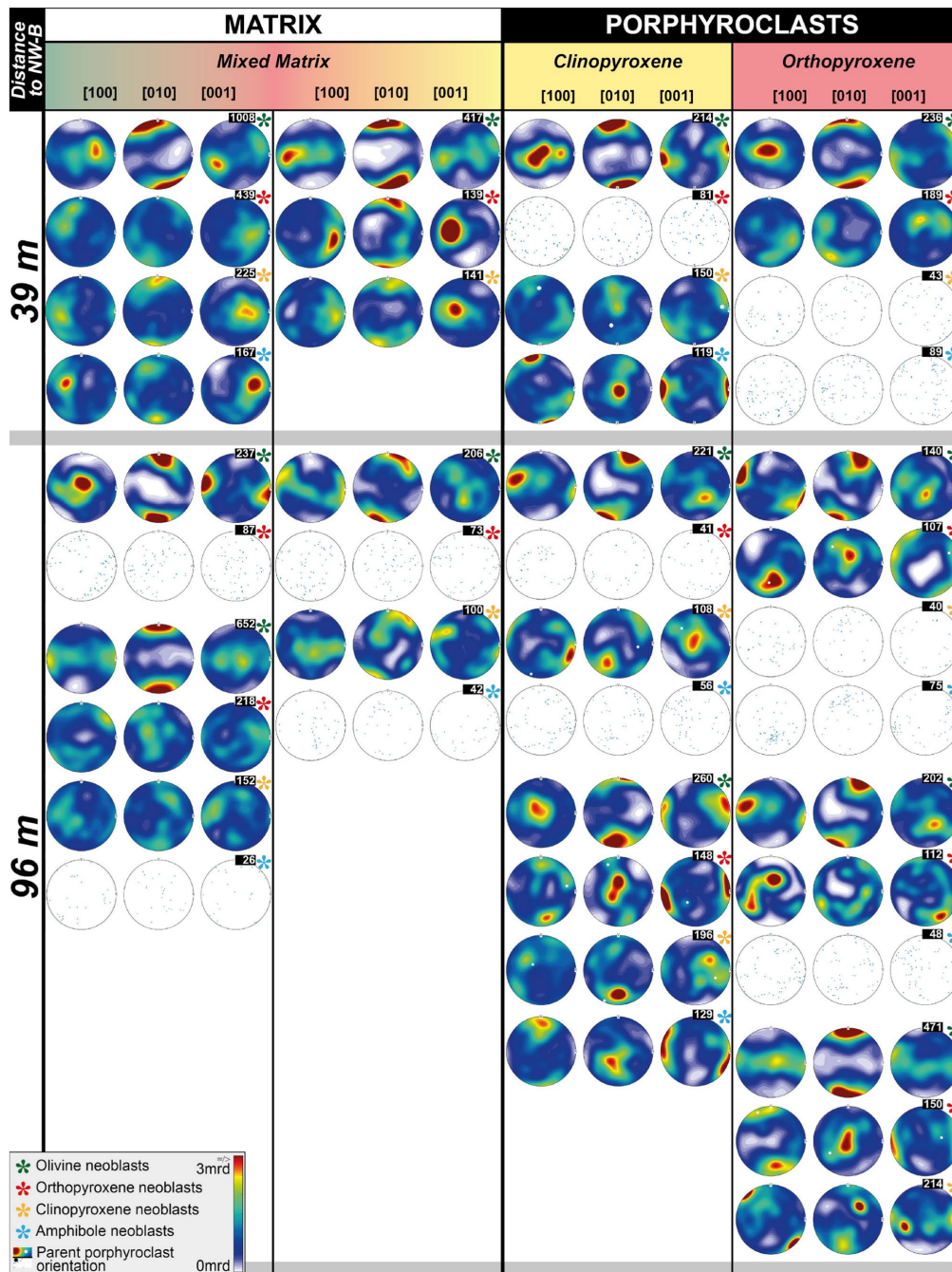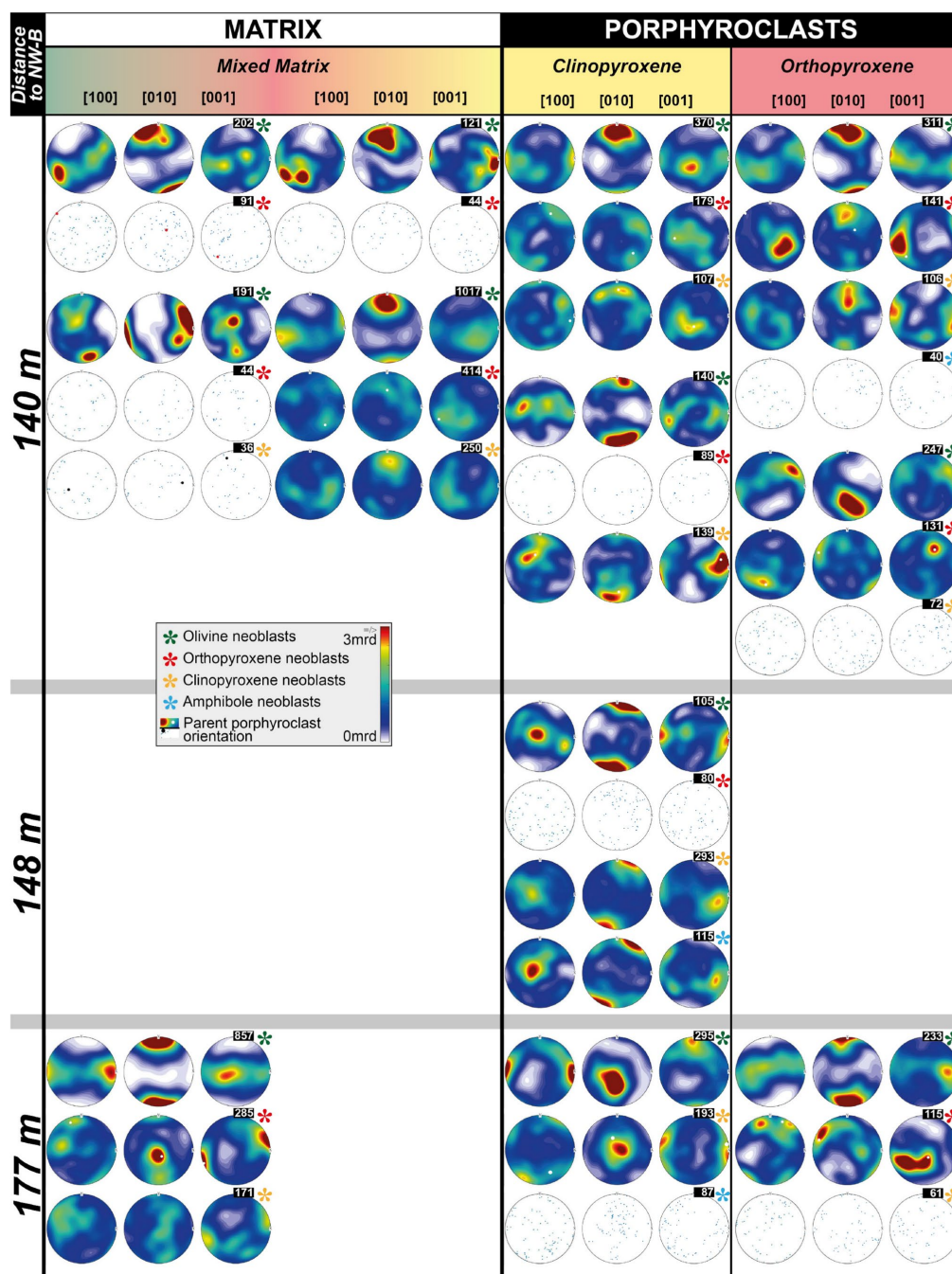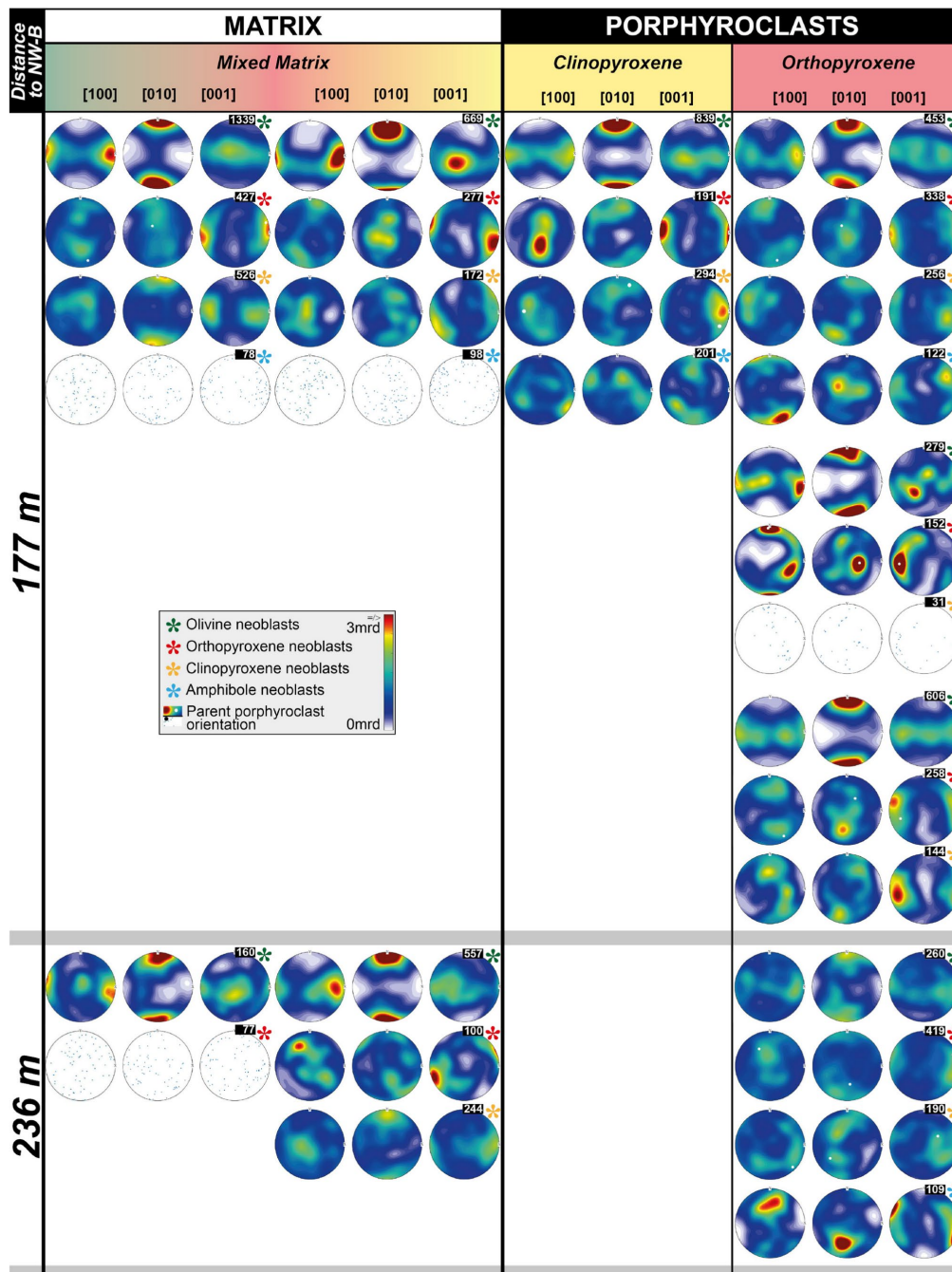
Figure 4.

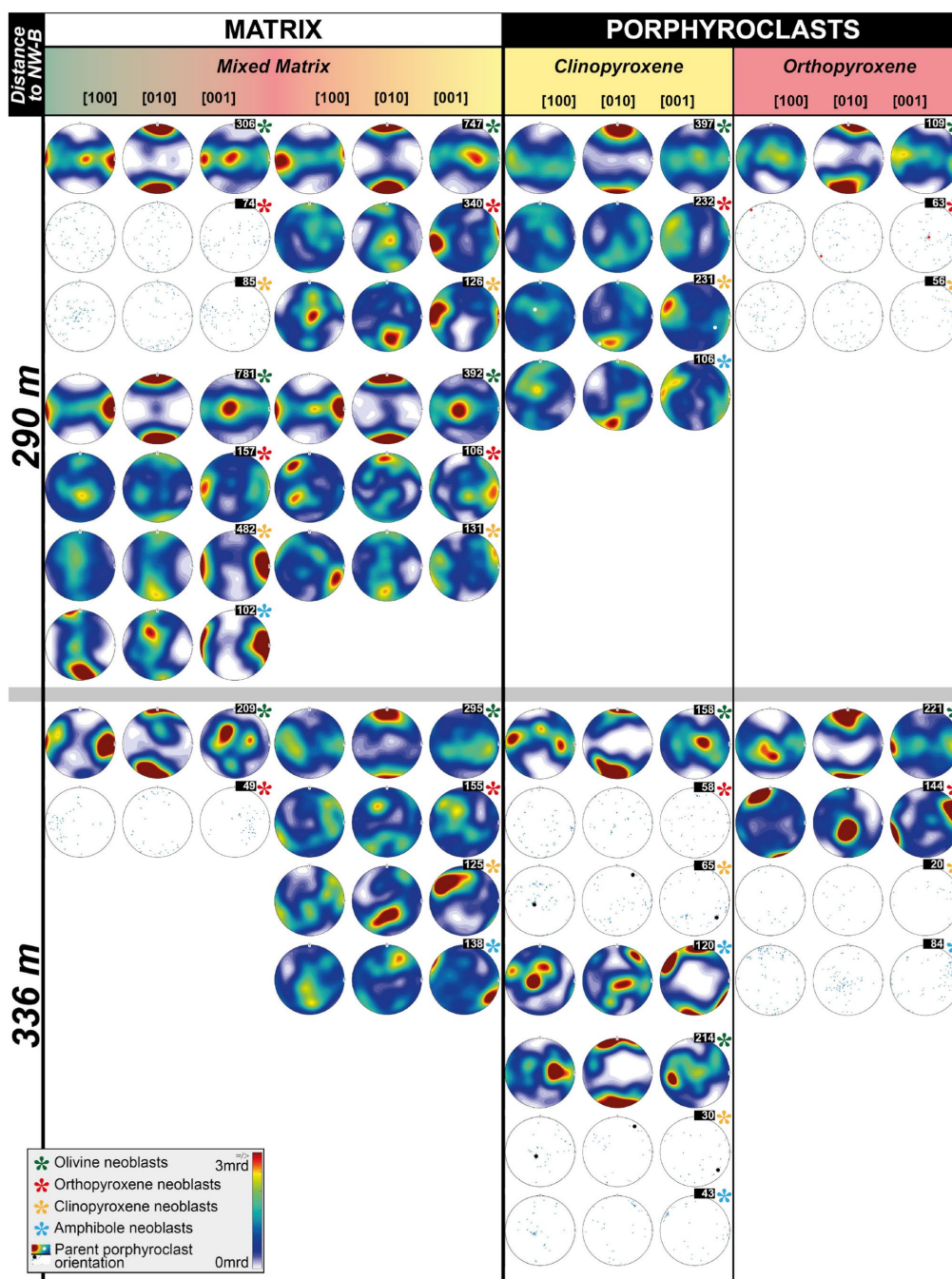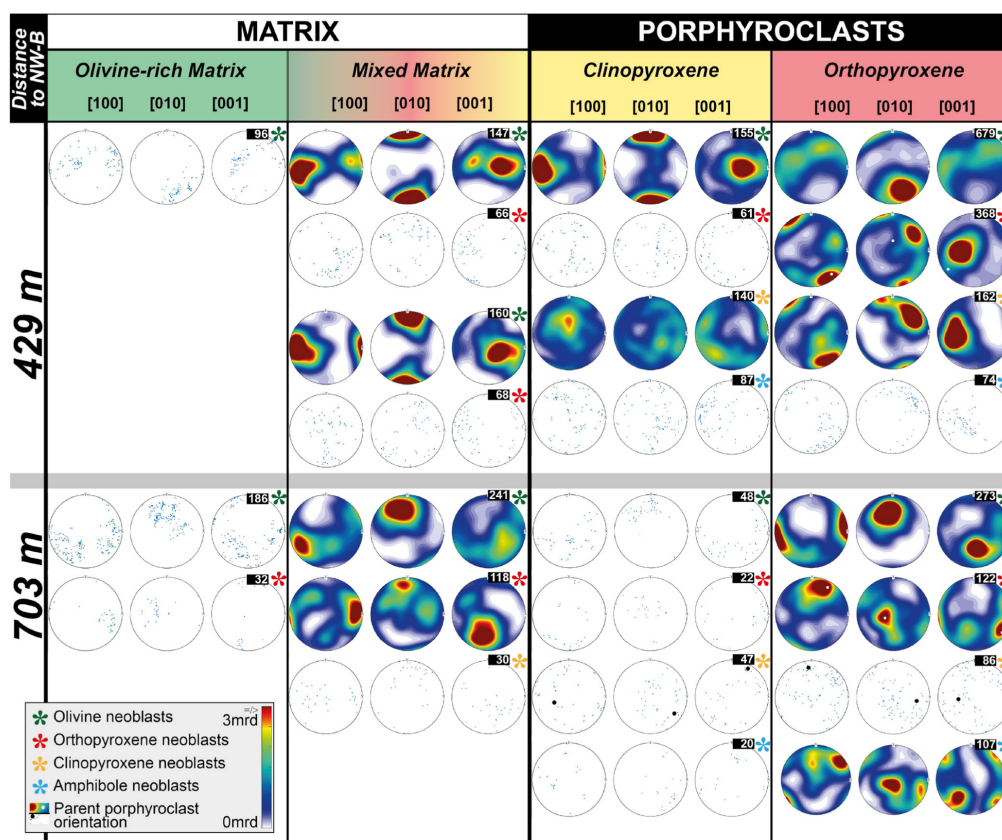**Figure 4.**

Figure 4.

Figure 4.

Figure 4. Orientation data of all microstructural domains plotted per phase and EBSD map as lower-pole figures of calculated texture (> 100 grains) or dots of grain orientations (< 100 grains). White numbers on black indicate the number of grains analyzed for the specific phase. The phase is indicated by the color of the asterisk. The grouping of pole figures correspondents to the microstructure, and a small spacing indicates neoblasts from the same microstructure.

present in layers consisting of both pyroxenes, spinel and minor olivine (Fig. 9bi), as clasts, or (Fig. 2fi and ii) as interstitial pyroxenes along grain boundaries of olivine clasts (Fig. 6bi). The isolated pyroxene clasts in tectonites are predominantly orthopyroxenes. In mylonitic samples, the contrast between porphyroclasts and matrix is marked by their strongly differing grain sizes (Fig. 2a–e). Most porphyroclasts are pyroxenes. Often clusters of intergrown pyroxenes ± spinel form porphyroclastic assemblages (Fig. 2di). These assemblages are predominantly present in deformed pyroxenitic layers or in areas with an increased pyroxene proportion (Fig. 2ci; lower half of the image). Occasionally, garnet surrounded by kelyphitic rims or coarse spinel grains (Fig. 2ei) also forms porphyroclasts. As both pyroxenes are present as (porphyro-)clasts in tectonites and mylonites, their microstructures were analyzed from 29 to 703 m distance to

the NW-B. In mylonitic samples, both pyroxenes show the formation of neoblast tails (Fig. 2a–e). Common characteristics of pyroxene neoblast tails are a mixed phase assemblage of pyroxenes, olivine, amphibole and spinel. The affiliation of neoblast tails to the parent porphyroclasts is given by the contrast in the phase composition and neoblast grain shape between tail and surrounding matrix, as well as by neoblast indentations into the parent porphyroclast (Figs. 7 and 8).

Orthopyroxene porphyroclasts

Orthopyroxene clasts (tectonites) and porphyroclasts (mylonites) are present in all samples. Their shape is variable (Fig. 2). However, towards the NW-B, highly elongated porphyroclasts (aspect ratios > 1 : 10) become more abundant. Neoblast formation around opx porphyroclasts is present in all mylonitic samples. Common characteris-
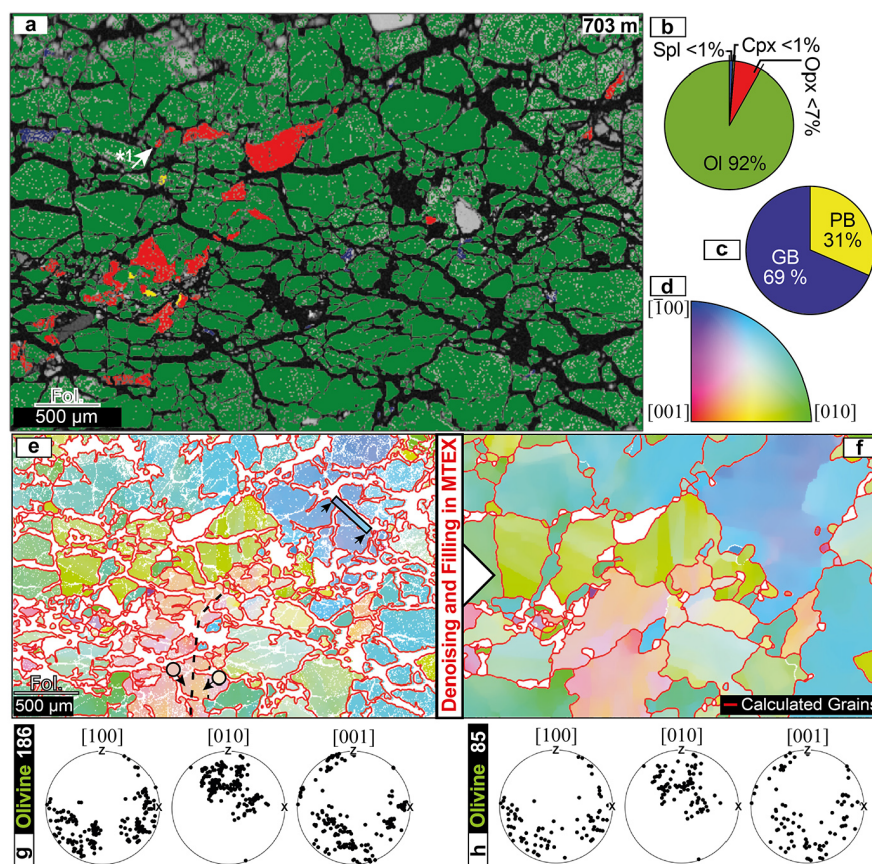
Figure 5. (a) Example microstructure of the olivine-rich matrix in a sample from 703 m distance to the NW-B. Area percentages (b), phase, and grain boundary percentages (c) are given in pie charts. The olivine orientation color key for the maps in panels (e) and (f) is given in panel (d). EBSD data reconstruction and denoising, which have been optimized for olivine, are shown in panels (e)–(h). (e) Original ol orientation data with calculated grain boundaries (red). Examples of intracrystalline deformation by the bending of the crystal lattice (box) and subgrain boundary (dashed line) covering and crossing multiple calculated fragmental grains are annotated. (f) Denoised and filled ol orientation map with calculated grain boundaries (red). Olivine orientation plots of original (g) and reconstructed data (h).

tics of neoblasts are low internal deformation, equiaxial grain shape, and often irregular boundaries (Fig. 8). At the tectonite–mylonite transition, the formation of neoblasts is weaker and rather arranged in diffuse patches around the porphyroclasts (Fig. 8bi). Here, the mixed neoblast assemblages are present at the parent clast grain boundary and extend along grain boundaries into the surrounding coarse-grained olivines (Fig. 8bi). With decreasing distance to the NW-B, opx porphyroclast neoblast assemblages become more abundant and form tails within the foliation (Fig. 8ai). The mineralogical assemblage of these tails consists of orthopyroxene (avg 41 %; range 16–66), olivine (avg 34 %; range 14–67), clinopyroxene (avg 20 %; range 1–48), amphibole (avg 3 %; range 1–7), and spinel (avg 2 %; range 1–6; Fig. 3n). Spinel

and especially amphibole form mostly interstitial grains. There are no clear trends in the phase assemblage related to the distance to the NW-B (Fig. 3n). Amphibole and spinel are constantly present as secondary phases with standard deviations of ± 2 % (amph) and ± 1 % (spl; Fig. 3n). For olivine and both pyroxenes, the phase abundances in opx neoblast tails can vary in a single thin section in the same magnitude as over the entire shear zone transect. Average grain sizes are 69 µm for opx (range 41–120) and reconstructed ol (range 53–99), 66 µm for cpx (range 34–115), 37 µm for amphibole (range 21–67), and 36 µm for spinel (range 20—6; Fig. 3). Apart from one excursion at around 250 m distance to the NW-B, the grain sizes are largely constant throughout the entire transect (Fig. 3). For a given opx tail, grains of
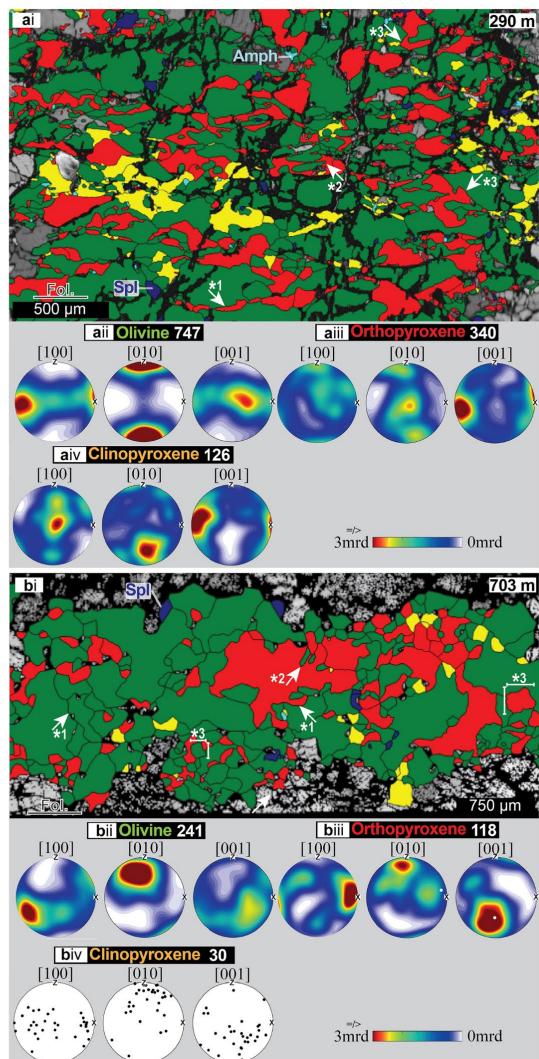
Figure 6. Example microstructures of the mixed matrix in 290 m (**ai**) and 703 m (**bi**) distance to the NW-B. (**a**) Mixed matrix with wedge- or film-shaped orthopyroxene (∗1) in between coarser olivine, indentations (∗2), and highly irregular phase boundaries (∗3). CPOs of olivine (**aii**), orthopyroxene (**aiii**), and clinopyroxene (**aiv**). (**b**) Mixed matrix of a tectonite sample with highly lobate grain and phase boundaries (∗1), indentations (∗2), and equiaxial grain shape (∗3). CPOs of olivine (**bii**) and orthopyroxene (**biii**) and a pole figure of the clinopyroxene orientations (**biv**).
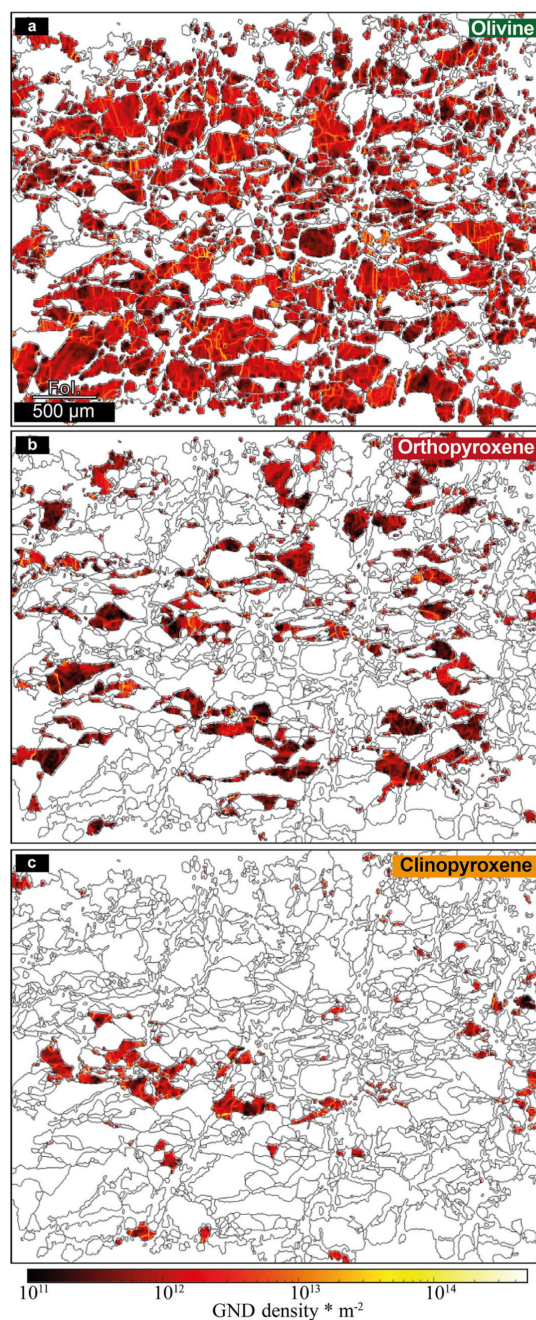
Figure 7. Geometrically necessary dislocation (GND) density maps of olivine (**a**), orthopyroxene (**b**), and clinopyroxene (**c**) from the mylonitic mixed matrix shown in Fig. 6ai. Note the presence of grain internal deformation in all phases and the formation of subgrain boundaries depicted by bright yellow lines of high GND density.
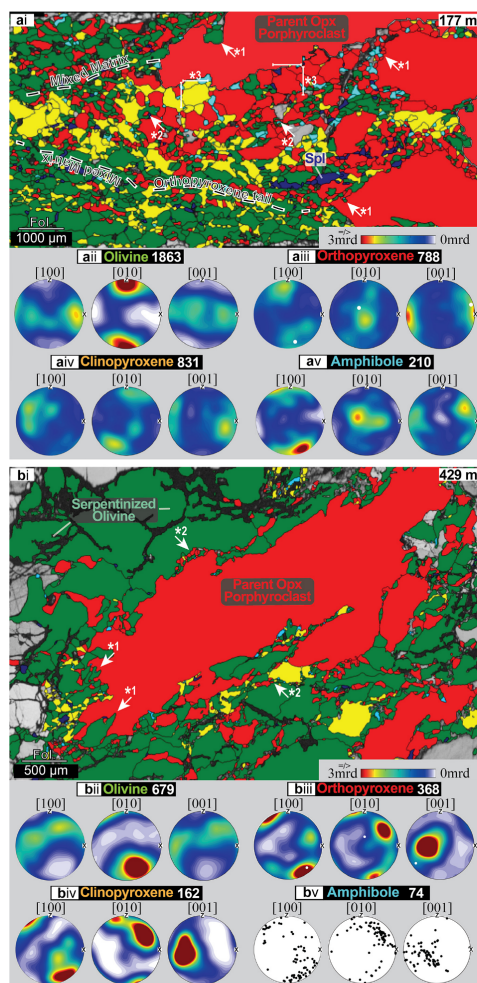
Figure 8. Example microstructures of orthopyroxene porphyroclasts with neoblasts at 177 m **(ai)** and 429 m **(bi)** distance to the NW-B. **(a)** Neoblast tail of opx and subordinate cpx porphyroclast assemblage. Annotated are neoblast indentations in parent porphyroclasts (*1), interstitial amph (amphibole) and spl (*2), and the equigranular grain shape (*3). Note the difference in phase composition and abundances and the grain size and shape between the neoblast tail and surrounding mixed matrix. CPOs of all present phases are given in panels **(aii–v)**, with white dots in panel **(aiii)** indicating the parent clast orientation. **(b)** Orthopyroxene porphyroclast with neoblast indentations (*1) and fine-grained mixed neoblast assemblages at its boundary (*2). Note the presence of fine-grained mixed neoblast along grain boundaries of the surrounding coarse olivine. CPOs of all present phases are given in panels **(bii–v)**, with white dots in panels **(biii)** indicating the parent clast orientation.

both pyroxenes and reconstructed olivine are mostly similar sized ($\pm 10\,\mu$m). Amphibole and spinel have similar, small grain sizes, with ECDs in general being half the size of pyroxene neoblasts. Average aspect ratios are 1.8 for opx, 1.9 for olivine, 1.8 for cpx, 1.8 for amphibole, and 1.9 for spinel, which is in general lower than in matrix domains (Table S2). In contrast to the excursion of the grain sizes, aspect ratios remain constant in all mylonitic samples. In the tectonite, the average aspect ratios are higher (Table S2). Phase boundaries clearly dominate ($77 \pm 4\,\%$) over grain boundaries (Fig. 3q). Apart from one outlier, these high phase boundary percentages are present over the entire shear zone (Fig. 3q). Although opx is mostly the predominant phase, olivine forms, on average, most of the phase boundaries (Table S2). Olivine neoblast CPOs are the weakest for all microstructural domains (avg max mrd 9; avg $M = 0.14$). The AG-type CPO is dominant, with girdle distributions of [100] and [001] in the foliation plane ($n = 11$; Fig. 4). Transitions to A- or B-type CPOs are formed by point maxima in these girdles (Fig. 8aii). Two clear A- and B-type CPOs are present for olivine neoblasts in opx tails (Fig. 4). Orthopyroxene neoblasts have the strongest opx CPOs of all microstructural domains (avg max mrd 12; avg $M = 0.07$). For almost all orthopyroxene porphyroclast–neoblast assemblages, opx neoblast CPOs are strongly dependent on the parent clast orientation (e.g., Fig. 8a and biii). This porphyroclast dependence is present in both strong and weak CPOs of orthopyroxene neoblasts. The common orthopyroxene CPO is formed by [001] parallel to the lineation. The [100] and [010] maxima do not show such a clear trend. Clino- and orthopyroxene CPOs are always for [001] and predominantly for [100] and [001] parallel to each other (e.g., Fig. 8biii and iv). With an average maximum mrd of 19 and an average M index of 0.19 cpx, neoblasts in opx porphyroclast tails form the strongest clinopyroxene CPOs of all microstructural domains. For all orthopyroxene tails, amphibole CPOs are related to the orthopyroxene neoblast CPOs and thereby also parallel to the parent clast orientation (e.g., Fig. 8a and bv).

Clinopyroxene porphyroclasts

In the tectonite, isolated clasts of clinopyroxene are less frequent than those of orthopyroxene (Fig. 2f). Here, beside the small interstitial cpx grains mentioned in the mixed-matrix section, coarser clinopyroxene grains are predominantly present in pyroxenite layers consisting of intergrown pyroxenes, spinel, and olivine (Fig. 9bi). Phase boundaries in these are irregular, whereas grain boundaries tend to be straight and angular (Fig. 9bi *1). Differentiation between the parent clast and neoblasts is not possible. In mylonitic samples, clinopyroxene porphyroclasts, either present in isolated (Fig. 2bii) or deformed assemblages of the above-described layers (Fig. 2dii), form tails of neoblasts, which are sweeping into the foliation. Compared to opx neoblast tails, those of clinopyroxene porphyroclasts are more pronounced – both

in frequency and in tail length (Fig. 2). Additionally, and in contrast to opx neoblast tails, neoblast tails of cpx porphyroclast are also present in mylonitic samples close to the tectonite–mylonite transition (Fig. 2eii). Neoblast tails of cpx porphyroclasts consist of 48 % clinopyroxene (range 22–88), 27 % olivine (range 7–56), 19 % orthopyroxene (range 4–40), 3 % amphibole (range 0–9), and 2 % spinel (range 1–10). For the major components (cpx, opx, and ol) no change in phase abundances is present over the transect (Fig. 3o). For the minor phases of amphibole and spinel, it seems that spinel is the prevailing secondary phase in distal parts of the mylonites and tectonites, whereas amphibole is more abundant closer to the NW-B (Fig. 3o). In most microstructures, spinel and amphibole occur separated from each other. Average grain sizes are 88 μm for cpx (range 53–177), 83 μm for reconstructed olivine (range 57–137), 70 μm for opx (range 40–116), 38 μm for amphibole (range 20–63), and 44 μm for spinel (range 23–112). The distribution of grain sizes is divided into coarse areas of primary phases (pyroxenes and olivine) and fine-grained areas of thoroughly mixed secondary (amphibole or spinel) and primary phases (Fig. 9ai *3). Primary-phase grain sizes are relatively constant over the first 300 m distance to the NW-B (Fig. 3). In the distal mylonitic part and in the tectonitic regime, their grain size increases. Amphibole and spinel average grain sizes are about half of the size of primary phases (Fig. 3). Their grain sizes tend to be constant over the entire transect. For both primary and secondary phases, a slight excursion towards bigger grain sizes at around ∼ 280 m distance to the NW-B is present. Average aspect ratios are 1.8 for cpx, 2.0 for olivine, 1.9 for opx, 1.9 for amphibole, and 1.9 for spl, which is in general lower than in matrix domains (Table S2). In contrast to the grain size, aspect ratios are more constant over the entire transect (Table S2). Phase boundaries form on average 72 % (± 10 %) of the total boundary length (Fig. 2i). This distribution is in general constant over the entire transect and independent of mylonitic or tectonitic unit. Amphibole is mostly affiliated to clinopyroxene (Table S2).

Olivine neoblasts CPOs in tails of clinopyroxene porphyroclasts are variable. Beside the most present A- and B-type (each $n = 4$) transitions to the AG type with point maxima in [100] and [010] girdles, pure AG types and one clear E type are present (Fig. 4). Their strength is moderate to strong (avg max mrd 12; avg $M = 0.15$). Clinopyroxene neoblast CPOs are weak (avg max mrd 15; avg $M = 0.07$). In most cases, the parent clinopyroxene porphyroclasts have an imprint on the neoblast orientation (e.g., Fig. 9aiv). However, compared to orthopyroxene, clinopyroxene maxima are often less pronounced and blurred and therefore more variable from their parent clast orientation. The [001] axes are largely parallel to the lineation. Occasionally ($n = 2$), [100] maxima are oriented parallel to the lineation. If present, orthopyroxene neoblasts are parallel to clinopyroxenes with their [001] and occasionally show 90° rotations for [100]
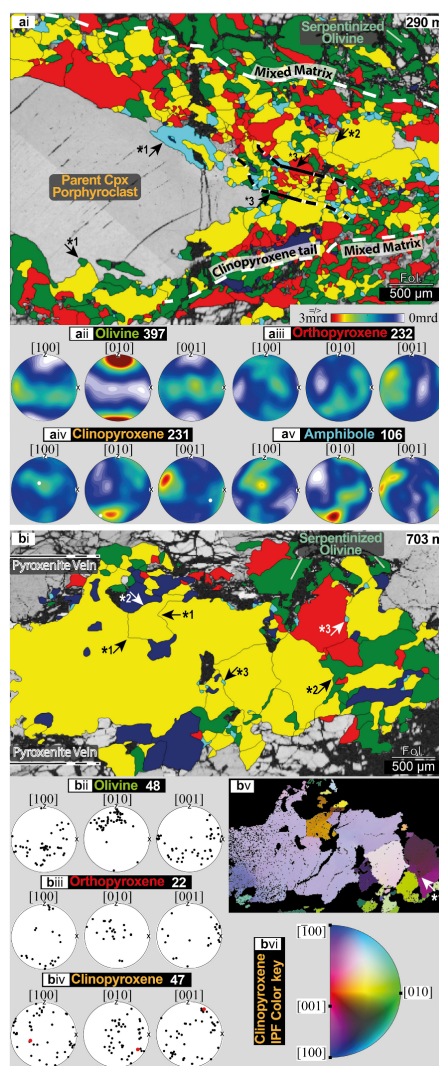

Figure 9. Example microstructures of clinopyroxene porphyroclast with a neoblast tail at 290 m (**ai**) and a cpx-dominated pyroxenite layer at 703 m (**bi**) distance to the NW-B. (**ai**) A clinopyroxene porphyroclast neoblast tail embedded in the mixed matrix with amphibole/ol indentations (*1) and interstitial amph (*2). Within the tail, a band of fine-grained neoblasts (*3) is present. CPOs of all phases are given in panels (**aii–v**). (**b**) A pyroxenite layer with straight grain (*1) and lobate and irregular phase boundaries (*2) and interstitial amph and spl (*3). Pole figures of ol (**bii**), opx (**biii**), and cpx (**biv**) orientations are given. The cpx orientation map (**bv**; color key in panel **bvi**) shows the internal grain deformation and subgrain boundaries (*1).

and [010]. Amphibole neoblasts are mostly oriented parallel to the pyroxenes (e.g., Fig. 9av).

4.1.3 Clinopyroxene–amphibole veins

In three samples, veins consisting of fine-grained (ECD < 10 µm) cpx and amphibole were analyzed. These veins crosscut porphyroclasts, tails, and the mixed matrix with an orientation of $\sim 45°$ to the foliation (Fig. 10). In olivine-rich domains, no such veins were found. The veins are best visible when crosscutting cpx porphyroclasts or pyroxenite layers (Fig. 10). Crosscutting previous structures oblique to the foliation, these veins are attributed to the late evolution of the Ronda peridotite. Because of the focus of this research on the mylonite formation, a detailed microstructural investigation was omitted. However, a short revision is given in Sects. 4.2 and 5.3.

4.2 Mineral chemistry

The major-element compositions of both pyroxenes (opx and cpx), olivine, amphibole, and spinel were determined from three samples with different distances to the NW-B (96, 177, and 290 m). Apart from the olivine-rich matrix, all microstructural domains (cpx and opx neoblast tails and mixed matrix) were analyzed for each sample if present. Neoblast tail measurements include the analysis of the parent pyroxene porphyroclast. There is a general trend for all analyzed phases of decreasing Mg# (molar Mg/(Mg + Fe)) with increasing distance to the NW-B (Figs. 11 and 12). Coupled to the decrease in Mg# is in most cases an increase in TiO_2 and a decrease in Cr_2O_3 (Figs. 11 and 12). In the following, deviations from this trend and phase-specific geochemical variations are presented. Detection limits (Table S1), the complete microprobe data (Table S3), and additional graphs (Fig. S4) are in the Supplement.

4.2.1 Orthopyroxene

All analyzed orthopyroxenes have with Mg# exceeding 0.89 enstatitic compositions (Fig. 11). In general, neoblasts of tails and in the mixed matrix have lower Cr_2O_3, Al_2O_3, and TiO_2 abundances than opx porphyroclasts of the same sample (Fig. 11). The decrease in Mg# with increasing distance to the NW-B is not only most prominent in opx porphyroclasts but also is present for all neoblasts. The complete range of this trend is from Mg# 0.89 at 290 m distance to Mg# 0.91 at 90 m distance to the NW-B. The Mg# decrease (increase in FeO) is coupled with an increase in the TiO_2 and a slight decrease in Cr_2O_3 (Fig. 11c and e).

4.2.2 Clinopyroxene

All analyzed clinopyroxenes have a diopsitic composition. For each analyzed sample, clinopyroxene porphyroclasts in general have lower Mg# and higher Al_2O_3 abundances than

associated neoblasts. For Na_2O, CaO, Cr_2O_3, and TiO_2, systematic differences between neoblasts and porphyroclasts of a given sample are not present (Figs. 11 and S4.1). However, the neoblasts have a bigger scatter in their composition of these oxides. For clinopyroxene, the Mg# decreases from 0.89 (290 m) to 0.93 (90 m distance to the NW-B). Compared to the opx, the Mg# decrease is more pronounced (Fig. 11). Like orthopyroxene, the decrease in Mg# is coupled to a decrease in Cr_2O_3 and an increase in TiO_2 (Fig. 11d and f). Additionally, Na_2O increases and CaO decreases with decreasing Mg#. Clinopyroxene neoblasts from a crosscutting amphibole–pyroxenitic vein deviate significantly from all other analysis by markedly lower Al_2O_3 and Na_2O abundances and increased CaO (Fig. 11; Table S3).

4.2.3 Olivine

All analyzed olivines have a forsteritic composition. Olivine neoblasts follow the trend of decreasing Mg# with increasing distance to the NW-B, which is independent from the microstructural domain (Fig. 12a). However, at 290 m distance to the NW-B, one group of olivine mixed-matrix neoblasts tends to have higher Mg# (Fig. 12a). Yet, with lower Mg# only present in distal samples, the decrease in the Mg# seems to strictly depend on the distance to the NW-B. CaO and NiO abundances do not vary (Figs. 12d and S4.1). Most of the Cr_2O_3 and all TiO_2 measurements lie beneath the detection limit and are therefore excluded from further analysis (Fig. S4.1).

4.2.4 Amphibole

All amphiboles are Ti–Cr-rich pargasites with in general variable abundances of K_2O (range 0–0.78 wt %), Cr_2O_3 (range 0.19–1.7 wt %); and TiO_2 (range 0.66–3.76 wt %; Figs. 12 and S4.2). Apart from one measurement carried out on a sample situated at 90 m distance to the NW-B, all amphiboles follow the trend of decreasing Mg# with increasing distance to the NW-B (Fig. 12b). Like both pyroxenes, Cr_2O_3 abundances decrease, and TiO_2 abundances increase with increasing Mg# (Fig. 12e and g). For TiO_2, four measurements show deviations from this trend with lower abundances. There are no systematic differences between amphiboles associated with ortho- and clinopyroxene tails or the mixed matrix. Na_2O and CaO abundances are, except for four measurements, constant for all samples and all microstructural domains (Fig. S4.2).

4.2.5 Spinel

Most spinels follow the trend of decreasing Mg# and increasing TiO_2 with increasing distance to the NW-B (Fig. 12c). However, coarse-grained spinels (ECD ~ 1 mm) associated with pyroxenes in the kelyphitic intergrow at 290 m distance to the NW-B show that Mg# are shifted to higher values (Fig. 12c). Additionally, spinels associated with cpx neoblast
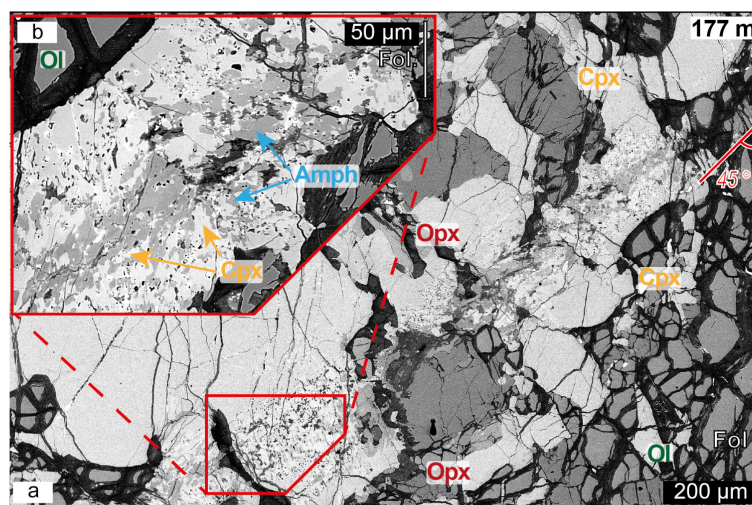
Figure 10. (a) Clinopyroxene amphibole vein crosscutting the mixed matrix and a clinopyroxene porphyroclast. Note the $\sim 45°$ angle between foliation and vein orientation. **(b)** Close-up view of the vein which shows the zoning in a cpx-rich rim and amph-rich center.

tails have in each sample the highest Mg# (Fig. 12c). High Mg# in these spinels are related to low TiO_2 and Cr_2O_3 values (Fig. 12f and h). In contrast to amphibole and both pyroxenes, Cr_2O_3 abundances increase with increasing distance to the NW-B (Fig. 12h).

5 Discussion

5.1 Formation of the microstructural domains – metasomatism by OH-bearing, evolved melt

5.1.1 Genesis of the mixed matrix

As the dominant microstructure of all analyzed samples, from 29 to 700 m distance to the NW-B, the mixed matrix is of particular importance for understanding the formation and evolution of the entire shear zone. Its constant microstructural characteristics are (1) a phase assemblage of interstitial secondary grains (opx, spl $\pm$ cpx) distributed in between coarse-grained pyroxenes and olivine; (2) high mixing intensities formed by the dispersed distribution of secondary phases; and (3) highly lobate phase boundaries and irregular grain shapes. All three characteristics indicate a formation by reactions (e.g., Dijkstra et al., 2002; Hidas et al., 2016; Newman et al., 1999; Tholen et al., 2022). Potential driving forces of such reactions in the upper mantle are metamorphism and/or metasomatism by melt–rock or fluid–rock interactions.

In other upper-mantle shear zones, metamorphic reactions were coupled to the garnet peridotite–spinel peridotite and, at shallower depth, spinel peridotite–plagioclase peridotite

transitions, which triggered continuous net transfer reactions (e.g., Furusho and Kanagawa, 1999; Newman et al., 1999; Tholen et al., 2022). As phase mixing in the Ronda shear zone is not bound to a specific phase association (grt or spl bearing), and no plagioclase is present, it is unlikely that metamorphic reactions were the dominant driving force for the neoblast formation in the matrix and in pyroxene tails.

As formerly elaborated by Hidas et al. (2016) in their study on ultramylonitic shear zones in Ronda's SSE plagioclase peridotites (location in Fig. 1), syn-kinematic net transfer, dissolution–precipitation reactions, and neoblast crystallization can also be catalyzed by fluids. In this regard, syn-kinematic amphibole precipitation and fluid channeling were also postulated to form mixed-phase assemblages and ultramylonites in the center of deformation of the Lanzo shear zone (Vieira Duarte et al., 2020). For a peridotitic composition at shallower upper-mantle conditions, Hidas et al. (2016) assume the formation of 1.0 wt %–1.4 wt % amphibole when fluid saturation is reached. However, despite all reported microstructural similarities (high mixing intensity, irregular phase boundaries, and interstitial or film-like shapes of orthopyroxenes), there are distinct differences between the NW Ronda shear zone and those mentioned above, making a fluid-driven metasomatism unlikely. First, in contrast to the well-dispersed amphibole in the matrix reported by Hidas et al. (2016; $\sim 1.6\%$) and Vieira Duarte et al. (2020; ≤ 30 vol %), amphibole in NW Ronda is mostly limited to pyroxene neoblast tails (avg 3 %). In the mixed matrix, amphibole is on average 1 %, which is again mostly associated with coarser-grained pyroxenes and especially cpx. The second difference is the lack of amphibole-bearing ultramy-
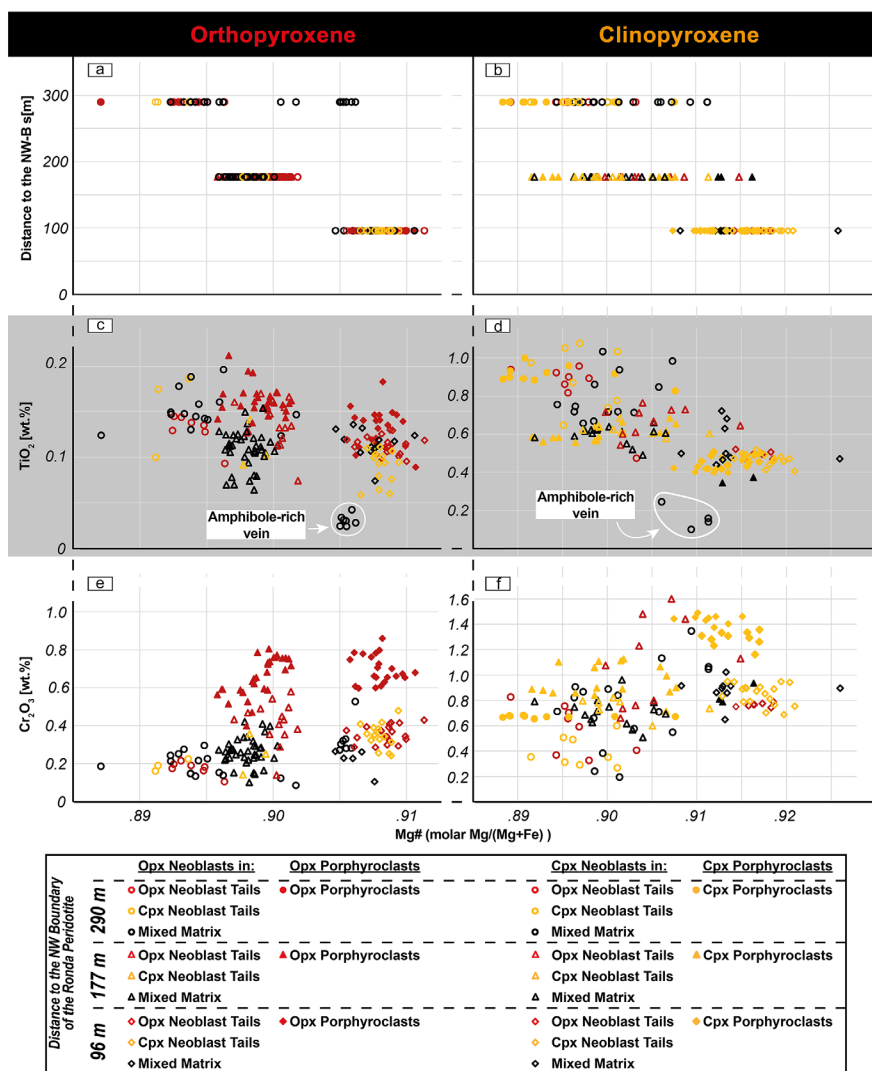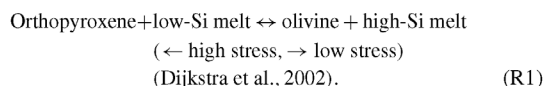
Figure 11. EPMA data of ortho- and clinopyroxene porphyroclasts and of neoblasts situated at 96, 177, and 290 m to the NW-B. Neoblasts were analyzed in cpx or opx porphyroclast tails and in the mixed matrix. **(a, b)** Mg# versus the distance to the NW-B. **(c, d)** TiO$_2$ versus Mg#. Pyroxenes of clinopyroxene–amphibole vein (Fig. 10) are indicated. **(e, f)** Cr$_2$O$_3$ versus Mg#.

lonites and no localization of the deformation coinciding with amphibole-rich assemblages (see Sect. 5.3).

Microstructural features such as interstitial grains with low dihedral angles, neoblast indentations in coarse-grained orthopyroxene, and highly irregular phase boundaries are furthermore considered to be evidence of melt–rock reactions and secondary crystallization from percolating melts (Dijkstra et al., 2002; Stuart et al., 2018; Suhr, 1993). In this regard, the commonly found irregular, highly lobate bound-

aries between olivine and orthopyroxene suggest a reaction already evoked by Dijkstra et al. (2002) for melt-assisted shearing in the Othris peridotite.

Orthopyroxene+low-Si melt $\leftrightarrow$ olivine + high-Si melt
$$(\leftarrow \text{high stress}, \rightarrow \text{low stress})$$
$$\text{(Dijkstra et al., 2002).} \qquad \text{(R1)}$$

Assuming a formation by percolating melt, the questions arise of its extent and composition. Melt percolation was re-
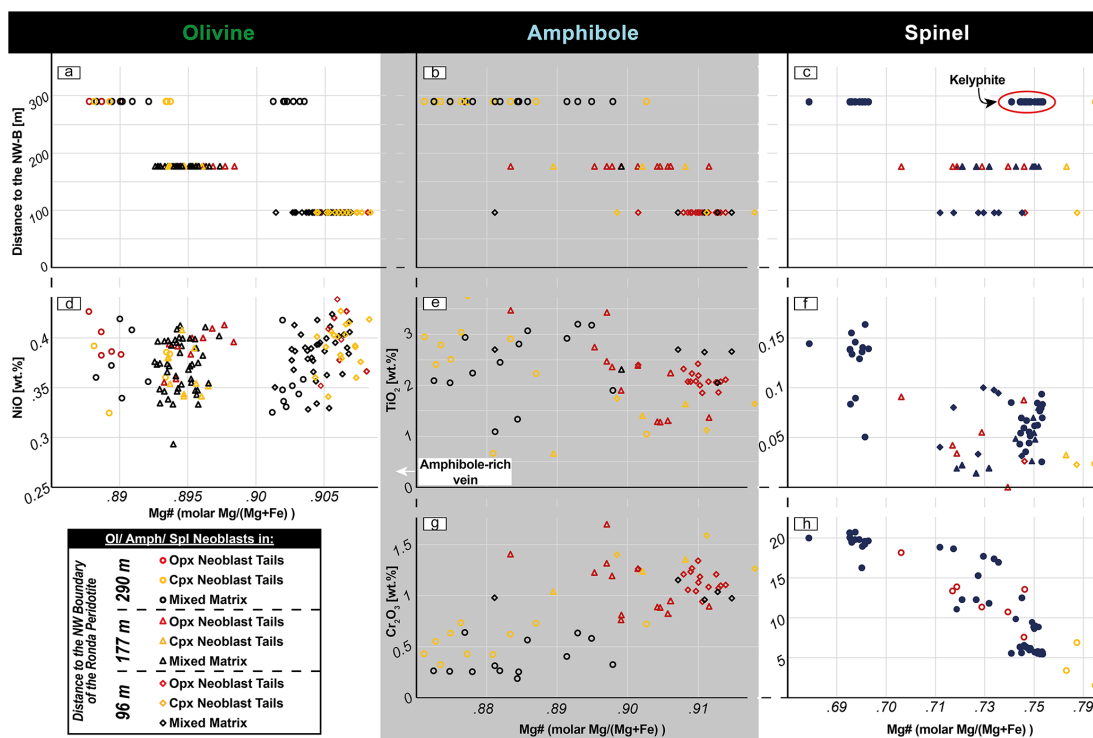
Figure 12. EPMA data of olivine, amphibole, and spinel neoblasts of cpx or opx porphyroclast tails and the mixed matrix at 96, 177, and 290 m distance to the NW-B. **(a–c)** Mg# in dependence of the distance to the NW-B. **(d)** Mg# versus NiO wt % for olivine neoblasts. **(e, f)** Mg# versus TiO_2 for amph and spl neoblasts. **(g, h)** Mg# versus Cr_2O_3 for amph and spl neoblasts.

ported to form lherzolite, plagioclase-bearing peridotite, and grt peridotite that replaced harzburgite and dunite in a process called refertilization (Beyer et al., 2006; Hu et al., 2020; Müntener and Piccardo, 2003; Le Roux et al., 2007). This process was also ascribed to form cpx-enriched tectonites in the refertilization front a few hundred meters ahead of the melting front between Ronda's coarse-grained peridotites and the tectonite unit (Lenoir et al., 2001). The melt origin is ascribed to the partial melting (2.5 %–6.5 % extraction) of the coarse-grained peridotites at conditions close to the anhydrous peridotite solidus ($T \geq 1200\,°C$) at 1.5 GPa (Lenoir et al., 2001). In their model, melting was triggered by a rapid transient heating event (Lenoir et al., 2001). Going further, Soustelle et al. (2009) postulated that Si-rich melts fertilized the spl tectonites of the NW Ronda shear zone up to 1.5 km ahead of the melting front. According to these authors, early melt pulses led to pyroxene and spinel crystallization in the form of irregularly shaped grains, whereas a late-stage, second-order percolation of an evolved melt caused the crystallization of interstitial, undeformed pyroxenes and spinel with a strongly enriched light rare earth element (LREE)

composition. In contrast to the data of Soustelle et al. (2009), which leave the mylonitic shear zone melt unaffected, we present microstructural evidence of melt presence up to the NW boundary of the Ronda massif. However, a change in the modal composition of refertilized lherzolites by neocrystallized pyroxenes, as commonly described for refertilization (e.g., Le Roux et al., 2007), is not documented in both studies. Moreover, syn-kinematic conditions of 800–900 °C and 1.95–2.00 GPa, postulated by Garrido et al. (2011) for the mylonites, refute a large-scale, syn-kinematic percolation of refertilizing basaltic melt, which should reset the temperature.

Similar microstructural evidence for syn-kinematic reactive melt percolation and melt–rock reactions such as irregular grain shape, lobate boundaries, and high mixing intensity have been reported for grt–spl mylonites of the Beni Bousera peridotite, which form the Moroccan counterpart of the Ronda massif on the southern limb of the Gibraltar arc (Fig. 1; Frets et al., 2014). Syn-kinematic conditions of 850–950 °C and ∼ 2.0 GPa, matching those obtained in NW Ronda, led to the assumption of a metasomatism

by small fractions of fluids or evolved melts, which did not reset the equilibrium temperatures (Frets et al., 2012, 2014). Amphibole presence in pyroxene neoblast tails (see Sect. 5.1.2), ubiquitous evidence of reaction-derived microstructures and pyroxene crystallization at syn-kinematic P–T conditions of 800–900 °C and 1.95–2.00 GPa point to a similar OH-bearing metasomatism by highly evolved melt in the NW Ronda shear zone. The geochemical imprint of this metasomatism is characterized by an increase in FeO (which means decreasing Mg#) and TiO$_2$ for olivine, pyroxenes, spinel, and amphibole in all microstructural domains towards the melting front or with increasing distance to the NW-B, respectively (Fig. 13). Interestingly, SE tectonites (data from Soustelle et al., 2009) and mylonites follow the same trend of decreasing Mg# with increasing distance to the NW-B (Fig. 13). However, an offset is present between SE tectonites analyzed by Soustelle et al. (2009), which decrease from higher Mg# ($\sim$0.92) than the mylonites and NW tectonites ($\sim$0.89) analyzed here and by Soustelle et al. (2009; Fig. 13). This possibility of multiphase melt pulses and over-printing of the mylonites by the NW tectonites is only indicated by the present sample set, but the evidence in support thereof is not conclusive. However, for the mixed matrix of all mylonitic and NW tectonitic samples analyzed, a pervasive metasomatism is suggested by the interstitial spinel and pyroxene neoblasts, high mixing intensities, highly lobate phase boundaries, and irregular grain shape. The low abundance of interstitial pyroxenes in the ol-rich matrix suggests that these represent areas slightly affected to unaffected by this metasomatism. The presence of amphibole and the geochemical data, although limited to three samples, suggests metasomatism by OH-bearing evolved melt.

5.1.2 On the origin of the pyroxene porphyroclasts and the formation of their neoblast tails

Pyroxene porphyroclasts are present in the entire transect. Especially in the tectonite, cpx porphyroclasts are often associated with pyroxenitic layers, which show a coarse-grained intergrowth of both pyroxenes, olivine, and spinel. Beside their formation by partial crystallization from percolating melts, Garrido and Bodinier (1999) interpreted these websteritic layers to have formed at the expense of garnet-bearing pyroxenites by melt–rock reactions. The kelyphitic structures in pyroxenite layers of mylonites, also described by Van Der Wal and Vissers (1996), corroborate the idea that these assemblages represent, at least partially, garnet breakdown products. This replacement of garnet-bearing by websteritic assemblages, which was so far associated with the melting or recrystallization front (Garrido and Bodinier, 1999), is present in our samples up to the tectonite–mylonite transition. Straight grain boundaries with 90° angles within the tectonitic pyroxenites suggest that these were partly annealed after having replaced garnet-bearing assemblages.
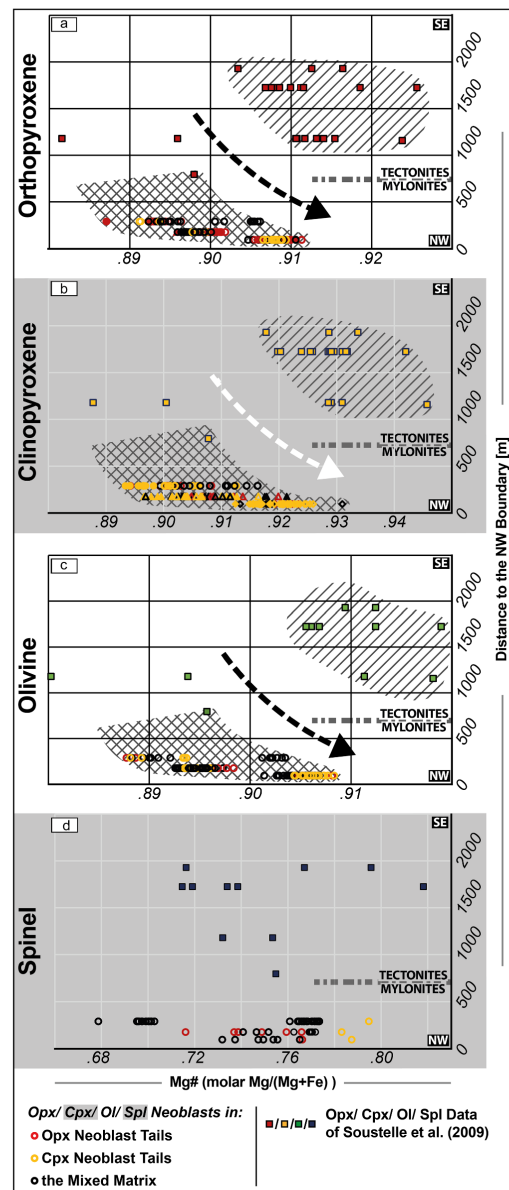

Figure 13. Mg# data of spinel tectonites (Soustelle et al., 2009) and spl–grt mylonites (this study) vs. distance to the NW-B. The transition between tectonites and mylonites is indicated around 700 m distance to the NW-B. The hatched area shows the geochemical signature of melt in tectonites. The crosshatched area shows the geochemical signature of melt in mylonites. Mg# of opx (**a**), cpx (**b**), olivine (**c**), and spl (**d**) is plotted against the distance to the NW-B. The location of the studied area by Soustelle et al. (2009) is indicated in Fig. 1. Arrows indicate the geochemical trend of increasing Mg# towards the NW-B.

Boudinage of the pyroxenite layers led to pinch-and-swell structures, which are present already in the SE part of the mylonite zone and described in detail by Précigout et al. (2013). The pyroxene-porphyroclast-rich areas and spinel–garnet–pyroxene clusters are interpreted to be the remnants of these pyroxenites. In the same samples (SE mylonites), cpx porphyroclasts form neoblast tails, and opx porphyroclasts are bordered by fine-grained patches of neoblasts. From there on, neoblast tails of both pyroxenes form essential microstructural domains in the mylonites. Their characteristics are (1) a polyphase assemblage of cpx, opx, ol, spl, and amph with (2) high mixing intensities (avg phase boundary percentages 77 % opx tails; 72 % cpx tails); (3) highly irregular phase boundaries of porphyroclasts and neoblasts; and (4) indentations of all neoblast phases into the porphyroclast (Figs. 3, 8, and 9). Again, all microstructural characteristics point to a formation by metasomatic reactions. These characteristics remain constant throughout the entire transect, suggesting that all neoblast tails were formed by the same process from both pyroxene porphyroclasts in all analyzed samples (mylonites and tectonite).

Amphibole presence and its reaction fabrics suggest, similar to the observations made in the mixed matrix, an OH-bearing metasomatism. Its indentations into the porphyroclasts underline its part of the primary neoblast assemblage. Pargasitic amphibole is stable up to ~ 3.8 GPa at 1000 °C, with its stability strongly depending on the amount of bulk H_2O (Mandler and Grove, 2016). Pargasite-bearing peridotites have been found in peridotite shear zones at similar, syn-kinematic P–T conditions to those present in NW Ronda (Garrido et al., 2011; Johanesen et al., 2014: 1.95–2/1.5 GPa, 800–900 °C; Hidas et al., 2016; Tholen et al., 2022). The common association of pyroxenes, olivine, and amphibole, indentations of amphibole into pyroxene porphyroclasts, also reported by Van der Wal (1993), and the observation that spinel is less abundant in areas with amphibole, and vice versa, suggest a reaction of pyroxenes, spinel, and amphibole. The replacement of clinopyroxene and spinel by amphibole in peridotites is commonly attributed to metasomatic reactions (e.g., Blatter and Carmichael, 1998; Bonadiman et al., 2014; Ishimaru et al., 2007). Hydrous melts were observed to form amphibole at the expense of primary orthopyroxene, olivine, and clinopyroxene (Rapp et al., 1999; Sen and Dunn, 1995). In their study of xenoliths from Antarctica, Coltorti et al. (2004) suggested a melt-assisted reaction, with the formation of amphibole at the expense of clinopyroxene and spinel shortly (a few thousand years) before their uplift. Their model implies a two-stage melt–rock evolution, with an initial crystallization of pyroxenes, olivine, and spinel being succeeded by the secondary crystallization of amphibole. However, the composition of the associated glass suggests that the metasomizing agent was a Na–alkali silicate melt. For Ronda, the limited geochemical data (three samples) suggests a Fe–Ti-enriched, OH-bearing melt by constant Na_2O abundances for clinopyrox-

ene clasts and neoblasts and Ti–Fe enrichment for pyroxenes. According to the experimental results of Wang et al. (2021), the composition of the crystallizing amphibole depends on the tectonic setting in addition to the metasomatic melt and peridotite composition. Relatively low Mg# and high Na_2O and TiO_2 abundances of the analyzed amphibole suggest a supra-subduction-zone metasomatism (Coltorti et al., 2007). Higher OH abundances in pyroxene neoblast tails are additionally indicated by olivine B-type CPOs, which is often associated with increased concentrations of H/Si (Jung et al., 2006; Jung and Karato, 2001; Mizukami et al., 2004). As no chemical difference is present between the neoblast tails and mixed matrix, both microstructural domains are thought to have been formed by OH-bearing metasomatism, most likely in the form of a hydrous, evolved melt.

5.2 Deformation in the NW Ronda shear zone

5.2.1 Differentiation between tectonites and mylonites by deformation-induced microstructures

Although the composition and the microstructures suggest a consistent metasomatic formation of the entire analyzed Ronda shear zone, differences in grain shape and, to a lesser extent, in the grain size between the mylonitic and the tectonitic mixed matrix suggest different deformation conditions and mechanisms of both units. The tectonitic mixed matrix is characterized by small, equiaxial, and interstitial grains of both pyroxenes and spinel between coarse pyroxenes and olivine. Neoblast formation in both the tectonitic mixed matrix and around orthopyroxene porphyroclasts at the tectonite–mylonite transition show weak dependence on the foliation. Additionally, tectonitic mixed-matrix orthopyroxene neoblasts have a CPO with [001] subperpendicular to the foliation, which is atypical for deformation-induced CPOs (e.g., Jung, 2017). Instead, the CPO of opx neoblasts is in most cases strongly connected to the parent clast orientation. Distributed neoblast precipitation, equiaxial neoblast grain shapes, and irregular CPO indicate in general weaker deformation and/or a certain degree of post-kinematic annealing in tectonites and SE mylonites. Nevertheless, strong CPO (A-type CPO; $M = 0.2$) and lobate grain boundaries indicate the deformation of olivine by dislocation creep.

On the other hand, microstructures of the mylonites indicate stronger deformation by (1) film-like pyroxenes oriented along grain boundaries subparallel to the foliation and (2) the increasing abundance of pyroxene neoblast tails elongated in the lineation. Similar film-like microstructures were observed in peridotite mylonites from the Othris shear zone (Dijkstra et al., 2002) and in ultramylonites from the plagioclase–tectonite unit in Ronda (Hidas et al., 2016). For Othris, this microstructure has been associated with the dependence of Reaction (R1) on local stress variations (Dijkstra et al., 2002). The low-stress, ol-crystallizing variant of Reaction (R1) forms highly irregular ol–opx phase boundaries

and ol indentations subperpendicular to the foliation. Wedge-shaped pyroxene neoblasts along grain boundaries subparallel to the foliation were interpreted as being high-stress precipitates of Reaction (R1). In NW Ronda, both low- and high-stress fabrics are present through film- or wedge-shaped pyroxenes in the mixed matrix and at porphyroclast boundaries adjacent to neoblast tails. For fluid-assisted dissolution–precipitation reactions in ultramylonites of Ronda, Hidas et al. (2016) inferred that the fluid composition can be locally controlled by the surrounding minerals, thus allowing the alternating dissolution and precipitation of olivine and orthopyroxene.

Regardless of the type of metasomatic agent, the comparison to the microstructures of Othris and Ronda in particular the highly lobate phase boundaries and the wedge-shaped pyroxenes along the foliation strongly point to the activity of incongruent, syn-kinematic dissolution–precipitation processes in the mylonitic unit (Hirth and Kohlstedt, 1995). Syn-kinematic diffusion with a stronger effect on smaller grains is additionally indicated by the tendency of mixed-matrix pyroxene neoblasts to lower TiO_2 and Cr_2O_3 abundances (Cherniak and Liang, 2012). In addition to grain-size-sensitive dissolution–precipitation creep, the CPOs of olivine and both pyroxenes, high dislocation densities in neoblasts of the mixed matrix, and the elongation of all present grains should result from dislocation creep. The localization of dynamic crystallization processes in olivine neoblasts is corroborated by the highest average M indices (0.14–0.20) of each microstructural domain, except for cpx in neoblast tails of opx porphyroclasts ($M = 0.19$), and the highest neoblast dislocation densities by GND concentration. Dominant slip systems are (010) in [100] for olivine (A type; e.g., Karato et al., 2008) and slip on (100) or on (010), with both directed towards [001] for orthopyroxene (Ohuchi et al., 2011; Ross and Nielsen, 1978). In the mylonites, the rheological impact of the olivine-rich matrix is considered to be rather small, since it forms competent lenses in the mixed matrix. In the mixed matrix, evidence of both grain-size-insensitive dislocation creep and grain-size-sensitive dissolution–precipitation creep corroborate the hypothesis of the activity of a dislocation creep-accommodated grain-size-sensitive deformation mechanism formerly proposed by Johanesen and Platt (2015) and Précigout et al. (2007). In contrast to the dislocation-creep-accommodated GBS (DisGBS; Hirth and Kohlstedt, 2003), as suggested by Précigout et al. (2007) and Précigout and Hirth (2014), Johanesen and Platt (2015) favor dislocation creep with a grain size sensitivity given by the grain boundary migration as the dominant recovery mechanism (DRX creep; Platt and Behr, 2011). Because microstructural evidence for both mechanisms is present (GBS – grain and phase boundary alignments; DRX creep – lobate grain boundaries), and DRX creep and DisGBS are dominant under approximately the same conditions of grain size and shear stress (Johanesen and Platt, 2015), neither mechanism can be excluded by this study. However,

microstructures of the NW Ronda shear zone clearly indicate the activity of both grain-size-insensitive dislocation creep and grain-size-sensitive dissolution–precipitation creep.

5.2.2 Timing and effect of metasomatism on deformation

Our data do not permit a firm conclusion about the timing of metasomatism. The dissolution–precipitation creep microstructures which shaped the mylonitic mixed matrix indicate, in accordance with the study of Othris mylonites, that melt was syn-kinematic (Dijkstra et al., 2002). Moreover, Frets et al. (2014) argued for syn- to late-kinematic metasomatism under near-solidus conditions for similar microstructures in the corresponding grt–spl mylonites of the Beni Bousera peridotite. In addition to enhancing the rate of dissolution–precipitation creep and lubricating grain boundaries for GBS (Hirth and Kohlstedt, 1995), metasomatic melt stimulates grain boundary pinning by crystallized secondary pyroxenes, which hinders grain growth and thereby stabilizes grain-size-sensitive deformation mechanisms (Linckens et al., 2011). Almost constant neoblast grain sizes in the mylonites indicate a deformation in the melt-affected area at constant stresses. However, microstructures of tectonites, which are interpreted to be formed by the same metasomatism (see Sect. 5.1) indicate weaker deformation. This could be explained either by a pre-kinematic metasomatism or annealing. Evidence for multiphase metasomatism of the tectonite unit brought up by Soustelle et al. (2009) is corroborated by different trends in Mg# of tectonites and mylonites and the final replacement of the grt-bearing pyroxenites by websteritic assemblages detected at the tectonite–mylonite transition. Both the replacement of grt-bearing pyroxenites and shifting geochemical trends could indicate that the tectonite–mylonite transition is an imprint of a later metasomatic front overprinting and annealing mylonitic microstructures under lower-stress conditions. As previously discussed in Sect. 5.1.1, additional data of the tectonite–mylonite transition are necessary to address these potential overprinting and annealing relationships of tectonites on mylonites. The controversy of crosscutting (Van Der Wal and Vissers, 1996) versus gradual contact (Précigout et al., 2007; Soustelle et al., 2009) between mylonites and tectonites is most likely part of this context.

5.2.3 Strain localization in the northwestern mylonites

A continuous decrease in grain size towards the NW-B (e.g., Obata, 1980; Précigout et al., 2007; Van Der Wal and Vissers, 1996) is not indicated by our data. Neoblast grain sizes of all phases and from all microstructural domains stay constant, with minor local excursions over the entire mylonitic shear zone. This observation of constant grain size with regional variations matches the study of Johanesen and Platt (2015) of rather constant grain size of recrystallized

olivine ($\sim 130\,\mu$m), which is based on optically traced grain boundaries. Accordingly, the average reconstructed olivine grain size of 103 μm for the mixed matrix and 107 μm for the ol-rich matrix lies in the range of the average recrystallized olivine grain size reported by Johanesen and Platt (2015) and Frets et al. (2014) for the grt–spl mylonite unit of both Ronda and Beni Bousera. For the mylonites, the postulated trend of a decreasing average grain size with decreasing distance to the NW-B could be explained by the increasing amount of neoblasts and the accompanying increase in the proportion of mixed matrix and neoblast tails.

An increase in the strain towards the NW-B is signified by the increase in the opx porphyroclast elongation to the final retort shape (Johanesen and Platt, 2015). This strain localization is accompanied by the decrease in the olivine CPO strength to a minimum of $M = 0.09$, as already reported by Précigout and Hirth (2014). Additionally, the proportion of intact pyroxene porphyroclasts to reacting porphyroclasts decreases towards the NW-B, indicating a strain dependence of neoblast tail formation. A positive feedback between deformation and neoblast formation rate was formerly reported by de Ronde and Stünitz (2007) in their experiments for the transition from plagioclase to spinel in olivine–plagioclase aggregates. An enhanced nucleation reaction rate was here explained by increasing deformation-induced defects in the reactant and the deformation-induced transportation of neoblasts away from the reaction interface, which thereby maintains a high chemical potential. For Ronda, a similar mechanism could clear the porphyroclast reaction interface of neoblasts and thereby lead to enhanced neoblast formation and tail elongation. An increasing number of neoblasts and the stabilization of their small grain size by mixing in turn enhances the share of the grain-size-sensitive deformation mechanism corroborated by the decrease in the CPO strength of olivine. Concomitant with the increase in the neoblast tails, the dominant olivine CPO changes within ~ 150 m distance to the NW-B from an A-type CPO, which indicates low water and intermediate stress conditions, to an AG-type CPO or occasionally a B-type CPO, which indicates increased water content and high stress (e.g., Jung, 2017). The increased presence of olivine B-type CPOs towards the NW-B was formerly interpreted to result from grain boundary sliding (GBS) rather from a change in the dominant slip system (Précigout and Hirth, 2014). However, over the entire mylonitic area, independent of the distance to the NW-B, olivine CPOs from pyroxene neoblast tails are predominantly B or AG types (Fig. 4). Pyroxene tail microstructures, which include, due to the scanning arrangement, areas of or transitions to the surrounding matrix, tend to have AG-type or A-type olivine CPOs. On the other hand, a stronger B type is commonly bound to a well-defined neoblast tail without large amounts of the surrounding matrix, thus highlighting the relation between the CPO type and microstructural location. Accordingly, the girdle distributions of olivine's [100] and [001] within the foliation plane present in the AG type

could result from a mix of A-type and B-type CPOs. The increased occurrence of amphibole in neoblast tails, especially in association with cpx, documents higher OH abundances. This in turn corroborates the association of the B-type CPO to increased concentrations of H/Si (Jung et al., 2006; Jung and Karato, 2001; Mizukami et al., 2004). The correlation of a stronger B-type with increased clinopyroxene abundances observed by Précigout and Hirth (2014), which was at odds with the B-type solely dependent on the increase in GBS towards the NW-B therefore fits with both of the previously presented observations: (1) the pronounced presence of amphibole and olivine B-type CPOs in pyroxene neoblast tails, and (2) the preferred association of amphibole with clinopyroxene. Accordingly, the decrease in the porphyroclasts and the increase in pyroxene neoblast tails towards the NW-B leads to an increase in the olivine neoblasts with a B-type orientation. However, the formation of olivine B-type CPOs by GBS in the mixed matrix close to the NW-B (< 100 m), as suggested by Précigout and Hirth (2014), cannot be ruled out. Although multiphase mixtures crystallized in the metasomatic neoblast tails of pyroxenes, no strain localization as reported for pyroxene reaction tails in other peridotite shear zones occurred in these microstructural domains (Hidas et al., 2013b; Tholen et al., 2022). The main reason for the lack of strain localization might be that all microstructural domains have similar percentages of phase boundaries and similar grain sizes. Therefore, no strain partitioning between the mixed matrix and the tails associated with a switch to a grain-size-sensitive deformation mechanism was achieved (e.g., Rutter and Brodie, 1988). The strong relation between neoblast and parent porphyroclast orientation implies an inherited orientation of the parent-phase neoblasts. The shared orientation of at least one preferred orientation for amphibole and second pyroxene neoblasts with parent-phase clast and neoblasts suggests topo- or epitactic growth (Putnis et al., 2006). The increase in finite strain towards the NW-B documented by porphyroclast elongation and neoblast tail formation possibly results from positive feedback between the formation of small, mixed neoblasts and its enhancing and stabilizing effect on grain-size-sensitive deformation mechanisms (Johanesen and Platt, 2015). Starting with the syn-kinematic to early-kinematic metasomatic formation of the neoblasts in the mixed-matrix and pyroxene porphyroclast tails, the localization of the strain might continue under subsolidus conditions by GBS, as suggested by Précigout and Hirth (2014).

5.3 Late-stage fluid infiltration

The crosscutting of entire cpx porphyroclasts by amphibole-filled cracks, the replacement of cpx exsolution lamellae by amphibole in opx porphyroclasts (Obata, 1980), and the formation of amphibole- and clinopyroxene-rich veins oblique to the foliation indicate a late-stage fluid infiltration, which post-dates the melt infiltration and deformation processes discussed above. Since these fabrics are largely restricted to

mylonites close to the NW-B, a fluid infiltration originating from the adjacent metasedimentary Jubrique unit seems plausible. Lower Ti abundances for amphibole, clino-, and orthopyroxene neoblasts and amphibole Mg# that are not comparable (<0.86) to those of other microstructural domains corroborate an independent formation process. Interestingly, the formation of serpentine seems to follow these structures.

5.4 Comparison to other upper-mantle shear zones and the significance of reactions for localized deformation

Like most studied upper-mantle shear zones, the results presented for the Ronda shear zone point to a key role of reactions in the evolution of upper-mantle shear zones (e.g., Dijkstra et al., 2004). A comparison between these studies suggests that the impact of reactions on the evolution of shear zones depends on the timing rather than on the type of reaction.

Tommasi et al. (2017) have shown that hydrous Si-rich melts significantly affect the mechanical strength of the upper mantle and favor a strain localization in the melt-affected region. Additionally, melt–rock reactions in low-strain domains of the Lanzo shear zone document the presence of melt during initial shearing (Kaczmarek and Müntener, 2008). Beside phase mixing by crystallization of pyroxene neoblasts interstitially and at the reacting boundaries of coarser olivine in combination with the activity of a grain-size-sensitive creep mechanism (Hirth and Kohlstedt, 2003; Platt and Behr, 2011), an additional effect is the reduction in the strength by the wetting of the phase and grain boundaries (e.g., Hirth and Kohlstedt, 1995). As these effects are solely dependent on the presence of melt, they are also most likely decisive for early localization of strain in the upper mantle.

For syn-kinematic, high-stress conditions during the later stages of the shear zone evolution, metasomatic and metamorphic reactions have elsewhere been shown to be important for the formation of ultramylonitic neoblast assemblages either in pyroxene porphyroclast tails or in ultramylonitic bands; in the shear zones of Othris and Erro–Tobbio, melt–rock reactions formed ultramylonitic, mixed tails dominated by pyroxene and olivine (Dijkstra et al., 2002; Linckens and Tholen, 2021). Metamorphic reactions in relation to the phase transitions of garnet, spinel, and plagioclase triggered reactions at pyroxene porphyroclasts and the formation of ultramylonitic assemblages in shear zones of the Uenzaru peridotite complex, the Turon de Técouère peridotite body, and the Lanzo peridotite massif (Furusho and Kanagawa, 1999; Newman et al., 1999; Tholen et al., 2022). Fluid-assisted dissolution–precipitation creep and the resulting ultramylonites were reported from shear zones at the transition of plagioclase to granular peridotite unit in central Ronda (Hidas et al., 2016) and in the Anita Peridotite (Czertowicz et al., 2016). Phase mixing with amphibole and/or chlorite in ultramylonitic assemblages was reported for Erro–Tobbio

(Hoogerduijn Strating et al., 1993; Linckens and Tholen, 2021) and the Shaka and Prince Edward transform faults (Kohli and Warren, 2020; Prigent et al., 2020). Diffusion creep and GBS as the dominant deformation process in these ultramylonitic assemblages result in a significant reduction in the mechanical strength, leading to further strain localization in the shear zones if the ultramylonitic areas start to become interconnected (e.g., de Ronde et al., 2005).

Based on the previous research, the observations from NW Ronda can be placed into the following hypothesis: metasomatic and metamorphic reactions result in reaction softening of the upper mantle by phase mixing and the activation of diffusion-driven and grain-size-sensitive deformation mechanisms which interact with dislocation creep. As these reactions are localized, they result in strain localization. The degree of strain localization seems to depend on the timing of the reaction in the course of the shear zone evolution but not on the nature of the reaction itself. In the case of the NW Ronda shear zone, pre-kinematic to early syn-kinematic metasomatism formed the mixed matrix and the neoblast tails over a kilometer-scale area and thereby shaped the early shear zone. High mixing intensities and resulting homogenous grain size in the mylonitic mixed matrix ensured that no further strain localization occurred in porphyroclasts reaction tails. Late-stage, syn-kinematic melt- or fluid-assisted and/or metamorphic reactions under high-stress conditions can lead to the formation of mixed ultramylonitic bands, which are not present in the examined NW Ronda shear zone but are described for Othris (Dijkstra et al., 2002), Erro-Tobbio (Linckens and Tholen, 2021), Uenzaru (Furusho and Kanagawa, 1999), Turon de Técouère (Newman et al., 1999), and the coarse granular peridotite unit of central Ronda (Hidas et al., 2016). In these bands, strain is further localized in the decimeter to centimeter scale by diffusion creep as the dominant deformation mechanism.

6 Conclusions

- Metasomatism formed (1) a mixed matrix by the crystallization of interstitial pyroxenes and (2) pyroxene porphyroclast neoblast tails by melt–rock reactions in the entire NW Ronda shear zone. Microstructural evidence comprises highly lobate grain boundaries, irregular grain shapes, and homogenously dispersed interstitial secondary phases that result in high mixing intensities. Geochemical analysis and the presence of amphibole indicate a metasomatism by Fe–Ti-enriched, OH-bearing evolved melt, which did not reset the equilibrium temperatures.

- Film- or wedge-shaped pyroxenes in the mylonitic mixed-matrix point to a pre-kinematic to syn-kinematic metasomatism. For the tectonite unit, the coarser grain size and equiaxial grain shapes suggest a pre-kinematic to early syn-kinematic melt presence and/or annealing,

which may be related to multiphase metasomatism. Evidence of the tectonite–mylonite transition being the imprint of a metasomatic front is found in shifted geochemical trends (Mg#) and the final replacement of garnet-bearing by websteritic assemblages in pyroxenite layers. Due to the limited geochemical data and sample density at the tectonite–mylonite transition, further analyses are needed to define the timing of metasomatism and confirm a potential overprint of tectonites on mylonites.

– CPO data and film- or wedge-shaped pyroxenes suggest grain-size-insensitive dislocation creep and grain-size-sensitive dissolution–precipitation creep as being the main deformation mechanisms. Grain-size-sensitive deformation is assisted by the pinning effect operating in the generally strongly mixed assemblages.

– Despite the nearly constant grain size for the entire mylonite unit, a strain gradient towards the NW is documented by increasing elongation of orthopyroxene porphyroclasts. The increase in the strain is accompanied by an increase in the neoblast abundance and a weakening and change in the olivine CPO, both suggesting enhanced grain-size-sensitive creep.

– Crosscutting amphibole veins indicate a late-stage fluid infiltration.

– The comparison to other upper-mantle shear zones highlights the significance of reactions for localized deformation at different scales. Hypothetically, the degree of strain localization seems to depend more on the timing of the reaction during the shear zone evolution than on the type of reaction. Pre-kinematic to early syn-kinematic melt infiltration localizes deformation in kilometer-scale melt-affected area, as present in NW Ronda. Syn-kinematic melt or fluid-assisted and/or metamorphic reactions under high-stress conditions hypothetically result in the formation of mixed ultramylonitic bands (not present in the investigated NW Ronda shear zone).

References

Bachmann, F., Hielscher, R., and Schaeben, H.: Texture analysis with MTEX-Free and open source software toolbox, Solid State Phenomena, 160, 63–68, https://doi.org/10.4028/www.scientific.net/SSP.160.63, 2010.

Balanyá, J. C., García-Dueñas, V., Azañón, J. M., and Sánchez-Gómez, M.: Alternating contractional and extensional events in the Alpujarride nappes of the Alboran Domain (Betics, Gibraltar Arc), Tectonics, 16, 226–238, https://doi.org/10.1029/96TC03871, 1997.

Barich, A., Acosta-Vigil, A., Garrido, C. J., Cesare, B., Tajčmanová, L., and Bartoli, O.: Microstructures and petrology of melt inclusions in the anatectic sequence of Jubrique (Betic Cordillera, S Spain): Implications for crustal anatexis, Lithos, 206–207, 303–320, https://doi.org/10.1016/j.lithos.2014.08.003, 2014.

Bercovici, D. and Ricard, Y.: Plate tectonics, damage and inheritance, Nature, 508, 513–516, https://doi.org/10.1038/nature13072, 2014.

Bergmann, R., Chan, R. H., Hielscher, R., Persch, J., and Steidl, G.: Restoration of manifold-valued images by half-quadratic minimization, Invers. Probl. Imag., 10, 281–304, https://doi.org/10.3934/ipi.2016001, 2016.

Beyer, E. E., Griffin, W. L., and O'Reilly, S. Y.: Transformation of archaean lithospheric mantle by refertilization: Evidence from exposed peridotites in the Western Gneiss Region, Norway, J. Petrol., 47, 1611–1636, https://doi.org/10.1093/petrology/egl022, 2006.

Blatter, D. L. and Carmichael, I. S. E.: Plagioclase-free andesites from Zitácuaro (Michoacán), Mexico: Petrology and experimental constraints, Contrib. Mineral. Petrol., 13, 121–138, https://doi.org/10.1007/s004100050411, 1998.

Bonadiman, C., Nazzareni, S., Coltorti, M., Comodi, P., Giuli, G., and Faccini, B.: Crystal chemistry of amphiboles: Implications for oxygen fugacity and water activity in lithospheric mantle beneath Victoria Land, Antarctica, Contrib. Mineral. Petrol., 167, 1–17, https://doi.org/10.1007/s00410-014-0984-8, 2014.

Booth-Rea, G., Ranero, C. R., Grevemeyer, I., and Martínez-Martínez, J. M.: Crustal types and tertiary tectonic evolution of the Alborán sea, western Mediterranean, Geochem. Geophy. Geosy., 8, 1–25, https://doi.org/10.1029/2007GC001639, 2007.

Borghini, G.: The spinel- to plagioclase-facies transition in mantle peridotites: Natural and experimental constraints, Plinius, 34, 43–45, 2008.

Boullier, A. M. and Gueguen, Y.: SP-Mylonites: Origin of some mylonites by superplastic flow, Contrib. Mineral. Petrol., 50, 93–104, https://doi.org/10.1007/BF00373329, 1975.

Bunge, H.-J.: Orientation Distributions, in: Texture Analysis in Materials Science, Butterworth, London, England, 42–46, https://doi.org/10.1016/B978-0-408-10642-9.50008-8, 1982.

Cherniak, D. J. and Liang, Y.: Ti diffusion in natural pyroxene, Geochim. Cosmochim. Ac., 98, 31–47, https://doi.org/10.1016/j.gca.2012.09.021, 2012.

Coltorti, M., Beccaluva, L., Bonadiman, C., Faccini, B., Ntaflos, T., and Siena, F.: Amphibole genesis via metasomatic reaction with clinopyroxene in mantle xenoliths from Victoria Land, Antarctica, Lithos, 75, 115–139, https://doi.org/10.1016/j.lithos.2003.12.021, 2004.

Coltorti, M., Bonadiman, C., Faccini, B., Grégoire, M., O'Reilly, S. Y., and Powell, W.: Amphiboles from suprasubduction and intraplate lithospheric mantle, Lithos, 99, 68–84, https://doi.org/10.1016/j.lithos.2007.05.009, 2007.

Cross, A. J. and Skemer, P.: Ultramylonite generation via phase mixing in high-strain experiments, J. Geophys. Res.-Solid, 122, 1744–1759, https://doi.org/10.1002/2016JB013801, 2017.

Czertowicz, T. A., Toy, V. G., and Scott, J. M.: Recrystallisation, phase mixing and strain localisation in peridotite during rapid extrusion of sub-arc mantle lithosphere, J. Struct. Geol., 88, 1–19, https://doi.org/10.1016/j.jsg.2016.04.011, 2016.

Davies, G. R., Nixon, P. H., Pearson, D. G., and Obata, M.: Tectonic implications of graphitized diamonds from the Ronda peridotite massif, southern Spain, Geology, 21, 471–474, https://doi.org/10.1130/0091-7613(1993)021<0471:TIOGDF>2.3.CO;2, 1993.

de Ronde, A. A. and Stünitz, H.: Deformation-enhanced reaction in experimentally deformed plagioclase-olivine aggregates, Contrib. Mineral. Petrol., 153, 699–717, https://doi.org/10.1007/s00410-006-0171-7, 2007.

de Ronde, A. A., Stünitz, H., Tullis, J., and Heilbronner, R.: Reaction-induced weakening of plagioclase-olivine composites, Tectonophysics, 409, 85–106, https://doi.org/10.1016/j.tecto.2005.08.008, 2005.

Dijkstra, A. H., Drury, M. R., Vissers, R. L. M., and Newman, J.: On the role of melt-rock reaction in mantle shear zone formation in the Othris Peridotite Massif (Greece), J. Struct. Geol., 24, 1431–1450, https://doi.org/10.1016/S0191-8141(01)00142-0, 2002.

Dijkstra, A. H., Drury, M. R., Vissers, R. L. M., Newman, J., and Van Roermund, H. L. M.: Shear zones in the upper mantle: Evidence from alpine- and ophiolite-type peridotite massifs, Geol. Soc. Spec. Publ., 224, 11–24, https://doi.org/10.1144/GSL.SP.2004.224.01.02, 2004.

Drury, M. R. and Urai, J. L.: Deformation-related recrystallization processes, Tectonophysics, 172, 235–253, https://doi.org/10.1016/0040-1951(90)90033-5, 1989.

Drury, M. R., Vissers, R. L. M., Van der Wal, D., and Hoogerduijn Strating, E. H.: Shear localisation in upper mantle peridotites, Pure Appl. Geophys., 137, 439–460, https://doi.org/10.1007/BF00879044, 1991.

Esteban, J. J., Sánchez-Rodríguez, L., Seward, D., Cuevas, J., and Tubía, J. M.: The late thermal history of the Ronda area, southern Spain, Tectonophysics, 389, 81–92, https://doi.org/10.1016/j.tecto.2004.07.050, 2004.

Esteban, J. J., Cuevas, J., Vegas, N., and Tubía, J. M.: Deformation and kinematics in a melt-bearing shear zone from the Western Betic Cordilleras (Southern Spain), J. Struct. Geol., 30, 380–393, https://doi.org/10.1016/j.jsg.2007.11.010, 2008.

Esteban, J. J., Cuevas, J., Tubía, J. M., Sergeev, S., and Larionov, A.: A revised Aquitanian age for the emplacement of the Ronda peridotites (Betic Cordilleras, southern Spain), Geol. Mag., 148, 183–187, https://doi.org/10.1017/S0016756810000737, 2011.

Frets, E., Tommasi, A., Garrido, C. J., Padrón-Navarta, J. A., Amri, I., and Targuisti, K.: Deformation processes and rheology of pyroxenites under lithospheric mantle conditions, J. Struct. Geol., 39, 138–157, https://doi.org/10.1016/j.jsg.2012.02.019, 2012.

Frets, E., Tommasi, A., Garrido, C., Vauchez, A., Mainprice, D., Targuisti, K., and Amri, I.: The beni bousera peridotite (rif belt, morocco): An oblique-slip low-angle shear zone thinning the subcontinental mantle lithosphere, J. Petrol., 55, 283–313, https://doi.org/10.1093/petrology/egt067, 2014.

Furusho, M. and Kanagawa, K.: Transformation-induced strain localization in a lherzolite mylonite from the Hidaka metamorphic belt of central Hokkaido, Japan, Tectonophysics, 313, 411–432, https://doi.org/10.1016/S0040-1951(99)00215-2, 1999.

Garrido, C. J. and Bodinier, J. L.: Diversity of mafic rocks in the Ronda peridotite: Evidence for pervasive melt-rock reaction during heating of subcontinental lithosphere by upwelling asthenosphere, J. Petrol., 40, 729–754, https://doi.org/10.1093/petroj/40.5.729, 1999.

Garrido, C. J., Gueydan, F., Booth-Rea, G., Précigout, J., Hidas, K., Padrón-Navarta, J. A., and Marchesi, C.: Garnet lherzolite and garnet-spinel mylonite in the Ronda peridotite: Vestiges of Oligocene backarc mantle lithospheric ex-

tension in the western Mediterranean, Geology, 39, 927–930, https://doi.org/10.1130/G31760.1, 2011.

Hidas, K., Booth-Rea, G., Garrido, C. J., Martínez-Martínez, J. M., Padrón-Navarta, J. A., Konc, Z., Gianconia, F., Frets, E., and Marchesi, C: Backarc basin inversion and subcontinental mantle emplacement in the crust: Kilometre-scale folding and shearing at the base of the proto-alborán lithospheric mantle (Betic Cordillera, southern Spain), J. Geol. Soc., 170, 47–55, https://doi.org/10.1144/jgs2011-151, 2013a.

Hidas, K., Garrido, C. J., Tommasi, A., Padrón-Navarta, J. A., Thielmann, M., Konc, Z., Frets, F., and Marchesi, C: Strain localization in pyroxenite by reaction-enhanced softening in the shallow subcontinental lithospheric mantle, J. Petrol., 54, 1997–2031, https://doi.org/10.1093/petrology/egt039, 2013b.

Hidas, K., Tommasi, A., Garrido, C. J., Padrón-Navarta, J. A., Mainprice, D., Vauchez, A., Barou, F., and Marchesi, C: Fluid-assisted strain localization in the shallow subcontinental lithospheric mantle, Lithos, 262, 636–650, https://doi.org/10.1016/j.lithos.2016.07.038, 2016.

Hiraga, T., Miyazaki, T., Yoshida, H., and Zimmerman, M. E.: sliding Comparison of microstructures in superplastically deformed synthetic materials and natural mylonites: Mineral aggregation via grain boundary sliding, Geology, 41, 959–962, https://doi.org/10.1130/G34407.1, 2013.

Hirth, G. and Kohlstedt, D.: Rheology of the upper mantle and the mantle wedge: A view from the experimentalists, Geophys. Monogr. Ser., 138, 83–105, https://doi.org/10.1029/138GM06, 2003.

Hirth, G. and Kohlstedt, D. L.: Experimental constraints on the dynamics of the partially molten upper mantle: deformation in the diffusion creep regime, J. Geophys. Res., 100, 1981–2001, https://doi.org/10.1029/94JB02128, 1995.

Hoogerduijn Strating, E. H., Rampone, E., Piccardo, G. B., Drury, M. R., and Vissers, R. L. M.: Subsolidus emplacement of mantle peridotites during incipient oceanic rifting and opening of the mesozoic tethys (voltri massif, NW Italy), J. Petrol., 34, 901–927, https://doi.org/10.1093/petrology/34.5.901, 1993.

Hu, W. J., Zhong, H., Chu, Z. Y., Zhu, W. G., Bai, Z. J., and Zhang, C.: Ancient Refertilization Process Preserved in the Plagioclase Peridotites: An Example From the Shuanggou Ophiolite, Southwest China, J. Geophys. Res.-Solid, 125, 1–21, https://doi.org/10.1029/2019JB017552, 2020.

Ishimaru, S., Arai, S., Ishida, Y., Shirasaka, M., and Okrugin, V. M.: Melting and multi-stage metasomatism in the mantle wedge beneath a frontal arc inferred from highly depleted peridotite xenoliths from the avacha volcano, Southern Kamchatka, J. Petrol., 48, 395–433, https://doi.org/10.1093/petrology/egl065, 2007.

Johanesen, K., Platt, J. P., Kaplan, M. S., and Ianno, A. J.: A revised thermal history of the Ronda peridotite, S. Spain: New evidence for excision during exhumation, Earth Planet. Sc. Lett., 393, 187–199, https://doi.org/10.1016/j.epsl.2014.01.024 2014.

Johanesen, K. E. and Platt, J. P.: Rheology, microstructure, and fabric in a large scale mantle shear zone, Ronda Peridotite, southern Spain, J. Struct. Geol., 73, 1–17, https://doi.org/10.1016/j.jsg.2015.01.007, 2015.

Jung, H.: Crystal preferred orientations of olivine, orthopyroxene, serpentine, chlorite, and amphibole, and implications for seismic anisotropy in subduction zones: a review, Geosci. J., 21, 985–1011, https://doi.org/10.1007/s12303-017-0045-1, 2017.

Jung, H. and Karato, S. I.: Water-induced fabric transitions in olivine, Science, 293, 1460–1463, https://doi.org/10.1126/science.1062235, 2001.

Jung, H., Katayama, I., Jiang, Z., Hiraga, T., and Karato, S.: Effect of water and stress on the lattice-preferred orientation of olivine, Tectonophysics, 421, 1–22, https://doi.org/10.1016/j.tecto.2006.02.011, 2006.

Kaczmarek, M. A. and Müntener, O.: Juxtaposition of melt impregnation and high-temperature shear zones in the upper mantle; field and petrological constraints from the lanzo peridotite (Northern Italy), J. Petrol., 49, 2187–2220, https://doi.org/10.1093/petrology/egn065, 2008.

Karato, S., Jung, H., Katayama, I., and Skemer, P.: Geodynamic Significance of Seismic Anisotropy of the Upper Mantle: New Insights from Laboratory Studies, Annu. Rev. Earth Planet. Sci., 36, 59–95, https://doi.org/10.1146/annurev.earth.36.031207.124120, 2008.

Kelemen, P. B. and Hirth, G.: A periodic shear-heating mechanism for intermediate-depth earthquakes in the mantle, Nature, 446, 787–790, https://doi.org/10.1038/nature05717, 2007.

Kilian, R., Bestmann, M., and Heilbronner, R.: Absolute orientations from EBSD measurements – as easy as it seems?, Geophys. Res. Abstr., 18, 8221, https://meetingorganizer.copernicus.org/EGU2016/EGU2016-8221.pdf (last access: 18 October 2023), 2016.

Kohli, A. H. and Warren, J. M.: Evidence for a Deep Hydrologic Cycle on Oceanic Transform Faults, J. Geophys. Res.-Solid, 125, 1–23, https://doi.org/10.1029/2019JB017751, 2020.

Lenoir, X., Garrido, C. J., Bodinier, J. L., Dautria, J. M., and Gervilla, F.: The recrystallization front of the Ronda periodite: Evidence for melting and thermal erosion of subcontinental lithospheric mantle beneath the Alboran basin, J. Petrol., 42, 141–158, https://doi.org/10.1093/petrology/42.1.141, 2001.

Le Roux, V., Bodinier, J. L., Tommasi, A., Alard, O., Dautria, J. M., Vauchez, A., and Riches, A. J. V.: The Lherz spinel lherzolite: Refertilized rather than pristine mantle, Earth Planet. Sc. Lett., 259, 599–612, https://doi.org/10.1016/j.epsl.2007.05.026, 2007.

Linckens, J. and Tholen, S.: Formation of ultramylonites in an upper mantle shear zone, Erro-Tobbio Italy, Minerals, 11, 1036, https://doi.org/10.3390/min11101036, 2021.

Linckens, J., Herwegh, M., Mntener, O., and Mercolli, I.: Evolution of a polymineralic mantle shear zone and the role of second phases in the localization of deformation, J. Geophys. Res.-Solid, 116, 1–21, https://doi.org/10.1029/2010JB008119, 2011.

Linckens, J., Herwegh, M., and Müntener, O.: Small quantity but large effect - How minor phases control strain localization in upper mantle shear zones, Tectonophysics, 643, 26–43, https://doi.org/10.1016/j.tecto.2014.12.008, 2015.

Lonergan, L.: Timing and kinematics of deformation in the Malaguide Complex, internal zone of the Betic Cordillera, southeast Spain, Tectonics, 12, 460–476, https://doi.org/10.1029/92TC02507, 1993.

Mameri, L., Tommasi, A., Signorelli, J., and Hansen, L. N.: Predicting viscoplastic anisotropy in the upper mantle: a comparison between experiments and polycrystal plasticity models, Phys. Earth Planet. Inter., 286, 69–80, https://doi.org/10.1016/j.pepi.2018.11.002, 2019.

Mandler, B. E. and Grove, T. L.: Controls on the stability and composition of amphibole in the Earth's mantle, Contrib. Mineral.

S. Tholen et al.: Melt-enhanced strain localization and phase mixing in a large-scale mantle shear zone   **1153**

Petrol., 171, 1–20, https://doi.org/10.1007/s00410-016-1281-5, 2016.

Mizukami, T., Wallis, S. R., and Yamamoto, J.: Natural examples of olivine lattice preferred orientation patterns with a flow-normal a-axis maximum, Nature, 427, 432–436, https://doi.org/10.1038/nature02179, 2004.

Müntener, O. and Piccardo, G. B.: Melt migration in ophiolitic peridotites: The message from Alpine-Apennine peridotites and implications for embryonic ocean basins, Geol. Soc. Spec. Publ., 218, 69–89, https://doi.org/10.1144/GSL.SP.2003.218.01.05, 2003.

Newman, J., Lamb, W. M., Drury, M. R., and Vissers, R. L. M.: Deformation processes in a peridotite shear zone: Reaction-softening by an H_2O-deficient, continuous net transfer reaction, Tectonophysics, 303, 193–222, https://doi.org/10.1016/S0040-1951(98)00259-5, 1999.

Obata, M.: The ronda peridotite: Garnet-, spinel-, and plagioclase-lherzolite facies and the P-T trajectories of a high-temprature mantle intrusion, J. Petrol., 21, 533–572, https://doi.org/10.1093/petrology/21.3.533, 1980.

Ohuchi, T., Karato, S., and Fujino, K.: Strength of single-crystal orthopyroxene under lithospheric conditions, Contrib. Mineral. Petrol., 161, 961–975, https://doi.org/10.1007/s00410-010-0574-3, 2011.

Pantleon, W.: Resolving the geometrically necessary dislocation content by conventional electron backscattering diffraction, Scripta Materialia, 58, 994–997, https://doi.org/10.1016/j.scriptamat.2008.01.050, 2008.

Platt, J. P. and Behr, W. M.: Grainsize evolution in ductile shear zones: Implications for strain localization and the strength of the lithosphere, J. Struct. Geol., 33, 537–550, https://doi.org/10.1016/j.jsg.2011.01.018, 2011.

Platt, J. P., Argles, T. W., Carter, A., Kelley, S. P., Whitehouse, M. J., and Lonergan, L.: Exhumation of the Ronda peridotite and its crustal envelope: Constraints from thermal modelling of a P-T-time array, J. Geol. Soc., 160, 655–676, https://doi.org/10.1144/0016-764902-108, 2003.

Platt, J. P., Kelley, S. P., Carter, A., and Orozco, M.: Timing of tectonic events in the Alpujárride Complex, Betic Cordillera, southern Spain, J. Geol. Soc., 162, 451–462, https://doi.org/10.1144/0016-764903-039, 2005.

Platt, J. P., Anczkiewicz, R., Soto, J. I., Kelley, S. P., and Thirlwall, M.: Early Miocene continental subduction and rapid exhumation in the western Mediterranean, Geology, 34, 981–984, https://doi.org/10.1130/G22801A.1, 2006.

Précigout, J. and Hirth, G.: B-type olivine fabric induced by grain boundary sliding, Earth Planet. Sc. Lett., 395, 231–240, https://doi.org/10.1016/j.epsl.2014.03.052, 2014.

Précigout, J. and Stünitz, H.: Evidence of phase nucleation during olivine diffusion creep: A new perspective for mantle strain localisation, Earth Planet. Sc. Lett., 455, 94–105, https://doi.org/10.1016/j.epsl.2016.09.029, 2016.

Précigout, J., Gueydan, F., Gapais, D., Garrido, C. J., and Essaifi, A.: Strain localisation in the subcontinental mantle – a ductile alternative to the brittle mantle, Tectonophysics, 445, 318–336, https://doi.org/10.1016/j.tecto.2007.09.002, 2007.

Précigout, J., Gueydan, F., Garrido, C. J., Cogné, N., and Booth-Rea, G.: Deformation and exhumation of the

Ronda peridotite (Spain), Tectonics, 32, 1011–1025, https://doi.org/10.1002/tect.20062, 2013.

Prigent, C., Warren, J. M., Kohli, A. H., and Teyssier, C.: Fracture-mediated deep seawater flow and mantle hydration on oceanic transform faults, Earth Planet. Sc. Lett., 532, 115988, https://doi.org/10.1016/j.epsl.2019.115988, 2020.

Puga, E., Nieto, J. M., Díaz De Federico, A., Bodinier, J. L., and Morten, L.: Petrology and metamorphic evolution of ultramafic rocks and dolerite dykes of the Betic Ophiolitic Association (Mulhacen Complex, SE Spain): Evidence of eo-Alpine subduction following an ocean-floor metasomatic process, Lithos, 49, 23–56, https://doi.org/10.1016/S0024-4937(99)00035-3, 1999.

Putnis, A., Niedermeier, D. R. D., and Putnis, C. V.: From epitaxy to topotaxy: The migration of reaction interfaces through crystals, Geochim. Cosmochim. Ac., 70, A509, https://doi.org/10.1016/j.gca.2006.06.1479, 2006.

Rapp, R. P., Shimizu, N., Norman, M. D., and Applegate, G. S.: Reaction between slab-derived melts and peridotite in the mantle wedge: Experimental constraints at 3.8 GPa, Chem. Geol., 160, 335–356, https://doi.org/10.1016/S0009-2541(99)00106-0, 1999.

Ross, J. V. and Nielsen, K. C.: High-temperature flow of wet polycrystalline estatite, Tectonophysics, 44, 233–261, 1978.

Rossetti, F., Faccenna, C., and Crespo-Blanc, A.: Structural and kinematic constraints to the exhumation of the Alpujarride Complex (Central Betic Cordillera, Spain), J. Struct. Geol., 27, 199–216, https://doi.org/10.1016/j.jsg.2004.10.008, 2005.

Rutter, E. H. and Brodie, K. H.: The role of tectonic grain size reduction in the rheological stratification of the lithosphere, Geol. Rundschau, 77, 295–307, https://doi.org/10.1007/BF01848691, 1988.

Sen, C. and Dunn, T.: Experimental modal metasomatism of a spinel lherzolite and the production of amphibole-bearing peridotite, Contrib. Mineral. Petrol., 119, 422–432, https://doi.org/10.1007/BF00286939, 1995.

Skemer, P., Katayama, I., Jiang, Z., and Karato, S.: The misorientation index: Development of a new method for calculating the strength of lattice-preferred orientation, Tectonophysics, 411, 157–167, https://doi.org/10.1016/j.tecto.2005.08.023, 2005.

Soustelle, V., Tommasi, A., Bodinier, J. L., Garrido, C. J., and Vauchez, A.: Deformation and reactive melt transport in the mantle lithosphere above a large-scale partial melting domain: The Ronda peridotite Massif, Southern Spain, J. Petrol., 50, 1235–1266, https://doi.org/10.1093/petrology/egp032, 2009.

Stuart, C. A., Piazolo, S., and Daczko, N. R.: The recognition of former melt flux through high-strain zones, J. Metamorph. Geol., 36, 1049–1069, https://doi.org/10.1111/jmg.12427, 2018.

Suades, E., and Crespo-blanc, A.: Onshore study of syn-orogenic olistostromic deposits in the Gibraltar Arc: a tool to reveal mountain front uplift, Geophys. Res. Abstr., 13, EGU 2011-5928-1, https://presentations.copernicus.org/EGU2011/EGU2011-5928_presentation.pdf (last access: 18 October 2023), 2011.

Suhr, G.: Evaluation of upper mantle microstructures in the Table Mountain massif (Bay of Islands ophiolite), J. Struct. Geol., 15, 1273–1292, https://doi.org/10.1016/0191-8141(93)90102-G, 1993.

Tholen, S., Linckens, J., Heckel, C., and Kemperle, M.: Reaction-induced phase mixing and the formation of

ultramylonitic bands, Tectonophysics, 827, 229230, https://doi.org/10.1016/j.tecto.2022.229230, 2022.

Tommasi, A. and Vauchez, A.: Heterogeneity and anisotropy in the lithospheric mantle, Tectonophysics, 661, 11–37, https://doi.org/10.1016/j.tecto.2015.07.026, 2015.

Tommasi, A., Langone, A., Padrón-Navarta, J. A., Zanetti, A., and Vauchez, A.: Hydrous melts weaken the mantle, crystallization of pargasite and phlogopite does not: Insights from a petrostructural study of the Finero peridotites, southern Alps, Earth Planet. Sc. Lett., 477, 59–72, https://doi.org/10.1016/j.epsl.2017.08.015, 2017.

Van der Wal, D.: Deformation process in mantle peridotites with emphasis on the Ronda peridotite of SW Spain, in: Vol. 102, Dissertation, Geologica Ultraiectina, 1–180, https://dspace.library.uu.nl/handle/1874/314998 (last access: 10 October 2023), 1993.

Van Der Wal, D. and Bodinier, J.-L.: Origin of the recrystallisation front in the Ronda peridotite by km-scale pervasive porous melt flow, Contrib. Mineral. Petrol., 122, 387–405, https://doi.org/10.1007/s004100050135, 1996.

Van Der Wal, D. and Vissers, R. L. M.: Uplift and emplacement of upper mantle rocks in the western Mediterranean, Geology, 21, 1119–1122, https://doi.org/10.1130/0091-7613(1993)021<1119:UAEOUM>2.3.CO;2, 1993.

Van Der Wal, D. and Vissers, R. L. M.: Structural petrology of the Ronda peridotite, SW Spain: Deformation history, J. Petrol., 37, 23–43, https://doi.org/10.1093/petrology/37.1.23, 1996.

Vauchez, A. and Garrido, C. J.: Seismic properties of an asthenospherized lithospheric mantle: Constraints from lattice preferred orientations in peridotite from the Ronda massif, Earth Planet. Sc. Lett., 192, 235–249, https://doi.org/10.1016/S0012-821X(01)00448-4, 2001.

Vieira Duarte, J. F., Kaczmarek, M. A., Vonlanthen, P., Putlitz, B., and Müntener, O.: Hydration of a mantle shear zone beyond serpentine stability: a possible link to microseismicity along ultraslow spreading ridges?, J. Geophys. Res.-Sol. Ea., 125, 1–24, https://doi.org/10.1029/2020JB019509, 2020.

Wang, C., Liang, Y., and Xu, W.: Formation of Amphibole-Bearing Peridotite and Amphibole-Bearing Pyroxenite Through Hydrous Melt-Peridotite Reaction and In Situ Crystallization: An Experimental Study, J. Geophys. Res.-Solid, 126, e2020JB019382, https://doi.org/10.1029/2020JB019382, 2021.

White, S. H., Burrows, S. E., Carreras, J., Shaw, N. D., and Humphreys, F. J.: On mylonites in ductile shear zones, J. Struct. Geol., 2, 175–187, https://doi.org/10.1016/0191-8141(80)90048-6, 1980.

Eidesstattliche Versicherung

Hiermit erkläre ich, Sören Tholen, an Eides statt, dass ich die vorliegende Dissertation selbstständig verfasst und keine anderen als die angegebenen Quellen und Hilfsmittel benutzt habe. Weiterhin erkläre ich, die Grundsätze der guten Wissenschaft beachtet zu haben. Mein Beitrag als Koautor zur Studie der Erro-Tobbio Scherzone (Kapitel 3) setzt sich zusammen aus Feldarbeit, Probenbearbeitung, mikroskopischer und analytischer Bearbeitung (EPMA, EBSD), Datenbearbeitung sowie Bild- und Textbearbeitung (im Wesentlichen Korrektur). Ich habe keine Hilfe einer kommerziellen Promotionsvermittlung in Anspruch genommen.

Ort, Datum, Unterschrift